

Annual reports on
NMR Spectroscopy

Volume 57



ANNUAL REPORTS ON

NMR SPECTROSCOPY

This page intentionally left blank

ANNUAL REPORTS ON

NMR SPECTROSCOPY

Edited by

G. A. WEBB

Royal Society of Chemistry, Burlington House, London, England

VOLUME 57



ELSEVIER

Amsterdam • Boston • Heidelberg • London • New York
Oxford • Paris • San Diego • San Francisco • Singapore
Sydney • Tokyo

Academic Press is an Imprint of Elsevier



ELSEVIER B.V.
Radarweg 29
P.O. Box 211, 1000 AE Amsterdam
The Netherlands

ELSEVIER Inc.
525 B Street, Suite 1900
San Diego, CA 92101-4495
USA

ELSEVIER Ltd
The Boulevard, Langford Lane
Kidlington, Oxford OX5 1GB
UK

ELSEVIER Ltd
84 Theobalds Road
London WC1X 8RR
UK

© 2006 Elsevier Ltd. All rights reserved.

This work is protected under copyright by Elsevier Ltd, and the following terms and conditions apply to its use:

Photocopying

Single photocopies of single chapters may be made for personal use as allowed by national copyright laws. Permission of the Publisher and payment of a fee is required for all other photocopying, including multiple or systematic copying, copying for advertising or promotional purposes, resale, and all forms of document delivery. Special rates are available for educational institutions that wish to make photocopies for non-profit educational classroom use.

Permissions may be sought directly from Elsevier's Rights Department in Oxford, UK: phone (+44) 1865 843830, fax (+44) 1865 853333, e-mail: permissions@elsevier.com. Requests may also be completed on-line via the Elsevier homepage (<http://www.elsevier.com/locate/permissions>).

In the USA, users may clear permissions and make payments through the Copyright Clearance Center, Inc., 222 Rosewood Drive, Danvers, MA 01923, USA; phone: (+1) (978) 7508400, fax: (+1) (978) 7504744, and in the UK through the Copyright Licensing Agency Rapid Clearance Service (CLARCS), 90 Tottenham Court Road, London W1P 0LP, UK; phone: (+44) 20 7631 5555; fax: (+44) 20 7631 5500. Other countries may have a local reprographic rights agency for payments.

Derivative Works

Tables of contents may be reproduced for internal circulation, but permission of the Publisher is required for external resale or distribution of such material. Permission of the Publisher is required for all other derivative works, including compilations and translations.

Electronic Storage or Usage

Permission of the Publisher is required to store or use electronically any material contained in this work, including any chapter or part of a chapter.

Except as outlined above, no part of this work may be reproduced, stored in a retrieval system or transmitted in any form or by any means, electronic, mechanical, photocopying, recording or otherwise, without prior written permission of the Publisher.

Address permissions requests to: Elsevier's Rights Department, at the fax and e-mail addresses noted above.

Notice

No responsibility is assumed by the Publisher for any injury and/or damage to persons or property as a matter of products liability, negligence or otherwise, or from any use or operation of any methods, products, instructions or ideas contained in the material herein. Because of rapid advances in the medical sciences, in particular, independent verification of diagnoses and drug dosages should be made.

First edition 2006

ISBN-10: 0-12-505457-2
ISBN-13: 978-0-12-505457-7
ISSN: 0066-4103 (Series)

∞ The paper used in this publication meets the requirements of ANSI/NISO Z39.48-1992 (Permanence of Paper).
Printed in the United Kingdom.

Working together to grow
libraries in developing countries

www.elsevier.com | www.bookaid.org | www.sabre.org

ELSEVIER

BOOK AID
International

Sabre Foundation

List of Contributors

W. Kremer, *Institut für Biophysik und Physikalische Biochemie, Universität Regensburg, P.O. Box, D-93040 Regensburg, Germany*

D. Raftery, *Department of Chemistry, Purdue University, 560 Oval Drive, West Lafayette, IN 47907, USA*

H. Saitô, *Himeji Institute of Technology, Harima Science Garden City, Hyogo, Japan and Center for Quantum Life Sciences, Hiroshima University, Kagamiyama, Higashi-Hiroshima, Japan*

B. Wrackmeyer, *Anorganische Chemie II, Universität Bayreuth, D-95440 Bayreuth, Germany*

Y. Yamamoto, *Department of Chemistry, University of Tsukuba, Tsukuba 305-8571, Japan*

This page intentionally left blank

Preface

It is a pleasure for me to introduce Vol. 57 of Annual Reports on NMR Spectroscopy. As is usual in this series the present volume consists of reports covering exciting work in many disparate areas of NMR spectroscopy.

The volume begins with an account of Applications of ^{29}Si NMR Parameters by B. Wrackmeyer; Y. Yamamoto reports on NMR Studies of 6-Type Haemoproteins Reconstituted with a Ring-Fluorinated Haem; Site Directed Solid State NMR on Membrane Proteins is covered by H. Saitô; W. Kremer reports on High Pressure NMR Studies in Proteins; and the volume is completed with an account of Xenon NMR Spectroscopy by D. Raftery.

My thanks are due to all of the contributors for their interesting and timely contributions on their chosen areas of NMR expertise. Thanks also go to the production staff at Elsevier for their help in the realisation of this volume.

*Royal Society of Chemistry
Burlington House
Piccadilly
London, UK*

G. A. WEBB
July 2005

This page intentionally left blank

Contents

List of Contributors	v
Preface	vii

Applications of ^{29}Si NMR Parameters BERND WRACKMEYER

1. Introduction	1
2. Experimental	3
3. Nuclear Spin Relaxation	5
4. Chemical Shifts $\delta^{29}\text{Si}$	9
5. Indirect Nuclear Spin-Spin Coupling Constants $^nJ(^{29}\text{Si},\text{X})$	24
6. Conclusions	40
References	40

NMR Studies of *b*-Type Haemoproteins Reconstituted with a Ring-Fluorinated Haem YASUHIKO YAMAMOTO

1. Introduction	52
2. Haemoprotein	53
3. ^{19}F Labeling of <i>b</i> -Type Haemoprotein Using Reconstitution	53
4. Effect of ^{19}F Labeling on the Electronic Structure of Porphyrin	56
5. NMR Spectral Comparison of Haem <i>bis</i> -Cyano Complexes	58
6. Properties of Myoglobins Reconstituted with Fluorinated Haems	61
7. ^{19}F NMR Spectral Properties of Myoglobins Reconstituted with Fluorinated Haems	63
8. ^{19}F NMR Studies of Myoglobins Reconstituted with Fluorinated Haems	66
9. Concluding Remarks	92
References	93

Site-Directed Solid-State NMR on Membrane Proteins HAZIME SAITÔ

1. Introduction	100
2. Isotope Enrichment	103
3. Site-Directed Assignment of ^{13}C NMR Peaks of Membrane Proteins	108

4. Backbone Dynamics and Structures in the Interfacial Domains of Bacteriorhodopsin from Purple Membrane	125
5. Backbone Dynamics in the Transmembrane α -Helices	142
6. Backbone Structures and Dynamics in Monomers	153
7. Membrane Proteins Overexpressed in <i>E. coli</i>	157
8. Membrane-Binding Protein	167
9. Concluding Remarks	170
Acknowledgments	171
References	171

High-Pressure NMR Studies in Proteins WERNER KREMER

1. Introduction	177
2. High-Pressure NMR spectroscopy	180
3. Application of high-pressure NMR spectroscopy on proteins	182
4. Conclusions	200
Acknowledgments	200
References	200

Xenon NMR Spectroscopy DANIEL RAFTERY

1. Introduction	206
2. Conventional Xenon NMR Studies	207
3. Hyperpolarized Xenon	227
4. Conclusion	260
Acknowledgements	260
References	261
Index	271

Applications of ^{29}Si NMR Parameters

BERND WRACKMEYER

Anorganische Chemie II, Universität Bayreuth, D-95440 Bayreuth, Germany

1. Introduction	1
2. Experimental	3
2.1 Referencing	3
2.2 Techniques for observing ^{29}Si resonances	3
3. Nuclear Spin Relaxation	5
4. Chemical Shifts $\delta^{29}\text{Si}$	9
4.1 General	9
4.2 Patterns of ^{29}Si chemical shifts	10
4.3 Isotope-induced ^{29}Si chemical shifts	19
5. Indirect Nuclear Spin–Spin Coupling Constants $^nJ(^{29}\text{Si},\text{X})$	24
5.1 General	24
5.2 One-bond couplings, $^1J(^{29}\text{Si},\text{X})$	25
5.3 Two- (geminal) and three-bond (vicinal) coupling constants, $^2J(^{29}\text{Si},\text{X})$ and $^3J(^{29}\text{Si},\text{X})$	36
5.4 Long-range coupling constants $^nJ(^{29}\text{Si},\text{X})$ with $n > 3$	39
6. Conclusions	40
References	40

Experimental techniques for the measurement of ^{29}Si nmr spectra (mainly for solutions) are briefly discussed, followed from considerations of the nuclear-spin relaxation mechanisms with emphasis on the ^{29}Si nucleus. Chemical shifts $\delta^{29}\text{Si}$ and indirect nuclear spin–spin coupling constants $^nJ(^{29}\text{Si},\text{x})$, the most prominent nmr parameters, are discussed in more detail. The increasing reliability of quantum chemical methods for the calculation of these parameters is pointed out. The relationship between the electronic structure and the nmr parameters $\delta^{29}\text{Si}$ and $^nJ(^{29}\text{Si},\text{x})$ is indicated.

1. INTRODUCTION

In most fields of silicon chemistry, NMR spectroscopy has become increasingly important. In the last three decades, the development of modern NMR techniques for solutions and also for the solid state has included major efforts to observe ^{29}Si NMR signals. The only magnetically active isotope of silicon, ^{29}Si , is a spin-1/2 nucleus with appreciable NMR properties (Tables 1 and 2). The negative sign of $\gamma(^{29}\text{Si})$ may give rise to a negative NOE (upon ^1H decoupling), which could lead to

Table 1. NMR properties of some spin-1/2 nuclei^a

Nucleus	N A. (%)	R ^{C b}	γ (10 ⁷ rad s ⁻¹ T ⁻¹)	Ξ (MHz)	Reference standard
¹ H	99.985	5.67 10 ³	26.7522	100.000000	SiMe ₄ , 1% in CDCl ₃
¹³ C	1.108	1.00	6.7283	25.145020	SiMe ₄ 1% in CDCl ₃
¹⁵ N	0.37	2.19 10 ⁻²	-2.7126	10.136767	MeNO ₂ (neat)
¹⁹ F	100	4.73 10 ³	25.1815	94.094003	CFCl ₃ (neat)
²⁹ Si	4.70	2.10	5.3190	19.867187	SiMe ₄ 1% in CDCl ₃
³¹ P	100	3.77 10 ²	10.8394	40.480747	H ₃ PO ₄ , 85% aq
⁷⁷ Se	7.58	3.02	5.1214	19.071523	Me ₂ Se (neat)
¹⁰³ Rh	100	0.180	-0.8468	3.160000	No compound
¹¹⁷ Sn	7.61	19.9	-9.589	35.632295	SnMe ₄ (neat)
¹¹⁹ Sn	8.58	25.7	-10.0318	37.290665	SnMe ₄ (neat)
¹²⁵ Te	6.99	12.8	-8.5087	31.549802	Me ₂ Te (neat)
¹⁹⁵ Pt	33.8	19.9	5.8383	21.400000	No compound
					$\delta^{195}\text{Pt}([\text{PtCl}_6]^{2-}) = +4533$
¹⁹⁹ Hg	16.84	5.68	4.8458	17.910841	HgMe ₂ (neat) ^c
²⁰⁷ Pb	22.6	11.9	5.6264	20.920597	PbMe ₄ (neat)

^aMost data taken from ref. 9, and some data are own unpublished measurements.^bReceptivity relative to that of ¹³C in natural abundance.^cAn alternative reference is a aqueous solution of Hg(ClO₄)₂; however, the frequency is defined less accurately.**Table 2.** NMR properties of some quadrupole nuclei^a

Nucleus	N.A. (%)	Spin I	Q (10 ⁻²⁸ m ²)	γ (10 ⁷ rad s ⁻¹ T ⁻¹)	Ξ (MHz)	Reference standard
² H	0.015	1	2.87 10 ⁻³	4.1066	15.350609	Si(CD ₃) ₄ (D ₁₂ -TMS)
⁶ Li	7.42	1	-6.4 10 ⁻⁴	3.9371	14.716106	LiCl, D ₂ O \approx 9.7 M
⁷ Li	92.58	3/2	-3.7 10 ⁻³	10.3976	38.863790	LiCl, D ₂ O \approx 9.7 M
¹¹ B	80.42	3/2	4.1 10 ⁻²	8.5847	32.083971	F ₃ B-OEt ₂ (CDCl ₃)
¹⁴ N	99.63	1	1.67 10 ⁻²	1.9338	7.226324	MeNO ₂ (neat)
¹⁷ O	0.037	5/2	6.11 10 ⁻²	-3.6280	13.556430	D ₂ O (liquid)
²⁷ Al	100	5/2	0.14	6.9762	26.056890	Al(NO ₃) ₃ , D ₂ O, 1.0 M

^aMost data taken from ref. 9, and some are own unpublished measurements.

cancelling of ²⁹Si NMR signals. In addition to the NOE, a further disadvantage, when compared with ¹³C, is the fact that the relaxation times T₁(²⁹Si) can be rather long. Therefore, it is rarely advisable to apply the experimental set-up, which is used for routine ¹³C{¹H} NMR spectra. However, various methods are available to circumvent most of the problems, and there are hardly any examples of diamagnetic silicon compounds that cannot be studied by ²⁹Si NMR spectroscopy.

The progress in ²⁹Si NMR has been the subject of several reviews.¹⁻⁸ Considering the enormous amount of NMR data, produced in the last decade, including many ²⁹Si NMR data, this review cannot aim for a complete assessment. Representative examples, mainly from the last decade, have been selected in order to show

applications of ^{29}Si NMR parameters. Various potential industrial applications of ^{29}Si NMR spectroscopy (e.g. in the field of silicones, other polymers containing silicon and silicates) have been lined out in previous reviews and will not be included here. Paramagnetic compounds, alloys, and most inorganic solids will not be discussed, and the main body of the data will deal with liquids. Some data from previous reviews will be included if they help to understand and classify new data.

2. EXPERIMENTAL

2.1. Referencing

Using modern NMR spectrometers, a fixed frequency can be defined as the reference for chemical shifts δX of those nuclei where an internal reference is not convenient (X other than ^1H or ^{13}C). In [Tables 1 and 2](#) such frequencies $\Xi(X)$ (in MHz) are listed, referring to $\Xi(^1\text{H}) = 100.000000$ MHz for tetramethylsilane (SiMe_4 or TMS).⁹ Multiplying $\Xi(X)$ with the appropriate factor, depending on the $^1\text{H}(\text{SiMe}_4)$ frequency of the individual NMR spectrometer, provides the exact reference frequency, and the handling of sometimes unpleasant chemicals can be avoided. This method is also convenient for SiMe_4 , which usually serves as the reference for chemical shifts $\delta^{29}\text{Si}$. In this way, $\delta^{29}\text{Si}$ data can be accurately reproduced if other experimental conditions (solvent, temperature and concentration) are comparable. Other referencing techniques should be discouraged.

For solid-state ^{29}Si NMR spectra, other referencing techniques are required. Usually a crystalline organosilicon compound is used (e.g. “ Q_8M_8 ”, octakis(trimethylsiloxy)octasilsesquioxane), which gives sharp and intensive ^{29}Si NMR signals under MAS conditions and ^1H decoupling. Since the $\delta^{29}\text{Si}$ values of this material are known (-109.3 , $+11.7$) relative to SiMe_4 , it serves as a reliable secondary reference.

2.2. Techniques for observing ^{29}Si resonances

Although the sensitivity to the NMR experiment for ^{29}Si is reasonably high ([Table 1](#)), the direct observation of ^{29}Si resonance signals by single-pulse techniques can be difficult. This is due to the negative NOE, which is frequently observed for organosilicon compounds upon ^1H decoupling. The application of inverse gated ^1H decoupling in order to suppress the NOE (maximum NOE $\eta_{\text{max}} = -2.51$) is also not straightforward since the relaxation times $T_1(^{29}\text{Si})$ are unknown in most cases, and may be rather long. In any case, inverse gated ^1H decoupling requires delay times of several seconds for complete suppression of the NOE and small pulse angles ($\leq 30^\circ$) because of long $T_1(^{29}\text{Si})$ and therefore, the efficiency of the NMR experiment is seriously decreased.

A first major breakthrough in ^{29}Si NMR spectroscopy, at least for organosilicon chemistry, can be traced to the application of INEPT or DEPT pulse

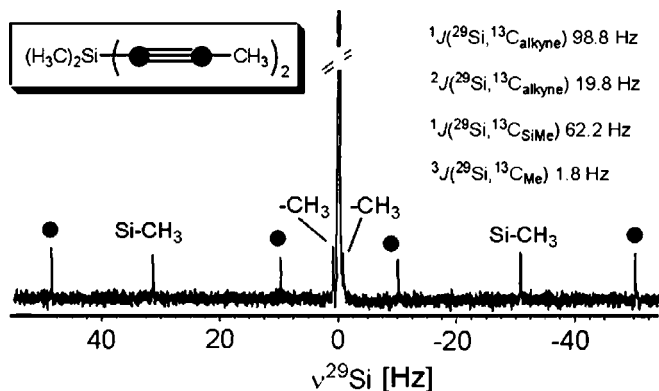


Fig. 1. 99.6 MHz $^{29}\text{Si}\{^1\text{H}\}$ NMR spectrum of $\text{Me}_3\text{Si}(\text{C}\equiv\text{C}-\text{Me})_2$ in CDCl_3 (1 transient, acquisition time 20 s; full-width in half-height of the central signal is 0.030 Hz). The ^{13}C satellites owing to ^{29}Si – ^{13}C spin–spin coupling are marked [see Scheme 15 for isotope-induced chemical shifts $^1\Delta^{12/13}\text{C}(^{29}\text{Si})$]. Adapted from ref. 105.

sequences,^{7a,8,10,11} based on scalar ^{29}Si – ^1H spin–spin coupling across one, two or three bonds to any number of protons (Fig. 1). This technique increases the ^{29}Si NMR sensitivity via $^1\text{H} \rightarrow ^{29}\text{Si}$ polarization transfer (PT) approximately by $|\gamma(^1\text{H})/\gamma(^{29}\text{Si})| = 5.02$, and the repetition time of the experiment depends no longer on $T_1(^{29}\text{Si})$ but on fairly short times $T_1(^1\text{H})$.

Four decades ago, heteronuclear $^1\text{H}\{\text{X}\}$ double-resonance CW experiments became possible, by which the NMR sensitivity of the ^1H nucleus was exploited in order to gain information on X nuclei. The prerequisite was scalar X– ^1H coupling. The development of two-dimensional (2D) NMR methods aimed for X/ ^1H correlations. In the beginning, for simplicity of the experiment, X resonances were observed and later on, in the so-called inverse experiments in $^1\text{H}/\text{X}$ correlations, ^1H resonances were observed with the encoded information on the ^{29}Si nuclei.^{8,12–14} The latter approach increased the sensitivity of the NMR experiment enormously, up to $[\gamma(^1\text{H})/\gamma(\text{X})]^{5/2} = 128$, and these experiments (e.g. HMQC, HSQC, HMBC) are now standard (Fig. 2) in all modern NMR spectrometers. A further gain in the performance could finally be achieved by the application of pulsed gradients^{15,16} for these methods (Fig. 3). Other methods of inverse detection or selective excitation can become important in the future.^[7b–e]

For liquids containing organosilicon compounds, in which any ^{29}Si – ^1H scalar coupling is present, ^{29}Si NMR spectra can be measured within reasonable time. In the absence of ^{29}Si – ^1H scalar coupling, the long relaxation times $T_1(^{29}\text{Si})$ can be a problem. For moderately concentrated solutions, single-pulse methods with small pulse angles will be sufficient for most purposes. For diluted solutions and exceedingly long times $T_1(^{29}\text{Si})$, the addition of paramagnetic relaxing agents should be considered.

Solid-state ^{29}Si NMR spectra of materials containing protons is usually obtained under experimental conditions rather similar to those well known for ^{13}C .^{17–19} Since

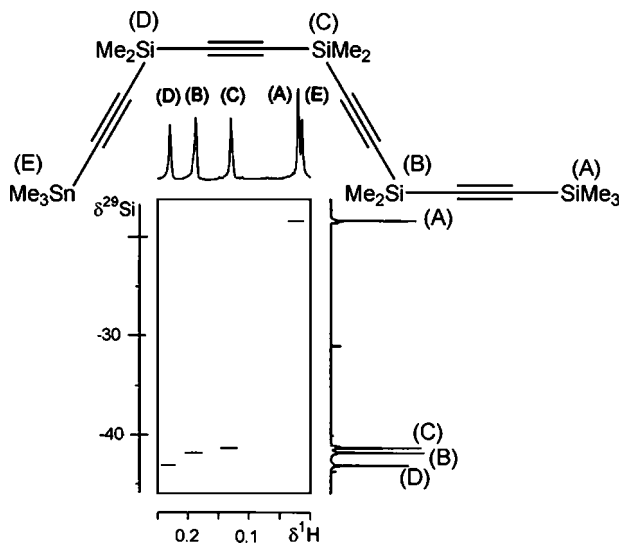


Fig. 2. Contour plot of the 500.1 MHz $^1\text{H}/^{29}\text{Si}$ HMQC NMR spectrum (with ^{29}Si decoupling in F_2) of the tetrayne $\text{Me}_3\text{Sn}-\text{C}\equiv\text{C}-\text{SiMe}_2-\text{C}\equiv\text{C}-\text{SiMe}_2-\text{C}\equiv\text{C}-\text{SiMe}_2-\text{C}\equiv\text{C}-\text{SiMe}_3$. The four different ^{29}Si sites are readily assigned to the ^1H resonances. These in turn can be used to assign the $^{13}\text{C}(\text{SiMe})$ and $^{13}\text{C}(\text{C}\equiv\text{C})$ signals in $^1\text{H}/^{13}\text{C}$ HMQC and HMBC experiments (not shown). Adapted from ref. 93d.

techniques related to cross polarization (CP) are usually applied together with MAS, the efficiency of the experiment depends on the magnetisation behaviour of both the protons and ^{29}Si nuclei. When the conditions for CP have been optimised, ^{29}Si NMR spectra can be obtained within rather short time (Fig. 4). Similar to liquid state, this situation becomes different in the absence of ^1H nuclei. Then, single-pulse techniques with long repetition times require a lot of spectrometer time (sometimes days) in order to get meaningful solid-state ^{29}Si NMR spectra²⁰ (e.g. in the case of silicon carbide²¹ or silicon nitride Si_3N_4 ²²).

3. NUCLEAR SPIN RELAXATION

Various relaxation mechanisms (DD, dipole–dipole; SC, scalar; SR, spin-rotation; CSA, chemical shift anisotropy) contribute to ^{29}Si nuclear spin relaxation, described by the time constants T_1 for spin-lattice (longitudinal) and T_2 for spin–spin (transversal) relaxation times (Eq. (1)).^{23,24} In the absence of scalar contributions it hold for liquids that $T_1 \approx T_2$.

$$(T_1)^{-1} = (T_1^{\text{DD}})^{-1} + (T_1^{\text{SR}})^{-1} + (T_1^{\text{SC}})^{-1} + (T_1^{\text{CSA}}) \quad (1)$$

In most organosilicon compounds, when studied at field strengths $B_B \leq 11.7\text{ T}$, DD and SR interactions dominate the relaxation (Fig. 5). The CSA mechanism is

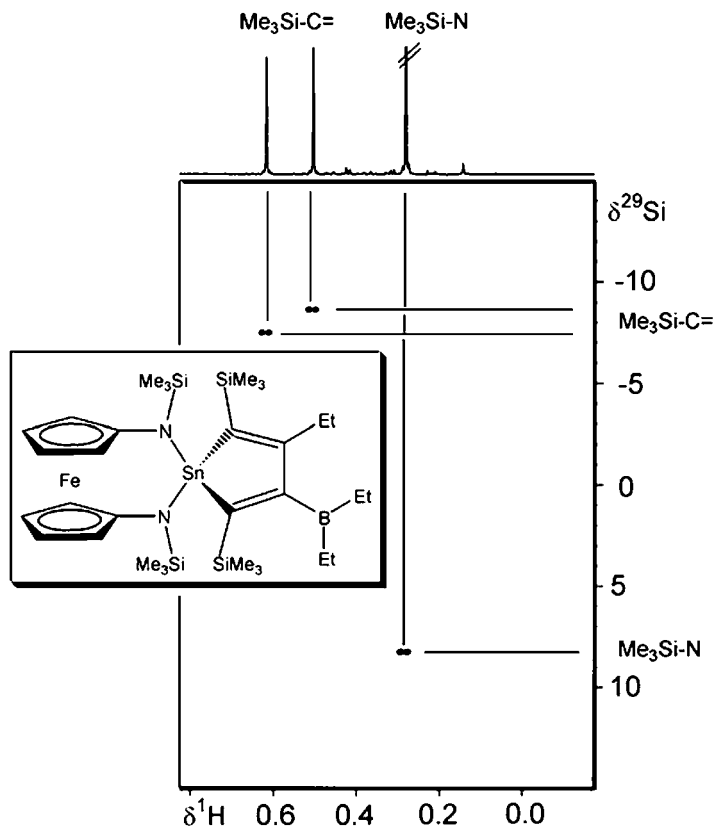


Fig. 3. Contour plot of the 500.1 MHz $^1\text{H}/^{29}\text{Si}$ gradient enhanced HSQC NMR spectrum (no ^{29}Si decoupling in F_2). For further NMR experiments see ref. 106.

expected to contribute for trigonal planar or linear surroundings of the silicon atom, geometries which are less common for silicon.

As already mentioned, DD interactions influence the appearance of $^{29}\text{Si}\{^1\text{H}\}$ NMR spectra because of the negative NOE (see also Fig. 5²⁵), and in some cases, this may cancel the ^{29}Si NMR signal (Eqs. (2) and (3)). Considering the opposite temperature dependence of DD and SR interactions, experimental conditions can be selected accordingly.

$$\text{NOE}_{\max} = 0.5[\gamma(^1\text{H})/\gamma(^{29}\text{Si})] = -2.51 \quad (2)$$

$$\text{Intensity}_{\text{signal}} = 1 + \text{NOE} \quad (3)$$

Scalar relaxation due to chemical exchange has the usual influence (broadening) on the appearance of ^{29}Si NMR spectra. A consequence of such exchange processes, depending on the rate of exchange, is that PT techniques may not work very well or sometimes not at all. Scalar relaxation of the second kind affects the line widths by $T_2^{\text{SC}}(^{29}\text{Si})$ if the silicon atom is bonded to one or more quadrupolar nuclei as in

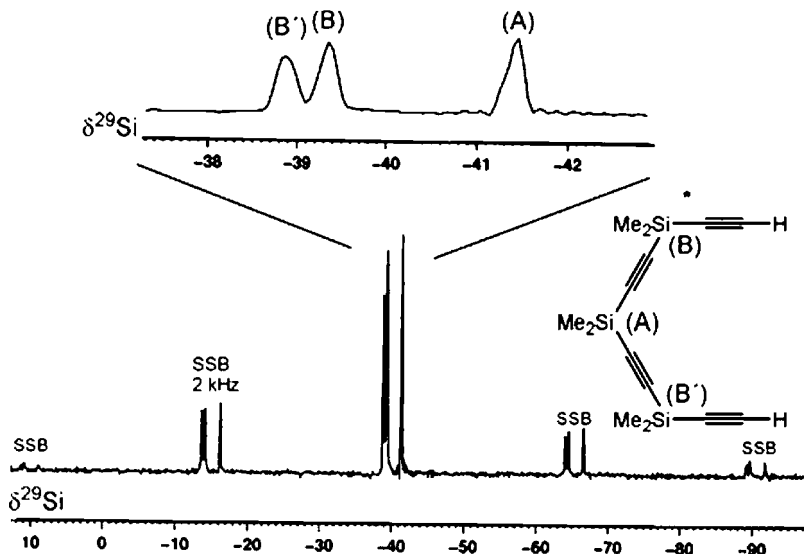


Fig. 4. Solid-state MAS $^{29}\text{Si}\{^1\text{H}\}$ NMR spectrum (79.7 MHz) of the tetrayne $\text{H}-\text{C}\equiv\text{C}-\text{SiMe}_2-\text{C}\equiv\text{C}-\text{SiMe}_2-\text{C}\equiv\text{C}-\text{SiMe}_2-\text{C}\equiv\text{C}-\text{H}$. The number of ^{29}Si NMR signals is in agreement with the results from X-ray crystallography, since the silicon atoms in the positions (B) are crystallographically non-equivalent.^{95a}

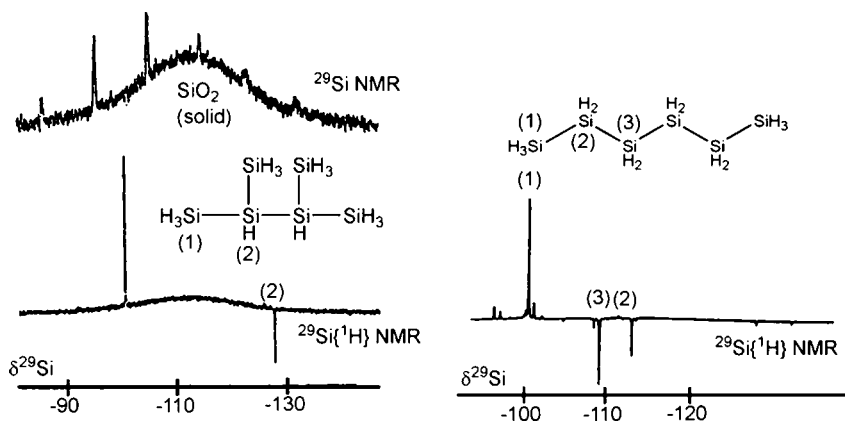


Fig. 5. 59.8 MHz ^{29}Si NMR spectra of two hexasilane isomers. The broad hump is the signal for silicate in the glass and serves for correct phasing of the signals. There is competition between dipole-dipole and spin-rotation interactions as dominant nuclear spin relaxation mechanisms for ^{29}Si nuclei. ^{29}Si nuclei in SiH_3 groups at a more peripheric position of the molecule relax predominantly by spin-rotation interactions as a result of the high mobility of these groups. The SiH_2 or SiH groups in the chains are less mobile and therefore, dipole-dipole interactions become competitive. Adapted from ref. 25.

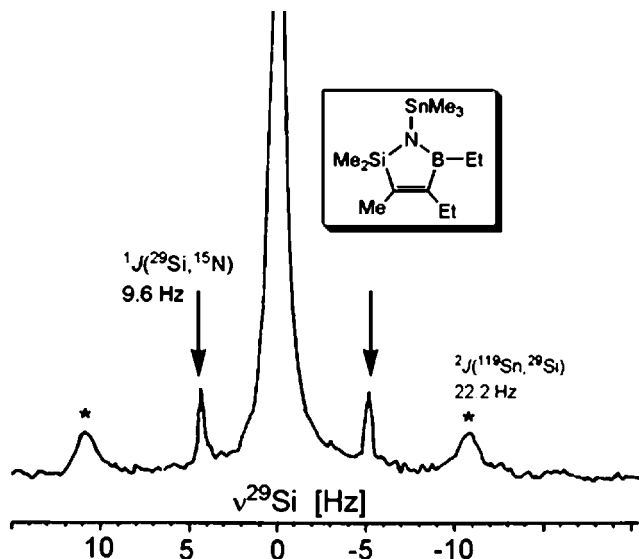


Fig. 6. 59.8 MHz $^{29}\text{Si}\{^1\text{H}\}$ NMR spectrum (HEED-INEPT (acquisition time 3 s, repetition delay 6 s and Hahn echo delay 0.6 s)). As a result of efficient transverse relaxation of the second kind, most of the induced magnetisation for the ^{14}N - ^{29}Si isotopomer decays in the course of the pulse sequence whereas that for the ^{15}N - ^{29}Si isotopomer is hardly affected. Adapted from ref. 29.

silicon halides²⁶ ($^{35/37}\text{Cl}$, $^{79/81}\text{Br}$, ^{127}I), in silicon nitrogen compounds^{27–29} (^{14}N) or in silylboranes (^1B , ^{11}B),³⁰ to name just three important classes of silicon compounds. Although quadrupole-induced nuclear spin relaxation of the quadrupolar nuclei is very efficient, scalar coupling to the ^{29}Si nucleus is not completely averaged, and the residual broadening of the ^{29}Si NMR signal (Fig. 6) indicates the spin dynamics of the respective quadrupolar nucleus.

If the relaxation time of the quadrupolar nucleus $T^Q(\text{X})$ is relatively long, the ^{29}Si NMR signal may exhibit the expected splitting pattern. This is known for ($\eta^5\text{-C}_5\text{H}_5$)Be-SiMe₃^{72a} ($^1J(^{29}\text{Si}-^9\text{Be}) = 51$ Hz) or trimethylsilyl borates (e.g. $^1J(^{29}\text{Si}, ^{11}\text{B}) = 74$ Hz for [Me₃Si-BH₃]^{72b}). Rather surprising examples, considering the low local symmetry around the nitrogen atoms, have been reported for ^{29}Si NMR signals resolved as triplets ($^1J(^{29}\text{Si}, ^{14}\text{N})$) for some *N*-silyl-aminoboranes,^{28,73} in which the nitrogen atoms bear the silyl and two boryl groups. In the case of the borazine (HBNSiMe₃)₃, calculations of the electric field gradient at the nitrogen atoms confirm the experimental findings.^{73a}

There are also examples of spin-1/2 nuclei with short-lived spin states, in particular in the cases of heavy nuclei such as ^{195}Pt ³¹ or ^{199}Hg ,³² for which chemical-shift-anisotropy relaxation can become efficient at high field strengths B_0 (Fig. 7).

In the solid state, ^{29}Si nuclear spin relaxation mechanisms are much less efficient when compared with solutions. In inorganic solids, the presence of small amounts (traces) of paramagnetic impurities accelerates the relaxation rate, which otherwise

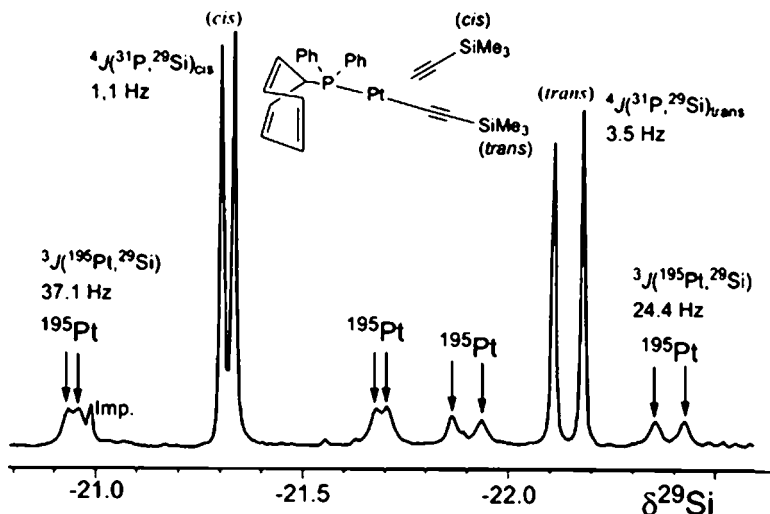


Fig. 7. 49.8 MHz $^{29}\text{Si}\{^1\text{H}\}$ NMR spectrum of the complex $[(\text{Ph}_2\text{PC}_7\text{H}_7)\text{Pt}(\text{C}\equiv\text{C}-\text{SiMe}_3)_2]$ dissolved in CD_2Cl_2 . The ^{29}Si NMR signals are split due to ^{31}P – ^{29}Si spin–spin coupling and accompanied by the ^{195}Pt satellites. These ^{195}Pt satellite signals are significantly broader than the respective central signals owing to efficient nuclear spin relaxation via the chemical-shift-anisotropy mechanism (short T_2^{CSA} (^{195}Pt)). Adapted from ref. 31b.

is extremely slow.^{21,22} Since nuclear spin relaxation of quadrupolar nuclei X can also be rather long in the solid state, it is frequently possible to observe the splitting of ^{29}Si NMR signals due to $J(^{29}\text{Si}, \text{X})$ in MAS ^{29}Si NMR spectra as shown for $^1J(^{29}\text{Si}, ^{14}\text{N})$ ^{64b} or $^1J(^{55}\text{Mn}, ^{29}\text{Si})$,^{75a} and even for $^2J(^{93}\text{Nb}, ^{29}\text{Si})$.^{75b} The patterns may be complicated by non-averaged quadrupolar interactions.⁷⁹

4. CHEMICAL SHIFTS $\delta^{29}\text{Si}$

4.1. General

Chemical shifts $\delta^{29}\text{Si}$ cover a range of approximately 1000 ppm, from ca. +600 to –400 with $\delta^{29}\text{Si}$ for SiMe_4 (TMS) at zero. Trends in the changes in $\delta^{29}\text{Si}$ values are similar to those found for $\delta^{73}\text{Ge}$,^{1,2,76} $\delta^{119}\text{Sn}$ ^{1,2,77} and $\delta^{207}\text{Pb}$.^{1,2,78} In principle, a comparison of $\delta^{29}\text{Si}$ and $\delta^{13}\text{C}$ values of structurally related compounds is also of interest. However, many silicon analogues of carbon compounds are not accessible by NMR measurements, and if they can be prepared, they usually differ greatly in the nature of stabilising substituents. There are also numerous silicon compounds of which the carbon analogues do not exist. However, it can be stated that the influence of multiple bonding and coordination number is similar for both $\delta^{29}\text{Si}$ and $\delta^{13}\text{C}$, at least as far as a general trend is concerned.

Calculations of ^{29}Si nuclear magnetic shielding is becoming increasingly reliable if electron correlation effects are included (e.g. MP2, MP4 or DFT methods) at the 6-311 + g(d,p) or a comparable level of theory^{33–37} (see Table 3 for some examples).

The extreme values found so far for $\delta^{29}\text{Si}$ are for divalent silicon (Scheme 1), with extreme deshielding for the cyclic silylene **1**³⁸ and extreme shielding for the silicocene **2**.³⁹ In the solid state of **2**, two different isomers are evident from the X-ray analysis³⁹ and also from the solid-state ^{29}Si NMR spectrum.⁴⁰ The cation **3**, $[\eta^5\text{-C}_5\text{Me}_5\text{Si}]^+$,⁴¹ has almost the same chemical shift $\delta^{29}\text{Si}$ as the neutral species **2**.

Expectedly, the $\delta^{29}\text{Si}$ data for most tetra-coordinate silicon atoms, including those for the pyramidal silyl anions, are relatively close to $\delta^{29}\text{Si} = 0$ (SiMe_4) within a range of about 200 ppm. However, these data possess a marked diagnostic value, since each class of compounds is characterised by typical $\delta^{29}\text{Si}$ data, which change in a systematic way due to substituent effects. Many of these trends have already been outlined in previous reviews,^{1–6} and an extensive data set has been collected. Therefore, this topic will not be treated here in detail.

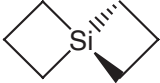
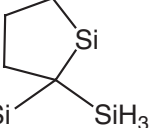
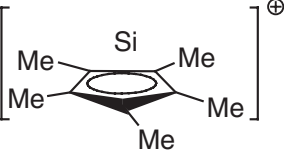
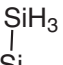
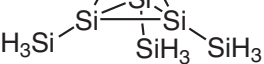
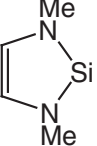
4.2. Patterns of ^{29}Si chemical shifts

4.2.1. Coordination number of silicon and electronic structure

In general, low magnetic shielding of ^{29}Si is typical for low-coordinated silicon atoms, as in silylenes^{42–44} (e.g. **1**³⁸ and **4–7** in Scheme 2), “free”⁴⁵ (e.g. **8–10**⁴⁵ in Scheme 3) or almost “free”⁴⁶ silyl cations, in contrast with silylene adducts⁴⁷ (Scheme 4). Low ^{29}Si nuclear magnetic shielding is typical for base-free silylene transition metal complexes^{48–51} (Scheme 5), and also for numerous compounds, where silicon is involved in multiple bonding with other elements^{38,52–58} (Scheme 6).


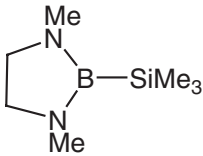
Major changes in ^{29}Si nuclear magnetic shielding, as it holds in general for nuclei other than ^1H , can be traced to the paramagnetic term σ^p (^{29}Si) of the shielding constant $\sigma(^{29}\text{Si})$. Any significant decrease in nuclear shielding is related to paramagnetic currents owing to rotation of electronic charge induced by the external magnetic field B_0 , mixing ground and excited states. These transitions must be magnetic-dipole-allowed (this excludes for example the electron-dipole allowed $\pi \rightarrow \pi^*$ transitions!), which means that certain $\sigma \rightarrow \sigma^*$, $\sigma \rightarrow \pi^*$ or $\pi \rightarrow \sigma^*$ transitions are relevant in this respect. This is shown in Fig. 8 in a simplified orbital scheme for a trigonal planar silyl cation (e.g. **8** or **9** in Scheme 3). The B_0 -induced rotation of electronic charge mixes the occupied σ orbitals (e.g. of Si–C bonds) with the virtual unoccupied orbital on the central silicon atom. If the energy difference between these orbitals is small, a large deshielding effect will be the result. This picture applies in a slightly modified way also to silylenes, where the Si–C or Si–N σ orbitals and the lone pair of electrons at the silicon have to be considered. The extreme ^{29}Si deshielding in **1** (Scheme 2) is the result of a fairly small HOMO-LUMO energy gap. In the bis(amino)silylenes **4–7**, this gap is much larger because of the electronegative nitrogen atoms, and also because of potential $\text{SiN}(\text{pp})\pi$ interactions. This model is supported by the calculation of the tensor components of $\sigma(^{29}\text{Si})$ for silylenes.⁵⁵

Table 3. Some calculated^a and experimental ^{29}Si chemical shifts

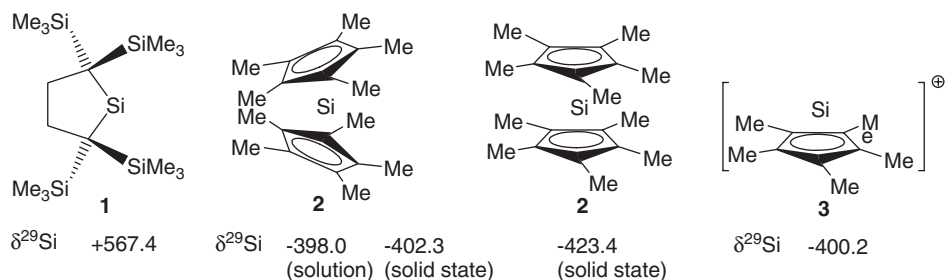
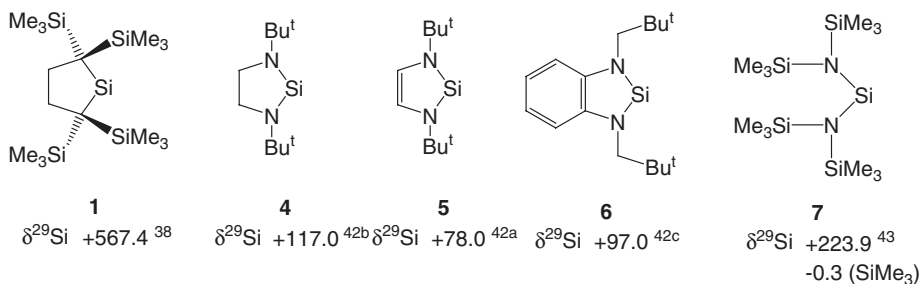
Compound	$\delta^{29}\text{Si}$ (calculated)	$\delta^{29}\text{Si}$ (experimental)
SiMe_4	0	0
$\text{Me}_2\text{Si}(\text{CH}_2)_5$	-3.7	
$\text{Me}_2\text{Si}(\text{CH}_2)_4$	+20.9	+16.8 ⁴
$\text{Me}_2\text{Si}(\text{CH}_2)_3$	+23.1	+18.4 ⁴
$\text{Me}_2\text{Si}(\text{CH}_2)_2$	-80.5	
	+47.1	+37.2 ¹⁰¹
$\text{Me}_2\text{Si}=\text{CMe}_2$		+50.3 (16) ^{53a}
$\text{H}_3\text{Si}-\text{Si}(\text{H})_2-\text{Si}(\text{H})_2-\text{Si}(\text{H})_2-\text{SiH}_3$	+626.5 (Si) -70.0 (SiH ₃)	+567.4 (1) ³⁸
		
$[(\text{H}_3\text{Si})_2\text{CH}]_2\text{Si}$	+628.4 (Si), -92.8 (SiH ₃)	
$[\text{Me}_3\text{Si}]^+$	+416.3	
	-468.3	-400.2 (4) ⁴¹
$\text{Me}_3\text{Si}-\text{SiH}_3$	-18.0, -102.0	
$\text{Me}_3\text{Si}-\text{Si}(\text{H})\text{Me}_2$	-13.9, -36.0	-18.9, -39.1 ^{115b}
	-205.5 (Si) -84.5 (SiH ₃)	Not observed (see ¹⁷⁷)
		
$\text{Me}_2\text{Si}=\text{SiMe}_2$	+109.3	90.4 (20) ^{55d}
$\text{Me}_3\text{Si}-\text{Si}\equiv\text{Si}-\text{SiMe}_3$	+134.4 (Si), +13.3 (SiMe ₃)	+91.5 (Si) (23) ^{54b}
$\text{Me}_2\text{Si}=\text{NMe}$	+77.7	+60.3 (19) ^{56c}
	+115.0	+78 ^{42a}

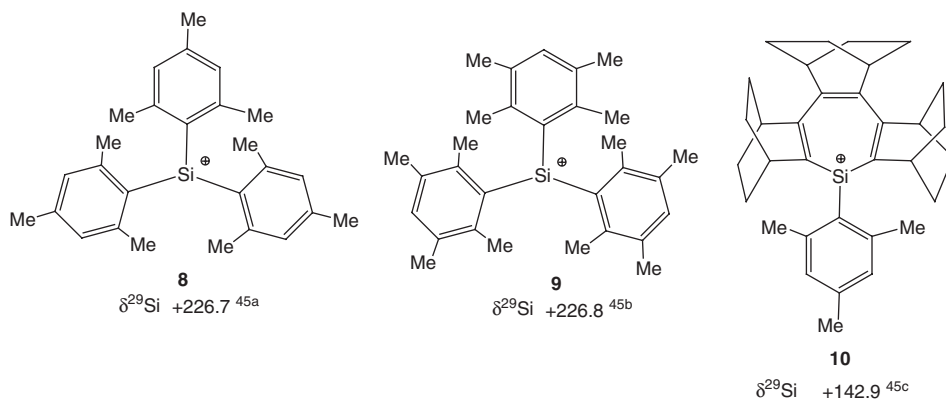
(continued)

Table 3. Continued

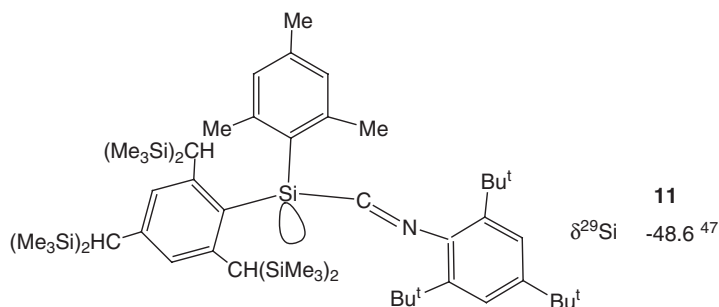
Compound	$\delta^{29}\text{Si}$ (calculated)	$\delta^{29}\text{Si}$ (experimental)
$\text{Me}_2\text{Si}=\text{P}-\text{SiMe}_3$	+257.0 (SiMe ₂), +9.2 (SiMe ₃)	+172 (Si = P) (22 ^o) ^{57a}
 Be—SiMe ₃	−26.1	−27.3 ^{72a}
 B—SiMe ₃	−24.5	−31.0 ¹³¹

^aGeometries were optimised for this review by B3LYP/6-311+G(d,p) calculations and the magnetic shielding constants $\sigma(^{29}\text{Si})$ were calculated (GIAO) at the same level of theory (Gaussian 98 or Gaussian 03 program packages¹⁷⁹). Calculated $\sigma(^{29}\text{Si})$ data are converted into $\delta^{29}\text{Si}$ by $\delta^{29}\text{Si} = \sigma(^{29}\text{Si}) [\text{SiMe}_4] - \sigma(^{29}\text{Si})$ with $\sigma(^{29}\text{Si}) [\text{SiMe}_4] = +340.1$ and $\delta^{29}\text{Si} (\text{SiMe}_4) = 0$. Experimental data are taken from previous reviews^{1–5} if not indicated otherwise.

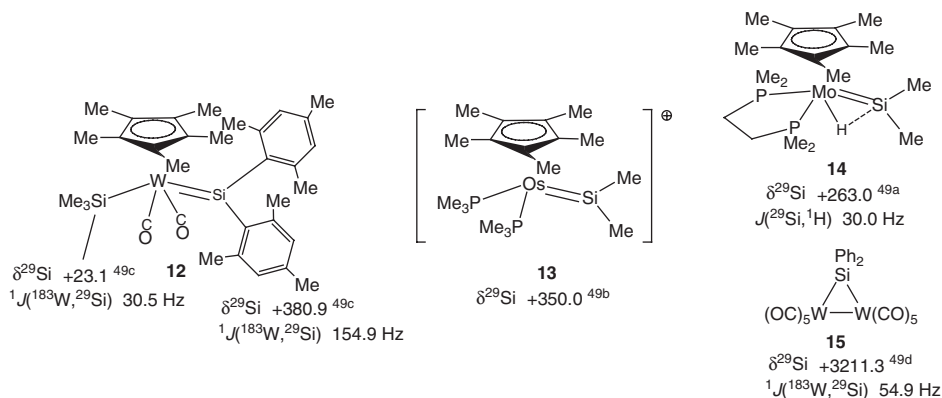
**Scheme 1.** Some extreme ^{29}Si chemical shifts ($\delta^{29}\text{Si}$) relative to $\delta^{29}\text{Si} (\text{SiMe}_4) = 0$.**Scheme 2.** Some ^{29}Si chemical shifts ($\delta^{29}\text{Si}$) of monomeric silylenes. Note the large difference between **1** and the bis(amino)silylenes **4–7**.



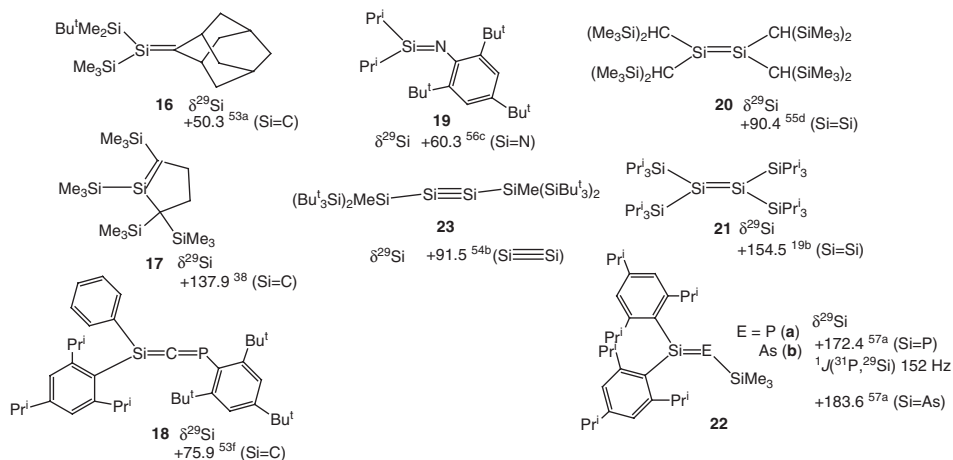
Scheme 3. Some ^{29}Si chemical shifts ($\delta^{29}\text{Si}$) of silyl cations, for which the presence of truly three-coordinate silicon atoms can be assumed. The increase in the ^{29}Si nuclear magnetic shielding in the case of the silatropylium derivative **10** can be ascribed to an increase in π electron density at the silicon atom.



Scheme 4. The ^{29}Si chemical shift ($\delta^{29}\text{Si}$) of the adduct of a diarylsilylene with an isonitrile (**11**) is observed in a range more typical of tetra-coordinate silicon, similar to silyl anions.



Scheme 5. Some ^{29}Si chemical shifts ($\delta^{29}\text{Si}$) of “base-free” silylene-metal complexes.



Scheme 6. Some ^{29}Si chemical shifts ($\delta^{29}\text{Si}$) of compounds containing silicon-element double and triple bonds.

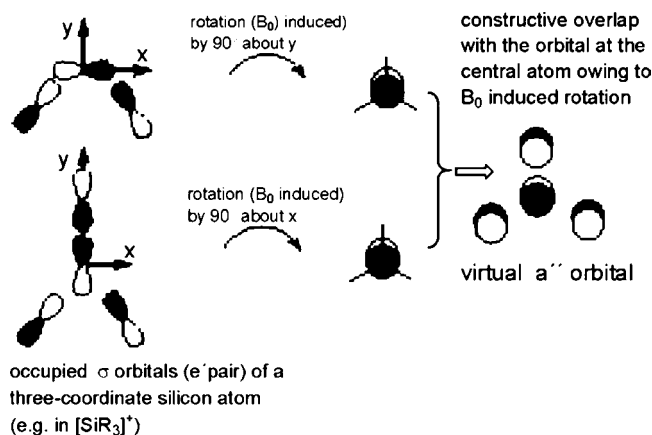


Fig. 8. Model for B_0 -induced rotation of charge involving ground and excited states, shown for a trigonal planar triorganosilyl cation. Both of the shown Si–C σ bonds overlap in a constructive way with the virtual π orbital centred at the silicon atom. See ref. 107 for the analogous view at comparable carbocations and trigonal boranes.

In the adduct **11**, the $\delta^{29}\text{Si}$ value is in the range of tetra-coordinate silicon compounds, similar to silyl anions, since the “vacant” orbital of low energy is no longer available for B_0 -induced charge rotation. In silylene transition metal complexes (Scheme 5), B_0 -induced charge rotation will also involve appropriate orbitals centred at the transition metal atom and, therefore, the ^{29}Si nuclear magnetic shielding becomes dependent on even more influences. In the complexes **12** and **13** (Scheme 5), there is a pronounced M–Si double bond character. In **14**, the hydride has to be considered as a bridge between Mo and Si, by which the Mo–Si bond order is

reduced. Nevertheless, the ^{29}Si nucleus is significantly deshielded (typical of many silyl transition metal complexes with activated Si–H bonds; *vide infra*). In the complex **15**, the Ph_2Si unit bridges the W–W bond. The ^{29}Si nuclear magnetic deshielding, in contrast to other three-member rings (*vide infra*), indicates that the W–Si bonds and metal-centred energetically low lying orbitals are involved.

In the cases of silicon-element multiple bonds (Scheme 6), it is again mainly the question for the relative energies of $\sigma \rightarrow \pi^*$ or $\pi \rightarrow \sigma^*$ transitions with major contributions from the silicon atom. However, the presence of a lone pair of electrons at an adjacent atom (e.g. in **22** at P or As) may also have some significant influence on ^{29}Si shielding. In the cases of disilenes and silaethenes, calculations and experimental determinations of the tensor components of $\sigma(^{29}\text{Si})$.^{18b,34,53a} confirm the major contributions to ^{29}Si nuclear magnetic shielding.

The data discussed so far show that there is some overlap with the range of $\delta^{29}\text{Si}$ for tetra-coordinated silicon. Selected $\delta^{29}\text{Si}$ data of tetra-coordinated silicon compounds are given in Tables 4 and 5. In the last decade, numerous $\delta^{29}\text{Si}$ data have been reported for compounds containing four-coordinate silicon with Si–chalcogen bonds, in particular Si–S and Si–Se bonds,^{59,60} and some examples with Si–Te bonds.⁶¹

A further increase in the coordination number of silicon from 4 to 5 (e.g. in silatranes) or 6 causes a significant increase in ^{29}Si nuclear shielding. This is shown in Scheme 7 by the change of about 100 ppm in the $\delta^{29}\text{Si}$ values of silicates bearing five⁶² or four organyl groups.⁶³

Table 4. $\delta^{29}\text{Si}$ data^a for some trimethylsilyl, dimethylsilyl and methylsilyl derivatives and for SiX_4 compounds

	$\delta^{29}\text{Si}$		$\delta^{29}\text{Si}$		$\delta^{29}\text{Si}$		$\delta^{29}\text{Si}$
$\text{Me}_3\text{Si-H}$	–15.5	Me_2SiH_2	–37.3	MeSiH_3	–65.2	SiH_4	–93.1
$\text{Me}_3\text{Si-F}$	35.4	Me_2SiF_2	8.8	MeSiF_3	–51.8	SiF_4	–113.6
$\text{Me}_3\text{Si-Cl}$	30.2	Me_2SiCl_2	32.2	MeSiCl_3	12.4	SiCl_4	–18.5
$\text{Me}_3\text{Si-Br}$	26.4	Me_2SiBr_2	19.9	MeSiBr_3	–18.2	SiBr_4	–93.6
$\text{Me}_3\text{Si-I}$	8.7	Me_2SiI_2	–33.7	MeSiI_3	–144.0	SiI_4	–346.2
$\text{Me}_3\text{Si-Ome}$	17.2	$\text{Me}_2\text{Si(Ome)}_2$	–2.5	MeSi(Ome)_3	–41.4	Si(Ome)_4	–79.2
$\text{Me}_3\text{Si-Sme}$	16.5	$\text{Me}_2\text{Si(Sme)}_2$	28.1	Me(Sme)_3	34.0	Si(Sme)_4	38.6
$\text{Me}_3\text{Si-SeBu}^b$	11.3	$\text{Me}_2\text{Si(SeBu)}_2^b$	18.1	Me(SeBu)_3^b	13.5	Si(SeBu)_4^b	1.9
$\text{Me}_3\text{Si-TeBu}^c$	–4.3	$\text{Me}_2\text{Si(TeBu)}_2^c$	–24.6	MeSi(TeBu)_3^c	–70.0	Si(TeBu)_4^c	–139.6
$\text{Me}_3\text{Si-NMe}_2$	5.9	$\text{Me}_2\text{Si(NMe}_2)_2$	–1.7	$\text{MeSi(NMe}_2)_3$	–17.5	$\text{Si(NMe}_2)_4$	–28.1
$\text{Me}_3\text{Si-Et}$	1.6	Me_2SiEt_2	4.6	MeSiEt_3	6.5	SiEt_4	8.4
$\text{Me}_3\text{Si-Vi}$	–6.8	Me_2SiVi_2	–13.7	MeSiVi_3	–20.6	SiVi_4	–22.5
$\text{Me}_3\text{Si-Ph}$	–5.1	Me_2SiPh_2	–9.4	MeSiPh_3	–11.9	SiPh_4	–14.0
$\text{Me}_3\text{Si-C}\equiv\text{CMe}^d$	–18.5	$\text{Me}_2\text{Si(C}\equiv\text{CMe)}_2^d$	–42.0	$\text{MeSi(C}\equiv\text{CMe)}_3^d$	–79.0	$\text{Si(C}\equiv\text{Cme)}_4^d$	–96.5
$\text{Me}_3\text{Si-SiMe}_3$	–19.8	$\text{Me}_2\text{Si(SiMe}_3)_2$	–48.7	—	—	$\text{Si(SiMe}_3)_4$	–135.5
$\text{Me}_3\text{Si-SnMe}_3$	–11.0	$\text{Me}_2\text{Si(SnMe}_2)_2^e$	–38.2	—	—	$\text{Si(SnMe}_3)_4^e$	–172.0

^aData taken from refs. 1–5 if not stated otherwise; for most compounds, several slightly different $\delta^{29}\text{Si}$ values have been reported owing to different experimental conditions (referencing, temperature, solvent and concentration).

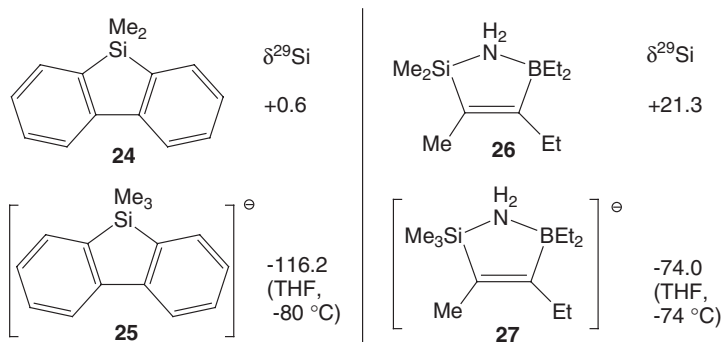
^bRef. 59b.

^cRef. 61a.

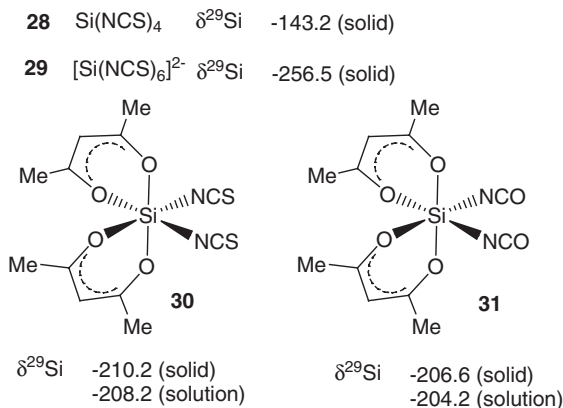
^dRef. 105.

Table 5. $\delta^{29}\text{Si}$ data for miscellaneous organosilicon compounds

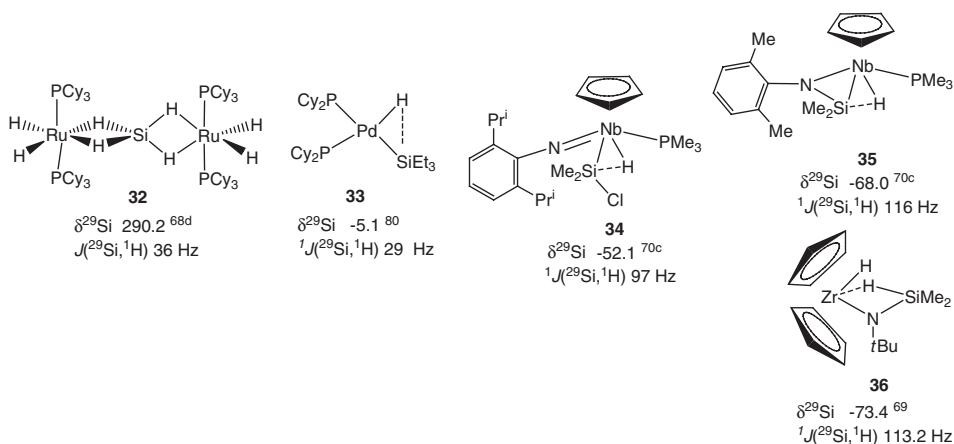
Class of compound	NMR parameters measured	Reference
β -Silyl carbocations	^{29}Si , ^{13}C NMR	184,185
C- and N-trimethylsilylazoles	^{29}Si , ^{13}C NMR	138
N-silylguanidinium and silylnitrilium ions	^{29}Si , ^{13}C NMR	174,194
Silylated cyclopentadiene derivatives and <i>ansa</i> -lanthanidocene complexes	^{29}Si , ^{13}C and ^{89}Y NMR	180
Silylated N,O-diacylhydroxylamines	^{29}Si , ^{13}C , ^{15}N NMR	190
Silylated benzhydroxamic acid derivatives	^{29}Si , ^{13}C , ^{15}N NMR	182
O-Silylated hydroxylamines	^{29}Si , ^{13}C , ^{15}N , ^{17}O NMR	186
Trimethylsilyloxonium ions	^{29}Si NMR	197
N-Silylated aluminum amides	^{29}Si NMR	193
Silylamid anions	^{29}Si , ^{15}N NMR	183,199
1,3-Disila-2-gallata and-indallenic anions	^{29}Si NMR	181
Tetrasilanes	^{29}Si NMR	187
Silyl group 14-element anions	^{29}Si NMR	191,198
Alkyn-1-ylsilanes η^2 -coordinated to Al or transition metals	^{29}Si , ^{13}C , ^{27}Al NMR	189, 200
η^2 alkenylsilane complexes	^{29}Si NMR	192
Silabenzene complexes (Ru)	^{29}Si NMR	195
Silylene iron complexes (dimers)	^{29}Si NMR	188
Silylene lanthanide complexes	^{29}Si NMR	196

**Scheme 7.** Examples for ^{29}Si chemical shifts ($\delta^{29}\text{Si}$) as a result of the change in the coordination number from 4 to 5.

The same trend is evident for the more Lewis-acidic silicon halides or pseudohalides,⁶⁴ when the coordination number is increased from 4 to 6 (Scheme 8). Variable temperature ^{20}Si NMR studies show the equilibrium between four-, five- and six-coordinate silicon atoms in imine and enaminechelate complexes.⁶⁵ There are numerous ^{29}Si NMR spectroscopic studies of hypervalent silicon



Scheme 8. Examples for ^{29}Si chemical shifts ($\delta^{29}\text{Si}$) as a result of the change in the coordination number from 4 to 6.

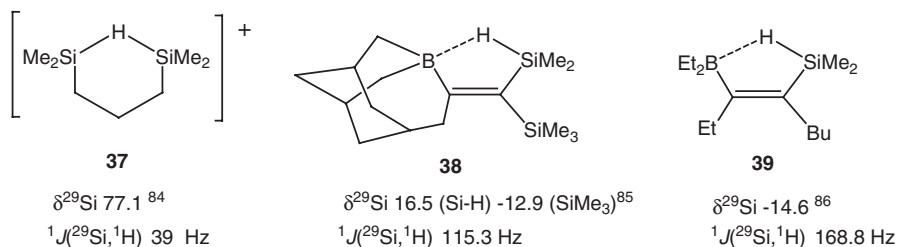


Scheme 9. Examples for ^{29}Si chemical shifts ($\delta^{29}\text{Si}$) of silane metal complexes, in which metal-H and Si-H bonding is present (agostic Si-M-H bonding; activation of Si-H bonds).

compounds,^{64–66} including, e.g. the determination of the ^{229}Si chemical shift tensor in fluorosilatrane.^{66c}

4.2.2. Activation of Si-H bonds

The activation of Si-H bonds by adjacent transition metals,^{67–71} or main group elements^{84–86} is important for the transformation of silanes. In many cases, the ^{29}Si nuclear shielding is markedly reduced (extremely so in the fluxional complex **32**, Scheme 9), accompanied by smaller values of coupling constants $J(^{29}\text{Si}, ^1\text{H})$ (see also the silylene complex **14**^{48a}). However, the $\delta^{29}\text{Si}$ values are not really a criterion for M-H-Si bridging, as can be seen from the data for **35** and **36** (Scheme 9).



Scheme 10. Examples of ^{29}Si NMR data for electron-deficient Si–H–Si and Si–H–B bridges. Note that the data indicate a much weaker Si–H–B bridge in **39** when compared with **38**.

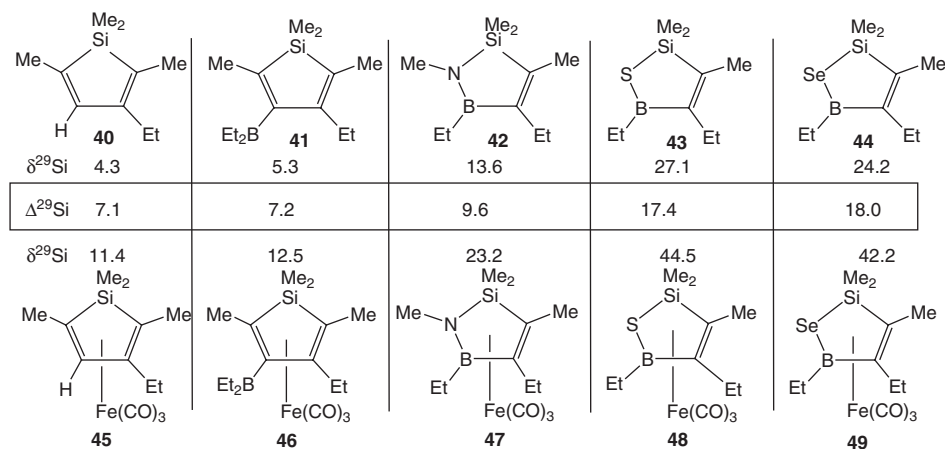
Electron-deficient hydrogen bridges between two silicon atoms (**37**) or between a silicon and a boron atom in **38** or **39** (Scheme 10) are characterised by more or less marked ^{29}Si deshielding. In the case of the Si–H–B bridge, the increase in the strength of the bridge goes together with ^{29}Si nuclear deshielding, increase in ^{11}B nuclear shielding, and significant changes in the magnitude of $^1J(^{29}\text{Si}, ^1\text{H})$. Interestingly, such Si–H–B bridges can be identified by unprecedented isotope-induced chemical shifts $^2\Delta^{10/11}\text{B}(^{29}\text{Si})$ (*vide infra*).

4.2.3. Effects of cyclic structures

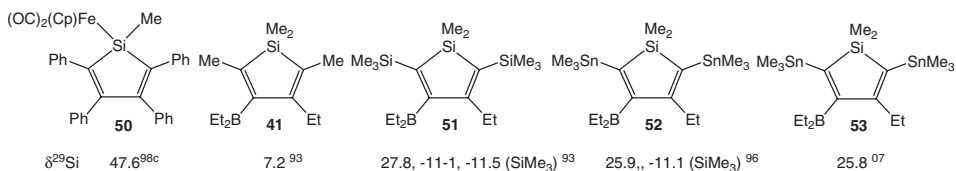
Cyclic structures are fairly common in silicon chemistry.^{1–6,92} Most frequently one finds four-,⁸⁷ five-⁸⁸ and six-member rings,⁸⁹ but there also examples for three-member rings,⁹⁰ and seven member or larger rings are also known.⁹¹ Usually, the ^{29}Si nuclear shielding in cyclic systems differs from non-cyclic analogues.¹³⁰ In cyclic hydrocarbons containing one or more silicon atom, ^{29}Si nuclei are well shielded in three-member rings, much less shielded in four- and five-member rings, and in six member or larger rings the ^{29}Si nuclear shielding is comparable with that for non-cyclic analogues. Silacyclopentadiene derivatives,^{88c,93} their dianions^{88a,b,d}, heterosiloles⁹⁴ and their transition metal complexes⁹⁵ (Scheme 11) are attractive compounds for ^{29}Si NMR studies. The $\delta^{29}\text{Si}$ values are markedly affected by heteroatoms in the ring, in particular by adjacent heteroatoms,⁹⁷ the effects being similar to those in comparable non-cyclic derivatives (see Table 4). Complexation of cyclic π systems also causes significant changes in the $\delta^{29}\text{Si}$ values, although the silicon atom is not directly involved in the bonding with the transition metal fragment.

The ^{29}Si shielding in siloles changes substantially with substituents at silicon, and there is also a large influence exerted by some substituents in 2,5-positions (Scheme 12). The silacyclopentadiene **52** is also an instructive example for the use of ^{29}Si NMR spectra in order to obtain information on various coupling constants (Fig. 9).

7-Silanorbornadienes (Fig. 10) appear to play a special role in the field of carbocyclic silanes, since they are characterised by significantly deshielded ^{29}Si nuclei^{98–100} (Scheme 13). This can be interpreted as the result of B_0 -induced paramagnetic currents involving $\sigma \rightarrow \pi^*$ and $\pi \rightarrow \sigma^*$ transitions. So far, derivatives bearing electronegative functional groups at the silicon atom in 7-position have not been studied as yet.



Scheme 11. Comparison of ^{29}Si chemical shifts ($\delta^{29}\text{Si}$) for silacyclopentadiene and heterosilacyclopentadiene derivatives and their $\text{Fe}(\text{CO})_3$ complexes. The shift difference $\Delta^{29}\text{Si}$ increases when the heteroatom is less integrated into the π system.



Scheme 12. The rather strong influence of substituents in 1- or in 2,5-positions on ^{29}Si chemical shifts ($\delta^{29}\text{Si}$) of silacyclopentadiene derivatives.

The presence of early transition metals in opposite position to the silicon atom in four-member rings causes significant ^{29}Si magnetic shielding when compared with analogous rings containing a main group element instead (Scheme 14).

4.3. Isotope-induced ^{29}Si chemical shifts

The advent of NMR spectrometers with external fields $B_0 \geq 4.6$ T has encouraged to measure isotope-induced chemical shifts $^n\Delta^{z/y}\text{X}(^{29}\text{Si})$ for pairs of isotopes $^z/y\text{X}$ (e.g. $^{10/11}\text{B}$, $^{12/13}\text{C}$, $^{14/15}\text{N}$) other than $^{1/2}\text{H}$ ¹⁰² with reasonable accuracy. Since the relative change in the masses of ^zX and ^yX are small except of $^{1/2}\text{H}$, the magnitude of $^n\Delta^{z/y}\text{X}(^{29}\text{Si})$ is also small (data given in ppb), and both high digital resolution and sharp ^{29}Si NMR signals are required in order to observe these effects. The theoretical basis for isotope-induced chemical shifts applies to $^n\Delta^{z/y}\text{X}(^{29}\text{Si})$ in the same way as for other nuclei.¹⁰³ In addition to vibrational effects as the result of different masses, electronic effects have to be taken into account. The latter become particularly important for the more heavy nuclei. In principle, the electronic effects should also be reflected by spin-spin coupling constants.

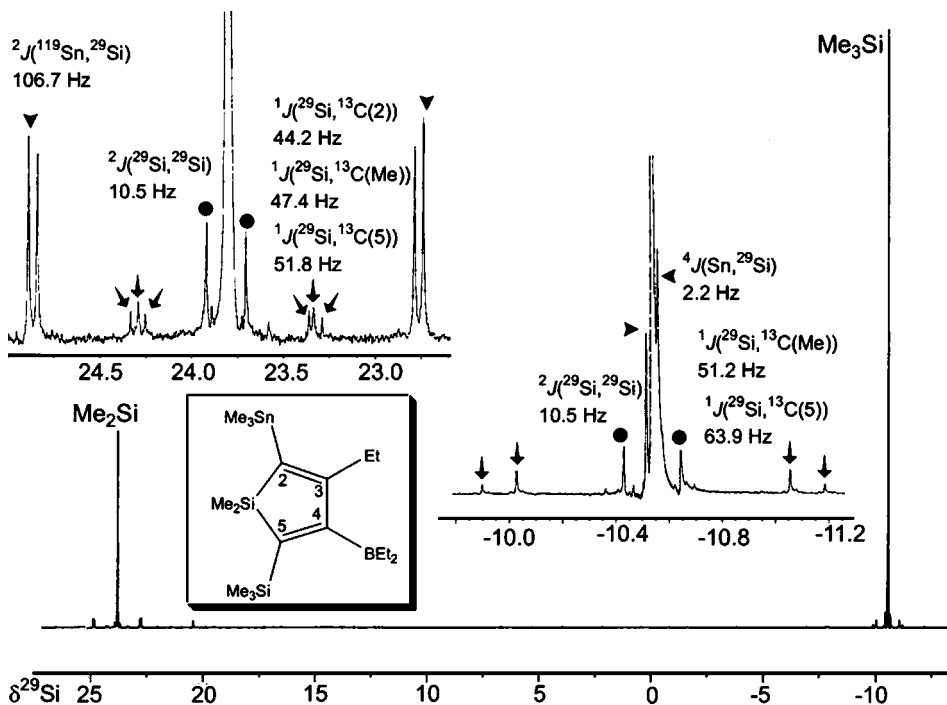


Fig. 9. 49.8 MHz $^{29}\text{Si}\{^1\text{H}\}$ NMR spectrum (INEPT) of an organometallic-substituted silacyclopentadiene derivative, showing various types of satellite signals owing to the presence of isotopomers containing two ^{29}Si , ^{29}S and ^{13}C or ^{117}Sn or ^{119}Sn , as indicated.^{95a} Note the large difference in ^{29}Si nuclear shielding for the SiMe_2 group in the ring and the SiMe_3 group in 5-position. See ref. 96 for further NMR data.

The first data for $^1\Delta^{12/13}\text{C}(^{29}\text{Si})$ and $^1\Delta^{14/15}\text{N}(^{29}\text{Si})$ have been reported in the 1980s,^{6,104} followed by more systematic studies^{6,105} (Scheme 15). Fig. 11 shows a ^{29}Si NMR spectrum with ^{13}C satellites for four different types of carbon atoms. The deviation from the mean positions of the ^{13}C satellites relative to the central ^{29}Si signal is given as $^1\Delta^{12/13}\text{C}(^{29}\text{Si})$ and $^2\Delta^{12/13}\text{C}(^{29}\text{Si})$. By using the HEED-INEPT or HEED-DEPT techniques, ^{15}N satellites can be readily assigned for many silicon–nitrogen compounds, and isotope-induced chemical shifts $^1\Delta^{14/15}\text{N}(^{29}\text{Si})$ can be determined (Fig. 12).

Usually the magnitude of isotope-induced chemical shifts for isotopes other than $^1/2\text{H}$ becomes very small with an increasing number of bonds separating the nuclei concerned. However, there are notable exceptions. Thus, isotope-induced chemical shifts across two bonds $^2\Delta^{10/11}\text{B}(^{29}\text{Si})$ have been measured in various boron compounds containing bridging hydrogen, oxygen and other heteroatoms between boron and silicon. The electron-deficient Si-H-B bridge is particularly intriguing. Although these bridges are rather weak, the observation of fairly large values $^2\Delta^{10/11}\text{B}(^{29}\text{Si})$ is straightforward, indicating unambiguously the presence of the Si-H-B bridge (Fig. 13).

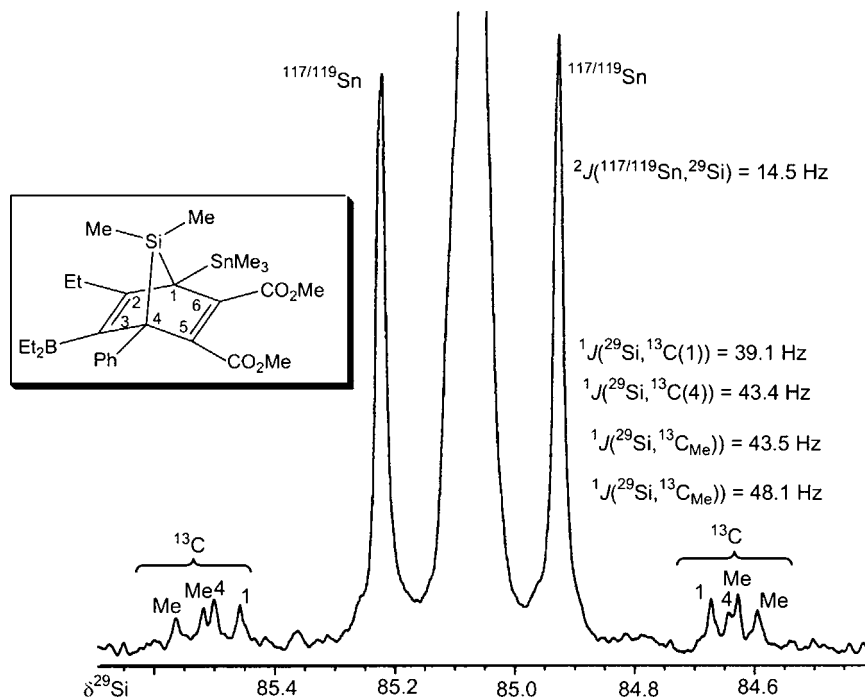
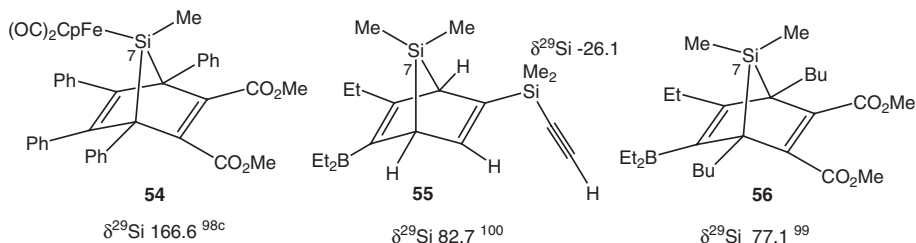
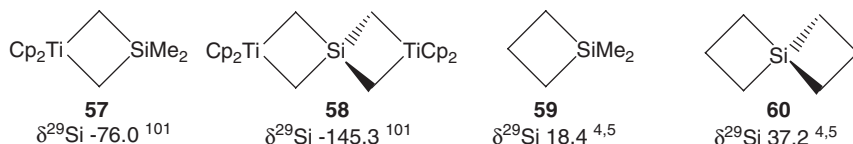


Fig. 10. 49.8 MHz $^{29}\text{Si}\{^1\text{H}\}$ NMR spectrum (INEPT) of a 7-silanorbornadiene derivative showing $^{117/119}\text{Sn}$ and ^{13}C satellites. The assignment of the latter is based on the ^{29}Si satellites observed in the ^{13}C NMR spectrum (not shown). Note the large deshielding of the ^{29}Si nucleus. Adapted from ref. 99.



Scheme 13. Rather extreme (for organosilanes) ^{29}Si chemical shifts ($\delta^{29}\text{Si}$) are typical of 7-silanorbornadiene derivatives.



Scheme 14. The surprisingly shielding influence for ^{29}Si nuclei induced by the presence of titanium complex fragments opposite to silicon in four-membered rings.

	$^1\Delta^{12/13}\text{C}(^{29}\text{Si})$ [ppb]		$^1\Delta^{14/15}\text{N}(^{29}\text{Si})$ [ppb]
SiMe_4	-6.0	$\text{Me}_3\text{Si-NEt}_2$	-11.0
$\text{Me}_3\text{Si-CH=CH}_2$	-4.5 (Me) -7.5 (C=)	$\text{Me}_3\text{Si-N(H)Bu}^t$	-14.0
$\text{Me}_3\text{Si-Ph}$	-4.4 (Me) -3.8 (Ph)	$\text{Me}_3\text{Si-N(H)Ph}$	-16.0
$\text{Me}_3\text{Si}-\text{C}\equiv\text{H}$	0 (Me) -15.0 (C \equiv)	$\text{Me}_3\text{Si(NH)}$	-10.7
$\text{Me}_3\text{Si}-\text{C}\equiv\text{Me}$	-0.1 (Me) -14.8 (C \equiv)	$\text{Me}_3\text{Si-NCO}$	-16.5
$\text{Me}_3\text{Si}-\text{C}\equiv\text{SiMe}_3$	0 (Me) -16.0 (C \equiv)	$\text{Me}_3\text{Si-NCS}$	-16.0
$\text{Me}_2\text{Si}-\text{C}\equiv\text{SiMe}_2$	-4.0 (Me) -8.0 (CH $_2$)	$\text{Me}_3\text{Si-NCN-SiMe}_3$	-16.0
$\text{Me}_2\text{Si}-\text{C}\equiv\text{C(H)}_2$	-1.0 (Me) -11.0 (C \equiv)	$\text{Me}_3\text{Si-N=C=C(SiMe}_3)_2$	-17.0
$\text{Me}_2\text{Si}-\text{C}\equiv\text{C(Me)}_2$	2.3 (Me) -9.2 (C \equiv)		
$\text{MeSi}-\text{C}\equiv\text{C(Me)}_3$	4.9 (Me) -5.2 (C \equiv)		
$\text{Si}-\text{C}\equiv\text{C(Me)}_4$	-1.9 (C \equiv)		
$\text{Me}_3\text{Si-NEt}_2$	-4.1		
$\text{Me}_3\text{Si-OMe}$	-0.8		
$\text{Me}_3\text{Si-OPh}$	-0.1		
$(\text{Me}_3\text{Si})_2\text{O}$	0.2		
$[\text{Me}_2(\text{Cl})\text{Si}]_2\text{O}$	5.8		
$\text{Me}_2\text{Si}[\text{OSiMe}_3]_2$	0.3 (SiMe $_3$) 4.9 (SiMe $_2$)		

Scheme 15. Examples for isotope-induced chemical shifts $^1\Delta^{12/13}\text{C}(^{29}\text{Si})$ and $^1\Delta^{14/15}\text{N}(^{29}\text{Si})$. Negative values in ppb indicate a shift of the ^{29}Si NMR signal for the heavy isotopomer to lower frequencies. Data taken from refs. 5,28,104 and 105.

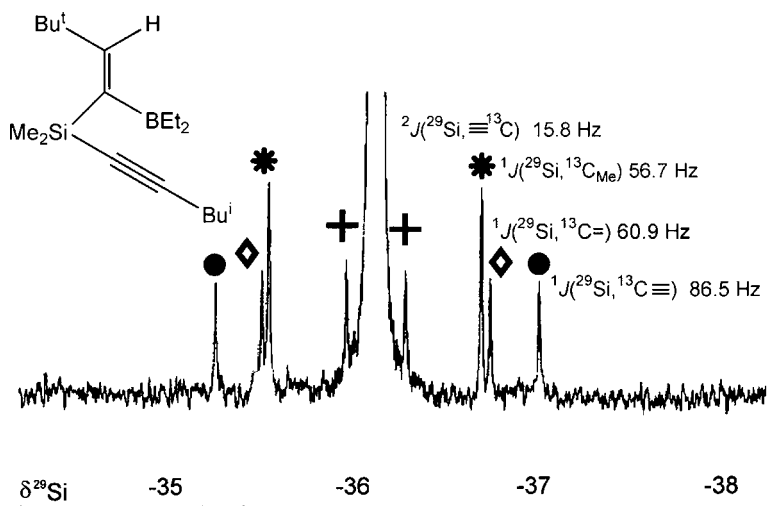


Fig. 11. 99.6 MHz $^{29}\text{Si}\{^1\text{H}\}$ NMR spectrum of the alkenyl(alkyn-1-yl)dimethylsilane in C_6D_6 showing ^{13}C satellites for different types of carbon atoms. The ^{13}C satellites are associated with isotope-induced chemical shifts $^n\Delta^{12/13}\text{C}(^{29}\text{Si})$ (+1.0 ppb for SiMe, -5.0 ppb for Si-C=, and -13.1 ppb for Si-C \equiv $^{12/13}\text{C}$ nuclei), which differ in a systematic way with n and the nature of the carbon atom (see also Scheme 15). Adapted from ref. 108.

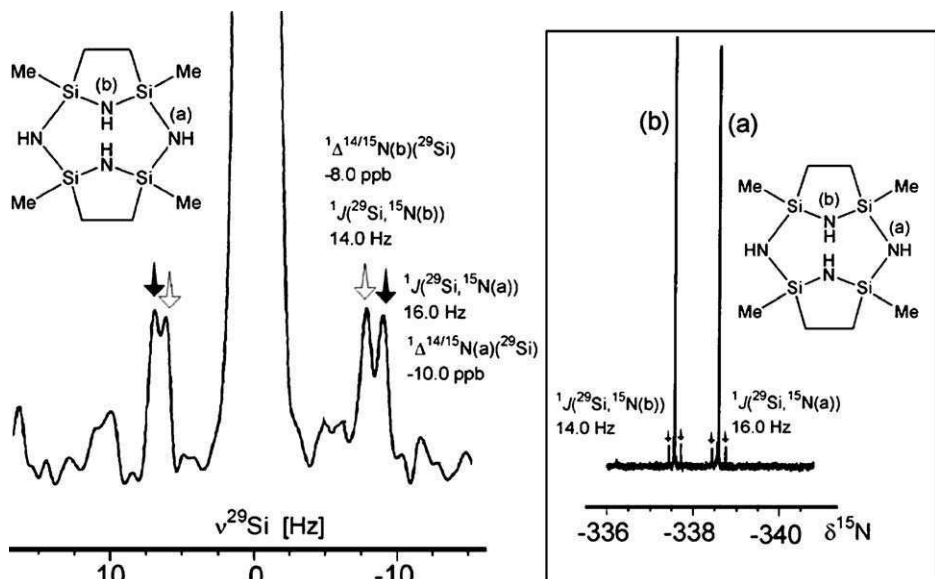


Fig. 12. 99.6 MHz $^{29}\text{Si}\{^1\text{H}\}$ and 50.4 MHz $^{15}\text{N}\{^1\text{H}\}$ NMR spectra (INEPT) of a tricyclic diaminomethylsilane (courtesy of G. Becker and R. Motz) dissolved in C_6D_6 . The ^{15}N satellites in the ^{29}Si NMR spectrum (the parent signal is partially suppressed by using the HEED-INEPT pulse sequence) are not symmetric because of the isotope-induced chemical shift $^1\Delta^{14/15}\text{N}(^{29}\text{Si})$. The assignment of the satellites is confirmed by the observation of the ^{29}Si satellite signals in the ^{15}N NMR spectrum (box).^{95a}

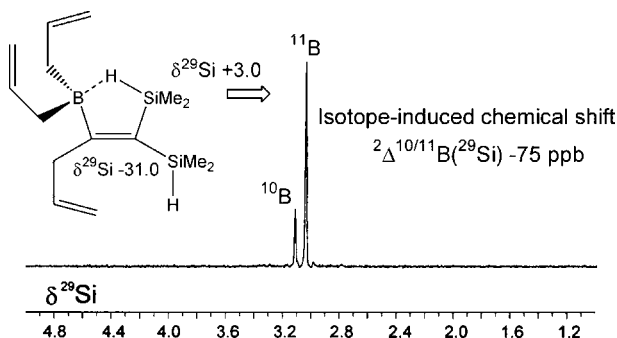


Fig. 13. Part of the 99.6 MHz $^{29}\text{Si}\{^1\text{H}\}$ NMR spectrum (INEPT) of an alkene derivative obtained by 1,1-allylboration of $\text{Me}_2(\text{H})\text{Si}-\text{C}\equiv\text{C}-\text{Si}(\text{H})\text{Me}_2$. The ^{29}Si NMR signal shown is shifted by more than 30 ppm to high frequency when compared with the other ^{29}Si NMR signal (not shown). In addition to the reduced ^{29}Si nuclear shielding, the pronounced isotope-induced chemical shift $^2\Delta^{10/11}\text{B}(^{29}\text{Si})$ is noteworthy. This effect is observed only when an electron-deficient Si-H-B bridge is present. Adapted from ref. 110.

5. INDIRECT NUCLEAR SPIN-SPIN COUPLING CONSTANTS ${}^nJ({}^{29}\text{Si}, \text{X})$

5.1. General

Major trends in indirect nuclear spin-spin coupling constants ${}^nJ({}^{29}\text{Si}, \text{X})$ have been summarised in previous reviews.¹⁻⁵ Although often neglected, modern NMR instrumentation can be used for straightforward experiments, in many cases, to determine the signs of the coupling constants $J({}^{29}\text{Si}, \text{X})$. Here it should be noted again that $\gamma({}^{29}\text{Si}) < 0$ and, therefore, the signs of $J({}^{29}\text{Si}, \text{X})$ and of the reduced coupling constants $K({}^{29}\text{Si}, \text{X})$ are opposite if $\gamma(\text{X}) > 0$. Usually at least three different types of nuclei are required for double-resonance experiments aiming for the determination of coupling signs. Two of these types of nuclei are called “active spins”, since their transitions are either observed or irradiated, and the third kind of nucleus is called the “passive spin”. The selective double-resonance experiments lead to the comparison of the signs of the two coupling constants, which involve the “passive spin” and the “active spins”. These experiments can be carried out as 1D selective double-resonance experiments, in a similar way as in the old times of CW NMR techniques, by observing differential effects for relevant transitions in the NMR spectra. Perhaps somewhat more elegant, 2D shift correlations (COSY, HETCOR, HSQC, HMQC and HMBC) can be carried out to serve for the same purpose, by observing the tilt of the cross peaks in the contour plot for the relevant transitions (Fig. 14). A positive tilt indicates that the reduced coupling constants K have alike signs, a negative tilt indicates opposite signs of K .

Since the natural abundance of ${}^{29}\text{Si}$ is only 4.7%, the determination of ${}^nJ({}^{29}\text{Si}, \text{X})$ from X NMR spectra requires the detection of weak ${}^{29}\text{Si}$ satellite signals. In addition to the signal-to-noise problem, the observation of these satellites may be difficult if the magnitude of the coupling constants is small and the satellites are close to the intensive parent signals. This is frequently the case for $\text{X} = {}^1\text{H}$ and $n \geq 2$ if the ${}^1\text{H}$ NMR signals are further split by spin-spin coupling of ${}^1\text{H}$ with other nuclei. In ${}^{29}\text{Si}\{{}^1\text{H}\}$ NMR spectra, the spin-spin coupling with other abundant or rare spin-1/2 nuclei is readily observed in most cases, since the ${}^{29}\text{Si}$ NMR signals are sharp (see e.g. Figs. 1 and 9–11 for $\text{X} = {}^{13}\text{C}$, Fig. 12 for $\text{X} = {}^{15}\text{N}$, Figs. 9–11 for $\text{X} = {}^{29}\text{Si}$ or ${}^{117/119}\text{Sn}$, Fig. 7 for $\text{X} = {}^{195}\text{Pt}$).

Recent developments in the quantum chemical treatment of NMR parameters include successful approaches to the calculation of indirect nuclear spin-spin coupling constants.^{119–121,133} This includes ${}^nJ({}^{29}\text{Si}, \text{X})$ values, at least for nuclei $\text{X} = {}^1\text{H}$, ${}^{11}\text{B}$, ${}^{13}\text{C}$, ${}^{15}\text{N}$, ${}^{29}\text{Si}$ and ${}^{31}\text{P}$. Some examples are given in Table 6 in order to demonstrate that the experimental trend is correctly reproduced. Some model compounds are not accessible experimentally. However, even for comparable compounds magnitude and sign of coupling constants have not always been reported. For Si-element single bonds, the Fermi contact (FC) term is the dominating mechanism. In the case of multiple bonding, the npn-contact terms (spin-dipole term (SD) and paramagnetic spin-orbital term (PSO)) have to be considered in addition to the Fermi contact (FC) term. These

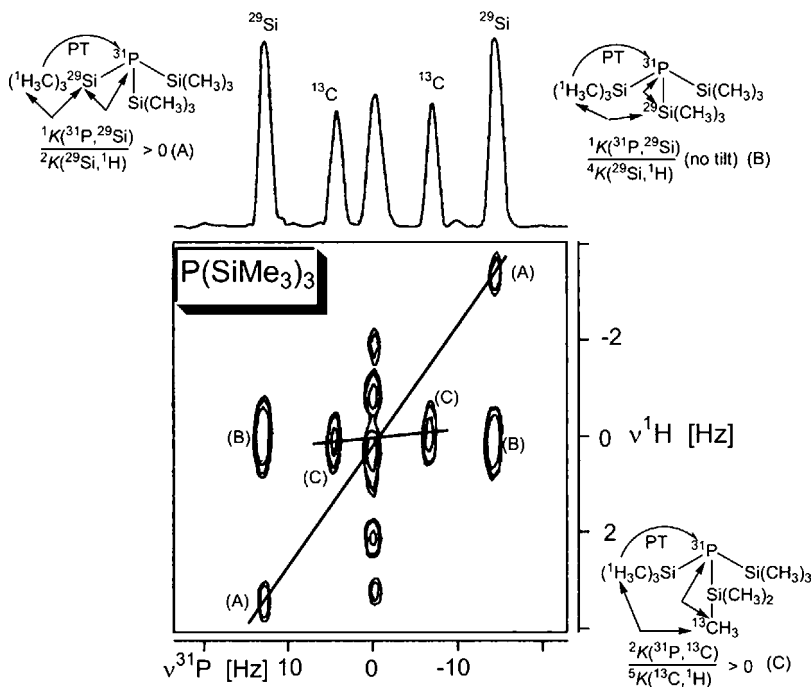


Fig. 14. Contour plot of the 2D 120 MHz $^{31}\text{P}/^1\text{H}$ HETCOR experiment for tris(trimethylsilyl)phosphane, $\text{P}(\text{SiMe}_3)_3$, in C_5D_5 . The experiment was modified by using a z-filter¹⁰⁹ in order to suppress most of the intensity of the central signal. This allows to observe the satellite signals almost undisturbed. The path of PT is indicated for each isotopomer. The active spins are ^{31}P and ^1H in each case, and the passive spin is either ^{29}Si or ^{13}C . In the case of ^{29}Si , there are two types of pairs of cross peaks for ^{29}Si satellites shown. The pair with lower intensity has a significant positive tilt which means that $^1K(^{31}\text{P}, ^{29}\text{Si})$ and $^2K(^{29}\text{Si}, ^1\text{H}_{\text{Me}})$ have alike signs. Since $^2K(^{29}\text{Si}, ^1\text{H}_{\text{Me}}) < 0$, it holds that $^1K(^{31}\text{P}, ^{29}\text{Si}) < 0$ ($^1J(^{31}\text{P}, ^{29}\text{Si}) > 0$!). The pair of crosspeaks with higher intensity results from PT across magnetically non-active silicon isotopes, and there is no tilt because of the small magnitude of $^4K(^{29}\text{Si}, \text{P}, \text{Si}, \text{C}, ^1\text{H})$. A very small tilt is indicated for ^{13}C satellites. (B. Wrackmeyer and U. Klaus, unpublished results).


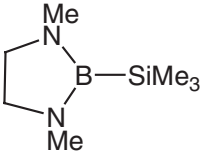
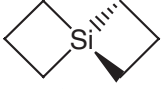
non-contact terms are important for Si-element double and triple bonds, in a similar way as has been pointed out for $\text{C}=\text{C}$, $\text{C}\equiv\text{C}$,^{120b,c} $\text{C}\equiv\text{N}$ and $\text{C}\equiv\text{P}$ bonds.^{121c}

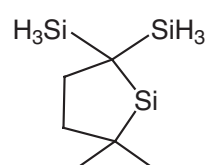
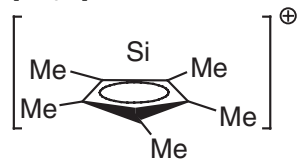
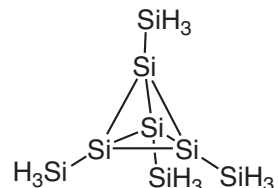
5.2. One-bond couplings, $^1J(^{29}\text{Si}, \text{X})$

5.2.1. Coupling Constants $^1J(^{29}\text{Si}, ^1\text{H})$

Coupling constants $^1J(^{29}\text{Si}, ^1\text{H})$ are readily determined either from the ^{29}Si satellite signals in the ^1H NMR spectra (Fig. 15) or from ^1H coupled ^{29}Si NMR spectra.¹²⁹ Extensive lists of data are given in previous reviews.¹⁻⁶ Changes in the magnitude of $^1J(^{29}\text{Si}, ^1\text{H})$ remind much of the well-known qualitative dependence of $^1J(^{13}\text{C}, ^1\text{H})$ on

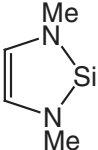
Table 6. Some calculated^a and experimental coupling constants $^1J(^{29}\text{Si}, \text{X})$ [Hz]

Compound	X	$^1J(^{29}\text{Si}, \text{X})$ (calculated) ^b	$^1J(^{29}\text{Si}, \text{X})$ (experimental) ^b
$\text{Me}_3\text{Si}-\text{H}$	^1H , ^{13}C	-168.8, -44.1	-184.0
 $\text{Be}-\text{SiMe}_3$	^9Be	+ 52.7	51.4 ^{72a}
$[\text{Me}_3\text{Si}-\text{BH}_3]$	^{11}B	-69.5 -103.3	-74.0 ^{72b} -97.0 ¹³¹
 $\text{B}-\text{SiMe}_3$			
SiMe_4	^{13}C	-44.3	-50.8
$\text{Me}_2\text{Si}(\text{CH}_2)_5$	^{13}C	-44.2 (Me), -42.9 (CH_2)	Not measured
$\text{Me}_2\text{Si}(\text{CH}_2)_4$	^{13}C	-42.5 (CH_3), -44.2 (CH_2)	Not measured
$\text{Me}_2\text{Si}(\text{CH}_2)_3$	^{13}C	-34.6 (CH_2), -37.0 (CH_2), + 14.3 (2J)	-44.6, -42.3, ¹⁷⁸ 16.4 ¹⁷⁸
$\text{Me}_2\text{Si}(\text{CH}_2)_2$	^{13}C	-53.6 (CH_3), -22.1 (CH_2)	—
 Si	^{13}C	-30.3	Not measured
$\text{Me}_2\text{Si}(\text{C}\equiv\text{C}-\text{Me})_2$	^{13}C	-100.0 ($\text{C}\equiv$), -56.5 (CH_3), -20.9 ($\equiv\text{C}$), -1.7 (CH_3)	-98.8, -62.2, -19.8, -1.8 ¹⁰⁵
$\text{Si}(\text{C}\equiv\text{C}-\text{Me})_4$	^{13}C	-130.6 ($\text{C}\equiv$), -28.3 ($\equiv\text{C}$), -2.2 (CH_3)	-127.0, -26.5, -1.0 ^{173a}
$\text{Me}_2\text{Si}=\text{CMe}_2$	^{13}C	-126.8 ($\text{Si}=\text{C}$), -50.1 ($\text{Si}-\text{CH}_3$)	—

	^{13}C	+ 42.1 (Si)	Not measured ³⁸
$[(\text{H}_3\text{Si})_2\text{CH}]_2\text{Si}$	^{13}C	+ 42.3 (Si)	—
$[\text{Me}_3\text{Si}]^+$	^{13}C	-32.1	—
	^{13}C	+ 12.5	Not measured ⁴¹
$\text{Me}_3\text{Si}-\text{SiH}_3$	^1H , ^{29}Si	-169.0, + 67.0	
$\text{Me}_3\text{Si}-\text{Si}(\text{H})\text{Me}_2$	^1H , ^{29}Si	-159.0, + 69.4	+ 84.6 (Si-Si)
	^{29}Si	-6.3 (Si-Si) + 54.3 (Si-SiH ₃)	Not observed ¹⁷⁷
$\text{Me}_2\text{Si}=\text{SiMe}_2$	^{29}Si	+ 164.5 (Si = Si), -44.0 (Si-CH ₃)	—
$\text{Me}_3\text{Si}-\text{Si}\equiv\text{Si}-\text{SiMe}_3$	^{29}Si	+ 291.7 (Si-Si), ^c + 52.0 (Si-SiMe ₃)	Not measured ⁵⁴
$(\text{H}_3\text{Si})_3\text{N}$	^{15}N	+ 3.2	+ 6.0
$(\text{Me}_3\text{Si})_2\text{NH}$	^{15}N , ^1H	+ 8.6, + 1.6 (Si-N-H)	+ 13.5, ... ²⁸
$\text{Me}_2\text{Si}=\text{NMe}_2$	^{15}N	+ 5.9	Not measured
$[(\text{H}_3\text{Si})_2\text{N}]_2\text{Si}$	^{15}N	-42.5 (Si), + 3.2 (SiH ₃)	Not measured

(continued)

Table 6. Continued

Compound	X	$^1J(^{29}\text{Si}, \text{X})$ (calculated) ^b	$^1J(^{29}\text{Si}, \text{X})$ (experimental) ^b
	¹⁵ N	−34.0	Not measured
Me ₃ Si–PH ₂	³¹ P	+ 59.0 ^d	+ 16.2 ¹⁴¹
(Me ₃ Si) ₃ P	³¹ P	+ 84.8 ^d	+ 27.2
Me ₂ Si=NMe	³¹ P	+ 263.2 (Si = P), + 118.0 (SiMe ₃)	153, 76 (22a) ^{57a}
Me ₃ Si–SeMe	⁷⁷ Se	+ 140.4	+ 110.2 (SeBu) ^{59b}
(Me ₃ Si) ₂ Se	⁷⁷ Se	+ 143.1	+ 109.8 ¹⁴⁶

^aGeometries were optimised for this review by B3LYP/6-311+G(d,p) calculations, and coupling constants were calculated at the same level of theory (Gaussian 03 program package¹⁷⁹). The data given are the sum of the contact contribution (FC) and the non-contact contributions (SD and SO). Experimental data are taken from previous reviews^{1–5} if not indicated otherwise.

^bNote that $\gamma(^{29}\text{Si}) < 0$, which means that all signs of J are opposite to those of the reduced coupling constants K for $\gamma(\text{X}) > 0$.

^cThe optimised geometry shows a *trans*-bent structure with bond angles at the central silicon atoms of 132.9° and the Si≡Si bond length of 209.2 pm.

^dThe trend of the experimental data is reproduced; however, the calculated $^1J(^{31}\text{P}, ^{29}\text{Si})$ values depend strongly on slight changes in the geometry at the phosphorus atom.

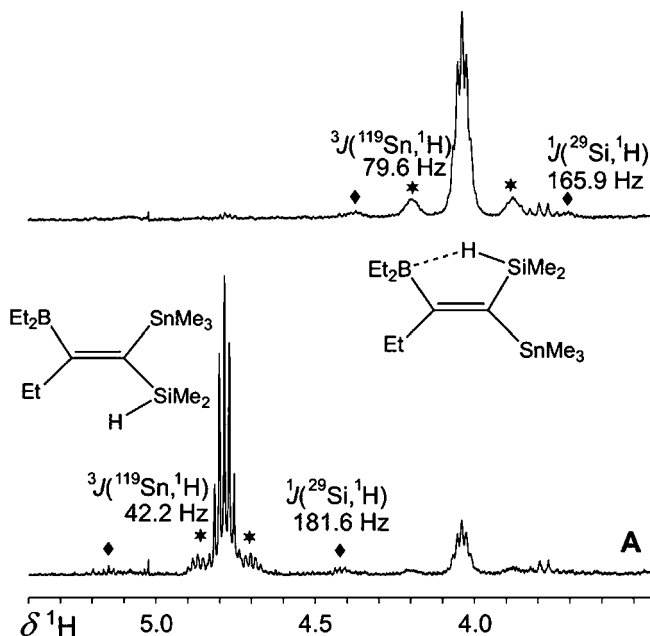


Fig. 15. 400 MHz ^1H NMR spectra for monitoring changes in a reaction mixture containing two different silanes. The $^1\text{H}(\text{Si}-\text{H})$ resonances are found in a typical range, accompanied by ^{29}Si satellite (in this case also by $^{117/119}\text{Sn}$ satellites). The different magnitude of $^1J(^{29}\text{Si}, ^1\text{H})$ is the result of a weak electron-deficient $\text{Si}-\text{H}-\text{B}$ bridge (smaller value) in one isomer, and the absence (larger value) of such a bridge in the other isomer. Adapted from ref. 93j.

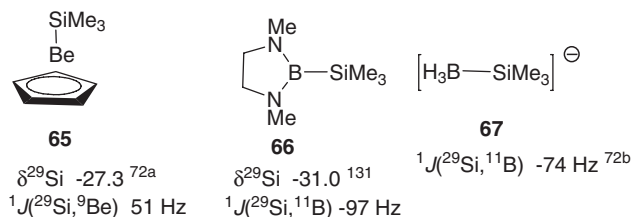
the s character of the respective hybrid orbitals in the carbon analogues. This includes in principle changes in $^1J(^{29}\text{Si}, ^1\text{H})$ for activated $\text{Si}-\text{H}$ bonds. Values >20 Hz for coupling constants $J(^{29}\text{Si}, ^1\text{H})$ are taken as a criterion for $\text{Si}-\text{H}$ bonding in complexes containing the $\text{R}_3\text{Si}-\text{M}-\text{H}$ unit. However, it seems that changes in these data are a complex function of both nature of the substituents R at silicon and the metal fragment itself.^{70b,80–83}

5.2.2. Coupling constants $^1J(^{29}\text{Si}, ^9\text{Be})$, $^1J(^{29}\text{Si}, ^{11}\text{B})$

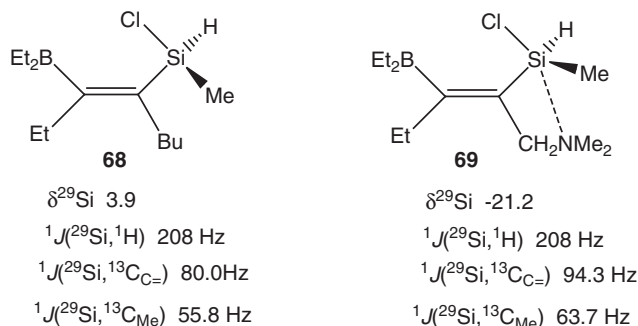
Only one example is known for $^1J(^{29}\text{Si}, ^9\text{Be}) = 51$ Hz in $(\eta^5\text{-C}_5\text{H}_5)\text{Be}-\text{SiMe}_3$ (**65**).^{72a} For tri-coordinate silylboranes, the ^{29}Si NMR signals are broad owing to partially relaxed $^{29}\text{Si}-^{11}\text{B}$ spin-spin coupling. In one case (**66**),¹³¹ the magnitude and sign of $^1J(^{29}\text{Si}, ^{11}\text{B})$ has been determined by $^1\text{H}\{^{29}\text{Si}\}$ heteronuclear double-resonance experiments. Resolved 1:1:1:1 quartets (**67**) as the result of $^1J(^{29}\text{Si}, ^{11}\text{B})$ are observed for silylborates^{72b} (Scheme 16).

5.2.3. Coupling constants $^1J(^{29}\text{Si}, ^{13}\text{C})$

All reduced coupling constants $^1K(^{29}\text{Si}, ^{13}\text{C})$ in organosilicon compounds containing tetravalent silicon are positive ($^1J(^{29}\text{Si}, ^{13}\text{C}) < 0$!). Possible exceptions (signs have not



Scheme 16. Examples for coupling constants $^1J(^{29}\text{Si}, ^9\text{Be})$ and $^1J(^{29}\text{Si}, ^{11}\text{B})$.



Scheme 17. Evidence for weak intramolecular N–Si coordination revealed by comparison of ^{29}Si NMR parameters.¹¹¹

been determined) may be found for triorganosilyl anions in analogy to the finding for triorganostannyl anions ($^1K(^{119}\text{Sn}, ^{13}\text{C}) < 0$ in $[\text{Me}_3\text{Sn}]\text{Li}^{74}$) and isoelectronic phosphanes ($^1K(^{31}\text{P}, ^{13}\text{C}) < 0$). In compounds containing divalent silicon, it can be predicted that the sign of $^1K(^{29}\text{Si}, ^{13}\text{C})$ is negative ($^1J(^{29}\text{Si}, ^{13}\text{C}) > 0$!)), and this is confirmed by calculation of the coupling constants (Table 6). Listings of representative data $^1J(^{29}\text{Si}, ^{13}\text{C})$ can be found in the previous reviews.^{1–6} Expectedly, changes in the magnitude of $^1J(^{29}\text{Si}, ^{13}\text{C})$ and $^1J(^{119}\text{Sn}, ^{13}\text{C})$ ^{77c,d,1127} for comparable compounds are similar, in most cases. Since this is also true for coordination numbers > 4 , it means that the magnitude of $^1J(^{29}\text{Si}, ^{13}\text{C})$ increases if the coordination number of Si increases, even if there is only an equilibrium present (Scheme 17). The NMR parameters for **68** are typical of Si coordination number 4. In the case of **69**, weak intramolecular N→Si coordination can be assumed, supported by the expected changes in $\delta^{29}\text{Si}$ and the increase in the magnitude of the coupling constants $^1J(^{29}\text{Si}, ^1\text{H})$ and $^1J(^{29}\text{Si}, ^{13}\text{C})$.¹¹¹ In the structure of **69**, the methyl carbon, the olefinic carbon and the hydride will be preferably adopt positions in the equatorial plane of a distorted trigonal bipyramid. Within the concept of rehybridisation,¹¹⁸ this causes an increase in the s character of the orbitals involved.

5.2.4. Coupling constants $^1J(^{29}\text{Si}, ^{29}\text{Si})$, $^1J(^{119}\text{Sn}, ^{29}\text{Si})$ And $^1J(^{207}\text{Pb}, ^{29}\text{Si})$

There is a wealth of compounds containing Si–Si bonds. The coupling constants $^1J(^{29}\text{Si}, ^{28}\text{Si})$ have been measured in some cases, either by direct observation of ^{29}Si

satellites in ^{29}Si NMR spectra^{61g,113–116,125,126} or by analysis of ^{29}Si satellites in ^1H NMR spectra.¹¹⁷ The reduced coupling constants $^1K(^{29}\text{Si}, ^{29}\text{Si})$ possess a positive sign in most cases,^{125,126} with the possible exception of silyl anions containing Si–Si bonds (e.g. $[(\text{Me}_3\text{Si})_3\text{Si}]^-$ with $^1J(^{29}\text{Si}, ^{29}\text{Si}) = \pm 19.0 \text{ Hz}$ ¹²⁶). The magnitude of $^1J(^{29}\text{Si}, ^{29}\text{Si})$ in disilanes depends, in a predictable way,¹¹⁴ upon the electronegativity of the substituents at the silicon atoms, and can be related to the s character of the Si–Si bond within the model of rehybridisation.¹¹⁸ In the frame of this simplified approach, it can also be predicted that the magnitude of $^1J(^{29}\text{Si}, ^{29}\text{Si})$ increases in going from disilanes to disilenes (Scheme 18), which is supported both by experiment¹¹⁶ and theory (see Table 6). Although there are no experimental data available for disilynes so far, the calculations for $\text{Me–Si}\equiv\text{Si–Me}$ (Table 6) predict a further increase in the magnitude of $^1J(^{29}\text{Si}, ^{29}\text{Si})$ and, therefore, the pattern of data $^1J(^{29}\text{Si}, ^{29}\text{Si})$ is fairly similar to that known for $^1J(^{13}\text{C}, ^{13}\text{C})$.¹²²

All known coupling constants $^1J(^{119}\text{Sn}, ^{29}\text{Si})$ appear to possess a positive sign.^{123,124} Some typical examples are given in Scheme 19. However, only a limited data set is available and therefore, it is well possible that changes in the coupling signs will be found. In principle, data $^1J(^{119}\text{Sn}, ^{29}\text{Si})$ can be readily determined either from ^{29}Si or from ^{119}Sn NMR spectra by observation of the respective satellite signals.^{124,127}

Although compounds containing Pb–Si bonds are rare, coupling constants $^1J(^{207}\text{Pb}, ^{29}\text{Si})$ and their signs (<0 ; $^1K(^{207}\text{Pb}, ^{29}\text{Si}) > 0$!) have been determined¹²⁸ (Scheme 20). These compounds deserve some interest since the Pb–Si bonding situation represents the extreme case in the series of Si-element bonds for group-14 elements.

5.2.5. Coupling constants $^1J(^{29}\text{Si}, ^{15}\text{N})$ and $^1J(^{31}\text{P}, ^{29}\text{Si})$

A large number of data $^1J(^{29}\text{Si}, ^{15}\text{N})$ has been summarised in two reviews.^{5,132} With few exceptions, it appears that the sign of $^1J(^{29}\text{Si}, ^{15}\text{N})$ is positive.^{3,134,135} The

$^1J(^{29}\text{Si}, ^{29}\text{Si})$ [Hz]		$^1J(^{29}\text{Si}, ^{29}\text{Si})$ [Hz]		$^1J(^{29}\text{Si}, ^{29}\text{Si})$ [Hz]				
70	Me ₃ Si-Si(H)Me ₂	84.6	76	H ₂ (Br)Si-SiH ₃	86.6	82	Me ₂ Si=Si(Mes)Xyl	158
71	Me ₃ Si-Si(Ph)Me ₂	86.1	77	H ₂ (I)Si-SiH ₃	83.4	83	Me ₂ Si=SiXyl ₂	155
72	Me ₃ Si-Si(Cl)Me ₂	94.0	78	Br ₂ (H)Si-SiH ₃	98.6	84	Xyl ₂ Si=Si(Mes)Xyl	156
73	Me ₃ Si-Si(F)Me ₂	98.7	79	Br ₃ Si-SiH ₃	117.7			
74	Me ₂ Si(SiMe ₃) ₂	73.2	80	I ₃ Si-SiH ₃	97.8			
75	Si(SiMe ₃) ₄	52.5	81	Br ₃ Si-Si(H)Br ₂	171.6			

Scheme 18. Examples for coupling constants $^1J(^{29}\text{Si}, ^{29}\text{Si})$.

$^1J(^{119}\text{Sn}, ^{29}\text{Si})$ [Hz]							
85	$\text{Me}_3\text{Sn–SiMe}_3$	+656	$\text{Bu}^t_2\text{Sn–SiMe}_2$		$\text{Bu}^t_2\text{Sn–SiMe}_2$		$\text{Bu}^t_2\text{Sn–SiMe}_2$
86	$\text{Me}_3\text{Sn–SiEt}_3$	650	$\text{Bu}^t_2\text{Sn–SiMe}_2$		$\text{Bu}^t_2\text{Sn–SiMe}_2$		$\text{Bu}^t_2\text{Sn–SiMe}_2$
87	$(\text{Me}_3\text{Sn})_2\text{SiMe}_2$	+504.0					
88	$(\text{Ph}_3\text{Sn})_2\text{SiPh}_2$	535.0	90		91		92
89	$(\text{Me}_3\text{Sn})_4\text{Si}$	+227.1	$^1J(^{119}\text{Sn}, ^{29}\text{Si})$	226		217	
			[Hz]				

Scheme 19. Examples for coupling constants $^1J(^{119}\text{Sn}, ^{29}\text{Si})$.

	$^1J(^{207}\text{Pb}, ^{29}\text{Si})$ [Hz]	$\delta^{29}\text{Si}$		$^1J(^{207}\text{Pb}, ^{29}\text{Si})$ [Hz]	$\delta^{29}\text{Si}$
93 $\text{Me}_3\text{Pb-SiMe}_3$	-764.2	6.8	98 $\text{Bu}^t_2\text{Pb}(\text{SiMe}_3)_2$	-180.0	12.0
94 $\text{Bu}^t_3\text{Pb-SiMe}_3$	-207.6	19.0	99 $\text{Bu}^t_2\text{Pb}[\text{Si}(\text{Bu}^t)\text{Me}_2]_2$	-80.6	30.2
95 $\text{Bu}^t_3\text{Pb-Si}(\text{Bu}^t)\text{Me}_2$	-102.5	34.7			
96 $\text{Bu}^t_3\text{Pb-Si}(\text{Ph})\text{Me}_2$	-151.4	13.3			
97 $\text{Bu}^t_3\text{Pb-SiMe}_2\text{SiMe}_3$	57.9	-12.2 (SiMe ₂) 6.0 (2J) -11.3 (SiMe ₃)			

Scheme 20. Examples for coupling constants $^1J(^{207}\text{Pb}, ^{29}\text{Si})$; data taken from ref. 128.

$\text{Me}_3\text{Si-X}$		$(\text{Me}_3\text{Si})_2\text{N-X}$	
X	$^1J(^{29}\text{Si}, ^{15}\text{N})$ [Hz]	X	$^1J(^{29}\text{Si}, ^{15}\text{N})$ [Hz]
N(H)Bu ^t	+17.2	H	+13.5
NEt ₂	19.2	Na	7.6
N=C=O	14.5	SiMe ₃	+7.7
N=C=S	12.2	SnMe ₃	6.9
N=C=C(SiMe ₃) ₂	+8.9	SnN(SiMe ₃) ₂	6.1
N=C=N-SiMe ₃	+16.9	SnCl ₃	3.8
N=N=N	0	TiCl ₃	1.5
N=S=O	0		
N=N-SiMe ₃	-13.7		
		(Me ₂ Si-NH) ₃	15.4
		(Me ₂ Si-NH) ₄	16.9
		Me ₂ (EtO)Si-N(H)Bu ^t	21.5
		Me(EtO) ₂ Si-N(H)Bu ^t	30.9
		(EtO) ₃ Si-N(H)Bu ^t	44.6
		Si[N(H)Pr] ₄	31.7
		Si(N=C=O) ₄	57.3
		[Si(N=C=S) ₆] ²⁻	36.1

Scheme 21. Examples for coupling constants $^1J(^{29}\text{Si}, ^{15}\text{N})$; see e.g. refs. 5, 28, 132 and 140.

exceptions known so far are mainly due to the influence of the lone pair of electrons at the nitrogen atom,¹³⁶ giving rise to substantial negative contributions to the FC term if energetically low-lying unoccupied orbitals can be mixed with the ground states by the external field B_0 . Thus, the value for $^1J(^{29}\text{Si}, ^{15}\text{N})$ in $\text{Me}_3\text{Si-NSO}$ is close to zero,²⁸ and a negative sign of $^1J(^{29}\text{Si}, ^{15}\text{N})$ has been determined and calculated in the case of $\text{Me}_3\text{Si-N}=\text{N-SiMe}_3$.¹³³ In any case, many values for $^1J(^{29}\text{Si}, ^{15}\text{N})$ are small, often < 10 Hz, and, therefore, inversion of the coupling sign is well possible. Typical examples in this respect are N-silylaminotin or titanium chlorides,¹³⁹ for which the magnitude of $^1J(^{29}\text{Si}, ^{15}\text{N})$ is even < 5 Hz (Scheme 21).

Many coupling constants $^1J(^{29}\text{Si}, ^{15}\text{N})$ have been measured either by detection of ^{15}N satellites in ^{29}Si NMR spectra (see e.g. Figs. 6 and 12), and for this purpose the application of the HEED-INEPT experiment²⁸ is particularly helpful. It is also possible to detect the ^{29}Si satellite signals in the ^{15}N NMR spectra even with ^{15}N at natural abundance (see e.g. Fig. 12). Frequently it is advisable to record the ^{15}N NMR spectra under conditions typical of the so-called “ultra-high resolution”,^{27,33,134c,137} since the natural transverse relaxation times $T_2(^{15}\text{N})$ can be extremely long which means that the ^{15}N NMR signals are very sharp. This technique is often fairly straightforward if PT can be applied (Fig. 16).

In silanes bearing electronegative substituents, the change in the $\delta^{29}\text{Si}$ values as the result of interactions with Lewis bases is accompanied by appropriate scalar coupling, e.g. $^{19}\text{Si-}^{15}\text{N}$ spin-spin coupling, if the exchange is slow. This is

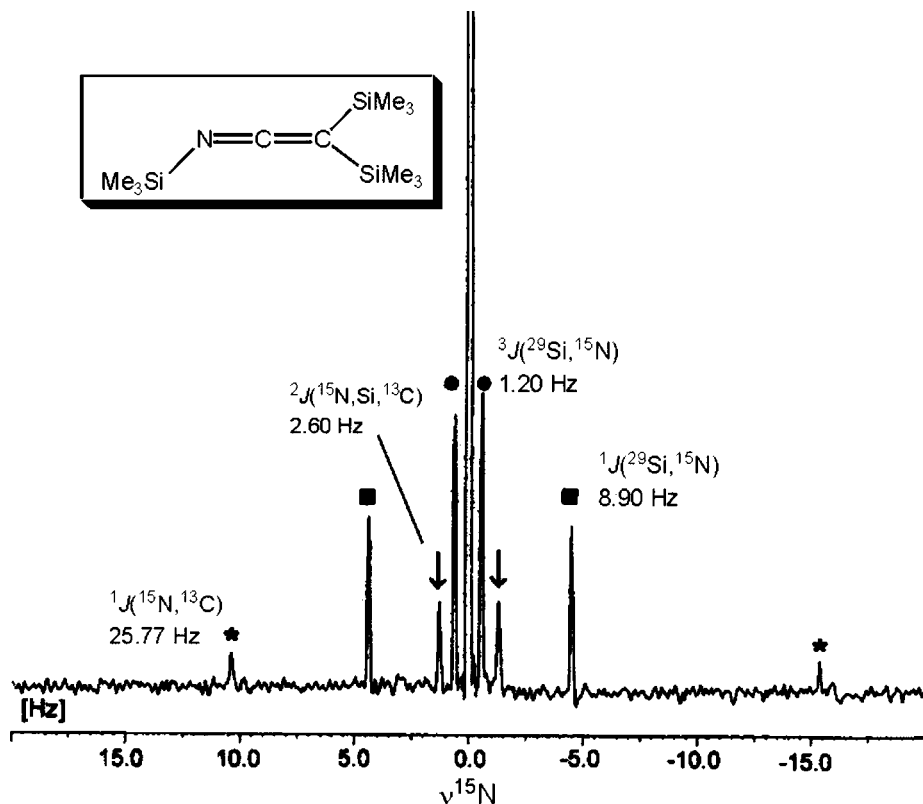
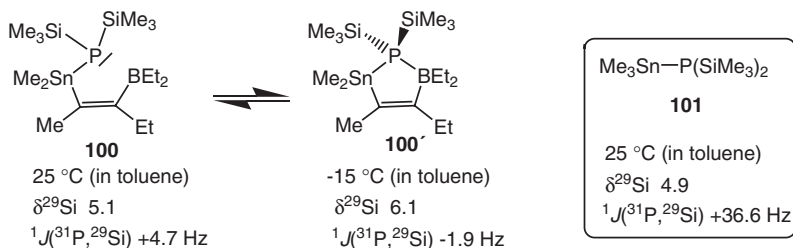


Fig. 16. 30.4 MHz $^{15}\text{N}\{^1\text{H}\}$ NMR spectrum of tris(trimethylsilyl)ketimine (INEPT, ultra-high resolution: 10 mm tube, 50/50 (v/v) in C_6D_6 , 23 °C, acquisition time 48 s, 128 transients, repetition delay 30 s; $h_{1/2} = 0.020$ Hz). ^{29}Si satellites are marked by filled squares and cycles, and ^{13}C satellites are marked by asterisks and arrows. Note the large isotope-induced chemical shift $^1\Delta^{12/13}\text{C}(^{15}\text{N}) = -82.6$ ppb. Adapted from ref. 137c2.

demonstrated for the adduct of $\text{Ph-C}\equiv\text{C-SiF}_3$ with one or two equivalents of ^{15}N -labelled pyridine.¹⁴⁷

Numerous coupling constants $^1J(^{31}\text{P}, ^{29}\text{Si})$ have been measured, mainly for silylphosphanes (values of $^1J(^{31}\text{P}, ^{29}\text{Si})$ are found of the order of 10–70 Hz^{1–5,57,157,175}), but also for the rare examples of derivatives with $\text{Si} = \text{P}$ bonds⁵⁷ (see Scheme 6). The sign of $^1J(^{31}\text{P}, ^{29}\text{Si})$ is invariably positive ($^1K(^{31}\text{P}, ^{29}\text{Si}) < 0$!) for three-coordinate phosphorus atoms^{94f,141,142} (the confusing statement in ref. 143 should be ignored). This is also evident for tris(trimethylsilyl)phosphane as shown in Fig. 14. It can be safely assumed that $^1J(^{31}\text{P}, ^{29}\text{Si})$ is positive for the $\text{Si} = \text{P}$ bond as in **21**^{57a} (Scheme 6) owing to the dominant influence of the lone pair of electrons at the phosphorus atom,¹³⁶ in agreement with calculations (Table 6). When the phosphorus lone pair becomes engaged in σ bonding, the sign of $^1J(^{31}\text{P}, ^{29}\text{Si})$ can change from positive to negative^{94f} ($^1K(^{31}\text{P}, ^{29}\text{Si}) > 0$!) as shown for compound **100** by the temperature-dependent equilibrium¹⁴⁴ in Scheme 22. The analogous behaviour is also well



Scheme 22. Dependence of magnitude and sign of $^1J(^{31}\text{P}, ^{29}\text{Si})$ on the coordination number of the phosphorus atom. Engagement of the lone pair of electrons at phosphorus in coordinative bonding reduces negative contributions to the FC term, and the sign of $^1K(^{31}\text{P}, ^{29}\text{Si})$ (opposite to $^1J(^{31}\text{P}, ^{29}\text{Si})$!) can become positive.¹⁴⁴

E = Se, Te	$^1J(^{77}\text{Se}, ^{29}\text{Si})$	$^1J(^{125}\text{Te}, ^{29}\text{Si})$		$^1J(^{77}\text{Se}, ^{29}\text{Si})$	$^1J(^{125}\text{Te}, ^{29}\text{Si})$ [Hz]
102 $\text{Me}_3\text{Si}-\text{EBu}$	110.8	281.8	105 $(\text{H}_3\text{Si})_2\text{E}$	110.6	--
103 $\text{Me}_2\text{Si}(\text{EBu})_2$	137.3	361.0	107 $(\text{Me}_3\text{Si})_2\text{E}$	109.2	274.6
104 $\text{MeSi}(\text{EBu})_3$	150.4	421.8	108 $(\text{Ph}_2\text{SiE})_3$	99.1	373.2
105 $\text{Si}(\text{EBu})_4$	180.2	454.9			

Scheme 23. Examples for coupling constants $^1J(^{77}\text{Se}, ^{29}\text{Si})$ and $^1J(^{125}\text{Te}, ^{29}\text{Si})$; data taken from refs. 59b,61a and 146.

established for $^1J(^{31}\text{P}, ^{13}\text{C})$ in phosphanes and phosphane complexes or phosphonium salts.

5.2.6. Coupling constants $^1J(^{77}\text{Se}, ^{29}\text{Si})$ and $^1J(^{125}\text{Te}, ^{29}\text{Si})$

The interest in the chemistry of sulphur, selenium and tellurium has recently led to numerous novel silicon–selenium and silicon–tellurium compounds, of which coupling constants $^1J(^{77}\text{Se}, ^{29}\text{Si})$ and $^1J(^{125}\text{Te}, ^{29}\text{Si})$ have been measured.^{58–61,95e} The positive sign of $^1J(^{77}\text{Se}, ^{29}\text{Si})$ ($^1K(^{77}\text{Se}, ^{29}\text{Si}) < 0$!) has been determined experimentally for several examples,^{94e,145,146} and is also predicted by calculations (Table 6). Since the known comparable data $^1J(^{77}\text{Se}, ^{29}\text{Si})$ and $^1J(^{125}\text{Te}, ^{29}\text{Si})$ follow the same trend it is reasonable to assume that the reduced coupling constants $^1K(^{77}\text{Se}, ^{29}\text{Si})$ and $^1K(^{125}\text{Te}, ^{29}\text{Si})$ possess alike signs. Some examples (102–108) for $^1J(^{77}\text{Se}, ^{29}\text{Si})$ and $^1J(^{125}\text{Te}, ^{29}\text{Si})$ are given in Scheme 23.

5.2.7. Coupling constants $^1J(^{29}\text{Si}, ^{19}\text{F})$

Coupling constants $^1J(^{29}\text{Si}, ^{19}\text{F})$ have attracted much attention, and consequently numerous data have been collected and cited in previous reviews.^{1–6,148} The values for $^1J(^{29}\text{Si}, ^{19}\text{F})$ range from about 120 to almost 400 Hz. There appears to be no straightforward relationship between the magnitude of $^1J(^{29}\text{Si}, ^{19}\text{F})$ (positive sign; $^1K(^{29}\text{Si}, ^{19}\text{F}) < 0$!) and structural features. However, the multiplicity of the ^{29}Si NMR signals serves in the usual way to assess the number and the type of ^{19}F nuclei bonded to silicon. The combination of temperature-dependent ^{19}F and ^{29}Si NMR

spectroscopy together with the observation of $^1J(^{29}\text{Si}, ^{19}\text{F})$ is particularly useful for the study of silicon fluorides with coordination number of silicon greater than 4.^{147,149–151} An instructive example is shown in Fig. 17, where Si–F–Si bridging and the fluxional character of this bridge become apparent.¹⁵¹ The magnitude of $^1J(^{29}\text{Si}, ^{19}\text{F})$ for the apical position of fluorine in a trigonal bipyramidal geometry at the silicon atom is usually smaller than that for equatorial positions.

5.2.8. Coupling constants $^1J(M, ^{29}\text{Si})$ (M = transition metal nucleus)

In the cases of various spin-1/2 transition metal nuclei M (^{57}Fe ,¹⁵³ ^{103}Rh ,¹⁵⁴ ^{182}W ,^{49c,155} ^{195}Pt ,¹⁵⁶ ^{199}Hg ¹⁵²), coupling constants $^1J(M, ^{29}\text{Si})$ have been measured, mainly from ^{29}Si NMR spectra. For quadrupolar nuclei M , the splitting is usually not resolved in the solution state ^{29}Si NMR spectra, but the value $^1J(M, ^{29}\text{Si})$ might be deduced from solid-state ^{29}Si NMR spectra, e.g. for $M = ^{55}\text{Mn}$.⁷⁵ It can be assumed that all reduced coupling constants $^1K(M, ^{29}\text{Si})$ possess a positive sign, in analogy to the experimental findings for $^1K(M, ^{119}\text{Sn})$. The data set is still fairly limited. However, certain trends, e.g. in analogy to $^1J(M, ^{13}\text{C})$, become already

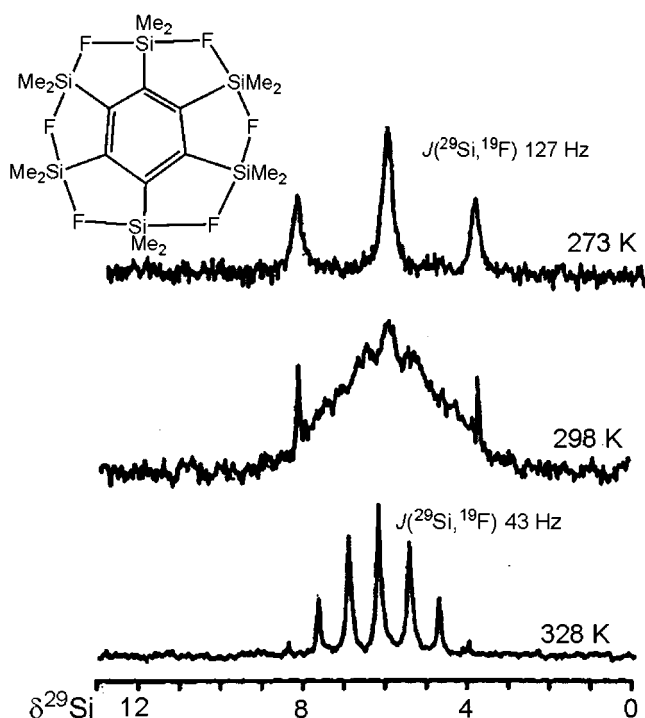


Fig. 17. 59.6 MHz $^{29}\text{Si}\{^1\text{H}\}$ NMR spectrum of hexakis(fluorodimethylsilyl)benzene (in C_7D_8) at variable temperature. At low temperature, the triplet splitting suggests a five-coordinate silicon atom bearing two fluoro substituents in equivalent (axial) positions (in the crystal, the positions are slightly different). At high temperature, the intramolecular exchange of the ^{19}F nuclei becomes fast, leading to a septet of the ^{29}Si NMR signal. Adapted from ref. 151.

$^1J(^{199}\text{Hg}, ^{29}\text{Si})$ [Hz]			$^1J(^{199}\text{Hg}, ^{29}\text{Si})$ [Hz]		
109	Me ₃ Si-Hg-Me	1393	115	Me ₃ Si-Hg-SiMe ₃	981
110	Me ₃ Si-Hg-Et	1227	116	(Me ₃ Si) ₃ Si-Hg-Si(SiMe ₃) ₃	432
111	Me ₃ Si-Hg-CH ₂ (CH ₃) ₃	1245	117	Me ₂ (Cl)Si-Hg-Si(Cl)Me ₂	1392
112	Me ₃ Si-Hg-Bu ^t	996	118	Cl ₂ (Me)Si-Hg-Si(Me)Cl ₂ (Et ₂ O)	2395
113	Me ₃ Si-Hg-C≡C-Bu	1950	119	Cl ₃ Si-Hg-SiCl ₃ (Et ₂ O)	3864
114	Me ₃ Si-Hg-C≡C-Ph	2001			

Scheme 24. Some coupling constants $^1J(^{199}\text{Hg}, ^{29}\text{Si})$ for silyl mercury derivatives; data taken from ref. 152.

evident. In the cases of $^1J(^{183}\text{W}, ^{29}\text{Si}) = 30.5$ and 143.9 Hz for complexes with formal W–Si single and double bonds, respectively^{49c} (see Scheme 5), the situation is similar to that for $^1J(^{183}\text{W}, ^{13}\text{C})$ for W–C single and double bonds. A fairly large data set is available for $^1J(^{199}\text{Hg}, ^{29}\text{Si})$ as shown for **109–119**,¹⁵² which shows a strong dependence on the nature of the other substituent(s) (Scheme 24). This is an expected behaviour, considering the polarizability of the Hg–Si bonds.

5.3. Two- (geminal) and three-bond (vicinal) coupling constants, $^2J(^{29}\text{Si}, \text{X})$ and $^3J(^{29}\text{Si}, \text{X})$

5.3.1. Coupling constants $^{2,3}J(^{29}\text{Si}, ^1\text{H})$ and $^{2,3}J(^{29}\text{Si}, ^{19}\text{F})$

The ever increasing performance of NMR spectrometers has provided a large set of data $^nJ(^{29}\text{Si}, \text{X})$ for $n > 1$. Frequently, these data are not used for structural assignment, very often they are not even reported (e.g. for $\text{X} = ^1\text{H}$). For $\text{X} = ^1\text{H}$ (or likewise ^{19}F), the ^{29}Si –X scalar couplings form the important basis for PT in 1D or 2D NMR experiments. The majority of data have been measured for organosilicon compounds with coupling across one or two carbon atoms. For intervening aliphatic carbon atoms, the sign of $^2J(^{29}\text{Si}, ^1\text{H})$ is positive ($^2K(^{29}\text{Si}, ^1\text{H}) < 0$!), in contrast to the situation for an intervening olefinic carbon atom where the sign of $^2J(^{29}\text{Si}, ^1\text{H})$ is usually negative ($^2K(^{29}\text{Si}, ^1\text{H}) > 0$!). In the case of alkylsilicon compounds, the variation in the magnitude of $^2J(^{29}\text{Si}, ^1\text{H})$ is relatively small (about 6.5 ± 3 Hz). However, the general trend reminds of that found for $^2J(^{119}\text{Sn}, ^1\text{H})$ for methyltin compounds. The absolute magnitude of coupling constants $^3J(^{29}\text{Si}, ^1\text{H})$ (negative sign; $^3K(^{29}\text{Si}, ^1\text{H}) > 0$!) in aliphatic frameworks or in phenylsilanes is similar to that of $^2J(^{29}\text{Si}, ^1\text{H})$ in alkylsilanes (note the opposite sign !). In alkenylsilanes, the usual trend is observed with $|^3J(^{29}\text{Si}, ^1\text{H})_{\text{trans}}| > |^3J(^{29}\text{Si}, ^1\text{H})_{\text{cis}}|$, and the values increase in the presence of electropositive substituents at the C = C bond.¹⁶⁰ There are also numerous examples for $^nJ(^{29}\text{Si}, ^1\text{H})$ ($n = 2, 3$) across heteroatoms,^{4,5} and it has been shown that this is useful to assess hypervalency of the silicon atom.¹⁶¹ In general the magnitude of $^2J(^{29}\text{Si}, ^{19}\text{F})$ (the sign is negative in most cases; $^2K(^{29}\text{Si}, ^{19}\text{F}) > 0$!) and $^3J(^{29}\text{Si}, ^{19}\text{F})$ values are larger than ^{29}Si – ^1H coupling constants. Trends have been pointed out and numerous data are listed.^{4,5,158,159}

5.3.2. Coupling constants $^{2,3}J(^{29}\text{Si}, ^{13}\text{C})$, $^{2,3}J(^{29}\text{Si}, ^{29}\text{Si})$, $^{2,3}J(^{119}\text{Sn}, ^{29}\text{Si})$ and $^2J(^{207}\text{Pb}, ^{29}\text{Si})$

Coupling constants $^nJ(^{29}\text{Si}, ^{13}\text{C})$ ($n > 1$) across carbon or other elements can be measured either from ^{13}C NMR (^{29}Si satellites) or from ^{29}Si NMR spectra (^{13}C satellites). In most cases, the magnitude of these coupling constants is relatively small (< 10 Hz) which makes it somewhat difficult to observe the satellites in routine NMR spectra.²⁰¹ In alkyn-1-ylsilanes, the absolute magnitude of $^2J(^{29}\text{Si}, \equiv ^{13}\text{C})$ (negative sign; $^2K(^{29}\text{Si}, \equiv ^{13}\text{C}) > 0$!) across the alkynyl carbon atom is > 10 Hz, and it increases with electronegative substituents at the silicon atom, following the trend set by the data $^1J(^{29}\text{Si}, ^{13}\text{C}\equiv)$ (Scheme 25).

The presence of two or more silicon atoms in different surroundings within the same molecule enables to measure coupling constants $^nJ(^{29}\text{Si}, ^{29}\text{Si})$ ($n > 1$) by detection of the ^{29}Si satellites in ^{29}Si NMR spectra (see e.g. Fig. 9 for $n = 2$ and an intervening sp^2 -hybridised carbon). Important applications are obvious for siloxane derivatives¹¹⁶ or silicates (with ^{29}Si enrichment),^{162–164} if it is possible to observe these two-bond couplings for $^{29}\text{Si}-\text{O}-^{29}\text{Si}$ units.

Geminal coupling constants $^2J(^{119}\text{Sn}, ^{29}\text{Si})$ are known for various classes of compounds, and their signs have been determined in some cases (Scheme 26).^{93j,134,165} They can be readily observed either from ^{119}Sn NMR (^{29}Si satellites) or from ^{29}Si NMR spectra ($^{119/117}\text{Sn}$ satellites; see Figs. 9 and 10). Changes in the magnitude of vicinal coupling constants $^3J(^{119}\text{Sn}, ^{29}\text{Si})$ across $\text{C}=\text{C}$ bonds are similar to those observed for analogous values $^3J(^{119}\text{Sn}, ^{13}\text{C})$.^{77c,77d,166}

In methane derivatives, where the carbon atom bears plumbyl and silyl substituents, the combination of 2D $^{13}\text{C}/^1\text{H}$ and $^{29}\text{Si}/^1\text{H}$ HETCOR was used (Fig. 18) in order to determine the sign of the coupling constant $^2J(^{207}\text{Pb}, ^{29}\text{Si})$ (positive; $^2K(^{207}\text{Pb}, ^{29}\text{Si}) < 0$!).¹⁶⁵

$^1J(^{29}\text{Si}, ^{13}\text{C}_{\text{alkyne}})$				$^2J(^{29}\text{Si}, ^{13}\text{C}_{\text{alkyne}})$			
	[Hz]				[Hz]		
120	$\text{Me}_3\text{Si}-\text{C}\equiv\text{C}-\text{Me}$	90.9	15.6	124	$\text{Me}_3\text{Si}-\text{C}\equiv\text{C}-\text{SiCl}_3$	68.2, 160.7 (SiCl_3)	11.2, 25.7 (SiCl_3)
121	$\text{Me}_2\text{Si}(\text{C}\equiv\text{C}-\text{Me})_2$	98.8	19.8	125	$\text{Bu}-\text{C}\equiv\text{C}-\text{SiCl}_3$	172.1	35.3
122	$\text{MeSi}(\text{C}\equiv\text{C}-\text{Me})_3$	112.2	22.8	126	$\text{Me}_3\text{Si}-\text{C}\equiv\text{C}-\text{SiH}_3$	75.1, 87.0 (SiH_3)	12.2, 13.6 (SiH_3)
123	$\text{Si}(\text{C}\equiv\text{C}-\text{Me})_4$	127.0	26.5	127	$\text{Ph}_2(\text{H})\text{Si}-\text{C}\equiv\text{C}-\text{Si}(\text{H})\text{Ph}_2$	83.9	13.1
				128	$\text{Si}_2(\text{C}\equiv\text{C}-\text{Bu})_6$	108.0	21.3

Scheme 25. Selected coupling constants $^1J(^{29}\text{Si}, ^{13}\text{C})$ and $^2J(^{29}\text{Si}, ^{13}\text{C})$ for alkyn-1-ylsilanes; data taken from refs. 85,95,172 and 173.

129	130	131	132	133	134
-25.4	-31.1	-38.0	+92.1	-7.6	-25.4
$^2J(^{119}\text{Sn}, ^{29}\text{Si})$ [Hz]					

Scheme 26. Geminal coupling constants $^2J(^{119}\text{Sn}, ^{29}\text{Si})$ across carbon,^{125,165,169,171} nitrogen^{134c} and phosphorus.¹⁴⁶ The signs have been determined by appropriate 2D HETCOR experiments.

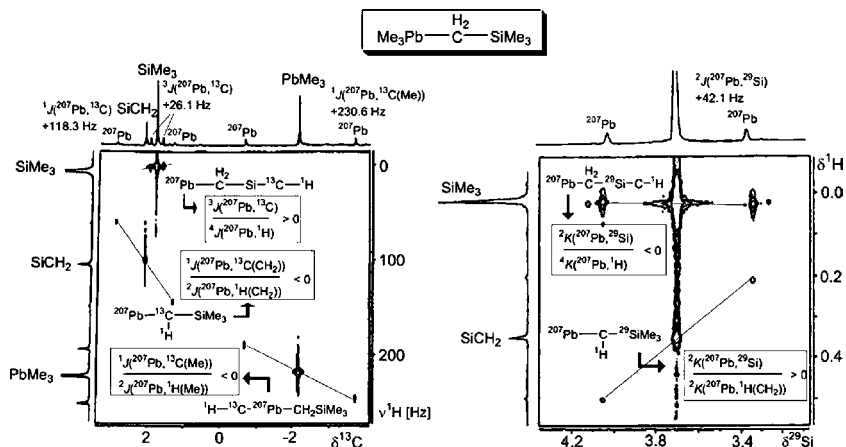
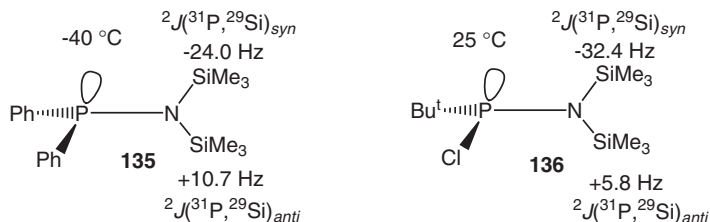


Fig. 18. Contour plots of the 2D 75.7 MHz $^{13}\text{C}/^1\text{H}$ (left) and 59.6 MHz $^{29}\text{Si}/^1\text{H}$ HETCOR (right) experiments carried out for trimethylplumbyl(trimethylsilyl)methane. The relevant cross peaks for satellites have been detected with the tilt in order to compare the signs of various reduced coupling constants as indicated. Since the absolute sign of $^2K(^{207}\text{Pb}, ^1\text{H}) < 0$ is known, other absolute signs of coupling constants become available. Adapted from ref. 165.

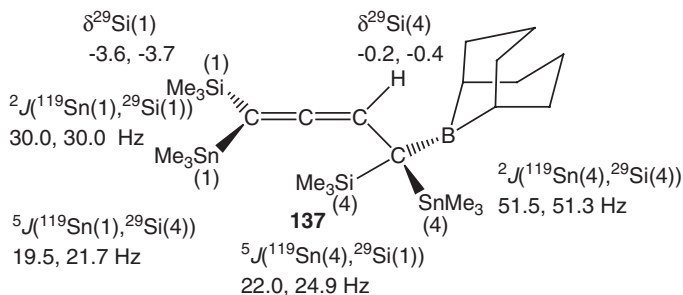
5.3.3. Coupling constants $^2J(^{29}\text{Si}, ^{15}\text{N})$ and $^2J(^{31}\text{P}, ^{29}\text{Si})$

The influence of the lone pair of electrons either on the nitrogen or the phosphorus atom on magnitude and sign of coupling constants is of particular interest,¹³⁶ since it might reveal structural information. This has hardly been exploited in the case of $^2J(^{29}\text{Si}, ^{15}\text{N})$, although the effect will be obvious. Usually the magnitude of $^2J(^{29}\text{Si}, ^{15}\text{N})$ is small and the measurement in natural abundance of the isotopes is not always straightforward. An assignment problem may arise if one- and two-bond couplings are observed at the same time as is the case in aminodisilane derivatives for $^1J(^{29}\text{Si}, ^{15}\text{N})$ and $^2J(^{29}\text{Si}, ^{15}\text{N})$, for which the magnitudes may be similar.¹⁷⁰ In these cases, if the couplings are measured from ^{15}N satellites in the ^{29}Si NMR spectra, the isotope-induced chemical shifts $|\Delta^{14/15}\text{N}(^{29}\text{Si})| \gg |\Delta^{14/15}\text{N}(^{29}\text{Si})|$ are helpful.

In contrast with amines, the inversion at the phosphorus atom in phosphanes is much more hindered and, therefore, the influence of the lone pair of electrons at the phosphorus atom becomes more readily apparent if the substituents prefer a particular orientation. This can be enforced by using bulky substituents (Scheme 27).¹⁶⁷ The effect has first been observed for $^2J(^{31}\text{P}, ^{13}\text{C})$ in aminophosphanes, where the J values are large and positive for a *syn*-orientation and small and negative for *anti*-orientation of the respective N–C bonds and the assumed orientation of the lone electron pair at the phosphorus atom.¹⁶⁸ The analogous stereochemical dependence is observed for $^2J(^{31}\text{P}, \text{N}, ^{29}\text{Si})$ as shown for the *N*-silylaminophosphanes **135** and **136** (Scheme 27).¹⁶⁷



Scheme 27. Stereochemical dependence of sign and magnitude of $^2J(^{31}\text{P}, \text{N}, ^{29}\text{Si})$ in N-silylaminophosphanes. The bulky groups at both phosphorus and nitrogen atoms cause hindered rotation about the P–N bond.^{167b}



Scheme 28. Long-range coupling constants $^5J(^{119}\text{Sn}, ^{29}\text{Si})$, in addition to $^2J(^{119}\text{Sn}, ^{29}\text{Si})$, in an organometallic-substituted allene. Since there are two chiral centres, a mixture of diastereomers is present.¹⁷⁶

5.3.4. Other two- and three-bond coupling constants $^{2,3}J(^{29}\text{Si}, \text{X})$

The multinuclear approach to NMR spectroscopy of organometallic compounds will provide more data on those coupling constants $^{2,3}J(^{29}\text{Si}, \text{X})$ that have not been studied in a systematic way so far (e.g. $\text{X} = ^{77}\text{Se}$, ^{125}Te and many transition metal nuclei).

5.4. Long-range coupling constants $^nJ(^{29}\text{Si}, \text{X})$ with $n > 3$

Spin–spin coupling between ^{29}Si and other nuclei X across four or more bonds is rarely observed, and there are no systematic studies so far. The limited data set prevents its application as a diagnostic criterion for the assignment of structural features. It can be expected that there will be more data for such compounds where a π system and a metal is involved in the transfer of scalar interactions. Thus, in those cases where one finds unusual large ^{119}Sn –X coupling constants, one may also look for measurable ^{29}Si –X spin–spin coupling. An example is $^5J(^{119}\text{Sn}, ^{29}\text{Si})$ for the allene derivative **137**¹⁷⁶ (Scheme 28).

The increasing analytic ability of modern NMR spectroscopy will make use of long-range coupling constants $^nJ(^{29}\text{Si}, \text{X})$ ($n > 3$) for assignment purposes, in particular for $\text{X} = ^1\text{H}$, when gradient-enhanced 2D HMQC experiments can be set up to detect ^{29}Si resonances as a consequence of very small scalar ^{29}Si – ^1H spin–spin coupling.

6. CONCLUSIONS

^{29}Si NMR spectroscopy in solution and, increasingly, in the solid state has become an indispensable tool in the multi-faceted silicon chemistry. The ^{29}Si NMR parameters are ideally suited to complement direct structural information from X-ray crystallography. Moreover they are extremely valuable in the investigation of dynamic properties both intermolecular and intramolecular. This includes the attractive chemistry of hypervalent silicon as well as the fascinating “playground” of low-coordinated silicon compounds. The excellent performance of modern NMR spectrometers has overcome most problems associated with the determination of ^{29}Si NMR parameters. The trend towards a multinuclear approach in NMR spectroscopy is certainly fortified by the availability of ^{29}Si NMR parameters.

REFERENCES

1. R. K. Harris, J. D. Kennedy, W. McFarlane and in, *NMR and the Periodic Table*, In: R. K. Harris, B. E. Mann, eds., Academic Press, London, 1978, pp. 329–377.
2. J. D. Kennedy and W. McFarlane, in *Multinuclear NMR*, J. Mason, ed., Plenum Press, New York, 1987, pp. 305–333.
3. E. A. Williams, in *The Chemistry of Organic Silicon Compounds*, Vol. 1, S. Patai and Z. Rappoport, eds., Wiley, New York, 1989, pp. 511–554.
4. H. C. Marsmann, ^{29}Si NMR spectroscopic results, in, *NMR – Basic Principles and Progress*, Vol. 17, P. Diehl, E. Fluck, and R. Kosfeld, eds., Springer, Berlin, 1981, pp. 65–235.
5. E. Kupce and E. Lukevics, in *Isotopes in Physical and Biomedical Sciences*, Vol. 2, E. Bunel and J. R. Jones, eds., Elsevier, Amsterdam, 1991, pp. 213–295.
6. (a) Y. Takeuchi and T. Takayama, *Chemistry of Organic Silicon Compounds*, Vol. 2, in Z. Rappoport and Y. Apeloig, eds., Wiley, Chichester, 1998, pp. 267–354; (b) D. Cory, A. Wong and W. M. Ritchey, *J. Organomet. Chem.*, 1982, **235**, 277.
7. (a) T. A. Blinka, B. J. Helmer and R. West, *Adv. Organomet. Chem.*, 1984, **23**, 193; (b) E. Kupce and B. Wrackmeyer, in *Advanced Applications of NMR to Organometallic Chemistry – Physical Organometallic Chemistry*, Vol. 1, M. Gielen, R. Willem and B. Wrackmeyer, eds., Wiley, Chichester, 1996, pp. 1–28; (c) M. Veshtort and R. G. Griffin, *ChemPhysChem*, 2004, **5**, 834; (d) M. Mishkovsky and L. Frydman, *ChemPhysChem*, 2004, **5**, 779; (e) E. Kupce, T. Nishida and R. Freeman, *Progr. NMR Spectrosc.*, 2003, **42**, 95.
8. J. Schraml, in *Chemistry of Organic Silicon Compounds*, Vol. 3, Chapter 3, Z. Rappoport and Y. Apeloig, eds., Wiley, Chichester, 2001, pp. 223–339.
9. R. K. Harris, E. D. Becker, S. M. Cabral de menezes, R. Goodfellow and P. Granger, *Pure Appl. Chem.*, 2001, **73**, 1795.
10. (a) G. A. Morris and R. Freeman, *J. Am. Chem. Soc.*, 1979, **101**, 760; (b) G. A. Morris, *J. Am. Chem. Soc.*, 1980, **102**, 428; (c) G. A. Morris, *J. Magn. Reson.*, 1980, **41**, 185; (d) D. P. Burum and R. R. Ernst, *J. Magn. Reson.*, 1980, **39**, 163.
11. (a) D. T. Pegg, D. M. Doddrell, W. M. Brooks and M. R. Bendall, *J. Magn. Reson.*, 1981, **44**, 32; (b) D. T. Pegg, D. M. Doddrell and M. R. Bendall, *J. Chem. Phys.*, 1982, **77**, 2745.
12. L. Müller, *J. Am. Chem. Soc.*, 1979, **101**, 4481. A. Bax, R. H. Griffey and B. L. Hawkins, *J. Magn. Reson.*, 1983, **55**, 301.
13. G. Bodenhausen and D. J. Ruben, *Chem. Phys. Lett.*, 1980, **69**, 185.
14. A. Bax and M. F. Summers, *J. Am. Chem. Soc.*, 1986, **108**, 2093.
15. (a) T. J. Norwood, *Chem. Soc. Rev.*, 1994, 59; (b) S. Berger, *Annu. Rep. NMR Spectrosc.*, 1997, **30**, 137; (c) T. Parella, *Magn. Reson. Chem.*, 1998, **36**, 467; (d) S. Berger and S. Braun, *200 and More NMR Experiments*, Wiley-VCH, Weinheim, 2004.

16. (a) L. E. Kay, P. Keifer and T. Saarinen, *J. Am. Chem. Soc.*, 1992, **114**, 10663; (b) R. Marek, L. Kralik and V. Sklenar, *Tetrahedron Lett*, 1997, **38**, 665.
17. (a) C. A. Fyfe, *Solid State NMR for Chemists*, C.F.C Press, Guelph, ON, 1983; (b) A. -R. Grimmer and B. Blümich, in *Solid State NMR I: Methods*, B. Blümich, ed., Springer, Berlin, 1994, pp. 3–62.
18. (a) M. J. Duer, in *Solid State Organometallic Chemistry – Physical Organometallic Chemistry*, Vol. 2, M. Gielen, R. Willem and B. Wrackmeyer, eds., Wiley, Chichester, 1999, pp. 227–277; (b) F. Babonneau and J. Maquet, *Polyhedron*, 2000, **19**, 315; (c) S. Kuroki, H. Kimura and I. Ando, *Annu. Rep. NMR Spectrosc.*, 2004, **52**, 201; (d) A. E. Aliev and K. D. M. Harris, *Struct. Bond.*, 2004, **108**, 1–53.
19. (a) R. West, J. D. Cavalieri, J. Duchamp and K. W. Zilm, *Phosphorus Sulfur Silicon*, 1994, **93–94**, 213; (b) R. West, J. D. Cavalieri, J. J. Buffy, C. Fry, K. W. Zilm, J. C. Duchamp, M. Kira, T. Iwamoto, T. Müller and Y. Apeloig, *J. Am. Chem. Soc.*, 1997, **119**, 4972; (c) M. Driess, T. Schaller and A. Sebald, *Solid State Nucl. Magn. Reson.*, 1997, **9**, 219; (d) S. Kimura, K. Okita, M. Ichitani, T. Sugimoto, S. Kuroki and I. Ando, *Chem. Mater.*, 2003, **15**, 255; (e) C. Bonhomme, P. Toledano, J. Maquet, J. Livage and L. Bonhomme-Courty, *J. Chem. Soc. Dalton Trans.*, 1997, 1617; (f) X. Helluy, J. Kümmerlen, C. Marschner and A. Sebald, *Monatsh. Chem.*, 1999, **130**, 147; (g) X. Helluy, J. Kümmerlen and A. Sebald, *Organometallics*, 1998, **17**, 5003; (h) X. Helluy, R. Pietschnig and A. Sebald, *Solid State Nucl. Magn. Reson.*, 2003, **24**, 286; (i) P. Bertani, J. Raya and J. Hirschinger, *C. R. Chimie*, 2004, **7**, 363.
20. (a) G. Engelhardt and D. Michel, *High-Resolution Solid State NMR of Silicates and Zeolites*, Wiley, Chichester, 1987; (b) G. Engelhardt, in *Solid State NMR II: Inorganic Matter*, B. Blümich, ed., Springer, Berlin, 1994, pp. 1–29; (c) H. Kollar, A. Wölker, H. Eckert, C. Panz and P. Behrens, *Angew. Chem.*, 1997, **109**, 2939; *Angew. Chem. Int. Ed.*, 1997, **36**, 2823; (e) C. A. Fyfe, D. H. Brouwer, A. R. Lewis and J. -M. Chezeau, *J. Am. Chem. Soc.*, 2001, **123**, 6882.
21. (a) G. W. Wagner, B. K. Na and M. A. Vannice, *J. Phys. Chem.*, 1989, **93**, 5061; (b) J. S. Hartmann, M. F. Richardson, B. L. Sherriff and B. G. Winsborrow, *J. Am. Chem. Soc.*, 1987, **109**, 6059.
22. K. R. Carduner, C. S. Blackwell, W. B. Hammond, F. Reidinger and G. R. Hatfield, *J. Am. Chem. Soc.*, 1990, **112**, 4676.
23. A. Abragam, *The Principles of Nuclear Magnetism*, Oxford University Press, Oxford, 1961, pp. 264–423.
24. (a) R. R. Ernst, G. Bodenhausen and A. Wokaun, *Principles of Nuclear Magnetic Resonance in One and Two Dimensions*, Clarendon Press, Oxford, 1987; (b) M. H. Levitt, *Spin Dynamics*, Wiley-VCH, Weinheim, 2002.
25. J. Hahn, *Z. Naturforsch. Teil B.*, 1980, **35**, 282.
26. V. Mlynarik, *Progr. NMR Spectrosc.*, 1986, **18**, 277.
27. E. Kupce and E. Lukevics, *J. Magn. Reson.*, 1988, **80**, 359.
28. E. Kupce and B. Wrackmeyer, *J. Magn. Reson.*, 1992, **97**, 568.
29. (a) B. Wrackmeyer, E. Kupce, R. Köster and G. Seidel, *Magn. Reson. Chem.*, 1995, **33**, 812; (b) B. Wrackmeyer, G. Kehr, H. Zhou and S. Ali, *Magn. Reson. Chem.*, 1996, **34**, 921.
30. T. Kajiwarra, N. Takeda, T. Sasamori and N. Tokitoh, *Organometallics*, 2004, **23**, 4723.
31. (a) M. Herberhold, T. Schmalz, W. Milius and B. Wrackmeyer, *J. Organomet. Chem.*, 2002, **641**, 173; (b) B. Wrackmeyer, B. Ullmann, R. Kempe and M. Herberhold, *Z. Anorg. Allg. Chem.*, 2005, **631**, 2629.
32. (a) R. Benn, H. Günther, A. Maercker, V. Menger and P. Schmitt, *Angew. Chem.*, 1982; (b) R. Benn, H. Günther, A. Maercker, V. Menger and P. Schmitt, *Angew. Chem. Int.*, 1982; (c) A. Sebald and B. Wrackmeyer, *Spectrochim. Acta*, 1986, **42A**, 1107.
33. C. Corminboeuf, J. Weber and T. Heine, *Chem. Phys. Lett.*, 2002, **357**, 1.
34. D. Auer, C. Strohmann, A. Arbuznikov and M. Kaupp, *Organometallics*, 2003, **22**, 2442.
35. T. Müller, *J. Organomet. Chem.*, 2003, **686**, 251.
36. M. Flock and C. Marschner, *Chem. Eur. J.*, 2002, **8**, 1024.
37. (a) M. Arshadi, D. Johnes, U. Edlund, C. -H. Ottosson and D. Cremer, *J. Am. Chem. Soc.*, 1996, **118**, 5120; (b) G. A. Olah, G. Rasul and G. K. S. Prakash, *J. Organomet. Chem.*, 1996, **521**, 271.

38. M. Kira, S. Ishida, T. Iwamoto and C. Kabuto, *J. Am. Chem. Soc.*, 1999, **121**, 9722.
39. P. Jutzi, U. Holtmann, D. Kanne, C. Krueger, R. Blom, R. Gleiter and I. Hyla-Kryspin, *Chem. Ber.*, 1989, **122**, 1629.
40. B. Wrackmeyer, A. Sebald and L. H. Merwin, *Magn. Reson. Chem.*, 1991, **29**, 260.
41. P. Jutzi, A. Mix, B. Rummel, W. W. Schoeller, B. Neumann and H. -G. Stammer, *Science*, 2004, **305**, 849.
42. (a) M. Denk, R. Lennon, R. Hayashi, R. West, A. V. Belyakov, H. P. Verne, A. Haaland, M. Wagner and N. Metzler, *J. Am. Chem. Soc.*, 1994, **116**, 2691; (b) M. Denk, J. C. Green, N. Metzler and M. Wagner, *J. Chem. Soc. Dalton Trans.*, 1994, 2405; (c) B. Gerhaus, M. F. Lappert, J. Heinicke, R. Boese and D. Blaesser, *Chem. Commun.*, 1995, 1931.
43. G. H. Lee, R. West and T. Müller, *J. Am. Chem. Soc.*, 2003, **125**, 8114.
44. (a) M. Kira, *J. Organomet. Chem.*, 2004, **689**, 4475; (b) N. J. Hill and R. West, *J. Organomet. Chem.*, 2004, **689**, 4165; (c) N. Tokitoh and R. Okazaki, *Coord. Chem. Rev.*, 2000, **210**, 251; (d) M. Haaf, T. A. Schmedake and R. West, *Acc. Chem. Res.*, 2000, **33**, 704.
45. (a) K. -C. Kim, C. A. Reed, D. W. Elliott, L. J. Mueller, F. Tham, L. Lin and J. B. Lambert, *Science*, 2002, **297**, 825; (b) J. B. Lambert and L. Lin, *J. Org. Chem.*, 2001, **66**, 8537; (c) T. Nishinaga, Y. Izukawa and K. Komatsu, *J. Am. Chem. Soc.*, 2000, **122**, 9312.
46. (a) P. Jutzi and E. -A. Bunte, *Angew. Chem.*, 1992, **104**, 1636; (b) P. Jutzi and E. -A. Bunte, *Angew. Chem. Int. Ed.*, 1992, **31**, 1605; (c) M. J. MacLachlan, S. C. Bourke, A. J. Lough and I. Manners, *J. Am. Chem. Soc.*, 2000, **122**, 2126; (d) T. Müller, C. Bauch, M. Ostermeier, M. Bolte and N. Auner, *J. Am. Chem. Soc.*, 2003, **125**, 2158.
47. (a) N. Takeda, H. Suzuki, N. Tokitoh and R. Okazaki, *J. Am. Chem. Soc.*, 1997, **119**, 1456; (b) B. Gehrhuis and M. F. Lappert, *J. Organomet. Chem.*, 2001, **617–618**, 209.
48. (a) B. V. Mork, D. T. Tilley, A. J. Schultz and J. A. Cowan, *J. Am. Chem. Soc.*, 2004, **126**, 10428; (b) P. B. Glaser, P. W. Wanandi and T. D. Tilley, *Organometallics*, 2004, **23**, 693; (c) K. Ueno, S. Asami, N. Watanabe and H. Ogino, *Organometallics*, 2002, **21**, 1326; (d) A. Gadek, A. Kochel and T. Szymanska-Burzar, *Organometallics*, 2003, **22**, 4860; (e) R. West and M. Denk, *Pure Appl. Chem.*, 1996, **68**, 785.
49. (a) D. A. Strauss, S. D. Grumbine and T. D. Tilley, *J. Am. Chem. Soc.*, 1990, **112**, 7801; (b) S. D. Grumbine, T. D. Tilley and A. L. Rheingold, *J. Am. Chem. Soc.*, 1993, **115**, 358; (c) S. D. Grumbine, T. D. Tilley, F. P. Arnold and A. L. Rheingold, *J. Am. Chem. Soc.*, 1993, **115**, 7884; (d) S. D. Grumbine, T. D. Tilley, F. P. Arnold and A. L. Rheingold, *J. Am. Chem. Soc.*, 1994, **116**, 5495; (e) J. C. Peters, J. D. Feldman and T. D. Tilley, *J. Am. Chem. Soc.*, 1999, **121**, 9871; (f) P. W. Wanadi, P. B. Glaser and T. D. Tilley, *J. Am. Chem. Soc.*, 2000, **122**, 972; (g) S. K. Grumbine, G. P. Mitchell, D. A. Straus and T. D. Tilley, *Organometallics*, 1998, **17**, 5607.
50. (a) J. D. Feldman, G. P. Mitchell, J. -O. Nolte and T. D. Tilley, *Can. J. Chem.*, 2003, **81**, 1127; (b) T. Sato, M. Okazaki and H. Tobita, *Chem. Lett.*, 2004, **33**, 868.
51. (a) M. Denk, R. K. Hayashi and R. West, *Chem. Commun.*, 1994, 33; (b) N. Metzler and M. Denk, *Chem. Commun.*, 1996, 23; (c) N. Metzler and M. Denk, *Chem. Commun.*, 1996, 2657; (d) J. M. Dysard and T. D. Tilley, *Organometallics*, 2000, **19**, 4726.
52. (a) M. Weidenbruch, *Eur. J. Inorg. Chem.*, 1999, 373; (b) M. Weidenbruch, *J. Organomet. Chem.*, 2002, **646**, 39; (c) J. Escudie, H. Ranaivonjatovo and L. Rigon, *Chem. Rev.*, 2000, **100**, 3639; (d) L. E. Gusel'nikov, *Coord. Chem. Rev.*, 2003, **244**, 149; (e) M. Weidenbruch, *Angew. Chem.*, 2005, **117**, 518; (f) M. Weidenbruch, *Angew. Chem. Int. Ed.*, 2005, **44**, 514; (g) M. Kira and T. Iwamoto, *J. Organomet. Chem.*, 2000, **611**, 236; (h) P. P. Power, *Chem. Rev.*, 1999, **99**, 3463; (i) R. Koch and M. Weidenbruch, *Angew. Chem.*, 2002, **114**, 1941; (j) R. Koch and M. Weidenbruch, *Angew. Chem. Int. Ed.*, 2002, **41**, 1861; (k) P. P. Power, *Chem. Commun.*, 2003, 2091; (l) M. Y. Lee and A. Sekiguchi, *Organometallics*, 2004, **23**, 2822.
53. Si=C bond; (a) J. J. Buffy, R. West, M. Bendikov and Y. Apeloig, *J. Am. Chem. Soc.*, 2001, **123**, 978; (b) M. Mickoleit, R. Kempe and H. Oehme, *Chem. Eur. J.*, 2001, **7**, 987; (c) M. Pötter, U. Bäumer, M. Mickoleit, R. Kempe and H. Oehme, *J. Organomet. Chem.*, 2001, **621**, 361; (d) B. Wrackmeyer and H. Oehme, *Z. Naturforsch. Teil B.*, 2001, **56**, 947; (e) K. Sakamoto, J. Ogasawara, Y. Kon, T. Sunagawa, C. Kabuto and M. Kira, *Angew. Chem.*, 2002, **114**, 1460;

- (f) K. Sakamoto, J. Ogasawara, Y. Kon, T. Sunagawa, C. Kabuto and M. Kira, *Angew. Chem.*, 2002, **114**, 1460; (g) K. Sakamoto, J. Ogasawara, Y. Kon, T. Sunagawa, C. Kabuto and M. Kira, *Angew. Chem. Int. Ed.*, 2002, **41**, 1402; (h) L. Rigon, H. Ranaivonjatovo, J. Escudie, A. Dubourg and H. -P. Declercq, *Chem. Eur. J.*, 1999, **5**, 774; (i) A. G. Brook, F. Abdesaken, G. Gutekunst and N. Plavac, *Organometallics*, 1982, **1**, 994; (j) G. Delpon-Lacaze, C. de Battisti and C. Couret, *J. Organomet. Chem.*, 1996, **514**, 59; (k) I. S. Ttoulkhonova, I. A. Guzei and R. West, *J. Am. Chem. Soc.*, 2004, **126**, 5336.
54. Si \equiv Si bond:; (a) A. Sekiguchi, R. Kinjo and M. Ichinohe, *Science*, 2004, **305**, 1755; (b) N. Wiberg, S. Kumar, G. Fischer and P. Mayer, *Z. Anorg. Allg. Chem.*, 2004, **530**, 1823.
55. Si = Si bond:; (a) M. Kira, T. Maruyama, C. Kabuto, K. Ebata and H. Sakurai, *Angew. Chem.*, 1994, **106**, 1575; (b) M. Kira, T. Maruyama, C. Kabuto, K. Ebata and H. Sakurai, *Angew. Chem. Int. Ed.*, 1994, **33**, 1489; (c) M. Kira, S. Ohya, T. Iwamoto, M. Ichinohe and C. Kabuto, *Organometallics*, 2000, **19**, 1817; (d) M. Ichinohe, Y. Arai, A. Sekiguchi, N. Takagi and S. Nagase, *Organometallics*, 2001, **20**, 4141; (e) S. Masamune, Y. Eriyama and T. Kawase, *Angew. Chem.*, 1987, **99**, 601; (f) S. Masamune, Y. Eriyama and T. Kawase, *Angew. Chem. Int. Ed.*, 1987, **26**, 584; (g) M. Ichinohe, K. Sanuki, S. Inoue and A. Sekiguchi, *Organometallics*, 2004, **23**, 3088; (h) V. Y. Lee, K. Takanashi, T. Matsuno, M. Ichinohe and A. Sekiguchi, *J. Am. Chem. Soc.*, 2004, **126**, 4758.
56. Si = N bond:; (a) M. Denk, K. Hayashi and R. West, *J. Am. Chem. Soc.*, 1994, **116**, 10813; (b) N. Wiberg, K. Schurz, G. Reber and G. Müller, *Chem. Commun.*, 1986, 591; (c) M. Hesse and U. Klingebiel, *Angew. Chem.*, 1986, **98**, 638; (d) M. Hesse and U. Klingebiel, *Angew. Chem. Int. Ed.*, 1986, **25**, 649.
57. Si = P, Si = As bond:; (a) M. Driess, H. Pritzkow, S. Rell and U. Winkler, *Organometallics*, 1996, **15**, 1745; (b) M. Driess, *Coord. Chem. Rev.*, 1995, **145**, 1.
58. Si = P bond:; (a) A. S. Ionkin and W. J. Marshall, *Organometallics*, 2003, **22**, 4136; (b) C. N. Smit and F. Bickelhaupt, Phosphorus Silicon, *Sulfur*, 1987, **30**, 357.
59. (a) H. G. Horn, *J. Prakt. Chem. Chem. Z.*, 1992, **334**, 201; (b) U. Herzog, *J. Prakt. Chem.*, 2000, **342**, 378; (c) U. Herzog and H. Borrmann, *J. Organomet. Chem.*, 2003, **675**, 42; (d) J. Chojnacki, B. Becker, A. Konitz, M. J. Potrzebowski and W. Wojnowski, *J. Chem. Soc. Dalton Trans.*, 1999, 3063; (e) U. Herzog and H. Borrmann, *J. Organomet. Chem.*, 2004, **689**, 564.
60. (a) U. Herzog and U. Böhme, *Silicon Chem*, 2003, **2**, 77; (b) U. Herzog and H. Borrmann, *J. Organomet. Chem.*, 2003, **681**, 5; (c) U. Herzog and H. Borrmann, *Inorg. Chem. Commun.*, 2003, **6**, 215.
61. (a) U. Herzog, *Main Group Met. Chem.*, 2001, **24**, 31; (b) U. Herzog, H. Lange, H. Borrmann, B. Walfort and H. Lang, *J. Organomet. Chem.*, 2004, **689**, 4909; (c) H. Lange, U. Herzog, H. Borrmann and B. Walfart, *J. Organomet. Chem.*, 2004, **689**, 4897; (d) U. Herzog, U. Böhme, E. Brendler and G. Rheinwald, *J. Organomet. Chem.*, 2001, **630**, 139; (e) U. Herzog and G. Rheinwald, *J. Organomet. Chem.*, 2001, **627**, 23; (f) U. Herzog and G. Rheinwald, *Eur. J. Inorg. Chem.*, 2001, 3107; (g) H. Lange and U. Herzog, *J. Organomet. Chem.*, 2002, **660**, 36.
62. (a) A. H. J. F. de Keijzer, F. J. J. de Kanter, M. Schakel, R. F. Schmitz and G. W. Klumpp, *Angew. Chem.*, 1996, **108**, 1183; (b) , *Angew. Chem. Int. Ed.*, 1996, **35**, 1127.
63. (a) R. Köster, G. Seidel, B. Wrackmeyer, K. Horchler and D. Schlosser, *Angew. Chem.*, 1989, **101**, 945; (b) R. Köster, G. Seidel, B. Wrackmeyer, K. Horchler and D. Schlosser, *Angew. Chem. Int. Ed.*, 1989, **28**, 918.
64. (a) R. Tacke, R. Bertermann, M. Penka and O. Seiler, *Z. Anorg. Allg. Chem.*, 2003, **629**, 2415; (b) O. Seiler, R. Bertermann, N. Buggisch, C. Burschka, M. Penka, D. Tebbe and R. Tacke, *Z. Anorg. Allg. Chem.*, 2003, **629**, 1403; (c) N. Kocher, J. Henn, B. Gostevskii, D. Kost, I. Kalikhman, B. Engels and D. Stalke, *J. Am. Chem. Soc.*, 2004, **126**, 5563.
65. (a) J. Wagler, U. Böhme, E. Brendler and G. Roewer, *Organometallics*, 2005, **24**, 1348; (b) J. Wagler, U. Boehme and G. Roewer, *Organometallics*, 2004, **23**, 6066; (c) I. Kalikhman, O. Girshberg, L. Lameyer, D. Stalke and D. Kost, *Organometallics*, 2000, **19**, 1927; (d) N. V. Timosheva, T. K. Prakasha, A. Chandrasekaran, R. O. Day and R. R. Holmes, *Inorg. Chem.*, 1996, **35**, 3614.

66. (a) A. R. Bassindale, M. Borbaruah, S. J. Glynn, D. J. Parker and P. G. Taylor, *J. Chem. Soc. Perkin Trans. 2*, 1999, 2099; (b) R. Tacke, M. Willeke, M. Penka and Z. Anorg, *Allg. Chem.*, 2001, **627**, 1236; (c) J. H. Iwamiya and G. E. Maciel, *J. Magn. Reson.*, 1991, **92**, 590; (d) E. Gomez, Z. Hernandez, C. Alvarez-Toledano, R. A. Toscano, V. Santes and P. Sharma, *J. Organomet. Chem.*, 2002, **648**, 280; (e) U. Herzog, *Main Group Met. Chem.*, 2001, **24**, 757; (f) D. Gudat, L. M. Daniels and J. G. Verkade, *J. Am. Chem. Soc.*, 1989, **111**, 8520; (g) K. Vojinovic, L. J. McLachlan, S. L. Hinchley, D. W. H. Rankin and N. W. Mitzel, *Chem. Eur. J.*, 2004, **10**, 3033.
67. (a) U. Schubert, *Adv. Organomet. Chem.*, 1990, **30**, 151; (b) J. J. Schneider, *Angew. Chem.*, 1996, **108**, 1132; (c) J. J. Schneider, *Angew. Chem. Int. Ed.*, 1996, **35**, 1068.
68. (a) W. A. Herrmann, N. W. Huber and J. Behm, *Chem. Ber.*, 1992, **125**, 1405; (b) X. Luo, G. J. Kubas, C. J. Burns, J. C. Bryan and C. J. Unkefer, *J. Am. Chem. Soc.*, 1995, **117**, 1159; (c) Y. -J. Kim, S.-C. Lee, K. Osakada, J.-C. Choi and T. Yamamoto, *J. Chem. Soc. Dalton Trans.*, 2000, 417; (d) I. Atheaux, B. Donnadieu, V. Rodriguez, S. Sabo-Etienne, B. Chaudret, K. Hussein and J. -C. Barthelot, *J. Am. Chem. Soc.*, 2000, **122**, 5664; (e) F. P. Lemke, K. J. Galat and W. J. Youngs, *Organometallics*, 1999, **18**, 1419.
69. L. Procopio, P. J. Carroll and D. H. Berry, *J. Am. Chem. Soc.*, 1994, **116**, 177.
70. (a) G. I. Nikonov, L. G. Kuzima, S. F. Vyboishchikov, D. A. Lemenovskii and J. A. K. Howard, *Chem. Eur. J.*, 1999, **5**, 2947; (b) S. R. Dubberley, S. K. Ignatov, N. H. Rees, A. G. Razuvaev, P. Mountford and G. I. Nikonov, *J. Am. Chem. Soc.*, 2003, **125**, 642; (c) G. I. Nikonov, P. Mountford, J. C. Green, M. A. Leech, L. G. Kuzmina, A. G. Razuvaev, N. H. Rees, A. J. Blake, J. A. K. Howard and D. A. Lemenovskii, *J. Chem. Soc. Dalton Trans.*, 2001, 2903; (d) S. K. Ignatov, N. H. Rees, B. R. Tyrrell, S. R. Dubberley, A. G. Razuvaev, P. Mountford and G. I. Nikonov, *Chem. Eur. J.*, 2004, **10**, 4991.
71. F. L. Taw, R. G. Bergman and M. Brookhart, *Organometallics*, 2004, **23**, 886.
72. (a) D. A. Saulys and D. R. Powell, *Organometallics*, 2003, **22**, 407; (b) W. Biffar, H. Nöth, H. Pommerening, R. Schwerthöffer, W. Storch and B. Wrackmeyer, *Chem. Ber.*, 1981, **114**, 49.
73. (a) B. Wrackmeyer, B. Schwarze, D. M. Durran and G. A. Webb, *Magn. Reson. Chem.*, 1995, **33**, 557; (b) B. Wrackmeyer and B. Schwarze, *Z. Anorg. Allg. Chem.*, 1996, **622**, 2048.
74. J. D. Kennedy and W. McFarlane, *J. Chem. Soc. Chem. Commun.*, 1974, 983.
75. (a) D. Christendat, I. S. Butler, D. F. R. Gilson and F. G. Morin, *Can. J. Chem.*, 1999, **77**, 1892; (b) H. -M. Kao and K. -W. Lii, *Inorg. Chem.*, 2002, **41**, 5644.
76. (a) P. J. Watkinson and K. M. Mackay, *J. Organomet. Chem.*, 1984, **275**, 39; (b) A. L. Wilkins, P. J. Watkinson and K. M. Mackay, *J. Chem. Soc. Dalton Trans.*, 1987, 2365; (c) E. Kupce, L. M. Ignatovich and E. Lukevics, *J. Organomet. Chem.*, 1989, **372**, 189.
77. (a) J. D. Kennedy and W. McFarlane, *Rev. Silicon Germanium Tin Lead Comp.*, 1974, **1**, 235; (b) P. J. Smith and A. P. Tupciauskas, *Annu. Rep. NMR Spectrosc.*, 1978, **8**, 291; (c) B. Wrackmeyer, *Annu. Rep. NMR Spectrosc.*, 1985, **16**, 73; (d) B. Wrackmeyer, *Annu. Rep. NMR Spectrosc.*, 1999, **38**, 203.
78. (a) B. Wrackmeyer and K. Horchler, *Annu. Rep. NMR Spectrosc.*, 1990, **22**, 249; (b) B. Wrackmeyer, *Annu. Rep. NMR Spectrosc.*, 2002, **47**, 1.
79. (a) A. C. Olivieri, *Magn. Reson. Chem.*, 1996, **34**, 365; (b) N. A. Davies, R. K. Harris and A. C. Olivieri, *Mol. Phys.*, 1996, **87**, 669.
80. R. C. Boyle, J. T. Mague and M. J. Fink, *J. Am. Chem. Soc.*, 2003, **125**, 3228.
81. (a) S. T. N. Freeman, L. L. Lofton and F. R. Lemke, *Organometallics*, 2002, **21**, 4776; (b) N. M. Yardi and F. R. Lemke, *Organometallics*, 2001, **20**, 5670.
82. D. L. Lichtenberger, *Organometallics*, 2003, **22**, 1599.
83. V. K. Dioumaev, B. R. Yoo, L. J. Procopio, P. J. Carroll and D. H. Berry, *J. Am. Chem. Soc.*, 2003, **125**, 8936.
84. T. Müller, *Angew. Chem.*, 2001, 113, 3123; *Angew. Chem. Int. Ed.*, 40 (2001) 3033.
85. B. Wrackmeyer, W. Milius and O. L. Tok, *Chem. Eur. J.*, 2003, **9**, 4732.
86. B. Wrackmeyer and O. L. Tok, *Magn. Reson. Chem.*, 2002, **40**, 406.
87. (a) A. Naka, J. Ikadi, J. Sakata, I. Miyahara, K. Hirotsu and M. Ishikawa, *Organometallics*, 2004, **23**, 2397; (b) M. Herberhold, A. Ayazi, W. Milius and B. Wrackmeyer, *J. Organomet. Chem.*, 2002,

- 656, 71; (c) B. Wrackmeyer, A. Ayazi, W. Milius and M. Herberhold, *J. Organomet. Chem.*, 2003, **682**, 180.
88. (a) S. -B. Choi and P. Boudjouk, *Tetrahedron Lett.*, 2000, **41**, 6685; (b) S. -B. Choi, P. Boudjouk and P. Wei, *J. Am. Chem. Soc.*, 1998, **120**, 5814; (c) B. Goldfuss, P. v. R. Schleyer and F. Hampel, *Organometallics*, 1996, **15**, 1755; (d) N. A. Troitski, S. N. Tandura, S. P. Kolesnikov, S. -B. Choi and P. Boudjouk, *Main Group Met. Chem.*, 2001, **24**, 1; (e) N. W. Mitzel, H. Schmidbaur, D. W. H. Rankin, B. A. Smart, M. Hofmann and P. v. R. Schleyer, *Inorg. Chem.*, 1997, **36**, 4360; (f) R. Köster, G. Seidel, B. Wrackmeyer and K. Horchler, *Chem. Ber.*, 1990, **123**, 1253; (g) R. Köster, G. Seidel and B. Wrackmeyer, *Chem. Ber.*, 1991, **124**, 1003.
89. (a) R. Köster, G. Seidel, R. Boese and B. Wrackmeyer, *Chem. Ber.*, 1990, **123**, 1013; (b) T. Heinrich, C. Burschka, M. Penka, B. Wagner and R. Tacke, *J. Organomet. Chem.*, 2005, **690**, 33.
90. B. Gehrhus and P. B. Hitchcock, *Organometallics*, 2004, **23**, 2848.
91. (a) H. Tsuji, A. Fukazawa, S. Yamaguchi, A. Toshimitsu and K. Taman, *Organometallics*, 2004, **23**, 3375; (b) T. Hascall, M. J. Drewitt and D. O'Hare, *Chem. Commun.*, 2001, 2600; (c) B. Wrackmeyer, E. V. Klimkina and W. Milius, *Struct. Chem.*, 2004, **15**, 333; (d) B. Wrackmeyer, E. V. Klimkina and W. Milius, *Inorg. Chem. Commun.*, 2004, **7**, 412; (e) R. Köster, G. Seidel, R. Boese and B. Wrackmeyer, *Z. Naturforsch. Teil B.*, 1995, **50**, 439.
92. S. Nagase, *Acc. Chem. Res.*, 1995, **28**, 469.
93. (a) R. Köster, G. Seidel, J. Süß and B. Wrackmeyer, *Chem. Ber.*, 1993, **126**, 1107; (b) R. Köster, G. Seidel, I. Klopp, C. Krüger, G. Kehr, J. Süß and B. Wrackmeyer, *Chem. Ber.*, 1993, **126**, 1385; (c) B. Wrackmeyer, G. Kehr, J. Süß and E. Molla, *J. Organomet. Chem.*, 1998, **562**, 207; (d) B. Wrackmeyer, G. Kehr, J. Süß and E. Molla, *J. Organomet. Chem.*, 1999, **577**, 82; (e) B. Wrackmeyer, O. L. Tok, M. H. Bhatti and S. Ali, *Collect. Czech. Chem. Commun.*, 2002, **67**, 822; (f) B. Wrackmeyer, W. Milius, E. V. Klimkina and Yu. N. Bubnov, *Chem. Eur. J.*, 2001, **7**, 775; (g) B. Wrackmeyer, O. L. Tok, K. Shahid and S. Ali, *Inorg. Chim. Acta.*, 2004, **357**, 1103; (h) B. Wrackmeyer, O. L. Tok, A. Khan and A. Badshah, *Z. Naturforsch. Teil B.*, 2005, **60**, 251; (i) B. Wrackmeyer, O. L. Tok, A. Khan and A. Badshah, *Appl. Organomet. Chem.*, 2005, **19**, 1249.
94. (a) R. Köster, G. Seidel, S. Kersch and B. Wrackmeyer, *Z. Naturforsch. Teil B.*, 1987, **42**, 191; (b) R. Köster, G. Seidel, G. Müller, R. Boese and B. Wrackmeyer, *Chem. Ber.*, 1988, **121**, 1381; (c) R. Köster, G. Seidel, R. Boese and B. Wrackmeyer, *Chem. Ber.*, 1987, **120**, 669; (d) R. Köster, G. Seidel and B. Wrackmeyer, *Chem. Ber.*, 1989, **122**, 1825; (e) B. Wrackmeyer, R. Köster and G. Seidel, *Magn. Reson. Chem.*, 1995, **33**, 493; (f) B. Wrackmeyer, G. Kehr, R. Köster and G. Seidel, *Magn. Reson. Chem.*, 1996, **34**, 625.
95. (a) B. Wrackmeyer, Unpublished results; (b) R. Köster, G. Seidel, R. Boese and B. Wrackmeyer, *Chem. Ber.*, 1988, **121**, 709; (c) R. Köster, G. Seidel, R. Boese and B. Wrackmeyer, *Chem. Ber.*, 1988, **121**, 597; (d) R. Köster, G. Seidel, R. Boese and B. Wrackmeyer, *Chem. Ber.*, 1988, **121**, 1941; (e) R. Köster, G. Seidel, R. Boese and B. Wrackmeyer, *Chem. Ber.*, 1988, **121**, 1955; (f) R. Köster, G. Seidel, B. Wrackmeyer and D. Schlosser, *Chem. Ber.*, 1989, **122**, 2055.
96. B. Wrackmeyer, G. Kehr and J. Süß, *Chem. Ber.*, 1993, **126**, 2221.
97. B. Wrackmeyer, *Chem. Commun.*, 1986, 397.
98. (a) H. Sakurai, H. Sakabo and Y. Nakadaira, *J. Am. Chem. Soc.*, 1982, **104**, 6156; (b) H. Sakurai, Y. Nakadaira, T. Koyama and H. Sakaba, *Chem. Lett.*, 1983, 213; (c) A. Marinetti-Mignani and R. West, *Organometallics*, 1987, **6**, 141.
99. B. Wrackmeyer, W. Milius, M. H. Bhatti and S. Ali, *J. Organomet. Chem.*, 2003, **665**, 196.
100. B. Wrackmeyer and J. Süß, *Z. Naturforsch. Teil B.*, 2002, **57**, 741.
101. B. J. J. Van de Heistee, G. Schat, O. S. Akkerman and F. Bickelhaupt, *Organometallics*, 1986, **5**, 1749.
102. (a) F. Berchier, Y. M. Pai, W. P. Weber and K. L. Servis, *Magn. Reson. Chem.*, 1986, **24**, 679; (b) H. Bürger, R. Eujen and H. C. Marsmann, *Z. Naturforsch. Teil B.*, 1974, **29**, 149.
103. C. J. Jameson, in *Isotopes in the Physical and Biomedical Sciences*, Vol. 2, E. Buncl and J. R. Jones, eds., Elsevier, New York, 1991, pp. 1–54.
104. S. Kersch, A. Sebald and B. Wrackmeyer, *Magn. Reson. Chem.*, 1985, **23**, 514.
105. B. Wrackmeyer, G. Seidel and R. Köster, *Magn. Reson. Chem.*, 2000, **38**, 529.

106. B. Wrackmeyer, H. E. Maisel, W. Milius and M. Herberhold, *J. Organomet. Chem.*, 2003, **680**, 271.
107. D. L. Bryce, R. E. Wasylshen and M. Gee, *J. Phys. Chem. A.*, 2001, **105**, 3633.
108. B. Wrackmeyer, H. E. Maisel, E. Molla, A. Mottalib, A. Badshah, M. H. Bhatti and S. Ali, *Appl. Organomet. Chem.*, 2003, **17**, 465.
109. E. Kupce and B. Wrackmeyer, *J. Magn. Reson.*, 1992, **99**, 338.
110. (a) B. Wrackmeyer, O. L. Tok and Yu. N. Bubnov, *Angew. Chem.*, 1999, **111**, 214; (b) B. Wrackmeyer, O. L. Tok and Yu. N. Bubnov, *Angew. Chem. Int. Ed.*, 1999, **38**, 124.
111. B. Wrackmeyer, K. Shahid and S. Ali, *Appl. Organomet. Chem.*, 2005, **19**, 277.
112. B. Wrackmeyer, Indirect nuclear ^{119}Sn -X spin-spin coupling, in *Physical Organometallic Chemistry, Advanced Applications of NMR to Organometallic Chemistry*, Vol. 1, M. Gielen, R. Willem and B. Wrackmeyer, eds., Wiley, Chichester, 1996, pp. 87–122.
113. (a) K. G. Sharp, P. A. Sutor, E. A. Williams, J. D. Cargioli, T. C. Farrar and K. Ishibitsu, *J. Am. Chem. Soc.*, 1976, **98**, 1977; (b) L. Müller, W. -W. du Mont, F. Ruthe, P. G. Jones and H. C. Marsmann, *J. Organomet. Chem.*, 1999, **579**, 156.
114. K. Hassler, W. Köll and K. Schenzer, *J. Mol. Struct.*, 1995, **348**, 353.
115. (a) H. Söllradl and E. Hengge, *J. Organomet. Chem.*, 1983, **243**, 257; (b) G. Engelhardt, R. Radeaglia, H. Kelling and R. Stendel, *J. Organomet. Chem.*, 1981, **212**, 51.
116. H. B. Yokelson, A. J. Millevolte, B. R. Adams and R. West, *J. Am. Chem. Soc.*, 1987, **109**, 4116.
117. K. Hassler, E. Hengge, F. Schrank and M. Weidenbruch, *Spectrochim. Acta.*, 1991, **47A**, 57.
118. H. A. Bent, *Chem. Rev.*, 1961, **61**, 275.
119. (a) R. H. Contreras, V. Barone, J. C. Facelli and J. E. Peralta, *Annu. Rep. NMR Spectrosc.*, 2003, **51**, 167; (b) T. Helgaker and M. Jaszunski, K. Ruud, *Chem. Rev.*, 1999, **99**, 293; (c) J. Gauss and J. F. Stanton, *Adv. Chem. Phys.*, 2002, **123**, 344; (d) J. Vaara, J. Jokisaari, R. E. Wasylshen and D. I. Bryce, *Progr. NMR Spectrosc.*, 2002, **41**, 233.
120. (a) I. Hermosilla, P. Calle, J. M. G. de la Vega and C. Sieiro, *J. Phys. Chem. A.*, 2005, **109**, 1114; (b) D. Cremer, E. Kraka, A. Wu and W. Lüttke, *ChemPhysChem.*, 2004, **5**, 349; (c) J. Gräfenstein and D. Cremer, *Chem. Phys. Lett.*, 2004, **383**, 332.
121. (a) J. E. Peralta, D. E. Scuseria, J. R. Cheeseman and M. J. Frisch, *Chem. Phys. Lett.*, 2003, **375**, 452; (b) T. Enevoldsen, L. Visscher, T. Saue, H. J. A. Jensen and J. Oddershede, *J. Chem. Phys.*, 2000, **112**, 3493; (c) B. Wrackmeyer, *Z. Naturforsch. Teil B.*, 2003, **58**, 1041; (d) Z. Biedrzycka and K. Kamienska-Trela, *Mol. Phys. Rep.*, 2001, **33**, 50; (e) J. Khandogin and T. Ziegler, *J. Phys. Chem. A.*, 2000, **104**, 113.
122. (a) K. Kamienska-Trela, in *Isotopes in the Physical and Biomedical Sciences*, Vol. 2, E. Buncl and J. R. Jones, eds., Elsevier, Amsterdam, 1991, pp. 297–365; (b) K. Kamienska-Trela, *Annu. Rep. NMR Spectrosc.*, 1995, **30**, 131; (c) V. Wray, *Progr. NMR Spectrosc.*, 1979, **13**, 177; (d) P. E. Hansen, *Org. Magn. Reson.*, 1978, **11**, 215.
123. J. D. Kennedy, W. McFarlane, G. S. Pyne and B. Wrackmeyer, *J. Chem. Soc. Dalton Trans.*, 1975, 386.
124. B. Wrackmeyer and P. Bernatowicz, *J. Organomet. Chem.*, 1999, **579**, 133.
125. E. A. Williams, J. D. Cargioli and P. E. Donahue, *J. Organomet. Chem.*, 1980, **192**, 319.
126. W. Biffar, T. Gasparis-Ebeling, H. Nöth, W. Storch and B. Wrackmeyer, *J. Magn. Reson.*, 1981, **44**, 54.
127. U. Herrmann, M. Schürmann and F. Uhlig, *J. Organomet. Chem.*, 1999, **585**, 211.
128. (a) B. Wrackmeyer and K. Horchler, *Z. Naturforsch. Teil B.*, 1989, **44**, 1195; (b) M. Herberhold, V. Tröbs and B. Wrackmeyer, *J. Organomet. Chem.*, 1997, **541**, 391.
129. A. Gupper and K. Hassler, *Eur. J. Inorg. Chem.*, 2001, 2007.
130. K. Strohfeldt, K. Andres, R. Bertermann, E. Wack, M. Kaupp and C. Strohmann, in *Organosilicon Chemistry V: From Molecules to Materials*, N. Auner and J. Weis, eds., Wiley-VCH, Weinheim, 2003, pp. 329–333.
131. H. Nöth, H. Fußstetter, B. Wrackmeyer and W. McFarlane, *Chem. Ber.*, 1977, **110**, 3172.
132. B. Wrackmeyer and E. Kupce, *Topics of Physical Organometallic Chemistry*, Vol. 4, in M. Gielen, ed., Freund Publishing House, Tel Aviv, 1992, pp. 289–352.

133. B. Wrackmeyer and C. Köhler, *Heteroatom Chem.*, 2005, **16**, 84.
134. (a) B. Wrackmeyer and H. Zhou, *Magn. Reson. Chem.*, 1990, **28**, 1066; (b) B. Wrackmeyer, J. Weidinger, H. Nöth, W. Storch, T. Seifert and M. Vosteen, *Z. Naturforsch. Teil B.*, 1998, **53**, 1494; (c) B. Wrackmeyer, M. Vosteen and W. Storch, *J. Mol. Struct.*, 2002, **602–603**, 177.
135. B. Wrackmeyer, G. Kehr and D. Wettinger, *Magn. Reson. Chem. S.*, 1998, **36**, 157.
136. V. M. S. Gil and W. von Philipsborn, *Magn. Reson. Chem.*, 1989, **27**, 409.
137. (a) A. Allerhand, R. E. Addleman and D. Osman, *J. Am. Chem. Soc.*, 1985, **107**, 5809; (b) A. Allerhand and S. R. Maple, *J. Am. Chem. Soc.*, 1987, **109**, 56; (c) B. Wrackmeyer and E. Kupce, *Z. Naturforsch. Teil B.*, 1998, **53**, 411.
138. L. I. Larina, M. S. Sorokin, A. I. Albanov, V. N. Elokhina, N. I. Protsuk and V. A. Lopyrev, *Magn. Reson. Chem.*, 1998, **36**, 110.
139. (a) B. Wrackmeyer, A. Pedall and J. Weidinger, *Z. Naturforsch. Teil B.*, 2001, **56**, 1009; (b) B. Wrackmeyer, J. Weidinger and W. Milius, *Z. Anorg. Allg. Chem.*, 1998, **624**, 98.
140. (a) B. Wrackmeyer, B. Distler, S. Gerstmann and M. Herberhold, *Z. Naturforsch. Teil B.*, 1993, **48**, 1307; (b) M. Herberhold, S. Gerstmann, W. Milius and B. Wrackmeyer, *Z. Naturforsch. Teil B.*, 1993, **48**, 249.
141. G. Fritz and H. Schäfer, *Z. Anorg. Allg. Chem.*, 1974, **409**, 137.
142. I. J. Colquhoun, J. D. Kennedy, W. McFarlane and R. J. Puddephatt, *J. Chem. Soc. Chem. Commun.*, 1975, 638.
143. S. Berger, S. Braun and H. -O. Kalinowski, *NMR Spectroscopy of the Non-Metallic Elements*, Wiley, Chichester, 1997, p. 945.
144. B. Wrackmeyer, S. Kersch and H. E. Maisel, *Main Group Met. Chem.*, 1998, **21**, 89.
145. (a) G. Pfisterer and H. Dreeskamp, *Ber. Bunsenges. Phys. Chem.*, 1969, **83**, 654; (b) C. H. W. Jones and R. D. Sharma, *J. Organomet. Chem.*, 1984, **268**, 113.
146. B. Wrackmeyer, G. Kehr, K. Bauer and U. Dörfler, *Main. Group Met. Chem.*, 1995, **18**, 1.
147. M. Nakash and M. Goldvaser, *J. Am. Chem. Soc.*, 2004, **126**, 3436.
148. (a) R. B. Johannesen, F. E. Brinckman and T. D. Coyle, *J. Phys. Chem.*, 1968, **72**, 660; (b) R. B. Johannesen, T. C. Farrar, F. E. Brinckman and T. D. Coyle, *J. Chem. Phys.*, 1966, **44**, 962.
149. (a) S. E. Johnson, R. G. Day and R. R. Holmes, *Inorg. Chem.*, 1989, **28**, 3182; (b) R. Damrauer and S. E. Danahey, *Organometallics*, 1986, **5**, 1490.
150. A. R. Bassindale, Y. I. Baukov, M. Borbaruah, S. J. Glynn, V. V. Negrebetsky, D. J. Parker, P. G. Taylor and R. Turtle, *J. Organomet. Chem.*, 2003, **669**, 154.
151. K. Ebata, T. Inada, C. Kabuto and H. Sakurai, *J. Am. Chem. Soc.*, 1994, **116**, 3595.
152. (a) M. J. Albright, T. F. Schaaf, A. K. Hovland and J. P. Oliver, *J. Organomet. Chem.*, 1983, **259**, 37; (b) A. Sebald and B. Wrackmeyer, *Spectrochim. Acta*, 1986, **42**, 1107.
153. E. Hengge, M. Eibl and F. Schrank, *J. Organomet. Chem.*, 1989, **369**, C 29.
154. (a) Y. Nishihara, M. Takemura and K. Osakada, *Organometallics*, 2002, **21**, 825; (b) M. -J. Fernandez, P. M. Balley, P. O. Bentz, J. S. Ricci, T. F. Koetzle and P. M. Maitlis, *J. Am. Chem. Soc.*, 1984, **196**, 5458.
155. (a) K. Ueno, A. Masuko and H. Ogino, *Organometallics*, 1997, **16**, 5023; (b) S. B. Duckett, D. M. Haddleton, S. A. Jackson, R. N. Perutz, M. Poliakoff and R. K. Upmacis, *Organometallics*, 1988, **7**, 1526.
156. H. Yamashita, M. Tanaka and M. Goto, *Organometallics*, 1997, **16**, 4696.
157. (a) R. Pietschnig, *Chem. Commun.*, 2004, 546; (b) M. Westerhausen, R. Löw and W. Schwarz, *J. Organomet. Chem.*, 1996, **513**, 213.
158. (a) J. Schraml, J. Vcelak, G. Engelhardt and V. Chvalovsky, *Coll. Czech. Chem. Commun.*, 1976, **41**, 3758; (b) J. C. Thompson, A. P. G. Wright and W. F. Reynolds, *J. Fluorine Chem.*, 1981, **17**, 509.
159. S. Berger, S. Braun and H.-O. Kalinowski, *NMR Spectroscopy of the Non-Metallic Elements*, Wiley, Chichester, 1997, pp. 623–625.
160. S. Bratovanov, W. Kozminski, J. Fässler, Z. Molnar, D. Nanz and S. Bienz, *Organometallics*, 1997, **16**, 3128.

161. I. Kalikhman, B. Gostevskii, V. Kingston, S. Krivonos, D. Stalke, B. Walfort, T. Kottke, N. Kocher and D. Kost, *Organometallics*, 2004, **23**, 4828.
162. (a) R. K. Harris and C. T. G. Knight, *J. Chem. Soc. Faraday Trans.*, 1983, **79**(2), 1525; (b) R. K. Harris, C. T. G. Knight and W. E. Hull, *J. Am. Chem. Soc.*, 1981, **104**, 1577.
163. (a) R. K. Harris, M. J. O'Connor, E. H. Curzon and O. W. Howarth, *J. Magn. Reson.*, 1984, **57**, 115; (b) C. T. G. Knight, R. J. Kirkpatrick and E. Oldfield, *J. Am. Chem. Soc.*, 1987, **109**, 1632; (c) R. K. Harris, K. A. Kinnear, G. A. Morris, M. J. Stchedroff, A. Samadi-Maybodi and N. Azizi, *Chem. Commun.*, 2001, 2422.
164. (a) R. K. Harris and R. H. Newman, *J. Chem. Soc. Faraday Trans. 2*, 1977, **73**, 1204; (b) E. Bertling-Kampf, M. Heimann, R. Kleibrink and H. C. Marsmann, *Z. Anorg. Allg. Chem.*, 1993, **619**, 1639; (c) C. T. G. Knight and R. K. Harris, *Magn. Reson. Chem.*, 1986, **24**, 872.
165. B. Wrackmeyer, K. Horchler and H. Zhou, *Spectrochim. Acta*, 1990, **46A**, 809.
166. T. N. Mitchell and C. Kummetat, *J. Organomet. Chem.*, 1978, **157**, 275.
167. (a) B. Wrackmeyer, E. Kupce, G. Kehr and J. Schiller, *Magn. Reson. Chem.*, 1992, **30**, 304; (b) B. Wrackmeyer, C. Köhler, W. Milius, R. Contreras, J. M. Grevy and Z. Garcia-Hernández, *Heteroatom Chem*, 2002, **13**, 667; (c) G. Bulloch, R. Keat and D. S. Rycroft, *J. Chem. Soc. Dalton Trans.*, 1978, 764.
168. (a) A. H. Cowley, M. J. S. Dewar, W. R. Jackson and W. B. Jennings, *J. Am. Chem. Soc.*, 1970, **92**, 5206; (b) M. P. Simonnin, R.-M. Lequan and F. J. Wehrli, *Chem. Commun.*, 1972, 1204; (c) K. Barlos, W. McFarlane, H. Nöth and B. Wrackmeyer, *J. Chem. Soc. Dalton Trans.*, 1979, 801.
169. B. Wrackmeyer and H. Zhou, *Spectrochim. Acta*, 1991, **47A**, 849.
170. B. Wrackmeyer, C. Stader and H. Zhou, *Spectrochim. Acta.*, 1989, **45A**, 1101.
171. B. Wrackmeyer, *Polyhedron*, 1986, **5**, 1709.
172. B. Wrackmeyer, O. L. Tok and Yu. N. Bubnov, *Appl. Organomet. Chem.*, 2004, **18**, 43.
173. (a) B. Wrackmeyer, O. L. Tok and A. Badshah, *Z. Naturforsch. Teil B.*, 2003, **58**, 809; (b) B. Wrackmeyer, W. Milius and A. Badshah, *J. Organomet. Chem.*, 2002, **656**, 97.
174. S. C. Chaudhry and D. Kummer, *J. Organomet. Chem.*, 1988, **339**, 241.
175. K. Hassler and S. Seidl, *Monatsh. Chem.*, 1988, **119**, 1241.
176. B. Wrackmeyer, C. Bihlmayer and M. Schilling, *Chem. Ber.*, 1983, **116**, 3182.
177. M. Ichinohe, M. Toyoshima, R. Kinjo and A. Sekiguchi, *J. Am. Chem. Soc.*, 2003, **125**, 13328.
178. B. Wrackmeyer and W. Biffar, *Z. Naturforsch. Teil B.*, 1979, **34**, 1270.
179. Gaussian 03, Revision B.02, M. J. Frisch, G. W. Trucks, H. B. Schlegel, G. E. Scuseria, M. A. Robb, J. R. Cheeseman, J. A. Montgomery Jr., T. Vreven, K. N. Kudin, J. C. Burant, J. M. Millam, S. S. Iyengar, J. Tomasi, V. Barone, B. Mennucci, M. Cossi, G. Scalmani, N. Rega, G. A. Petersson, H. Nakatsuji, M. Hada, M. Ehara, K. Toyota, R. Fukuda, J. Hasegawa, M. Ishida, T. Nakajima, Y. Honda, O. Kitao, H. Nakai, M. Klene, X. Li, J. E. Knox, H. P. Hratchian, J. B. Cross, C. Adamo, J. Jaramillo, R. Gomperts, R. E. Stratmann, O. Yazyev, A. J. Austin, R. Cammi, C. Pomelli, J. W. Ochterski, P. Y. Ayala, K. Morokuma, G. A. Voth, P. Salvador, J. J. Dannenberg, V. G. Zakrzewski, S. Dapprich, A. D. Daniels, M. C. Strain, O. Farkas, D. K. Malick, A. D. Rabuck, K. Raghavachari, J. B. Foresman, J. V. Ortiz, Q. Cui, A. G. Baboul, S. Clifford, J. Cioslowski, B. B. Stefanov, G. Liu, A. Liashenko, P. Piskorz, I. Komaromi, R. L. Martin, D. J. Fox, T. Keith, M. A. Al-Laham, C. Y. Peng, A. Nanayakkara, M. Challacombe, P. M. W. Gill, B. Johnson, W. Chen, M. W. Wong, C. Gonzalez and J. A. Pople, Gaussian Inc., Pittsburgh PA (2003).
180. J. Eppinger, M. Spiegler, W. Hieringer, W. A. Herrmann and R. Anwander, *J. Am. Chem. Soc.*, 2000, **122**, 3080.
181. N. Nakata, R. Izumi, V. Ya. Lee, M. Ichinohe and A. Sekiguchi, *J. Am. Chem. Soc.*, 2004, **126**, 5058.
182. J. Schraml, M. Kivalova, L. Soukopova, V. Blechta and O. Exner, *J. Phys. Org. Chem.*, 1999, **12**, 668.
183. J. Schneider, E. Popowski and H. Reinke, *Z. Anorg. Allg. Chem.*, 2003, **629**, 55.
184. J. B. Lambert, C. Liu and T. Kouliev, *J. Phys. Org. Chem.*, 2002, **15**, 667.
185. J. B. Lambert, C. Liu and S. Keinan, *Org. Biomol. Chem.*, 2003, **1**, 2559.

186. N. W. Mitzel and U. Lohsehand, *Angew. Chem.*, 1997, **109**, 2897.
187. M. K. Denk, K. Hatano and A. J. Lough, *Eur. J. Inorg. Chem.*, 1998, 1067.
188. R. S. Simons, K. J. Galat, J. D. Bradshaw, W. J. Youngs, C. A. Tessier, G. Aullon and S. Alvarez, *J. Organomet. Chem.*, 2001, **628**, 241.
189. C. Cui, S. Köpke, R. Herbst-Irmer, H. W. Roesky, M. Noltemeyer, H. -G. Schmidt and B. Wrackmeyer, *J. Am. Chem. Soc.*, 2001, **123**, 9091.
190. J. Schraml, J. Mindl, J. Roithova, V. Blechta, J. Sykora, L. Soukupova, J. Karban, M. Bartlova and O. Exner, *Organometallics*, 2004, **23**, 2157.
191. T. Fukawa, M. Nakamoto, V. Ya. Lee and A. Sekiguchi, *Organometallics*, 2004, **23**, 2376.
192. M. Horacek, P. Stepnicka, J. Kubista, R. Gyepes and K. Mach, *Organometallics*, 2004, **23**, 3388.
193. C. J. Carmalt, S. J. King, J. D. Mileham, E. Sabir and S. A. Tocher, *Organometallics*, 2004, **23**, 2939.
194. S. R. Bahr and P. Boudjouk, *J. Am. Chem. Soc.*, 1993, **115**, 4514.
195. J. M. Dysard and T. D. Tilley, *Organometallics*, 2001, **20**, 1195.
196. X. Cai, B. Gehrhus, P. B. Hitchcock and M. F. Lappert, *Can. J. Chem.*, 2000, **78**, 1484.
197. G. A. Olah, H. Doggweiler, J. D. Fellberg and S. Frohlich, *J. Org. Chem.*, 1985, **50**, 4847.
198. M. Nanjo, E. Nanjo and K. Mochida, *Eur. J. Inorg. Chem.*, 2004, 2961.
199. A. Kawachi and K. Tamao, *J. Am. Chem. Soc.*, 2000, **121**, 1919.
200. F. J. Zuno-Cruz, A. L. Carrasco and M. J. Rosales-Hoz, *Polyhedron*, 2002, **21**, 1105.
201. (a) E. Kupce and B. Wrackmeyer, *Magn. Reson. Chem.*, 1992, **30**, 950; (b) E. Kupce, E. Lukevics and B. Wrackmeyer, *Magn. Reson. Chem.*, 1994, **32**, 326.

This page intentionally left blank

NMR Studies of *b*-Type Haemoproteins Reconstituted with a Ring-Fluorinated Haem

YASUHIKO YAMAMOTO

Department of Chemistry, University of Tsukuba, Tsukuba 305-8571, Japan

1. Introduction	52
2. Haemoprotein	53
3. ¹⁹ F Labeling of <i>b</i> -Type Haemoprotein Using Reconstitution	53
4. Effect of ¹⁹ F Labeling on the Electronic Structure of Porphyrin	56
5. NMR Spectral Comparison of Haem <i>bis</i> -Cyano Complexes	58
6. Properties of Myoglobins Reconstituted with Fluorinated Haems	61
7. ¹⁹ F NMR Spectral Properties of Myoglobins Reconstituted with Fluorinated Haems	63
8. ¹⁹ F NMR Studies of Myoglobins Reconstituted with Fluorinated Haems	66
8.1 Protein-induced perturbation on the haem electronic structure	66
8.2 Haem orientation	74
8.3 Haem electronic structure in deoxy myoglobin	77
8.4 Acid-alkaline transition in ferric myoglobin	79
8.5 Oxy and carbonmonoxy myoglobins	83
8.6 ¹⁹ F relaxation mechanism	87
9. Concluding Remarks	92
References	93

Taking advantage of fluorine labeling technique for NMR studies of biological systems, combined with the use of ring-fluorinated haems, allows the observation of well-resolved ¹⁹F signals in all of the accessible oxidation, spin, and ligation states of b-type haemoproteins, thus providing potential spectroscopic probes for characterizing the haem active site. An analysis of the effects of the introduced fluorine atom(s) on the nature of the protein often provides valuable information about the protein architecture. The method provides a new means for the detailed characterisation of the haem electronic structure in various b-type haemoproteins in their physiologically active forms and to delineate their structure-function relationships. Sensitivity of the method to the electronic and dynamic properties of the haem active site in the proteins is described.

1. INTRODUCTION

A number of reviews on NMR studies of haemoproteins have already appeared, some^{1–7} comprehensive and others^{8–26} more focused. As described in those reviews, ¹H is by far the most popular nucleus for NMR investigations of the structural and electronic properties of haemoproteins, because of its high detection sensitivity and high natural abundance. However, most ¹H NMR signals resonate in the shift range of –5 to 20 ppm and, consequently, a detailed study of haemoproteins is often hampered by severe signal overlapping, especially as the size of the protein becomes larger. Therefore, with larger proteins, it is necessary to employ stable isotopic labeling in order to resolve and assign the signals of interest.²⁷ When such signals cannot be adduced from the spectrum of the native system, an exogenous fluorine spin can be introduced.^{28–99} By analogy with the use of paramagnetic species,³ the problem of the signal overlapping can easily be overcome. Additionally, an analysis of the effects of the introduced exogenous atom(s) on the nature of the protein often provides valuable information about the structure–function relationship of the protein. Furthermore, in addition to solution ¹⁹F NMR studies, solid-state ¹⁹F NMR methods for studying biologically relevant molecules are also quite promising.^{100–113}

In this chapter, ¹⁹F NMR^{114–122} studies of haemoproteins are reviewed with emphasis on the characterisation of electronic and dynamic properties of the haem active site. Owing to the absence of interfering background signals, the introduction of a fluorine atom(s) into specific site(s) of the proteins facilitates the observation of their signals in various oxidation, spin, and ligation states, which are expected to serve as potential spectroscopic probes for characterizing the electronic nature of the haem active site.^{116,117,121,122} ¹⁹F is a 100% naturally abundant nucleus with nuclear spin $I = 1/2$ and, because of a relatively high gyromagnetic ratio, ¹⁹F NMR is about 83% as sensitive as ¹H NMR. Furthermore, its high gyromagnetic ratio facilitates the observation of dipole connectivity between the ¹⁹F nuclei or between the ¹⁹F and ¹H nuclei, which provides valuable information about molecular structure. The van der Waals radius of a fluorine atom is only slightly larger than that of a hydrogen atom, i.e., 0.135 and 0.11 nm for fluorine and hydrogen, respectively, and hence the introduction of fluorine atom(s) into a molecule of interest is expected to perturb its structure only slightly. However, care should be taken regarding large perturbations in the electronic structure of the molecule, which may be caused by ¹⁹F labeling due to its high electronegativity.

Additionally, because of the wider spectral range for ¹⁹F NMR than ¹H NMR, the former is considerably more sensitive to the local magnetic environment than the latter, providing not only a better resolution of signals, but also a larger dynamic range, namely the superior ability to differentiate between signals arising from various species which are in a dynamic equilibrium. Therefore, it is more likely that individual signals will be resolved on ¹⁹F NMR and the signals will in turn be a sensitive probe for the detailed characterisation of proteins at the atomic level. Furthermore, according to the Q value which relates to the contact coupling constant of a given nucleus with the π spin density of an attached sp^2 carbon, the NMR signal of a fluorine side-chain is much more sensitive to the haem porphyrin

π -system than that of a haem side-chain proton, as manifested, for example, in the Q_{CH}^{H} ($= -75.6 \text{ MHz}^{123}$) and Q_{CF}^{F} ($= -410 \text{ MHz}^{124}$) values. Finally, ^{19}F relaxation exhibits a relatively large chemical shift anisotropy contribution and valuable information about the dynamic nature of the molecules can be inferred through the analysis of ^{19}F relaxation.¹²⁵

2. HAEMOPROTEIN

Because of their ubiquitousness and abundance as well as their many unique physicochemical properties arising primarily from the presence of a haem group, usually an iron–protoporphyrin IX complex (protohaem; structure shown in Fig. 1A), haemoproteins are the most studied group of proteins. Haem is the prosthetic group of a number of proteins possessing remarkably different functions, i.e., oxygen storage or transport proteins (myoglobin (Mb) or haemoglobin(Hb)), electron transfer proteins (cytochromes, etc.), oxidase enzymes (peroxidase, catalase, etc.), and gas sensor proteins (Fix L¹²⁶, Haem AT¹²⁷, etc.). Since these proteins contain the same prosthetic group at their active sites, their functional differences are thought to arise from differences in the way that they interact with the haem.

Mb, a typical haemoprotein, is a monomeric protein with a molecular weight of about 17 kDa, and a single haem is embedded in its protein moiety, which consists of eight helices (A–H). The haem iron is bound to the protein matrix through the proximal His residue (His F8), the 8th residue in the F helix (Fig. 2). In general, the haem iron in Mb is either in the ferrous or ferric state. The numbers of electrons in the 3d orbitals of ferrous and ferric iron are 6 and 5, respectively. Hence, the total spin quantum number S is an integer and half-integer for ferrous and ferric irons, respectively. Depending upon the degree of spin pairing of electrons in the 3d orbitals, ferrous haem iron can have 4, 2, or 0 unpaired electrons, corresponding to $S = 2, 1$, or 0, respectively, and for ferric haem iron $S = 5/2, 3/2$, or $1/2$ with 5, 3, or 1 unpaired electrons, respectively. Based on an octahedral ligand field, the energy levels of the five 3d orbitals of the iron atom are split into two groups in such a way that the energies of the d_{z^2} and $d_{x^2-y^2}$ orbitals are higher than those of the other three orbitals, d_{xy} , d_{yz} , and d_{xz} .⁵ The spin state of a haemoprotein depends on the chemical nature of the ligand. For the ferrous haem iron, the deoxy form (deoxy Mb; Fig. 2B) is penta-coordinated with a high-spin configuration, $S = 2$, and the oxy form (MbO₂) or carbonmonoxy form (MbCO) possesses a low-spin configuration, $S = 0$. On the other hand, the binding of ligands of relatively weak field strength such as H₂O to ferric haem iron gives a high-spin state $S = 5/2$ (met-aquo Mb), and a low-spin state $S = 1/2$ is achieved with a strong ligand such as CN[−] (met-cyano Mb).

3. ^{19}F LABELING OF *b*-TYPE HAEMOPROTEIN USING RECONSTITUTION

A technique called reconstitution, combined with the use of fluorinated haems,^{116,128–133} can be used to introduce fluorine atom(s) selectively and specifically

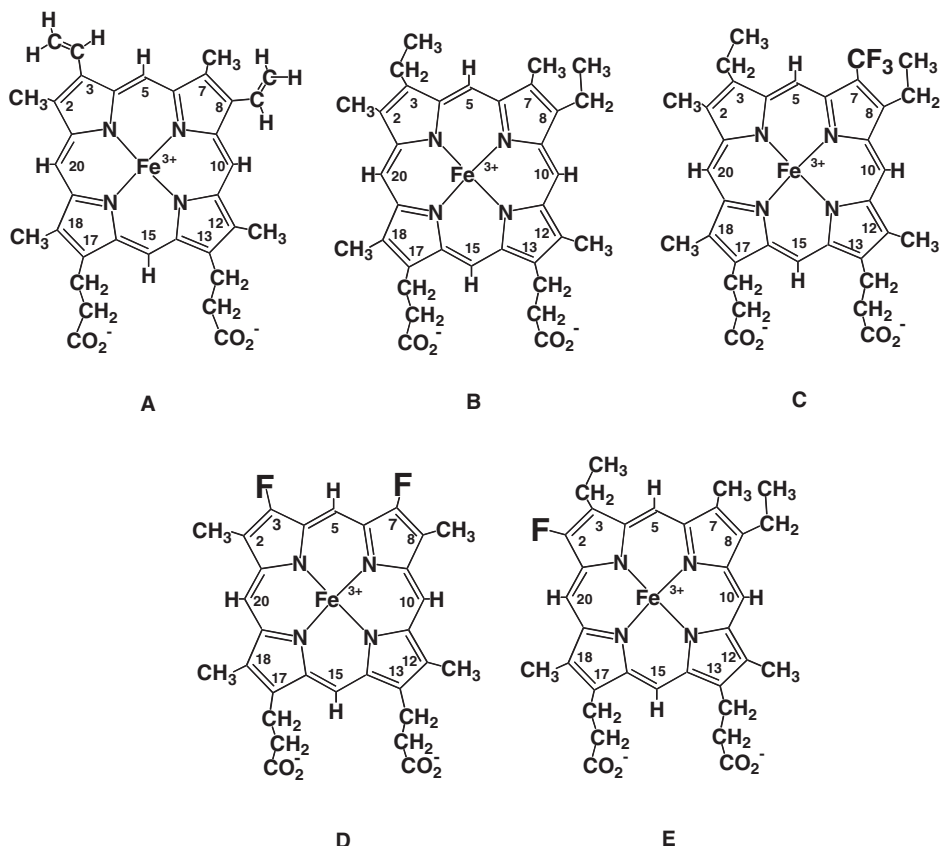


Fig. 1. The structures of protohaem (A), mesohaem (B), 7-PF (13,17-*bis*(2-carboxylatoethyl)-3,8-diethyl-2,12,18-trimethyl-7-trifluoro-methylporphyrinatoiron(III)) (C), 3,7-DF (13,17-*bis*(2-carboxyethyl)-2,8,12,18-tetramethyl-3,7-difluoroporphyrinatoiron(III)) (D), and 2-MF (13,17-*bis*(2-carboxylatoethyl)-3,8-diethyl-2-fluoro-7,12,18-trimethylporphyrinatoiron(III)) (E). Iron-free porphyrins of protohaem and mesohaem are called protoporphyrin and mesoporphyrin, respectively, and those of 7-PF, 3,7-DF, and 2-MF are indicated as 7-PFP, 3,7-DFP, and 2-MFP, respectively.

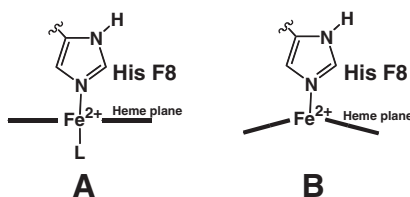
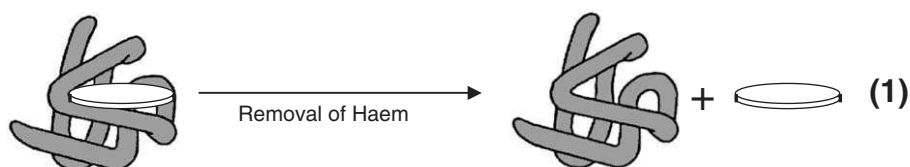


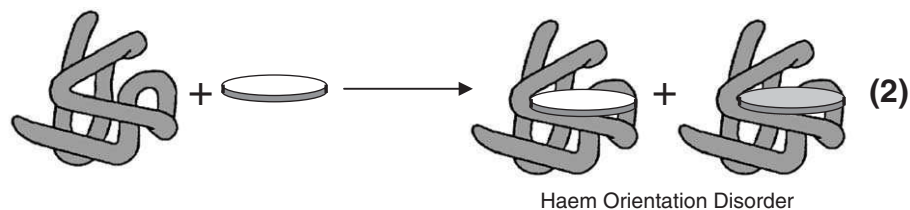
Fig. 2. Schematic representation of haem iron coordination structures in ferrous hexacoordinated (A) and pentacoordinated (B) states. L in A represents an exogenous ligand such as O₂ or CO.

into the active sites of *b*-type haemoproteins. This ^{19}F labeling technique is completely different from that utilized for the ordinary proteins.^{28–32} As schematically illustrated in Fig. 3, haem was extracted from a native protein according to the method described previously.¹³⁴ Since there is no covalent bond

Preparation of apoprotein



Reconstitution



Haem reorientation reaction

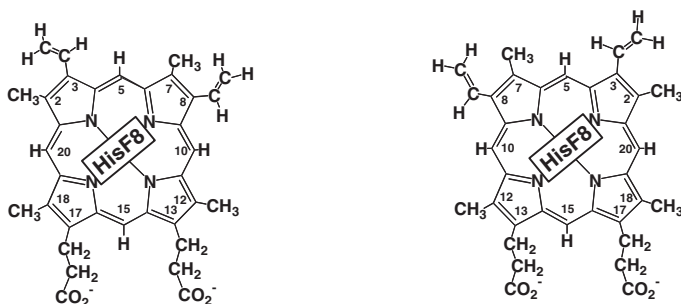
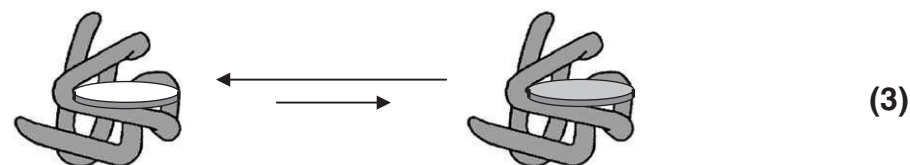


Fig. 3. Schematic representation of preparation of apoprotein (1), reconstitution (2), and haem reorientation reaction (3). Two possible orientations of haem relative to His F8 are illustrated at the bottom; normal form (left) represents the orientation found in the crystal structure of sperm whale Mb¹⁶⁷ and reversed one (right) that with the haem rotated 180° about the 5,15-H *meso*-proton axis from that of the normal form.

between the haem and the protein moiety in a *b*-type haemoprotein, partial unfolding of the protein at pH <2.7 promotes haem release. The released haem is extracted from the apoprotein solution using 2-butanone. Then the apoprotein solution is exhaustively dialyzed against water to remove any 2-butanone distributed. The apoprotein solution is adjusted to neutral pH and then a stoichiometric amount of the haem of interest is mixed in to reconstitute the holoprotein. Using the reconstitution technique, the desired haems and even non-haem compounds can be incorporated into *b*-type haemoproteins.

It has been supposed that the reaction between haem and apoprotein proceeds in a specific manner and yields the native holoprotein instantaneously.^{135,136} Paramagnetic ¹H NMR studies of native and reconstituted Mbs, however, revealed that the reaction of haem with the apoprotein initially yields ~1:1 mixture of two isomers and both components are present in the native protein.^{137–139} The time course of the ¹H NMR spectrum of reconstituted protein demonstrated that one form is converted into the other, thermodynamically favored, form and the rate at which the equilibrium mixture is attained is on the hour or day rather than the millisecond time scale as originally thought. Therefore, the presence of the haem orientation disorder as well as the dynamics of the haem reorientation reaction need to be taken into account in the structural and functional study of reconstituted proteins.

Aiming at incorporation into Mb, several fluorinated haems have been synthesized (Fig. 1C–E).^{114,116,128–133} The initial attempts to incorporate fluorine atom(s) into haem were focused on the substitution of a perfluoromethyl group, CF₃, for the haem methyl group.^{128–132} The introduction of a strongly electron-withdrawing CF₃ group into the porphyrin ring, however, greatly affects the π -system of the haem and has marked effects on the physicochemical properties of haems as well as Mbs reconstituted with such fluorinated haems.^{132,133,140–142} On the other hand, ring fluorination of porphyrin is expected to induce a relatively small perturbation of the haem electronic structure due to a repulsive interaction between electrons in the π -orbitals of the fluorine atom and the π -system of the porphyrin ring, and therefore provides a suitable ¹⁹F NMR probe for the structure study of the haemoproteins.^{114,116,117,120}

4. EFFECT OF ¹⁹F LABELING ON THE ELECTRONIC STRUCTURE OF PORPHYRIN

The electronic structures of the porphyrins were compared through the analysis of the ¹H NMR spectra of their dimethyl ester derivatives (Fig. 4). The fluorinated porphyrins exhibited typical spectral patterns similar to those of protoporphyrin and mesoporphyrin. In general, the shifts of the signals are affected by the ring current of the porphyrin macrocycle and the electronic inductive effect of nearby substituents and the ring-current shift is also modulated by the electronic contribution of the substituents. Since four *meso* protons, namely, protons bound to carbons at the 5, 10, 15, and 20 positions occupy the same orientation relative to the porphyrin macrocycle, in-plane asymmetry of the haem electronic structure is reflected directly

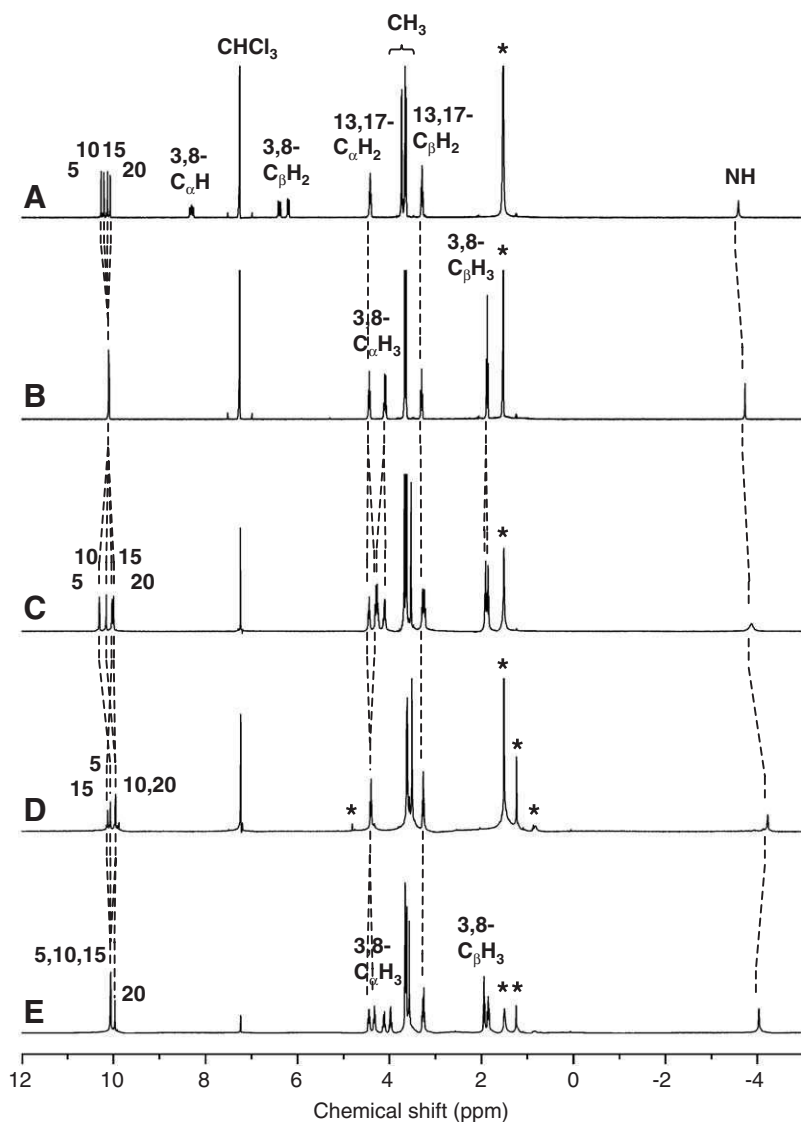


Fig. 4. ^1H NMR spectra of protoporphyrin (A), mesoporphyrin (B), 7-PFP (C), 3,7-DFP (D), and 2-MFP (E) dimethylesters in CDCl_3 at 25°C .

in a spread of haem *meso*-proton signals. The values of 0.20, 0.01, 0.31, 0.17, and 0.09 ppm were observed for the *meso*-proton signals of protoporphyrin, mesoporphyrin, 7-PFP, 3,7-DFP, and 2-MFP, respectively. The smaller spread for mesoporphyrin than protoporphyrin indicated that the substitution of ethyl groups for the vinyl groups of the latter enhances a four-fold symmetry of the porphyrin electronic structure in the former. Furthermore, since mesoporphyrin and 7-PFP

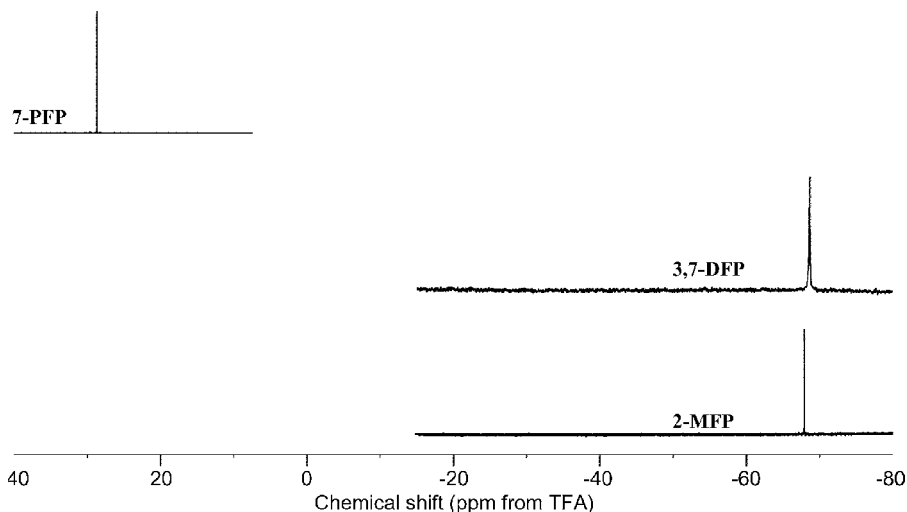


Fig. 5. ^{19}F NMR spectra of 7-PFP, 3,7-DFP, and 2-MFP dimethylesters in CDCl_3 at 25 $^\circ\text{C}$.

possess the same molecular structures except for the 7-position which has a CH_3 group for the former and CF_3 group for the latter, the larger spread for 7-PFP than mesoporphyrin dictated that the four-fold symmetry of the porphyrin electronic structure in mesoporphyrin is distorted by the replacement of CH_3 by CF_3 due to the strong electron-withdrawing property of CF_3 . On the other hand, as observed in the slightly larger spread of the *meso*-proton signals for 2-MFP than for mesoporphyrin, demonstrated that the replacement of a CH_3 group by F induces only a small distortion in the four-fold symmetry of the electronic structure of the porphyrin. Furthermore, 3,7-DFP exhibited the spread comparable to that of protoporphyrin. These results confirmed the substantially smaller perturbation of the ring fluorination, relative to that of the CF_3 substitution, on the porphyrin electronic structure, as expected from the comparative study between benzene derivatives bearing fluoro and CF_3 groups. The ^{19}F NMR spectra of 7-PFP, 3,7-DFP, and 2-MFP are compared in Fig. 5. The signal of 7-PFP resonates at ~ 30 ppm and those of 3,7-DFP and 2-MFP at ~ -70 ppm.

5. NMR SPECTRAL COMPARISON OF HAEM *bis*-CYANO COMPLEXES

The effects of the fluorine substitution on the haem electronic structure were more obvious in the paramagnetic complex. The ^1H NMR spectra of the *bis*-cyano forms of protohemin, mesohaem, 7-PF, 3,7-DF, and 2-MF are compared in Fig. 6. The observed shift (δ_{obs}) of a paramagnetically shifted signal is given by the sum of the diamagnetic (δ_{dia}) and paramagnetic contributions (δ_{para}).¹⁴³ Since the δ_{dia} values of the corresponding proton signals for the haems are expected to be similar to each other, as reflected in the spectra of Fig. 4, the shift difference between the

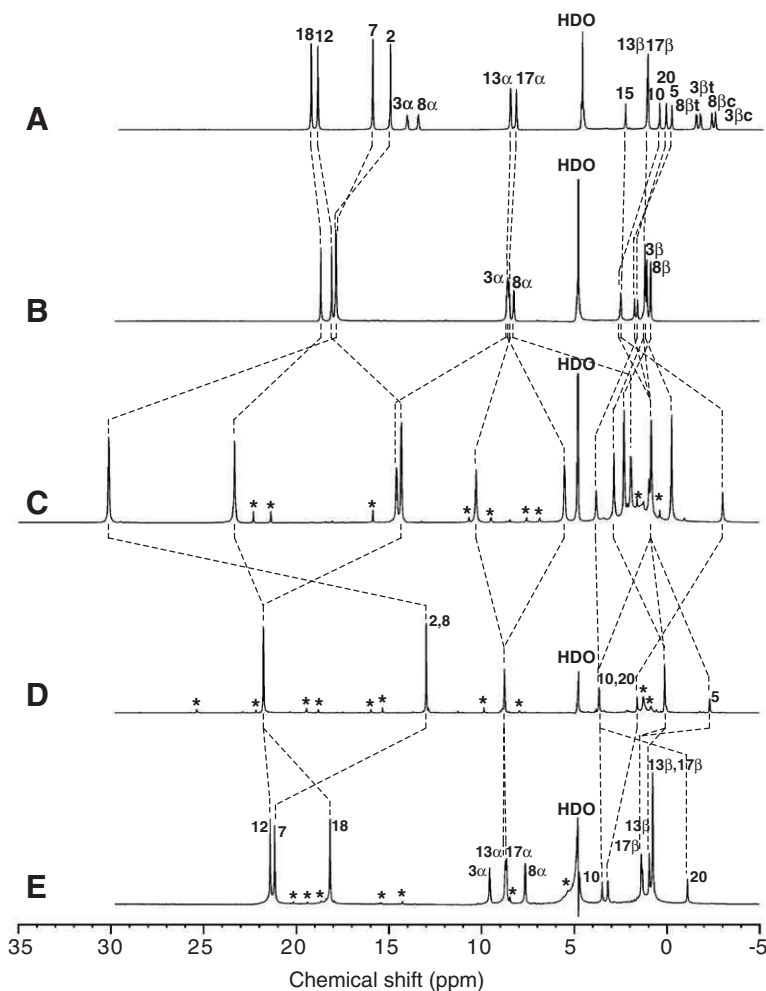


Fig. 6. ^1H NMR spectra of protohaem (A), mesohaem (B), 7-PF (C), 3,7-DF (D), and 2-MF (E) *bis*-cyano complexes in D_2O at pH 8.5 and 25°C .

corresponding signals in the ^1H NMR spectra of the haem *bis*-cyano complexes is largely attributed to δ_{para} , and can be interpreted in terms of the interaction of its proton with an unpaired electron. Since the contact contribution (δ_c) is predominant in the δ_{para} values for haem methyl ^1H NMR signals,² they have been used as a sensitive probe for the haem electronic structure.⁵⁻⁷ The magnitude as well as the pattern of the distortion of the porphyrin π -system from four-fold symmetry due to asymmetric substitutions of haem peripheral side-chains has been shown to be sharply and semiquantitatively manifested in the spread of the haem methyl proton signals of the *bis*-cyano form.² The values of 4.3, 0.8, 15.8, 8.8, and 3.2 ppm were obtained for the spreads of the haem methyl proton signals for protohaem, mesohaem, 7-PF, 3,7-DF, and 2-MF, respectively, at 25°C . The C_2

symmetry of the haem electronic structure of 3,7-DF, about the 5-H–15-H *meso*-proton axis, is manifested in the observation of only seven ^1H NMR signals in the spectrum. The largest spread for 7-PF, together with the large difference in the value between mesohaem and 7-PF, clearly demonstrated the significant effects of the CF_3 substitution on the porphyrin π -system. In contrast to the CF_3 substitution, ring fluorination in 2-MF and 3,7-DF induced relatively small alterations on the haem electronic structure as reflected in the small spreads of the haem methyl proton signals.^{116,117} Consequently, the bonding interaction of the pyrrole nitrogen atoms of porphyrin to iron in 7-PF could be considerably different from those in the other haems due to its porphyrin π -system being significantly distorted from four-fold symmetry.

The ^{19}F NMR spectra of 7-PF, 3,7-DF, and 2-MF *bis*-cyano complexes are compared in Fig. 7. The effect of fluorine substitution on the delocalisation of the unpaired electrons from the iron to the porphyrin π -system is characterised through an analysis of the ^{19}F shift. For example, the δ_{obs} difference of ~ 10 ppm between the signals for 2-MF and 3,7-DF *bis*-cyano complexes, i.e., -27.98 and -18.15 ppm for the former and the latter at 25°C , respectively, can be interpreted as follows. Since their δ_{dia} value are similar to each other, as shown in the spectra of Fig. 5, and the pseudo-contact shift (δ_{pc}) is not significantly influenced by the haem peripheral side-chains, the shift difference is attributed largely to the difference in the δ_{c} shift of the contact term. For the shift of a signal arising from a fluorine atom bound to an aromatic carbon, the shifts due to spin polarization through the σ bond (δ_{sp}) and direct delocalisation through π -orbitals (δ_{dd}) contribute to the δ_{c} value.^{7,9} Both δ_{sp} and δ_{dd} are proportional to the unpaired electron density at the aromatic carbon, to which a fluorine atom is bound, although they are different in sign as well as in

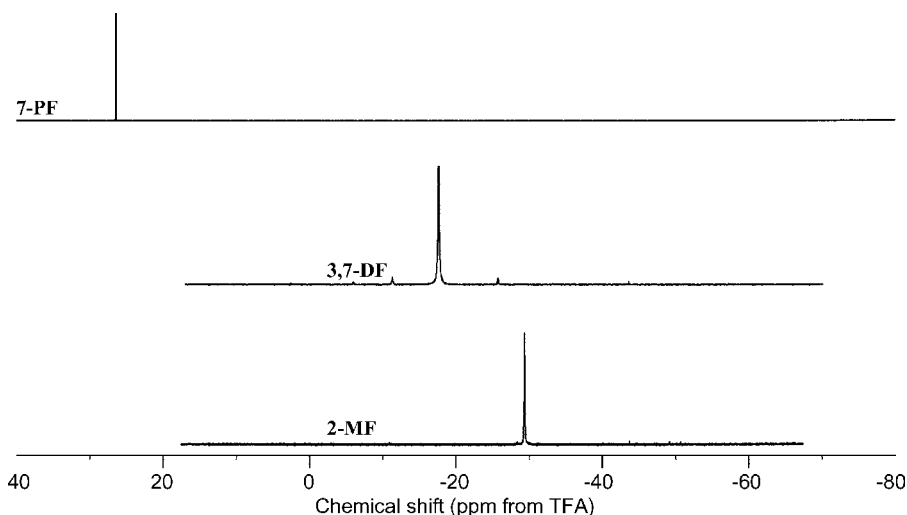


Fig. 7. ^{19}F NMR spectra of 7-PF, 3,7-DF, and 2-MF *bis*-cyano complexes in D_2O at pH 8.5 and 25°C .

magnitude. The positive contact interaction for the observed ^{19}F signals indicates that the δ_{dd} contribution is predominant in the shift of the signal arising from the substituted fluorine atoms. The fact that the δ_{dd} shift for the signal of the 3,7-DF *bis*-cyano complex is larger than that of the 2-MF *bis*-cyano complex indicates that the unpaired electron density delocalised from the iron orbital to the porphyrin π -system is larger for the former complex. This could be attributed to the difference in the number of substituted fluorine atoms. Although the electron-withdrawing ability of the fluorine atom is expected to be diminished by a strong repulsive interaction between the electrons in the π -orbitals of the fluorine atom and in the π -orbital of the carbon atom, when a fluorine atom is bound to an sp^2 carbon,¹⁴⁴ the comparison of the ^{19}F shift between the 2-MF and 3,7-DF *bis*-cyano complexes suggests that the delocalisation of the unpaired electron from the haem iron to the π -system of porphyrin increases with the number of substituted fluorine atoms. Finally, the signal of the 7-PF *bis*-cyano complex resonates at ~ 30 ppm, as if the δ_{para} value almost completely vanishes.

6. PROPERTIES OF MYOGLOBINS RECONSTITUTED WITH FLUORINATED HAEMS

The effects of ^{19}F labeling on Mb structure were examined through the analysis of the ^1H NMR spectra of Mbs reconstituted with 7-PF, 3,7-DF, or 2-MF, Mb(7-PF), Mb(3,7-DF), or Mb(2-MF), respectively. In the ^1H NMR spectrum of MbCO, a single methyl proton signal is resolved in the furthest low-frequency-shifted region, ~ -2.5 ppm, due to the ring-current effect of the haem, and this signal has been assigned to the $\gamma\text{-CH}_3$ proton of the Val E11.¹⁴⁵ The shifts for the Val E11 $\gamma\text{-CH}_3$ proton signals of the reconstituted Mbs are similar with each other (Fig. 8). The similarity in the Val E11 $\gamma\text{-CH}_3$ proton shift among the Mbs strongly suggests that their active site structures are highly alike.

^1H NMR spectra of met-cyano Mbs reconstituted with fluorinated haems are compared in Fig. 9. A low-frequency-shifted methyl proton signal at ~ -3 ppm has been assigned to Ile FG5 $\delta\text{-CH}_3$ proton,¹⁴⁶ and the similarity in the Ile FG5 $\delta\text{-CH}_3$ proton shift among the proteins also suggests that the haem active site structure is not significantly altered by the modification of haem peripheral substituents.

Furthermore, in the ^1H NMR spectra of deoxy Mbs reconstituted with fluorinated haems, haem methyl and His F8, the N_δH proton signals are observed in the shift range of 15–25 and at ~ 75 ppm, respectively (Fig. 10), as observed in the spectrum of native deoxy Mb.^{147,148} These spectral properties also suggest that the introduction of fluorine atoms as haem substituents does not significantly perturb the structure of the haem active site in deoxy Mb. The His F8 N_δH proton shift has been shown to be sensitive to the His–Fe bonding interaction.^{149,150} Due to the haem orientation disorder,^{137–139} two His F8 N_δH proton signals were observed in the spectrum of Mb(7-PF) (Fig. 10). His F8 N_δH proton shifts for the reconstituted Mbs were close to the value for the corresponding signal of native Mb, not only confirming the formation of pentacoordinated haems with the coordination of His

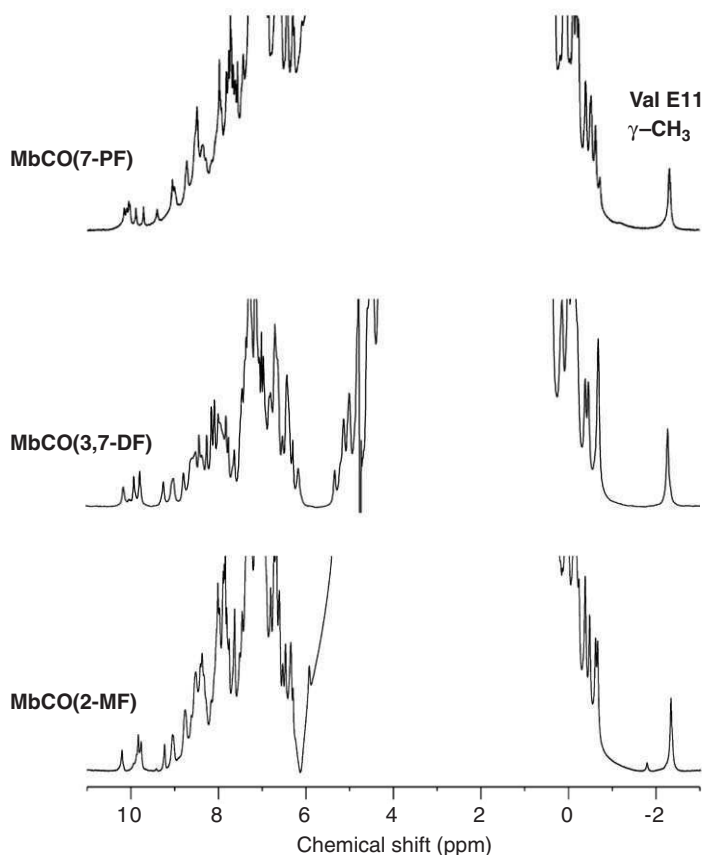


Fig. 8. ^1H NMR spectra of MbCO(7-PF), MbCO(3,7-DF), and MbCO(2-MF) in D_2O at pH 7.0 and 25°C .

F8 in the proteins, but also indicating that the His–Fe bonding interaction was not significantly affected by the alteration of the porphyrin π -system exerted by the substitution of fluorine atom(s) as peripheral side-chain(s).

In contrast to the spectral similarities in MbCO, met-cyano Mb, and deoxy Mb among the reconstituted proteins, paramagnetically shifted signals of met-aquo Mb are largely different from each other (Fig. 11). Despite the sizeable contribution of the δ_{pc} value, due to zero-field splitting, to the δ_{para} value in the system of met-aquo Mb, the contract contribution dominates in the δ_{para} value.¹⁵¹ The large difference in the paramagnetically shifted signals among the protein manifests high sensitivity of these signals to the haem electronic structure, because the similarity in the haem active site structure among the proteins is supported by the fact that the spectra of the other forms of the proteins are highly alike.

Finally, P_{50} values (partial pressure of O_2 when half of the total Mb is oxygenated) of Mb reconstituted with mesohaem (Mb(meso)), Mb(7-PF), Mb(3,7-DF), Mb(2-MF),

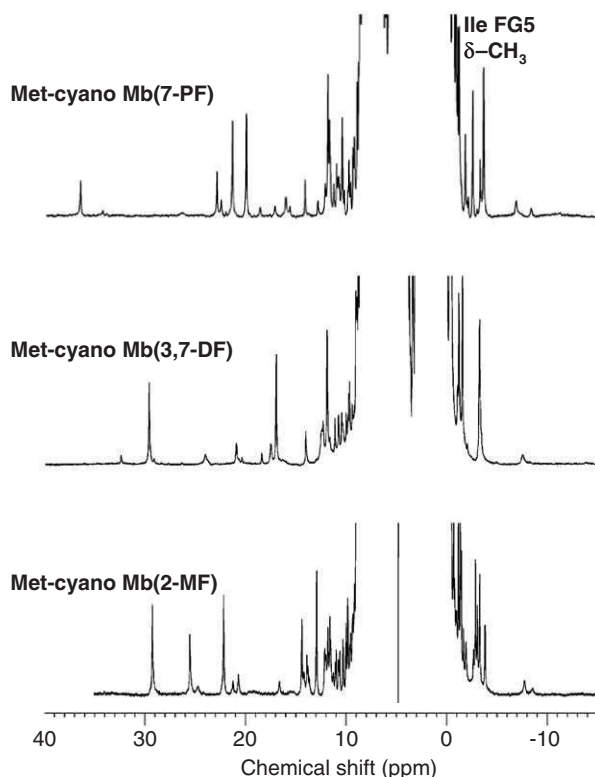


Fig. 9. ^1H NMR spectra of met-cyano Mb(7-PF), met-cyano Mb(3,7-DF), and met-cyano Mb(2-MF) in 90% H_2O /10% D_2O at pH 7.0 and 25 °C.

and native Mb are summarized in Table 1. The oxygen affinity of Mb was not so affected by the haem replacement. These functional similarities among the Mbs confirmed that the haem active site structure was not greatly affected by the haem replacement.

7. ^{19}F NMR SPECTRAL PROPERTIES OF MYOGLOBINS RECONSTITUTED WITH FLUORINATED HAEMS

The ^{19}F NMR spectra of various forms of Mb(7-PF), Mb(3,7-DF), and Mb(2-MF) are illustrated in Figs. 12–14. Two well-separated signals were observed in each spectrum and the unequal intensities of the signals in the spectra of Mb(2-MF) as well as Mb(7-PF) reflected the fractions of the two isomers due to the haem orientation disorder.^{137–139} The shifts and spread of the signals depended crucially upon the type of the ^{19}F labeling, i.e., 7-PF vs. 3,7-DF, 2-MF, and their δ_{para} values tend to exhibit larger low-frequency shifts with an increasing number of unpaired electrons. The spectra of the reconstituted Mbs in five different states are compared

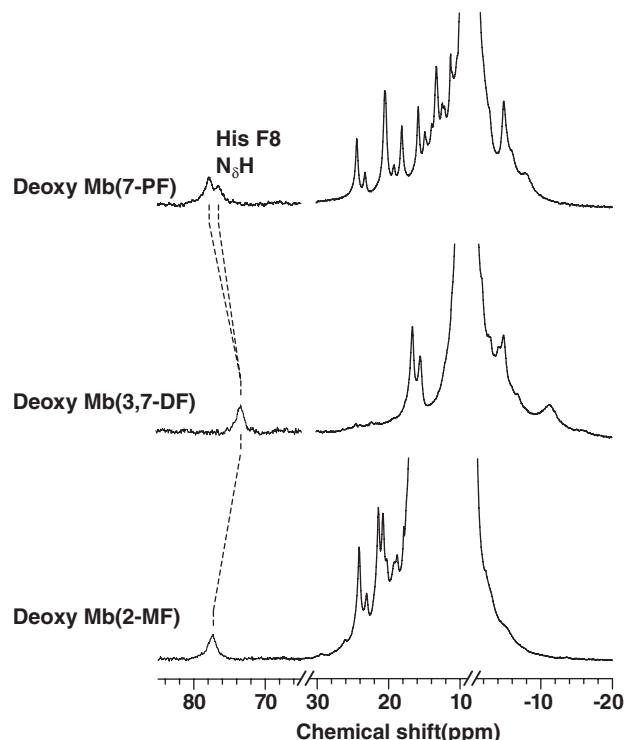


Fig. 10. ^1H NMR spectra of deoxy Mb(7-PF), deoxy Mb(3,7-DF), and deoxy Mb(2-MF) in 90% $\text{H}_2\text{O}/10\%$ D_2O at pH 6.5 and 25 °C.

in Figs. 15–19. The spectral pattern for diamagnetic MbCO and MbO₂ are almost the same as each other with the appearance of the signals at ~ 30 and ~ -70 ppm for Mb(7-PF) and Mb(3,7-DF), Mb(2-MF), respectively.

In the case of met-cyano Mb, the signals for Mb(7-PF) are observed at ~ 20 and ~ 35 ppm and those for Mb(3,7-DF) and Mb(2-MF) at ~ -45 and ~ -15 ppm. The similarity in the spectral pattern between Mb(3,7-DF) and Mb(2-MF) is expected from the similarity in the orientation of the introduced fluorine atom(s), relative to the protein matrix, between the proteins. The ^{19}F signals in the spectrum of deoxy Mb(7-PF) were remarkably narrower than those of deoxy Mb(3,7-DF) and deoxy Mb(2-MF), i.e., the line widths of ^{19}F signals were ~ 200 Hz for deoxy Mb(7-PF) and ~ 700 Hz for deoxy Mb(3,7-DF) and deoxy Mb(2-MF) (Fig. 18). This is in sharp contrast to the ^1H NMR spectra (Fig. 10), which exhibited similar line widths for the corresponding signals among the proteins. These results could be attributed to the difference in the chemical shift anisotropy between CF_3 in 7-PF and fluorine atom(s) covalently bonded to porphyrin in 3,7-DF and 2-MF, because the relaxation mechanism due to chemical shift anisotropy contributes much more significantly to ^{19}F relaxation than to ^1H relaxation.¹²⁵ Additionally, Curie spin relaxation mechanism^{152–155} is considerably reduced for the ^{19}F relaxation of CF_3 in

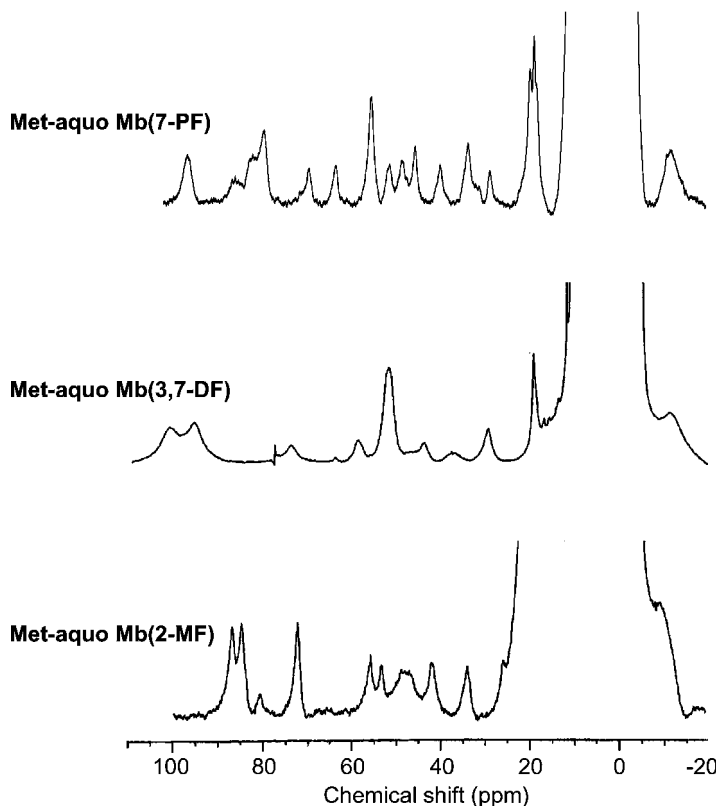


Fig. 11. ^1H NMR spectra of met-aquo Mb(7-PF), met-aquo Mb(3,7-DF), and met-aquo Mb(2-MF) in 90% H_2O /10% D_2O at pH 7.0 and 25 °C.

Table 1. Spectrophotometric and functional properties of reconstituted Mbs

Mb	Absorption maxima (nm) ^a		$\text{p}K_{\text{a}}$ ^b	P_{50} ^c (mmHg)
	Met-aquo	Met-cyano		
Protohaem ^d	408	423	8.84	0.58
Mesohaem	396	411	9.43	0.38
7-PF	399	414	8.57	1.1
3,7-DF	392	407	8.4	0.53
2-MF	393	409	8.54	0.12

^aAt pH 6.0, in 100 mM phosphate buffer, at room temperature.

^b $\text{p}K_{\text{a}}$ of acid–alkaline transition in reconstituted Mb met-aquo, in 10 mM phosphate buffer, at room temperature.

^cPartial pressure of O_2 at $[\text{Mb}] = [\text{MbO}_2]$, in 100 mM phosphate buffer (pH 7.2) at 20 °C.

^dNative Mb.

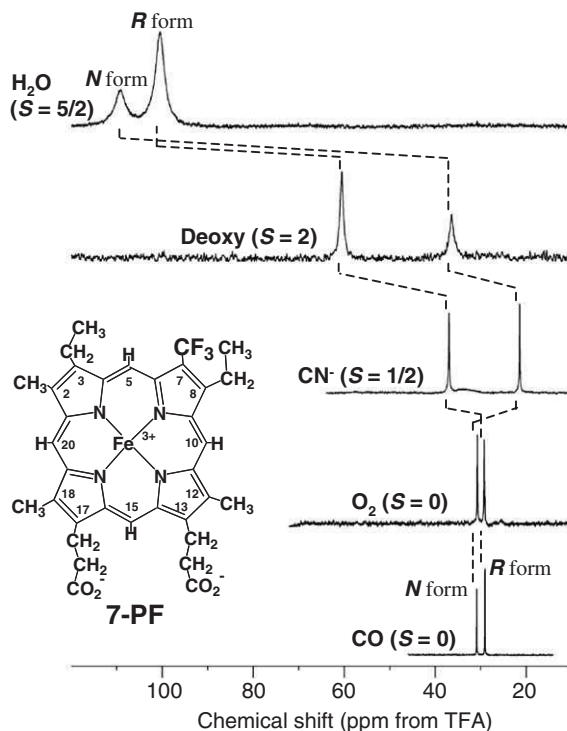


Fig. 12. ^{19}F NMR spectra of Mb(7-PF) with various oxidation, spin, and ligation states of haem iron at pH 7.0 and 25°C .

7-PF, because of its rapid rotation about the C_3 -axis. In the spectra of met-aquo Mbs, the broadening of the ^{19}F signals is further enhanced, especially for Mb(3,7-DF) and Mb(2-MF) (Fig. 19).

The spread of the two signals in the spectra of MbCO and met-cyano Mb are compared with those of 7-PFP, 3,7-DFP, and 2-MFP in Figs. 20–22. Due to the δ_{para} value, the spreads of the signals in the spectra of met-cyano Mbs are increased considerably, compared with those in the spectra of MbCOs. In the case of met-cyano Mb, the orientation of His F8 imidazole, relative to the haem, modulates the haem electronic structure through the interaction of the p_π -orbital of imidazole with the highest energy d_π -orbital where the unpaired electron resides (Fig. 23).^{155–162}

8. ^{19}F NMR STUDIES OF MYOGLOBINS RECONSTITUTED WITH FLUORINATED HAEMS

8.1. Protein-induced perturbation on the haem electronic structure

Rhombic perturbation of haem electronic structure induced by asymmetric interaction of haem with the protein matrix has been thought to be relevant to the

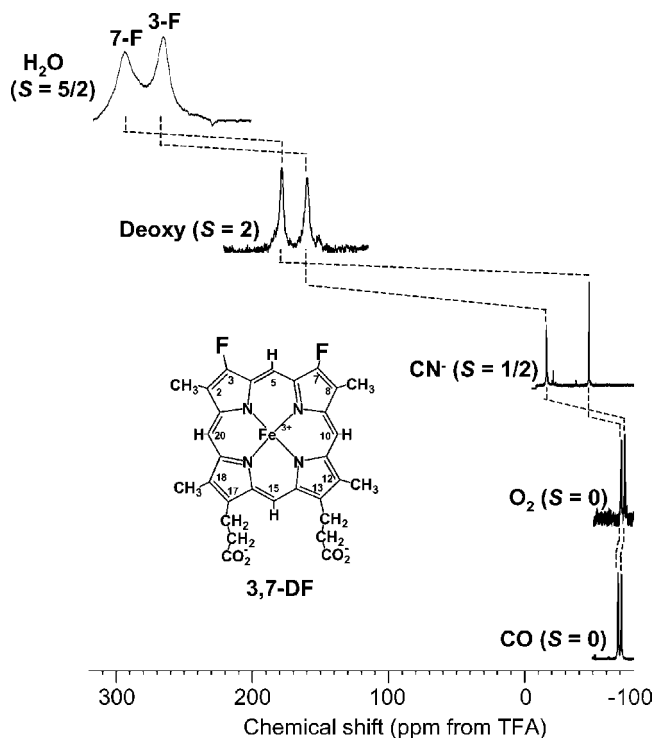


Fig. 13. ^{19}F NMR spectra of Mb(3,7-DF) with various oxidation, spin, and ligation states of haem iron at pH 7.0 and 25 °C.

functional properties of haemoproteins.^{163–166} In-plane asymmetry of the haem electronic structure in the paramagnetic protein is reflected in a distinct spread of haem peripheral methyl proton signals. The analysis of the paramagnetic shift pattern of these signals has provided a qualitative description for the effects of haem–protein interaction on the haem electronic structure.^{155–162} Studies of the haem methyl proton shift patterns of various native and reconstituted haemoproteins have revealed that the orientation of the axial His imidazole plane relative to the nitrogens of the haem^{155–160} and the electronic nature of haem substituents^{161,162} contribute to the rhombicity of the haem electronic structure. One of the difficulties in characterizing the effects of haem–protein interaction on the electronic structure of haem active sites arises from the intrinsic asymmetry in the molecular structure of native haem, iron–protoporphyrin IX. C_2 symmetric 3,7-DF (structure in D of Fig. 1) is useful for a quantitative analysis of the influences of the asymmetric haem–protein interaction on the haem electronic structure.

The C_2 symmetry of the electronic structure of 3,7-DF *bis*-cyano complex along the 5-H–15-H *meso*-proton axis is clearly reflected in its ^1H and ^{19}F NMR spectra (Figs. 4–7). Upon incorporation of 3,7-DF into apoMb, the degeneracy of the two ^{19}F signals is removed, as indicated in Fig. 13. The observation of two signals in the spectrum of MbCO(3,7-DF) is not due to the presence of haem orientation

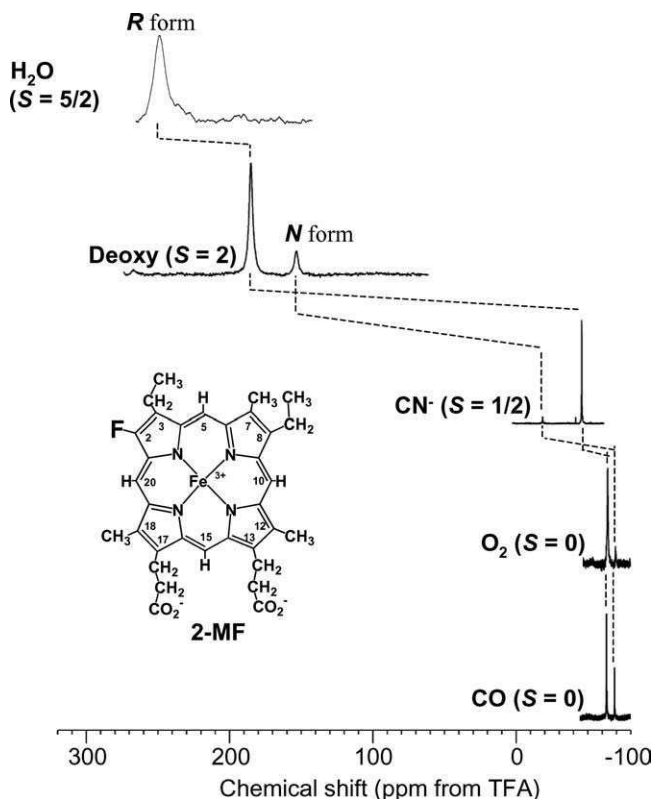


Fig. 14. ^{19}F NMR spectra of Mb(2-MF) with various oxidation, spin, and ligation states of haem iron at pH 7.0 and 25 °C.

isomers,^{137–139} because 3,7-DF possesses a two-fold rotation axis along the 5-H–15-H *meso*-proton axis, but results from the removal of the degeneracy of the magnetic environments for the two fluorine atoms of the haem by haem–protein interaction. The separation of the two signals increases dramatically in the spectrum of met-cyano Mb(3,7-DF). In the spectrum of deoxy Mb(3,7-DF), two signals are resolved and are high-frequency-shifted by >200 ppm relative to those of MbCO(3,7-DF).

A fixed orientation of the axial ligands and/or asymmetry of protein environment could remove the degeneracy of the magnetic environments for the two fluorine atoms of 3,7-DF in the active site of Mb. Since, according to the X-ray structure,¹⁶⁷ the 3- and 7-F atoms of 3,7-DF in Mb are likely to be located at least 0.5 nm away from the centre of gravity of the nearby benzene rings of aromatic amino acid side-chains, the separation of the ^{19}F signals observed in the spectrum of MbCO(7-PF) is attributed largely to an asymmetric bonding interaction between haem iron and the axial His imidazole. This result demonstrates that a fixed orientation of the axial ligands induces a sizeable rhombic perturbation on the electronic structure of the haem in the active site of the haemoprotein.

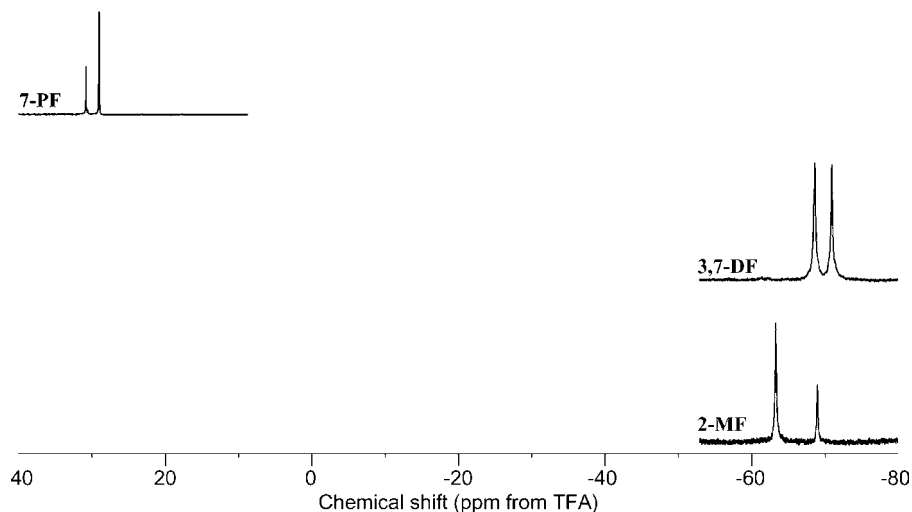


Fig. 15. ^{19}F NMR spectra of MbCO(7-PF), MbCO(3,7-DF), and MbCO(2-MF) at pH 7.0 and 25 °C.

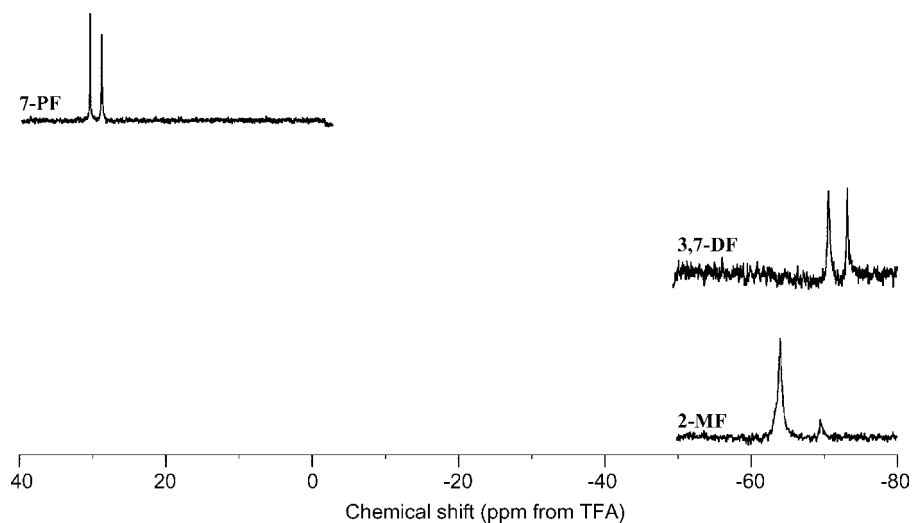


Fig. 16. ^{19}F NMR spectra of MbO₂(7-PF), MbO₂(3,7-DF), and MbO₂(2-MF) at pH 7.0 and 25 °C.

Since studies on met-cyano Mbs reconstituted with a wide variety of chemically modified hemins have demonstrated that the δ_{pc} value due to the localized unpaired electron at iron is essentially independent of haem side-chain substituents,¹⁵⁹ the value of -6 ppm for δ_{pc} of 3- and 7-F signals can be calculated from the equation reported for native met-cyano Mb.¹⁴⁶ Therefore, using the δ_{obs} value of the

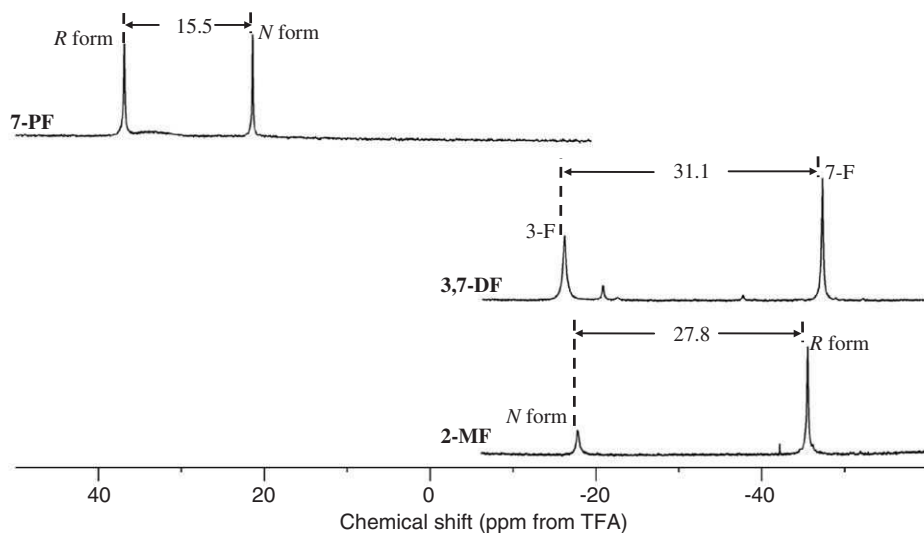


Fig. 17. ^{19}F NMR spectra of met-cyano Mb(7-PF), met-cyano Mb(3,7-DF), and met-cyano Mb(2-MF) at pH 7.0 and 25 °C.

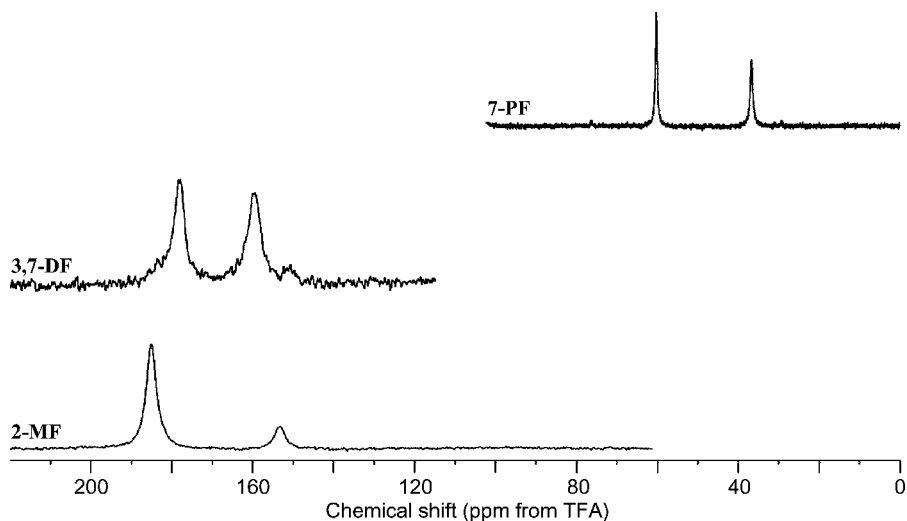


Fig. 18. ^{19}F NMR spectra of deoxy Mb(7-PF), deoxy Mb(3,7-DF), and deoxy Mb(2-MF) at pH 6.5 and 25 °C.

corresponding signals in the spectrum of MbCO as the δ_{dia} value, the δ_{c} values of +58 and +30 ppm for 3- and 7-F signals, respectively, of met-cyano Mb are obtained from their δ_{obs} and the estimated δ_{pc} values. Thus, the shift difference of ~ 30 ppm between the signals of met-cyano Mb(3,7-DF) is attributed to the difference in their δ_{c} values. This result is consistent with the fact that the orbital

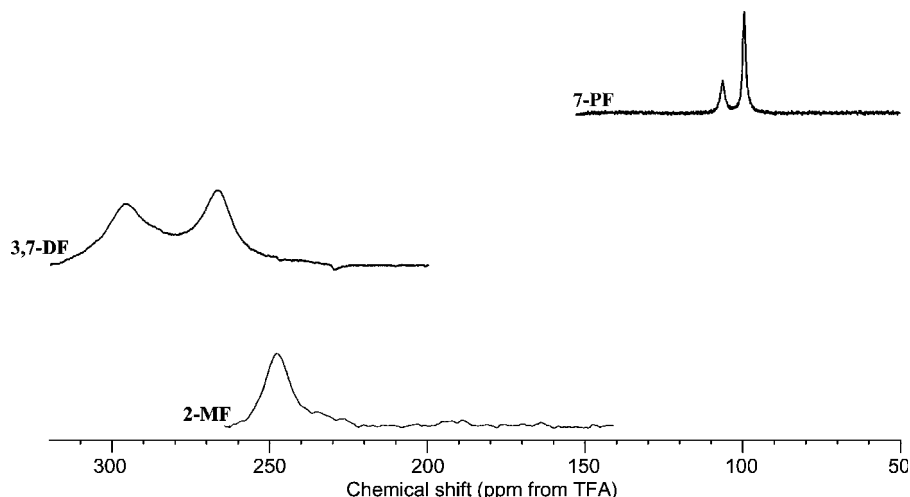


Fig. 19. ^{19}F NMR spectra of met-aquo Mb(7-PF), met-aquo Mb(3,7-DF), and met-aquo Mb(2-MF) at pH 7.0 and 25°C .

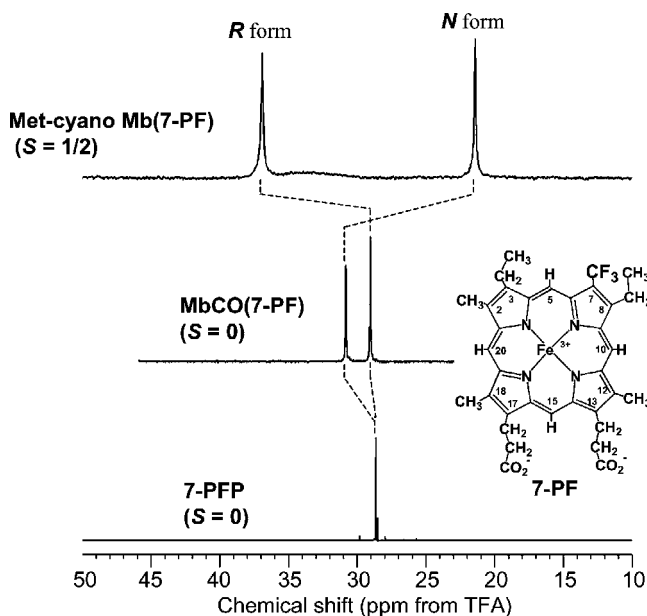


Fig. 20. ^{19}F NMR spectra of 7-PFP dimethylester, MbCO(7-PF), and met-cyano Mb(7-PF) at 25°C .

ground state, $(d_{xy})^2(d_{xz})^2(d_{yz})$, of met-cyano Mb, as expected from the crystallographic orientation of axial His plane with respect to the haem,¹⁶⁷ leads to larger delocalised unpaired electron density in pyrrole I than in pyrrole II (Fig. 23). It has been shown that chemical functionality of the haem periphery contributes to raising

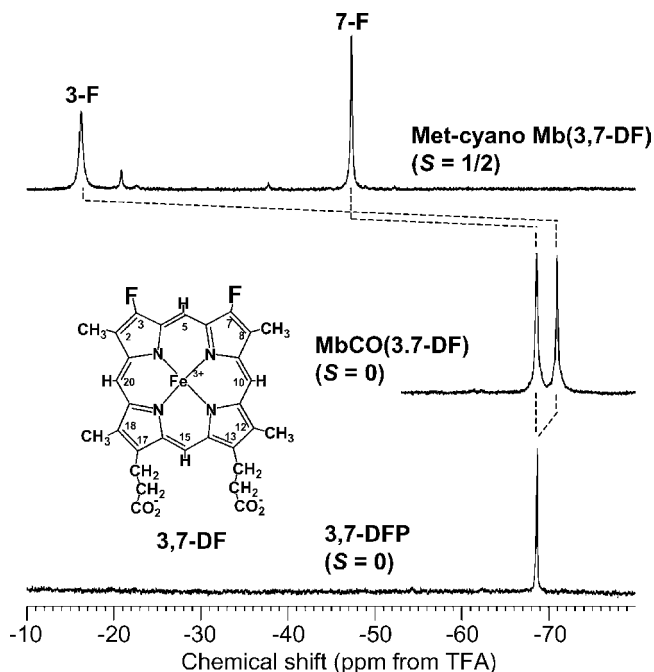


Fig. 21. ^{19}F NMR spectra of 3,7-DFP dimethylester, MbCO(3,7-DF), and met-cyano Mb(3,7-DF) at 25 °C.

the orbital degeneracy of the haem iron and that such influences can account for orbital ground states that are not necessarily aligned with the axial His orientation.¹⁶⁰ This result demonstrated the contribution of asymmetric Fe–His bonding to the in-plane asymmetry of the haem electronic structure. Furthermore, the estimated δ_c values indicate that the unpaired electron density at the pyrrole carbon to which the 3-F atom is bound is almost twice as large as that at the carbon to which 7-F is bound. The remarkable difference in line width between the two signals can be qualitatively interpreted in terms of a ligand-centred dipolar contribution, which accounts for modulation of the dipole–dipole interaction between the nucleus and the delocalised unpaired electron spins in both the fluorine and the pyrrole carbon to which fluorine is bonded, and the contact hyperfine coupling interaction.¹⁶⁸

In spite of its physiological importance, only a few NMR studies have been reported on the properties of the haem active site in deoxy Mb and deoxy Hb.^{147,148,169–175} This is due to the poor resolution of the signals and difficulties in signal assignments.¹⁴⁷ Non-degeneracy of the two signals in the ^{19}F NMR spectrum of the reconstituted deoxy Mb clearly demonstrates a protein-induced rhombic perturbation on the haem electronic structure in the ferrous high-spin complex. The high-frequency shift of >200 ppm observed for the ^{19}F signals is predominantly attributed to δ_c , although a small pseudo-contact contribution exists due to

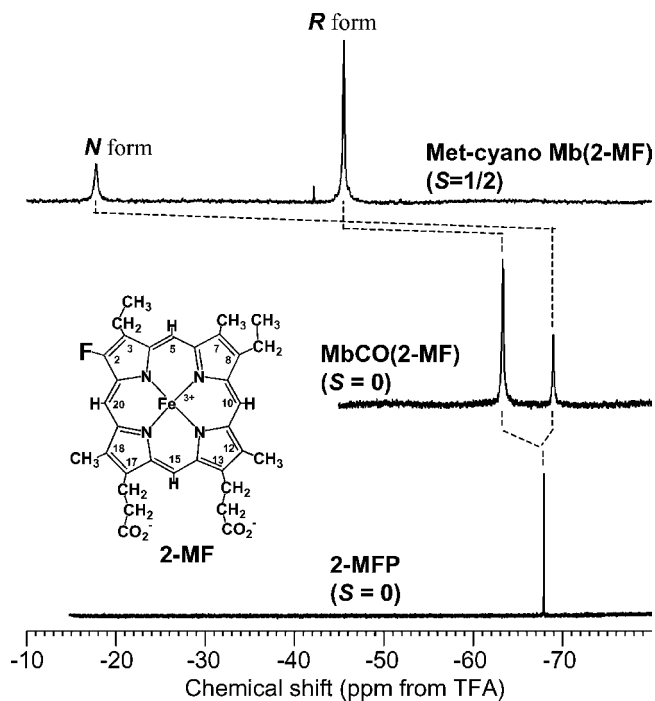


Fig. 22. ^{19}F NMR spectra of 2-MFP dimethylester, MbCO(2-MF), and met-cyano Mb(2-MF) at 25°C.

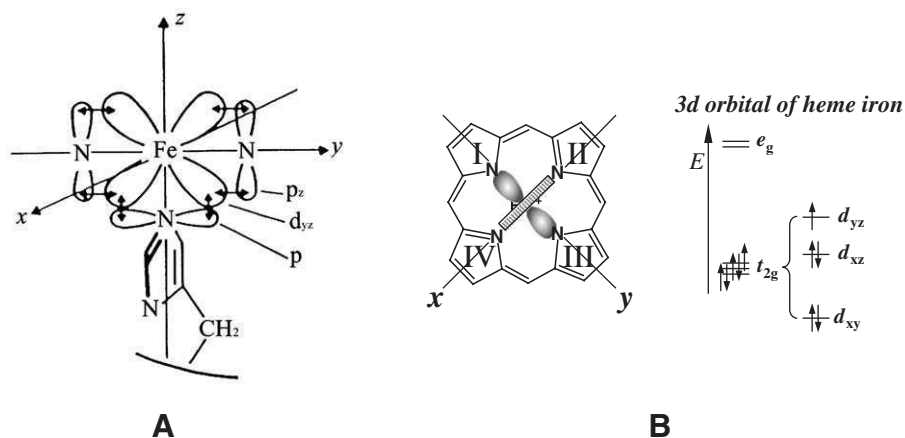


Fig. 23. Delocalisation of unpaired electron in haem (A) and the effect of the proximal histidine imidazole orientation on the haem electronic structure (B).

magnetic anisotropy arising from zero-field splitting.¹⁴⁸ The fact that the shift difference between the ^{19}F signals in deoxy Mb is smaller than that in met-cyano Mb, despite a much larger high-frequency shift in the former, would be interpreted as indicative of the predominance of the σ -delocalisation mechanism over a π -mechanism for a delocalisation of the unpaired electron. This result has been predicted by the conclusion deduced from model compound studies that, in the case of the ferrous high-spin state, where both σ bonding $d_{x^2-y^2}$ and π bonding d_{xz} and d_{yz} orbitals are singly occupied (Fig. 24), the σ -mechanism is predominant for the haem side-chains.¹⁷⁶

As has been shown in the ^1H NMR spectra of the ferric high-spin complex, the σ spin delocalisation contributes predominantly to the δ_c value, although the contribution from the π spin delocalisation cannot be neglected.^{2,176} The fact that the shift difference between 3- and 7-F signals is smaller for met-aquo Mb than for met-cyano Mb could be interpreted as indicative of the predominance of the σ spin delocalisation contribution to the δ_c value in the former complex.

8.2. Haem orientation

The nature of the molecular recognition between the haem and proteins in *b*-type haemoproteins is not sufficiently specific to force a single orientation of the prosthetic group within its protein matrix.⁶ Although their crystal structures have invariably shown that the haem possesses a unique orientation within the protein, a solution NMR study has clearly demonstrated that the haem in these proteins is seated in two different orientations that differ by 180° rotation of the haem plane, about the 5,15-H *meso*-proton axis, relative to the protein matrix (Fig. 3), and that the haem orientational disorder is present in almost all native *b*-type haemoproteins.^{137–139} The dominant component in Mb possesses the same haem orientation

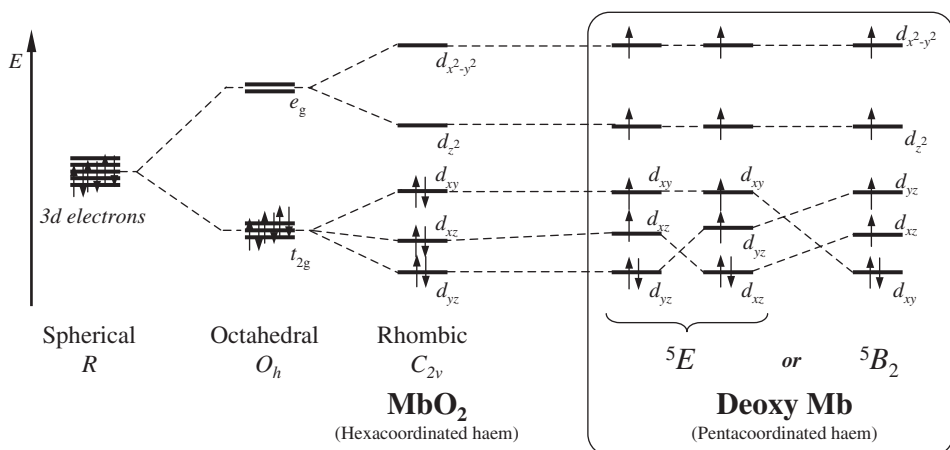


Fig. 24. The iron 3d electrons splitting patterns for different spin states.

as found in the crystal structure, called the normal form; a protein with a reversed haem orientation is called the reversed form.

The functional consequence of the haem orientation appears to be dependent on the particular protein. The influence of the haem orientation on the O₂ affinity is negligible in sperm whale Mb,¹⁷⁷ but is relatively significant in insect (*Chironomus thummi thummi*) Hbs.¹⁶³ Similarly, the Bohr effect of the insect Hb,¹⁶³ the autoxidation rate of oxy-Mb¹⁷⁸ and tetrameric human adult oxy-Hb,¹⁷⁹ the redox potential of ferricytochrome *b*₅,¹⁶⁴ and the thermal spin equilibrium for both met-azido insect Hb¹⁸⁰ and ferricytochrome *b*₅¹⁸¹ have been reported to be influenced by the haem orientation. Thus, an understanding of the molecular mechanism underlying the modulation of functional properties for *b*-type haemoproteins through the interaction of the prosthetic haem periphery with the protein matrix demands detailed scrutiny of the influence of the haem orientation on the molecular and electronic structures of the haem-active site.

Although the haem orientation disorder in *b*-type haemoproteins is most readily detected by ¹H NMR spectroscopy, the characterisation of the effect of the haem orientation on the electronic structure of the active site in physiologically relevant forms of the protein is often hampered by the resolution of the signals.^{138,179} Taking advantage of the utility of ¹⁹F NMR spectroscopy, combined with the use of ring-fluorinated haems, allows the observation of well-resolved ¹⁹F signals in all of the accessible oxidation, spin, and ligation states of the protein, which provide potential spectroscopic probes for characterizing the haem active site.¹¹⁶

As shown in Fig. 14, the reconstitution of apoMb with 2-MF results in the splitting of the ¹⁹F signal into two peaks due to the haem orientation disorder. Assuming that the haem-protein interaction in Mb(2-MF) is similar to that in the crystal structure of native Mb,¹⁶⁷ the fluorine atoms in the normal and reversed forms are expected to be located at ~1.18 and ~0.40 nm, respectively, from the Ile FG5 δ-CH₃ proton. The intramolecular NOE connectivity between fluorine and Ile FG5 δ-CH₃ proton in Mb(2-MF) unequivocally demonstrate that the reverse orientation of the haem is predominant in the protein. The Mb(meso) is favored in the normal form with the equilibrium ratio of 5.5 ± 0.6 between the normal and the reversed forms.¹³⁹ Consequently, differences in the physicochemical properties between the methyl group and the fluorine atom at the 2-position appear to be a critical determinant for the major haem orientation in these reconstituted Mbs. The X-ray structure revealed that the haem side-chains at the 2-, 3-, 7-, and 8-positions in the normal form are in close contact with (Val E10, Ala E14, Leu F4), (Leu E15, Leu G5, Ile G8, Ile G12, Phe H15), (Leu B13, Ile FG5, Tyr G4, Ile G8), and (Leu B13, Phe CD1, Thr C4, Lys C7, Ile FG5, Tyr G4), respectively.¹⁶⁷ All of the possible orientations of 2-MF and mesohemin at the active site of Mb are illustrated in Fig. 25. The results demonstrated both that the energy level of the structure in Fig. 25B is lower than that of Fig. 25A and that Fig. 25C is energetically more stable than Fig. 25D. Considering the steric hindrance between the haem peripheral side-chains and the surrounding protein, the energy levels of Fig. 25A and B are expected to be lower than those of Fig. 25C and D, respectively, because of the difference in the size of the substituents at the 2-position. Consequently, these orientational states are

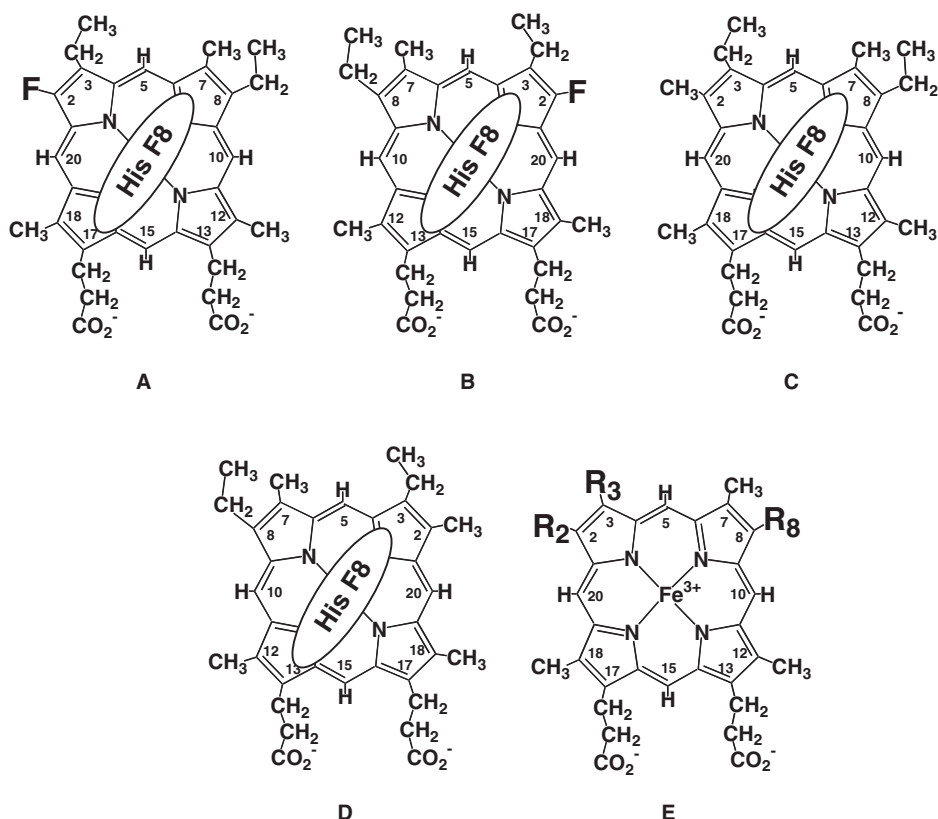


Fig. 25. Possible orientations of 2-MF and mesohaem relative to His F8. Normal and reverse forms of (A, B) Mb(2-MF); (C, D) Mb(meso). The numbering system of porphyrin is indicated in (E).

aligned as Fig. 25B < A < C < D in the order of increasing energy level. The small difference in their energy levels can be understood by the fact that the energy difference between Fig. 25B and Fig. 25D is solely accounted for by the difference in the steric hindrance between the protein and the fluorine atom or the methyl group at the haem 2-position in the reversed form. Furthermore, in the normal form, the protein-haem contacts at the haem 8- and 3-position exerts a larger steric hindrance than those at the haem 2- and 7-positions, respectively. Similar conclusions were derived from X-ray studies, which revealed that 8-isopropyl-3-vinyldeuteroheemin ($R_2 = -CH_3$, $R_3 = -CH = CH_2$, $R_8 = -CH(CH_3)_2$) in the haem structure of Fig. 25E possesses the reverse orientation in the active site of Mb, whereas 3,8-diisopropyldeuteroheemin ($R_2 = -CH_3$, $R_3 = R_8 = -CH(CH_3)_2$) and 3-isopropyl-8-vinyldeuteroheemin ($R_2 = -CH_3$, $R_3 = -CH(CH_3)_2$, $R_8 = -CH = CH_2$) are predominantly in the normal form.^{182,183} The fact that 8-ethyldeuteroheemin ($R_2 = -CH_3$, $R_3 = -H$, $R_8 = -CH_2CH_3$) is preferentially in the reversed form,

whereas mesohemin and 3-ethyldeuteroheemin ($R_2 = -CH_3$, $R_3 = -CH_2CH_3$, $R_8 = -H$) are in the normal form,¹⁸² is also consistent with these results.

8.3. Haem electronic structure in deoxy myoglobin

Since the *d*-orbital splittings derived from the 5E , $(d_{xz})^2(d_{yz})(d_{xy})(d_{z^2})(d_{x^2-y^2})$ or $(d_{yz})^2(d_{xz})(d_{xy})(d_{z^2})(d_{x^2-y^2})$, and the 5B_2 , $(d_{xy})^2(d_{xz})(d_{yz})(d_{z^2})(d_{x^2-y^2})$ states for the high-spin d^6 system with $S = 2$ are close in energy (Fig. 24),¹⁷⁰ the contributions of these electronic states to the electronic and magnetic nature of deoxy Mb and Hb complicated the interpretation of their 1H NMR spectra in terms of structural features of their haem active sites. The previous 1H NMR study demonstrated that the haem electronic structure inferred from the analysis of paramagnetic shifts of peripheral side-chain proton signals of high-spin ferrous haem in deoxy Mb has reflected a combination of both the σ and π spin delocalisation.¹⁷⁰ Furthermore, in the absence of adequate model compounds for the 1H NMR properties of deoxy Mb,^{170,184} the 1H NMR study of deoxy Mb and deoxy Hb almost comes to a deadlock. ^{19}F NMR study provides useful information as to the fundamental understanding of the electronic nature of high-spin ferrous haem in deoxy Mb as well as possibly in deoxy Hb.¹²⁰

Since the haem methyl proton signals of MbCO were observed in the narrow chemical shift range between 2 and 4 ppm,¹⁴⁵ the spreads of the haem methyl proton signals in the spectra of deoxy Mb (Fig. 10) reflected the hyperfine shift pattern of the haem methyl proton signals. Hence the larger dispersion of the haem methyl proton signals in the spectrum of Mb(7-PF) could be attributed to the significant π spin delocalisation.

Using the ^{19}F shifts for the corresponding MbCOs as the δ_{dia} values (Fig. 26), together with the δ_{pc} values reported for native deoxy Mb,¹⁷⁰ the contact contributions for the ^{19}F signals could be calculated (Table 2). As shown in Table 2, the δ_c values for the signals of Mb(7-PF) were considerably smaller than those of Mb(3,7-DF) and Mb(2-MF). This result is parallel to the previous 1H NMR observation that the paramagnetic shifts of pyrrole proton signals are much larger than those of haem methyl proton signals in the spectra of deoxy Mb¹⁷⁰ and high-spin ferrous model haem complexes.¹⁸⁴ This has been interpreted in terms of the significant σ spin transfer in high-spin ferrous haems. The signals due to the normal and reversed forms of Mb(7-PF), i.e., 7-CF₃(N) and 7-CF₃(R) signals, exhibited the δ_c values of ~ 3 and ~ 33 ppm, respectively, and they were considerably smaller than the values of ~ 250 ppm for the signals of Mb(3,7-DF) and Mb(2-MF). The smaller δ_c value for 7-CF₃(N) than for 7-CF₃(R) implied that the electron density in pyrrole II of Mb(7-PF) is smaller than that in pyrrole I (Fig. 23B). The δ_c values of the signals for high-spin ferrous haems have been shown to result from a combination of σ and π spin delocalisation.¹⁷⁰ The contribution of the σ spin delocalisation to the δ_c values of 7-CF₃(N) and 7-CF₃(R) signals should be relatively small because of the presence of two single bonds intervening between the pyrrole carbon and fluorine atoms in 7-PF. Therefore the δ_c shift difference of ~ 30 ppm observed for

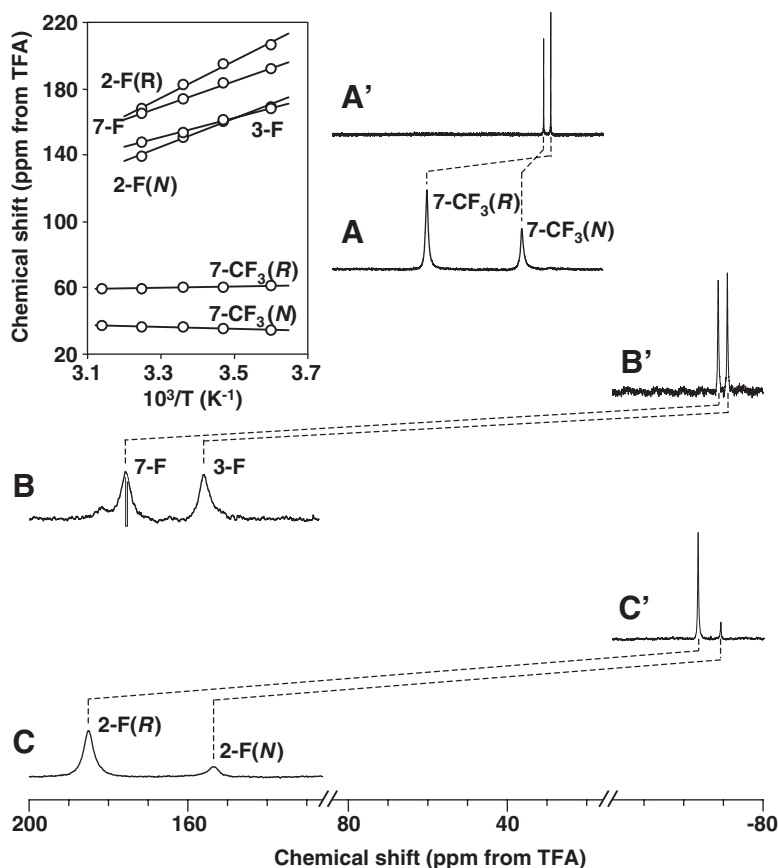


Fig. 26. 376 MHz ^{19}F NMR spectra of (A) Mb(7-PF), (B) Mb(3,7-DF), and (C) Mb(2-MF) at 25 °C, in 90% $\text{H}_2\text{O}/10\%$ D_2O , pH 6.5. (A–C) Deoxy Mbs and (A'–C') MbCOs. The corresponding signals are connected by a broken line.

the ^{19}F signals of Mb(7-PF) was predominantly attributed to the π spin delocalisation. In the ^5E state, the degeneracy of the energy levels for the two configurations is removed by the interaction between a d_π -orbital and the π -orbital of the Fe-bound nitrogen atom of His F8 imidazole and, depending upon the relative energy of the d_{xz} and d_{yz} orbitals, π spin delocalisation occurs into either of the pyrroles I, III or II, IV (Fig. 23B). On the other hand, the non-degenerate $^5\text{B}_2$ state delocalises twice as much spin density to the porphyrin π -system and the delocalisation occurs equally to all pyrroles because there are π spins in both the d_{xz} and d_{yz} orbitals (Fig. 24). The large shift difference, together with the relatively small δ_c values, for the signals of Mb(7-PF) strongly suggested a significant contribution of the ^5E state to the ground state of its haem electronic structure. Thus, the significant π spin delocalisation in high-spin ferrous 7-PF was also reflected in the hyperfine shift pattern of the haem methyl proton signals. In contrast to the ^{19}F signals of

Table 2. ^{19}F chemical shifts of deoxy Mbs reconstituted with fluorinated haems in 90% $\text{H}_2\text{O}/10\% \text{ } ^2\text{H}_2\text{O}$ (pH 6.5) at 25°C

Mb	δ_{obs}^a (ppm)	δ_{dia}^b (ppm)	δ_{pc}^c (ppm)	δ_{c}^d (ppm)	Curie intercept ^e (ppm)
<i>Mb</i> (7- <i>PF</i>)					
7- $\text{CF}_3(\text{N})^f$	36.0	30.9	~ 2	~ 3	60
7- $\text{CF}_3(\text{R})^f$	60.3	29.1	~ -2	~ 33	50
<i>Mb</i> (3,7- <i>DF</i>)					
3-F	154.9	-70.9	~ -2	~ 228	-40
7-F	173.8	-68.5	~ 2	~ 240	-90
<i>Mb</i> (2- <i>MF</i>)					
2-F(N) ^f	150.9	-69.0	~ -2	~ 222	-100
2-F(R) ^f	182.3	-63.3	~ 2	~ 244	-150

^aObserved shift.^bDiamagnetic shift observed for MbCO.^cParamagnetic δ_{pc} taken from Ref. 170.^dParamagnetic δ_{c} .^eIntercept of the Curie plots, shift vs. reciprocal of absolute temperature.^fN and R in the parentheses represent the normal and reversed forms, respectively.

Mb(7-PF), the signals of Mb(3,7-DF) and Mb(2-MF) exhibited similarly large δ_{c} values of ~ 250 ppm, demonstrating the predominant contribution of $^5\text{B}_2$ state to their haem electronic structures.

The contributions of multiple states to the ground state of the electronic structure of Mb(7-PF) were also manifested in its anomalous Curie plots, the observed shift vs. reciprocal of absolute temperature, as shown in the inset of Fig. 26. Although the plots for the ^{19}F signals of Mb(3,7-DF) and Mb(2-MF) essentially obey Curie's law, those for 7- $\text{CF}_3(\text{N})$ signal of Mb(7-PF) do not. Such an anomaly was not observed in the Curie plots for the resolved haem methyl proton signals illustrated. These results demonstrated that the haem CF_3 ^{19}F signal is more sensitive to the electronic nature of haem than is the haem CH_3 proton signal. Finally, the contribution of multiple states to the ground state of the haem electronic structures of Mb(3,7-DF) and Mb(2-MF) could not be ruled out because the shifts to $T^{-1} \rightarrow 0$ in the Curie plots for their ^{19}F signals are remarkably different from the diamagnetic reference shifts of the corresponding signals (Table 2).

8.4. Acid-alkaline transition in ferric myoglobin

The haem active site in ferric Mb (metMb) exhibits a characteristic pH-dependent structure change known as the acid-alkaline transition.¹⁸⁵ MetMb possessing highly conserved distal His E7 has H_2O and OH^- as coordinated ligands under low and high pH conditions, respectively.¹⁸⁵⁻¹⁸⁹ As illustrated in Fig. 27, the acid-alkaline transition in metMb comprises three distinct reactions, i.e., interconversion of the

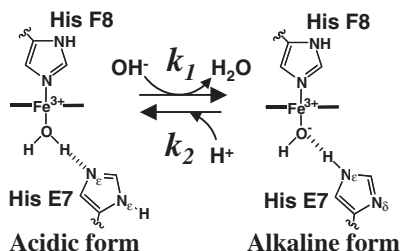


Fig. 27. Schematic representation of the acid–alkaline transition in metMb.

coordinated ligand between H_2O and OH^- , tautomerism of the His E7 imidazole, and deprotonation/protonation of the His E7 N_δH , which take place simultaneously through a molecular mechanism similar to the proton relay of serine protease.¹⁹⁰ Furthermore, since the transition is associated with the deprotonation/protonation process, the equilibrium constant is usually represented as the “ $\text{p}K_a$ ” value in analogy with the ionization equilibrium of an acid. For the scaffold of the conserved globin fold in Mbs, the $\text{p}K_a$ value has been shown to remarkably vary with the protein, ranging from 7.2 to 10.^{185–189} Thus, the acid–alkaline transition in metMb sharply reflects the structural features of the haem active site in the protein, which could be relevant to the protein function.^{186–189}

In the pH dependence of ^{19}F NMR spectrum of metMb(7-PF), two signals were observed under low and high pH conditions (Fig. 28).¹²² It has been shown that Mb(7-PF) exists as a mixture of isomers possessing two haem orientations, with a ratio of 1.0 : 2.2 for normal(N) form : reversed (R) form at equilibrium.¹²⁰ Therefore, the observed signals could be assigned on the basis of their intensities. With increasing pH, the signals of the normal and reversed forms exhibited progressive low-frequency shifts of ~ 40 and ~ 30 ppm, respectively. The acid–alkaline transition in the protein was manifested in these large pH-induced shift changes attributable to a change in the spin state between the acidic (essentially $S = 5/2$) and alkaline (mainly $S = 1/2$) forms. Quantitative fitting of their pH-dependent shifts to the Henderson–Hasselbach equation yielded $\text{p}K_a$ values of 8.32 ± 0.03 and 8.62 ± 0.03 for the normal and reversed forms of metMb(7-PF), respectively (Fig. 29). On the other hand, an optical study of metMb(7-PF) yielded a $\text{p}K_a$ value of 8.57 ± 0.03 (Fig. 30), which is close to the weight-averaged $\text{p}K_a$ value of those for the normal and reversed forms obtained on ^{19}F NMR.

The effect of the CF_3 substitution on the $\text{p}K_a$ value was analysed on the basis of comparison between metMb(7-PF) and metMb(meso). The optical study yielded a $\text{p}K_a$ value of 9.43 ± 0.03 for metMb(meso) (Fig. 31), and therefore the substitution of CF_3 for the haem peripheral CH_3 side-chain at position 7 lowered the $\text{p}K_a$ value by about 1 pH unit. Ferrihaem in metMb carries a net positive charge, and hence needs to be stabilized through neutralization on electrostatic interaction with nearby polar groups in the hydrophobic haem pocket of the protein. As far as the stability of the ferrihaem in the protein is concerned, the alkaline form is more stable than the acidic one because of neutralization of the cationic character of the

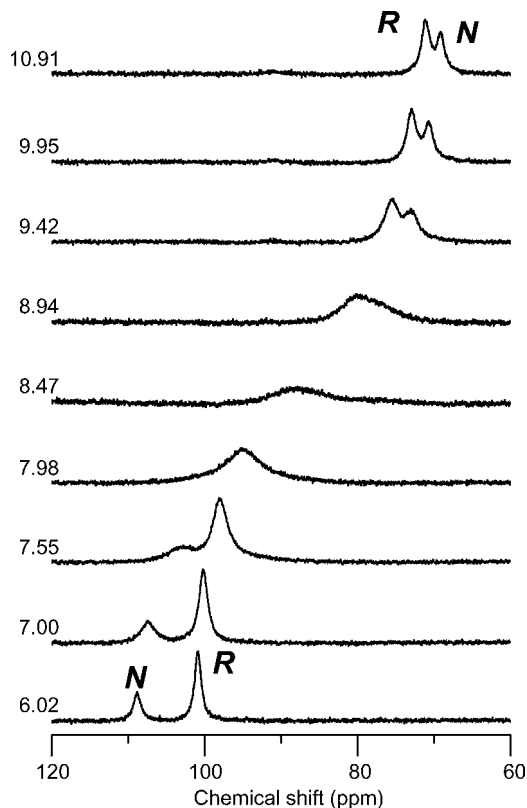


Fig. 28. 470 MHz ^{19}F NMR spectra of metMb(7-PF) at 25 °C and the indicated pH values. Signals due to the N and R forms illustrated in Fig. 3 are observed.

ferrihaem by the coordinated OH^- . The substitution of strongly electron-withdrawing CF_3 is expected to partly enhance the positive charge at the haem iron of ferrihaem, which in turn further destabilizes the acidic form. Consequently, the equilibrium of the transition is shifted toward the alkaline form by the CF_3 substitution, leading to a decrease in the $\text{p}K_{\text{a}}$ value, as observed on comparison of metMb(7-PF) and metMb(meso). These results constitute persuasive evidence for a previous proposal that the reactivity of the haem iron is regulated through the electronic nature of haem peripheral side-chains.¹⁸⁸

A distinct difference in the $\text{p}K_{\text{a}}$ value has been detected between the normal and reversed forms of metMb(7-PF) (Fig. 29). The characterisation of the dynamics of the transition in the reversed form indicates that the k_2 value is diffusion-controlled (see below), and therefore the k_2 values of the normal and reversed forms should be similar. Consequently, the difference in $\text{p}K_{\text{a}}$ value between the two forms can be attributed to the effect of the haem orientation, with respect to the protein, on the k_1 value, and hence the stability of the acidic form. In the acidic form, the hydrogen bond between the coordinated ligand and His E7 contributes not only to stabilization

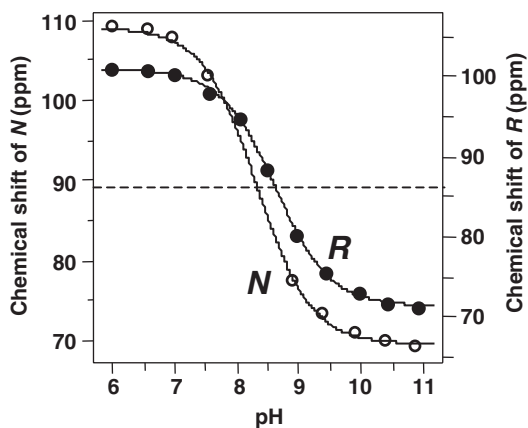


Fig. 29. Plots of the shifts of the ^{19}F NMR signals of metMb(7-PF) at 25 °C as a function of pH. The $\text{p}K_{\text{a}}$ values of 8.32 ± 0.03 and 8.62 ± 0.03 were obtained for the N and R forms, respectively. The vertical scales for the plots of the two signals were adjusted to highlight the difference in $\text{p}K_{\text{a}}$ value between them.

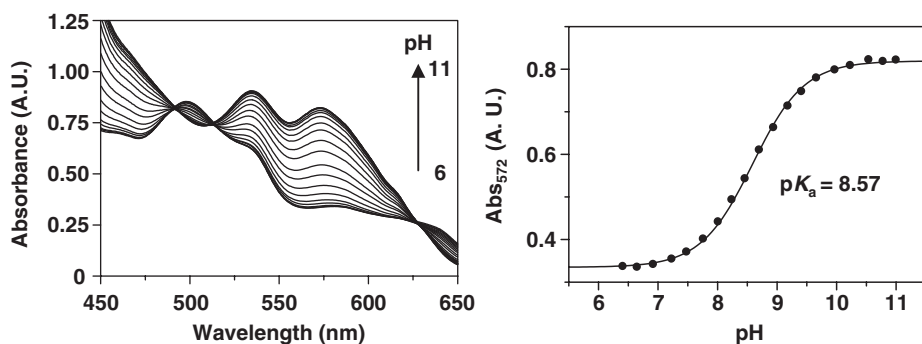


Fig. 30. The pH-dependent optical spectra of metMb(7-PF) (A) and the $\text{p}K_{\text{a}}$ value of 8.57 ± 0.03 were obtained from the plots of absorbance at 572 nm against pH (B).

of the H_2O coordination to the haem iron, but also to neutralization of the cationic character of the ferrihaem by the partial negative charge of the oxygen atom, induced by polarization of the O–H bond due to the hydrogen bond. Therefore, the stronger hydrogen bonding interaction could result in a higher $\text{p}K_{\text{a}}$ value because of the greater stability of the acidic form.¹⁹¹ The difference in the strength of the hydrogen bonding interaction between the normal and reversed forms could arise from displacement of the haem iron, relative to the protein, possibly exerted by differential haem–protein contacts in the two forms.¹⁷⁸

As shown in the series of spectra in Fig. 28 the signals are narrowest in the extreme pH regions and considerably broaden at the $\text{p}K_{\text{a}}$ value.¹⁹² Excess line broadening could arise from exchange of the CF_3 group between the acidic and alkaline forms of the protein. Using the familiar equation for the fast exchange

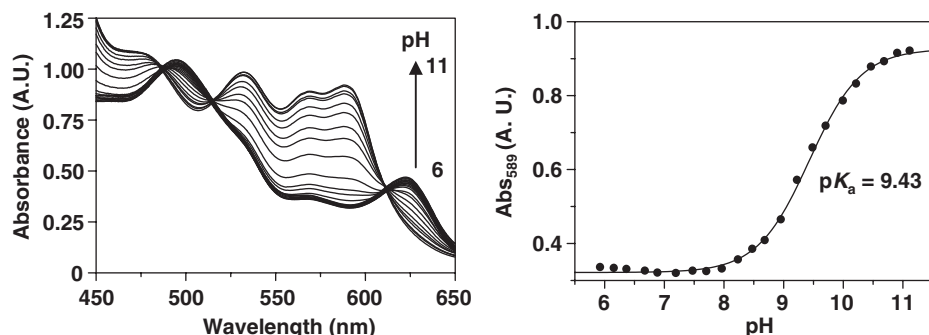


Fig. 31. The pH-dependent optical spectra of metMb(meso) (A) and the pK_a value of 9.43 ± 0.03 were obtained from the plots of absorbance at 572 nm against pH (B).

limit,¹⁹² the $k_2 = (1.1 \pm 0.2) \times 10^5 \text{ s}^{-1}$ was obtained for the reversed form of metMb(7-PF). Additionally, using the obtained k_2 value, combined with the pK_a value of 8.62 ± 0.03 , $k_1 = (2.6 \pm 0.5) \times 10^{10} \text{ M}^{-1} \text{ s}^{-1}$ was determined. Both the k_1 and k_2 values were within the ranges estimated previously for native metMb and metMbs reconstituted with various chemically modified haems.^{187,188} The obtained k_2 value for metMb(7-PF) is comparable to the exchange rate of histidyl imidazole NH protons fully exposed to the solvent,¹⁹³ indicating that the deprotonation/protonation of His E7 N δ H associated with the transition is essentially a diffusion-controlled process. In fact, according to the X-ray crystal structure,¹⁶⁷ the His E7 N δ H proton is completely exposed to the solvent, although the His E7 residue is mostly buried in the protein matrix. Furthermore, analysis of the temperature dependence of the k_2 value, determined from the temperature dependence of the line width (Fig. 32), using Arrhenius plots, yielded a value of $20.9 \pm 3 \text{ kJ mol}^{-1}$ for the activation energy of the transition. The relatively small activation energy of the transition was consistent with the absence of a large conformation change in the protein upon the transition.

Finally, due to signal overlapping, the pH dependence of the ^1H NMR spectra of metMb(7-PF) (Fig. 33) is so complex that it does not allow a detailed thermodynamic and dynamic study on the acid–alkaline transition. Furthermore, as illustrated in Figs. 34–37, the electronic nature of the haem active sites in the acidic and alkaline forms and its temperature dependence can be much more easily characterised by ^{19}F NMR than ^1H NMR. Especially, the intermediate ligand field strength for OH^- ligand is clearly reflected in the anti-Curie behavior of the ^{19}F NMR signal for the reversed form, namely, the paramagnetic shift increases with increasing temperature (Fig. 36).

8.5. Oxy and carbonmonooxy myoglobins

Characterisation of the nature of O_2 and CO binding to respiratory haemoproteins is of paramount importance for understanding the molecular mechanisms

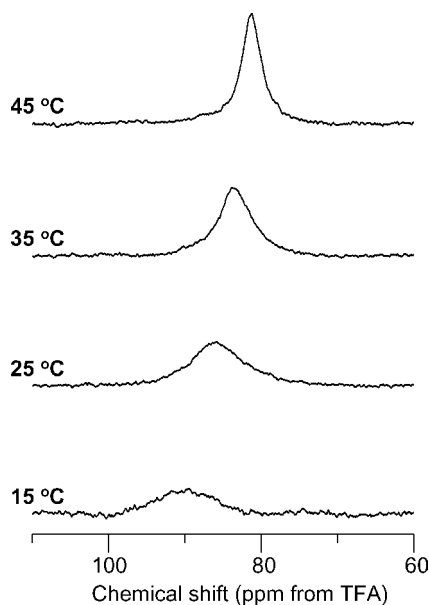


Fig. 32. 470 MHz ^{19}F NMR spectra of metMb(7-PF) in 90% H_2O /10% D_2O , pH 8.62, at the indicated temperatures.

responsible for the control of their physiological activities.¹⁹⁴ Despite detailed structural^{195,196} and spectroscopic^{197–199} information on, as well as theoretical consideration²⁰⁰ of, the binding of these ligands to haemoproteins and iron–porphyrin complexes, little experimental evidence has been reported so far as to the effects of O_2 and CO binding on the haem electronic structure of haemoproteins. Although ^1H NMR is the most powerful spectroscopic method for elucidating the haem electronic structure of proteins, the haem electronic structure of diamagnetic haemoproteins has not been fully characterised.^{145,201–206} One of difficulties associated with NMR characterisation of the haem electronic structure of diamagnetic haemoproteins is the asymmetric nature of the haem electronic structure of native haem, which often obscures subtle changes in the haem electronic structure of diamagnetic haemoproteins. Furthermore, the sensitivity of the haem peripheral side-chain proton signals to the porphyrin π -system is relatively low due to the rather weak interaction between the pyrrole carbon p_π -orbital and the proton orbital, as manifested in the small Q values for the π spin delocalisation in a paramagnetic system.⁴ In order to overcome these difficulties, a ring-fluorinated C_2 -symmetric haem 3,7-DF has been incorporated into the apoprotein of sperm whale Mb. In 3,7-DF, a change in the porphyrin π -system leads to a distortion of its C_2 -symmetric electronic structure, which can be readily detected as the separation of two ^{19}F NMR signals.¹¹⁶

In the ^{19}F NMR spectra of $\text{MbO}_2(3,7\text{-DF})$ and $\text{MbCO}(3,7\text{-DF})$ (Fig. 38), due to a protein-induced rhombic perturbation, the equivalency of the two fluorine atoms of 3,7-DF was removed and two well-resolved signals are observed in each

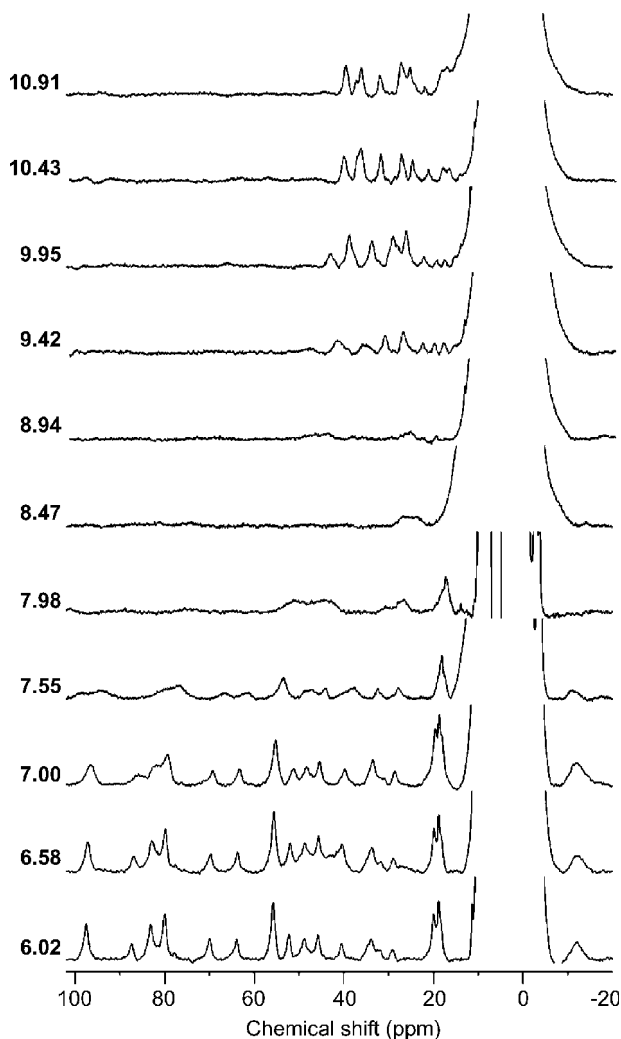


Fig. 33. 500 MHz ^1H NMR spectra of metMb(7-PF) in 90% H_2O /10% D_2O at 25 °C and the indicated pH values.

spectrum.¹¹⁷ In the spectrum of the mixture of $\text{MbO}_2(3,7\text{-DF})$ and $\text{MbCO}(3,7\text{-DF})$ (Fig. 38B), the two sets of signals are separately observed, demonstrating that the time scale of the ligand exchange between O_2 and CO in the protein is slow compared with the NMR time scale. The time scale of the ligand exchange between O_2 and CO, estimated from the shift difference between the corresponding signals for MbO_2 and MbCO in Fig. 38B is within the range of the values reported.²⁰⁷ The shift differences of more than 2.0 ppm between the corresponding signals of $\text{MbO}_2(3,7\text{-DF})$ and $\text{MbCO}(3,7\text{-DF})$ were considerably larger than those observed for the haem peripheral side-chain ^1H signals,¹⁴⁵ demonstrating the high sensitivity

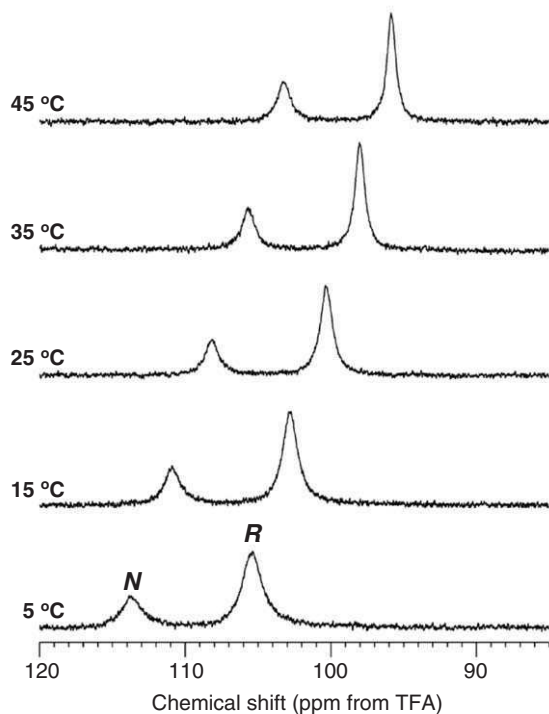


Fig. 34. 470 MHz ^{19}F NMR spectra of metMb(7-PF) in 90% H_2O /10% D_2O (pH 6.03) at the indicated temperatures.

of the ^{19}F signals to the haem electronic structure. Furthermore, the observed ^{19}F shift difference for the present reconstituted Mbs is considerably larger than those observed for Mb reconstituted with difluorovinyl deuterohaem,¹¹⁹ i.e., 0.6–1.3 ppm, demonstrating a higher sensitivity of the NMR signal for the fluoro group to the porphyrin π -system of haem than that for the fluorovinyl group.

In the absence of detailed structural information on the haem active sites in these reconstituted Mbs, the observed ^{19}F shifts could not be interpreted quantitatively in terms of the haem electronic structure. However, the electron density of a pyrrole carbon atom bearing a fluorine atom could be inferred from the observed ^{19}F shift.²⁰⁸ A comparison of the ^{19}F shifts indicates that the signals for $\text{MbO}_2(3,7\text{-DF})$ are low-frequency-shifted relative to the corresponding signals for $\text{MbCO}(3,7\text{-DF})$, indicating that the electron density in the porphyrin π -system of $\text{MbCO}(3,7\text{-DF})$ is lower than that of $\text{MbO}_2(3,7\text{-DF})$. Thus, the effect of $\text{Fe } d_\pi \rightarrow \text{CO } \pi^*$ back-donation^{209,210} on the haem electronic structure of MbCO is clearly detected on ^{19}F NMR.

Since C_2 -symmetric 3,7-DF does not possess the haem orientation disorder,^{137–139} the equivalency of the two fluorine atoms of 3,7-DF is abolished primarily by bonding interactions between the haem iron and the axial ligands, and the asymmetry in the chemical environment around the haem. X-ray crystal studies¹⁶⁷

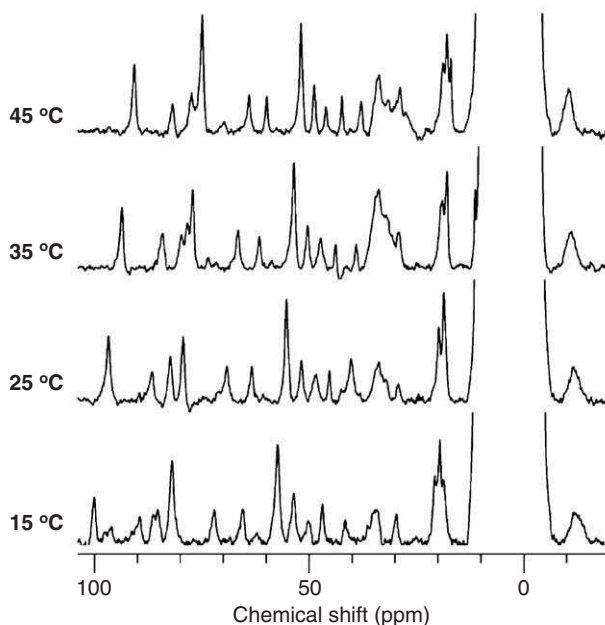


Fig. 35. 500 MHz ^1H NMR spectra of metMb(7-PF) in 90% H_2O /10% D_2O (pH 6.03) at the indicated temperatures.

demonstrate that the Fe–C–O unit in MbCO prefers a linear geometry ($\angle \text{Fe–C–O} = 171^\circ$) to maximize the Fe $d_\pi \rightarrow \text{CO } \pi^*$ back-donation,^{209,210} while the Fe–O–O unit in MbO₂ is greatly bent ($\angle \text{Fe–O–O} = 123^\circ$), although the orientation of the His F8 imidazole with respect to the haem is essentially the same in them (Fig. 39). Since the structural similarity of the haem active site in Mb possessing 3,7-DF to that of native Mb was supported by the functional and spectroscopic data, the increased non-equivalency between 3- and 7-F in MbO₂(3,7-DF), relative to that in MbCO(3,7-DF), could be attributed to the bent Fe–O–O coordination with respect to the haem. Thus, the ^{19}F NMR signals of 3,7-DF embedded in Mb are particularly sensitive to the in-plane asymmetry of the haem electronic structure induced by coordination of axial ligands to the haem iron.

8.6. ^{19}F relaxation mechanism

The analysis of nuclear relaxation has provided a wealth of information about structural and dynamic properties of molecules. Particularly, in the case of metalloproteins carrying unpaired electron(s), dynamic nature of the molecule is sharply manifested in paramagnetic relaxation observed on paramagnetically shifted NMR signals.^{7,168} The field dependence of ^{19}F NMR signals arising from MbCO ($S = 0$), met-cyano Mb ($S = 1/2$), deoxy Mb ($S = 2$), and met-aquo Mb

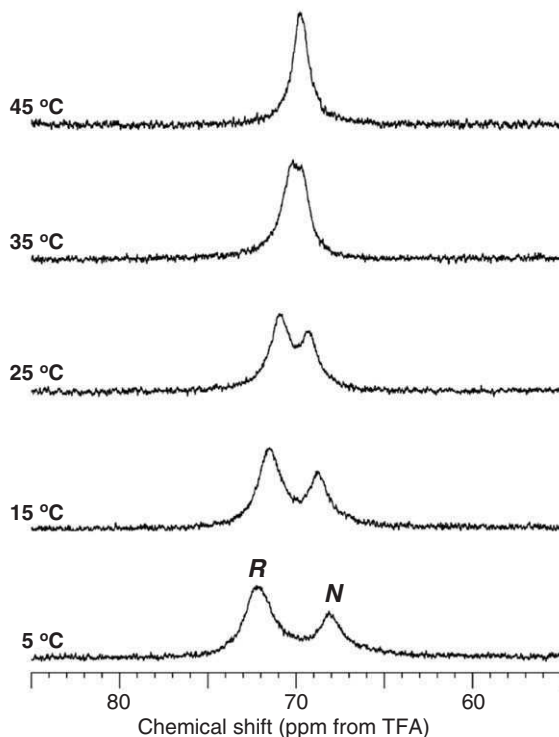


Fig. 36. 470 MHz ^{19}F NMR spectra of metMb(7-PF) in 90% H_2O /10% D_2O (pH 10.98) at the indicated temperatures.

($S = 5/2$) reconstituted with 3,7-DF¹¹⁶ was characterized in order to evaluate ^{19}F relaxation mechanism in the protein with a variety of magnetic properties (Fig. 40). Since the fluorine atoms introduced to 3,7-DF are dynamically fixed to the porphyrin ring, analysis of the field strength dependence of the line width of the ^{19}F signals provides the correlation time (τ_r) of the haem accommodated in the active site of Mb.

The nuclear relaxation rate (R_{obs}) in a paramagnetic system is expressed as the sum of diamagnetic (R_{dia}) and paramagnetic (R_{para}) terms¹⁶⁸:

$$R_{\text{obs}} = R_{\text{dia}} + R_{\text{para}}. \quad (1)$$

R_{dia} is written as the sum of the contributions of dipole–dipole interaction ($R_{\text{dia}}^{\text{DD}}$), chemical shift anisotropy ($R_{\text{dia}}^{\text{CSA}}$), and others ($R_{\text{dia}}^{\text{other}}$):

$$R_{\text{dia}} = R_{\text{dia}}^{\text{DD}} + R_{\text{dia}}^{\text{CSA}} + R_{\text{dia}}^{\text{other}}. \quad (2)$$

The contribution of $R_{\text{dia}}^{\text{CSA}}$ to nuclear spin–lattice ($R_{1\text{dia}}$) and spin–spin ($R_{2\text{dia}}$) relaxation rates, $R_{1\text{dia}}^{\text{CSA}}$ and $R_{2\text{dia}}^{\text{CSA}}$, depends on the magnetic field strength and can be written as follows:²¹¹

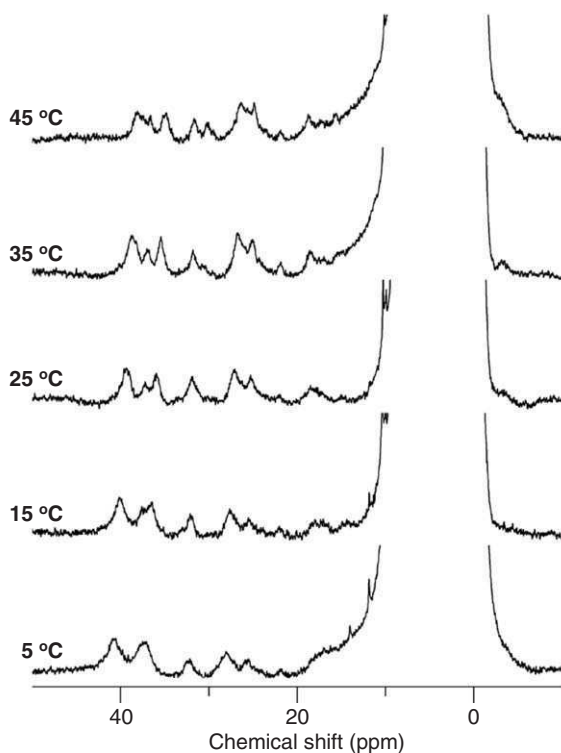


Fig. 37. 500 MHz ^1H NMR spectra of metMb(7-PF) in 90% H_2O /10% D_2O (pH 10.98) at the indicated temperatures.

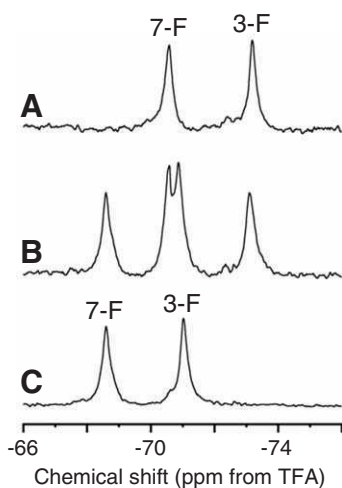


Fig. 38. 376 MHz ^{19}F NMR spectra of Mb(3,7-DF) in 90% H_2O /10% D_2O (pH 7.0) at 25 °C. (A) MbO_2 , (B) a mixture of MbO_2 and MbCO , and (C) MbCO .

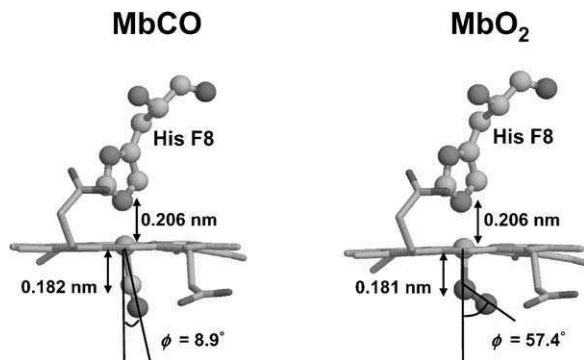


Fig. 39. The coordination structure of CO and O₂ in the crystal structure of native sperm whale MbCO and MbO₂.¹⁹⁵

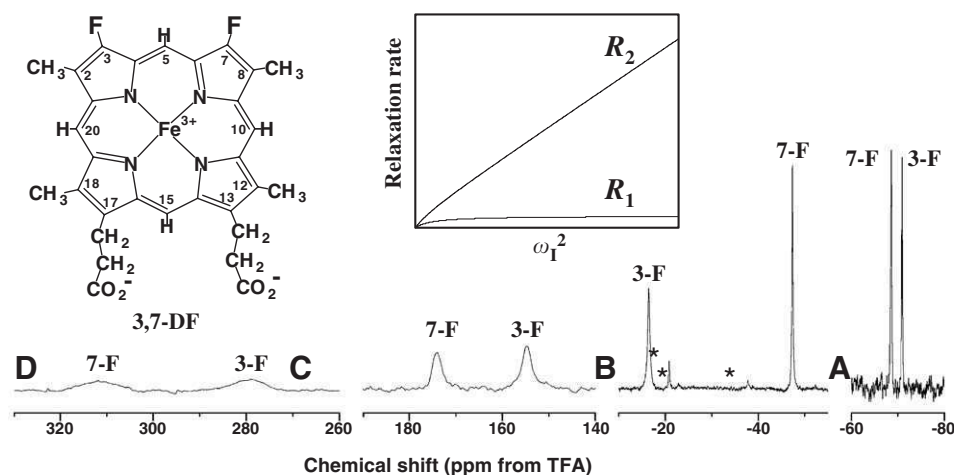


Fig. 40. The 376 MHz ¹⁹F NMR spectra of (A) MbCO(3,7-DF), (B) met-cyano Mb(3,7-DF), (C) deoxy Mb(3,7-DF), and (D) met-aquo Mb(3,7-DF) in 90% H₂O/10% D₂O, pH 7.0, at 25 °C. The signal assignments are indicated with the spectra. Peak labeled by an asterisk is due to impurity. The plots of nuclear spin–lattice (*R*₁) and spin–spin (*R*₂) relaxation rates against the square of the magnetic field strength are schematically illustrated in the inset.

$$R_{\text{Idia}}^{\text{CSA}} = \frac{6}{40} \omega_1^2 \Delta_z^2 \left(1 + \frac{\eta^2}{3} \right) J(\omega_1), \quad (3)$$

$$R_{\text{2dia}}^{\text{CSA}} = \frac{1}{40} \omega_1^2 \Delta_z^2 (3J(\omega_1) + 4J(0)), \quad (4)$$

$$J(\omega_1) = \frac{2\tau_r}{1 + \omega_1^2 \tau_r^2}, \quad (5)$$

where Δ_z is associated with the principal components of the chemical shift tensor, η is the asymmetric parameter of the molecule under consideration, and $J(\omega_1)$ represents the spectral density function.

However, R_{para} is expressed as the sum of the contributions of metal-centred ($R_{\text{para}}^{\text{MC}}$) and ligand-centred ($R_{\text{para}}^{\text{LC}}$) dipolar terms, contact hyperfine interaction ($R_{\text{para}}^{\text{C}}$), and Curie spin relaxation ($R_{\text{para}}^{\text{Curie}}$)¹⁶⁸:

$$R_{\text{para}} = R_{\text{para}}^{\text{MC}} + R_{\text{para}}^{\text{LC}} + R_{\text{para}}^{\text{C}} + R_{\text{para}}^{\text{Curie}}. \quad (6)$$

Using the Solomon–Bloembergen equations,^{212,213} together with the expression for $R_{\text{para}}^{\text{Curie}}$ ^{152–154} paramagnetic contributions to nuclear spin–lattice and spin–spin relaxation rates ($R_{1\text{para}}$ and $R_{2\text{para}}$) in a paramagnetic system are expressed by

$$\begin{aligned} R_{1\text{para}} = & \frac{2}{15} \left(\frac{\mu_0}{4\pi} \right)^2 \gamma_{\text{I}}^2 \beta_{\text{e}}^2 \mu_{\text{B}}^2 S(S+1) \left(\gamma_{\text{M}}^{-6} + \sum \rho^2 \gamma_{\text{L}}^{-6} \right) \\ & \times \left[\frac{\tau_{\text{c2}}}{1 + (\omega_{\text{I}} - \omega_{\text{S}})^2 \tau_{\text{c2}}^2} + \frac{3\tau_{\text{c1}}}{1 + \omega_{\text{I}}^2 \tau_{\text{c1}}^2} + \frac{6\tau_{\text{c2}}}{1 + (\omega_{\text{I}} + \omega_{\text{S}})^2 \tau_{\text{c2}}^2} \right] \\ & + \frac{2}{3} S(S+1) \left(\frac{A}{h} \right)^2 \left[\frac{\tau_{\text{e2}}}{1 + (\omega_{\text{I}} + \omega_{\text{S}})^2 \tau_{\text{e2}}^2} \right] \\ & + \frac{2}{5} \left(\frac{\mu_0}{4\pi} \right)^2 \frac{\omega_{\text{I}}^2 \beta_{\text{e}}^4 \mu_{\text{B}}^4 S^2 (S+1)^2}{(3kT)^2 r_{\text{M}}^6} \left(\frac{3\tau_{\text{r}}}{1 + \omega_{\text{I}}^2 \tau_{\text{r}}^2} \right), \end{aligned} \quad (7)$$

$$\begin{aligned} R_{2\text{para}} = & \frac{1}{15} \left(\frac{\mu_0}{4\pi} \right)^2 \gamma_{\text{I}}^2 \beta_{\text{e}}^2 \mu_{\text{B}}^2 S(S+1) \left(\gamma_{\text{M}}^{-6} + \sum \rho^2 \gamma_{\text{L}}^{-6} \right) \\ & \times \left[4\tau_{\text{c1}} + \frac{3\tau_{\text{c2}}}{1 + (\omega_{\text{I}} - \omega_{\text{S}})^2 \tau_{\text{c2}}^2} + \frac{3\tau_{\text{c1}}}{1 + \omega_{\text{I}}^2 \tau_{\text{c1}}^2} + \frac{6\tau_{\text{c2}}}{1 + \omega_{\text{S}}^2 \tau_{\text{c2}}^2} + \frac{6\tau_{\text{c2}}}{1 + (\omega_{\text{I}} + \omega_{\text{S}})^2 \tau_{\text{c2}}^2} \right] \\ & + \frac{1}{3} S(S+1) \left(\frac{A}{h} \right)^2 \left[\tau_{\text{e1}} + \frac{\tau_{\text{e2}}}{1 + (\omega_{\text{I}} - \omega_{\text{S}})^2 \tau_{\text{e2}}^2} \right] \\ & + \frac{1}{5} \left(\frac{\mu_0}{4\pi} \right)^2 \frac{\omega_{\text{I}}^2 \beta_{\text{e}}^4 \mu_{\text{B}}^4 S^2 (S+1)^2}{(3kT)^2 r_{\text{M}}^6} \left(4\tau_{\text{c2}} + \frac{3\tau_{\text{r}}}{1 + \omega_{\text{I}}^2 \tau_{\text{r}}^2} \right), \end{aligned} \quad (8)$$

$$\tau_{\text{c1}}^{-1} = T_{\text{le}}^{-1} + \tau_{\text{r}}^{-1} + \tau_{\text{ex}}^{-1}, \quad (9)$$

$$\tau_{\text{c2}}^{-1} = T_{2\text{e}}^{-1} + \tau_{\text{r}}^{-1} + \tau_{\text{ex}}^{-1}, \quad (10)$$

$$\tau_{\text{c1}}^{-1} = T_{\text{le}}^{-1} + \tau_{\text{ex}}^{-1}, \quad (11)$$

$$\tau_{\text{c2}}^{-1} = T_{2\text{e}}^{-1} + \tau_{\text{ex}}^{-1}, \quad (12)$$

where, in the present case, r_{M} and r_{L} are the distance between the F and Fe and F–C bond length, respectively, ρ is the unpaired electron density at carbon and fluorine atoms at the positions 3 and 7 on the porphyrin, (A/h) is the apparent hyperfine coupling constant for ^{19}F , and ω_{I} and ω_{S} are the Larmor frequencies of ^{19}F and the

electron, respectively, T_{1e} and T_{2e} are the electron longitudinal and transverse relaxation times, respectively, and τ_{ex} is the electron exchange time. The other parameters represent usual meanings. In large molecules with highly resolved NMR spectra, $T_{1e}, T_{2e} \ll \tau_r$ and at high magnetic field, $\omega_I^2 T_{1e}^2 \ll 1$, $1 < \omega_S^2 T_{1e}^2$, and $1 < \omega_S^2 T_{2e}^2$, Eqs. (7) and (8) are reduced to the equations^{214,215}

$$R_{1para} = \frac{2}{15} \left(\frac{\mu_0}{4\pi} \right)^2 \gamma_I^2 \beta_e^2 \mu_B^2 S(S+1) \left(\gamma_M^{-6} + \sum \rho^2 \gamma_L^{-6} \right) T_{1e}, \quad (13)$$

$$R_{2para} = \frac{7}{15} \left(\frac{\mu_0}{4\pi} \right)^2 \gamma_I^2 \beta_e^2 \mu_B^2 S(S+1) \left(\gamma_M^{-6} + \sum \rho^2 \gamma_L^{-6} \right) T_{1e} \\ + \frac{1}{3} S(S+1) \left(\frac{A}{\hbar} \right)^2 T_{1e} + \frac{4}{5} \left(\frac{\mu_0}{4\pi} \right)^2 \frac{\omega_I^2 \beta_e^4 \mu_B^4 S^2 (S+1)^2}{(3kT)^2 r_M^6} \tau_r. \quad (14)$$

Eq. (14) dictates that R_{2para} depends on the field strength due to the contribution of R_{para}^{Curie} , the third term on the right-hand side of the equation. Nuclear spin–lattice ($R_1 = R_{1dia} + R_{1para}$) and spin–spin ($R_2 = R_{2dia} + R_{2para}$) relaxation rates of a paramagnetic Mb are schematically plotted against the square of the applied field strength, ω_I^2 (the inset of Fig. 40).

As shown in the spectra of Fig. 40, the contributions of the paramagnetic relaxation mechanisms to R_2 is reflected in the considerable broadening of the signals with an increase in the S value. In the case of diamagnetic MbCO, the increase in the line width of the signals observed at higher magnetic field is attributed solely to R_{2dia}^{CSA} . For paramagnetic met-cyano, deoxy, and met-aquo Mbs, R_{para}^{Curie} , in addition to the R_{dia}^{CSA} contribution, plays a significant role in the field strength dependence of the line width of the signals. Assuming that the R_{dia}^{CSA} contribution is independent of the oxidation, ligation, and spin states of Mb, the R_{para}^{Curie} contribution in each paramagnetic form of Mb could be obtained from the analysis of the relationship between the line width of the signals and the field strength using the R_{dia}^{CSA} contribution estimated from the study of the field-dependent line width for the signals of MbCO through Eq. (4). Then the τ_r value of Mb^{216,217} can be estimated from the R_{para}^{Curie} contribution. Thus, the study on the field dependence of the line width of the NMR signals arising from immobilized fluorine atom(s) introduced to the active site of Mb allows the determination of the τ_r value.

9. CONCLUDING REMARKS

This chapter has described the potential applicability of ^{19}F NMR in combination with fluorinated haems for the detailed characterisation of structural properties of the haem active sites in *b*-type haemoproteins. By virtue of ^{19}F NMR in studying biological macromolecules, molecular and electronic structures of haem active sites in the proteins can be readily characterised from the analysis of the NMR parameters of well-resolved signals. Furthermore, ^{19}F NMR also allows quantitative characterization of the dynamic processes occurring at the haem active site in Mb. The present method provides a new means of studying in detail, structural

properties that are relevant to the functional regulation of various *b*-type haemoproteins to delineate their structure–function relationships.

REFERENCES

1. J. S. Morrow and F. R. N. Gurd, *CRC Crit. Rev. Biochem.*, 1975, **3**, 221.
2. G. N. La Mar, in *Biological Application of Magnetic Resonance*, R. G. Shulman, ed., Academic Press, New York, 1979, p. 305.
3. O. Jardetzky and G. C. K. Roberts, *NMR in Molecular Biology*, Chap. III, Academic Press, New York, 1981.
4. I. Bertini and C. Luchinat, *NMR of Paramagnetic Molecules in Biological Systems*, Benjamin/Cummings Publishing, Menlo Park, CA, 1986.
5. Y. Yamamoto, *Annu. Rep. NMR Spectrosc.*, 1998, **36**, 1.
6. G. N. La Mar, J. D. Satterlee and J. S. de Ropp, in *The Porphyrin Handbook*, K. M. Kadish, K. M. Smith and R. Guilard, eds., Academic Press, New York, 2000, p. 185.
7. I. Bertini, C. Luchinat and G. Parigi, *Solution NMR of Paramagnetic Molecules*, Elsevier, Amsterdam, 2001.
8. K. Wüthrich, *Struct. Bond.*, 1970, **8**, 53.
9. G. N. La Mar, in *NMR of Paramagnetic Molecules, Principles and Applications*, G. N. La Mar, W. Dew. Horrocks, Jr. and R. H. Holm, eds., Academic Press, New York, 1973, p. 85.
10. R. G. Shulman, in *ESR and NMR of Paramagnetic Species in Biological and Related systems*, I. Bertini and R. S. Drago, eds., Reidel, Dordrecht, 1979, p. 135.
11. K. Wüthrich, *NMR in Biological Research: Peptide and Proteins*, Chap. 6, North-Holland, Amsterdam, 1976.
12. I. Morishima, S. Ogawa, T. Inubushi and T. Iizuka, *Adv. Biophys.*, 1978, **11**, 217.
13. R. M. Keller and K. Wüthrich, in *Biological Magnetic Resonance*, Vol. 3, L. J. Berliner and J. Reuben, eds., Plenum Press, New York, 1981, p. 1.
14. C. Ho and I. M. Russu, *Method Enzymol.*, 1981, **76**, 278.
15. H. M. Goff, in *Iron Porphyrins*, Part 1, A. B. P. Lever and H. B. Gray, eds., Addison-Wesley, Reading, MA, 1983, p. 239.
16. J. D. Satterlee, *Annu. Rep. NMR Spectrosc.*, 1986, **17**, 79.
17. J. D. Satterlee, *Met. Ions Biol. Syst.*, 1986, **21**, 121.
18. I. Bertini, P. Turano and A. J. Vila, *Chem. Rev.*, 1993, **93**, 2833.
19. F. A. Walker and U. Simonis, in *Biological Magnetic Resonance*, Vol. 12, L. J. Berliner and J. Reuben, eds., Plenum Press, New York, 1993, p. 133.
20. J. D. Satterlee, S. Alam, Q. Yi and J. E. Erman, in *Biological Magnetic Resonance*, Vol. 12, L. J. Berliner and J. Reuben, eds., Plenum Press, New York, 1993, p. 275.
21. C. Luchinat and S. Ciurli, in *Biological Magnetic Resonance*, Vol. 12, L. J. Berliner and J. Reuben, eds., Plenum Press, New York, 1993, p. 357.
22. L. Banci, M. Piccioli and A. Scozzafava, *Coord. Chem. Rev.*, 1992, **120**, 1.
23. J. S. de Ropp, L. P. Yu and G. N. La Mar, *J. Biomol. NMR*, 1991, **1**, 175.
24. G. N. La Mar and J. S. de Ropp, in *Biological Magnetic Resonance*, Vol. 12, L. J. Berliner and J. Reuben, eds., Plenum Press, New York, 1993, p. 1.
25. A. V. Xavier, D. L. Turner and H. Santos, *Methods Enzymol.*, 1993, **227**, 1.
26. M. Rivera and G. A. Caignan, *Anal. Bioanal. Chem.*, 2004, **378**, 1464.
27. J. L. Markley and M. Kainosho, in *NMR of Macromolecules*, Chap. 5, G. C. K. Roberts, ed., Oxford University Press, Oxford, 1993.
28. B. D. Sykes and W. E. Hull, *Methods Enzymol.*, 1978, **49**, 270.
29. C. Frieden, S. D. Hoeltzli and I. J. Ropson, *Protein Sci.*, 1993, **2**, 2007.
30. J. T. Gerig, *Prog. NMR Spectrosc.*, 1994, **26**, 293.
31. P. G. Gettins, *Int. J. Biol. Macromol.*, 1994, **16**, 227.
32. M. A. Danielson and J. J. Falke, *Annu. Rev. Biophys. Biomol. Struct.*, 1996, **25**, 163.

33. W. H. Huestis and M. A. Raftery, *Biochem. Biophys. Res. Commun.*, 1972, **49**, 1358.
34. J. T. Gerig and R. S. McLeod, *J. Am. Chem. Soc.*, 1973, **95**, 5725.
35. W. E. Hull and B. D. Sykes, *Biochemistry*, 1974, **13**, 3431.
36. W. E. Hull and B. D. Sykes, *J. Chem. Phys.*, 1975, **63**, 867.
37. W. E. Hull and B. D. Sykes, *Biochemistry*, 1976, **15**, 1535.
38. B. J. Kimber, J. Feeney, G. C. Roberts, B. Birdsall, D. V. Griffiths, A. S. Burgen and B. D. Sykes, *Nature*, 1978, **271**, 184.
39. P. K. Mascharak, M. C. Smith, W. H. Armstrong, B. K. Burgess and R. H. Holm, *Proc. Natl. Acad. Sci. USA*, 1982, **79**, 7056.
40. J. T. Gerig, J. C. Klinkenbirk and R. A. Nieman, *Biochemistry*, 1983, **27**, 2076.
41. F. C. Knowles, *Arch. Biochem. Biophys.*, 1984, **230**, 327.
42. M. Brauer and B. D. Sykes, *Biochemistry*, 1986, **25**, 2187.
43. M. P. Gamcsik, J. T. Gerig and R. B. Swenson, *Biochim. Biophys. Acta*, 1986, **874**, 372.
44. U. Tollemar, K. Cunningham and J. W. Shriver, *Biochim. Biophys. Acta*, 1986, **873**, 243.
45. M. P. Gamcsik, J. T. Gerig and D. H. Gregory, *Biochim. Biophys. Acta*, 1987, **912**, 303.
46. L. E. Kay, J. M. Pascone, B. D. Sykes and J. W. Shriver, *J. Biol. Chem.*, 1987, **262**, 1984.
47. G. S. Rule, E. A. Pratt, V. Simplaceanu and C. Ho, *Biochemistry*, 1987, **26**, 549.
48. E. Li, S. J. Quian, L. Nader, N. C. Yang, A. d'Avignon, J. C. Sacchettini and J. I. Gordon, *J. Biol. Chem.*, 1989, **264**, 17041.
49. E. Li, S. J. Qian, N. C. Yang, A. d'Avignon and J. I. Gordon, *J. Biol. Chem.*, 1990, **265**, 11549.
50. L. A. Luck and J. J. Falke, *Biochemistry*, 1991, **30**, 4248.
51. L. A. Luck and J. J. Falke, *Biochemistry*, 1991, **30**, 4257.
52. E. Li, S. J. Qian, N. S. Winter, A. d'Avignon, M. S. Levin and J. I. Gordon, *J. Biol. Chem.*, 1991, **266**, 3622.
53. P. Gettins, J. Choay, B. C. Crews and G. Zettlmeiss, *J. Biol. Chem.*, 1992, **267**, 21946.
54. I. J. Ropson and C. Frieden, *Proc. Natl. Acad. Sci. USA*, 1992, **89**, 7222.
55. S. K. Drake, R. B. Bourret, L. A. Luck, M. I. Simon and J. J. Falke, *J. Biol. Chem.*, 1993, **268**, 13081.
56. R. B. Bourret, S. K. Drake, S. A. Chervitz, M. I. Simon and J. J. Falke, *J. Biol. Chem.*, 1993, **268**, 13089.
57. G. D. Henry, S. Maruta, M. Ikebe and B. D. Sykes, *Biochemistry*, 1993, **32**, 10451.
58. S. Hamman, M. Atta, A. Ehrenberg, P. Wilkins, H. Dalton, C. Beguin and M. Fontecave, *Biochem. Biophys. Res. Commun.*, 1993, **195**, 594.
59. S. M. Lui and J. A. Cowan, *J. Am. Chem. Soc.*, 1994, **116**, 4483.
60. J. Scheuring, J. Lee, M. Cushman, H. Patel, D. A. Patrick and A. Bacher, *Biochemistry*, 1994, **33**, 7634.
61. M. A. Danielson, H. P. Biemann, D. E. Koshland, Jr. and J. J. Falke, *Biochemistry*, 1994, **33**, 6100.
62. S. D. Hoeltzli and C. Frieden, *Biochemistry*, 1994, **33**, 5502.
63. C. Lian, H. Le, B. Montez, J. Patterson, S. Harrell, D. Laws, I. Matsumura, J. Pearson and E. Oldfield, *Biochemistry*, 1994, **33**, 5238.
64. S. D. Hoeltzli and C. Frieden, *Proc. Natl. Acad. Sci. USA*, 1995, **92**, 9318.
65. L. A. Luck, J. E. Vance, T. M. O'Connell and R. E. London, *J. Biomol. NMR*, 1996, **7**, 261.
66. D. Heintz, H. Kany and H. R. Kalbitzer, *Biochemistry*, 1996, **35**, 12686.
67. S. D. Hoeltzli and C. Frieden, *Biochemistry*, 1996, **35**, 16843.
68. Z. Y. Sun, E. A. Pratt, V. Simplaceanu and C. Ho, *Biochemistry*, 1996, **35**, 16502.
69. F. J. van der Bolt, R. H. van den Heuvel, J. Vervoort and W. J. van Berkel, *Biochemistry*, 1997, **36**, 14192.
70. H. Duewel, E. Daub, V. Robinson and J. F. Honek, *Biochemistry*, 1997, **36**, 3404.
71. D. V. Laurents and R. L. Baldwin, *Biochemistry*, 1997, **36**, 1496.
72. C. Y. Wong and M. R. Eftink, *Biochemistry*, 1998, **37**, 8938.
73. M. Bouchard, C. Pare, J. P. Dutasta, J. P. Chauvet, C. Gicquaud and M. Auger, *Biochemistry*, 1998, **37**, 3149.
74. S. D. Hoeltzli and C. Frieden, *Biochemistry*, 1998, **37**, 387.

75. S. Maruta, G. D. Henry, T. Ohki, T. Kambara, B. D. Sykes and M. Ikebe, *Eur. J. Biochem.*, 1998, **252**, 520.
76. A. Jongejan, J. A. Jongejan and J. A. Duine, *Protein Eng.*, 1998, **11**, 185.
77. Q. S. Zhang, L. Shen, E. D. Wang and Y. L. Wang, *Protein Chem.*, 1999, **18**, 187.
78. R. Peteranderl, M. Rabenstein, Y. K. Shin, C. W. Liu, D. E. Wemmer, D. S. King and H. C. Nelson, *Biochemistry*, 1999, **38**, 3559.
79. L. Schmitt, J. J. Boniface, M. M. Davis and H. M. McConnell, *J. Mol. Biol.*, 1999, **286**, 207.
80. L. A. Luck, J. I. Barse, A. M. Luck and C. H. Peck, *Biochem. Biophys. Res. Commun.*, 2000, **270**, 988.
81. H. W. Lee, J. H. Sohn, B. I. Yeh, J. W. Choi, S. Jung and H. W. Kim, *J. Biochem.*, 2000, **127**, 1053.
82. M. C. Loewen, J. Klein-Seetharaman, E. V. Getmanova, P. J. Reeves, H. Schwalbe and H. G. Khorana, *Proc. Natl. Acad. Sci. USA*, 2001, **98**, 4888.
83. C. Hammann, D. G. Norman and D. M. Lilley, *Proc. Natl. Acad. Sci. USA*, 2001, **98**, 5503.
84. H. S. Duewel, E. Daub, V. Robinson and J. F. Honek, *Biochemistry*, 2001, **40**, 13167.
85. B. Salopek-Sondi and L. A. Luch, *Protein Eng.*, 2002, **15**, 855.
86. K. Oxenoid, F. D. Sonnichsen and C. R. Sanders, *Biochemistry*, 2002, **41**, 12876.
87. B. Schuler, W. Kremer, H. R. Kalbitzer and R. Jaenicke, *Biochemistry*, 2002, **41**, 11670.
88. R. A. Rodriguez-Mias and M. Pellecchia, *J. Am. Chem. Soc.*, 2003, **125**, 2892.
89. Y. N. Yao, Q. S. Zhang, X. Z. Yan, G. Zhu and E. D. Wang, *FEBS Lett.*, 2003, **547**, 197.
90. C. Frieden, S. D. Hoeltzi and J. G. Bann, *Methods Enzymol.*, 2004, **380**, 400.
91. A. J. Doerr, M. A. Case, I. Pelczar and G. L. McLendon, *J. Am. Chem. Soc.*, 2004, **126**, 4192.
92. J. G. Bann and C. Frieden, *Biochemistry*, 2004, **43**, 13775.
93. L. G. Scott, B. H. Geierstanger, J. R. Williamson and M. Hennig, *J. Am. Chem. Soc.*, 2004, **126**, 11776.
94. G. L. Abbott, G. E. Blouse, M. J. Perron, J. D. Shore, L. A. Luck and A. G. Szabo, *Biochemistry*, 2004, **43**, 1507.
95. Q. Shu and C. Frieden, *Biochemistry*, 2004, **43**, 1432.
96. M. Neerathilingam, L. H. Greene, S. A. Colebrooke, I. D. Campbell and D. Staunton, *J. Biomol. NMR*, 2005, **31**, 11.
97. H. Li and C. Frieden, *Biochemistry*, 2005, **44**, 2369.
98. Q. Shu and C. Frieden, *J. Mol. Biol.*, 2005, **345**, 599.
99. G. Anderluh, A. Razpotnik, Z. Podlesek, P. Macek, F. Separovic and R. S. Norton, *J. Mol. Biol.*, 2005, **347**, 27.
100. A. S. Ulrich, *Prog. NMR Spectrosc.*, 2004, **46**, 1.
101. L. M. McDowell, M. Lee, R. A. McKay, K. S. Anderson and J. Schaefer, *Biochemistry*, 1996, **35**, 3328.
102. S. L. Grage and A. S. Ulrich, *J. Magn. Reson.*, 1999, **138**, 98.
103. S. L. Grage and A. S. Ulrich, *J. Magn. Reson.*, 2000, **46**, 81.
104. S. Rozovsky, G. Jogl, L. Tong and A. E. McDermott, *J. Mol. Biol.*, 2001, **310**, 271.
105. J. Salgado, S. L. Grage, L. H. Kondejewski, R. S. Hodges, B. N. McElhaney and A. S. Ulrich, *J. Biomol. NMR*, 2001, **21**, 191.
106. S. J. Kim, L. Cegelski, D. R. Studelska, R. D. O'Connor, A. K. Mehta and J. Schaefer, *Biochemistry*, 2002, **41**, 6967.
107. S. L. Grage, J. Wang, T. A. Cross and A. S. Ulrich, *Biophys. J.*, 2002, **83**, 3336.
108. R. W. Glaser and A. S. Ulrich, *J. Magn. Reson.*, 2003, **164**, 104.
109. S. Afonin, R. W. Glaser, M. Berditchevskaia, P. Wadhvani, K. H. Guhrs, U. Mollmann, A. Perner and A. S. Ulrich, *Chembiochem.*, 2003, **4**, 1151.
110. S. Wi, N. Sinha and M. Hong, *J. Am. Chem. Soc.*, 2004, **126**, 12754.
111. R. W. Glaser, C. Sachse, U. H. Durr, P. Wadhvani and A. S. Ulrich, *J. Magn. Reson.*, 2004, **168**, 153.
112. S. Afonin, U. H. Durr, R. W. Glaser and A. S. Ulrich, *Magn. Reson. Chem.*, 2004, **42**, 195.
113. J. J. Buffy, A. J. Waring and M. Hong, *J. Am. Chem. Soc.*, 2005, **127**, 4477.

114. A. Suzuki, T. Tomizawa, T. Hayashi, T. Mizutani and H. Ogoshi, *Bull. Chem. Soc. Jpn.*, 1996, **69**, 2923.
115. J. G. Pearson, B. Montez, H. Le, E. Oldfield, E. Y. Chien and S. G. Sligar, *Biochemistry*, 1997, **36**, 3590.
116. Y. Yamamoto, Y. Hirai and A. Suzuki, *J. Biol. Inorg. Chem.*, 2000, **5**, 455.
117. Y. Hirai, Y. Yamamoto and A. Suzuki, *Bull. Chem. Soc. Jpn.*, 2000, **73**, 2309.
118. M. R. Thomas and S. G. Boxer, *Biochemistry*, 2001, **40**, 8588.
119. C. Poliart, J.-F. Briand, F. Tortevoie, J. Leroy, G. Simonneaux and A. Bondon, *Magn. Reson. Chem.*, 2001, **39**, 615.
120. Y. Yamamoto, S. Nagao, Y. Hirai, T. Inose, N. Terui, H. Mita and A. Suzuki, *J. Biol. Inorg. Chem.*, 2004, **9**, 152.
121. Y. Hirai, S. Nagao, H. Mita, A. Suzuki and Y. Yamamoto, *Bull. Chem. Soc. Jpn.*, 2004, **77**, 1485.
122. S. Nagao, Y. Hirai, A. Suzuki and Y. Yamamoto, *J. Am. Chem. Soc.*, 2005, **127**, 4146.
123. E. T. Strom, G. R. Underwood and D. Jurkowitz, *Mol. Phys.*, 1972, **24**, 901.
124. D. R. Eaton, A. D. Josey, W. D. Phillips and R. E. Benson, *Mol. Phys.*, 1962, **5**, 407.
125. W. E. Hull and B. D. Sykes, *J. Mol. Phys.*, 1975, **98**, 121.
126. M. David, M. -L. Daveran, J. Batut, A. Dedieu, O. Domergue, J. Ghai, C. Hertig, P. Boistard and D. Kahn, *Cell*, 1988, **54**, 671.
127. S. Hou, R. W. Larsen, D. Boudko, C. W. Riley, E. Karatan, M. Zimmer, G. W. Ordal and M. Alam, *Nature*, 2000, **403**, 640.
128. R. W. Kaesler and E. LeGoff, *J. Org. Chem.*, 1982, **47**, 5243.
129. H. Ogoshi, M. Hommma, K. Yokota, H. Toi and A. Aoyama, *Tetrahedron Lett.*, 1983, **24**, 929.
130. M. Hommma, K. Aoyagi, Y. Aoyama and H. Ogoshi, *Tetrahedron Lett.*, 1983, **24**, 4343.
131. H. Toi, M. Hommma, A. Suzuki and H. Ogoshi, *J. Chem. Soc. Chem. Commun.*, 1985, 1791.
132. H. Ogoshi, H. Mizushima, H. Toi and Y. Aoyama, *J. Org. Chem.*, 1986, **51**, 2366.
133. K. M. Snow and K. M. Smith, *J. Org. Chem.*, 1989, **54**, 3270.
134. F. W. J. Teale, *Biochim. Biophys. Acta*, 1959, **35**, 543.
135. Q. H. Gibson and E. Antonini, *Biochem. J.*, 1960, **77**, 328.
136. M. Y. Rose and J. S. Olson, *J. Biol. Chem.*, 1983, **258**, 4298.
137. G. N. La Mar, D. L. Budd, D. B. Viscio, K. M. Smith and K. C. Langry, *Proc. Natl. Acad. Sci. USA*, 1978, **75**, 5755.
138. G. N. La Mar, N. L. Davis, D. W. Parish and K. M. Smith, *J. Mol. Biol.*, 1983, **168**, 887.
139. G. N. La Mar, H. Toi and R. Krishnamoorthi, *J. Am. Chem. Soc.*, 1984, **106**, 6395.
140. T. Yoshimura, H. Toi, S. Inaba and H. Ogoshi, *Inorg. Chem.*, 1991, **30**, 4315.
141. T. Yoshimura, H. Toi, S. Inaba and H. Ogoshi, *Bull. Chem. Soc. Jpn.*, 1992, **65**, 1915.
142. T. Yoshimura, H. Kamada, H. Toi, S. Inaba and H. Ogoshi, *Inorg. Chim. Acta*, 1992, **208**, 9.
143. J. P. Jesson, in *NMR of Paramagnetic Molecules*, G. N. La Mar, W. D. Horrocks, Jr. and R. H. Holm, eds., Academic Press, New York, 1973, p. 1.
144. R. D. Chambers, *Fluorine in Organic Chemistry*, Wiley, New York, 1973.
145. B. C. Mabbutt and P. E. Wright, *Biochim. Biophys. Acta*, 1985, **832**, 175.
146. S. D. Emerson and G. N. La Mar, *Biochemistry*, 1990, **29**, 1545.
147. C. M. Bougault, Y. Dou, M. Ikeda-Saito, K. C. Langry, K. M. Smith and G. N. La Mar, *J. Am. Chem. Soc.*, 1998, **120**, 2113.
148. Y. Yamamoto, K. Iwafune, R. Chûjô, Y. Inoue, K. Imai and T. Suzuki, *J. Biochem.*, 1992, **112**, 414.
149. G. N. La Mar, D. L. Budd and H. Goff, *Biochem. Biophys. Res. Commun.*, 1977, **77**, 104.
150. K. Nagai, G. N. La Mar, T. Jue and H. F. Bunn, *Biochemistry*, 1982, **21**, 842.
151. Y.-H. Kao and J. T. J. Lecomte, *J. Am. Chem. Soc.*, 1993, **115**, 9754; 1994, **116**, 6991.
152. M. Gueron, *J. Magn. Reson.*, 1975, **19**, 58.
153. A. J. Vega and D. Fiat, *Mol. Phys.*, 1976, **31**, 347.
154. K. Wüthrich, J. Hochmann, R. M. Keller, G. Wagner, M. Brunorin and C. Giacometti, *J. Magn. Reson.*, 1975, **19**, 111.
155. R. G. Shulman, S. H. Glarum and M. Karplus, *J. Mol. Biol.*, 1971, **57**, 93.
156. T. C. Traylor and A. P. Berzini, *J. Am. Chem. Soc.*, 1980, **102**, 2844.

157. Y. Yamamoto, N. Nanai, R. Chûjô and T. Suzuki, *FEBS Lett*, 1990, **264**, 113.
158. N. V. Shokhirev and F. A. Walker, *J. Phys. Chem.*, 1995, **99**, 17795.
159. R. O. Louro, I. J. Correia, L. Brennan, I. B. Coutinho, A. V. Xavier and D. L. Turner, *J. Am. Chem. Soc.*, 1998, **120**, 13240.
160. U. Kolczak, J. B. Hauksson, N. L. Davis, U. Pande, J. S. de Ropp, K. C. Langry, K. M. Smith and G. N. La Mar, *J. Am. Chem. Soc.*, 1999, **121**, 835.
161. F. A. Walker and U. Simonis, *Biol. Magn. Reson.*, 1993, **12**, 133.
162. I. Bertini, C. Luchinat, G. Parigi and F. A. Walker, *J. Biol. Inorg. Chem.*, 1999, **4**, 515.
163. K. Gersonde, H. Sick, M. Overkamp, K. M. Smith and D. W. Parish, *Eur. J. Biochem.*, 1986, **157**, 393.
164. F. A. Walker, D. Emrich, J. E. Rivera, B. J. Hanquet and D. H. Buttlair, *J. Am. Chem. Soc.*, 1988, **110**, 6234.
165. S. Sarma, B. Dangi, C. Yan, R. J. DiGata, D. L. Banville and R. D. Guiles, *Biochemistry*, 1997, **36**, 645.
166. S. Sarma, R. J. DiGata, D. B. Goodin, C. J. Miller and R. D. Guiles, *Biochemistry*, 1997, **36**, 5658.
167. G. S. Kachalova, A. N. Popov and H. D. Bartunik, *Science*, 1999, **284**, 473.
168. T. J. Swift, in: *NMR of Paramagnetic Molecules*, G. N. La Mar, W. D. Horrocks, Jr. and R. H. Holm, eds., Academic Press, New York, 1973, p. 53.
169. G. N. La Mar, K. Nagai, T. Jue, D. L. Budd, K. Gersonde, H. Sick, T. Kagimoto, A. Hayashi and F. Taketa, *Biochem. Biophys. Res. Commun.*, 1980, **96**, 1172.
170. G. N. La Mar, N. L. Davis, R. D. Johnson, W. S. Smith, J. B. Hauksson, D. L. Budd, F. Dalichow, K. C. Langry, I. K. Morris and K. M. Smith, *J. Am. Chem. Soc.*, 1993, **115**, 3869.
171. L. Banci, I. Bertini, S. Marconi and R. Pierattelli, *Eur. J. Biochem.*, 1993, **215**, 431.
172. G. N. La Mar, F. Dalichow, X. Zhao, Y. Dou, M. Ikeda-Saito, M. L. Chiu and S. G. Sligar, *J. Biol. Chem.*, 1994, **269**, 29629.
173. S. C. Busse and T. Jue, *Biochemistry*, 1994, **33**, 10934.
174. D. Ma, R. Musto, K. M. Smith and G. N. La Mar, *J. Am. Chem. Soc.*, 2003, **125**, 8494.
175. I. Bertini, C. Luchinat, P. Turano, G. Battaini and L. Casella, *Chemistry*, 2003, **9**, 2316.
176. H. M. Goff, in *Iron Porphyrin*, Part I, A. B. P. Lever ABP and H. B. Gray, eds., Addison-Wesley, Reading, MA, 1983, p. 237.
177. W. R. Light, R. J. Rhofls, G. Palmer and J. S. Olson, *J. Biol. Chem.*, 1987, **262**, 46.
178. Y. Yamamoto, T. Nakashima, E. Kawano and R. Chûjô, *Biochim. Biophys. Acta*, 1998, **1388**, 349.
179. Y. Yamamoto and G. N. La Mar, *Biochemistry*, 1986, **25**, 5288.
180. G. N. La Mar, P. D. Burns, J. T. Jackson, K. M. Smith, K. C. Langry and P. Strittmatter, *J. Biol. Chem.*, 1981, **256**, 237.
181. J. Z. Wu, G. N. La Mar, L. P. Yu, K. B. Lee, F. A. Walker, M. L. Chiu and S. G. Sligar, *Biochemistry*, 1991, **30**, 2156.
182. K. Miki, Y. Ii, M. Yukawa, A. Owatari, Y. Hato, S. Harada, Y. Kai, N. Kasai, Y. Hata, N. Tanaka, M. Kakudo, Y. Katsube, K. Kawabe, Z. Yoshida and H. Ogoshi, *J. Biochem.*, 1986, **100**, 269.
183. K. Miki, S. Harada, Y. Hato, S. Iba, Y. Kai, N. Kasai, Y. Katsube, K. Kawabe, Z. Yoshida and H. Ogoshi, *J. Biochem.*, 1986, **100**, 227.
184. H. Goff and G. N. La Mar, *J. Am. Chem. Soc.*, 1977, **99**, 6599.
185. E. Antonini and M. Brunori, in *Hemoglobins and Myoglobins in their Reactions with Ligands*, North-Holland, Amsterdam, 1971, p. 43.
186. G. M. Giacometti, A. Da Ros, E. Antonini and M. Brunori, *Biochemistry*, 1975, **14**, 1584.
187. T. Iizuka and I. Morishima, *Biochim. Biophys. Acta*, 1975, **400**, 143.
188. T. M. McGrath and G. N. La Mar, *Biochim. Biophys. Acta*, 1978, **534**, 99.
189. U. Pande, G. N. La Mar, J. T. L. Lecomte, F. Ascoli, M. Brunori, K. M. Smith, R. K. Pandey, D. W. Parish and V. Thanabal, *Biochemistry*, 1986, **25**, 5638.
190. J. D. Robertus, J. Kraut, R. A. Alden and J. J. Birktoft, *Biochemistry*, 1972, **11**, 4293.
191. W. S. Caughey, B. Chance, R. W. Estabrook and T. Yonetani, eds., *Hemes and Hemoproteins*, Academic Press, New York, 1966, p. 276.

192. J. L. Sudmeier, J. L. Evelhoch and N. B.-H. Jonsson, *J. Magn. Reson.*, 1980, **40**, 377.
193. K. Wüthrich, *NMR of Proteins and Nucleic Acids*, Wiley-Interscience Publication, New York, 1986, p., 24
194. B. A. Springer, S. G. Sligar, J. S. Olson and G. N. Phillips, Jr., *Chem. Rev.*, 1994, **94**, 699.
195. J. Vojtěchovský, K. Chu, J. Berendzen, R. M. Sweet and I. Schlichting, *Biophys. J.*, 1999, **77**, 2153.
196. F. Schotte, M. Lim, T. A. Jackson, A. V. Smirnov, J. Soman, J. S. Olson, G. N. Phillips, Jr., M. Wulff and P. A. Anfinrud, *Science*, 2003, **300**, 1944.
197. S. M. Decatur, G. D. DePillis and S. G. Boxer, *Biochemistry*, 1996, **35**, 3925.
198. J. A. Lukin, V. Simplaceanu, M. Zou, N. T. Ho and C. Ho, *Proc. Natl. Acad. Sci. USA*, 2000, **97**, 10354.
199. L. K. Sanders, W. D. Arnold and E. Oldfield, *J. Porphyrins Phthalocyanines*, 2001, **5**, 323.
200. D. A. Case, B. H. Huynh and M. Karplus, *J. Am. Chem. Soc.*, 1979, **101**, 4433.
201. C. Dalvit and C. Ho, *Biochemistry*, 1985, **24**, 3398.
202. C. Dalvit and P. E. Wright, *J. Mol. Biol.*, 1987, **194**, 329.
203. C. Dalvit, L. Tennant and P. E. Wright, *FEBS Lett.*, 1987, **213**, 289.
204. C. Schaeffer, C. T. Creascu, J. Mispelter, M. C. Garel, J. Rosa and J. M. Lhoste, *Eur. J. Biochem.*, 1988, **173**, 317.
205. Y. Thériault, T. C. Pochapsky, C. Dalvit, M. L. Chiu, S. G. Sligar and P. E. Wright, *J. Biomol. NMR*, 1994, **4**, 491.
206. S. L. Alam, B. F. Volkman, J. L. Markley and J. D. Satterlee, *J. Biomol. NMR*, 1998, **11**, 119.
207. R. J. Rohlf, A. J. Mathews, T. E. Carver, J. S. Olson, B. A. Springer, K. D. Edeberg and S. G. Sligar, *J. Biol. Chem.*, 1990, **265**, 3168.
208. A. Saika and C. P. Slichter, *J. Chem. Phys.*, 1954, **22**, 26.
209. J. P. Collman, J. L. Brauman, T. R. Halbert and K. S. Suslick, *Proc. Natl. Acad. Sci. USA*, 1976, **73**, 3333.
210. C. G. Kalodimos, I. P. Gerothanassis, R. Pierattelli and A. J. Troganis, *Inorg. Biochem.*, 2000, **79**, 371.
211. A. Abragam, *Principles of Nuclear Magnetism*, Oxford University Press, Oxford, 1961.
212. I. Solomon, *Phys. Rev.*, 1955, **99**, 559.
213. N. Bloembergen, *J. Chem. Phys.*, 1957, **27**, 572.
214. S. W. Unger, T. Jue and G. N. La Mar, *J. Magn. Reson.*, 1985, **61**, 448.
215. Y. Yamamoto, *J. Magn. Reson.*, 1994, **B 103**, 72.
216. E. Oldfield, R. S. Norton and A. Alerhand, *J. Biol. Chem.*, 1975, **250**, 6368.
217. A. G. Marshall, K. M. Lee and P. W. Martin, *J. Am. Chem. Soc.*, 180, **102**, 1460.

Site-Directed Solid-State NMR on Membrane Proteins

HAZIME SAITÔ*

*Himeji Institute of Technology, Harima Science Garden City, Hyogo, Japan and
Center for Quantum Life Sciences, Hiroshima University, Kagamiyama, Higashi-Hiroshima,
Japan*

1. Introduction	100
2. Isotope Enrichment	103
2.1 Uniform or extensive isotope enrichment	103
2.2 Selective enrichment by [1- ¹³ C]glucose or [2- ¹³ C]glycerol	104
2.3 Site-directed (or amino-acid specific) ¹³ C enrichment	105
3. Site-Directed Assignment of ¹³ C NMR Peaks of Membrane Proteins	108
3.1 Regio-specific assignment of peaks	108
3.2 Conformation-dependent ¹³ C chemical shifts in the solid	109
3.3 Site-directed assignment of peaks based on site-directed mutagenesis	111
3.4 Spectral editing using Mn ²⁺ -induced spectral broadening	116
3.5 Conformation-dependent ¹³ C chemical shifts in membrane proteins	123
4. Backbone Dynamics and Structures in the Interfacial Domains of Bacteriorhodopsin from Purple Membrane	125
4.1 Surface dynamics	125
4.2 Blue membrane	132
4.3 Surface structure	134
5. Backbone Dynamics in the Transmembrane α -Helices	142
5.1 Kinked structure	142
5.2 M-like state	143
5.3 Long-distance interaction among residues for information transfer	148
6. Backbone Structures and Dynamics in Monomers	153
6.1 bR mutants incapable of forming 2D lattice	153
6.2 bR structure in lipid bilayer	155
7. Membrane Proteins Overexpressed in <i>E. coli</i>	157
7.1 Phoborhodopsin and its cognate transducer	158
7.2 Diacylglycerol kinase	165
8. Membrane-Binding Protein	167
9. Concluding Remarks	170
Acknowledgements	171
References	171

*Address correspondence to: #203, 3-15-21 Sumiyoshi-honmachi, Higashinada-ku, Kobe, Japan 658-0051

*Well-resolved, fully visible ^{13}C NMR signals of membrane proteins were successfully recorded either at ambient or at lower temperatures when they were embedded in lipid bilayers constituting a 2D crystalline lattice, as manifested from site-directed ^{13}C NMR studies on $[3\text{-}^{13}\text{C}]\text{Ala}$ and/or $[1\text{-}^{13}\text{C}]\text{Val}$ -labeled bacteriorhodopsin (bR) from purple membrane, instead of uniformly labeled preparations. It is emphasized that recording ^{13}C NMR spectra by dipolar decoupled magic angle spinning (DD-MAS) is essential to detect signals from rather flexible portions of fully hydrated membrane proteins, in addition to recording signals from static portions by cross-polarization-magic angle spinning (CP-MAS). The resulting ^{13}C NMR signals were site-directly assigned to specific residues utilizing site-directed mutants, otherwise global conformational changes were introduced by such mutations. Conformational features of bR with emphasis on surface area, as defined by surface complex, were discussed together with its biological significance, on the basis of the conformation-dependent displacement of the ^{13}C chemical shifts. Further, slow local membrane dynamics with frequencies of 10^5 or 10^4 Hz, which is important for biological functions, was analyzed as viewed from specifically suppressed ^{13}C NMR signals of certain regions caused by interference of fluctuation frequency with frequency of proton-decoupling or magic angle spinning. This approach has been further extended to reveal the conformation and dynamics of a variety of ^{13}C -labeled membrane proteins that are overexpressed from *Escherichia coli* and subsequently not always involved in a 2D crystalline lattice by ^{13}C NMR: they include phototaxis receptor protein (pharaonis phoborhodopsin), its transducer (pHtrII), and membrane enzyme (diacylglycerol kinase). In such cases, it was found that several ^{13}C NMR signals could be suppressed from amino-acid residues located at the flexible portions such as loops and transmembrane α -helices near to the membrane surface, as a result of interference of dominant frequency for conformational fluctuations of the order of 10^4 - 10^5 Hz. This means that protein-protein contact in the 2D crystalline lattice significantly regulates the protein dynamics. It is therefore important to search for the most appropriate experimental condition to be able to observe the full ^{13}C NMR signals of the membrane proteins under consideration, including the choice of the most appropriate ^{13}C -labeled amino acids, temperature, ionic state, etc.*

1. INTRODUCTION

The most important physical property of biological membranes is that they serve as permeability barriers to the passage of polar ions and molecules, because such charged species cannot remain in the nonpolar interior of lipid bilayers. Naturally, membrane proteins having at least one segment of peptide chain traversing the lipid bilayer as a result of incorporation into such lipid bilayers serve as active mediators between the cell and its environment. In particular, such membrane proteins play crucial roles in maintaining various activities of cells such as the transport of appropriate molecules into or out of the cell, catalysis of chemical reaction, and receiving and transducing chemical signals from the cell environment, channel, etc.¹ Many integral membrane proteins in the membrane environment are assembled into oligomeric complexes rather than monomers as revealed by crystallographic studies, to form tertiary and quaternary structures that are believed to be necessary

for biological functions.^{2,3} Indeed, the presence of oligomeric complexes has been confirmed for a variety of membrane proteins as viewed from their three-dimensional (3D) pictures revealed either from two-dimensional (2D) or 3D crystals, including light-driven proton pump bacteriorhodopsin (bR),⁵⁻⁸ chloride pump halorhodopsin^{9,10} and phototaxis receptor sensory rhodopsin II (phoborhodopsin),¹¹⁻¹³ photosynthetic reaction center,¹⁴ light-harvesting complex,^{15,16} cytochrome *c* oxidase,^{17,18} potassium and mechanosensitive channels,^{19,20} bovine rhodopsin,²¹ calcium pump of sarcoplasmic reticulum,²² etc.

On the contrary, there remains an alternative view that such an oligomerization process is not always essential for the biological function of membrane proteins: most of their biological activities are known to be also retained in a monomeric form as solubilized in detergents or reconstituted in lipid bilayers. For instance, the functional unit responsible for the photocycle of bR, as a typical membrane protein, is the monomer itself,²³⁻²⁵ except that the lifetimes of the L and N intermediates are significantly shorter in the monomer.^{26,27} The light-dark adaptation is affected by the aggregation state of bR²⁴ and an increase in the relative amplitude of the slow component of bR excited state decay is observed in the monomer, which is due to the increase in the concentration of the 13-*cis*-retinal isomer in the ground state of the light-adapted bR²⁸ for the trimeric form of bR, although bR is a naturally occurring 2D crystal as purple membrane (PM) comprising the trimeric form packed to a hexagonal lattice.

In this connection, it is very important to clarify how the 3D structure and dynamics of membrane proteins of interest could be modified by converting the monomeric form as encountered in a lipid bilayer into the 2D crystal form in the presence of their specific protein-protein and lipid-protein interactions leading to the formation of oligomers. X-ray crystallography and multidimensional solution NMR spectroscopy have proved to be standard and indispensable techniques to reveal the 3D structure of a variety of biological molecules, including biologically active peptides, globular proteins, membrane proteins, etc. Application of these approaches to a variety of membrane proteins, however, is not always straightforward as compared with that of globular proteins, because of extreme difficulty in crystallization of membrane proteins essential for X-ray diffraction study as compared with globular proteins, and enormously broadened line widths arising from their increased molecular mass in the presence of surrounding lipid bilayers hampering the revelation of such structures.

As an alternative means, it is a natural consequence to expect that high-resolution solid-state NMR could be conveniently utilized to reveal the 3D structure and dynamics of a variety of membrane proteins, because the expected NMR line widths available from solid-state NMR are not any more influenced by *motional fluctuation of proteins under consideration as a whole* as encountered in solution NMR. For instance, an attempt was made to determine 3D structure of *uniformly* ¹³C-labeled α -spectrin SH3 domain as a globular protein, based on distance constraints estimated from ¹³C-¹³C proton-driven spin-diffusion (PDSD) measurements for well-resolved peaks,^{29,30} although structural data were unavailable from missing signals of the N- and C-termini caused by local fluctuation motions.

It should be expected, however, that ^{13}C NMR signals of *uniformly or densely* ^{13}C -labeled, fully hydrated membrane proteins could be substantially broadened or suppressed^{31–37} at ambient temperature, because their backbone or side-chain carbons of certain residues could undergo *local fluctuation motions* with either correlation times of the order of less than 10^{-8} or 10^{-4} – 10^{-5} s that vary depending upon the portions under consideration, especially for flexible residues at the N- and C-terminal residues or loops, respectively, as encountered for bR as described below.^{31,32} Therefore, the above-mentioned approach is not always useful for fully hydrated membrane proteins that could undergo a variety of fluctuation motions. Instead, 3D structural data for transmembrane portions were successfully obtained from ^{15}N NMR data of uniformly (but not densely) ^{15}N -labeled proteins in either a mechanically or a magnetically aligned system,^{38–41} as far as such samples were prepared at relatively lower humidity. Still, no structural information is available from residues located at un-oriented or flexible N- or C-terminal residues as well as at interhelical loops.

In contrast, the site-directed ^{13}C NMR approach on *selectively* ^{13}C -labeled membrane proteins from a 2D crystalline state is a very valuable means to reveal conformational feature as well as the dynamics of *whole areas* of *fully hydrated* proteins, including both N- or C-terminal residues as well as interhelical loops. This is because a number of *fully hydrated* membrane proteins of biological relevance in a 2D crystal or monomeric state are far from being a rigid body as conceived,^{35–37} at least at *ambient temperature*, in spite of currently available 3D structural models revealed by cryo-electron microscope or X-ray diffraction studies on “so-called” crystalline preparations at low temperature.^{5–22} Indeed, they are very flexible and undergo various kinds of molecular motions with correlation times of the order of 10^{-2} – 10^{-8} s, depending upon crystalline or monomeric preparations and the site of interest. This picture is readily available from site-directed solid-state ^{13}C NMR studies on bR from PM (2D crystal)^{31–35} as well as from monomeric *pharaonis* phoborhodopsin (*ppR* or sensory rhodopsin II),⁴² its transducer (*pHtrII*),⁴³ and *E. coli* diacylglycerol kinase (*DGK*).⁴⁴ This view is also readily recognized by the fact that their hydrophilic loops or N- or C-terminal residues are fully exposed to an isotropic aqueous phase, while their hydrophobic transmembrane α -helices are embedded within the fluid liquid crystalline environment of lipid bilayers.

Especially, it is important to reveal the general features of a site-directed NMR approach on membrane proteins in the monomeric form as compared with that of the 2D or 3D crystalline samples so far accumulated, because a number of biologically important membrane proteins from overexpressed systems are present as monomers when they are reconstituted into lipid bilayers. In such cases, several ^{13}C NMR signals of the interhelical loops are missing from $[3\text{-}^{13}\text{C}]\text{Ala}$ -labeled membrane proteins,^{37,42,45,46} although ^{13}C NMR spectra are fully visible from the 2D crystalline preparations of fully hydrated membrane proteins.^{32,36} In the latter, however, several signals from the loops and some transmembrane α -helices are also missing depending upon the type of ^{13}C -labeled species used.³⁴ It is therefore very important to obtain a convenient way to determine how such monomeric form of membrane proteins can be converted into a 2D crystalline form in order to achieve maximum structural information from ^{13}C NMR approach for this purpose.

Indeed, this type of a dynamic picture of membrane proteins is more pronounced when they are present as monomers in lipid bilayers instead of the 2D or 3D crystalline states, because the intermolecular contact responsible for leading to such oligomerization is absent as manifested from a comparative ^{13}C NMR study on PM and reconstituted bR in lipid bilayers.^{45,46} This dynamic picture is obviously disadvantageous as viewed from the aspect of revealing the 3D structure, however. It is therefore desirable to prepare better crystalline samples even in the case for solid-state NMR studies by searching for the optimum experimental conditions although this requirement is, of course, less stringent as compared with that of the sample for X-ray diffraction.

2. ISOTOPE ENRICHMENT

2.1. Uniform or extensive isotope enrichment

In general, it is not easy to distinguish individual NMR signals from the respective residues in membrane proteins in which their peaks are heavily crowded, because of the increased number of amino-acid residues. The resulting signals are also broadened due to the increased molecular mass consisting of a complexed mixture with surrounding lipids. Therefore, an appropriate isotope enrichment, rather than labeling, by the most common ^{13}C or ^{15}N nuclei with larger chemical shift ranges through biosynthesis by cell cultures or chemical synthesis, is essential to enhance their peak intensities and selectivity of their particular labeled signals from background signals arising from residues of natural abundance. The extent of isotope enrichment is naturally desirable to be as high as possible up to 100% for a sample to be used for a solid-state NMR. Extensive isotope enrichment for globular proteins of molecular weights up to 10 kDa has proved to afford a better spectral resolution comparable to that of solution NMR when uniform isotope substitution, using [^{13}C]glucose, [$^{13}\text{C}_2$]acetate, and/or $^{15}\text{NH}_4\text{Cl}$ as sole sources for ^{13}C or ^{15}N nuclei is utilized.^{47–49} The spectra were recorded for microcrystalline preparations by an ultra-high-field spectrometer utilizing fast magic angle spinning, high-power proton decoupling ($\omega_1/2\pi \gg 70$ kHz) with an efficient decoupling scheme such as TPPM (two-pulse phase modulation)⁵⁰ or XiX (X-inverse-X),⁵¹ and homonuclear ^{13}C – ^{13}C J decoupling.⁴⁷

In contrast to rigid crystalline globular proteins, surface residues of such loops and N- or C-terminal residues of bR as a typical membrane protein turned out to be very flexible at ambient temperature, even if they are embedded in lipid bilayer to form naturally occurring 2D crystals (PM). This kind of flexibility is essential to exhibit its specific biological function. Nevertheless, it is cautioned that spectral resolution of such ^{13}C -labeled proteins might be desperately deteriorated, if a directly bonded ^{13}C – ^{13}C sequence is present in the dense ^{13}C spin networks undergoing fluctuation motions with frequency from 10^4 to 10^5 Hz, as manifested from the extremely broadened ^{13}C CP-MAS NMR spectra of [1,2,3- $^{13}\text{C}_3$]Ala-labeled bR from PM, as demonstrated in Fig. 1.³⁴ The resulting spectral resolutions turned out

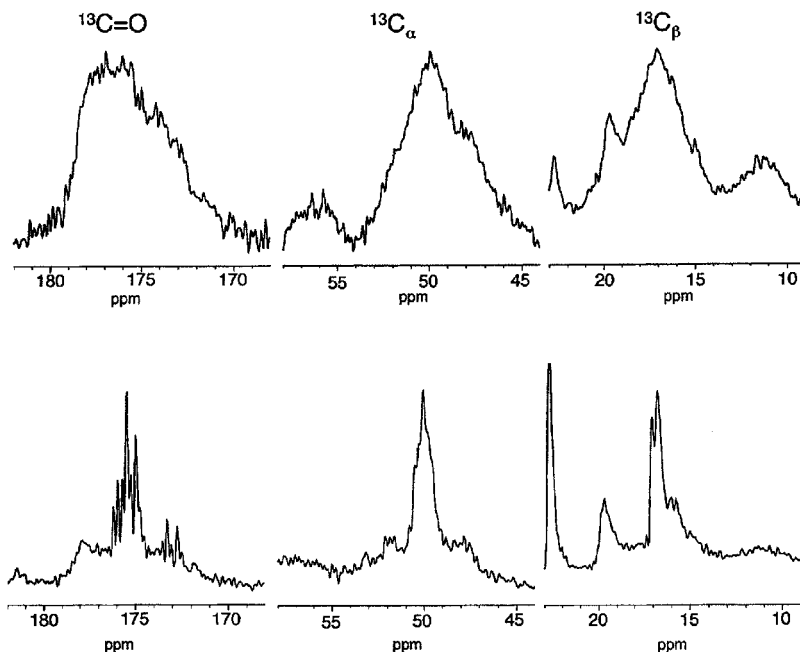


Fig. 1. ^{13}C CP-MAS NMR spectra (upper traces) and DD-MAS NMR spectra (lower traces) of $^{13}\text{C}=\text{O}$, $^{13}\text{C}_\alpha$, and $^{13}\text{C}_\beta$ carbons from $[1,2,3\text{-}^{13}\text{C}_3]\text{Ala}$ -labeled bacteriorhodopsin from PM.³⁴ Reproduced with permission from the Japanese Biochemical Society.

to be hopelessly poor, although the well-resolved signals are visible by *single-pulse* DD (dipolar decoupled)-MAS NMR spectra of the carbonyl region. This DD-MAS NMR technique is especially useful in recording signals of membrane proteins with various flexible portions, even though this fact has been ignored in many instances. The observation of such extremely broadened signals is mainly caused by their shortened spin-spin relaxation times arising from an increased number of relaxation pathways modulated by their fluctuation motions through a number of ^{13}C - ^{13}C homonuclear dipolar and scalar spin interactions, etc.

In this case, no meaningful information is available from the featureless ^{13}C NMR signals. On the contrary, better spectral resolution has been achieved by ^{13}C CP-MAS and DD-MAS NMR spectra of $[3\text{-}^{13}\text{C}]\text{Ala}$ - or $[1\text{-}^{13}\text{C}]\text{Val}$ -labeled bR from PM,^{33,35-37} in which problems arising from dense ^{13}C spin networks of directly bonded ^{13}C - ^{13}C pairs that cause such accelerated transverse spin relaxation rate are not any more present.

2.2. Selective enrichment by $[1\text{-}^{13}\text{C}]\text{glucose}$ or $[2\text{-}^{13}\text{C}]\text{glycerol}$

It is advisable to avoid uniform isotope enrichment for *fully hydrated* membrane proteins in order to prevent creation of a directly bonded ^{13}C - ^{13}C pair. This is

because indirect one-bond J couplings as well as dipolar ^{13}C – ^{13}C interactions can cause severe line broadenings in the solid-state NMR in which the maximum isotope enrichment is required to achieve a better spectral sensitivity. This type of line broadening, however, cannot be removed even if high-speed magic angle spinning ($>25\text{ kHz}$) is employed. In addition, the weak ^{13}C – ^{13}C dipolar couplings arising from any remote ^{13}C – ^{13}C interaction turn out to be obscured by the strong dipolar couplings due to spin diffusion within the dense ^{13}C spin network and by the dipolar truncation mechanism.⁵² In solution NMR, analysis of side-chain dynamics by ^{13}C spin relaxation is complicated by contributions from ^{13}C – ^{13}C scalar and dipolar couplings. To overcome the latter complication, the ^{13}C label using $[1\text{-}^{13}\text{C}]$ glucose or $[2\text{-}^{13}\text{C}]$ glycerol as the sole carbon sources has been introduced to isolate groups in an alternating ^{12}C – ^{13}C – ^{12}C -labeling pattern in solution NMR.⁵³ Taking this labeling strategy, Hong and Jakes⁵⁴ and Hong⁵⁵ prepared selectively and extensively ^{13}C -labeled proteins suitable for solid-state NMR. They showed that for amino acids synthesized in the linear part of the biosynthetic pathways, $[1\text{-}^{13}\text{C}]$ glucose preferentially labels the ends of the side-chains, while $[2\text{-}^{13}\text{C}]$ glycerol labels the C_α of 10 amino-acid residues, including Gly, Cys, Ser, Ala, Leu, Val, His, Phe, Tyr, and Trp as well as C_β of Val residue, although two pairs of coupled ^{13}C spins, Val $\text{C}_\alpha/\text{C}_\beta$, and Leu $\text{C}_\beta/\text{C}_\gamma$ are still present. Typically, they used a modified M9 medium containing, per liter, 1 g $^{15}\text{NH}_4\text{Cl}$, 4 g $[2\text{-}^{13}\text{C}]$ glycerol, 3 g KH_2PO_4 , 6 g Na_2HPO_4 , 1 mM MgSO_4 , the unlabeled amino acids Asp, Asn, Arg, Gln, Glu, Ile, Lys, Met, Pro, and Thr at $150\text{ }\mu\text{g/mL}$ each, and $100\text{ }\mu\text{g/mL}$ ampicillin. They showed that the maximum labeling level is up to 50%.

Even in the absence of the problems of dense spin network, it should also be taken into account that a ^{13}C NMR signal from an expected site is not always fully visible if the motional frequency of internal fluctuation, if any, is interfered by either the frequency of proton decoupling or magic angle spinning, as encountered for a variety of membrane proteins at ambient temperature.^{42–46,56} This is also possible for a variety of labels ($[3\text{-}^{13}\text{C}]$ Ala, $[1\text{-}^{13}\text{C}]$ Gly, Ala, or Val) used. This kind of information, however, is extremely useful to locate a residue in which the fluctuation motions with timescales of a millisecond or microsecond of biological significance are present, once ^{13}C NMR peaks of interest are site-directly assigned to amino-acid residues located at the particular site in advance, as discussed below.

2.3. Site-directed (or amino-acid specific) ^{13}C enrichment

In order to obtain more simple spectral features, it is advised to try alternative site-directed (or amino-acid-specific) enrichment in which one of the unlabeled amino-acid residues is replaced by a selectively ^{13}C -labeled amino acid such as $[3\text{-}^{13}\text{C}]$ Ala, $[1\text{-}^{13}\text{C}]$ Ala, Val, etc. in the growth TS medium, as shown in Table 1⁵⁷ for bR from *H. salinarum* or M9 medium for a variety of membrane proteins expressed from *E. coli*.⁵⁸ It is also possible to combine two different kinds of amino-acids such as $[3\text{-}^{13}\text{C}]$ Ala and $[1\text{-}^{13}\text{C}]$ Val simultaneously, when there is no overlap of peaks with each other nor direct ^{13}C – ^{13}C connectivity. This approach is therefore the simplest

Table 1. TS and M9 media for amino-acid specific enrichment

TS medium (pH 6.6, 2L scale)					
NaCl					500 g
MgSO ₄ · 7H ₂ O					40 g
KCl					2 g
KNO ₃					200 mg
KH ₂ PO ₄					300 mg
K ₂ HPO ₄					300 mg
Sodium citrate 2H ₂ O					1 g
L-Ala	430 mg	L-Arg	800 mg	L-Asp	450 mg
L-Cys	100 mg	L-Glu	2600 mg	Gly	120 mg
L-His	300 mg	L-Ile	440 mg	L-Leu	1600 mg
L-Lys	1700 mg	L-Met	370 mg	L-Phe	260 mg
L-Pro	100 mg	L-Ser	610 mg	L-Thr	500 mg
L-Tyr	400 mg	L-Trp	50 mg	L-Val	1000 mg
Glycerol	2 g = 0.1% (g/ml)				
Metal salt solution 2 mL					
[Metal salt solution consisting of: 100 mL (0.1 N HCl)]					
CaCl ₂ · 2H ₂ O				700 mg	
CuSO ₄ · 5H ₂ O				5 mg	
FeCl ₂ · 4H ₂ O				230 mg	
ZnSO ₄ · 7H ₂ O				44 mg	
MnSO ₄ · H ₂ O				30 mg	
M9 medium (pH 7.4, 1 L scale)					
Non-labeled amino acids (except for Trp) each 100 mg					
Trace metal solution 1.0 mL, consisting of:					
[concentrated trace metal solution (100 mL scale)]					
4 mM	ZnSO ₄ 7H ₂ O				115 mg
1 mM	MnSO ₄ 4·5H ₂ O				23.2 mg
4.7 mM	H ₃ BO ₃				29.1 mg
0.7 mM	CuSO ₄ · 5H ₂ O				17.5 mg
2.5 mM	CaCl ₂ · 2H ₂ O				36.8 mg
1.8 mM	FeCl ₂ · 4H ₂ O				35.8 mg
Adding the following, after autoclaving:					
1 M MgSO ₄	3 mL				
1 M CaCl ₂	150 µL				
20% glucose	10 mL (2 g/L)				
Trp (100 mg/10 mL)	10 mL (100 mg/mL)				
¹³ C-labeled amino acid (100 mg/10 mL)	10 mL (100 mg/L)				
Antibiotics (the amount varies depending upon protein to be overexpressed and bacterium)					

means to incorporate one or two kinds of amino acid residue(s) as an isolated spin system, which is essential for observation of the narrowest NMR signals for membrane proteins even if fluctuations with a variety of frequencies are present depending upon their environment either in a 2D crystal or a monomer. In principle,

all the ^{13}C signals thus obtained could be readily ascribed to the incorporated amino-acid residues, unless otherwise metabolic conversion, for instance, from incorporated Asp to Glu or Trp residues is not ignored, as encountered for $[4-^{13}\text{C}]\text{Asp}$ -labeled bR in which the scrambling was confirmed by a ^{14}C isotope experiment.⁵⁹ No such conversion, however, has been noted when amino-acids such as Ala and Val are incorporated into bR. Therefore, well-resolved ^{13}C NMR signals are available from $[3-^{13}\text{C}]\text{Ala}$ -bR from PM as illustrated in Fig. 2. All the signals located at positions between 14.5 and 18 ppm can be exclusively ascribed to Ala C_β signals located at various sites, because there are no overlaps of signals from other amino-acid residues, nor accelerated transverse relaxation process in the absence of a directly bonded ^{13}C – ^{13}C pair. Background ^{13}C NMR signals from unlabeled amino-acid residues can be also usually ignored because of the highest level of

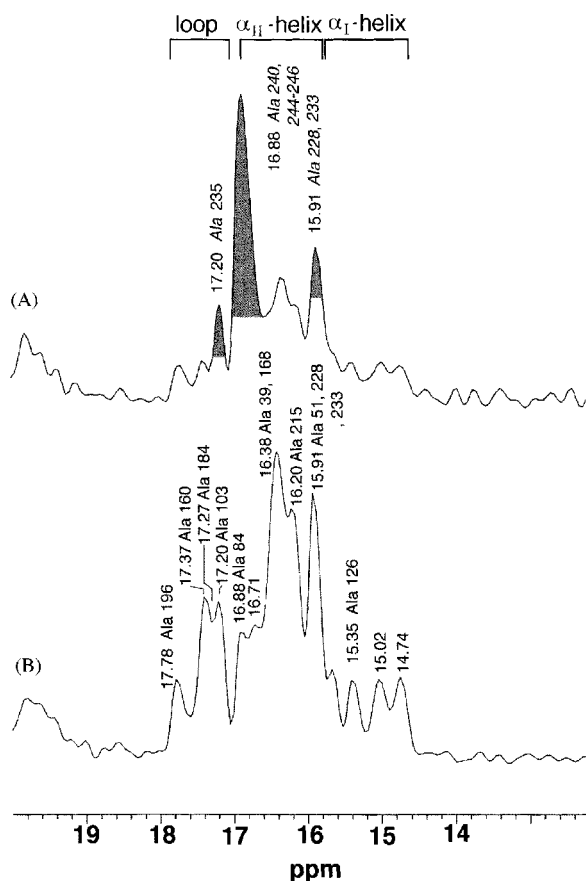


Fig. 2. Comparison of ^{13}C DD-MAS (A) and CP-MAS (B) NMR spectra of $[3-^{13}\text{C}]\text{Ala}$ -labeled bacteriorhodopsin from PM. The three peaks marked by gray on the upper trace are from the Ala residues located at the N- and C-terminal moieties.⁶⁰ Reproduced with the permission from the Biophysical Society.

isotope enrichment, except for the case of [1- ^{13}C]Gly labeled bR in which a possibility of contributions from a variety of other amino-acid residues at natural abundance should be taken into account.

It is cautioned that this kind of an excellent spectral resolution of [3- ^{13}C]Ala-bR from PM could be again severely deteriorated, when spectra are recorded either under the conditions of lower humidity than relative humidity (r.h.) 90%^{36,61} or at a temperature below -10°C .⁶² This may be a consequence of similarity of the data between the temperature-dependent spectral change and the dehydration/rehydration behavior of PM studied by measurements of the lamellar spacing by neutron diffraction.⁶³ Still, no sufficient structural information relating to a 3D structure is available from loops or N- or C-terminal residues under such conditions, however. It is again emphasized that better spectral resolution can be achieved only when the ^{13}C NMR spectra are recorded for ^{13}C -labeled proteins of 2D crystalline lattice at ambient temperature.

3. SITE-DIRECTED ASSIGNMENT OF ^{13}C NMR PEAKS OF MEMBRANE PROTEINS

3.1. Regio-specific assignment of peaks

For integral membrane proteins embedded in a membrane, the hydrophobic portion of the polypeptide chain passes through at least once or several times, usually as α -helices but in some cases as β -strands. The hydrophilic N- and C-terminal residues, protruding from either side of the membrane, are exposed to the aqueous phase to result in an undergoing fast fluctuation motions by taking the random coil form. The interhelical loops between the transmembrane α -helices are located at the membrane surface. G-protein-coupled receptors (GPCRs) form the largest known family among integral membrane proteins of all genes encoded in the genomes of higher eukaryotes and their highly conserved topology is made up of seven transmembrane helices like bR as their prototype protein. They function as a transducer of extracellular signals like hormone, pheromones, odorants, or light into the activation of intracellular G-protein complex, as demonstrated by rhodopsin as a typical GPCR, a mammalian photoreceptor protein of 40 kDa covalently linked to 11-*cis*-retinal through Lys 296.

It is very helpful to compare the ^{13}C NMR spectra of [3- ^{13}C]Ala-labeled proteins recorded by the DD-MAS technique (Fig. 2A) with those recorded by the CP-MAS technique (Fig. 2B), to distinguish the ^{13}C NMR signals of a rather flexible N- or C-terminus from those of immobilized portions arising from the transmembrane helices, in view of their differential spin-lattice relaxation times.³⁶ In fact, the ^{13}C NMR spectra are readily visible from the whole area of the membrane proteins by the DD-MAS experiment when they are labeled by [3- ^{13}C]Ala, because their spin-lattice relaxation times are of the order of 0.5 s^{32,36} and sufficiently short compared with repetition times usually taken as 4 s. In contrast, the ^{13}C NMR

signals from such regions are almost completely suppressed by the CP-MAS experiment owing to time-averaged dipolar interactions in the presence of their flexible fluctuation motions, as manifested from the ^{13}C NMR spectra of $[3-^{13}\text{C}]\text{Ala}$ -labeled proteins.³⁷ This is not always true, however, for ^{13}C NMR observations of nuclei with longer spin-lattice relaxation times of the order of 20 s, such as carbonyl groups of the transmembrane α -helices of bR labeled by $[1-^{13}\text{C}]\text{amino acids}$.³⁶ In such cases, the ^{13}C NMR signals from the transmembrane α -helices are usually not visible by the DD-MAS experiment that usually utilizes shorter repetition times.

Further regio-specific assignments of the observed ^{13}C NMR peaks to the transmembrane α -helices, loops and N- or C-terminus is readily feasible in view of their respective ^{13}C chemical shifts, corresponding to the α -helix form, turned structure, and random coil forms, respectively, with reference to the conformation-dependent displacements of the ^{13}C chemical shifts, to be described in the next section.

3.2. Conformation-dependent ^{13}C chemical shifts in the solid^{35,36,63,64}

^{13}C chemical shifts of polypeptides, taking particular secondary structures such as the α -helix, β -sheet, etc. in the solid-state and random coil in solution, can be conveniently used as reference data to determine the local conformation of amino-acid residues of interest. This is readily made possible in the solid because such ^{13}C chemical shifts are free from time-averaged processes due to conformational fluctuations as frequently encountered in solution NMR. Recording ^{13}C NMR spectra of polypeptides by taking the β -sheet form is made possible in the solid, although no solution NMR data are available due to a sparing solubility in solution. As demonstrated in Table 2, the two kinds of major conformations, the α -helix or β -sheet form in addition to the random coil form in solution, are readily distinguished for a variety of polypeptides with reference to their significant ^{13}C NMR peak positions for the C_α , C_β and carbonyl carbons.^{64,65} The ^{13}C chemical shifts for the random coil form in CF_3COOH or in aqueous solution in the presence of a few drops of H_2SO_4 are located at the midpoint of the peak positions between the α -helix and β -sheet forms, reflecting the time averaging among allowed conformations.⁶⁶ In general, the backbone C_α and $\text{C}=\text{O}$ ^{13}C shifts of the α -helix (ordinary α -helix or α_1 -helix) forms are significantly displaced to high frequency (by 3.5–8.0 ppm) with respect to those of the β -sheet forms, while the side chain C_β peak of the α -helix form is displaced to low frequency (by 3.4–5.2 ppm) with respect to that of the β -sheet form. The differences, Δ , of the ^{13}C chemical shifts between the α -helix and β -sheet form up to 8 ppm for the C_α , C_β , and $\text{C}=\text{O}$ carbons do not vary strongly among a variety of amino acid residues (Table 2), although the absolute ^{13}C chemical shifts for the C_α and C_β carbons are strongly affected by the chemical structure of the individual amino-acid residues. Further, it is noteworthy that the ^{13}C NMR signals of the random coil form are resonated at positions between the above-mentioned α -helix and β -sheet forms.

Table 2. ^{13}C chemical shifts characteristic of the α -helix, β -sheet and random coil forms (ppm from TMS)^a

Amino acid Residues in Polypeptides	C_α				C_β				$\text{C} = 0$			
	α -helix	β -sheet	Random coil ^c	Δ^b	α -helix	β -sheet	Random coil ^c	Δ^b	α -helix	β -sheet	Random coil ^c	Δ^b
Ala	52.4	48.2	51.1	4.2	14.9	19.9	15.7	-5.0	176.4	171.8	176.1	4.6
	52.3	48.7		3.6	14.8	20.0		-5.2	176.2	171.6		4.6
	52.8	49.3		3.5	15.5	20.3		-4.8	176.8	172.2		4.6
Leu	55.7	50.5	55.2	5.2	39.5	43.3	39.7	-3.8	175.7	170.5	175.7	5.2
	55.8	51.2		4.6	43.7 ^d	39.6 ^d		4.1	175.8	171.3		4.5
Val	65.5	58.4	61.2	7.1	28.7	32.4	31.7	-4.6	174.9	171.8	174.4	3.1
		58.2				32.4				171.5		
Ile	63.9	57.8	61.1	6.1	34.8	39.4	37.1	-3.7	174.9	172.7	175.8	2.2
		57.1				33.1				171.0		
Glu(OBzl)	56.4	51.2		5.2	25.6	29.0		-3.4	175.6	171.0		4.6
	56.8	51.1		5.7	25.9	29.7		-3.8	175.4	172.2		3.2
Asp(OBzl)	53.4	49.2		4.2	33.8	38.1		-4.3	174.9	169.8		5.1
	53.6 ^e				34.2 ^e				174.9			
Lys ^f	57.4				29.9				176.5			
Lys(Z)	57.6	51.4		6.2	29.3	28.5		-0.8	175.7	170.4		5.3
Arg ^f	57.1				28.9				176.8			
Phe	61.3	53.2		8.1	35.0	39.3		-4.3	175.2	169.0		6.2
Met	57.2	52.2		5.0	30.2	34.8		-4.6	175.1	170.6		4.5
Gly		43.2								168.4		
		44.3								168.4		
										169.2		
									171.6 ^g	168.5		3.1

^aRefs. 64,65^bDifference in the ^{13}C chemical shifts of the α -helix form relative to those of the β -sheet form.^cIn CF_3COOH solution. A few drops of H_2SO_4 was added in the cases of $(\text{Ile})_n$ and $(\text{Leu})_n$.^dThis assignment should be reversed.^eErroneously assigned from the left-handed α -helix.^fData taken from the data of salt-induced α -helix in neutral aqueous solution.^gAveraged values from the data of polypeptides containing ^{13}C -labeled glycine residues.

Such conformation-dependent displacements of the ^{13}C chemical shifts for particular amino-acid residues depending upon their secondary structures can be conveniently utilized as a means to elucidate the local conformations of the respective amino-acid residues for any given proteins or peptides, since all the ^{13}C chemical shifts of the amino-acid residue, adopting unfolded conformations in solution, turn out to be independent of all neighboring residues except for the proline residue.⁶⁷ Therefore, the transferability of these parameters for the particular residues from the simple model polypeptides to more complicated proteins is excellent and can be applied to any type of proteins, as far as the amino acid residues under consideration are virtually static (rigid) as in silk fibroin,⁶⁸ collagen,^{69,70} and synthetic transmembrane peptides of bR in the solid.⁷¹

3.3. Site-directed assignment of peaks based on site-directed mutagenesis

The first step to this end is to locate the peak(s) of reduced peak intensity, if any, in the ^{13}C NMR spectra of ^{13}C -labeled mutants of membrane proteins, in which specific amino-acid residues of interest are replaced with others, as compared with those of the wild type. The feasibility of this approach has been extensively explored as a convenient means to be able to assign the well-resolved ^{13}C NMR peaks of bR. For this purpose, the locations of the individual amino-acid residues are illustrated in the primary sequence of bR taking into account the possible secondary structure based on the data of X-ray diffraction studies as shown in Fig. 3. They are marked as [3- ^{13}C]Ala (circle), [1- ^{13}C]Val (rectangular), Ala (circle), Pro (square), Trp (oval), etc. For instance, the Ala C_β ^{13}C NMR peaks of Ala 196 (F-G loop) and 126 (at the corner of helix D) in [3- ^{13}C]Ala-labeled bR are straightforwardly assigned to the peaks whose intensities are significantly reduced in the site-directed mutants A196G and A126G, respectively, as shown in Fig. 4,⁶⁰ since no additional spectral change was noted by the introduction of this sort of site-directed mutagenesis. Here, the so-called α_{I} - (ordinary right-handed α -helix) and α_{II} -helices are defined on the basis of the conformation-dependent ^{13}C chemical shifts of [3- ^{13}C]Ala-labeled bR with reference to the ^{13}C chemical shifts of $(\text{Ala})_n$ in the solid and in hexafluoroisopropanol (HFIP) solution, respectively.³¹ The so-called latter α_{II} -helix was originally proposed by Krimm and Dwivedi⁷² as an anomalous α -helix found for bR embedded in membrane by infrared spectra, although no such anomaly was noted later by X-ray diffraction studies.⁶ Nevertheless, this definition is still useful to characterize the manner of an α -helix form in membrane proteins and should be ascribed to a residue whose time-averaged deviation of torsion angles at ambient temperature is different from that of static ones at low temperature and leads to anharmonicity associated with local anisotropic fluctuation.⁷¹

In many instances, however, a more complicated spectral change in the difference spectrum can arise from an accidental overlap of signal under consideration with that of another residue and an accompanied local conformational change is introduced by site-directed mutagenesis as encountered in A84 and A39V.³³ It is straightforward to assign the peak at 16.88 ppm to Ala 84 from helix C, as it is

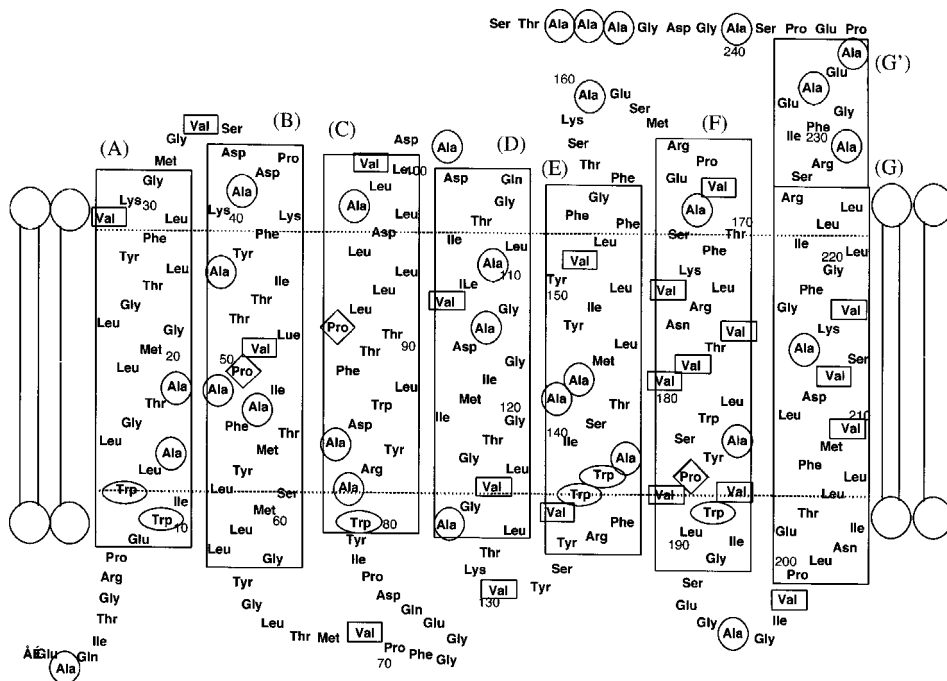


Fig. 3. Schematic representation of the primary structure of bacteriorhodopsin taking into account its secondary structure based on X-ray diffraction studies. Residues marked by circle, rectangular box, diamond, and oval are Ala, Val, Pro, and Trp, respectively.

decreased in A84G as compared with the wild type, although an additional signal of Ala 240 from the C-terminal moiety taking the random coil form is superimposed upon it. In addition, the most intense peak at 16.40 ppm of A39 V in the DD-MAS NMR spectrum free from efficiency of cross-polarization is clearly decreased as compared with the wild type. Several other peaks are also modified, as seen by the increased peak intensity at 16.26 ppm in the CP-MAS NMR spectrum as well as the low-frequency displacement of the peak Ala 103 at 17.20 to 17.10 ppm at the loop region. This is because Ala 39 is located at the turn of the helix B at its cytoplasmic end (see Fig. 3) and its replacement with Val may result in an accompanied modified secondary structure of helix B at the cytoplasmic end and the C–D loop through interactions among cytoplasmic loops and the C-terminal α -helix. The assigned Ala C_β peaks so far obtained by the site-directed mutagenesis are summarized in Table 3.

Accidental overlaps of signals inevitably occur owing to the fact that only 12 and 9 peaks are resolved for $[3-^{13}\text{C}]\text{Ala}$ - and $[1-^{13}\text{C}]\text{Val}$ -labeled bR, respectively, in spite of 29 Ala and 21 Val residues being involved.^{60,73,74} Therefore, it is also possible to utilize another type of ^{13}C -labeled probe such as Gly, Pro, Ile, etc., in order to obtain additional information about conformation and dynamics to get rid of the inconvenience caused by the accidental overlaps of ^{13}C NMR signals. This approach is very important as viewed from the differential sensitivity to the protein

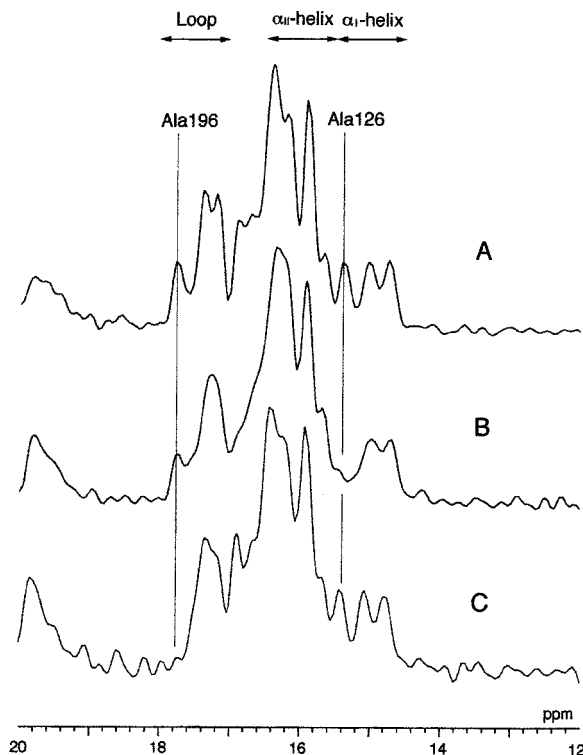


Fig. 4. Site-specific assignment of the ^{13}C NMR signals of $[3\text{-}^{13}\text{C}]\text{Ala}$ -labeled bacteriorhodopsin from PM (A), as compared with those of its site-directed mutants, A126G (B), and A196G (C) mutants.⁶⁰ Reproduced with permission from the Biophysical Society.

dynamics between the Ala C_β and carbonyl carbons of a variety of amino acid residues, to be described later. The most suitable alternative probes other than $[3\text{-}^{13}\text{C}]\text{Ala}$ are $[1\text{-}^{13}\text{C}]\text{Val}$ or Ile instead of $[1\text{-}^{13}\text{C}]\text{Ala}$, Gly , etc. in which ^{13}C NMR signals from the interfacial domains could be suppressed^{34,75} due to the interference of the frequency of fluctuation motion with the frequency of the magic angle spinning,⁷⁶ are described in the next section.

At least nine ^{13}C NMR signals are resolved in the ^{13}C NMR spectrum of $[1\text{-}^{13}\text{C}]\text{Val}$ -labeled bR as illustrated in Fig. 5⁷⁷. Tanio *et al.*⁷³ showed that the ^{13}C NMR signal of the lowest frequency occurs at 171.1 ppm of $[1\text{-}^{13}\text{C}]\text{Val}$ -labeled bR is ascribed to Val 101, on the basis of the comparative ^{13}C NMR spectra of wild-type (A) and V101A mutant (B) (Fig. 6), although this peak was also assigned to Val 199 superimposed upon the peak of Val 101 with reference to the data of V199A.⁷³ In a similar manner, the peak at 172.0 ppm turns out to be ascribed to both Val 49 and Val 130. Accordingly, the ^{13}C NMR signals of $[1\text{-}^{13}\text{C}]\text{Val}$ -bR are well-resolved and assigned to Val residues in the loop regions, Val 34 (A–B loop), 69 (B–C loop), 101 (C–D loop), 130 (D–E loop), and 199 (F–G loop),^{73,74} with reference to the data of the site-directed mutants and data obtained using enzymatic cleavage. Therefore,

Table 3. Assigned ^{13}C chemical shifts for $[3\text{-}^{13}\text{C}]\text{Ala}$ and $[1\text{-}^{13}\text{C}]\text{Val}$ residues in $[3\text{-}^{13}\text{C}]\text{Ala}$ -, $[1\text{-}^{13}\text{C}]\text{Val}$ -labeled bacteriorhodopsin from purple membrane

	Chemical shifts	Ala residues	Val/Pro/Ile/Trp residues
$[3\text{-}^{13}\text{C}]\text{Ala}^{a,b}$			
Loop	17.78	196	
Loop	17.36	160	
α_{II} -helix	17.27	184	
Loop, α_{II} -helix	17.19	103, 235	
Random coil, α_{II} -helix	16.88	240, 244–246, 84	
α_{II} -helix	16.38	39, 168	
α_{II} -helix	16.52	81	
α_{II} -helix	16.20	215	
α_{II} -helix	16.14	53	
α_{II} -helix	15.92	51	
α_{II} -helix	15.91–15.67	228, 233	
α_{I} -helix	15.02	126	
$[1\text{-}^{13}\text{C}]\text{Val}^c$			
Loop	171.07		101, 199
Loop, α -helix	171.99		49, 130
Loop	172.84		34, 69
α -helix	173.97		151, 167, 180
α -helix	174.60		136, 179, 187
α -helix	174.99		217
α -helix	177.04		29, 213
$[1\text{-}^{13}\text{C}]\text{Pro}^d$			
Loop	173.1		
Random coil	174.4, 174.6		236, 238
α -helix	174.3		50
α -helix	176.0		91
α -helix	177.7		186
$[1\text{-}^{13}\text{C}]\text{Ile}^c$			
Loop	171.2, 172.9		78, 198
Random coil	173.5		4
α -helix	175.4		222
$[1\text{-}^{13}\text{C}]\text{Trp}^c$			
α -helix	175.0		189
α -helix	175.8		182

^aRef. 35.

^bRef. 101.

^cRef. 74.

^dRef. 83.

they can be utilized as very convenient diagnostic probes to examine a plausible change in the conformation or dynamics or both in the cytoplasmic and extracellular loops of bR as a function of pH, ionic strength, temperature, etc. The assigned peaks for $[1\text{-}^{13}\text{C}]\text{Val}$ -labeled bR so far obtained are based on a variety of mutants,^{73–75} V29A, V34A, V49A, V101A, V130A, V151A, V167L, V179M, V180A, V187L, V199A, V213A, V217A as summarized in Table 3. The assigned ^{13}C chemical shifts of $[1\text{-}^{13}\text{C}]\text{Pro}$ -, Ile- and Trp-bR are summarized in Table 3, based on the ^{13}C NMR spectra of their appropriate site-directed mutants.⁷⁴ It is noted from Table 3 that the C_β ^{13}C NMR peaks of the loop regions available from

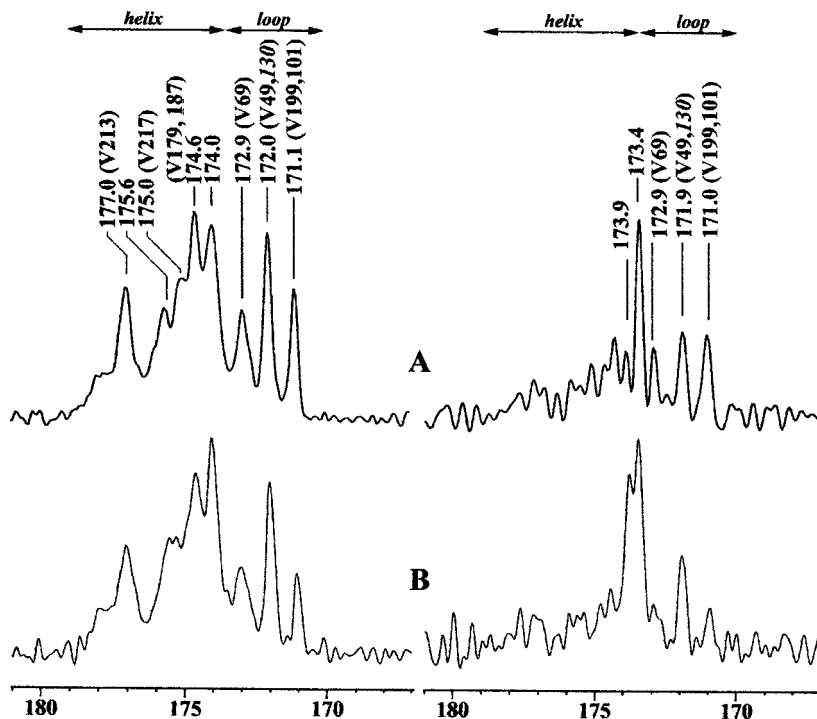


Fig. 5. ^{13}C CP-MAS (left) and DD-MAS (right) NMR spectra of $[1-^{13}\text{C}]\text{Val}$ -labeled wild type (A) and V101A mutant (B) of bacteriorhodopsin, respectively.⁷⁷ Reproduced with permission from the IOS Press.

$[3-^{13}\text{C}]\text{Ala}$ -bR are resonated at higher frequency than those of the α -helix forms, although Ala 184 and 235 are accidentally overlapped by the peaks of the loops. It is also noted that the peak position of the random coil is located at the boundary that divides them. On the contrary, the ^{13}C chemical shifts of the loop regions of $[1-^{13}\text{C}]\text{Val}$, Pro, Ile are at lower frequency than those of the α -helix form, except for Val 49, and the peak positions of the α -helices are located at the higher frequency side with respect to that of the random coil. The unusually low-frequency shift of the ^{13}C NMR peak of Val 49 in the Val-Pro sequence is due to the so-called proline effect in which the carbonyl ^{13}C chemical shift of the amino acid residue in the Val-Pro sequence is displaced to lower frequency by 1.4–2.5 ppm.^{78,79}

It is cautioned, however, that this approach cannot always be utilized for mutants in which any single mutation at a certain key position causes global conformational change as encountered for the ^{13}C NMR spectra of $[3-^{13}\text{C}]\text{Ala}$ -labeled D85N mutant of bR.⁸⁰ Caution is also a prerequisite for several ^{13}C -labeled proteins in which certain signals from the surface areas are preferentially suppressed when the frequency of fluctuation motions, if any, interferes with the frequency of the magic angle spinning or proton decoupling of the order of 10^4 – 10^5 Hz,^{76,81} as described in Section 4.1.

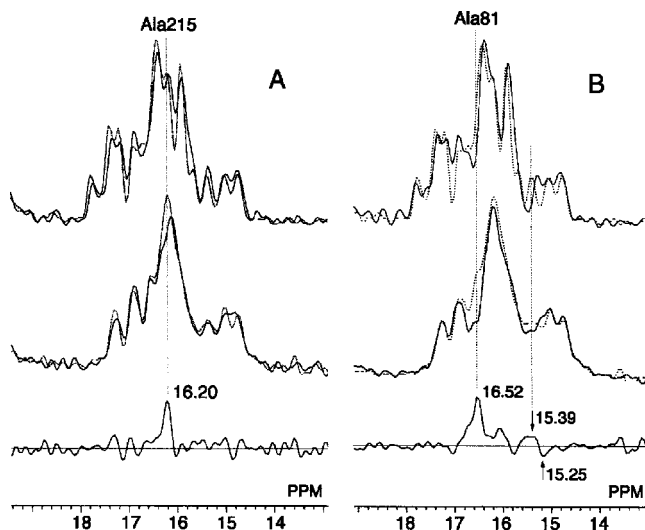


Fig. 6. ^{13}C CP-MAS NMR spectra of $[3\text{-}^{13}\text{C}]\text{Ala}$ -labeled A215G (A) and A81G (B) in the absence (top solid traces) and presence (mid solid traces) of $40\ \mu\text{M}$ Mn^{2+} ion. The corresponding spectra of the $[3\text{-}^{13}\text{C}]\text{Ala}$ -labeled wild-type bR are superimposed on the top and middle traces as dotted traces. Difference spectra between the spectra of the wild-type and mutant bRs in the presence of the Mn^{2+} ion are shown as the bottom traces.⁶⁰ Reproduced with permission from the Biophysical Society.

3.4. Spectral editing using Mn^{2+} -induced spectral broadening

Even under such situations, the present approach using site-directed mutations for the assignment of peaks turns out to be still effective, as far as such accompanied conformational changes remain relatively local and their sites of the reduced peak intensities by site-directed mutation can be readily identified. This type of peak assignment, however, is also made easier, if many of the superimposed signals from other residues, located at the surface, could be preferentially removed. This can be achieved by editing the spectra utilizing Mn^{2+} -ion-induced line broadenings from the observed spectral pattern, when their sites under consideration are located at the membrane surfaces. For this purpose, Tuzi *et al.* proposed a unique way to preferentially remove such perturbed signals arising from the residues located near a site at the surface to which Mn^{2+} ion can bind.⁸² In fact, the ^{13}C NMR spectra of bR labeled by $[3\text{-}^{13}\text{C}]\text{Ala}$ -, $[1\text{-}^{13}\text{C}]\text{Pro}$ -, Val -, Ala -, etc. were compared between preparations with and without Mn^{2+} ion.^{82,83} This approach is very effective when several modified ^{13}C NMR peaks from surface residues are due to an accompanied conformational change arising from the site-directed mutagenesis that can be preferentially broadened by the accelerated transverse relaxation rate in the presence of specific dipole-dipole interactions between Mn^{2+} ions and the carbons under consideration. The broadened line widths ($1/\pi T_{2C}$), which are expressed by a function of distances between electron and nuclear spins, r , and the correlation time of

rotational reorientation of the spin pair (τ_r) based on the Solomon–Bloembergen equation, can be described as follows:^{84,85}

$$1/T_{2c} = [S(S+1)\gamma_c^2 g^2 \beta^2 / (15r^6)] [4\tau_{c1} + 3\tau_{c1}/(1 + \omega_c^2 \tau_{c1}^2) + 13\tau_{c2}(1 + \omega_c^2 \tau_{c2}^2)] \quad (1)$$

$$1/\tau_{c1} = 1/T_{1e} + 1/\tau_r + 1/\tau_m, \quad 1/\tau_{c2} = 1/T_{2e} + 1/\tau_r + 1/\tau_m$$

where T_{2c} is the spin–spin relaxation time of a ^{13}C nucleus, r the distance between the ^{13}C nucleus and Mn^{2+} ion, S the total electron spin, ω_c and ω_e are the nuclear and electronic Larmor precession frequencies, γ_c the gyromagnetic ratio of ^{13}C , g the g factor of Mn^{2+} , β the Bohr magneton, T_{1e} and T_{2e} are the spin–lattice and spin–spin relaxation times of an electron, τ_r the rotational correlation time of the Mn^{2+} –bR complex and τ_m is the lifetime of the Mn^{2+} complex. The g -factor and T_{1e} of Mn^{2+} are assumed to be identical to those of an aqua ion. τ_m is assumed to be longer than T_{1e} (3×10^{-9} s). When τ_r is longer than T_{1e} , the line width corresponding to the calculated $1/\pi T_{2c}$ value becomes greater than 100 Hz in the area within 8.7 Å of Mn^{2+} ion.⁸² Therefore, the upper bound of the interatomic distances between the ^{13}C nuclei in bR and the Mn^{2+} bound to the hydrophilic surface for the production of suppressed peaks is thus estimated as 8.7 Å.⁸²

Utilizing this procedure, the emerging 16.20 ppm peak in the presence of the Mn^{2+} ion, superimposed upon complicated ^{13}C NMR spectra of [3- ^{13}C]Ala-labeled bR, was selected by the difference spectrum between the wild type and the A215G mutant (Fig. 6A, left bottom) and straightforwardly assigned to Ala 215, even though respective spectra without Mn^{2+} ion are rather complicated due to the presence of accompanied spectral changes due to inevitable, conformational changes (Fig. 6A, left top and middle). In a similar manner, the 16.52 ppm peak was also unequivocally assigned to Ala 81 in view of the difference spectrum between wild type and A81G in the presence of Mn^{2+} ion (Fig. 6B, right bottom). It is noteworthy that the resulting conformational changes occur even in the inner part of the transmembrane α -helix by replacement of Ala 81 with Gly and result in a dispersion signal at 15.39 and 15.25 ppm.

It is also very important to examine in more detail how the present approach to edit spectra by utilizing Mn^{2+} ion-transverse relaxation is useful as a diagnostic means to assign the ^{13}C NMR peaks of bR labeled with [1- ^{13}C]Gly, Ala-, Leu, Val-, Ile-, Trp-, Pro-, etc. It appears from Fig. 7B that in addition to the main peak, a broad envelope centered at 175 ppm is present for the ^{13}C CP-MAS NMR spectra of [1- ^{13}C]Gly labeled bR as a background signal ascribable to several superimposed ^{13}C NMR signals from amino-acid residues with substituents at C_α ^{64,65} of natural abundance such as Ala, Leu, and Val. Instead, the intense ^{13}C NMR peak at 171.7 ppm recorded by the CP-MAS and DD-MAS NMR spectra arose from the α -helical segments, as viewed from the conformation-dependent ^{13}C chemical shifts for [1- ^{13}C]Gly residues.^{63,64} It is also noteworthy that most of the peak intensity from the Gly residues involved in the α -helix, as detected by the DD-MAS NMR, is suppressed by the Mn^{2+} ion, whereas the corresponding peak from the CP-MAS NMR is not. This means that the ^{13}C NMR signals of the Gly residues located at the interfacial regions from [1- ^{13}C]Gly labeled bR could be preferentially

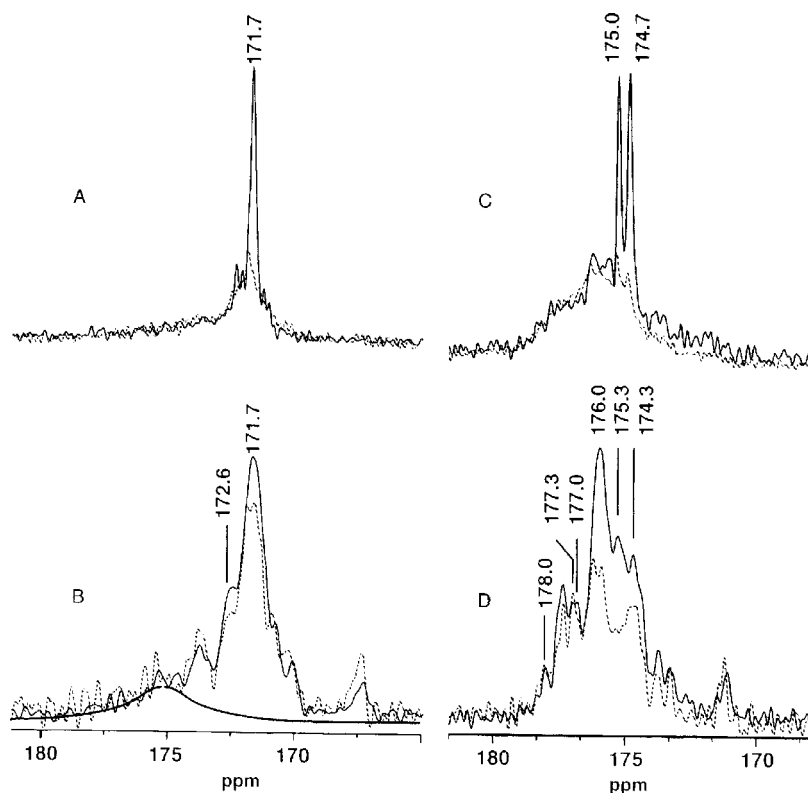


Fig. 7. ^{13}C DD-MAS (A and C) and CP-MAS (B and D) NMR spectra of the $[1-^{13}\text{C}]$ Gly and Leu-labeled bR from PM, respectively, without (solid traces) and with $40\ \mu\text{M}\ \text{Mn}^{2+}$ ion (dotted traces).⁷⁴ Reproduced with permission from John-Wiley and Son, Ltd.

suppressed due to the interference of the fluctuation frequency with that of the magic angle spinning, as will be discussed later in Section 4.1.

In general, the ^{13}C CP-MAS NMR signals of bR labeled with $[1-^{13}\text{C}]$ amino-acid residues, except for Gly, spread over the region between 171 and 178 ppm. In particular, the ^{13}C NMR signals resonating at higher frequency than 174.9 ppm are ascribed to those of the α -helix, whereas the lower frequency signal than this are assigned to either a turned structure in the loop or β -sheet. As demonstrated in the schematic representation shown in Fig. 3, there appears no Leu residue involved in the N- or C-terminal moieties which take randomly coiled segments and their signals can be easily evaluated in view of the ^{13}C chemical shifts of $[3-^{13}\text{C}]$ Ala- or $[1-^{13}\text{C}]$ Ala-, Pro-, Ile-labeled bR.^{36,74,83} Therefore, it is unlikely that Leu residues are involved in the segment of the random coil form in spite of the possibility of the observed peak positions in the intense signals at 175.0 and 174.7 ppm, which are visible by the DD-MAS NMR (Fig. 9C) but not by CP-MAS NMR (Fig. 2D). It is probable that these signals may arise from residue(s) rather than the incorporated $[1-^{13}\text{C}]$ Leu by scrambling.

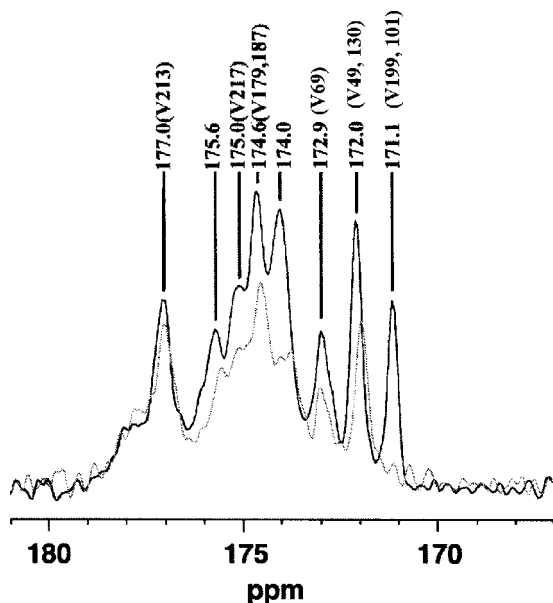


Fig. 8. ^{13}C CP-MAS NMR spectra of $[1-^{13}\text{C}]\text{Val}$ -labeled bR from PM without (solid trace) and with $40\ \mu\text{M}$ Mn^{2+} ion (gray trace). ^{13}C NMR peaks of Val 130 and 101 are superimposed upon the peaks of Val 49 and 199, respectively.⁷⁵ Reproduced with permission from Elsevier.

As demonstrated in Fig. 8, the ^{13}C NMR spectra of $[1-^{13}\text{C}]\text{Val}$ -bR were compared under the conditions with and without Mn^{2+} ion. The ^{13}C peak intensities of $[1-^{13}\text{C}]\text{Val}$ residues located at the loop regions, Val 69 (172.9 ppm) from B–C loop, Val 130 (172.0 ppm) from D–E loop and Val 101 and 199 (171.0 ppm) from the C–D and E–F loops, respectively, are almost completely suppressed by the accelerated transverse relaxation effect in the presence of $40\ \mu\text{M}$ Mn^{2+} ion, although those of the inner part of the transmembrane α -helix including Val 213 (177.0 ppm) and 49 (172.0 ppm) are not.⁷⁵ This finding is obviously consistent with the secondary structure in Fig. 3 together with the prediction based on Eq. (1).

It is surprising to note that the ^{13}C relative intensities of peaks in $[1-^{13}\text{C}]\text{Trp}$ recorded by the DD-MAS NMR with (gray) and without Mn^{2+} ion (black) given in Fig. 9 and Phe-labeled bR (data not shown) are almost the same as those recorded by the CP-MAS NMR. In general, it is well recognized that ^{13}C DD-MAS NMR observation of signals from the transmembrane α -helices of bR labeled with $[1-^{13}\text{C}]\text{amino acids}$ is very difficult because of expected spin–lattice relaxation times which might be of the order of 10–20 s.³⁴ In contrast, it is found that such ^{13}C NMR signals from $[1-^{13}\text{C}]\text{Trp}$ - or Phe-labeled bR can be easily recorded by the DD-MAS method, probably because the ^{13}C spin–lattice relaxation times of the transmembrane α -helices of $[1-^{13}\text{C}]\text{Trp}$ - and Phe-labeled bR are made shorter by at least one order of magnitude as compared with those of other amino-acid residues such as Gly, Ala, and Val.³⁴ Obviously, this is caused by the presence of the two-site jump

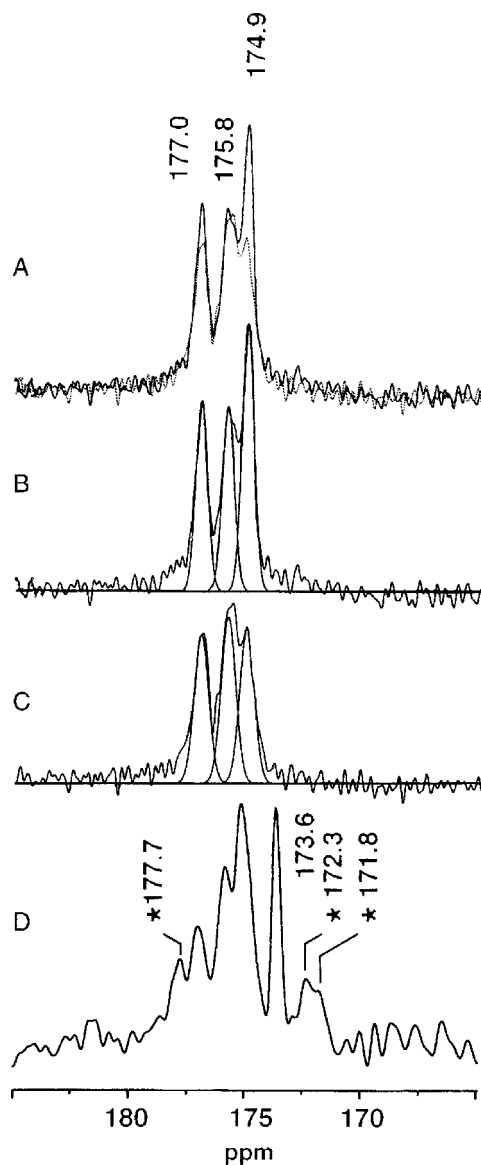


Fig. 9. ^{13}C CP-MAS NMR spectra of [1- ^{13}C]Trp-labeled bR without (solid trace) and with $40\ \mu\text{M Mn}^{2+}$ ion (dotted trace) (A), deconvoluted spectra without (B) and with $40\ \mu\text{M Mn}^{2+}$ ion (C), and corresponding ^{13}C DD-MAS NMR spectrum (D). Several asterisked peaks arose from ^{13}C signals probably scrambled from incorporated [1- ^{13}C]Trp.⁷⁵ Reproduced with permission from John-Wiley and Son, Ltd.

motions of the aromatic side-chains, especially in the membrane environment that could serve as a sink of the shortened spin-lattice relaxation times.^{86,87} It is noticeable that the ^{13}C NMR peaks of $[1-^{13}\text{C}]\text{Trp}$ -labeled bR are distributed in a rather narrow range (ca. 2 ppm) as compared with those of $[1-^{13}\text{C}]\text{Val}$ -labeled bR (6 ppm) described above, because there is neither Trp residue in the loop regions nor involvement in a specific sequence Trp-Pro that would result in the displacement of the peaks to low frequency, if any (see Fig. 3). The peak intensities of the two α -helical peaks resonated at 177.0 and 174.9 ppm are appreciably suppressed by the accelerated relaxation rate caused by the proximity of the Trp residue close to the bound Mn^{2+} ions at the surface areas, although the ^{13}C Trp peaks so far assigned are limited to Trp 182 and 189 ascribed to 175.8 and 174.9 ppm, respectively, utilizing the site-directed mutants W128F and W189F.⁷⁴ Indeed, Trp 182 is located at the inner part of the transmembrane α -helix, which is not influenced by the added Mn^{2+} ion, whereas Trp 189 is present at the shaded area, which could be strongly influenced by the Mn^{2+} ion, as illustrated in Fig. 10.

Three of the transmembrane α -helices (helices B, C, and F) are involved in a kink at positions of Pro 51, 91, and 186 among a total of 11 Pro residues, because the Pro residues lack the proton donors required for the hydrogen bonds of normal α -helix,

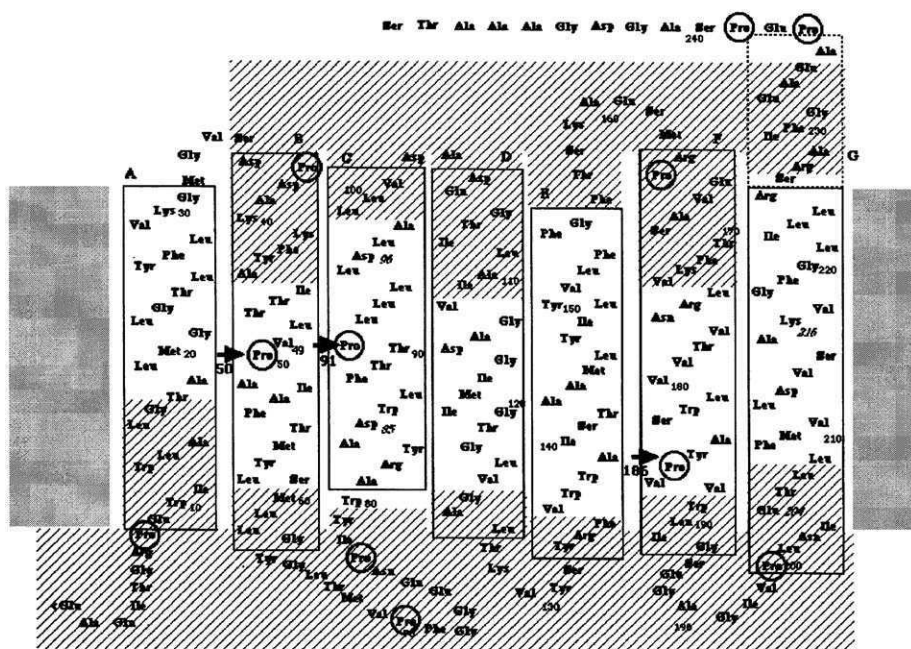


Fig. 10. Schematic representation of the secondary structure of bR. Shaded areas represent residues located within 8.7 Å from oxygens included in the potential cation binding sites. Pro residues are circled and Pro 50, 91, and 186 are indicated by the arrows.⁸³ Reproduced with permission from Elsevier.

according to the model structure of bR reported by X-ray diffraction studies.⁴⁻⁸ Naturally, these kinks contribute to efficient packing of the α -helices around the retinal. It is expected that the ^{13}C NMR signals of these three kinds of Pro residues located at the inner part of the transmembrane α -helices can be readily distinguished from those of the others located near the surfaces based on the Mn^{2+} -induced transverse relaxation rates, as described already. These three residues are located at positions separated more than 8.7 \AA from the surface, whereas the rest are located at positions within 8.7 \AA as shaded areas (Fig. 10). Consistent with this prediction, Tuzi *et al.*⁸³ showed that the following three resonance peaks remain at 177.7, 176.0 and 174.3 ppm (Fig. 11B) from the total seven resolved peaks (Fig. 11A) when the ^{13}C CP-MAS NMR spectra of $[1-^{13}\text{C}]\text{Pro}$ -labeled bR were recorded in the presence of $40\text{ }\mu\text{M}$ Mn^{2+} ion. In contrast, only two peaks occur at 174.4 and 174.6 ppm in the corresponding DD-MAS spectrum (Fig. 11C). The other peaks in the CP-MAS spectrum (Fig. 11A) are almost completely suppressed in the DD-MAS spectrum (Fig. 11C) due to their longer spin-lattice relaxation times (of the order of 10–20 s as found for $[1-^{13}\text{C}]\text{Val}$ - or Ala -labeled bR) as compared with the repetition time (4 s).^{34,73} The major peaks in the DD-MAS NMR spectrum with shorter spin-lattice relaxation times (of the order of 1 s⁷³), superimposed upon the ^{13}C NMR signals from the naturally abundant carbonyl peaks are obviously ascribed to Pro 236 and 238 located at the flexible C-terminal tail of the bR protruding from the cytoplasmic membrane surface. Naturally, such signals from the residues fully exposed to the surface are suppressed by the fast transverse relaxation rate by the Mn^{2+} ion. The three peaks at 174.3, 176.0 and 177.7 ppm, visible by the

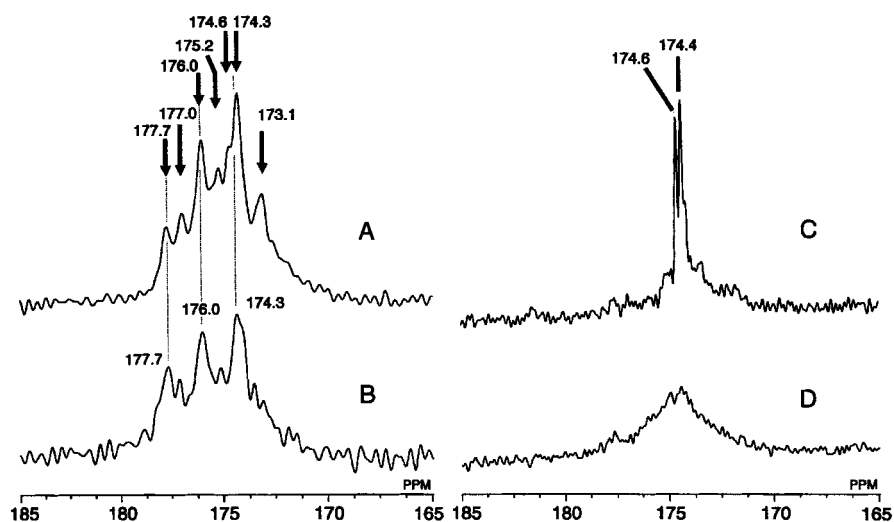


Fig. 11. ^{13}C CP-MAS NMR spectra of $[1-^{13}\text{C}]\text{Pro}$ -labeled wild-type bR from PM in the presence (A) and absence (B) of $40\text{ }\mu\text{M}$ Mn^{2+} ion, and ^{13}C DD-MAS NMR spectra of $[1-^{13}\text{C}]\text{Pro}$ -labeled wild-type bR in the presence (C) and absence (D) of $40\text{ }\mu\text{M}$ Mn^{2+} ion.⁸³ Reproduced with permission from Elsevier.

CP-MAS NMR spectrum in the presence of 40 μM Mn^{2+} ion, are assigned to Pro 50, 91, and 186 with reference to ^{13}C NMR spectra of P50G, P91G, and P186A mutants, respectively.⁸³

3.5. Conformation-dependent ^{13}C chemical shifts in membrane proteins

The existence of the conformation-dependent displacement of the ^{13}C chemical shifts for polypeptides and proteins, as discussed in Section 3.2, was initially proposed for the interpretation of the ^{13}C NMR spectral data available from the solids as early as 1985 by Saitô and coworkers.^{63,64,88} The conformation-dependent ^{13}C chemical shifts turned out to be well related by the local conformation of the amino-acid residues defined by a set of torsion angles (ϕ and ψ) as demonstrated for the ^{13}C chemical shifts of the Ala C_β carbons with reference to the theoretically evaluated counter map of the ^{13}C chemical shift (nuclear shielding constant) for the Ala-residue from N-acetyl-N'-methylalanine amide.⁸⁹⁻⁹¹ In the case of carbonyl ^{13}C chemical shifts, however, the effect of hydrogen bonding is more significant than that of the local conformation.⁸⁹ It was therefore shown, on the basis of the experimental data and the predicted values given by this chemical shift map, that the map successfully predicts the ^{13}C chemical shifts of the Ala residues in polypeptides and fibrous proteins.^{92,93} Instead of utilizing the ^{13}C chemical shifts from solid peptides, however, Spera and Bax⁹⁴ proposed an alternative approach utilizing the database of the ^{13}C chemical shifts from globular proteins in solution, in which the C_α and C_β chemical shifts are empirically related to the torsion angles determined by X-ray diffraction studies. Later, this relationship has been utilized to determine the protein backbone angle restraints package as TALOS.⁹⁵ Wishart *et al.*⁹⁶ found, on the basis of the chemical shift database for a variety of proteins, that their ^1H , ^{13}C , and ^{15}N chemical shifts reveal strong correlations to protein secondary structure and later proposed an automated ^1H and ^{13}C chemical shift prediction program SHIFTY.⁹⁷ Similar correlations have been proposed by several authors based on the ^{13}C NMR data on globular proteins or calculated spectra.⁹⁸⁻¹⁰⁰

It is cautioned, however, that the use of such a database from solution NMR is not always appropriate for the interpretation of solid-state NMR data, because of a possible source of errors arising from the chemical shift references for the solid and solution NMR studies. Moreover, further larger dispersions of chemical shifts from the solution NMR of globular proteins cannot always be ignored. Such data, however, are not always free from ambiguities in choosing the appropriate chemical shifts of the "random coil," which are essential for data collection in solution NMR. These are simply treated as hidden parameters, and not always as necessary parameters for the interpretation of the solid-state NMR, unless ^{13}C NMR data of the fully hydrated samples are concerned. In fact, the ^{13}C chemical shift data available from such databases are in many instances "biased" as a reference for solid-state NMR because of choice of reference data for both solid and solution NMR. It is advised therefore to utilize the database from the solid state, if one aims to interpret the ^{13}C chemical shift data from solid-state NMR.^{64,65}

In membrane proteins, however, it should be borne in mind that the secondary structures of *fully hydrated* membrane proteins are far from *static* under physiological condition, in spite of proposed models available from diffraction studies on crystalline samples at lower temperature. Indeed, they are very flexible even in the 2D crystal, because they are embedded in flexible lipid bilayers at ambient temperature, undergoing various kinds of molecular motions with correlation times of the order of 10^{-2} – 10^{-8} s. In fact, it is notable from [Tables 2 and 3](#) that the spread of the distribution of the conformation-dependent ^{13}C chemical shifts of membrane proteins is much larger than that of the reference polypeptides in the solids: ^{13}C chemical shifts of the α -helix forms spread over 3 and 2 ppm for [1- ^{13}C]Val- or Pro-, and [3- ^{13}C]Ala-labeled bR, respectively; and ^{13}C NMR peaks from the turned structures located at the loop region of [1- ^{13}C]Val-bR spread over 3 ppm. It may well be recognized, therefore, that the concept of the conformation-dependent displacement of ^{13}C chemical shifts as predicted under static condition should be modified to some extent in such flexible membrane proteins.

Most of the ^{13}C NMR peaks from the transmembrane α -helices occur at the peak position of the α_{II} -helix rather than α_{I} -helix form, as far as the ^{13}C chemical shifts of [3- ^{13}C]Ala-labeled bR are concerned with reference to those of (Ala)_n in HFIP solution, consistent with the prediction by Krimm and Dwivedi⁷² based on IR measurements (see [Table 3](#)). This is also true for a variety of membrane proteins other than bR, including phoborhodopsin ppR, its transducer pHtrII and *E. coli* DGK.^{37,42–44} The estimated proportion of the α_{II} -helix form in the transmembrane peptides of bR in lipid bilayers, however, is much less than that estimated from the Ala C $_{\beta}$ signals as in the case of Ala 14, 53, and 139 as judged from the carbonyl ^{13}C shift with reference to the peak positions of (Ala)_n in HFIP solution.⁷⁰ Therefore, most of the α_{II} forms as judged by the ^{13}C chemical shifts of the Ala C $_{\beta}$ carbons should not always be interpreted in terms of the *static* picture as proposed on the basis of infrared spectral data⁷² but of the dynamic picture of membrane proteins undergoing a variety of fluctuation motions in the environment of the lipid bilayers.⁸² In fact, it is conceivable that the ^{13}C NMR peaks of the Ala C $_{\beta}$ in the transmembrane peptides pointed toward the lipid bilayers could be much influenced by the local fluctuation of the peptide unit in the lipid bilayers, whereas those of the carbonyl groups are not, because they are not in direct contact with the lipids.⁸² Consistent with this view, it is also interesting to note that the ^{13}C NMR signals of the [3- ^{13}C]Ala-labeled cytoplasmic or amphipathic α -helices protruding from the membrane surfaces of bR,^{33,34} ppR,⁴² pHtrII⁴³, and *E. coli* diacylglycerol, which undergo fluctuation motions with correlation times of the order of 10^{-6} s, occur at the peak positions of the α_{II} -helix, even though they are not embedded within lipid bilayers. Indeed, the ^{13}C chemical shifts of the above-mentioned Ala C $_{\beta}$ from the cytoplasmic α -helix in bR are shifted to higher frequency when the temperature is raised.¹⁰¹

Nevertheless, it is also demonstrated that the above-mentioned cytoplasmic α -helix can be considered as the normal α_{I} -helix rather than the α_{II} -helix as judged by the ^{13}C chemical shifts of the C $_{\alpha}$ and C=O carbons.³⁴ Therefore, the ^{13}C NMR signals of the more flexible transmembrane α -helices in membrane proteins and

their fragments in lipid bilayers, or cytoplasmic and amphipathic α -helices protruding from the membrane surfaces can be interpreted in terms of the *dynamic-dependent displacements of ^{13}C chemical shifts* as viewed from their Ala C_β signals. As mentioned earlier, the ^{13}C chemical shifts of the $\text{C}=\text{O}$ carbons are more sensitive to the manner of hydrogen bonding rather than that of the secondary structure as defined by a set of torsion angles (φ , ψ).⁸⁹ In this connection, it should be cautioned that the database of the ^{13}C chemical shifts accumulated from globular proteins without this sort of fluctuation motion should be treated more carefully.

4. BACKBONE DYNAMICS AND STRUCTURES IN THE INTERFACIAL DOMAINS OF BACTERIORHODOPSIN FROM PURPLE MEMBRANE

4.1. Surface dynamics

4.1.1. Site-directed suppression of ^{13}C NMR signals by slow motional fluctuations

As demonstrated already, the ^{13}C NMR spectra of ^{13}C -labeled membrane proteins including bR are not always fully visible at ambient temperature, depending upon the types of incorporated ^{13}C labels. For instance, the ^{13}C NMR signals of $[1-^{13}\text{C}]\text{Ala}$ -labeled bR from PM with and without $40\ \mu\text{M}$ Mn^{2+} ion turned out to be very similar,⁷⁵ because the ^{13}C NMR signals from the interfacial domains located within approximately $8.7\ \text{\AA}$ from the membrane surface were already suppressed by the failure of peak narrowing. This is due to the interference of the motional frequency of internal fluctuation with the frequency of the magic angle spinning (to be described below in more detail), and not because of the accelerated transverse relaxation by the added Mn^{2+} ion.³⁴ In contrast, it is shown that the corresponding ^{13}C NMR signals from this region are fully visible from $[3-^{13}\text{C}]\text{Ala}$ -labeled bR of PM taking the 2D crystal, as judged by careful comparison of individual peak intensities between the experimental and deconvoluted peaks by taking into account the relative proportions of the contributed residues.³² Indeed, the ^{13}C NMR peaks of Ala C_β are sensitive to the fluctuation frequency interfering with the frequency of proton decoupling ($\approx 10^5\ \text{Hz}$), whereas those of the $\text{C}=\text{O}$ signals are sensitive to a fluctuation frequency interfering with the frequency of the magic angle spinning ($\approx 10^4\ \text{Hz}$).^{76,81}

Theoretically, the expected ^{13}C NMR linewidth $1/\pi T_2^{\text{C}}$, under CP-MAS or DD-MAS NMR conditions, depends strongly on either the coherent frequency of the proton decoupling or the magic angle spinning, when they interfere with the frequency of the corresponding incoherent random fluctuation motion, if any.^{76,81} In such cases, the overall relaxation rate $1/T_2^{\text{C}}$ can be dominantly determined by the following second or third terms instead of the first term of the static component by

$$1/T_2^{\text{C}} = (1/T_2^{\text{C}})^{\text{S}} + (1/T_2^{\text{C}})^{\text{M}}_{\text{DD}} + (1/T_2^{\text{C}})^{\text{M}}_{\text{CS}} \quad (2)$$

where $(1/T_2^{\text{C}})^{\text{S}}$ is the transverse component due to static C–H dipolar interactions,

and $(1/T_2^C)_{DD}^M$ and $(1/T_2^C)_{CS}^M$ are the transverse components due to the fluctuation of the dipolar and chemical shift interactions in the presence of the internal fluctuation motions, respectively. The latter two terms are given as a function of the correlation time τ_c by

$$(1/T_2^C)_{DD}^M = \Sigma(4\gamma_I^2\gamma_S^2\hbar^2/15r^6)I(I+1)(\tau_c/(1+\omega_I^2\tau_c^2)) \quad (3)$$

$$(1/T_2^C)_{CS}^M = (\omega_0^2\delta^2\eta^2/45)(\tau_c/(1+4\omega_I^2\tau_c^2) + 2\tau_c/(1+\omega_r^2\tau_c^2)) \quad (4)$$

Here, ω_I and ω_S are the gyromagnetic ratios of the I and S nuclei, respectively, and r is the internuclear distance between the spins I and S. ω_o and ω_I are the carbon resonance frequency and the amplitude of the proton decoupling RF field, respectively. ω_r is the rate of spinner rotation. δ the chemical shift anisotropy and η the asymmetric parameter of the chemical shift tensor.

Clearly, the transverse relaxation rate is dominated by modulation of either dipolar interactions or chemical shift anisotropies, if internal fluctuations cannot be ignored as in the membrane proteins. It is expected that a decoupling field of 50 kHz is sufficient to reduce the static component and the $(1/T_2^C)_{CS}^M$ term will be dominant in the overall $1/T_2^C$, as far as carbonyl groups with larger chemical shift anisotropies are concerned.³⁴ In addition, it is expected that the C_α carbon signal could also be affected by both the $(1/T_2^C)_{DD}^M$ and $(1/T_2^C)_{CS}^M$ terms, depending upon the frequency range of either 50 kHz (ω_I) or 4 kHz (ω_r), respectively. Of course, it is possible to avoid the above-mentioned interference with a frequency of the order of 10^4 Hz by increasing the spinning rate up to as fast as 20 kHz. In this case, however, one should take special precaution to prevent unnecessary heating of the samples as well as dehydration due to the centrifuging effect on fully hydrated membrane proteins. On the contrary, it is obvious that spinning the sample at about 4 kHz is more preferable as one of the best ways to detect fluctuation motions of the order of 10^4 Hz, if any.

This means that the observation of such site-directed suppression of peaks with respect to the spectra of the wild type protein provides one a very convenient and unambiguous means to detect the presence of conformational fluctuation motions at specific residues under certain conditions. For instance, several ^{13}C NMR signals from the loop region as well as some transmembrane α -helices of bR are significantly suppressed for the $[3-^{13}\text{C}]\text{Ala}$ -labeled D85N mutant or bacterio-opsin in which the retinal-helix interactions are completely removed or partly modified^{33,80} as a result of respective modified protein dynamics. In this connection, it is interesting to note that the ^{13}C DD-MAS NMR signals of the C-terminal α -helix (helix G', as illustrated in Fig. 12) in $[1-^{13}\text{C}]\text{Ala}$ -labeled bR from PM (2D crystal) are visible at a temperature 0°C in the presence of fluctuation motions with the correlation times of the order of 10^{-6} s as judged from the carbon spin-lattice relaxation times T_1^C and spin-spin relaxation times T_2^C under the high-power proton decoupling,³⁴ but are also almost completely suppressed at a temperature below -10°C by DD-MAS NMR as a result of reduced correlation times to the order of 10^{-4} s leading to their suppressed peak intensities. Of course, they are fully visible at ambient temperature as far as the correlation time is of the order of 10^{-6} s³⁴, which

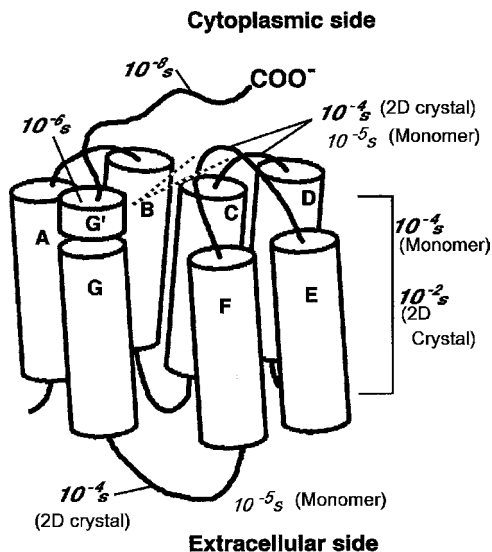


Fig. 12. Schematic representation of secondary structure and dynamics for bR as a typical membrane protein, consisting of the C-terminal α -helix (helix G' protruding from the membrane surface), its interaction with the C-D and E-F loops (dotted lines) leading to the cytoplasmic surface complex, and seven transmembrane α -helices (A–G). Note that the protein dynamics differ substantially between 2D crystals (PM) and regenerated monomeric species in lipid bilayer.

is free from such interference. This finding is consistent with the earlier experiment utilizing a hydrophobic fluorescence probe by Renthall and coworkers,¹⁰² who claimed that the C-terminal tail of bR is held at the membrane surface with motion on a timescale of 13–25 ns.

Experimentally, it is possible to evaluate a relative contribution of the ^{13}C NMR signals (f) from residues located at the surface areas by comparing their peak intensities in the presence (I) with those in the absence of $40\ \mu\text{M}$ Mn^{2+} ion (I_0) (as discussed in Section 3.4) as

$$f = 1 - I/I_0, \quad (5)$$

provided that the relative contributions of the surface areas are defined as residues located within $8.7\ \text{\AA}$ from the membrane surface, leading to completely suppressed peaks by the accelerated transverse relaxation process caused by the Mn^{2+} ion. Alternatively, the predicted proportion of residues near the surface ($8.7\ \text{\AA}$ from the membrane surface), g , are defined by

$$g = n/n_0 \quad (6)$$

where n and n_0 are the number of respective residues located within such areas and total number of such residues, respectively. If $f = g$, there are no suppressed peaks in the surface areas due to interference with slow fluctuation motions. If $f < g$, ^{13}C

NMR signals from the surface areas might be suppressed to some extent due to interference with the fluctuation frequencies.

Interestingly, the relative contributions, f , thus obtained by the $[1-^{13}\text{C}]\text{Val-}$ and Ile- labeled bR from PM are in good agreement with the proportions of the respective residues, g , estimated from the expected number of these residues within 8.7 \AA from the negatively charged residues, as summarized in Table 4.⁷⁴ In contrast, it is shown that the relative proportions f of the ^{13}C NMR signals from the surface areas of $[1-^{13}\text{C}]\text{Gly-}$, Ala- , Leu-bR are substantially lower than the expected g values: they are 0.12, 0 and 0.11 for $[1-^{13}\text{C}]\text{Gly}$, Ala- , Leu-bR , respectively, while the expected proportions based on the predicted number of these residues from the surface areas are 0.67, 0.62, and 0.49, respectively. These findings indicate that ^{13}C NMR signals from the surface areas of these systems are substantially suppressed even in the absence of the Mn^{2+} ion due to the interference of the incoherent low-frequency motions with the coherent frequency of the magic angle spinning, as demonstrated for $[1-^{13}\text{C}]\text{Ala-}$ labeled bR.⁷⁵ This is also true for the ^{13}C NMR peak intensities of $[1-^{13}\text{C}]\text{Phe-}$ and Trp- labeled preparations, owing to the presence of low-frequency conformational fluctuations present in these residues that interferes with the frequency of the magic angle spinning.

It appears that such *low-frequency, residue-specific* dynamics, leading to completely or partially suppressed peaks in the absence of Mn^{2+} ion, is well related to the possibility of conformational fluctuations for bR from PM labeled with $[1-^{13}\text{C}]\text{Gly}$, Ala , Leu , Phe , Trp , etc. caused by the time-dependent deviation from the torsion angles corresponding to the lowest energy minimum of a particular conformation. Naturally, it is conceivable that conformational space allowed for such a fluctuation is strongly related to the presence or absence of bulky side-chains at C_α : the allowed space for such Val or Ile residues may be limited to a very narrow

Table 4. Comparison of relative proportion (f) of the ^{13}C NMR signals from the surface areas as estimated from the ^{13}C NMR intensity ratio with (I) and without (I_0) Mn^{2+} ion^a

	Estimated from ^{13}C signals ($1-I/I_0$), f	Predicted amounts of residues near the surface (8.7 \AA from the membrane surface), g	Suppressed ^{13}C NMR peaks from the surface area by slow motions
Gly	0.14	0.67	Suppressed
Ala	$\approx 0^b$	0.62	Almost completely suppressed
Leu	0.11	0.49	Suppressed
Phe	0.24	0.55	Suppressed
Trp	0.24	0.38	Suppressed
Val	0.41	0.38	None
Ile	0.50	0.56	None

^aRef. 74.

^bRef. 45.

area expressed in a Ramachandran map, together with a limited χ_1 rotation around the C_α - C_β bond. Here, the side-chains at the C_α are expressed by C_α - C_β H(X)(Y), where X and Y are substituents on C_β . This minimum, however, may be very shallow for Gly residues in view of the widely allowed conformational space. The low-frequency, residue-specific backbone dynamics discussed above may be present also for the Ala, Leu, Phe, and Trp residues, because the backbone dynamics in these systems could be coupled with a possible rotational motion of the χ_1 angle around the C_α - C_β bond, as represented schematically by the C_α - C_β H₂-Z, where Z is H, isopropyl, phenyl or an indole group.

Accordingly, it is concluded that the ^{13}C NMR signals of [1- ^{13}C]Val and Ile residues among a variety of [1- ^{13}C]amino-acid residues can serve as the most appropriate probes, to examine the local conformation and dynamics of bR from PM especially at the surface area. Otherwise, it should be anticipated that the carbonyl ^{13}C NMR signals are not fully visible from those located at the membrane surface (Ala, Leu, Phe, and Trp), because of interference between the fluctuation frequency and the frequency of magic angle spinning.

4.1.2. *Distinction of the flexible portion by cross-polarization, relaxation parameters, and order parameters*

As demonstrated earlier, the interfacial domains of bR, consisting of the N- or C-terminus and the interhelical loops protruding from the membrane surfaces, are very flexible at ambient temperature owing to exposure to the aqueous phase even in 2D or 3D crystalline preparations, as compared with those of the transmembrane α -helices, as far as their fully hydrated preparations are concerned. It is therefore expected that the distinction of such flexible interfacial domains from the transmembrane α -helices can be readily made possible by means of a differential cross-polarization rate or relaxation parameters, including the spin-lattice relaxation times T_1^C and spin-spin relaxation times under proton decoupling T_2^C , depending upon the fluctuation frequencies under consideration. In particular, ^{13}C NMR signals of the rapidly fluctuating C-terminus can be readily distinguished from those of the transmembrane α -helices, as viewed from the presence of their peaks as indicated by the gray peaks in the DD-MAS NMR spectra of [3- ^{13}C]Ala-labeled bR from PM but by the absence in the corresponding CP-MAS NMR (Fig. 2⁶⁰) due to averaged dipolar interactions by fast fluctuation motions (see Fig. 12). Engelhard and coworkers¹⁰³ also demonstrated, on the basis of a ^{13}C NMR study of [3- ^{13}C] and [4- ^{13}C]Pro-labeled bR, that the first part of the C-terminus is fixed to the membrane via salt bridges between divalent cations and negative charges of the C-terminus as well as by loops. As will be discussed in more detail later, it was shown^{101,104} that the cytoplasmic loops and the C-terminal α -helix are not always present independently but are held together to form the cytoplasmic surface complex, which undergoes fluctuation motions with a correlation time of the order of 10^{-4} s as manifested from the suppressed ^{13}C peak intensities of [1- ^{13}C] or [2- ^{13}C]Ala-labeled bR,³⁴ as schematically illustrated in Fig. 12. The timescale for the fluctuation motions of the transmembrane α -helices was previously estimated to be

of the order of 10^{-2} s, as estimated from a possible chemical exchange process among various conformations undergoing slow anisotropic fluctuation (Fig. 12).⁶¹

The measurement of the ^{13}C spin–lattice relaxation times, T_1^C , for $[1-^{13}\text{C}]\text{Gly-}$, Ala-, or Val-, and $[2-^{13}\text{C}]$ or $[3-^{13}\text{C}]\text{Ala-}$ labeled bR from PM has proved to be also very useful for locating such rather flexible portions protruding from the membrane surfaces.^{32,34,73} In fact, the T_1^C values of the transmembrane α -helices for the first three carbons determined by CP-MAS NMR are of the order of 16–24 s, whereas those of the C-terminus or loops are 1–2 s as determined by DD-MAS NMR. In this connection, the presence of two distinct T_1^C values for the single peak at 172.0 ppm of $[1-^{13}\text{C}]\text{Val-}$ labeled bR, 15.2 and 1.22 s by CP-MAS and DD-MAS, respectively,⁷³ can be unequivocally explained in terms of the two superimposed peaks originating from different portions, namely, Val 49 from the transmembrane α -helix and Val 130 from the D–E loop as confirmed by examination of the respective site-directed mutants.^{73,74} Recording the ^{13}C NMR spectra of the $[1-^{13}\text{C}]\text{Val-}$ labeled transmembrane α -helices by DD-MAS NMR measurements is not always suitable because of such long T_1^C values as compared with acceptable repetition times. Distinction of the ^{13}C NMR signals among the transmembrane α -helices, C-terminal α -helices, loops, and random coil is also feasible from their respective differential backbone dynamics by careful examination of the T_1^C values of $[2-^{13}\text{C}]\text{-}$ or $[3-^{13}\text{C}]\text{Ala-}$ labeled bR from PM, although their changes as viewed from $[3-^{13}\text{C}]\text{Ala-}$ labeled bR are much smaller when compared to those of the others mentioned above.³⁴

Carbon spin–spin relaxation times under proton decoupling T_2^C can provide motional information about the individual carbon site of interest, in contrast to the case of proton spin–lattice relaxation times in the rotating frame in which information on individual sites would be masked by the presence of the rapid spin–spin process. It is noted, however, that the T_2^C values strongly depend on the frequencies of proton decoupling or magic angle spinning as demonstrated in Eqs. (2)–(4),^{76,81} although such motions, if any, would result in suppressed peaks as demonstrated above rather than the expected changes in the relaxation parameters. It is shown that the peak occurs at the lowermost frequency at 171.1 ppm of $[1-^{13}\text{C}]\text{Val-}$ labeled bR from PM ascribable to Val 199 and Val 101 from the loop regions that exhibit a T_2^C value of 14.1 ms as compared with the values of the transmembrane α -helices (5–10 ms).⁷³ Such distinctions, however, disappear on several mutants including T46V, D85N, D96N, and E204Q because of the presence of interactions between Asp 96 and the backbone near the extracellular surface at Val 199.

It is emphasized that the absence of these ^{13}C NMR peaks from the loop region of $[1-^{13}\text{C}]\text{Ala-}$ and $[2-^{13}\text{C}]\text{Ala-}$, $[1-^{13}\text{C}]\text{Gly}$, or Phe-labeled bR from PM indicates that the turned structure of the loop is not static at ambient temperature as anticipated from that of the globular protein, but slowly fluctuates among various preferred conformations. To clarify this point further, the surface dynamics of bR was examined by measurements of site-specific $^{13}\text{C-}^1\text{H}$ dipolar couplings in $[3-^{13}\text{C}]\text{Ala-}$ labeled bR.¹⁰⁵ Motions of slow or intermediate frequency (correlation time $< 50\ \mu\text{s}$) scale down the $^{13}\text{C-}^1\text{H}$ dipolar couplings according to the motional amplitude. The 2D dipolar and chemical shift (DIP-SHIFT) correlation technique¹⁰⁶ was utilized to obtain the dipolar coupling strength for each resolved peak

in the ^{13}C MAS spectrum, providing the molecular order parameter of the respective site. To this end, typical dipolar dephasing curves available from the DIP-SHIFT experiment are shown in Fig. 13, with the best-fit simulations scaled by the scaling factor of the homonuclear frequency-switched Lee Goldburg (FSLG) decoupling scheme.¹⁰⁷ The order parameter as the ratio between the measured (motionally averaged) dipolar coupling and the rigid limit value in which the dipolar couplings are scaled to 1/3 by the rotation of the Ala methyl groups (22.8 kHz) is utilized as a measure of additional motional fluctuation of the $\text{C}_\alpha\text{--C}_\beta$ vector. Typical order parameters for the mobile sites in bR from PM are between 0.25 and 0.29. These can be assigned to Ala 103 of the C–D loop and Ala 235 at the C-terminal α -helix which protrudes from the membrane surface, and Ala 196 of the F–G loop, as well as to Ala 228 and Ala 233 of the C-terminal α -helix and Ala 51 from the

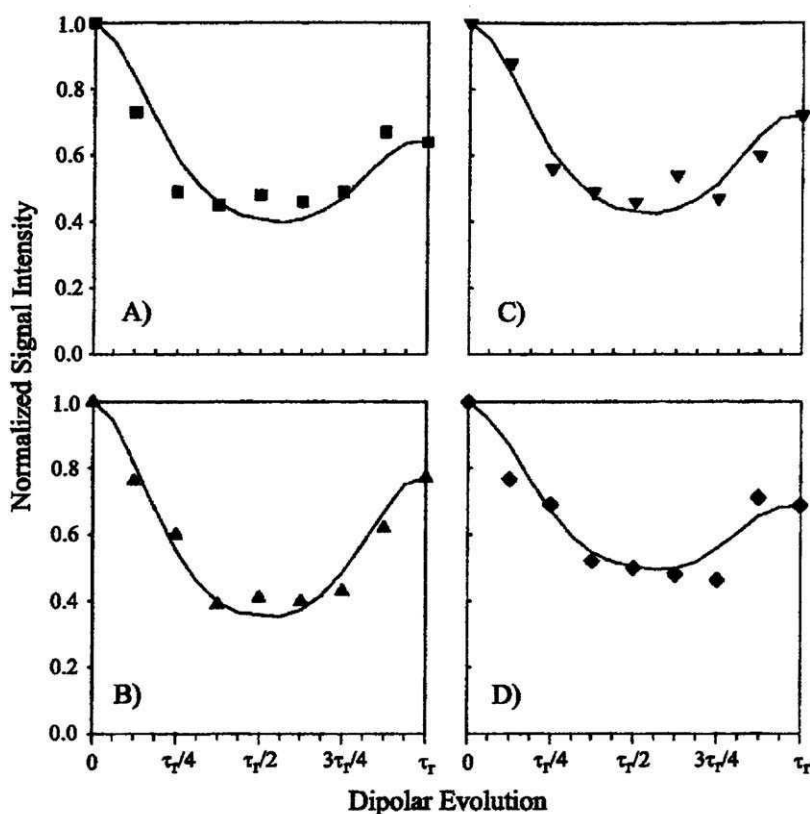


Fig. 13. $^{13}\text{C}\text{--}^1\text{H}$ dipolar dephasing curves for the signals at 16.0 ppm (A: Ala 51, 228, and 233), 16.5 ppm (B: Ala 81), 17.0 ppm (C: Ala 184), and 17.2 ppm (D: Ala 103 and 235). The solid lines represent best-fit numerical simulations with a dipolar coupling of 3.8 kHz (A), 4.3 kHz (B), 3.8 kHz (C), and 3.3 kHz (D), translating into order parameters of 0.29, 0.33, 0.29, and 0.25, respectively.¹⁰⁵ Reproduced with permission from Springer.

transmembrane α -helix. Such order parameters depart significantly from the value of 0.33 for rotating methyl groups and are obviously direct evidence for the fluctuation motions of the Ala C_α - C_β vectors of the intact preparations of fully hydrated bR at ambient temperature. The order parameter for Ala 160 from the expectantly more flexible E-F loop, however, is unavailable under the highest field conditions (749.98 MHz for ^1H frequency), probably because of the increased chemical shift anisotropy together with intrinsic fluctuation motions result in an unresolved ^{13}C NMR signal, based on Eq. (4).

4.2. Blue membrane

In view of its highly halophilic growth condition (ca. 4 M NaCl), it is expected that cation binding to negatively charged lipid head groups and amino-acid residues located at the membrane surface plays an important role in protein dynamics as well as its secondary structure through lipid-protein interactions as a result of partial electric shielding of the negatively charged groups and/or through assembly of the surface structure owing to the formation of salt bridges among charged residues from loops and cytoplasmic α -helix or metal ion-mediated interactions.^{61,108} Lowering the pH of the medium or removal of such cations from the PM (which increases the apparent pK_a value of Asp 85), however, shifts the absorbance maximum from 568 (PM) to 604 nm (blue membrane), hereafter referred to as acid or deionized blue membrane, respectively.^{109–111} In particular, the blue membrane has an altered photocycle and no proton transport activity.¹⁰⁹

In order to gain insight into the protein dynamics and secondary structure, Tuzi *et al.*⁶⁰ recorded the ^{13}C CP-MAS NMR spectra of $[3-^{13}\text{C}]$ Ala-labeled acid-blue and deionized blue membranes, as illustrated in Fig. 14. It is interesting to note that the ^{13}C NMR spectra of two kinds of blue membranes, deionized (pH 4) and acid blue at pH 1.2 are very similar and different from that of the native PM. This suggests that when the surface pH is lowered, either by removal of cations or by lowering the bulk pH, a substantial change is induced in the secondary structures of the protein as well as in their dynamics. In particular, the ^{13}C NMR signals at 17.78–17.20 and 16.41 ppm which are ascribable to Ala residues at the CD, EF, and FG loop regions involving Ala 103, 160, and 196 and those at the transmembrane F, G', B α -helices involving Ala 184, 235, 39, and 168 of $[3-^{13}\text{C}]$ Ala-labeled bR from PM (Fig. 14A) are suppressed in the acid-blue and deionized blue forms (Figs. 14B and C), although the rest of the peaks were broadened as a whole. Further, it was shown that the ^{13}C CP-MAS and DD-MAS NMR spectra of deionized $[3-^{13}\text{C}]$ Ala-labeled 160G mutant of bR are very similar to those of the wild-type, even though their spectral patterns in the purple form are quite different especially at the loop regions in which signals occur at high frequency.¹⁰⁴ The absence of such ^{13}C NMR signals from the loops and some transmembrane α -helices should be obviously ascribed to the changes in the protein dynamics in which an increased fluctuation frequency, from the order of 10^2 Hz in PM to the order of 10^5 Hz in blue membranes, interferes with the frequency of the proton decoupling, to result in suppressed peaks, on the

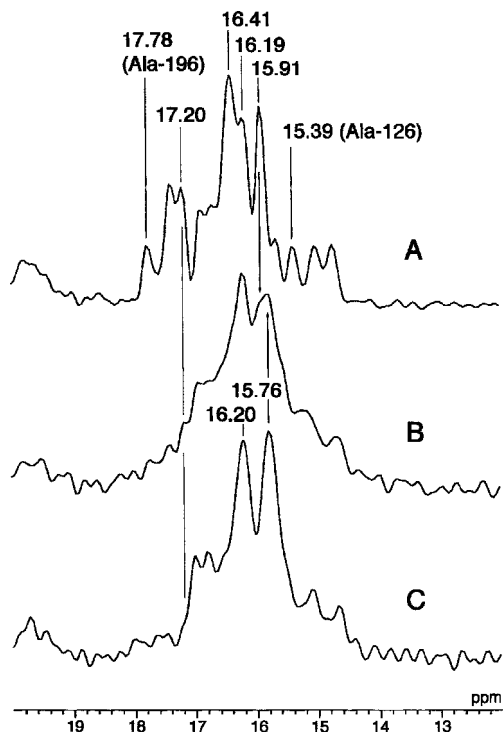


Fig. 14. ^{13}C CP-MAS NMR spectra of $[3\text{-}^{13}\text{C}]\text{Ala}$ -labeled bR from PM at neutral pH (A), its acid blue form at pH 1.2 (B), and its deionized blue form (pH 4) (C).⁶⁰ Reproduced with permission from the Biophysical Society.

basis of the arguments described in Section 4.1. This interpretation is in contrast to the previous one in which the ^{13}C NMR signals of interest were considered to be displaced to low frequency in the blue membranes.⁶⁰

It is interesting to compare the ^{13}C CP-MAS (left) and DD-MAS (right) NMR spectra of $[1\text{-}^{13}\text{C}]\text{Val}$ -labeled bR from PM (Fig. 15A) with those of $[1\text{-}^{13}\text{C}]\text{Val}$ -labeled deionized blue membrane (Fig. 15B), in order to gain insight into its dynamic features as viewed from the ^{13}C NMR spectra of $[1\text{-}^{13}\text{C}]\text{Val}$ -labeled preparation.¹¹² Fig. 15C shows the ^{13}C CP-MAS and DD-MAS NMR of the regenerated Na^+ - purple form. Two things are noteworthy in Fig. 15: first, the ^{13}C NMR spectra of Na^+ - purple are not always the same as those of the native PM. This is consistent with a view that surface secondary structure is stabilized by divalent cations through cation-mediated linkages,¹⁰⁴ to be discussed in more detail in the next section. Second, the ^{13}C NMR peak intensities ascribable to the loop regions of the blue membrane are substantially suppressed both in the CP-MAS and the DD-MAS NMR spectra, consistent also with those of the ^{13}C NMR spectra of $[3\text{-}^{13}\text{C}]\text{Ala}$ -labeled preparations (see Fig. 14). However, it is rather surprising to note that the extent of the peak suppression by the blue membrane is not always the

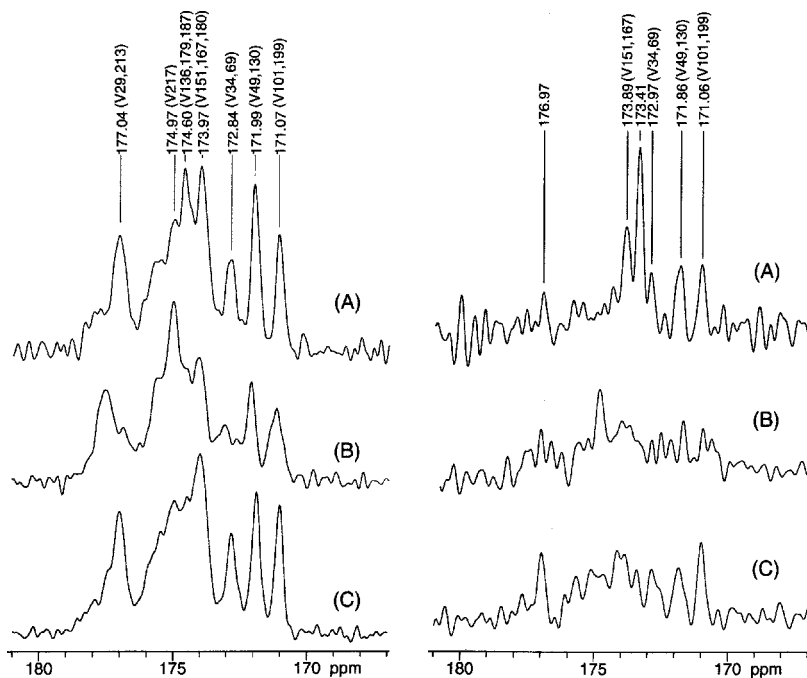


Fig. 15. ¹³C CP-MAS (left) and DD-MAS (right) NMR spectra of [1-¹³C]Val-labeled PM (A), deionized blue membrane (B) and regenerated Na⁺-PM from deionized blue membrane (C).

same for the ¹³C CP-MAS and DD-MAS spectra. This may be a consequence of the presence of a distribution in the fluctuation frequencies in the blue membranes.

4.3. Surface structure

Naturally, it is anticipated that the surface structure of membrane proteins is generally very important for exhibiting their biological functions, because any biological signals could be initiated or received at the membrane surfaces. Nevertheless, the surface structure of bR is still obscured, or inconsistent, among a variety of 3D structures so far revealed by cryoelectron microscopy and X-ray diffraction studies.⁵⁻⁹ This is because it can be easily altered by a variety of intrinsic or environmental factors such as the crystallization process either in the 2D or 3D crystals, temperature, pH, ionic strength, crystallographic contact, etc.^{35,113} In addition, the dynamic picture of membrane proteins to be observed at the physiological temperature can be lost when all of the 3D structures have been obtained at cryogenic temperatures. As an alternative means, fluorescence,^{102,114} spin labeling,¹¹⁵ and atomic force microscopy (AFM)¹¹³ techniques have been utilized to probe such structures at ambient temperature, although these techniques are not always free

from plausible perturbations due to steric hindrance by the introduced probes, except for the case of AFM. For this reason, the surface structure to be discussed on the basis of the conformation-dependent ^{13}C chemical shift (δ) herein should not be considered as a static picture compatible with that available from diffraction studies in spite of the data available from solid-state NMR but as a picture consisting of dynamic equilibrium among various conformers available from solution NMR:

$$\delta = \sum_i p_i \delta_i \quad (7)$$

where p_i is the fraction of the conformer i under consideration.

It appears, from the ^{13}C NMR data described above, that mono- or divalent cations present in the growth medium of bR (Table 1) play an essential role for regulating the protein dynamics, especially at the membrane surface, through stabilization of its secondary structure at the membrane surface consisting of several negatively charged amino-acid residues (see Fig. 3), besides their potential role for maintaining neutral surface pH. The presence of the specific cation-binding sites to bR was initially proposed to explain the alterations of color and the above-mentioned function of bR,^{116,117} although Szundi and Stoeckenius demonstrated that a lowered surface pH, induced by the removal of nonspecific surface-bound cations, can explain the purple-to-blue transition.^{118,119} Obviously, the latter view is consistent with the similarity of the ^{13}C NMR spectra of [3- ^{13}C]Ala-labeled bR between the cation-free and acid-blue membranes, as shown in Fig. 14.

Nevertheless, it is also probable that the above-mentioned dynamic change is not simply caused by neutralization of the surface pH owing to the non-specific cation binding but by stabilization of the secondary structure by the specific cation binding leading to an assembly of specific surface structure, as already noted in the dynamic structure. Undoubtedly, the current site-directed ^{13}C NMR spectroscopy is an unrivaled means to be able to clarify the dynamics as well as the structural features of the membrane surface that cannot be revealed by diffraction methods.⁵⁻⁸ For this purpose, Tuzi *et al.*⁶⁰ compared the ^{13}C NMR spectra of [3- ^{13}C]Ala-labeled bR from PM with those of Na^+ -regenerated PM prepared from the deionized blue membrane at neutral pH, as illustrated in Fig. 16. Here, the ^{13}C CP-MAS (A) and DD-MAS (B) NMR spectra of the Na^+ purple form of bR (black traces) are superimposed on the spectra of the native purple form (gray traces). Indeed, most of the transmembrane α -helices are restored in the Na^+ purple form as viewed from the very similar spectral pattern between Na^+ purple and PM. Only the four peaks arising from the loops and C-terminal α -helix designated by the arrows in Fig. 16 differ between the Na^+ and the native purple form in the presence of 10 mM NaCl. These spectral changes are ascribed to a local conformational change near the specific cation-binding site(s) caused by replacement of divalent cations with the Na^+ ion. However, the remaining peak positions at the loop region as well the peak intensity at 15.91 ppm ascribable to the C-terminal α -helix are not always identical. Interestingly, the ^{13}C NMR spectra of the Na^+ purple form treated with 5 μM Ca^{2+} ion exhibits characteristics intermediate between those of the native purple form and the Na^+ form. The broadened or less intense peak at 15.91 ppm in the spectra of the Na^+ purple form becomes narrower and approaches the line shape in

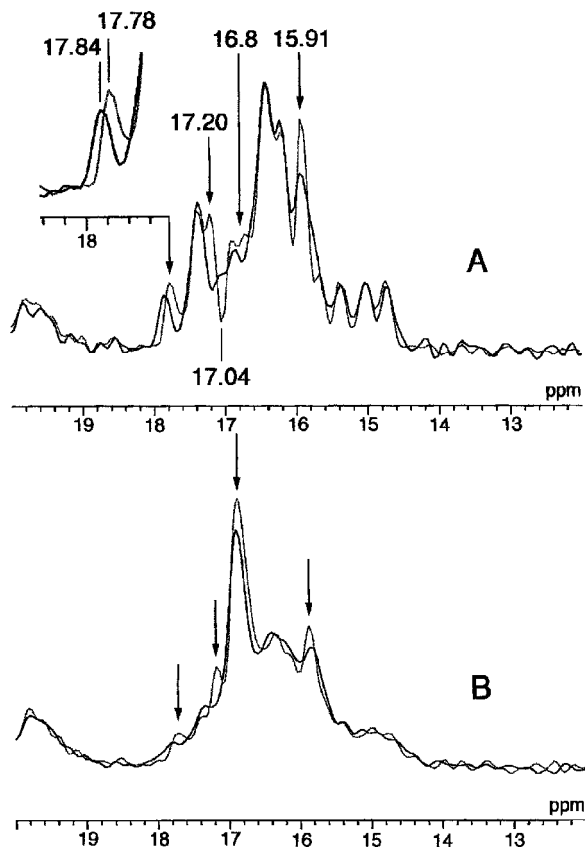


Fig. 16. Comparison of ^{13}C CP-MAS (A) and DD-MAS (B) NMR spectra of $[3-^{13}\text{C}]\text{Ala}$ -labeled bR at pH 7.0 between native purple form (gray traces) and Na^+ purple form (black traces).⁶⁰ Reproduced with permission from the Biophysical Society.

the spectra of the native PM by Ca^{2+} treatment. This spectral change can be ascribed to a recovery of the cytoplasmic surface complex consisting of the C-terminal α -helix and C-D and E-F loops in the presence of a divalent cation.^{31,34,35} The most preferred binding site for the divalent cations is further revealed as near Ala 196 at the extracellular side instead of the expected site near Asp 85,⁶⁰ by utilizing $5\ \mu\text{M}$ Mn^{2+} ion as probe for the transverse relaxation agent instead of Ca^{2+} ion.

Several pieces of evidence have been presented on how specific surface electrical charges at the cytoplasmic surface are involved in efficient proton uptake during the photocycle in relation to the biological significance of the above-mentioned surface complex. Riesle *et al.*¹²⁰ proposed that the surface-exposed amino acids Asp 36 (A-B loop), Asp 102, and Asp 104 (C-D loop) and Glu 161 (E-F loop) seem to collect efficiently protons from the aqueous bulk phase and funnel them to the

entrance of the cytoplasmic proton pathway. Checover *et al.*^{121,122} showed that a dominant “proton binding cluster” of the wild-type protein consists of Asp 104, Glu 161, and Glu 234 (C-terminal α -helix), together with Asp 36 as a mediator to deliver the proton to a channel. In particular, replacement of Glu 234 (C-terminal α -helix, designated by G' in Fig. 3) with cysteine disrupted the structure of the cluster,¹²¹ probably through disruption of the surface structure. It is anticipated, therefore, that such a surface structure could be altered by site-directed mutations at the key positions mentioned above, through modified salt bridges and/or metal ion-mediated interactions.

To gain insight into this problem, Yonebayashi *et al.*¹⁰⁴ examined how the cytoplasmic surface structure of [3-¹³C]Ala-labeled bR, consisting of the C-terminal α -helix and cytoplasmic loops, is altered by site-directed mutation at the former (R 227Q) and the latter (A160G, E166G, and A168G) and by cation binding with reference to the displaced ¹³C NMR peaks of Ala 228, Ala 233 (C-terminal α -helix), Ala 103 (C–D loop), and Ala 160 (E–F loop). In fact, deletion of the C-terminal α -helix by papain or mutation at the C-terminal α -helix and E–F loop resulted in a substantial conformational change in the loop region of the ¹³C chemical shifts (Ala 103 and Ala 160) as viewed from the displaced ¹³C chemical shifts as compared with those of the intact bR, as summarized in Table 5. Most notably, lowering the temperature of bR from 40°C to –10°C results in the displaced ¹³C NMR peak of the C-terminal α -helix to a low frequency direction by about 0.41 ppm.³⁴ In contrast, the low-frequency displacement of the ¹³C chemical shifts of Ala C _{β} peaks of α -helix to the normal position, 15.5 ppm at –10°C, correspond to the α -helical Ala C _{β} peak of (Ala)_n in the solid-state.^{63,64,88} This can be ascribed to a recovery of the perturbed α_{II} -helix to the unperturbed α_I -helix form.¹⁰⁴ This is because a fluctuating or perturbed α -helix conformation with a low-frequency motion could be recognized as an α_{II} -helix form as viewed from the high frequency displacement of the ¹³C NMR signals.⁷¹

It appears, therefore, that the C-terminal α -helix as an unperturbed form, encountered for WT at low temperature, could be readily visualized by an “open” form consisting of the C-terminal α -helix extended straightforwardly from the G'-helix (Fig. 17A). This can be schematically shown as a vertical cylinder protruding from the membrane surface that is free from mutual interactions with nearby loops, as illustrated in Fig. 17A as superimposed upon the drawing by Grigorieff *et al.*⁴ It is expected that this type of the “open” form is dominant under the condition that the pH is lower than 4.5.¹⁰¹ In addition the M-like state of D85N at pH 10⁸⁰ and mutants at the C-terminal α -helix (R227Q) and in the vicinity of the E–F loop (E166G and A168G), due to the loop regions and the cytoplasmic ends of the helices acquiring motional flexibility with a frequency range of up to 10⁵ Hz, resulting in the selectively suppressed ¹³C NMR signals of [2-¹³C]Ala-bR³⁴ and 16.38 ppm ascribable to Ala 39 (helix B)⁷³ and 168 (helix F) in [3-¹³C]Ala-bR,¹⁰⁴ respectively. In contrast, it is plausible that in order to facilitate the maximum mutual interactions with the nearby loops the tilted C-terminal α -helix toward the direction to the helices B and F might be more preferable as a “capped” form (see Fig. 17B). Undoubtedly, this form

Table 5. Displacements of ¹³C chemical shifts of the C-terminal α-helix and loops from [3-¹³C]Ala-labeled bacteriorhodopsin and its mutants (Ref. 104)

		C-terminal α-helix	Loop (ppm)		References
		Ala 228, 233 (ppm)	Ala 103	160	
Wild type	20°C ^a	15.91	17.19	17.36	<i>b,c</i>
	40°C	16.40	17.62		<i>b,c</i>
	−10°C	15.50	17.58	17.30	<i>b,c</i>
A160G	20°C	15.91	17.61		<i>d</i>
	0°C	15.67	17.43	—	<i>d</i>
WT	high ionic strength (100 mM NaCl)	15.89	17.56	17.37	<i>b</i>
	decreased pH (pH 4.5)	15.89/15.67	17.57	17.27	<i>e</i>
	(pH 1.2)	15.76	<i>f</i>	<i>f</i>	<i>e</i>
	Deionized	15.76	<i>f</i>	<i>f</i>	<i>e</i>
	Added Ca ²⁺	15.91	17.51	17.37–17.15	<i>d</i>
	papain-cleaved	None	17.52	17.27	<i>b</i>
	R227Q (C-terminal α-helix)	15.88/15.68	17.54	17.28	<i>d</i>
	A228G (C-terminal α-helix)	15.87	17.58	17.32	<i>b</i>
D85N	(pH 7) (C-helix)	15.84	17.59	17.40	<i>g</i>
	(pH 10) (C-helix)	15.87/15.61	<i>f</i>	<i>f</i>	<i>g</i>
E166G	(F-helix)	15.91/15.68	17.53	17.30	<i>d</i>
A168G	(F-helix)	15.91/15.68	17.53	17.30	<i>d</i>

^aReference state: pH 7, 10 mM NaCl, 20°C, unless otherwise specified.
^bRef. 101.
^cRef. 33.
^dRef. 104.
^eRef. 60.
^fPeaks suppressed.
^gRef. 80.

is more suitable to prevent the accelerated fluctuation motions in the cytoplasmic ends of the B and F helices (Fig. 3) by forming a cytoplasmic structure or cytoplasmic complex. This means that the cytoplasmic surface complex of WT at ambient temperature is formed among the C-terminal α-helix and C–D and E–F loops and probably the A–B loop. This results in the loss of stability of the C-terminal α-helix itself, mainly due to stereochemical requirement for the formation of complex through salt bridges among charged residues and/or cation-mediated interactions utilizing divalent cations such as the Ca²⁺ ion (see Table 6).¹⁰⁴

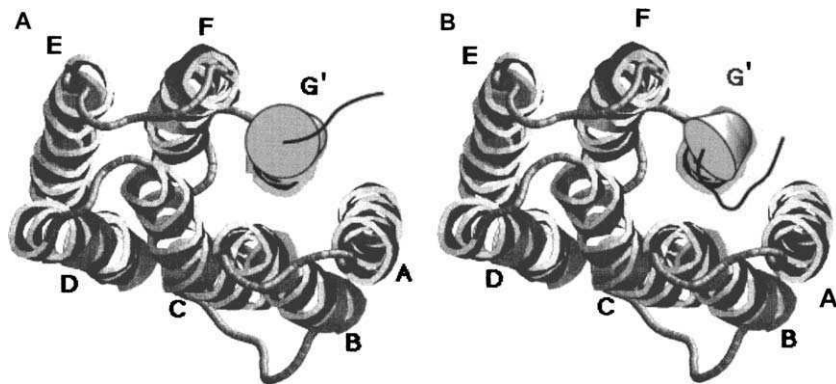


Fig. 17. Schematic representation of the C-terminal α -helix (G' as added *cylinder*) superimposed upon the 3D structure (cytoplasmic side) of bR by Grigieff *et al.* *Small capital letters, A–G, denote the transmembrane helices.* A. An “open” form in which the C-terminal α -helix is straightforwardly extended from helix G. B. A “capped” form in which the C-terminal α -helix is tilted toward the direction of the B- and F-helices to be able to interact with the nearby loops through salt bridges and/or metal ion-mediated bonding.¹⁰⁴ Reproduced with permission from Springer.

Table 6. Summary of conditions leading to formed or disrupted cytoplasmic complex as judged from the ^{13}C chemical shifts of the C-terminal α -helix (Ref. 104)

	Formed	Disrupted	Reference
Wild type	Ambient temperature ($>0^\circ\text{C}$)	Low (-10°C)	^a
	High ionic strength ($>10\text{ mM NaCl}$)	Deionized	^b
	Neutral pH	Low pH <4.5	^c
Mutants		D85N (pH >10)	^d
		R227Q	^b
		E166G	^b
		A168G	^b

^aRef. 101.

^bRef. 104.

^cRef. 60.

^dRef. 80.

Such surface structure should be realized as a rapidly interconverting system, at least, between the above-mentioned two forms as described by Eq. (7), although the relative proportions of these forms vary depending upon the environmental factors such as temperature, pH, ionic strength, etc. It is also pointed out that such a conformational change illustrated in Fig. 17 might be related to the consequence of the conformational switch responsible for proton uptake after the release of a proton from the extracellular surface in the photocycles. This view is obviously consistent

with that of the presence of a cytoplasmic surface complex that plays an important role in facilitating the efficient proton uptake by preventing unnecessary fluctuations in the cytoplasmic surface of the WT, by taking into account the recent findings by Checover *et al.*^{121,122} Consistent with this view, Brown *et al.* also showed that Arg 227 located at the end of the helix G plays an important role through a cluster of interacting residues to facilitate proton transfer from the cytoplasmic domain.¹²³

It is expected that partial neutralization of negatively charged residue(s) by site-directed mutagenesis would also lead to the modified cytoplasmic structure as viewed from a ^{13}C NMR spectral change, if such a mutation site is located at the above-mentioned "proton-binding cluster." Indeed, Asp 102 and 104 are located at the C-D loop constituting cytoplasmic surface complex, because Asp 36, 38, 102, and 104 and Glu 161 seem to efficiently collect protons from the aqueous bulk phase and funnel them to the entrance of the CP proton pathway.¹²⁰⁻¹²² In order to gain insight into such a possibility, Arakawa¹¹² recorded the ^{13}C NMR spectra of $[1-^{13}\text{C}]\text{Val}$ -labeled D102N, D104N, and D102/104N as illustrated in Fig. 18. Obviously, at least two types of arrowed peaks at 171.5–171.6 and 172.4–172.6 ppm emerge in these mutants from the degenerated peaks of the wild type at 171.9 (Val 49/130) and 172.8 ppm (Val 34/69), respectively (see the top trace of Fig. 16), as a reference for wild-type bR from PM. Naturally, it is likely that such affected peaks, both at the peak positions and intensities accompanied by a plausible conformational change at the C-D loop, could be transmitted to subsequent conformational

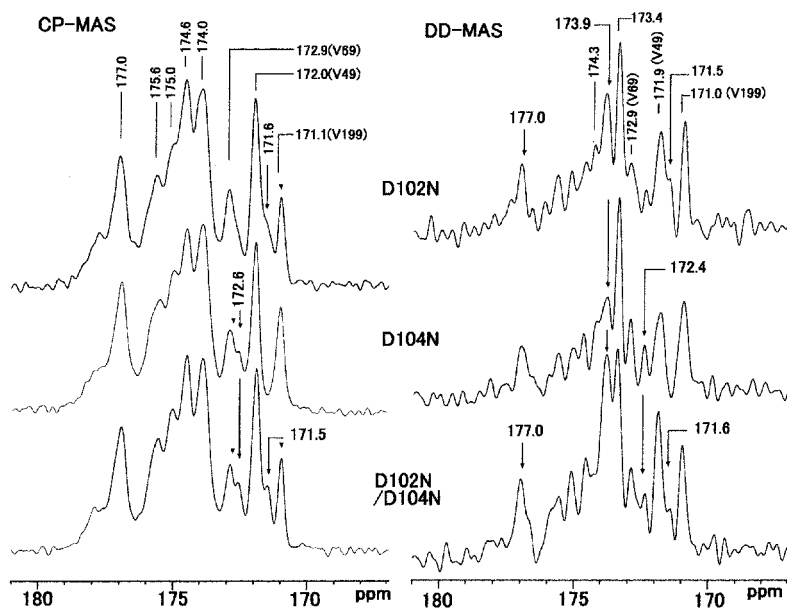


Fig. 18. ^{13}C CP-MAS (left) and DD-MAS (right) NMR spectra of $[1-^{13}\text{C}]\text{Val}$ -labeled D102N (top), D104N (middle), and D102N/D104N (bottom) mutants. The arrowed peaks emerged in these mutants from the spectra of the wild type.¹¹²

changes at Val 130 at D–E loop and Val 34 at A–B loop through movements in the transmembrane helices, B, C, D, and E, in view of the schematic representation of bR taking into account of the secondary structure in Fig. 3. This finding indicates that such a conformational change of bR from PM, if any, turns out to be more conveniently visualized by this sort of characteristic displacement of ^{13}C NMR signals from $[1-^{13}\text{C}]\text{Val}$ -labeled bR than that of $[3-^{13}\text{C}]\text{Ala}$ -labeled bR.¹²⁴

Even though the negatively charged amino-acid residues are associated with the binding site for protons and a variety of mono- or divalent cations as discussed above, the most preferred cation-binding site is located at the F–G loop near Ala 196 on the extracellular surface.⁶⁰ Besides, several negatively charged amino-acid residues, Glu or Asp residues located at the cytoplasmic (CP) surfaces turns out to be also involved as additional sites for loosely bound divalent cation, essential for stabilization of EC structure and proton pump activity.^{125,126} Among four Glu residues (Glu 9, 74, 194, and 204) located at the EC surface, a proton is transferred, during photocycle, from the protonated Schiff base to the proton acceptor Asp 85 and another proton is subsequently released on the EC side from the proton releasing complex (Glu 204, Glu 194, and a bound water). Lazarova *et al.* showed that Glu 194 is the group that controls the pKa of Asp 85.¹²⁷ To clarify the contribution of the extracellular (EC) Glu residues to the conformation and dynamics of bR, Saitô *et al.*¹²⁸ recorded the ^{13}C NMR spectra of $[3-^{13}\text{C}]\text{Ala}$ - or $[1-^{13}\text{C}]\text{Val}$ -labeled bR and a variety of mutants in which extracellular Glu residues are replaced with Gln: E9Q, E74Q, E194Q/E204Q (2Glu), E9Q/E194Q/E204Q (3Glu) and E9Q/E74Q/E194Q/E204Q (4Glu). Replacements of Glu 9 or 74 as well as Glu 194/204 at the EC surface by glutamine(s) induced conformational changes at the cytoplasmic (CP) surface structure consisting of the C-terminal α -helix and loops, as viewed from the ^{13}C NMR spectra of $[3-^{13}\text{C}]\text{Ala}$ - and $[1-^{13}\text{C}]\text{Val}$ -labeled proteins.

As demonstrated in Fig. 19, the ^{13}C CP-MAS (left) and DD-MAS (right) NMR spectra were recorded for $[3-^{13}\text{C}]\text{Ala}$ -labeled 2Glu (C and D), 3Glu (E and F) and 4Glu (G and H) as well as those of the wild-type (A and B), respectively. The resulting spectral lines from whole areas of these mutants were significantly broadened, as encountered with those of the wild-type, owing to partially failed proton decoupling interfering with the fluctuation frequency of the order of 10^5 Hz.⁸¹ As a result, the three well-resolved low-frequency peaks 15.34, 15.02, and 14.74 ppm of wild-type are no longer resolved for these multiple mutants, as in the cases of $[3-^{13}\text{C}]\text{Ala}$ -labeled bO³³ or D85N mutant.⁸⁰ In addition, the increased peak intensities at 19.83 ppm from the lipid methyl group of 3Glu and 4Glu as recorded by the DD-MAS spectra are interpreted in terms of increased numbers of surrounding lipid molecules due to the presence of a disrupted or disorganized trimeric structure.⁴⁰

Therefore, the multiple mutants containing at least both E194Q and E204Q cause a retinal–protein perturbation that is not seen in the individual single mutants, consistent with the altered absorption spectrum. In addition, the ^{13}C NMR signals at 17.78 (Ala 196 from the F–G loop) and 15.91 ppm (Ala 228 and 233 at the C-terminal α -helix) of these mutants are appreciably suppressed as compared to those of the wild-type in the CP-MAS NMR only, other peaks occur at 16.33 (Ala 39 and 168) and 16.20 ppm (Ala 15) (both the CP ends of B and F helices, respectively).

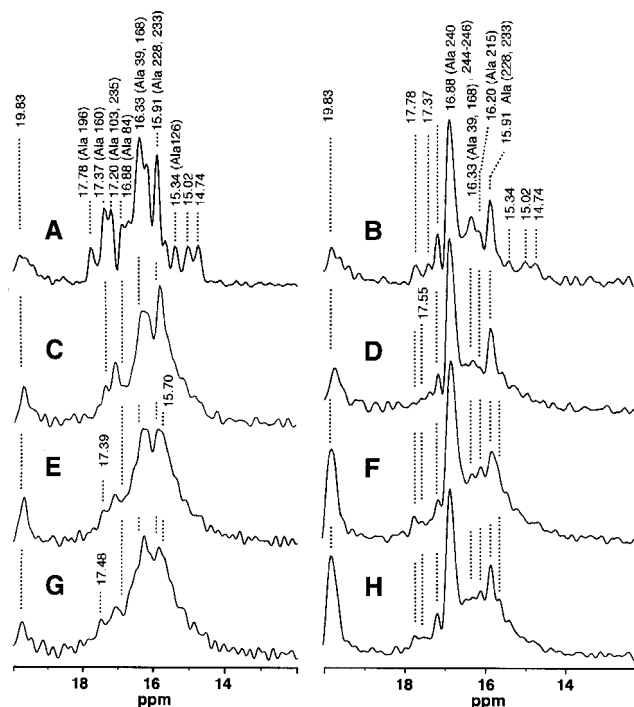


Fig. 19. ^{13}C CP-MAS (left) and DD-MAS (right) NMR spectra of $[3-^{13}\text{C}]\text{Ala}$ -labeled wild type (A and B), E194Q/E204Q (2Glu) (C and D), E9Q/E194Q/E204Q (3Glu) (E and F), and E9Q/E74Q/E194Q/E204Q (4Glu) (G and H) mutants. The assigned peaks so far performed are indicated at the top traces.¹²⁸ Reproduced with permission from the Biophysical society.

Major dynamic changes induced for the triple or quadruple mutants are clearly seen from the broadened ^{13}C NMR peaks of the $[3-^{13}\text{C}]\text{Ala}$ -labeled 3Glu and 4Glu mutants due to acquired global fluctuation motions of the order of 10^{-4} – 10^{-5} s arising from the disrupted trimeric form. In such mutants, ^{13}C NMR signals of $[1-^{13}\text{C}]\text{Val}$ -labeled 3Glu and 4Glu mutants were substantially suppressed from Val residues near to the CP and EC surfaces (including 8 Å depth from the surface) in spite of the presence or absence of $40\ \mu\text{M}\ \text{Mn}^{2+}$ ion. It is therefore concluded that these Glu residues at the EC surface also play an important role in maintaining the native secondary structure of bR in the PM.

5. BACKBONE DYNAMICS IN THE TRANSMEMBRANE α -HELICES

5.1. Kinked structure

Based on the site-directed mutants together with the Mn^{2+} -induced spectral editing described in Section 3.4, the ^{13}C NMR positive peak at 17.27 ppm in the difference

spectrum between [3- ^{13}C]Ala-labeled wild-type bR and A184G mutant in the presence of the Mn^{2+} ion is unequivocally ascribed to Ala 184 located at the helix F as revealed by an X-ray diffraction study at low temperatures in spite of the ^{13}C NMR peak position in the loop region, as illustrated in Fig. 20C.⁸² It is likely that this sort of anomaly could be caused by an altered conformation and dynamics of the transmembrane α -helix F at Ala 184 at ambient temperature in the lipid bilayer caused by the presence of a kinked structure at Pro 186, which results in the absence of the intrahelical hydrogen bond between Trp 182 and Pro 186, as demonstrated in Fig. 21. In fact, it is noted that this anomaly disappears when the ^{13}C CP-MAS NMR spectrum of [3- ^{13}C]Ala-labeled P186A mutant is recorded in the presence of the Mn^{2+} ion, as illustrated in Fig. 20D: the Ala 184 signal at 17.27 ppm is displaced to a low frequency from the normal position of the α -helix by removal of the kinked structure by replacement of Pro 186 with Ala.

In order to clarify how a conformational change in the transmembrane α -helix is induced in the helix F, Saitô *et al.*⁷⁵ recorded the ^{13}C NMR spectra of WT and P186 mutant of [3- ^{13}C]Ala,¹⁸⁴[1- ^{13}C]Val¹⁸⁷-labeled transmembrane peptide F (164–194) both in the lipid bilayer and in the solid. Interestingly, the ^{13}C NMR signal of the [3- ^{13}C]Ala-labeled fragment occurs at 17.4 ppm which corresponds to the loop region in the DMPC bilayer (Fig. 22A), while the corresponding peak from the P186L mutant occurs at 15.8 ppm of the normal α -helix conformation. It is noted that the former peak position is very close to that of 17.27 ppm as observed for the intact wild-type protein from PM. In addition, the ^{13}C chemical shift of [1- ^{13}C]Val¹⁸⁷ of the wild-type fragment occurs at 172.0 ppm far from the α -helix region, while the corresponding peak of P186L mutant is at the normal α -helix region (Fig. 22B).⁷⁵ In contrast, no evidence of the kinked structure is present in the solid, because the ^{13}C chemical shifts of the [3- ^{13}C]Ala¹⁸⁴ and [1- ^{13}C]Val¹⁸⁷-labeled peaks are almost the same for the transmembrane peptides corresponding to the wild-type and the P286L mutant. This means that the spectral change caused by the kinked structure is more pronounced in the lipid bilayer in which conformational and dynamic changes could be more easy than in the more flexible environment in the lipid bilayer.

The three Pro residues that serve as the kinked structures in PM are located in the inner part of the transmembrane α -helices, Pro 186 (helix F), Pro 50 (helix B), and Pro 91 (helix C) among the total 10 Pro residues, as pointed out already in Section 4.1. It is emphasized that the acquired protein dynamics due to the presence of the kinked structure and its physiological significance can be visualized by solid-state NMR alone. This aspect will be discussed in more detail in the following section.

5.2. M-like state

Photoisomerization of the retinal from the all-*trans* to the 13-*cis* form initiates proton transfer steps from the cytoplasmic to the extracellular side via the J, K, L, M, N, and O intermediates of a cyclic reaction.¹²⁹ These intermediate states can be distinguished over picosecond to millisecond ranges, and a series of the cycle is completed in less than 10 ms. Global conformational changes of the protein

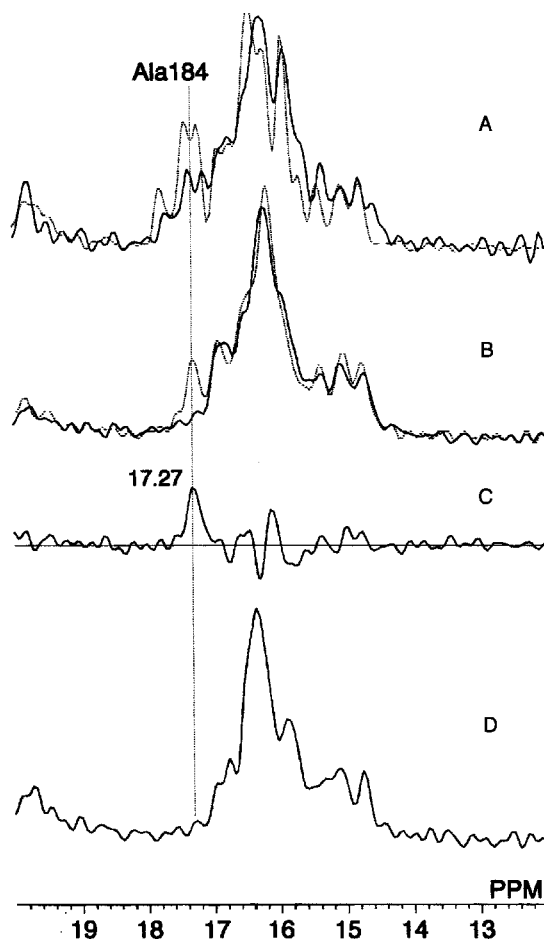


Fig. 20. ^{13}C CP-MAS NMR spectra of the $[3\text{-}^{13}\text{C}]\text{Ala}$ -labeled A184G in the absence (A) and (B) presence of the Mn^{2+} ion. The corresponding spectra of $[3\text{-}^{13}\text{C}]\text{Ala}$ -labeled wild-type bR are superimposed as dotted traces. (C) Difference spectrum between the spectra of the wild-type and mutant bRs in the presence of Mn^{2+} ion. (D) ^{13}C CP-MAS NMR spectra of $[3\text{-}^{13}\text{C}]\text{Ala}$ -labeled P186A in the presence of the Mn^{2+} ion.⁸² Reproduced with permission from the Biophysical Society.

backbone occur in the M and/or N intermediates with a deprotonated and a protonated retinal Schiff base, respectively. Such global conformational changes may be part of the proton access switch between the deprotonation and reprotonation of the Schiff base.^{130,131} Kamikubo *et al.*¹³² showed on the basis of low-resolution X-ray diffraction studies that characteristic conformational changes of the M intermediate occur at helices B and G and the change of the N intermediate occurs at helices F and G. Therefore, D85N and D85N/D96N mutants at alkaline pH with the unprotonated Schiff base can be conveniently used as an excellent model system

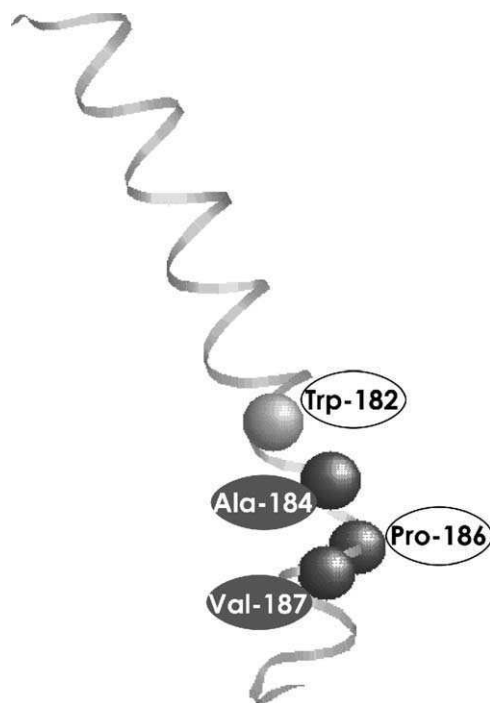


Fig. 21. A proposed kinked structure in the transmembrane α -helix F (164–194) in the lipid bilayer, caused by lack of the intrahelical hydrogen bond between Trp 182 and Pro 186.⁷⁵ Reproduced with permission from Elsevier.

to achieve an M-like state *at ambient temperature without illumination* to clarify this problem, because a resultant structural change in these systems is very similar to that of the M photointermediate according to previous X-ray diffraction studies.^{130,133}

It is expected that such global conformational as well as concomitant dynamic changes, if any, could be suitably examined by the site-directed solid-state NMR approach, utilizing the conformation-dependent displacement of peaks,^{35,63,64} as well as the preferentially suppressed peak intensities,^{34–36} so far examined. In reflecting such a global conformational change, the ^{13}C NMR spectrum of $[1-^{13}\text{C}]\text{Val}$ -labeled D85N (Fig. 23, top trace) is substantially varied even at neutral pH as compared with that of the wild-type (Fig. 5, top (left)). The intense ^{13}C NMR peak at 172.03 ppm from the wild-type is ascribed to the superimposed signals from Val 49 (B helix) and Val 130 (D–E loop) (Fig. 5). The corresponding peak from D85N, however, is split into the following two components:¹³⁴ the intense ^{13}C NMR peak for Val 49 is displaced to 172.30 ppm by an accompanied conformational change, while the peak for Val 130 is almost completely suppressed at neutral pH. In contrast, the former peak is almost completely suppressed at pH 10 as a result of acquired local fluctuation motion at the helix B with a frequency of 10^4 Hz,

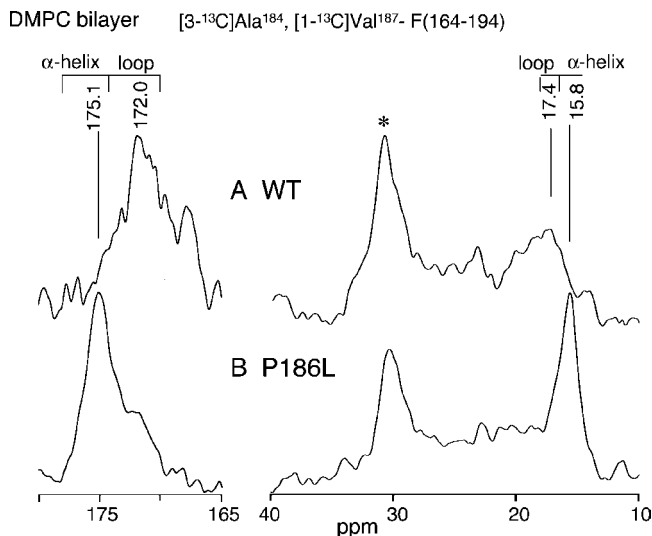


Fig. 22. ^{13}C CP-MAS NMR spectra of wild type (A) and P186L mutant (B) of chemically synthesized $[3\text{-}^{13}\text{C}]\text{Ala}^{184}$, $[1\text{-}^{13}\text{C}]\text{Val}^{187}$ -labeled transmembrane peptide F (164–194) incorporated in DMPC bilayer, recorded at ambient temperature.⁷⁵ Reproduced with permission from Elsevier.

concomitant with deprotonation of Schiff base at the M-like state. The latter peak emerges again at the same time at 171.80 ppm at $\text{pH} > 8$ caused by passing through fluctuation motions with frequencies from 10^4 to 10^5 Hz. Of course, such preferentially suppressed peaks either at neutral or alkaline pH are ascribed to the interference of an acquired fluctuation frequency either at the D–E loop or at the helix B, respectively, with the frequency of magic angle spinning.⁷⁶ This interpretation is consistent with the spectral behavior of Val 130 from $[1\text{-}^{13}\text{C}]\text{Val}$ -labeled D85N/V49A as a function of pH, described below.¹³⁴ This interpretation is therefore in contrast to the previous one by Kawase *et al.*⁸⁰ in which such spectral change was interpreted in terms of the pH-induced displacement of peaks alone.

Kawase *et al.*⁸⁰ and later Kira *et al.*¹³⁴ examined the ^{13}C NMR spectra of $[3\text{-}^{13}\text{C}]\text{Ala}$ -, $[1\text{-}^{13}\text{C}]\text{Val}$ -, Pro-labeled D85N, D85N/V49A, and D85N/D96N mutants at both neutral (protonated) and alkaline pH (> 10) (unprotonated), as compared with those of the wild-type. The peak intensities of the three to four ^{13}C NMR signals of the $[3\text{-}^{13}\text{C}]\text{Ala}$ -labeled residues from the transmembrane α -helices, including Ala 39, 51, and 53 (helix B) and 215 (helix G), were suppressed in D85N and D85N/D96N proteins both in the CP-MAS and DD-MAS spectra, irrespective of the pH, as demonstrated by Kawase *et al.*⁸⁰ This observation is due to the conformational change and subsequent acquisition of the low-frequency motions, which interfere with the frequency of the proton decoupling.⁸¹ Greater spectral changes were achieved as mentioned above,^{80,134} however, at pH 10, which indicate large-amplitude motions of the transmembrane helices upon deprotonation of the Schiff base and the formation of the M-like state in the absence of illumination

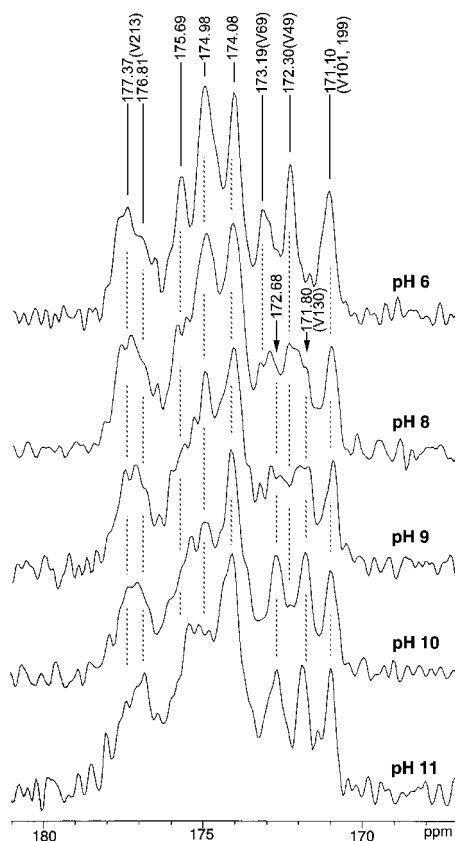


Fig. 23. ^{13}C CP-MAS NMR spectra of the $[1-^{13}\text{C}]\text{Val}$ -labeled D85N mutant at various pH values (from 6 to 11).¹³⁴ Reproduced with permission from Springer.

(see Fig. 24). A similar pH-dependent spectral change was noted for the $[1-^{13}\text{C}]\text{Val}$ -labeled D85N/V49A mutant: the less intense Val 130 at pH 7 (171.95 ppm) is recovered at pH 8 and 9 in a similar manner to the case of D85N mentioned above. However, the whole spectra were almost completely suppressed at pH 10, but they were fully recovered again after the pH was lowered.¹³⁴ This is obviously caused by an accelerated conformational fluctuation which might be triggered by relaxed helix–helix interactions in the absence of any van der Waals contact between Lys 216 at the Schiff base and Val 49 residues of the wild-type. In fact, it was shown that the peptide $\text{C}=\text{O}$ of Val 49 forms a hydrogen bond with a water molecule connected to Asp 85.¹³⁵ Nevertheless, local dynamics at Pro 50 neighbored with Val 49 turned out to be unchanged irrespective of the charged state of SB as viewed from the ^{13}C NMR of $[1-^{13}\text{C}]\text{Pro}50$. This is because the ^{13}C NMR peak intensity of $[1-^{13}\text{C}]\text{Pro}50$ residues in D85N mutant among three Pro residues active as hinges was unchanged even at pH 10, while the peak intensities of the remaining two Pro residues, Pro 91 and Pro 186, were completely suppressed (see Fig. 11).

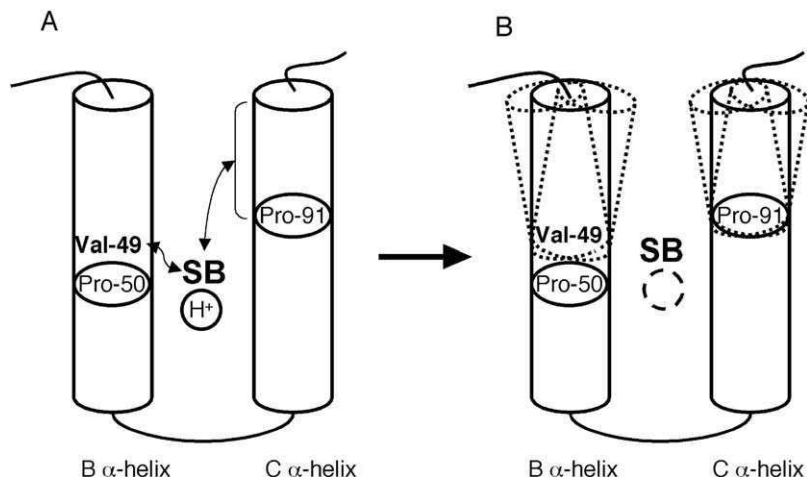


Fig. 24. Schematic representation of dynamic behavior of the B and C α -helices of D85N accompanied with protonation of Schiff base, as viewed from the ^{13}C NMR spectral behavior of Val 49 and Pro 91, described in the text. (A) Ground state at pH 7, and (B) M-like state at pH 10.¹³⁴ Reproduced with permission from Springer.

Undoubtedly, acquisition of such fluctuation motion at the cytoplasmic side of the transmembrane B and C α -helices in the M-like state of D85N mutant (Fig. 24B) is responsible for a transient environmental change from the hydrophobic to hydrophilic conditions both at the Asp 96 and Schiff base (SB) as compared with the ground state (Fig. 24A), resulting in a reduced $\text{p}K_a$ value of Asp 96 in the M-like state, which makes proton uptake more efficient. Further, it is demonstrated that the presence of the van der Waals contact of Val 49 with Lys 216 at the Schiff base is essential to trigger this sort of dynamic change, as revealed from the ^{13}C NMR data of the D85N/V49A mutant.

5.3. Long-distance interaction among residues for information transfer

As pointed out already, proton transfer in bR is activated by photoisomerization of all the *trans*-retinal to the *13-cis* form, followed by proton transfer from the retinal Schiff base to Asp 85, release of a proton from residues or water molecule(s) at the extracellular surface, and uptake from the cytoplasmic surface through reprotonation of the Schiff base by Asp 96. This results in a proton transfer from the cytoplasmic to the extracellular side.^{135,136} It appears that this process proceeds with induced conformation and/or dynamic changes at both the extracellular and cytoplasmic side owing to protonation of Asp 85.^{81,137} This means that the information of the protonation at Asp 85 should be transmitted to both the extracellular and the cytoplasmic regions, through specific side-chains or through backbone interactions.

Tanio *et al.*^{73,138} recorded the ^{13}C NMR spectra of a variety of mutants, [$1\text{-}^{13}\text{C}$]Val-labeled V49A, V199A, T46V, T46V/V49A, D96N, and D85N (along with the cytoplasmic half channel) and [$3\text{-}^{13}\text{C}$]Ala-labeled E194, E194D, E204Q, Y83F, D85N, and D85N/R82Q mutants (along with the extracellular proton transfer chain), in order to clarify how such interactions, if any, could be modified by changes of electric charge or polarity in mutants. This is based on the expectation that such interaction should also exist in bR even in the unphotolyzed state, among backbone, side-chains, bound water molecules, etc. Results with the T46V mutant suggest that there is a long-distance effect on the backbone conformation between Thr 46 and Val 49.⁷³ From the spectra of the D85N and E204Q mutants there also appears to be coupling between Val 49 and Asp 85 and between Asp 85 and Glu 204, respectively.⁷³ Further, the low- and high-frequency displacements (or possibly peak suppression by acquired fluctuation frequency to the order of 10^5 Hz) of the single carbon signals of Ala 196 (in the F–G loop) and Ala 126 (at the extracellular end of helix D), respectively, reveal conformational (or dynamic) differences in E194D, E194Q and E204Q from the wild-type.¹³⁸ The same kind of conformational change at Ala 126 is noted in the Y83F mutant, which lacks the van der Waals contact between Tyr 83 and Ala 126 present in the wild type. Indeed, the absence of a negative charge at Asp 85 in D85N induced global conformational as well as dynamic changes as described already, as well as the local conformational changes at Ala 126 and Ala 196 as in other mutants. Unexpectedly, however, no such change at Ala 126 was observed in R82Q (even though Asp 85 is protonated at pH 6) or D85N/R82Q mutant. The changes induced in the Ala126 signal when Asp 85 is uncharged could be interpreted in terms of displacement of the positive charge at Arg 82 in the photocycle toward Tyr 83, where Ala 126 is located. This is because the underlying spectral change might be interpreted in terms of the presence of a perturbed Ala 126 mediated by Tyr 83 located between Arg 82 and Ala 126.¹² Indeed, the reorientation of Arg 82 has been later observed by X-ray diffraction studies on the M intermediate of the wild-type¹³⁹ and D96N and E204Q,^{140,141} in which Asp 85 is protonated and the Schiff base is deprotonated. Petkova *et al.*^{141a} also proposed, on the basis of a ^{15}N NMR study on [$\eta_{1,2}\text{-}^{15}\text{N}_2$]-labeled bR and D85N mutant, that one arginine, probably Arg 82, is perturbed in the M intermediate trapped at -44°C in the presence of 0.3 M guanidine chloride and D85N, respectively.

As illustrated in Figs. 25 and 26, it is also possible to examine how local conformational changes of remote residues in the inner part of the transmembrane α -helices, for instance, at either Ala 81, 84 (helix C), 53, 51 (helix B), or 215 (helix G) residues whose relative locations can be visualized based on recent X-ray diffraction data⁶ as shown in Fig. 26.⁷⁷ This approach is made possible by spectral editing by the Mn^{2+} ion-induced selective line broadening for the residues at the surface areas, as illustrated in Fig. 25. It is shown⁷⁷ that local conformational changes are found to be induced at the site of Ala 53, 84, 126, and 215 located at the vicinity of Asp 85 in E204Q mutant (Fig. 25B), although no spectral change was induced at the vicinity of Ala 81, 51, and 184. The E204D mutant exhibited more localized and smaller perturbations to Ala 53 and 215. A distinct spectral change at Ala 84 is still distinguishable (Fig. 25C). This means that site-directed mutation at the side-chain

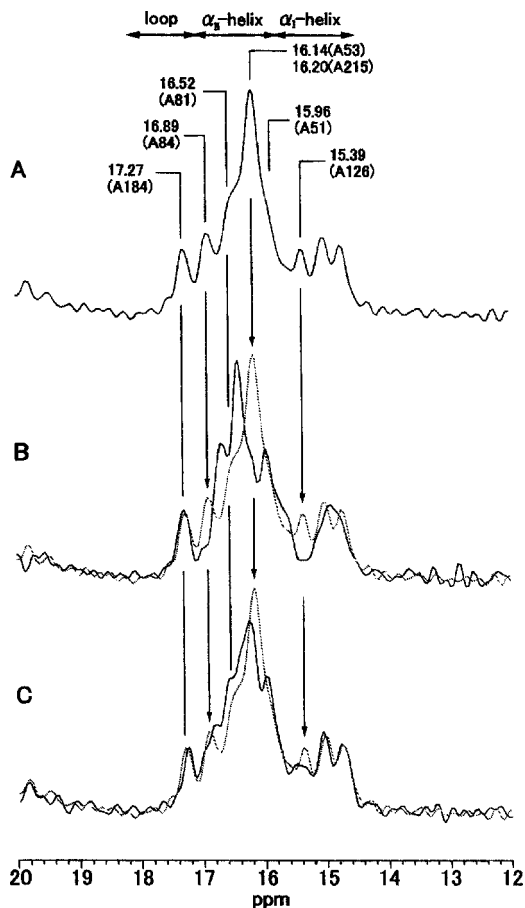


Fig. 25. ^{13}C CP-MAS NMR spectra of the [3- ^{13}C]Ala-labeled wild type (A), E204Q (B), and E204D (C) mutants. All spectra were recorded in the presence of 40 μM Mn^{2+} ion. Dotted spectra in the traces B and C are from 40 μM Mn^{2+} -treated wild type.⁷⁷ Reproduced with permission from the IOS Press.

of E204 induced a local conformational change near to the retinal (as viewed from the signals of Ala 53 and 215) and the proton channel (as viewed from the effect of Asp 85) and this effect is more prominent in the E204Q mutant. In contrast, a conformational change at Ala 81 is distinct for the E194Q mutant but not detectable for E194D.

In order to reveal a possible involvement of Arg 82 and Thr 89, it is more preferable to utilize the R82Q mutant with pK_a 7.2, responsible for protonation at Asp 85, instead of the wild-type with pK_a of ca. 2.5.¹⁴² In fact, it was shown that the ^{13}C NMR signals of [1- ^{13}C]Val-labeled Val 213 and Val 49 of the R82Q mutant are appreciably shifted to low frequency by raising the pH, owing to induced local

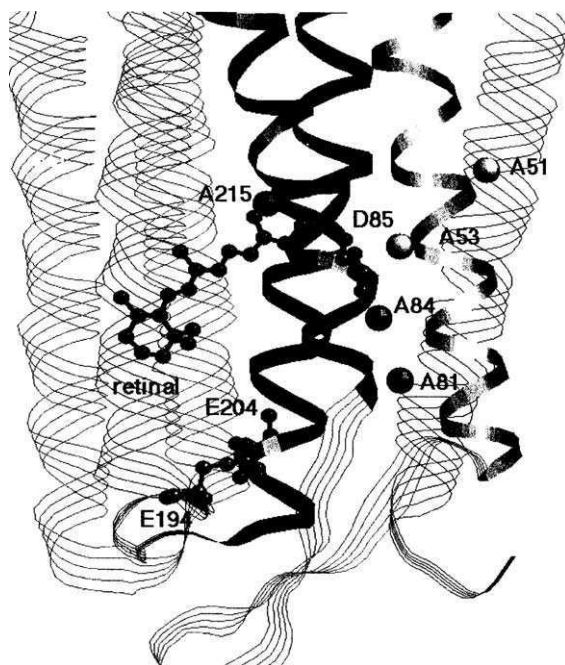


Fig. 26. Relative locations of Ala residues whose peaks are changed by mutations of side-chains in Glu 204 and Glu 194 shown upon the 3D structure of bR.⁷⁷ Reproduced with permission from the IOS Press.

conformational changes.⁷⁷ The apparent pK_a for R82Q as determined by a plot of the displaced ^{13}C NMR peaks of Val 213 and 49 residues in R82Q mutant against pH is 8.3 and 8.2, respectively (Fig. 27A, and B), which is close to that of 7.8 for Asp 85 as determined by the absorption maximum and coupled with the charged state of Asp 85. In contrast, the pK_a value of the wild-type is 8.8, as viewed from the displacement of the ^{13}C NMR signal of Val 49 in spite of a pK_a 7.8 from the absorption spectra, and seems to be coupled with an unidentified amino-acid residue via an interaction with Thr 89. In fact, there appears to be no pH-dependent change in the pH-titration study for T89S mutant (Fig. 27C). This means that these induced local conformational changes at the helices B and G are strongly influenced by the deprotonated state of Asp 85 in R82Q. In other words, the backbone conformational and fluctuation changes are mediated by the reduced interactions among the helices B, C, and G, and by the structural change of the side chains of Arg 82, both of which are induced by the protonation of Asp 85. Such structural and fluctuation changes would cause long-distance effects between the cytoplasmic and extracellular surface regions and regulation of the pK_a of internal amino acids in bR, as in the lowered pK_a of Asp 96 in D85N.⁸⁰

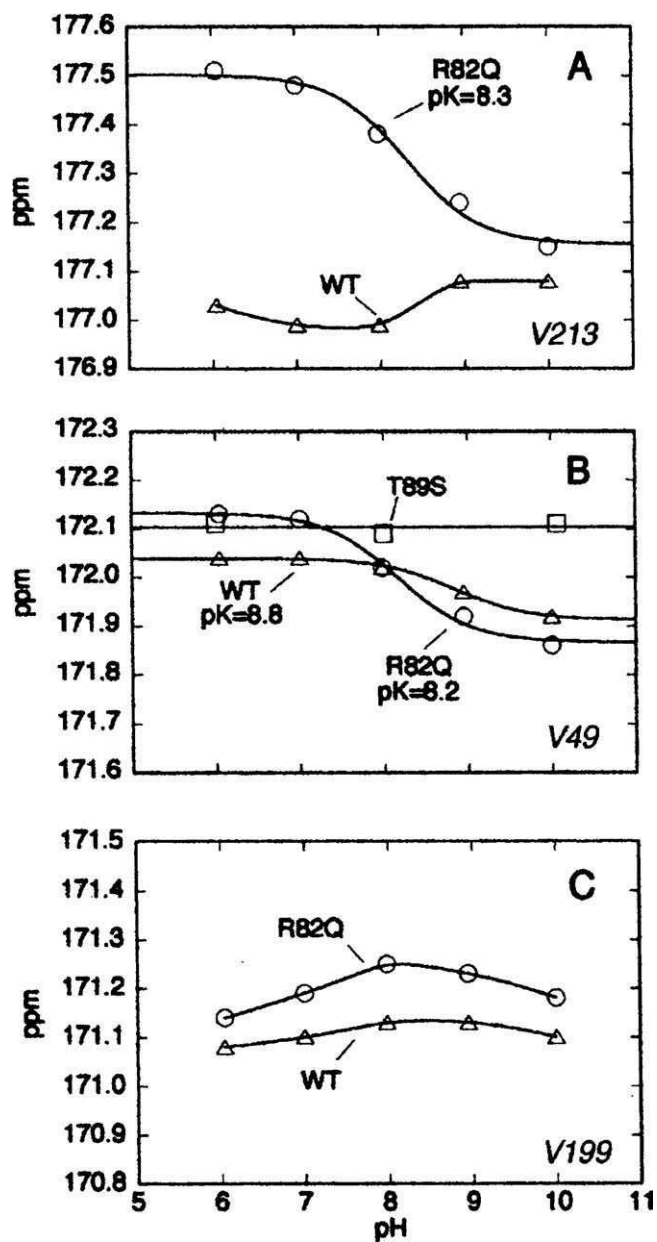


Fig. 27. Plots of ^{13}C NMR peaks of Val 213 (A), Val 49 (B), and Val 199 (C) in R82Q (circles), T89S (square) and WT (triangles) against pH.⁷⁷ Reproduced with permission from the IOS Press.

6. BACKBONE STRUCTURES AND DYNAMICS IN MONOMERS

So far, we have discussed the ^{13}C NMR data of bR from PM consisting of its trimeric form packed to a 2D hexagonal crystalline lattice or X-ray diffraction data on a 3D crystal in the presence of detergents.^{4–8} Under such conditions, the ^{13}C NMR signals are fully visible as far as the fully hydrated [3- ^{13}C]Ala- or [1- ^{13}C]Val-labeled bR from PM are examined at ambient temperature. As regarding the role of the underlying lipid-protein interactions leading to effective protein-protein interactions in PM, specific high-affinity binding of lipids to bR may be critical for lattice assembly. In such an arrangement of the bR trimer, 10 lipid molecules per bR monomer, comprising 6–7 phospholipids, 2–3 sulfoglycolipids, and 1 squalene fill the space between the proteins.^{143,144} Indeed, the presence of such negatively charged endogenous lipids is essential for the 2D crystalline array of bR when one attempts to regenerate it by incorporation into the dimyristoylphosphatidylcholine (DMPC) bilayer.¹⁴⁵

It is expected, however, that the backbone dynamics could be substantially modified when such a 2D lattice assembly is distorted or disrupted as in bacterio-opsin (bO) prepared from either an hydroxylamine-treated bR or retinal-deficient E1001 strain in which retinal–helix interactions is absent owing to lack of retinal.³³ The resultant protein dynamic change caused by the removed retinal through the modified helix–helix interaction resulted in the preferentially suppressed ^{13}C NMR signals of [3- ^{13}C]Ala-labeled bO at the loops and transmembrane α -helices near to the membrane surface. At the same time, the ^{13}C NMR spectrum of [1- ^{13}C]Val-labeled bO was also partly suppressed especially in the region of the loops at lower frequency by acquisition of the fluctuation motions.³³

6.1. bR mutants incapable of forming 2D lattice

It was shown by the presence of the bilobed feature in CD spectra that the trimeric structure is preserved for the bR mutant W12L but is disrupted for W80L.⁴⁵ A possibility of the disrupted trimeric structure, however, is expected for these mutants, because the side-chain of one of these two Trp residues, which are oriented outward from the transmembrane α -helices at the interface for lipid–protein interactions, is absent in these mutants.⁴⁵ In particular, Krebs and Isenbarger¹⁴⁶ showed that the interaction between sulfoglycolipid, 3-sulfate-Gal β 1-6Man α 1-2Glc α -1-archaeol (S-TGA-1), in the interior of the bR trimer and Trp 80 is thought to be crucial for the lattice assembly. This is due to the fact that the trimeric form is disrupted by substitution of Trp 80 with smaller amino acids as in the W80L mutant. To clarify the potential role of these Trp residues for the stabilization of the 2D lattice, Saitô *et al.*⁴⁵ compared the ^{13}C NMR spectra of [3- ^{13}C]Ala-labeled W12L and W80L with those of the wild-type, as demonstrated in Fig. 28. It is noteworthy that the relative peak intensities of the lipid per transmembrane α -helices are increased appreciably as a result of the disrupted crystalline lattice. This is judged from the substantially increased peak intensity of the surrounding lipid methyl group (marked by the asterisk) at 19.0 ppm⁶¹ with respect to the

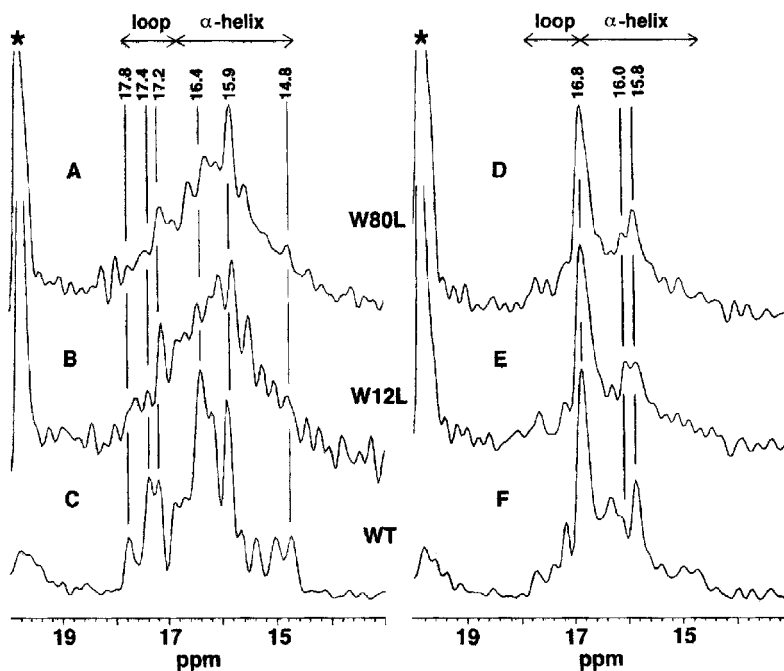


Fig. 28. ^{13}C CP-MAS (left) and DD-MAS (right) NMR spectra of $[3\text{-}^{13}\text{C}]\text{Ala}$ -labeled W80L (A and D), W12L (B and E), and wild-type (C and F). The intense asterisked peak at 19.8 ppm for W80L and W12L is ascribed to the lipid methyl group.⁴⁵ Reproduced with permission from Elsevier.

protein peak at 16.8 ppm (Ala 84 and 240, 244–246 at the C-terminal end, which is indifferent from the manner of crystalline packing); these values were evaluated, from the spectra in which the lipid methyl peak is not overscaled, as 22 and 10 for W80L and W12L, respectively, with reference to 1 for the wild type. Further, the ^{13}C NMR signals from the transmembrane α -helices were substantially broadened for the W12L and W80L mutants as compared with those of the wild type, except for the peaks from the C-terminal residues protruding from the membrane surface, including the peaks at 16.8 and 15.8 ppm from the C-terminal end undergoing random fluctuation motions and Ala 228 and 233 from the C-terminal α -helix, G', respectively, connected to the transmembrane α -helix G^{33,35,101} (see Fig. 3). This finding indicates that the trimeric structure is not restored both in W12L and W80L, although the CD measurement is less sensitive to this change for W12L mutant.

In addition, the ^{13}C NMR signals from the loops and several ^{13}C NMR peaks from the transmembrane α -helices near to the surface, including Ala 39, 53, 168, and 215 were preferentially suppressed^{33,35,101} in these mutants as encountered when retinal–protein interactions are substantially modified as in the case of D85N mutant⁸⁰ or they are absent as in bO.³³ This is due to the acquired internal fluctuation with a correlation time of 10^{-5} s, which interferes with the proton decoupling frequency of 50 kHz.⁸¹ Further, it should be noted that the ^{13}C CP-MAS

NMR spectra of the [1- ^{13}C]Ala- and Val-labeled mutants are almost completely suppressed, owing to the presence of fluctuations in the transmembrane α -helices with a timescale of 10^{-4} s, which interferes with the magic angle spinning. The present finding indicates that the hexagonal lattice in the 2D crystals regulates the protein dynamics of the individual helices, restraining molecular fluctuation of the transmembrane helices from the 10^4 Hz of proteins from a disrupted or disorganized lattice (monomer) to 10^2 Hz in the crystalline lattice consisting of the trimeric structures. This situation is schematically displayed together with their corresponding correlation times in Fig. 12.

6.2. bR structure in lipid bilayer

It is anticipated that oligomerization as well as lattice formation is not always straightforward for a number of membrane proteins overexpressed in a host cell like *E. coli*, unless identification and incorporation of such specific endogenous lipids to promote the formation of a 2D lattice are seriously taken into account. As a reference system to examine the ^{13}C NMR spectra of such proteins by site-directed NMR approach, it seems to be very important to gain an insight into how the ^{13}C NMR spectra of [3- ^{13}C]Ala- or [1- ^{13}C]Val-labeled bR incorporated into neutral lipid bilayers such as egg phosphatidylcholine (PC), dimyristoylphosphatidylcholine (DMPC) or dipalmitoylphosphatidylcholine (DPPC) are modified by the presence or absence of a 2D crystalline lattice.

For this reason, it is very important to record the ^{13}C NMR spectra of [3- ^{13}C]Ala- or [1- ^{13}C]Val-labeled bR reconstituted into a variety of lipid bilayers with different gel-to-liquid crystalline phase transition temperatures at various temperatures. The absorption maximum of the reconstituted bR preparations at 560 nm is very similar to that of delipidated bR (558–562 nm) as compared with that of intact bR from PM (568 nm) and close to that of the solubilized protein in detergents as a monomer (550 nm).¹⁴⁷ In fact, well-resolved ^{13}C NMR spectra were recorded for the [3- ^{13}C]Ala-labeled bR reconstituted into an egg PC bilayer together with the intense peak ascribable to the lipid methyl group at 19.7 ppm as shown in Fig. 29, although several peaks from the loops and some transmembrane α -helical regions occur at higher frequencies, 17.8–17.4 ppm from PM. These are still suppressed as a characteristic feature of the monomeric form as mentioned above, in a similar manner to that of the W80L and W12L mutants (see Fig. 28).⁴⁶ Obviously, the peak at 19.7 ppm arises from the endogenous lipids from *Halobacteria* which are tightly associated with bR during the process of reconstitution into the lipid bilayer. Further, it is noteworthy that the ^{13}C NMR spectra of [1- ^{13}C]Val-labeled bR in lipid bilayers are almost completely suppressed at ambient temperatures because of the acquired fluctuation motions in the transmembrane α -helices with a frequency of the order of 10^4 Hz in the absence of a 2D crystalline lattice.^{45,46}

In the presence of such endogenous lipids, it is anticipated that the 2D lattice assembly could be formed when the temperature of bR in neutral lipid bilayers is lowered to that of the gel phase in the presence of higher ionic strengths.¹⁴⁵ Saitô *et al.*⁴⁶ showed that this is the case at low temperature in the presence of a 10 mM

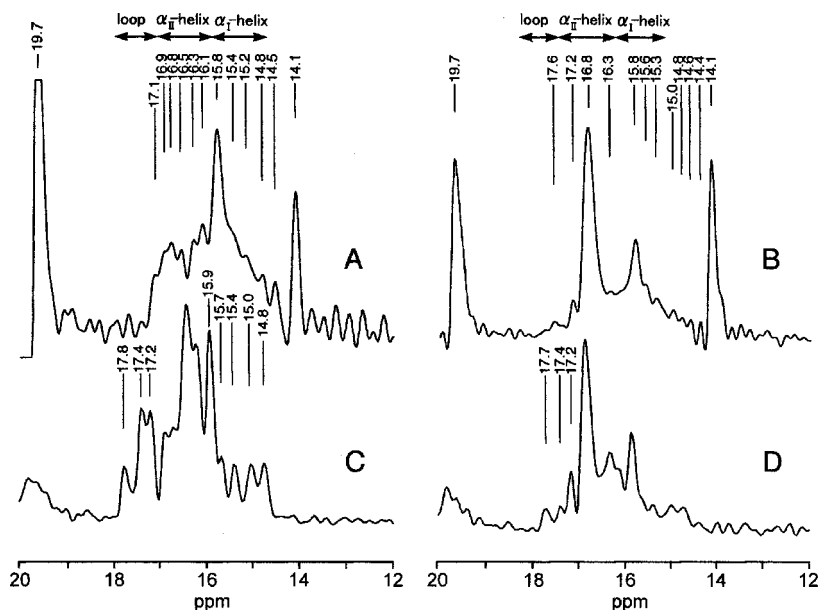
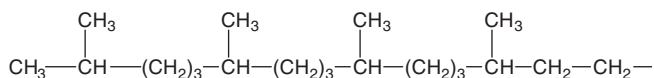


Fig. 29. ^{13}C CP-MAS (left) and DD-MAS (right) NMR spectra of $[3\text{-}^{13}\text{C}]\text{Ala}$ -labeled bR reconstituted into the egg PC bilayer (A and B; 1:50 mol ratio) and from PM (C,D). The intense peaks at 19.7 and 14.1 ppm are ascribed to lipid methyl groups from *Halobacterium* and egg PC, respectively.⁴⁶ Reproduced with permission from Elsevier.

NaCl solution in DMPC or DPPC bilayers adopting the gel phase: the phase behavior of the surrounding lipids can be conveniently examined by means of the methylene ^{13}C chemical shift of the fatty acyl chains as a sensitive probe, either the gel (*trans*: 32.6 ppm) or the liquid crystalline phase (*gauche/trans*: 30.3 ppm).^{40,71} It turns out that the characteristic ^{13}C NMR spectra of the 2D crystalline lattice were observed for $[3\text{-}^{13}\text{C}]\text{Ala}$ -labeled bR reconstituted in the DMPC or the DPPC bilayer at temperatures below 0 or 20°C adopting the gel phase, respectively.⁴⁶ Besides, it is interesting to note that the ^{13}C NMR peak of the methyl signal from the endogenous lipids at 19.7 ppm, which is ascribed to the side-methyl group of the (3R, 7R, 11R)-15-tetramethylhexadecyl (I) group⁶¹ as fatty the acyl chain of the phospholipids from *Halobacterium*, is



substantially suppressed at lowered temperature both in the CP-MAS and DD-MAS NMR spectra. Their spectral features are changed from the liquid crystalline to the gel state forming a crystalline lattice. This type of peak suppression is obviously caused by a slowed fluctuation motion with a frequency of the order of 10^5 Hz as a result of a specific lipid-protein interaction within the 2D crystalline lattice.

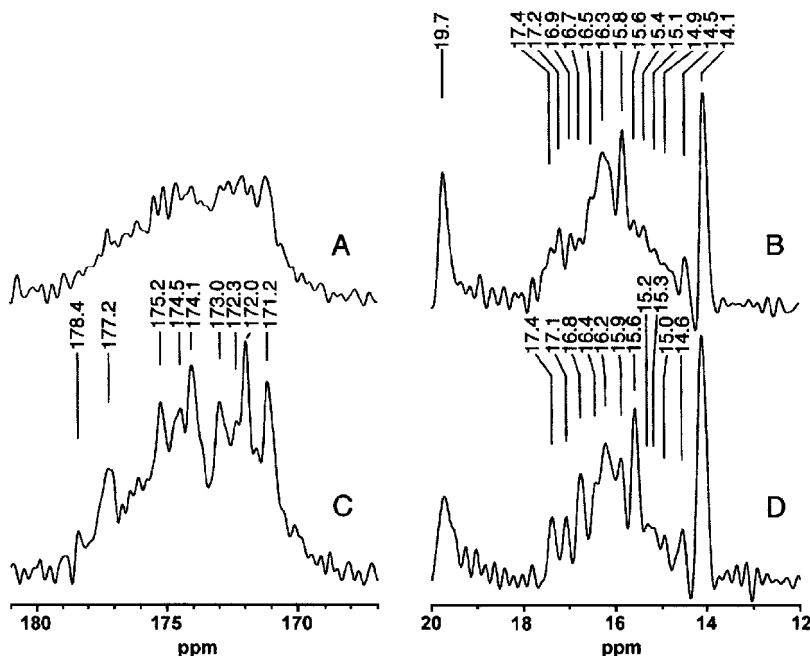


Fig. 30. ^{13}C CP-MAS NMR spectra of $[1-^{13}\text{C}]\text{Val}$ - (left) and $[3-^{13}\text{C}]\text{Ala}$ -labeled bR (right) reconstituted into DPPC bilayer (1:50 mol ratio) at 20°C (A, B) and 0°C (C and D). ^{13}C NMR signals from carbonyl and methyl regions are given at higher frequency (A, C) and lower frequency (B, D), respectively.⁴⁶ Reproduced with permission from John-Wiley and Son, Ltd.

In the case of $[1-^{13}\text{C}]\text{Val}$ -bR, which is sensitive to fluctuation motions of 10^4 Hz, this condition is more stringent than that of $[3-^{13}\text{C}]\text{Ala}$ -bR, which is sensitive to fluctuation motions of 10^5 Hz. A ^{13}C NMR spectral pattern characteristic of 2D lattice is achieved at 0°C as viewed from the $[1-^{13}\text{C}]\text{Val}$ -labeled bR in the DPPC bilayer (Fig. 30C), while this feature is achieved from the $[3-^{13}\text{C}]\text{Ala}$ -labeled bR at 20°C (Fig. 30B). Therefore, a suitable choice of ^{13}C -labeled amino acid, either $[3-^{13}\text{C}]\text{Ala}$ or $[1-^{13}\text{C}]\text{Val}$ as well as the manner of protein aggregation is very important for the study of the conformation and dynamics of membrane proteins by the site-directed ^{13}C NMR approach, as summarized in Tables 7 and 8.

7. MEMBRANE PROTEINS OVEREXPRESSED IN *E. COLI*

It is interesting to extend the present approach, utilizing site-directed ^{13}C NMR so far established for bR and its mutants from both the 2D crystalline or monomeric preparations, to various types of membrane proteins. They include *pharaonis* phoborhodopsin (*ppR*) consisting of seven transmembrane α -helices linked to retinal as a photoreceptor active for negative phototaxis,¹⁴⁸ its cognate transducer *pHtrII* consisting of the two transmembrane α -helices to yield signaling for phototaxis¹⁴⁹

Table 7. ¹³C NMR peak intensities of ¹³C-labeled bR recorded by CP-MAS NMR^a

	2D crystal			Monomer		
	[3- ¹³ C]Ala-labeled	[1- ¹³ C]Ala-labeled	[1- ¹³ C]Ala-labeled	[3- ¹³ C]Ala-labeled	[1- ¹³ C]Ala-labeled	[1- ¹³ C]Val-labeled
C-terminal α-helix	+ ^b	+ ^b	c	+ ^b	+ ^b	c
Loop	+	—	+	—	—	±
Transmembrane α-helix	+	±	+	±	—	±

^akey: +; fully visible, ±; partially suppressed, —; completely suppressed.

^bThese peaks are also visible by DD-MAS NMR.

^cNo Val residue is present in the C-terminal α-helix.

Table 8. ¹³C NMR spectral features of a variety of membrane proteins recorded in intact preparation or in lipid bilayers at ambient temperature (Ref. 37)

		Number of transmembrane α-helices	[3- ¹³ C]Ala-labeled ^a	[1- ¹³ C]Val-labeled ^a	Fluctuation frequency of transmembrane α-helices (Hz)	References
bR	2D crystal	(7) _n	+++	+++	10 ²	61
	monomer (WT)	7	++	+	10 ⁴ –10 ⁵	46
	monomer (W80L)	7	++	—	10 ⁴	45
ppR	monomer	7	++	+	10 ⁴ –10 ⁵	42
ppR*/pHtrII ^b	2:2 complex	7+2	++	+	10 ⁴	42
pHtrII	aggregated	(2) _n	+	+	10 ³	43
pHtrII*/ppR	2:2 complex	2+7	+	—	10 ⁴	43
DGK	monomer	3	+	—	10 ⁴	44

^a+++ , well-resolved and fully visible; ++ , well-resolved but signals from the loop and some transmembrane α-helices are missing; + , broadened; - , suppressed.

^bAsterisked proteins were ¹³C-labeled.

activated by receiving incoming light through formation of a tightly complexed form with ppR, and *E. coli* diacylglycerol kinase (DGK), which catalyzes conversion of diacylglycerol and MgATP to phosphatic acid and MgADP.¹⁵⁰

7.1. Phoborhodopsin and its cognate transducer

7.1.1. Phoborhodopsin

Halobacterium salinarum membrane contains a family of four photoactive retinal proteins, called archaeal rhodopsins that are similar to our visual pigments in their

structure and photochemistry: bR and halorhodopsin (hR) harvest solar energy by light-driven transport of proton and chloride, respectively.¹⁵¹ Sensory rhodopsin I (sR I) and phoborhodopsin II (pR or sensory rhodopsin II, sR II) are photoreceptors active as positive and negative phototaxis, respectively, that use the energy of absorbed photons to send signals to the flagellar motor via HtrI and HtrII, respectively.¹⁴⁸ Here, *pharaonis* phoborhodopsin (ppR) is a pigment protein from *Natronobacterium pharaonis* and corresponds to the pR of *H. salinarum* with 50% homology of amino-acid sequence.¹⁵²

These two photoreceptors with proton transport are activated to yield signaling for phototaxis, through their plausible conformational changes, after receiving incoming light they are tightly complexed to their respective cognate transducers consisting of two transmembrane helices (TM1 and TM2) of HtrI and HtrII, respectively.¹⁵³ It is believed that the activation of the transducer HtrII by its receptor pR leads to a conformational change of TM2 that propagates to the tip of the coiled-coil cytoplasmic domain, as illustrated in Fig. 31A.¹⁴⁹ A ribbon diagram of the top view from the cytoplasmic side for 2:2 complex of ppR (seven transmembrane α -helices, A-G and A'-G') and pHtrII (1-114) (TM1, TM2, TM1', and TM2') as revealed by X-ray diffraction is also shown in Fig. 31B. The next steps in the signaling cascade involve the homodimeric histidine kinase CheA, the coupling protein CheW, and the response regulators/aspartate kinase CheY and CheB, in analogy to the bacterial sensory system.^{154,155} Phosphorylated (P) CheY functions as a switch factor of the flagellar motor. CheB (a methyltransferase) together with CheR (a methyltransferase) are involved in the adaptation processes of the bacteria.

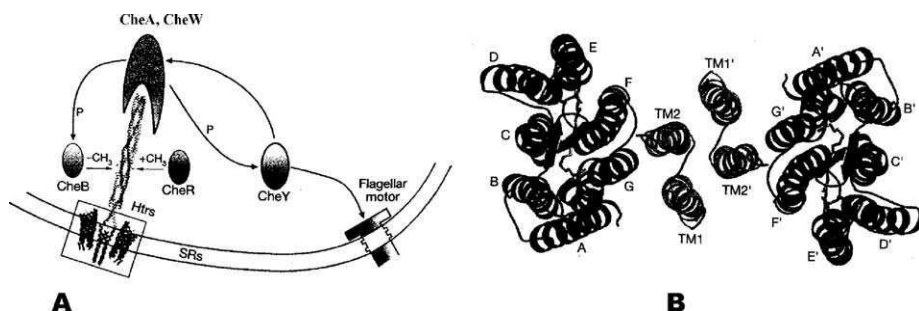


Fig. 31. (A) Two-component signaling cascade. The activation of the transducer HtrII by its receptor SRII (ppR) leads to a conformational change of TM2 that propagates to the tip of the coiled-coil cytoplasmic domain, based on the structure taken from Ref. 156. The next steps in the signaling cascade involve the homodimeric histidine kinase CheA, the coupling protein CheW, and the response regulators/aspartate kinases CheY and CheB. Phosphorylated (P) CheY functions as a switch factor of the flagellar motor. CheB (a methyltransferase) together with CheR (a methyltransferase) are involved in the adaptation process of the bacteria. (B) Ribbon diagram of the top view from the cytoplasmic side of the receptor-transducer complex. α -helices in the receptors and transducers are indicated by A-G, A'-G' and TM1, TM2, TM1', and TM2', respectively.¹⁴⁹ Reproduced with permission from Nature Publishing Group.

It is anticipated that *ppR* reconstituted in egg PC bilayer at ambient temperature is present as a monomer in view of the absence of endogenous lipids as in *Halobacteria* and also in comparative site-directed ^{13}C NMR data with those of reconstituted *bR* and its mutants in lipid bilayers^{45,46} as discussed in the previous section. However, oligomeric structures consisting of dimeric or trimeric forms were revealed by cryo-electron microscopic or X-ray diffraction studies on 2D or 3D crystals containing such lipids at low temperature.^{11–13} Arakawa *et al.*⁴² showed that the ^{13}C NMR spectra of [3- ^{13}C]Ala-labeled *ppR* reconstituted in egg PC bilayer (Fig. 32B) exhibited the spectral pattern characteristic of the monomeric state: ^{13}C NMR signals are absent from the loop regions in spite of the presence of three Ala residues, in a similar manner to that observed for the reconstituted *bR* in lipid bilayers (Figs. 29A and B). Instead, seven ^{13}C NMR signals are resolved for the transmembrane α -helices, at 16.8–15.0 ppm, consisting of the normal α_1 -helices and α_{11} -helices⁷¹ in the presence of low-frequency fluctuation motions. In addition there is a peak at 14.1 ppm arising from egg PC.

It is notable that the ^{13}C NMR peak of *ppR* at 15.9 ppm ascribable to the Ala residues located at the cytoplasmic α -helix is readily distinguished in the DD-MAS NMR spectrum (Fig. 32B, right) in a similar manner to that of *bR* but is suppressed in the CP-MAS NMR spectrum (Fig. 32B, left). This is because this portion is too flexible in the absence of the cognate transducer, *pHtrII*, with fluctuation frequencies $> 10^8$ Hz to be observed by the CP-MAS NMR, as compared with that of *bR* in which the C-terminal α -helix is held together with A–B, C–D, E–F loops through salt bridges or metal-ion-mediated interactions leading to prevent ion of any unnecessary fluctuation¹⁰⁴ (see Fig. 12). Nevertheless, it is interesting to note that distinct dynamic changes are accompanied for *ppR* by complex formation with the truncated cognate transducer *pHtrII* (1–159), as revealed by the increased peak intensity at 15.9 ppm (asterisked) ascribable to the C-terminal α -helix by ^{13}C CP-MAS NMR, together with the improved spectral resolution for signals from the whole area (Fig. 32A). This observation is consistent with a view that the accompanied change in the “effective molecular mass” from the system of 7 transmembrane α -helices (*ppR* alone) to 18 transmembrane α -helices of the complex $[2 \times (7 + 2)]$ transmembrane α -helices as a 2:2 complex results in a change of the fluctuation frequency from 10^4 – 10^5 to 10^4 Hz.^{37,42} In particular, the increased intensity in the CP-MAS NMR spectrum at 15.9 ppm is caused by efficient magnetization owing to the immobilized cytoplasmic α -helix due to the complex formation. Therefore, it appears that the mutual helix–helix interaction between the extended TM2 helix of *pHtrII* (1–159) beyond the surface and the cytoplasmic α -helix of *ppR* plays also an important role for stabilization of the complex, as schematically illustrated in Fig. 33.

It is noteworthy that the ^{13}C CP-MAS NMR spectrum of the transmembrane α -helices from [1- ^{13}C]Val-labeled *ppR* in egg PC bilayer is clearly visible, although the corresponding peaks from the loops are partly suppressed. Interestingly, the former peaks are appreciably suppressed in the presence of the transducer *pHtrII* (1–159) as revealed by the ^{13}C CP-MAS NMR spectrum when compared with those of free *ppR*, leaving no spectral change in the loop regions. It is also notable that a

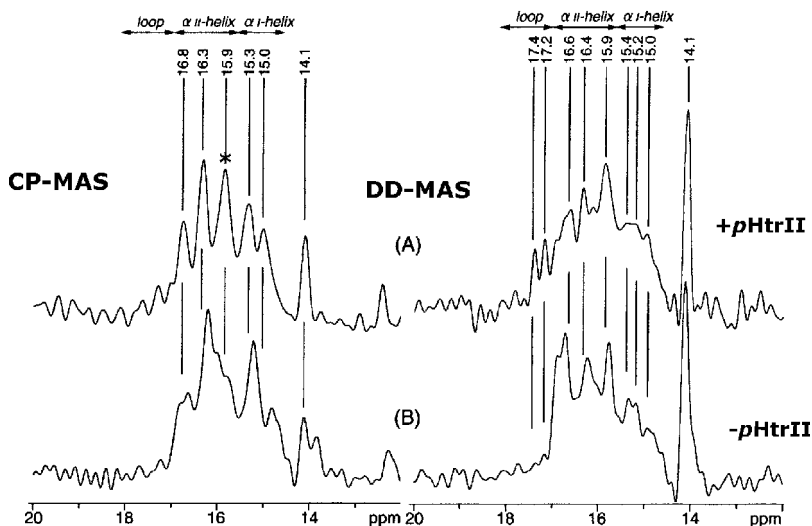


Fig. 32. Comparison of the ^{13}C CP-MAS (left) and DD-MAS (right) NMR spectra of $[3-^{13}\text{C}]\text{Ala}$ -labeled phoborhodopsin (*ppR*) in the presence (A) or absence (B) of its truncated transducer (*pHtrII* (1–159)). The asterisked peak of the CP-MAS NMR spectrum in the upper trace indicates the peak of the C-terminal α -helix.³⁷ Reproduced with permission from Elsevier.

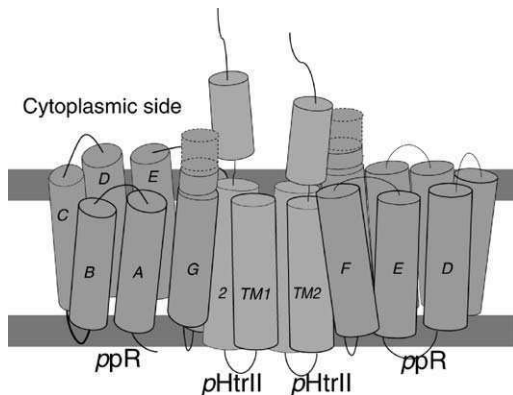


Fig. 33. Schematic representation of 2:2 complex between *ppR* and *pHtrII*.¹⁵⁹

reduced lipid–protein interaction by diluting the polar lipids by neutral lipids as in the present experimental condition is more preferable for observation of better ^{13}C NMR signals from the $[1-^{13}\text{C}]\text{Val-bR}$ preparation. This may be the reason why better ^{13}C NMR spectra were obtained for *ppR* expressed in *E. coli* that lacks polar lipids. It is worthwhile, however, to examine the conditions to record the maximum ^{13}C NMR signals under the condition of 2D array in the presence of such polar lipids at low temperature.

7.1.2. Cognate transducer

The cognate transducer *pHtrII* is composed of a cytoplasmic domain divided into linker, methylation, and signaling regions, in addition to the transmembrane domain consisting of the two helices, TM1 and TM2.¹⁴⁸ The truncated transducer *pHtrII* (1–159) under consideration consists of the C-terminal residue protruding from the cytoplasmic membrane surface (82–159) mainly as linker (Fig. 34) that may participate in the coiled-coil form responsible for phototaxis besides the two transmembrane α -helices.¹⁴⁹ by analogy with the X-ray diffraction picture of four-helical-bundle structure of the cytoplasmic domain of a serine chemotaxis receptor.¹⁵⁶ Indeed, each monomer is a ≈ 70 turn α -helix folded back on itself to form two long antiparallel coiled-coil structures.¹⁵⁶

Fig. 35 illustrates the ^{13}C DD-MAS (left) and CP-MAS (right) NMR spectra of the $[3-^{13}\text{C}]\text{Ala}$ -labeled *pHtrII* (1–159) recorded at ambient temperature from the samples reconstituted in an egg PC bilayer, where panels A and B are from the complex with *ppR*, and C and D are from uncomplexed *pHtrII* (1–159). All of the Ala C_β ^{13}C NMR signals from the protein (15.0–16.7 ppm) recorded by DD-MAS NMR can be assigned to the peak position of the α_{II} -helix (16.7–15.5 ppm) and its boundary with the ordinary α_{I} -helix (15.5–15.0 ppm), with reference respectively to the ^{13}C chemical shifts of $(\text{Ala})_n$ in hexafluoroisopropanol (HFIP) solution or solid state:^{31,36,70,72} this is the case because no ^{13}C NMR signal appears at the position of the random coil (16.9 ppm) or β -structure (19.9 ppm).^{35,36,60,63,64} Of course, this α_{II} -helix is not visible in the X-ray diffraction study, because the truncated *pHtrII*(1–114) used in the X-ray diffraction lacks the corresponding cytoplasmic α -helical region revealed by the solid-state NMR.

The intense α_{II} -helical ^{13}C NMR peaks resonated at 16.7 and 16.3 ppm are clearly seen as a doublet peak for *pHtrII* (1–159) complexed with *ppR*, besides a broad envelope at 15.5 ppm, as recorded by the DD-MAS NMR (Fig. 35A) but

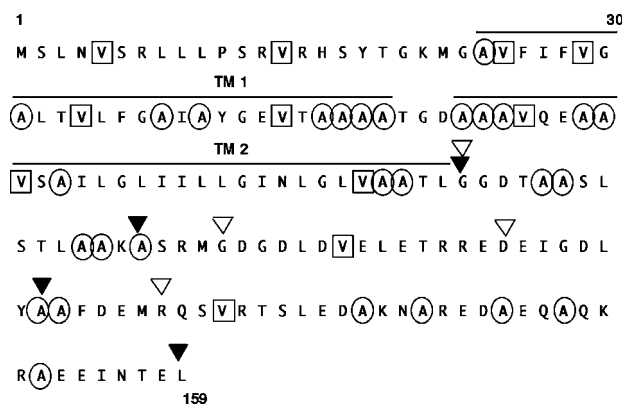


Fig. 34. Amino-acid sequence of truncated *pharaonis pHtrII* (1–159). Two transmembrane α -helices, TM1 and TM2, are shown by the bars above the sequence. Location of ^{13}C -labeled.⁴³

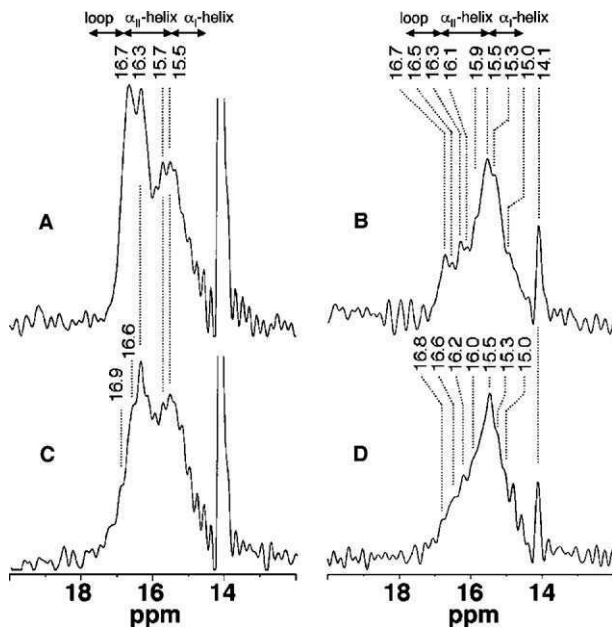


Fig. 35. ^{13}C DD-MAS (left) and CP-MAS (right) NMR spectra of $[3\text{-}^{13}\text{C}]\text{Ala}$ -labeled *pharionis* truncated pHtr II (1–159) in the complex with ppR (A, B), reconstituted in the egg PC bilayer, as compared with those in the absence of ppR (C and D). ^{13}C NMR signals of the low-frequency region (12–20 ppm) from the $[3\text{-}^{13}\text{C}]\text{Ala}$ proteins alone are presented. The intense or sharp ^{13}C NMR signal resonated at the highest peak position 14.1 ppm is ascribed to the methyl peak of the egg PC.⁴³

substantially suppressed by the CP-MAS NMR (Fig. 35B), leaving the signals of the low-frequency envelope peaks at 15.5 ppm unchanged. This is the case where the peaks under consideration were preferentially suppressed by a reduced cross polarization rate owing to the presence of rapid molecular motion (with a correlation time or fluctuation frequency of the order of $<10^{-6}$ s (or $>10^6$ Hz)). This finding is consistent with the previous observations about the C-terminal α -helix protruding from the surface of bR^{34–36,104} and ppR.⁴² The relative proportion of the high-frequencies doublet, which is suppressed by CP-MAS NMR, to the low-frequency envelope peaks, including contributions from the unsuppressed peaks extending to the peak position of the α_{II} -helix in this DD-MAS NMR experiment, is found to be 38%: 62% as judged from the relative peak intensities recorded by the ^{13}C DD-MAS and CP-MAS spectra, respectively (Figs. 35A and B). This is very close to the relative proportions of the Ala residues involved in the C-terminal cytoplasmic α -helix as compared to those of the transmembrane α -helices, 43%:57%. Therefore, the high-frequency α_{II} -helix and low-frequency envelope peaks are fully visible and unambiguously assigned, respectively, to the cytoplasmic and transmembrane α -helices. It is therefore emphasized that the observed cytoplasmic α_{II} -helix (82–159) revealed by the site-directed NMR could be a candidate for participation in the

coiled-coil portion of the full-length transducer that plays an essential role for the signal transduction. In this connection, it is emphasized that the present NMR approach could be a very useful means for the identification of this type of a secondary structure, if any.

Surprisingly, the high-frequency doublet peaks of the ^{13}C NMR signals of $[3\text{-}^{13}\text{C}]\text{Ala-}p\text{HtrII}(1\text{--}159)$ in the absence of $pp\text{R}$ are not always fully visible at ambient temperature even by the DD-MAS method (Fig. 35C). The resulting dynamic change leads to a failure in our attempt to fully detect the ^{13}C NMR signals by narrowing the peaks in the free state, due to interference of the incoherent frequency of the motional fluctuations with the coherent frequency of the proton decoupling essential for the successful peak narrowing.⁸¹ The lowered fluctuation frequencies in the cytoplasmic α -helix of $p\text{HtrII}$ (1–159) from $>10^6$ Hz of the complexed to the order of 10^5 Hz (5×10^4 Hz) of the free states, results in the preferentially suppressed peak intensities at 16.7 and 16.3 ppm, as a result of interference of the fluctuation frequency with the proton-decoupling frequency, as viewed from the ^{13}C NMR signals of the $[3\text{-}^{13}\text{C}]\text{Ala}$ -labeled residues. It appears, however, that this observation conflicts with our expectation: fluctuation motions of the cytoplasmic α -helices of the transducer alone should be more pronounced in the free state than in the complexed state, because the frequency of the local fluctuation motions in the free state also depends upon the resulting reduced “effective molecular mass” and interhelical interactions. In fact, this view was confirmed when one compares the fluctuation frequencies of the transmembrane α -helices of $pp\text{R}$ as estimated from the ^{13}C NMR spectra of $[1\text{-}^{13}\text{C}]\text{Val-}pp\text{R}$ with and without $p\text{HtrII}$ as summarized also in Table 8,³⁷ although the corresponding spectral changes are rather less pronounced as compared with those of the present observation for $[1\text{-}^{13}\text{C}]\text{Val-}p\text{HtrII}(1\text{--}159)$. This obvious conflict, however, may be compromised only when the uncomplexed transducers are not present as monomer or dimer but exist as aggregated or clustered forms in the lipid bilayer. This finding also rules out the possibility that this moiety is a random coil even in the absence of $pp\text{R}$. Otherwise, it would be expected that the intensity of the ^{13}C NMR signal from the random coil would appear at the characteristic peak position of 16.9 ppm, and should be invariant in spite of the presence or absence of $pp\text{R}$.

7.1.3. Signal transduction

It is thought that light excitation of $pp\text{R}$ complexed with $p\text{HtrII}$ induces an outward movement of its helix F, as revealed by time-resolved spin-labeled $pp\text{R}$.¹⁵⁷ It was also shown that the flap-like movement of the helix F of $pp\text{R}$ upon light excitation induces a conformational change in the transmembrane domain of the spin-labeled transducer, together with the arrangement of the receptor-transducer 2:2 complex with a 2-fold symmetry axis by distance measurements by spin-labeled $pp\text{R}$ and transducer.¹⁵⁸ An important outcome of this work is the decoupling of the TM2 motion from the return of the photoreceptor to the ground state, which enables the transducer to exist separately in the active state and to operate independently of the photoreceptor.

This view is consistent with the data present already^{42,43} and recent site-directed solid-state NMR of [3-¹³C]Ala-labeled *ppR* and its complex with *pHtrII*(1–159) by Kawamura *et al.*^{159,160} In particular, Kawamura *et al.*¹⁶⁰ found evidence of the role of specific interactions between the C-terminal α -helix of *ppR* and the extended α -helix of *pHtrII* for the stability of the former in the ground state. This is based on a comparative study on the wild-type and *ppR* (1–220), in a similar manner to that of *bR* to make the proton uptake efficient (see Fig. 17B). It turned out, however, that this kind of interaction is broken for the D75N mutant of *ppR* taking activated state¹⁶¹ (corresponding to the M-like state in *bR*) without photoillumination, to weaken the interaction between *ppR* and *pHtrII* (1–159) and to make *pHtrII* (1–159) rigid, as viewed from the ¹³C NMR spectra of [3-¹³C]Ala-labeled *pHtrII* (1–159).¹⁶⁰

7.2. Diacylglycerol kinase

Diacylglycerol kinase (DGK) from *E. coli* is a small, 121 amino acid, integral membrane protein that catalyzes the conversion of diacylglycerol and MgATP to phosphatic acid and MgADP. It has been shown that DGK is homotrimeric both in the micellar system and in 1-palmitoyl-2-oleyl-sn-glycero-3-phosphocholine (POPC) vesicles.^{162,163} The topology of DGK as revealed by the sequence data and β -lactamase and β -galactosidase fusion experiment consists of three transmembrane domains and two cytoplasmic domains, as shown schematically in Fig. 36.^{164,165} Wen *et al.*¹⁶⁶ showed that DGK is extremely tolerant to sequence changes with three-quarters of the residues tolerating non-conservative changes. The conserved residues are distributed with approximately the same frequency in the soluble and transmembrane portions of the protein, but the most critical active-site residues

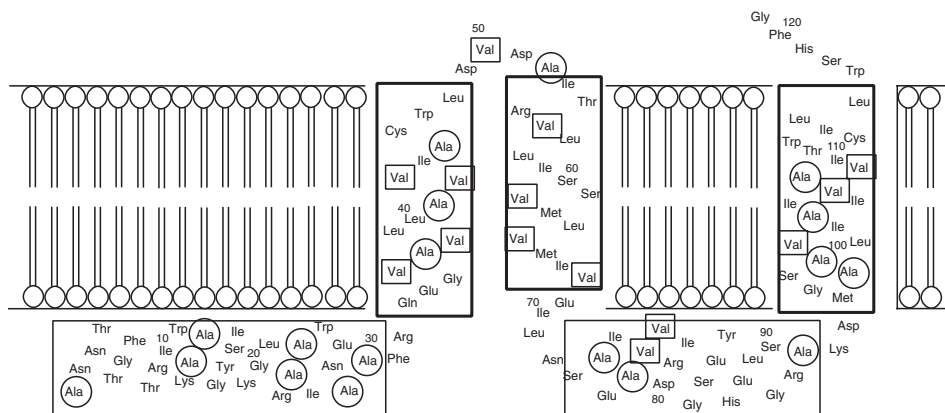


Fig. 36. Schematic representation of conformation and topology of DGK based on the published data. Ala and Val residues used for ¹³C-labeling are shown as circled and boxed residues, respectively.⁴⁴ Reproduced with permission from Elsevier.

appear to residues in the second cytoplasmic domain. In addition, mutant/wild-type subunit mixing experiments indicate that these active site residues are shared between subunits within the trimer.^{166,167}

Yamaguchi *et al.*⁴⁴ recorded the ^{13}C NMR spectra of $[3-^{13}\text{C}]\text{Ala}$ -labeled *E. coli* DGK reconstituted in a POPC bilayer, using the CP-MAS and DD-MAS methods as shown in Fig. 37. It is expected that these labeled Ala residues can be utilized as intrinsic probe to examine the conformation and dynamics of both transmembrane and cytoplasmic domains in view of their distribution as shown in Fig. 37. Surprisingly, the ^{13}C NMR spectra of $[3-^{13}\text{C}]\text{Ala}$ -labeled DGK recorded by both the methods are broadened to yield rather featureless peaks at physiological temperatures, both in DM solution (spectrum not shown) or in lipid bilayers of the liquid crystalline phase. The ^{13}C NMR spectra of $[3-^{13}\text{C}]\text{Ala}$ -labeled DGK recorded by the DD-MAS (A-C) and CP-MAS (E-F) methods in POPC bilayers are substantially broadened as far as the samples are retained in the lipids of the liquid crystalline phase at temperatures between 20°C and -5°C (Fig. 37). The intense peaks at 16.8 ppm are more pronounced in the DD-MAS spectra and ascribed to Ala residues involved in the α -helix form of the N-terminal region as a result of protruding from the membrane surface. They can be assigned to the Ala residues located at the more flexible N-terminal α -helical regions anchored at the membrane surface rather than to the transmembrane α -helices aligned with the membrane normal. The spectral resolution of the CP-MAS NMR spectrum, however, was substantially improved to yield the four peaks 14.5, 15.5, 16.0, and 16.7 ppm at

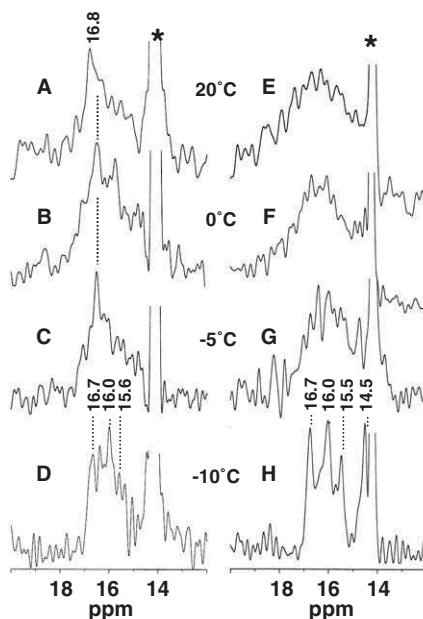


Fig. 37. ^{13}C DD-MAS (left) and CP-MAS (right) NMR spectra of $[3-^{13}\text{C}]\text{Ala}$ -DGK in POPC bilayer at various temperatures. The asterisked peaks are ascribed to the methyl peak from POPC.⁴⁴ Reproduced with permission from Elsevier.

–10°C just below the phase-transition temperature of the POPC bilayer (–5°C). This situation is also realized in the DPPC bilayer in which the gel-to-liquid crystalline phase transition occurs at 41°C, as evaluated from the peak position of saturated fatty acyl chains from the lipid bilayer:⁷¹ the well-resolved spectra consisting of up to six peaks ascribable to the transmembrane and amphipathic α -helices and loops were observed at temperatures below 35°C but the spectrum was broadened at 45°C for the liquid crystalline phase.

It is also notable that the ^{13}C NMR spectra of [1- ^{13}C]Val-labeled DGK were completely suppressed at temperatures corresponding to the liquid crystalline phase of both the POPC and DPPC bilayers but those including the peaks from the loops were recovered to some extent in the gel-phase lipids.⁴⁴ This means that the broadened or completely suppressed peaks of the ^{13}C NMR spectra of [3- ^{13}C]Ala- and [1- ^{13}C]Val-labeled DGK in the lipid bilayers of the liquid crystalline phase are ascribed to the presence of the interference of motional frequencies of DGK with the frequencies of the proton decoupling or the magic angle spinning (10^5 or 10^4 Hz, respectively). While DGK can be tightly packed in the gel phase lipids, DGK is less tightly packed at physiological temperatures, where it becomes more mobile. The fact that the enzyme activity is low under conditions where motions are restricted and high when conformational fluctuations can occur suggests that the acquisition of low-frequency backbone motions, on the microsecond to millisecond timescale, may facilitate the efficient enzymatic activity of DGK. This means that the dynamic aspect is very important to understand the function of this enzyme, even if a crystallographic observation is unsuccessful.

The present observations demonstrate that the site-directed ^{13}C NMR approach is very useful for probing the conformation and dynamics of the membrane proteins in a membrane environment, as summarized in Table 8.

8. MEMBRANE-BINDING PROTEIN

So far, we were concerned with site-directed solid-state NMR studies on fully hydrated integral membrane proteins in which anisotropic spin interactions leading to broadened line widths are not averaged as they are in solution NMR but a variety of motions with various timescale from millisecond to microsecond are persistent because of integration into the lipid bilayer. It is still difficult to obtain structural information for peripheral membrane proteins which are not integrated but bound to a membrane surface, because the persistent anisotropic interaction with the membrane surface still hampers the utilization of the solution NMR approach.

The pleckstrin homology (PH) domain of phospholipase C- δ 1 (PLC- δ 1) is one of the most extensively studied, because it has been proposed that it regulates the membrane localization of PLC- δ 1^{168,169} through its high-affinity specific interaction with phosphatidylinositol 4,5-bisphosphate (PIP₂)¹⁷⁰ and with D-*myo*-inositol 1,4,5-trisphosphate (IP₃). A high-resolution structural model of phospholipase C- δ 1 (PLC- δ 1) pleckstrin homology (PH) domain forming a complex with IP₃ has been

determined by X-ray diffraction.¹⁷¹ Structural information of PLC- $\delta 1$ at the membrane surface is indispensable, because functionally more important interactions with its ligand, PIP₂, or other proteins included in the signal transduction pathways takes place in the membrane surface.

Tuzi *et al.*^{172,173} examined the ¹³C DD-MAS (B) and CP-MAS (A) NMR spectra of [3-¹³C]Ala-labeled PH domain complexed with PIP₂ in a PC/ PIP₂ bilayer with reference to the peak positions available from the complex with IP₃ in solution (vertical peaks at the bottom), as shown in Fig. 38. Five resolved peaks, occur at 18.82, 16.99, 15.83, 15.37, and 14.41 ppm; these were assigned to the five Ala residues incorporated, Ala 112, 88, 116, 118, and 21, respectively, with reference to the ¹³C chemical shifts of the respective site-directed mutants which are replaced by other types of residue. It is interesting to note that the local conformations of the C-termini of the $\alpha 2$ -helix and $\beta 7$ -strand are altered by the membrane localization of

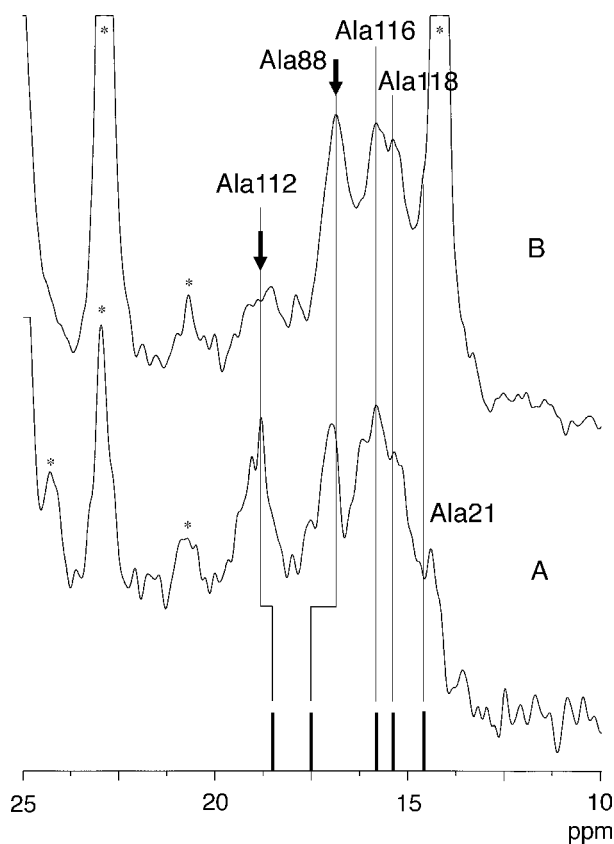


Fig. 38. High-resolution solid-state NMR spectra of the [3-¹³C]Ala-labeled PLC- $\delta 1$ PH domains forming complex with PC/PIP₂ vesicles obtained by (A) the CPMAS and (B) the DDMAS method. Assignments of the individual signals are shown at the top of the spectra. The vertical bars at the bottom of the spectra indicate the chemical shifts of the [3-¹³C]Ala signals for the PLC- $\delta 1$ PH domain-IP₃ complex in solution.¹⁷²

the PH domain, as viewed from the displaced peaks of Ala 88, which is included in the $\alpha 2$ -helix and of Ala 112. This is located at the C-terminus of the $\beta 7$ -strand flanking with the C-terminus of the $\beta 5/\beta 6$ loop. However, the N- and C-terminal α -helices, containing Ala 116, 118 and 21, located at the surface opposite to the ligand binding site of the PH domain show virtually no conformational changes (see Fig. 39 for their locations). Taking into account the highly amphipathic nature of

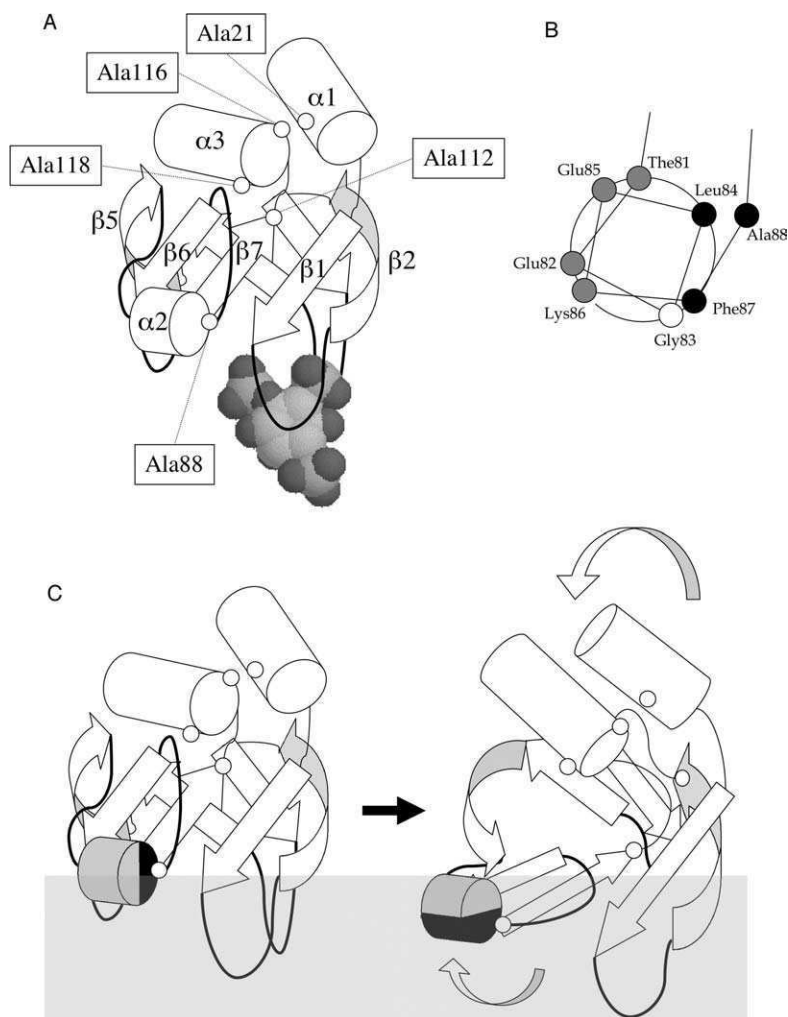


Fig. 39. (A) A schematic representation of the three-dimensional structure of the PLC- $\delta 1$ PH domain. The α -helices and β -sheets are indicated by cylinders and arrows, respectively. Ala residues are indicated by open circles. IP₃ is shown by a CPK model. (B) The amphipathic $\alpha 2$ -helix viewed from the C-terminus. Hydrophilic and hydrophobic residues are shown by gray and black circles, respectively. (C) A model of the conformational change of the PLC- $\delta 1$ PH domain-induced at the membrane surface.¹⁷²

the $\alpha 2$ -helix as shown by a helical wheel in Fig. 39B, it is plausible to predict a hydrophobic interaction between the hydrophobic face of the $\alpha 2$ -helix and the hydrophobic inner layer of the lipid bilayer. Further, it is proposed that the orientation of the $\alpha 2$ -helix causes an opening of the hydrophobic cluster between the $\alpha 2$ -helix and the $\beta 7$ strand, as illustrated in Fig. 39C.

It is therefore concluded that site-directed solid-state NMR provides an excellent means to probe the conformational features of membrane-binding proteins which cannot be examined by any other spectroscopic means.

9. CONCLUDING REMARKS

It is demonstrated that well-resolved ^{13}C NMR signals of fully hydrated membrane proteins are successfully recorded at ambient temperature, as far as they are selectively labeled with $[3\text{-}^{13}\text{C}]\text{Ala}$ and/or $[1\text{-}^{13}\text{C}]\text{Val}$ and embedded in lipid bilayers, as manifested from the ^{13}C NMR studies on bR and its mutants from PM. For this purpose, it is also important to record the ^{13}C NMR spectra by a single-pulse, dipolar decoupled-magic angle spinning (DD-MAS) in order to detect signals from the flexible portions located at the membrane surface from which ^{13}C signals are suppressed by the CP-MAS experiment. It is demonstrated that this site-directed NMR approach is an unrivaled means for revealing the conformation and dynamics of membrane proteins on the basis of the conformation-dependent displacement of ^{13}C chemical shifts and the preferentially suppressed peaks by CP-MAS alone or by both CP-MAS and DD-MAS NMR, depending upon the types of respective fluctuation motions. In particular, slow local motions with a fluctuation frequency of the order of $10^4\text{--}10^5$ Hz, which are very important in relation with their biological functions can be readily detected by the preferentially suppressed peaks due to the interference of the fluctuation frequency with the frequency of the proton decoupling or the magic angle spinning.

It should be taken into account, however, that several the ^{13}C NMR signals from the loops and some transmembrane α -helices are preferentially suppressed when ^{13}C NMR spectra of $[3\text{-}^{13}\text{C}]\text{Ala}$ -labeled bR were recorded in a *monomeric* state as in a reconstituted lipid bilayer. In addition, the ^{13}C NMR signals were almost completely suppressed when the ^{13}C NMR spectra were recorded for $[1\text{-}^{13}\text{C}]\text{Ala}$ - or Val -labeled bR in lipid bilayers. This is obviously caused by accelerated backbone dynamics with a fluctuation frequency from 10^2 Hz in the 2D crystal to 10^4 Hz in the monomeric state in the absence of specific protein-protein interactions as well as lipid-protein interactions in the absence of specific endogeneous lipids. Keeping this fact in mind, this approach turns out to be very useful to examine the conformation and dynamics of a variety of membrane proteins such as a photoreceptor protein (*pharaonis* phoborhodopsin; ppR), its transducer pHtrII (1–159), receptor-transducer complex [ppR/pHtrII (1–159)], and a membrane enzyme (diacylglycerol kinase; DGK), which are overexpressed in *E. coli* and present as monomers. In fact, several ^{13}C NMR signals are missing from the amino-acid residues located at the

flexible portions such as loops and transmembrane α -helices near to the membrane surface as compared with the data from the 2D crystalline preparation. In such cases, it is also very important to search for the best experimental conditions leading to the observation of the full ^{13}C NMR signals.

ACKNOWLEDGEMENTS

The author thanks Professors Akira Naito of Yokohama National University and Satoru Tuzi of the University of Hyogo for stimulating discussions.

REFERENCES

1. C. Branden and J. Tooze, *Introduction to Protein Structure*, 2nd edition, Garland Publishing, New York, 1999.
2. B. J. Bormann and D. M. Engelman, *Annu. Rev. Biophys. Biomol. Struct.*, 1992, **21**, 223–242.
3. M. H. B. Stowell and D. C. Rees, *Adv. Protein Chem.*, 1995, **46**, 279–311.
4. N. Grigorieff, T. A. Ceska, K. H. Downing, J. M. Baldwin and R. Henderson, *J. Mol. Biol.*, 1996, **259**, 393–421.
5. E. Pebay-Peyroula, G. Rummel, J. P. Rosenbusch and E. M. Landau, *Science*, 1997, **277**, 1676–1681.
6. H. Luecke, H. T. Richter and J. K. Lanyi, *Science*, 1998, **280**, 1934–1937.
7. L. Essen, R. Siebert, W. D. Lehman and D. Oesterhelt, *Proc. Natl. Acad. Sci. USA*, 1998, **95**, 11673–11678.
8. H. Sato, K. Takeda, K. Tani, T. Hino, T. Okada, M. Nakasako, N. Kamiya and T. Kouyama, *Acta Crystallogr.*, 1999, **D 55**, 1251–1256.
9. W. A. Havelka, R. Henderson, J. A. Heymann and D. Oesterhelt, *J. Mol. Biol.*, 1993, **234**, 837–846.
10. M. Kolbe, H. Besir, L. -O. Essen and D. Oesterhelt, *Science*, 2000, **288**, 1390–1396.
11. E. R. S. Kunji, E. N. Spudich, R. Grishammer, R. Henderson and J. L. Spudich, *J. Mol. Biol.*, 2001, **308**, 279–293.
12. H. Luecke, B. Shoberg, J. K. Lanyi, E. N. Spudich and J. L. Spudich, *Science*, 2001, **293**, 1499–1503.
13. A. Royant, P. Nollert, K. Edman, R. Neutze, E. M. Landau, E. Pebay-Peyroula and J. Navaro, *Proc. Natl. Acad. Sci. USA*, 2001, **98**, 10131–10136.
14. J. Deisenhofer, O. Epp, K. Miki, R. Huber and H. Michel, *Nature*, 1985, **318**, 618–624.
15. W. K. Kuhlbrandt, D. N. Wang and Y. Fujiyoshi, *Nature*, 1994, **367**, 614–621.
16. G. McDermott, S. M. Prince, A. A. Freer, A. M. Hathornthwaite-Lawless, M. Z. Papiz, R. J. Cogdell and N. W. Isaacs, *Nature*, 1995, **374**, 517–521.
17. S. Iwata, C. Ostermeier, B. Ludwig and H. Michel, *Nature*, 1995, **376**, 660–669.
18. T. Tsukihara, H. Aoyama, E. Yamashita, T. Tomizaki, H. Yamaguchi, K. Shinzawa-Itoh, R. Nakashima, R. Yaono and S. Yoshikawa, *Science*, 1996, **272**, 1136–1144.
19. D. A. Doyle, J. M. Cabral, R. A. Pfuetzner, A. Kuo, J. M. Gulbis, S. L. Cohen, B. T. Chait and R. MacKinnon, *Science*, 1998, **280**, 69–77.
20. G. Chang, R. H. Spencer, A. T. Lee, M. T. Barclay and D. C. Rees, *Science*, 1998, **282**, 2220–2226.
21. K. Palczewski, T. Kumasaka, T. Hori, C. A. Behnke, H. Motoshima, B. A. Fox, I. Le Trong, D. C. Teller, T. Okada, R. E. Stenkamp, M. Yamamoto and M. Miyano, *Science*, 2000, **289**, 739–745.
22. C. Toyoshima, M. Nakasako, H. Nomura and H. Ogawa, *Nature*, 2000, **405**, 647–655.
23. N. A. Dencher and M. P. Heyn, *FEBS Lett.*, 1979, **108**, 307–310.
24. N. A. Dencher, K. -D. Kohl and M. P. Heyn, *Biochemistry*, 1983, **22**, 1323–1334.
25. S. J. Milder, T. E. Thorgeirsson, L. J. Mierke, R. M. Stroud and D. S. Kliger, *Biochemistry*, 1991, **30**, 1751–1761.

26. N. A. Dencher and M. P. Heyn, *Methods Enzymol.*, 1978, **88**, 5–10.
27. G. Varo and J. K. Lanyi, *Biochemistry*, 1991, **30**, 7165–7171.
28. J. Wang, S. Links, C. D. Heyes and M. A. El-Sayed, *Biophys. J.*, 2002, **83**, 1557–1566.
29. F. Castellani, B. van Rossum, A. Diehl, M. Schubert, K. Rehbein and H. Oschkinat, *Nature*, 2002, **420**, 98–102.
30. F. Castellani, B. J. van Rossum, A. Diehl, K. Rehbein and H. Oschkinat, *Biochemistry*, 2003, **42**, 11476–11483.
31. S. Tuzi, S. Naito and H. Saitô, *Biochemistry*, 1994, **33**, 15046–15052.
32. S. Tuzi, S. Yamaguchi, A. Naito, R. Needleman, J. K. Lanyi and H. Saitô, *Biochemistry*, 1996, **35**, 7520–7527.
33. S. Yamaguchi, S. Tuzi, M. Tanio, A. Naito, J. K. Lanyi, R. Needleman and H. Saitô, *J. Biochem. (Tokyo)*, 2000, **127**, 861–869.
34. S. Yamaguchi, S. Tuzi, K. Yonebayashi, A. Naito, R. Needleman, J. K. Lanyi and H. Saitô, *J. Biochem. (Tokyo)*, 2001, **129**, 373–382.
35. H. Saitô, S. Tuzi, S. Yamaguchi, M. Tanio and A. Naito, *Biochim. Biophys. Acta*, 2000, **1460**, 39–48.
36. H. Saitô, S. Tuzi, M. Tanio and A. Naito, *Annu. Rep. NMR Spectrosc.*, 2002, **47**, 39–108.
37. H. Saitô, *Chem. Phys. Lipids*, 2004, **132**, 101–112.
38. S. J. Opella, C. Ma and F. M. Maassi, *Meth. Enzymol.*, 2001, **339**, 285–313.
39. F. M. Marassi, *Biophys. J.*, 2001, **80**, 994–1003.
40. S. J. Opella and F. M. Marassi, *Chem. Rev.*, 2004, **104**, 3587–3606.
41. A. C. Zeri, M. F. Mesleh, A. A. Nevzorov and S. J. Opella, *Proc. Natl. Acad. Sci. USA*, 2003, **100**, 6458–6463.
42. T. Arakawa, K. Shimono, S. Yamaguchi, S. Tuzi, Y. Sudo, N. Kamo and H. Saitô, *FEBS Lett.*, 2003, **36**, 237–240.
43. S. Yamaguchi, K. Shimono, Y. Sudo, S. Tuzi, A. Naito, N. Kamo and H. Saitô, *Biophys. J.*, 2004, **86**, 3131–3140.
44. S. Yamaguchi, S. Tuzi, J. U. Bowie and H. Saitô, *Biochim. Biophys. Acta*, 2004, **1698**, 97–105.
45. H. Saitô, T. Tuchida, K. Ogawa, T. Arakawa, S. Yamaguchi and S. Tuzi, *Biochim. Biophys. Acta*, 2002, **1565**, 97–106.
46. H. Saitô, K. Yamamoto, S. Tuzi and S. Yamaguchi, *Biochim. Biophys. Acta*, 2003, **1616**, 127–136.
47. S. K. Straus, T. Bremi and R. R. Ernst, *Chem. Phys. Lett.*, 1996, **262**, 709–715.
48. J. Pauli, M. Baldus, B. Van Rossum, H. de Groot and H. Oschkinat, *Chembiochem.*, 2001, **2**, 272–281.
49. M. Ernst, A. Detken, A. Böckmann and B. H. Meier, *J. Am. Chem. Soc.*, 2003, **125**, 15807–15810.
50. A. E. Bennett, C. M. Riensra, M. Auger, K. V. Lakshmi and R. G. Griffin, *J. Chem. Phys.*, 1995, **103**, 6951–6958.
51. A. Detken, E. H. Hardy, M. Ernst and B. H. Meier, *Chem. Phys. Lett.*, 2002, **356**, 298–304.
52. S. Kiihne, M. A. Mehta, J. A. Stringer, D. M. Gregory, J. C. Shiels and G. P. Drobny, *J. Phys. Chem. A*, 1998, **102**, 2274–2282.
53. D. M. LeMaster and D. M. Kushlan, *J. Amer. Chem. Soc.*, 1996, **118**, 9255–9264.
54. M. Hong and K. Jakes, *J. Biomol. NMR*, 1999, **14**, 71–74.
55. M. Hong, *J. Magn. Reson.*, 1999, **139**, 389–401.
56. H. Saitô, K. Yamamoto, S. Tuzi and S. Yamaguchi, *Biochim. Biophys. Acta*, 2003, **1616**, 127–136.
57. H. Onishi, E. M. McCance and N. E. Gibbons, *Can. J. Microbiol.*, 1965, **11**, 365–373.
58. H. Kandori, K. Shimono, Y. Sudo, M. Iwamoto, Y. Shichida and N. Kamo, *Biochemistry*, 2001, **40**, 9238–9246.
59. M. Engelhard, B. Hess, D. Emeis, G. Metz, W. Kreutz and F. Siebert, *Biochemistry*, 1989, **28**, 3967–3975.
60. S. Tuzi, S. Yamaguchi, M. Tanio, H. Konishi, S. Inoue, A. Naito, R. Needleman, J. K. Lanyi and H. Saitô, *Biophys. J.*, 1999, **76**, 1523–1531.
61. S. Tuzi, A. Naito and H. Saitô, *Eur. J. Biochem.*, 1993, **28**, 837–844.
62. S. Tuzi, A. Naito and H. Saitô, *Eur. J. Biochem.*, 1996, **239**, 294–301.
63. R. E. Lechner, F. Fitter, N. A. Dencher and T. Hauss, *J. Mol. Biol.*, 1998, **277**, 593–603.

64. H. Saitô, *Magn. Reson. Chem.*, 1986, **24**, 835–852.
65. H. Saitô and I. Ando, *Annu. Rep. NMR Spectrosc.*, 1989, **21**, 209–290.
66. H. Saitô, R. Tabeta, A. Shoji, T. Ozaki and I. Ando, *Macromolecules*, 1983, **16**, 1050–1057.
67. O. W. Howarth and D. M. J. Lilley, *Prog. NMR Spectrosc.*, 1978, **12**, 1–40.
68. M. Ishida, T. Asakura, M. Yokoi and H. Saitô, *Macromolecules*, 1990, **23**, 88–94.
69. H. Saitô, R. Tabeta, A. Shoji, T. Ozaki, I. Ando and T. Miyata, *Biopolymers*, 1984, **23**, 2279–2297.
70. H. Saitô and M. Yokoi, *J. Biochem. (Tokyo)*, 1992, **111**, 376–382.
71. S. Kimura, A. Naito, S. Tuzi and H. Saitô, *Biopolymers*, 2001, **58**, 78–88.
72. S. Krimm and A. M. Dwivedi, *Science*, 1982, **216**, 407–408.
73. M. Tanio, S. Inoue, K. Yokota, T. Seki, S. Tuzi, R. Needleman, J. K. Lanyi, A. Naito and H. Saitô, *Biophys. J.*, 1999, **77**, 431–442.
74. H. Saitô, J. Mikami, S. Yamaguchi, M. Tanio, A. Kira, T. Arakawa, K. Yamamoto and S. Yamaguchi, *Magn. Reson. Chem.*, 2004, **42**, 218–230.
75. H. Saitô, S. Yamaguchi, H. Okuda, A. Shiraishi and S. Tuzi, *Solid State Nucl. Magn. Reson.*, 2004, **25**, 5–14.
76. D. Suwelack, W. P. Rothwell and J. S. Waugh, *J. Chem. Phys.*, 1980, **73**, 2559–2569.
77. S. H. Saitô, R. Kawaminami, M. Tanio, T. Arakawa, S. Yamaguchi and S. Tuzi, *Spectroscopy*, 2002, **16**, 107–120.
78. D. A. Torchia and J. R. Lyerla, *Biopolymers*, 1974, **13**, 97–114.
79. D. S. Wishart, C. G. Bigam, A. Holm, R. S. Hodges and B. D. Sykes, *J. Biomol. NMR*, 1995, **5**, 67–81.
80. Y. Kawase, M. Tanio, A. Kira, S. Yamaguchi, S. Tuzi, A. Naito, M. Kataoka, J. K. Lanyi, R. Needleman and H. Saitô, *Biochemistry*, 2000, **39**, 14472–14480.
81. W. P. Rothwell and J. S. Waugh, *J. Chem. Phys.*, 1981, **74**, 2721–2732.
82. S. Tuzi, J. Hasegawa, R. Kawaminami, A. Naito and H. Saitô, *Biophys. J.*, 2001, **81**, 425–434.
83. S. Tuzi, A. Naito and H. Saitô, *J. Mol. Struct.*, 2003, **654**, 205–214.
84. I. Solomon, *Phys. Rev.*, 1955, **99**, 559–565.
85. N. Bloembergen, *J. Chem. Phys.*, 1957, **27**, 572–573.
86. M. Kamihira, A. Naito, K. Nishimura, S. Tuzi and H. Saitô, *J. Phys. Chem. B*, 1998, **102**, 2826–2834.
87. M. Kamihira, A. Naito, S. Tuzi and H. Saitô, *J. Phys. Chem. A*, 1999, **103**, 3356–3363.
88. H. Saitô, R. Tabeta, A. Shoji, T. Ozaki, I. Ando and T. Asakura, in *Magnetic Resonance in Biology and Medicine*, G. Govil, C. L. Kheterpal and A. Saran, eds., Tata McGraw-Hill, New Delhi, 1985, 195–215.
89. I. Ando, H. Saitô, R. Tabeta, A. Shoji and T. Ozaki, *Macromolecules*, 1984, **17**, 457–461.
90. N. Asakawa, H. Kurosu and I. Ando, *J. Mol. Struct.*, 1994, **323**, 279–285.
91. A. C. de Dios, J. G. Pearson and E. Oldfield, *Science*, 1993, **260**, 1491–1496.
92. H. Saitô, R. Tabeta, A. Shoji, T. Ozaki, I. Ando and T. Miyata, *Biopolymers*, 1984, **23**, 2279–2297.
93. H. Saitô, R. Tabeta, T. Asakura, Y. Iwanaga, A. Shoji, T. Ozaki and I. Ando, *Macromolecules*, 1984, **17**, 1405–1412.
94. S. Spera and A. Bax, *J. Amer. Chem. Soc.*, 1991, **113**, 5490–5492.
95. G. Cornilescu, F. Delaglio and A. Bax, *J. Biomol. NMR*, 1999, **13**, 289–302.
96. D. S. Wishart, B. D. Sykes and F. M. Richards, *J. Mol. Biol.*, 1991, **222**, 311–333.
97. D. S. Wishart, M. S. Watson, R. F. Boyko and B. D. Sykes, *J. Biomol. NMR*, 1997, **10**, 329–336.
98. M. Iwadata, T. Asakura and M. P. Williamson, *J. Biol. NMR*, 1999, **13**, 199–211.
99. S. Luca, D. V. Filippov, J. H. van Boom, H. Oschkinat, H. J. M. de Groot and M. Baldus, *J. Biol. NMR*, 2001, **20**, 325–331.
100. X. -P. Xu and D. A. Case, *J. Biol. NMR*, 2001, **21**, 321–333.
101. S. Yamaguchi, K. Yonebayashi, H. Konishi, S. Tuzi, A. Naito, J. K. Lanyi, R. Needleman and H. Saitô, *Eur. J. Biochem.*, 2001, **268**, 2218–2228.
102. R. Renthal, N. Dawson, J. Tuley and P. Horowitz, *Biochemistry*, 1983, **22**, 5–12.
103. M. Engelhard, S. Finkler, G. Metz and F. Siebert, *Eur. J. Biochem.*, 1996, **235**, 526–533.
104. K. Yonebayashi, S. Yamaguchi, S. Tuzi and H. Saitô, *Eur. Biophys. J.*, 2003, **32**, 2–11.
105. P. Barré, S. Yamaguchi, H. Saitô and D. Huster, *Eur. Biophys. J.*, 2003, 578–584.

106. A. C. Kolbert, H. J. M. De Groot, M. H. Levitt, M. G. Munowitz, J. E. Roberts, G. S. Harbison, J. Herzfeld and R. G. Griffin, in *Multinuclear Magnetic Resonance in Liquid and Solids — Chemical Applications*, P. Granger and R. K. Harris, eds, Kluwer, Dordrecht, 1990, 339–354.
107. A. Bielecki, A. C. Kolbert and M. H. Levitt, *Chem. Phys. Lett.*, 1989, **155**, 341–345.
108. T. A. Moore, M. E. Edgerton, G. Parr, C. Greenwood and R. N. Perham, *Biochem. J.*, 1978, **171**, 469–476.
109. P. C. Mowery, R. H. Lozier, Q. Chae, Y. W. Tseng, M. Taylor and W. Stoeckenius, *Biochemistry*, 1979, **18**, 4100–4107.
110. U. Fischer and D. Oesterheld, *Biophys. J.*, 1979, **28**, 211–230.
111. Y. Kimura, A. Ikegami and W. Stoeckenius, *Photochem. Photobiol.*, 1984, **40**, 641–646.
112. T. Arakawa, MS Thesis, Himeji Institute of Technology, Hyogo, Japan, 2002.
113. J. B. Heymann, D. J. Muller, E. M. Landau, J. P. Rosenbusch, E. Pabay-Peyroula, G. Buldt and A. Engel, *J. Struct. Biol.*, 1999, **128**, 243–249.
114. J. Marque, K. Kinoshita Jr., R. Govindjee, A. Ikegami, T. G. Ebrey and J. Otomo, *Biochemistry*, 1986, **25**, 5555–5559.
115. H. J. Steinhoff, R. Mollaaghababa, C. Altenbach, K. Hideg, M. Krebs, H. G. Khorana and W. L. Hubbell, *Science*, 1994, **266**, 105–107.
116. C. H. Chang, J. G. Chen, R. Govindjee and T. Ebrey, *Proc. Natl. Acad. Sci. USA*, 1985, **82**, 396–400.
117. M. Ariki and J. K. Lanyi, *J. Biol. Chem.*, 1986, **261**, 8167–8174.
118. I. Szundi and W. Stoeckenius, *Proc. Natl. Acad. Sci. USA*, 1987, **84**, 3681–3684.
119. I. Szundi and W. Stoeckenius, *Biophys. J.*, 1989, **56**, 369–383.
120. J. Riesle, D. Oesterheld, N. A. Dencher and J. Heberle, *Biochemistry*, 1996, **35**, 6635–6643.
121. S. Checover, E. Nachliel, N. A. Dencher and M. Gutman, *Biochemistry*, 1997, **36**, 13919–13928.
122. S. Checover, Y. Marantz, E. Nachliel, M. Gutman, M. Pfeiffer, J. Tittor, D. Oesterheld and N. A. Dencher, *Biochemistry*, 2001, **40**, 4281–4292.
123. L. S. Brown, Y. Yamazaki, A. Maeda, L. Sun, R. Needleman and J. K. Lanyi, *J. Mol. Biol.*, 1994, **239**, 401–414.
124. S. Yamaguchi, PhD Thesis, Himeji Institute of Technology, Hyogo, Japan, 2000.
125. C. Sanz, T. Lazarova, F. Seplucré, R. González-Moreno, J. L. Bourdelande, E. Querol and E. Padrós, *FEBS Lett.*, 1999, **4556**, 191–195.
126. C. Sanz, M. Márquez, A. Peralvarez, S. Elouatik, F. Seplucré, E. Querol, T. Lazarova and E. Padrós, *J. Biol. Chem.*, 2001, **276**, 40788–40794.
127. T. Lazarova, C. Sanz, E. Querol and E. Padrós, *Biophys. J.*, 2000, **78**, 2022–2030.
128. H. Saitô, S. Yamaguchi, K. Ogawa, S. Tuzi, M. Márquez, C. Sanz and E. Padrós, *Biophys. J.*, 2004, **86**, 1673–1681.
129. S. P. Balashov, *Biochim. Biophys. Acta*, 2000, **1460**, 75–94.
130. M. Kataoka, H. Kamikubo, F. Tokunaga, L. S. Brown, Y. Yamazaki, A. Maeda, M. Sheves, R. Needleman and J. K. Lanyi, *J. Mol. Biol.*, 1994, **243**, 621–638.
131. J. K. Lanyi and B. Schobert, *J. Mol. Biol.*, 2002, **321**, 727–737.
132. H. Kamikubo, T. Oka, Y. Imamoto, F. Tokunaga, J. K. Lanyi and M. Kataoka, *Biochemistry*, 1997, **36**, 12282–12287.
133. L. S. Brown, H. Kamikubo, L. Zimanyi, M. Kataoka, F. Tokunaga, P. Verdegem, J. Lugtenburg and J. K. Lanyi, *Proc. Natl. Acad. Sci. USA*, 1997, **94**, 5040–5044.
134. A. Kira, M. Tanio, S. Tuzi and H. Saitô, *Eur. Biophys. J.*, 2004, **33**, 580–588.
135. Y. Yamazaki, S. Tuzi, H. Saitô, H. Kandori, R. Needleman, J. K. Lanyi and A. Maeda, *Biochemistry*, 1996, **35**, 4063–4068.
136. A. H. Dioumaev, H. -T. Richter, L. S. Brown, M. Tanio, S. Tuzi, H. Saitô, Y. Kimura, R. Needleman and J. K. Lanyi, *Biochemistry*, 1998, **37**, 2496–2505.
137. Y. Yamazaki, M. Hatanaka, H. Kandori, J. Sasaki, W. F. Karstens, J. Raaps, J. Lugtenburg, M. Bizounok, J. Herzfeld, R. Needleman, J. K. Lanyi and A. Maeda, *Biochemistry*, 1995, **34**, 7088–7093.
138. M. Tanio, S. Tuzi, S. Yamaguchi, R. Kawaminami, A. Naito, R. Needleman, J. K. Lanyi and H. Saitô, *Biophys. J.*, 1999, **77**, 1577–1584.

139. H. J. Sass, G. Buldt, R. Gessenich, D. Hehn, D. Neff, R. Schlesinger, J. Berendzen and P. Ormos, *Nature*, 2000, **406**, 649–653.
140. H. Leucke, B. Schobert, H. T. Richter, J. P. Cartailier and J. K. Lanyi, *Science*, 1999, **286**, 255–260.
141. H. Leucke, B. Schobert, J. P. Cartailier, H. T. Richter, A. Rosengarth, R. Needleman and J. K. Lanyi, *J. Mol. Biol.*, 2000, **300**, 1237–1255.
- 141a. A. Petkova, J. G. Hu, M. Bizounok, M. Simpson, R. G. Griffin and J. Herzfeld, *Biochemistry*, 1999, **38**, 1562–1572.
142. L. S. Brown, Y. Gat, M. Sheves, Y. Yamazaki, A. Maeda, R. Needleman and J. K. Lanyi, *Biochemistry*, 1994, **33**, 12001–12011.
143. M. Kates, N. Moldoveanu and L. C. Stewart, *Biochim. Biophys. Acta*, 1993, **1169**, 46–53.
144. N. Grigorieff, E. Beckmann and F. Zelmlin, *J. Mol. Biol.*, 1995, **254**, 404–415.
145. B. Sternberg, C. L'Hostis, C. A. Whiteway and A. Watts, *Biochim. Biophys. Acta*, 1992, **1108**, 21–30.
146. M. P. Krebs and T. A. Isenbarger, *Biochim. Biophys. Acta*, 2000, **1460**, 15–26.
147. M. Tani, S. Tuzi, S. Yamaguchi, H. Konishi, A. Naito, R. Needleman, J. K. Lanyi and H. Saitô, *Biochim. Biophys. Acta*, 1998, **1375**, 84–92.
148. W. D. Hoff, K. -W. Jung and J. L. Spudich, *Annu. Rev. Biophys. Biomol. Struct.*, 1997, **26**, 223–258.
149. V. I. Gordeliy, J. Labahn, R. Moukhametzianov, R. Efremov, J. Granzin, R. Schlesinger, G. Buldt, T. Savopol, A. J. Scheidig, J. P. Klare and M. Engelhard, *Nature*, 2002, **419**, 484–487.
150. C. R. Sanders II, L. Czerski, O. Vinogradova, P. Badola, D. Song and S. O. Smith, *Biochemistry*, 1996, **35**, 8610–8618.
151. J. K. Lanyi, *J. Struct. Biol.*, 1999, **124**, 164–178.
152. R. Seidel, B. Scharf, M. Gautel, K. Kleine, D. Oesterheld and M. Engelhard, *Proc. Natl. Acad. Sci. USA*, 1995, **92**, 3036–3040.
153. X. -N. Zhang, J. Zhu and J. L. Spudich, *Proc. Natl. Acad. Sci. USA*, 1999, **96**, 857–862.
154. J. J. Falke and G. L. Hazelbauer, *Trends Biochem. Sci.*, 2001, **26**, 257–265.
155. J. L. Spudich and H. Luecke, *Curr. Opinion Struct. Biol.*, 2002, **12**, 540–546.
156. K. K. Kim and H. Yokota, S-H. Kim., *Nature*, 1999, **400**, 787–792.
157. A. -A. Wegener, I. Chizov, M. Engelhard and H. -J. Steinhoff, *J. Mol. Biol.*, 2000, **301**, 881–891.
158. A. -A. Wegener, J. P. Klare, M. Engelhard and H. -J. Steinhoff, *EMBO J.*, 2001, **20**, 5312–5319.
159. I. Kawamura, N. Kihara, S. Tuzi, Y. Ikeda, K. Nishimura, H. Saitô, N. Kamo and A. Naito, The 1st Asia-Pacific NMR Symposium, Yokohama (2005).
160. I. Kawamura, Y. Ikeda, Y. Sudo, M. Iwamoto, K. Shimono, S. Tuzi, H. Saitô, Naoki Kamo, Akira Naito, Pacificchem 2005, Honolulu (2005).
161. E. N. Spudich, W. Zhang, M. Alam and J. L. Spudich, *Proc. Natl. Acad. Sci. USA*, 1997, **94**, 4960–4965.
162. O. Vinogradova, P. Badola, L. Czerski, F. D. Sonnichsen and C. R. Sanders II, *Biophys. J.*, 1997, **72**, 2688–2701.
163. B. M. Gorzelle, J. K. Nagy, K. Oxenoid, W. L. Lonzer, D. M. Cafiso and C. R. Sanders, *Biochemistry*, 1999, **38**, 16373–16382.
164. R. L. Smith, J. F. O'Toole, M. E. Maguire and C. R. Sanders II, *J. Bacteriol.*, 1994, **176**, 5459–5465.
165. C. R. Sanders II, L. Czerski, O. Vinogradova, P. Badola, D. Song and S. O. Smith, *Biochemistry*, 1996, **35**, 8610–8618.
166. J. Wen, X. Chen and J. U. Bowie, *Nat. Struct. Biol.*, 1996, **3**, 141–148.
167. F. W. Lau, X. Chen and J. U. Bowie, *Biochemistry*, 1999, **38**, 5521–5527.
168. M. E. Cifuentes, L. Honkanen and M. Rebecchi, *J. Biol. Chem.*, 1993, **268**, 11586–11593.
169. F. Ramirez and M. K. Jain, *Protein Struct. Funct. Genet.*, 1991, **9**, 229–239.
170. M. J. Rebecchini, A. Peterson and S. McLaughlin, *Biochemistry*, 1992, **31**, 12742–12747.
171. K. M. Ferguson, M. A. Lemmon, J. Schlessinger and P. B. Sigler, *Cell*, 1995, **83**, 1037–1046.
172. S. Tuzi, N. Uekama, M. Okada, S. Yamaguchi, H. Saitô and H. Yagisawa, *J. Biol. Chem.*, 2003, **278**, 28019–28025.
173. S. Tuzi, N. Uekama, M. Okada and H. Yagisawa, in *Modern Magnetic Resonance*, G.A. Webb, ed., Springer, Berlin, in press.

This page intentionally left blank

High-Pressure NMR Studies in Proteins

WERNER KREMER

*Institut für Biophysik und Physikalische Biochemie, Universität Regensburg, P.O.Box,
D-93040 Regensburg, Germany*

1. Introduction	177
2. High-Pressure NMR spectroscopy	180
3. Application of high-pressure NMR spectroscopy on proteins	182
3.1 Linear tetrapeptides at pressure between 0.1 and 200 MPa	185
3.2 Pressure-stability of phospholipid bicelles: Measurement of residual dipolar couplings	190
3.3 Pressure-stabilized functional important conformers	191
3.4 Protein structures under pressure	198
4. Conclusions	200
Acknowledgments	200
References	200

High-pressure biochemistry started to emerge in the 1960s and 1970s and focused on the effects of pressure on proteins, nucleoproteins and membranes. During the same time, NMR spectroscopy was combined with high pressure since it is the only generally applicable method to monitor pressure-induced structural changes at the atomic level in solution. However, up to now the application of many, if not most, of the currently available multidimensional high-resolution NMR experiments is impossible under high pressure in protein solutions due to the restricted volume of the high-pressure glass cells, which causes a poor signal-to-noise ratio. In addition, a prerequisite for the understanding of pressure effects on proteins is the knowledge about the dependence on ^1H chemical shifts in random coil model tetrapeptides and buffer systems. Furthermore, we review various high-pressure NMR experiments on proteins and the recent advances made in this field.

1. INTRODUCTION

The application of high pressure is capable of delivering a wealth of important information about the physicochemical properties of proteins, especially folding as well as the dynamics and structure of folding intermediates.¹ In combination with NMR spectroscopy, the stability of proteins can be studied at atomic resolution without chemical perturbations, such as denaturants (for a review see ref. 2). Thus, high-pressure NMR spectroscopy can yield local information about mechanical and

dynamical properties of proteins and can be used to stabilize folding and unfolding intermediates. In addition, at pressures of 200 MPa, the phase behaviour of water allows the observation of protein denaturation in aqueous solution at temperatures down to 255 K.³ High pressure influences protein aggregation and association as well.^{1,4-12} The application of high-pressure NMR spectroscopy towards biochemistry has been reviewed several times,^{3,13-17} and a new series of meetings (International Conference in High Pressure Biosciences and Biotechnology, HPBB) as well as the recent special edition of applications of high pressure to biomolecules (BBA 1595, 2002) shows the growing attention of the scientific community in this field. Recent advances in high-pressure NMR spectroscopy on folding intermediates and denatured states of proteins have been covered by the Akasaka group.^{2,18-22}

For NMR experiments under high pressure on commercially available NMR instruments home-built high-pressure apparatus were designed independently by Yamada²³ and the group of Lüdemann.²⁴ With these systems pressures up to 200 MPa were reached. Wagner²⁵ used this technique to study pressure effects on ring-flip motions in the basic pancreatic trypsin inhibitor (BPTI). In 1972, Jonas^{26,27} introduced a probe, which can be pressurized and allowed to extend the pressure range for NMR spectroscopy up to 1000 MPa.^{16,28,29} Nevertheless, the design of special metallic high-pressure probes may lead to severe problems. The big advantage of the 'Yamada glass cell method' (for review see refs. 30,31,32) is its use in all commercially available probes and thus availability for all modern NMR applications to proteins. However, the restricted volume of the high-pressure glass cells causes a poor signal-to-noise ratio, which up to now renders the application of most of the multidimensional NMR experiments impossible. To overcome this problem cells made of sapphire or zirconium oxide were introduced by a number of groups³³⁻³⁶ to increase the amount of sample in the detection coil. Synthetic quartz cells³⁷ were designed to extend the pressure range for NMR spectroscopy up to 600 MPa.

There are generally two responses of proteins towards the application of pressure. They result from the property that pressure favours states with a smaller specific volume. This is described by the standard equations which define the reaction volume ΔV and activation volume ΔV^\ddagger of a thermodynamic reaction:

$$\left(\frac{\delta \ln K}{\delta p}\right)_T = -\frac{\Delta V}{RT} \text{ and } \left(\frac{\delta \ln k}{\delta p}\right)_T = -\frac{\Delta V^\ddagger}{RT} \quad (1)$$

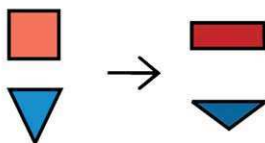
where K is the equilibrium constant, k the rate constant, p the pressure, T the absolute temperature and R the gas constant. Thus, any equilibrium in a population of conformers of proteins, including low-lying excited states and partially or completely unfolded conformations, connected with a non-zero volume change will be shifted towards the more compact state by the application of hydrostatic pressure. The volume decrease in proteins observed upon partial or complete unfolding of the native structure depends on three kinds of interactions: (1) Ionic pairs in aqueous solution are strongly destabilized by hydrostatic pressure due to the electrostrictive

effect of the separated charges, thus favouring the dissociation and disruption of ionic interactions under pressure. (2) Exposure of hydrophobic groups to water leads to a hydrophobic solvation layer favouring the unfolding of proteins at elevated pressure. (3) Evolutionary selected areas with non-optimized packing density through van der Waals' forces are key points where volume fluctuations can be probed by pressure, this is displaying the high anisotropy of compressibility found in proteins. These issues were discussed in detail by Silva *et al.*¹ and Akasaka^{19,20,22} and are summarized in Fig. 1.

The underlying molecular and energetic origins for protein misfolding and aggregation (for review see refs. 38 and 39–42) leading to amyloidosis and disorders like, e.g. the transmissible spongiform encephalopathies (TSEs) and Alzheimer's disease (AD) are still an open question.

One possibility to investigate oligomeric proteins and protein aggregates is high-hydrostatic pressure.¹ As an example, the protein transthyretin (TTR) can be viewed. Under normal conditions native TTR forms a stable tetramer. Compression of TTR leads to a monomeric molten-globule like intermediate. Upon decompression TTR forms a tetrameric pre-aggregate with a conformation different from the native form leading to fibrillar aggregation. A repeated compression changes the conformation from fibrillar structures back to a monomeric molten-globule like intermediate state. The structure of such an intermediate state with pre-amyloidogenic properties can be characterized by keeping it at a temperature of 4°C and

a) Pressure effect on each conformation



b) Shift of the conformational equilibrium

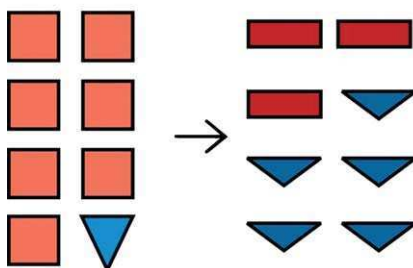


Fig. 1. Schematic representation of pressure effects in proteins connected with a nonzero volume change. (a) Pressure effect on a single conformation represents a highly anisotropic compression. (b) Shift of any equilibrium in a population of conformers of proteins towards a more compact state.

avoiding the aggregation that way.¹ In this sense, an elegant alternative to investigating multiple misfolding pathways of the proteins involved in neurodegenerative diseases with denaturing agents is applying hydrostatic pressure, which allows studying intermediate forms in the folding pathway of such proteins different from those obtained by denaturing agents^{43–46} (for review see refs. 41,47). As seen in case of the prion protein pressure induces scrapie-like prion-protein misfolding and amyloid-fibril formation.^{48–51} Irreversible aggregation of *shaPrP*(90–231) was observed above 450 MPa, and incubation of *shaPrP*(90–231) at 600 MPa overnight led to the formation of amyloid fibrils, whereas pressures up to 200 MPa lead to reversible effects and recovery of the original structure after pressure release.⁴⁸

Fine-tuning of temperature and pressure would lead to a stabilization of the intermediate pre-amyloidogenic conformations from proteins involved in neurodegenerative diseases and subsequently to a structural characterization of such an intermediate. The combination with NMR spectroscopy would allow a structure determination of pre-amyloidogenic intermediates at the atomic level. This review describes the experimental technique used for proteins and will summarize the recent advances made in the sampling of the conformational space of proteins by high-pressure NMR spectroscopy pioneered by Akasaka.

2. HIGH-PRESSURE NMR SPECTROSCOPY

As pointed out above, high-pressure NMR spectroscopy is the most exciting method for studying the structural anisotropy and conformational dynamics of proteins. At present two conceptually different methods are applied for high-pressure NMR experiments: (i) specifically designed non-magnetic metal autoclaves^{26,29} and (ii) the so-called Yamada glass cell method.^{23,32,37} Pressurizing of the whole probe allows to obtain very high pressures,^{28,29} but may result in severe problems: (a) limitation of space in high-resolution, high-field NMR spectrometers, (b) perturbations of the magnetic field homogeneity and (c) the difficulty to construct reliable low impedance radiofrequency feedthroughs through the thick metal parts of the autoclaves. However, the Yamada glass cell method can be applied much easier since it does not require special probes. A disadvantage of the glass cell method is the inherent low sensitivity since the sample volume contained in the thick-walled sample tubes is rather small. Typically, borosilicate or quartz-glass capillaries with an outer diameter of 1–5 mm and an inner diameter of 0.1–1.2 mm are required to withstand a pressure up to 200 MPa.

The typical active volume in 5 mm capillaries is 50 μ L. Such a small amount of sample material within the NMR coils causes a poor signal-to-noise ratio, which limits useful applications of most of the multidimensional NMR experiments important in protein science. Therefore, a number of groups were investigating set ups with larger active volumes.^{34,35}

The maximum pressure p_{\max} obtainable is a function of the tensile strength τ of the material and the quotient outer and inner diameters d_o and d_i . It can be

approximated by

$$p_{\max} = \tau \ln(d_0^2/d_i^2) \quad (2)$$

In Table 1, mechanical and physical parameters of different materials used for the production of high-pressure capillaries are listed. Quartz and sapphire display a much higher tensile strength than borosilicate glass. The effective tensile strength given in Table 1 includes the possible existence of faults in the material, which substantially reduces the maximum pressure the capillaries can resist, their number is also much dependent on the details of fabrication process. As the probability for faults decreases with size of the piece of material, small capillaries can endure much higher forces. Selected quartz capillaries with an outer diameter of 3 mm and an inner diameter of 1 mm were reported to sustain pressures up to 400 MPa. Yamada even reported that quartz capillaries made out of synthetic quartz can withstand pressures up to 600 MPa.³⁷

The use of sapphire cells with 5 mm outer diameter and 0.8 mm wall was first suggested by Roe³³ for pressures up to 41.5 MPa. Urbauer *et al.*³⁴ reported that sapphire cells with 5 mm outer diameter and 1 mm inner diameter tolerate pressures up to 100 MPa (US patent No. 5977772).

Arnold *et al.*³⁵ were using single crystalline sapphire cells with an inner diameter of 1.73 mm and an outer diameter of 3.18 mm, available from Saphikon (Milford, NH, U.S.A.). In contrast to amorphous materials such as borosilicate and quartz glass, sapphire single crystal should contain only few faults due to the manufacturing method. However, the commercially available sapphire cells have still a large spread in their quality and have to be tested before use. Although most cells can be used up to 200 MPa, some of them burst at pressures below 70 MPa but also pressures above 350 MPa were reached.³⁵ A disadvantage of sapphire compared to borosilicate glass is its high thermal expansion coefficient, which may lead to mechanical problems when changing the temperature.

In general, the sapphire cells can be used with a structure according to the descriptions of Price and Lüdemann³² for borosilicate glass cells. Here, the pressurizing fluid (methyl cyclohexane : methyl cyclopentane:50:50) is pressurized externally by a pressure bench which is connected to the autoclave by a 6 m high-strength steel tube

Table 1. Physical and mechanical properties of the materials used for high-pressure NMR capillaries

	Borosilicate Glass	Quartz Glass	Sapphire	
Producer	Schott	Qsil	Saphikon	
Tensile strength [Nmm ⁻²]	7	50	140	
Coefficient of expansion [10 ⁻⁶ K ⁻¹]	3	0.5	8.8	7.9
Temperature of processing [K]	825–1260	1700–2100	>2053	
Magnetic susceptibility [10 ⁻⁹ m3kg ⁻¹]	−0.86	−0.49	−0.21	−0.25

Note: Owing to its single crystalline structure, the coefficient of expansion and magnetic susceptibility of sapphire are tensorial quantities (the left side, values parallel, right side perpendicular to the principal axis of the system). (After ref. 36.)

with an inner diameter of 100 μm . The pressure is transmitted onto the NMR sample by a Teflon hose closed by a Teflon plug, which simultaneously serves as separation of the organic solvent from the biological sample (Fig. 2). For sealing the glass-cell system, Price and Lüdemann³² used cone-shaped nipples. These nipples are tightly pressed into the cone-shaped bore of the autoclave. Since the radial forces applied to the capillary tube increase with its diameter, only small diameters in the contact area of the capillary with the sealing cone can be used. This does not present a problem for glass-cell systems because the glass cells can be shaped appropriately in this region. Since the outer diameter of the sapphire capillary is constant over its length Arnold *et al.*³⁵ devised another type of pressure sealing for the sapphire cells (Fig. 2). To fix the capillaries within the autoclave a 30-mm-long cylinder-shaped TiAl_6V_4 nipple was used, which was glued around the end of the capillary. The small gap between the bore of the autoclave and the nipple ($<10\ \mu\text{m}$) is sealed by an O-ring. The O-ring is forced to the walls of the autoclave by a cone-shaped brass cylinder. A glass rod is used to fill up the inner volume of the sapphire cell outside the NMR coil, to reduce the amount of sample fluid needed to fill the sample tube. To prevent the probe from damages caused by an explosion, a Teflon protection hose is applied to the lower end of the capillaries (Fig. 2). The improvements achieved by using the new sapphire cells were shown by Arnold *et al.*³⁵ through the comparison of ^1H - ^{15}N -HSQC-spectra measured on a sample of a 0.5 mM sample of the cold shock protein (Csp) from *Thermotoga maritima*. It was first measured in the sapphire cell with an outer diameter of 3.2 mm and an inner diameter of 1.8 mm and then under identical experimental conditions in the glass cell with 5 mm outer diameter and 1.2 mm inner diameter. Fig. 3 shows part of the spectra measured with this equipment. The data were plotted at the same contour level. It is obvious that the signal-to-noise ratio is much better using the sapphire cell as to be expected from the approximately two times larger active volume, and thus filling factor, in the probe. 1D traces through the maximum of the amide H^{N} cross-peak of K19 in the 2D-HSQC spectra are depicted in the bottom part of Fig. 3. The signal-to-noise ratio calculated from 1D traces is increased by a factor of 2. The 3 mm sapphire cell system can also be used in a 5 mm probe head leading to a further improvement in signal-to-noise ratio.

In conclusion, sapphire cell systems, as well as other systems to increase the filling factor in the NMR detection coil, allow a detection of pressure effects in peptides and proteins with a much higher sensitivity than that obtained in conventional systems and should allow the application of most modern experiments in multi-dimensional high-resolution NMR spectroscopy at elevated pressures.

3. APPLICATION OF HIGH-PRESSURE NMR SPECTROSCOPY ON PROTEINS

Pressure is an additional external parameter for a solute-solution system. Its increase can induce structural changes in a biomolecule via a volume change of the solute system. In addition to the dynamical information gained by the NMR relaxation measurements the pressure-induced structural changes observed in

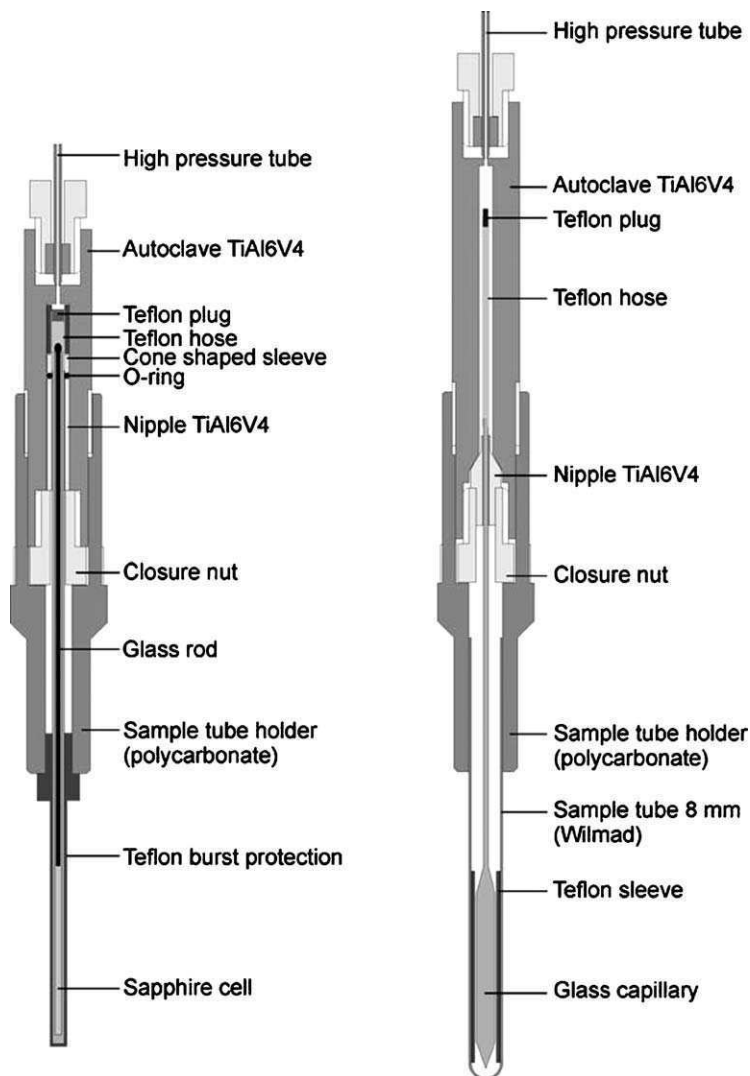


Fig. 2. Borosilicate glass and sapphire high-pressure systems. (Left) Sapphire-cell system with O-ring gasket. The pressurizing fluid and sample are separated by a Teflon shrink hose, which is closed by a Teflon plug. Outer diameter of the sapphire cell is 3.18 mm; inner diameter, 1.73 mm. As burst protection, either a Teflon hose with 0.2- mm wall thickness or an especially manufactured closed Teflon tube (outer diameter, 4.8 mm, inner diameter, 3.5 mm) was used (Right) Glass-cell system with cone-shaped metal sealing. The Duran 50 borosilicate glass capillary is glued into a cone-shaped TiAl₆V₄ nipple. Outer diameter of the glass capillary is 5.0 mm; inner diameter, 1.2 mm. (After ref. 35.)

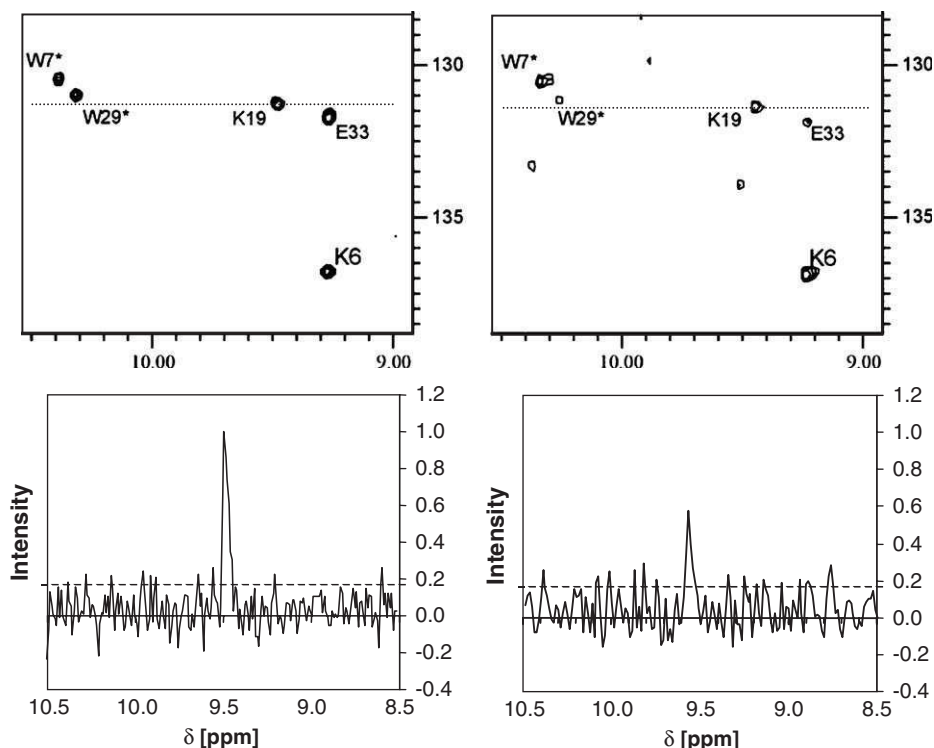


Fig. 3. Sensitivity obtainable in high-pressure borosilicate glass cells and sapphire cells. The sample contained 0.5 mM uniformly ^{15}N -enriched Csp from *Thermotoga maritima* (TmCsp) in 50 mM phosphate buffer (pH 6.5), 20 mM NaCl, 0.2 mM Na-EDTA, 0.1 μM NaN_3 , 10% D_2O and 90% $^1\text{H}_2\text{O}$. Gradient selected sensitivity enhanced ^1H - ^{15}N -HSQC spectra were recorded under identical experimental conditions either in a sapphire cell (left) with an outer diameter of 3.18 mm, inner diameter of 1.72 mm or a borosilicate glass capillary (right) with an outer diameter of 5.0 mm and an inner diameter of 1.2 mm. Data were recorded with a 8 mm inverse triple-resonance probe at 600 MHz proton frequency. Total acquisition time, approximately 2.5 h; resolution, 2048 points in the direct dimension and 256 points in the indirect dimension. The temperature was adjusted to 303 K. (Top) Only a small part of the spectra are shown and plotted at the same contour levels for the two experiments. (Bottom) 1-D trace through the maximum of the H^{N} -signal of K19. (After ref. 35.)

high-pressure NMR spectroscopy will give information about conformational equilibria in proteins and nucleic acids. Akasaka has discussed this in a number of reviews.^{2,18–21} Proteins are sensitive to high pressure since they exhibit “packing defects” and display local melting points for denaturation.¹ The application of pressure induces generally a change in the chemical shift as well as a change in signal intensities. Both parameters, chemical shift and signal intensity, are usually used to analyze the pressure-induced effects.² We will discuss the recent advances made in high-pressure NMR spectroscopy on proteins in the following sections.

3.1. Linear tetrapeptides at pressure between 0.1 and 200 MPa

A prerequisite for a qualitative as well as quantitative analyses of chemical shift data of proteins with elevating pressure is the comparison with standard parameters from random-coil peptides to separate specific structural features from unspecific factors characteristic for a given amino acid residue. Very early in NMR spectroscopy, Bundi and Wüthrich^{52,53} introduced the tetrapeptides Gly–Gly–X–Ala as reference compounds for the random-coil structures. They reported the ^1H -chemical shifts of these peptides in aqueous solution with X representing one of the 20 DNA-encoded amino acids. Later on, ^{13}C - and ^{15}N -chemical shifts of these peptides were published.^{54,55} ^1H - and ^{31}P -chemical shifts are also reported for the phosphorylated forms of these peptides with X = P-His, P-Asp, P-Ser, P-Thr, P-Tyr and P-Hyp.^{56–58}

The interpretation of chemical shift effects induced by pressure in proteins is still in its infancy, although at least some of the changes can be consistently interpreted in structural terms, e.g. the change of the H^{N} -chemical shifts could be associated with the change of the length of intramolecular hydrogen bond under pressure.^{59,60} Arnold *et al.*⁶¹ reported a data basis for the chemical shift changes with pressure for random-coil peptides.

Generally, the pH of a solution is dependent on pressure (for buffer systems with low-pressure coefficients see e.g. ref. 62). Since a pressure-induced pH shift of the solvent can also lead to shifts of the resonances, possible pH-dependent shifts have to be separated from “pure” pressure-induced shifts. For this reason generally buffer solutions, which are very insensitive to pressure, are chosen, i.e. buffers with the least dissociation volume (e.g. Tris, MES, etc.). However, the advantage of solution NMR spectroscopy is the near-physiological environment of proteins, where physiological buffers are mainly based on phosphate compounds.⁶³ In the buffering range of the phosphate buffer, the negative dissociation volume leads to a decrease of about 0.4 pH units when increasing the pressure from 0.1 to 100 MPa.⁶⁴ The pressure dependence of the chemical shifts of the amino acid X in the tetrapeptides Gly–Gly–X–Ala was determined by Arnold *et al.*⁶¹ at two different pH values separated by 0.4 pH units. At ambient pressure the pH of the samples was adjusted to 5.0 and 5.4, respectively, before varying the pressure. In some cases they completed the data by experiments at pH 7.0.

For the tetrapeptide Gly–Gly–X–Ala, the $\text{p}K_{\text{a}}$ values were determined by NMR spectroscopy.⁵³ They are 3.9 for Asp, 4.3 for Glu, 10.3 for Tyr and 11.1 for Lys. The $\text{p}K_{\text{a}}$ value of the C-terminal carboxyl group is approximately 3.3 and varies slightly when the amino acid in position X is exchanged.⁵³ Since only the $\text{p}K_{\text{a}}$ values of the side chains of Glu and His are close to pH 5.0 and 5.4 used in their experiments⁶¹, specific pH effects could only be expected for these two residues.

The chemical shifts usually can be represented as a linear function of pressure for the random-coil peptides, only for a few examples significant deviations from linearity can be observed (Fig. 4), which are the backbone amide proton resonance of glutamate and the side-chain NH – resonance H^{e1} of tryptophan. However, for a complete description of the data, the dependence of the chemical shifts δ on the

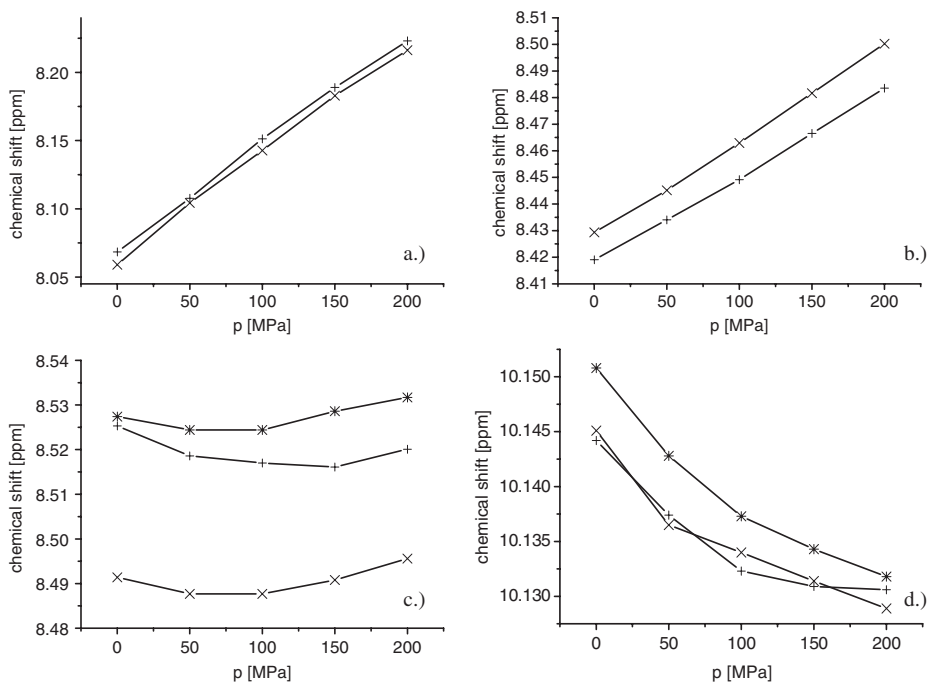


Fig. 4. Pressure dependence of chemical shifts of selected tetrapeptides Gly-Gly-X-Ala. The chemical shifts, δ (ppm), are plotted as function of the pressure p (MPa) at different pH values. The amino acid X is Cys (a), Asp (b), Glu (c), and Trp (d). Measurements were performed at pH 5.0 (x), pH 5.4 (+), and pH 7.0 (*). (After ref 61.)

pressure p was fitted by Arnold *et al.*⁶¹ with two models, with the linear relationship

$$\delta = \delta_o + \delta_{\Delta p}(p - p_o) \quad (3)$$

and a second-order polynomial

$$\delta = \delta_o + \delta'_{\Delta p}(p - p_o) + \delta'_{\Delta 2p}(p - p_o)^2 \quad (4)$$

Here δ_o is the chemical shift at atmospheric pressure $p_o = 0.1$ MPa, $\delta_{\Delta p}$ the linear pressure coefficient, and $\delta'_{\Delta p}$ and $\delta'_{\Delta 2p}$ the first- and second-order pressure coefficients. The chemical shifts δ_o at atmospheric pressure and the linear pressure coefficients δ_{Δ} obtained from a regression analysis are listed in Tables 2 and 3 for all proton resonances of the 20 common amino acids X. In addition, the first- and second-order coefficients defined in Eqs. (3) and (4) are summarized for the backbone amide resonances in Table 2.

In general, the largest pressure-dependent shift changes are observed for the backbone amide protons (see Table 2). The mean linear pressure coefficient $\langle \delta'_{\Delta p} \rangle$ for the backbone amide resonances is 0.38 ppm/GPa with a root mean square deviation of 0.20 ppm/GPa. The mean value is close to the values observed in proteins. The spread in pressure coefficients is clearly larger in proteins than in the

Table 2. Chemical shifts and pressure coefficients of the amide and H^α-protons of amino acid X in Gly–Gly–X–Ala at 305 K in aqueous solution at pH 5.4

X3	First-Order Model			Second-Order Model			First-Order Model		
	δ_0^{HN} (ppm)	$\delta_{\Delta p}^{\text{HN}}$ (ppm/GPa)		δ_0^{HN} (ppm)	$\delta_{\Delta p}^{\text{HN}}$ (ppm/GPa)	$\delta_{\Delta p^2}^{\text{HN}}$ (ppm GPa ⁻²)	$\delta_0^{\text{H}\alpha}$ (ppm)	$\delta_{\Delta p}^{\text{H}\alpha}$ (ppm)	
Ala	8.283	0.537	±0.018	8.281	0.63	−0.44	4.326	−0.080	±0.024
Arg	8.376	0.338	±0.006	8.376	0.35	−0.06	4.361	−0.077	±0.006
Asn	8.503	0.307	±0.018	8.504	0.26	0.34	4.720	−0.046	±0.006
Asp	8.418	0.323	±0.006	8.419	0.29	0.18	4.634	0.026	±0.006
Cys	8.070	0.781	±0.024	8.409	0.38	0.010	4.565	0.010	±0.006
Gln	8.440	0.335	±0.012	8.440	0.33	0.05	4.349	−0.068	±0.006
Glu	8.522	−0.026	+0.024	8.521	−0.15	0.53	4.293	0.110	±0.012
Glu ^{met}	8.714	0.300	+0.006	8.709	0.53	−0.98			
Gly	8.403	0.133	±0.006	8.403	0.12	0.05	3.959	0.060	±0.012
His	8.367	0.502	±0.018	8.364	0.60	−0.51	4.713	−0.020	±0.006
Ile	8.204	0.501	±0.024	8.200	0.63	−0.66	4.189	−0.058	±0.036
Leu	8.319	0.436	±0.030	8.317	0.53	−0.47	4.345	−0.088	±0.006
Lys	8.403	0.337	±0.018	8.403	0.36	−0.25	4.301	−0.075	±0.006
Met	8.428	0.383	±0.018	8.426	0.45	−0.34	4.479	−0.089	±0.012
Phe	8.301	0.489	±0.018	8.301	0.47	0.10	4.614	−0.042	±0.006
Pro _{cis}							4.568	0.024	±0.006
Pro _{trans}							4.416	−0.007	±0.006
Ser	8.356	0.396	±0.006	8.352	0.48	−0.34	4.495	0.010	±0.006
Thr	8.251	0.633	±0.018	8.249	0.72	−0.44	4.353	0.016	±0.006
Trp	8.181	0.457	±0.018	8.178	0.57	−0.57	4.652	−0.068	±0.006
Tyr	8.194	0.336	±0.006	8.193	0.38	−0.20	4.590	−0.011	±0.006
Val	8.191	0.517	±0.018	8.189	0.61	−0.45	4.146	−0.035	±0.006

Glu^{met} are the chemical shifts and pressure coefficients taken from the amide protons of Gly–Gly–Glu–Ala methyl. (Modified after ref. 62.)

Table 3. Chemical shifts and pressure coefficients of the side-chain protons of amino acid X in Gly–Gly–X–Ala at 305 K in aqueous solution at pH 5.4. (After ref. 62.)

X3	Atom	Atom			Atom	Atom			
		δ_0 (ppm)	$\delta_{\Delta p}$ (ppm/GPa)			δ_0 (ppm)	$\delta_{\Delta p}$ (ppm/GPa)		
Ala	H $^{\beta 2}$	1.400	−0.031	± 0.012					
Arg	H $^{\beta 2}$	1.885	−0.097	± 0.006	H $^{\gamma 2/\gamma 3}$	1.661	−0.083	± 0.006	
	H $^{\beta 3}$	1.773	−0.035	± 0.006	H $^{\delta 2/\delta 3}$	3.211	−0.082	± 0.006	
					H $^{\epsilon}$	7.236	−0.204	± 0.012	
Asn					H $^{\eta 11/\eta 12/\eta 21/\eta 22}$	6.680	−0.090	± 0.042	
	H $^{\beta 2}$	2.842	0.009	± 0.006	H $^{\delta 21}$	7.573	0.214	± 0.012	
	H $^{\beta 3}$	2.755	0.032	± 0.006	H $^{\delta 22}$	6.966	0.417	± 0.006	
Asp	H $^{\beta 2}$	2.729	0.128	± 0.006					
	H $^{\beta 3}$	2.592	0.089	± 0.006					
Cys	H $^{\beta 2}$	2.977	−0.050	± 0.012					
	H $^{\beta 3}$	2.926	0.014	± 0.042					
Gln	H $^{\beta 2}$	2.124	−0.071	± 0.006	H $^{\gamma 2/\gamma 3}$	2.380	−0.032	± 0.006	
	H $^{\beta 3}$	2.000	−0.023	± 0.006	H $^{\epsilon 21}$	7.532	0.260	± 0.006	
					H $^{\epsilon 22}$	6.929	0.395	± 0.012	
Glu	H $^{\beta 2}$	2.086	−0.023	± 0.006	H $^{\gamma 2/\gamma 3}$	2.301	0.089	± 0.006	
	H $^{\beta 3}$	1.949	−0.077	± 0.018					
His	H $^{\beta 2}$	3.284	−0.025	± 0.006	H $^{\delta 2}$	7.311	0.089	± 0.006	
	H $^{\beta 3}$	3.210	0.006	± 0.006	H $^{\epsilon}$	8.546	0.243	± 0.018	
Ile	H $^{\beta}$	1.872	0.027	± 0.018	H $^{\gamma 12}$	1.458	−0.243	± 0.024	
					H $^{\gamma 13}$	1.190	−0.065	± 0.018	
					(H $^{\gamma 2}$) $_3$	0.923	−0.058	± 0.006	
					(H $^{\delta 1}$) $_3$	0.870	−0.078	± 0.006	
					H $^{\gamma/\beta 2/\beta 3}$	1.626	−0.041	± 0.018	
Leu	H $^{\gamma/\beta 2/\beta 3}$				(H $^{\delta 1}$) $_3$	0.931	−0.060	± 0.006	
					(H $^{\delta 2}$) $_3$	0.888	−0.061	± 0.006	
					H $^{\gamma 2/\gamma 3}$	1.437	−0.174	± 0.030	
					H $^{\delta 2/\delta 3}$	1.688	−0.109	± 0.006	
Lys	H $^{\beta 2}$	1.845	−0.096	± 0.012	H $^{\epsilon 2/\epsilon 3}$	3.004	−0.073	± 0.006	
		H $^{\beta 3}$	1.772	−0.075	± 0.012	(H $^{\xi}$) $_3$	7.260	0.368	± 0.018
						(H $^{\epsilon}$) $_3$ H $^{\beta 2}$	2.109	−0.058	± 0.006
Met	(H $^{\epsilon}$) $_3$ H $^{\beta 2}$	2.109	−0.058	± 0.006	H $^{\gamma 2/\gamma 3}$	2.590	−0.079	± 0.006	
		H $^{\beta 3}$	2.013	−0.007	± 0.006	H $^{\delta 1/\delta 2}$	7.287	−0.029	± 0.006
Phe	H $^{\beta 2}$	3.121	−0.035	± 0.006	H $^{\epsilon 1/\epsilon 2}$	7.386	0.015	± 0.006	
		H $^{\beta 3}$	3.056	0.031	± 0.006	H $^{\xi}$	7.328	0.025	± 0.006
						H $^{\gamma 3}$	1.906	−0.103	± 0.006
Pro $_{cis}$	H $^{\beta 2}$	2.384	−0.056	± 0.006	H $^{\beta 3/\gamma 2}$	2.188	−0.083	± 0.006	
		H $^{\beta 3/\gamma 2}$	2.188	−0.083	± 0.006	H $^{\delta 2/\delta 3}$	3.558	−0.101	± 0.006
						H $^{\delta 2/\delta 3}$	3.632	−0.077	± 0.006
Pro $_{trans}$	H $^{\beta 2}$	2.266	−0.020	± 0.006	H $^{\beta 3/\gamma 2/\gamma 3}$	2.015	−0.082	± 0.006	
		H $^{\beta 3/\gamma 2/\gamma 3}$	2.015	−0.082	± 0.006				
Ser	H $^{\beta 2/\beta 2}$	3.874	−0.024	± 0.006					
Thr	H $^{\beta}$	4.241	−0.003	± 0.006	(H $^{\gamma 2}$) $_3$	1.213	−0.036	± 0.006	
Trp	H $^{\beta 2}$	3.281	−0.047	± 0.012	H $^{\delta 2}$	7.271	0.059	± 0.006	
		H $^{\beta 3}$	3.268	0.026	± 0.006	H $^{\epsilon 1}$	10.141	−0.071	± 0.012

(continued)

Table 3. Continued

X3	Atom				Atom			
		δ_0 (ppm)	$\delta_{\Delta p}$ (ppm/Gpa)			δ_0 (ppm)	$\delta_{\Delta p}$ (ppm/GPa)	
Tyr	$H^{\beta 2}$	3.120	−0.050	± 0.006	$H^{\epsilon 3}$	7.654	−0.078	± 0.006
					$H^{\zeta 2}$	7.179	−0.011	± 0.006
					$H^{\zeta 3}$	7.515	0.021	± 0.006
					$H^{\eta 2}$	7.251	−0.006	± 0.006
					$H^{\delta 1/\delta 2}$	7.146	−0.019	± 0.006
Val	$H^{\beta 3}$	2.915	0.033	± 0.006	$H^{\epsilon 1/\epsilon 2}$	6.849	0.000	± 0.006
	H^{β}	2.114	−0.026	± 0.006	$(H^{\gamma 1})_3 (H^{\gamma 2})_3$	0.943	−0.068	± 0.006

random-coil peptides, which vary between the minimum value 0.0 ppm/GPa (Glu) and 0.78 ppm/GPa (Cys). Whereas for amide protons in proteins in the average downfield shifts are observed with increasing pressures, for the H^{α} -resonances usually upfield shifts are observed. In our random-coil peptides the average shift is −0.025 ppm/GPa and ranges from −0.08 (Ala) to 0.11 ppm/GPa (Glu). Again the average values in native proteins are close to that of the random-coil peptides but the variation of the pressure coefficients is much larger.

For the side-chain resonances, Arnold *et al.*⁶¹ found rather small pressure-induced shifts. The only exception are side-chain protons, which can be engaged in hydrogen bonds and are part of polar or charged groups indicative for hydrogen bonding to water. Interestingly, side-chain amide protons of Asn and Gln show different pressure coefficients for their two stereospecifically different protons. The pro-Z proton shows always a larger dependence on pressure (Table 2). In HPr from *S. carnosus* some of the side-chain amide protons were stereospecifically assigned. At 298 K, the mean linear pressure coefficients are 0.27 and 0.53 ppm/GPa for the pro-E and the pro-Z protons, respectively.⁶⁵ The reason for this different behaviour is not known but the random-coil data show that they are not due to specific structural features of the HPr-protein. In most proteins the pressure-induced changes of chemical shifts can be fitted well by a linear dependence, but there are also exceptions where clearly nonlinear dependences were observed. They serve as indicators for a conformational equilibrium shifted by pressure. In the random-coil peptides the nonlinearities were vanishing for most of the residues showing that larger deviations from the linearity do not occur in unstructured peptides. Only the backbone amide of Glu and the side-chain NH of Trp showed some nonlinear behaviour (Fig. 4). However, the quantitative analysis shows that the contribution is very small (Tables 2 and 3). For glutamate the first-order coefficient is very small independent of the pH. This is probably due to internal hydrogen bonds of the carboxyl group to peptide amides. Indeed, the methylation of the C-terminal carboxyl group, which has a pK_a -value of approximately 3.3 led to a disappearance of the nonlinear pressure dependence indicating an interaction between the Glu $^1H^N$ and the C-terminal Ala in the nonmethylated form (see Table 2).

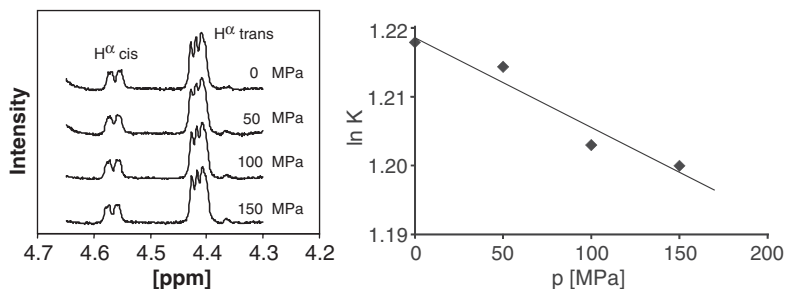


Fig. 5. Left: 1-D ^1H spectra of the H^α protons of proline in the tetrapeptide GGPA. The sample contained 5 mM GGPA in 50 mM Tris/HCl buffer (pH 7.0) and 0.1 mM DSS in 99% D_2O . (Left) Part of 1D ^1H -NMR spectra at various pressures showing the H^α signal of proline in *cis*- and *trans*- conformation, respectively. The pressure was changed from 0.1 to 150 MPa in steps of 50 MPa at a temperature of 305 K. (Right) The logarithm of the equilibrium constant K (the ratio of the integrals of the signals of the *trans*- to the *cis*-conformer) is plotted as function of pressure p . (After ref 35.)

The peptide bond involving the imino group of a proline residue usually exists in *cis*- and *trans*-conformations. In NMR spectroscopy, the two conformations can be distinguished on the basis of their characteristic chemical shifts. From the integration of their resonance lines the relative populations and hence the equilibrium constant $K = [\textit{trans}]/[\textit{cis}]$ can be determined. At 0.1 MPa and 305 K, $K = 3.381 \pm 0.008$. Increasing pressure leads to a higher population of the *cis*-isomer of the peptide bond. From the dependence of K on the pressure p the change of the partial molar volume ΔV^0 can be calculated as -0.25 mL/mol at 305 K for the transition from the *trans*-configuration to the *cis*-configuration (Fig. 5). A possible explanation for the effect found is the breakage of two H-bonds, which are forming γ -turns⁶⁶ in the short peptide GGPA between the carboxyl C and the amide N of the C-terminal alanine and the second glycine but may also represent differences of the partial charges of the peptide bond itself in the two isomers.

The pressure-dependent shifts in the model-peptides Gly–Gly–X–Ala are relatively small as to be expected for nonstructured peptides but are characteristic for specific atoms in a given amino acid. The largest shift changes are observed for protons of groups involved in hydrogen bonding to water. The data presented here provide a solid basis for the interpretation of pressure-induced chemical shift changes in proteins and allow to separate specific effects as pressure-induced conformational changes of the protein from unspecific effects caused by the pressure-dependent direct interaction between the solvent molecules and solvent-exposed residues.

3.2. Pressure-stability of phospholipid bicelles: Measurement of residual dipolar couplings

As pointed out before, the strongly restricted sample volume (usually $< 50 \mu\text{L}$) together with the low filling factor of the coil is a major problem in high-pressure NMR spectroscopic studies of protein solutions. Thus, due to the relatively poor

signal-to-noise ratio, the detection of NOESY spectra of sufficient quality for structural work is impossible, since the concentration of many protein solutions is limited to values of 1–3 mM. Residual dipolar couplings (RDCs) are used very often in NMR spectroscopic protein structure determination.^{67–69} RDCs are capable of replacing NOE information to a very high extent.⁷⁰ In solutions of diamagnetic proteins, RDCs are commonly induced by the addition of magnetically orienting media to the solutions. Phospholipid bicelles are frequently used as orienting medium, e.g. in mixtures of dimyristoylphosphatidylcholine (DMPC) and dihexanoylphosphatidylcholine (DHPC). Brunner *et al.*⁷¹ investigated the pressure stability of this medium and demonstrated the possibility to measure RDCs in high-pressure experiments.

Brunner *et al.*⁷¹ analyzed mixtures, which finally contained DMPC, DHPC, and CTAB in a molar ratio of $q:1:0.1$ ($3 \leq q \leq 3.5$). The total lipid concentration (DMPC+DHPC) of the thus prepared stock solution was 15 wt.-%. They monitored the pressure stability of DMPC/DHPC bicelles by measuring the ^2H NMR signals of D_2O added to the solutions. They measured the quadrupole splitting Δ for a mixture with $q = 3.3$ as a function of pressure at various temperatures. The result of this measurement is summarized in Fig. 6. To evaluate the pressure stability of bicelles, they defined the ‘decay pressure’, $p_{1/2}$, at which the ^2H NMR doublet splitting, Δ , drops down to 1/2 of its initial value (see Fig. 6B). It is remarkable that the pressure stability of the bicelles strongly increases with the temperature. For $T > 335\text{ K}$, the oriented phase remains stable up to ca. 200 MPa. Brunner *et al.*⁷¹ noted that the bicelles were extremely temperature-stable (up to ca. 375 K, the maximum temperature applied in their experiments). The most likely reason for the extraordinarily high-temperature stability of DMPC/DHPC bicelles observed in their experiments is the addition of CTAB to the solutions. In order to demonstrate the feasibility of measuring RDCs under high pressure, ^1H -coupled ^1H - ^{15}N HSQC experiments of *TmCsp* in a bicellar solution were performed.⁷¹ Fig. 7A and B show a selected region of the ^1H -coupled ^1H - ^{15}N HSQC spectrum of 1 mM *TmCsp* in isotropic and bicellar solution, respectively, measured at 336 K and a pressure of 150 MPa. The residual ^1H - ^{15}N dipolar couplings are the difference between the effective coupling constants observed in isotropic and bicellar solution. The presence and long-term stability of magnetically oriented phospholipid bicelles were detected by ^2H NMR spectroscopy before and after the acquisition of the HSQC spectrum. The doublet splitting, Δ , remained constant within the experimental error. The common phospholipid bicelle are highly pressure-stable especially at elevated temperatures. This allows to make use of RDCs for the study of structural changes induced by high pressure in proteins. Since NOEs are usually difficult to observe in high-pressure NMR spectroscopy, the measurement of the RDCs can provide an independent source of direct quantitative structural information.

3.3. Pressure-stabilized functional important conformers

In general, protein function involves fluctuations of the protein structure, which can be probed by high-pressure NMR spectroscopy. Chemical shifts have been used in a

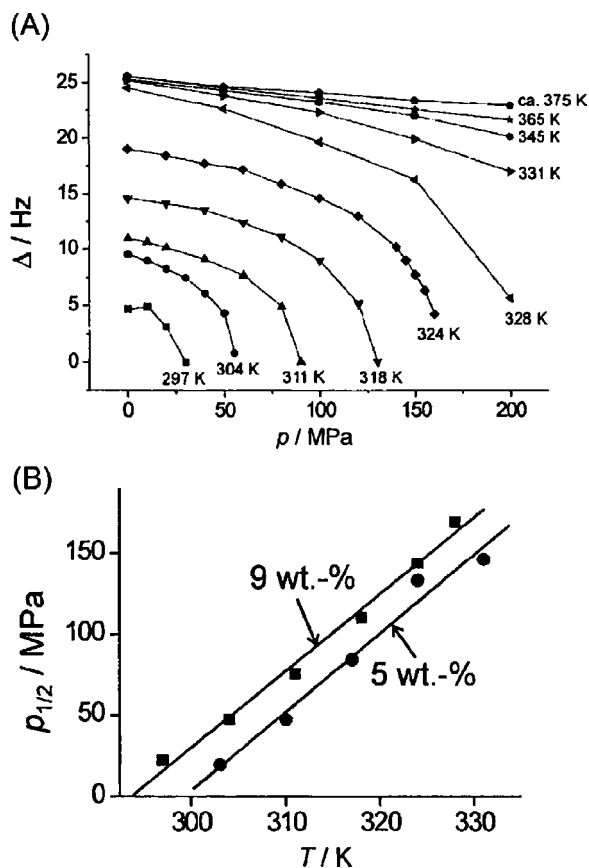


Fig. 6. (A) ^2H NMR doublet splitting, Δ , as a function of pressure, p , observed for D_2O in a mixture containing 9 wt.-% DMPC/DHPC bicelles ($q = 3.3$, CTAB-doped) measured at various temperatures. (B) 'Decay pressure,' $p_{1/2}$, at which the ^2H NMR doublet splitting, Δ , drops down to 1/2 of its initial value as a function of temperature for 5 wt.-% (filled circles) and 9 wt.-% (filled squares) total lipid concentration. (After ref. 71.)

number of proteins to report conformational changes under pressure. A reversible change of chemical shifts with pressure was found in apomyoglobin,⁷² α -lactalbumin,⁷³ β -lactoglobulin,⁷⁴ BPTI,^{59,75–77} DHFR,^{78,79} gurmarin,⁸⁰ HPr,^{66,81,82} the immunoglobulin-binding domain of protein G⁶⁰, lysozyme,^{83–85} melittin α -helix,⁸⁶ P13^{MTCP1},⁸⁷ prion,^{43,45,46} RalGDS–RBD,⁸⁸ the RalGDS–RBD–Rap1A complex⁸⁹ and ubiquitin.^{90–92} As an example for a typical 2-D NMR spectrum see the ^1H – ^{15}N HSQC spectrum of Ral-GDS (Fig. 8). Each amino acid residue gives a cross-peak at a specific position (chemical shift) (Fig. 8). The response of the protein to pressure is detected as continuous shifts of individual cross-peaks (or ^1H , ^{15}N , or ^{13}C signals) (see Fig. 8). Microscopic effects of pressure include compression of hydrophobic core,⁸³ hydrogen bond shortening,^{59,60,75} change of torsion angles,⁷⁵ compression of the vicinity of cavities⁸⁴ and effects on protein dynamics.^{76,93} The amide ^1H shift is

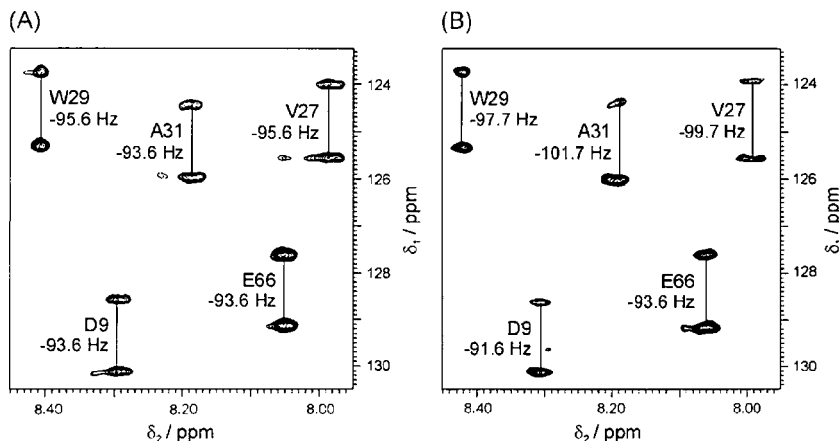


Fig. 7. Selected region from the ^1H -coupled ^1H - ^{15}N HSQC spectrum of 1 mM *TmCsp* in isotropic solution (A) and in a solution containing 5 wt.-% DMPC/DHPC bicelles ($q = 3.0$, CTAB-doped) measured at 336 K and a pressure of 150 MPa. The effective ^1H - ^{15}N coupling constant giving rise to the doublet splitting in indirect spectral dimension (δ_1) is given together with the assignment of the signals. (After ref 71.)

mainly determined by the magnetic anisotropy from neighboring peptide groups and is closely correlated with the hydrogen-bonding state of the NH group.^{59,60,75–77} The ^{15}N -pressure shift depends on changes in the local electronic environment, and gives a qualitative measure of fluctuation in torsion angles φ , ψ and χ .⁷⁶ The magnitude of the shift reflects the extent of the change in the average conformation at each site. The magnitude of the pressure-induced chemical shift in Fig. 8 may be used as a qualitative measure of the conformational fluctuation at that site.⁸⁸ In BPTI,^{59,75–77} gurmarin,⁸⁰ and the immunoglobulin-binding domain of protein G⁶⁰ as well as in simple helical peptides,^{86,94} the ^1H and ^{15}N chemical shifts of most amide groups are surprisingly linear with pressure. The strong linear behaviour of the chemical shift is known from peptide studies described above.⁶¹ The observation of a linear dependence of ^1H and ^{15}N chemical shifts on pressure indicates that no structural transition occurs and the experiment monitors relatively simple compression within the folded state. In contrast, many proteins show nonlinear pressure shifts of the amide ^1H and ^{15}N chemical shifts, including apomyoglobin,⁷² α -lactalbumin,⁷³ β -lactoglobulin,⁷⁴ DHFR,^{78,79} HPr,^{65,82} P13^{MTCP1},⁸⁷ RalGDS-RBD,⁸⁸ the RalGDS-RBDRap1 A complex,⁸⁹ prion^{43,45,46} and ubiquitin,^{90–92} including a part of lysozyme.^{83,84} The nonlinearity can only be explained by shifting low-lying excited states with a nonzero volume change to the more compact state of the solute-solvent system with increasing pressure^{18–20} (Fig. 1B). As Akasaka and Li¹⁸ pointed out, the extent of nonlinearity as a sum over all the amide residues of a protein is strongly correlated with the density of the cavities within the interior of the protein; the larger the density of cavities in a protein, the larger the nonlinearity of chemical shifts for the protein.¹⁸ Low-lying excited states seem to be associated with hydration of water-accessible cavities. Many of these proteins even undergo local unfolding at higher pressures in

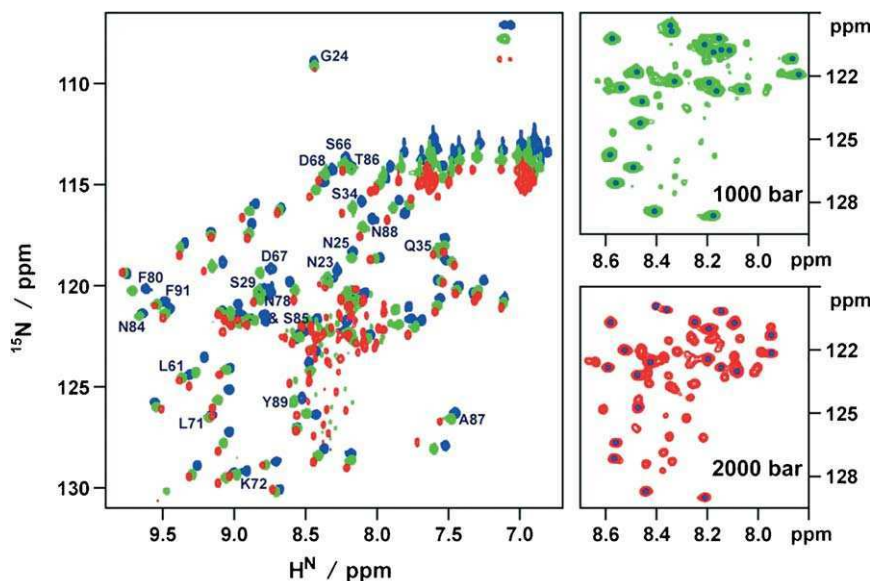


Fig. 8. Pressure effects observable in ^1H - ^{15}N HSQC spectra of RalGDS-RBD (residues 11–97). Data were recorded at 297 K and various pressures. (a) Overview plot showing the backbone and side-chain amide cross-peaks at 3 MPa (30 bar, blue), 100 MPa (1000 bar, green), and 200 MPa (2000 bar, red). (b) and (c) Close up views of a selected region of the ^1H - ^{15}N HSQC spectra recorded at 100 MPa (1000 bar, b) and 200 MPa (2000 bar, c). The cross-peaks corresponding to the native structure are labelled by blue dots. (After ref. 89.)

regions close to the cavities. Currently it is discussed that these low-lying excited states and the associated conformational dynamics are closely correlated with the functions of these proteins.

Such structural or shape fluctuations can be probed by a quantitative analysis of the pressure-dependent NMR spectral changes. Changes in NOE intensities were observed in most side-chain protons of hen lysozyme⁸³ and BPTI^{59,75–77} at 200 MPa, indicating rearrangements in side-chain packing through nonoptimized packing density or changes in tertiary structure under pressure. Williamson *et al.*⁸⁵ found indications in hen egg white lysozyme (HEWL) that the α -helical domain is compressed by approximately 1% at 200 MPa, as a result of tighter packing of helices. On the other hand, the β -domain undergoes both expansion and compression, resulting in almost no overall compression. One finding is that fluctuations are larger around water-containing cavities. It seems that the observed fluctuations are coupled with water molecules penetrating into and out of cavities and are evolutionarily designed to facilitate diffusion-controlled reactions like substrate binding and/or product dissociation.

It has been shown that a number of proteins such as apomyoglobin,⁷² α -lactalbumin,⁷³ β -lactoglobulin,⁷⁴ DHFR,^{78,79} P13^{MTCP1},⁸⁷ prion,^{43,45,46} RalGDS-RBD⁸⁸ and ubiquitin,^{90–92} are unfolding within 200–400 MPa. Some of them start to partial

unfold^{43,46,74,78,88,89} producing a variety of intermediately folded conformers, which include locally unfolded conformers, the so-called ‘molten globule (MG),’ and totally unfolded conformers. Such a local unfolding is normally detected by the appearance of two separate groups of cross-peaks in 2-D NMR spectra (as for RalGDS–RBD, see Fig. 8). Whether the conformational change involves unfolding, can be judged from the chemical shift position of the cross-peaks after the conformational change (Fig. 8). As seen in the case of RalGDS–RBD (see Fig. 8), the relative intensities of each pair of the cross-peaks allow us to calculate an equilibrium constant (and ΔG) at individual amino acid sites as a function of pressure, and the stability difference (ΔG_0) and the volume difference (ΔV_0) between the two conformers are obtained at 0.1 MPa.

In apomyoglobin in the pressure range from 3 to 300 MPa,⁷² the equilibrium is shifted from N (native) to I (intermediate), from I to MG, and from MG to U (unfolded) in sequence, as the pressure is increased. This means that the partial molar volume V of apomyoglobin decreases in the following order: $N > I > MG > U$. This order coincides with the decreasing order of the tertiary structure (“conformational order”) of apomyoglobin.⁷² In various other globular proteins examined at or below physiological temperatures, there is a parallel between the partial molar volume V of a protein and its conformational order, suggesting that this correlation is common to globular proteins. Akasaka and coworkers have put this into a theorem: The partial molar volume of a protein decreases in parallel with the decrease in its conformational order⁷² (for review see refs. 18,19,21).

As pointed out before, any equilibrium in a population of conformers of proteins, including low-lying excited states, connected with a nonzero volume change will be shifted toward the more compact state by the application of hydrostatic pressure. Such low-lying excited states have been found by high-pressure NMR in a number of proteins having important cellular functions, such as apomyoglobin,⁷² α -lactalbumin,⁷³ β -lactoglobulin,⁷⁴ DHFR,^{78,79} HPr,^{65,95} prion,^{43,45,46} RalGDSRBD,^{88,89} P13^{MTCP188} and ubiquitin.^{90–92} We will discuss in the following these intermediate conformers, which are apparently designed by nature for functional purposes.

Kitahara *et al.*^{78,79} were investigating dihydrofolate reductase (DHFR), which catalyses a reduction of dihydrofolate to tetrahydrofolate with the aid of a cofactor NADPH. In the folate-bound form of DHFR from *Escherichia coli*, they observed only one cross-peak for each amino acid in the ^{15}N – ^1H 2-D NMR spectrum at 0.1 MPa; but with increasing pressure, some of them split into two cross-peaks. The new cross-peaks increase as the old ones decrease in intensity with increasing pressure. Kitahara, *et al.*⁷⁸ showed that two conformers coexist at all pressures and that the population of the rare conformer increases to $\sim 50\%$ at 200 MPa. They concluded that the rare conformer has a smaller partial molar volume than the first ($\Delta V_0 = -25 \text{ mL/mol}$ at 15°C) and predicted the population of the rare conformer at 0.1 MPa to be $\sim 11\%$. The difference in the two conformers is visible in the hinge parts of the M20 loop, the C-helix, and the F-helix, surrounding the cofactor-binding pocket. They concluded from linewidth analysis that the folate-bound DHFR undergoes a hinge motion between the “closed” and “open” forms of the NADPH-binding pocket at a rate of $< 20/\text{s}$. The fluctuation of the M20 loop to the open conformer seemed to be necessary for the cofactor NADPH to bind.

In a separate NMR measurement at ambient pressure, Kitahara *et al.*⁷⁸ could show the presence of signals of the open conformer nearly at the expected population of (~13% compared to ~11%) at positions of predicted chemical shifts. The open or ligand awaiting conformation is actually sampled by the proteins under native condition, which would be a kind of trigger conformation for an enzyme to bind a substrate, a cofactor, or an allosteric effector. Since the open conformers are meant to be minor, as they are more prone to ligand binding than the closed conformers, these open conformers in various enzymes can be stably trapped and structurally characterized under pressure.

Another example where an open conformer was found at high pressure is bovine β -lactoglobulin,⁷⁴ which binds a fatty acid within the central cavity.^{96,97} Kuwata *et al.*⁷⁴ analysed the pressure dependencies of ^1H and ^{15}N chemical shifts and cross-peak intensities between 3 and 200 MPa. Some ^1H - ^{15}N cross-peaks were found to be lost with increasing pressure, showing local conformational disorder. The analysis of the cross-peak intensities as a function of pressure suggests large-amplitude conformational fluctuations in the protein, represented by disorder in either side of the β -barrel.⁷⁴ These include the hydrophobic core side (βF - βH) and the noncore side (βB - βE) and are producing intermediates I_1 and I_2 .⁷⁴ The intermediates represent higher-energy conformers with $\Delta G_0 = 6.5 \pm 2.0$ and 4.6 ± 1.3 kcal/mol (27.2 ± 8.4 and 19.3 ± 5.4 kJ/mol) and $\Delta V_0 = -90.0 \pm 35.2$ and -57.4 ± 14.4 mL/mol.⁷⁴ The analysis of high-pressure NMR measurements revealed that β -lactoglobulin has large-amplitude fluctuations leading to intermediates I_1 and I_2 with partially disordered barrel structures. Such intermediates could be necessary for the interaction with small hydrophobic ligands such as palmitic acid, which has to enter into the central cavity of the β -barrel.⁷⁴

In the case of ubiquitin, Kitahara *et al.*^{90,91} used ^1H - ^{15}N 2D NMR spectroscopy at elevated pressures from 0.1 to 370 MPa and found that it fluctuates between four major conformers (N_1 , N_2 , I and U) at pH 4.5 at 0°C .⁹¹ From the analysis of chemical shifts and cross-peak intensities as a function of pressure, they calculated that the partial molar volume decreases in the following way: $\text{N}_1 > \text{N}_2 > \text{I} > \text{U}$ (ΔV of -24 , -58 and -27 mL/mol, for each step), and that the C-terminal domain close to the C-terminal reactive site is partially disordered in the conformer N_2 and fully disordered in the conformer I .

An elegant alternative to investigating multiple misfolding pathways of the proteins involved in neurodegenerative diseases with denaturing agents is applying hydrostatic pressure, which allows studying intermediate forms in the folding pathway different from those obtained by denaturing agents. As one example the prion protein can be viewed. According to the 'protein only' hypothesis, prions as causative agents of TSEs in humans and animals are principally composed of the infectious isomer, PrP^{Sc} , of the cellular prion protein, PrP^{C} . The conversion and thus the propensity of PrP^{C} to adopt alternative folds leads to the species-specific propagation of the disease. Therefore, knowledge about the structure of the metastable intermediates of PrP^{C} and the conformational equilibrium that is involved are critical for understanding the underlying mechanism. Kuwata *et al.*⁴³ carried out ^1H - ^{15}N 2D NMR measurements under variable pressure and temperature on

Syrian hamster prion protein *shaPrP*(90–231), and found a metastable intermediate conformer of $\text{PrP}^c(\text{PrP}^I)$ in which helices B and C are preferentially disordered. They found that the intermediate PrP^I coexists with normal PrP^c at a population of $\sim 1\%$ under a closely physiological condition (pH 5.2 and 30°C). Kremer *et al.*⁴⁶ investigated the pressure dependence of two isoforms of the human prion protein. They had to carry out ^1H – ^{15}N TROSY experiments developed for high-molecular-weight proteins,^{98–101} suggesting that an aggregating mechanism was leading to very broad NMR signals. A thorough analysis of the data led them to conclude at least for the human prion protein a two-step behaviour for the interconversion between the cellular form and the intermediate form. One process on the fast timescale could be detected, which clustered to the residues in the core of the helices II and III, and a slow exchange process leading to the disappearance of the signals involving the loop between strand $\beta 1$ and helix $\alpha 1$ (Fig. 9). They found that the fast process was conferred to a ΔG_0 of about 3.2 kJ/mol and the slow process to a ΔG_0 of 14.2 kJ/mol leading to the suggestion of the following folding funnel for the human protein (Fig. 10).

Pressure is known as the method of choice to dissociate dimers, tetramers and oligomers into monomers.^{1,41,102} Recently, Foguel and Silva⁴¹ discussed pressure results on the amyloidogenic proteins TTR, ataxin, α -synuclein and the prion protein. They concluded that stable intermediates can be achieved by utilizing appropriate pressure and temperature conditions. In combination with high-resolution multidimensional NMR spectroscopy such intermediates can be characterized in atomic detail. Tachibana and coworkers^{103,104} showed for the disulphide-deficient lysozyme variant (OSS) that an amyloid-like fibril assembled at ambient pressure can be dissociated through elevated pressure. OSS is unfolded in the absence of denaturant and forms a soluble assembly with a sedimentation coefficient of 17 S and high amount of intermolecular β -sheet structure.¹⁰⁴ They showed that this material spontaneously forms amyloid-like fibrils and that pressure can dissociate the 17 S assembly of OSS, leading to a monomeric intermediate observable by NMR spectroscopy.¹⁰⁴

Pressure-jump studies were carried out to characterize the kinetics of the folding–unfolding processes in proteins with a whole number of different spectroscopic methods^{105,106} (for review see 107 and 108). In case of the small protein $\text{p13}^{\text{MTCP1}}$, Kitahara *et al.*⁸⁷ were able to report a real-time observation of pressure-jump unfolding kinetics by $2\text{D}^1\text{H}$ – ^{15}N NMR spectroscopy due to its very long relaxation times at high pressure revealed by fluorescence studies. Within the dead-time (50 min for 2-D NMR^{87}) after the pressure jump to 300 MPa, a series of ^{15}N – ^1H HSQC spectra of unfolding of $\text{p13}^{\text{MTCP1}}$ was measured with a midpoint of 70 min accumulation time while the native conformer changed to that of alternate folded conformers. In a separate equilibrium high-pressure NMR experiment, Kitahara *et al.*⁸⁷ could show that the conformers observed in the pressure-jump kinetic experiments were identical to the conformers found in equilibrium at this pressure. In addition, Kitahara and Akasaka⁹¹ could demonstrate for ubiquitin the close identity of a pressure-stabilized folding intermediate with a kinetic intermediate found in a pulse-labeling ^1H – ^2H exchange NMR study.

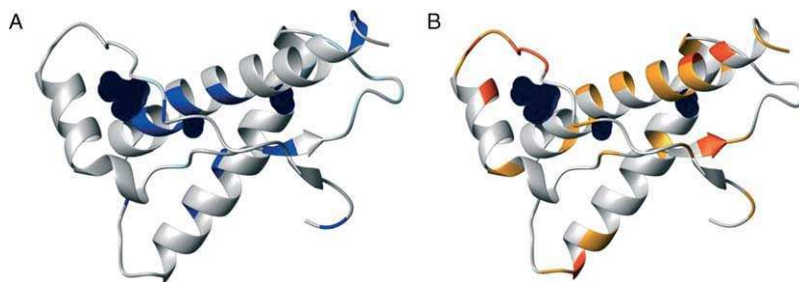


Fig. 9. Ribbon representation of the NMR structure of the human prion protein isoform *huPrP*(121–230) (taken from PDB 1QM2). Residues conferring to the fast process with molar free energy values at ambient pressure (ΔG_0) of about 3.2 kJ/mol are coloured blue (A) and residues involved in the slow process with molar free energy values at ambient pressure (ΔG_0) of about 14.2 kJ/mol coloured orange and red (B). Residues with very low-pressure stability (ΔG_0 lower than the mean value plus one standard deviation) are coloured red. Cavities were calculated using a probe radius of 0.12 nm. (After ref 46.)

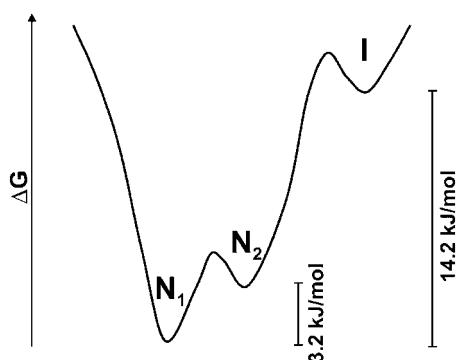


Fig. 10. Schematic representation of the energy landscape of folding for the human prion protein isoform *huPrP*(121–230) as revealed by results from ^1H – ^{15}N TROSY spectra at elevated pressures. (After ref. 46.)

3.4. Protein structures under pressure

A prerequisite for structural work on proteins is the detection of NOESY spectra of sufficient quality. In high-pressure NMR spectroscopy, a protein concentration up to 10 mM is necessary for high-quality NOESY spectra due to the restricted volume in the high-pressure glass cell. For ubiquitin, a small and highly water-soluble protein up to 10 mM, Kitahara *et al.*⁹² were able to determine high-resolution NMR structures at 3 and at 300 MPa. They were able to pinpoint down the structural changes resulting from the conformational fluctuations already characterized

before.⁹¹ In Fig. 11, A–E, a ribbon diagram and a surface representation of the two structures (PDB-code: 3 MPa, 1V80; 300 MPa, 1V81) is shown. These structures represent NMR snapshots of the fluctuating ubiquitin structure. Kitahara *et al.*⁹² concluded from the comparative structural analysis of ubiquitin at the two pressures that there is substantial change in one localized region of the protein involving the C-terminal segment from residues 70–76, the entire helix from residues 23–34, and the connected loop region from residues 35–40. This change in surface area of the protein is accompanied with a partial opening/closing of the core and increased/decreased hydration.⁹²

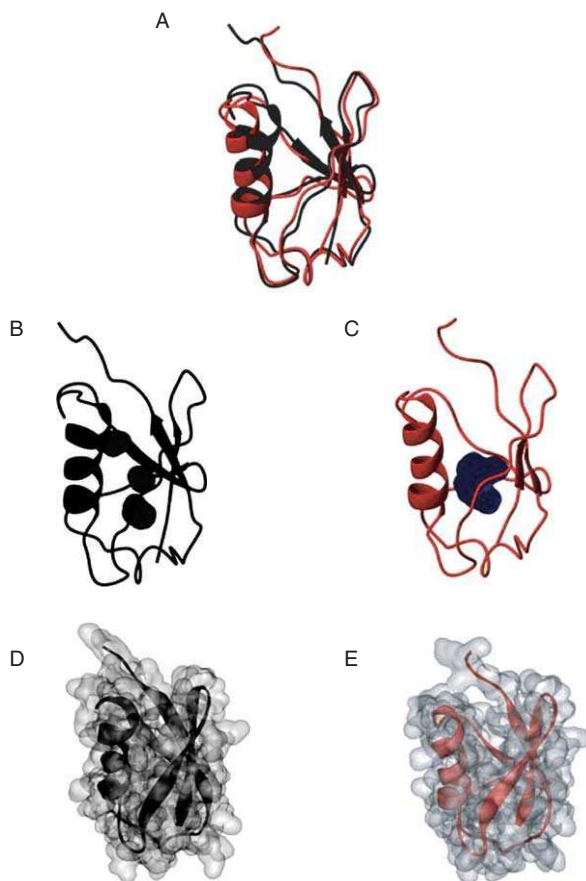


Fig. 11. NMR snapshots of fluctuating ubiquitin. Ribbon representation of the NMR structures of ubiquitin at 3 MPa (B, black taken from PDB 1V80) and 300 MPa (C, red taken from PDB 1V81) and a superposition of the two structures (A). (D) and (E), Molecular surface representation of the two structures with the ribbon representation superimposed. Cavities (B, C) and surfaces (D, E) were calculated using a probe radius of 0.12 nm. (Modified after ref. 92.)

4. CONCLUSIONS

The conformational space of a protein is determined by the variables temperature and pressure. The pressure sensitivity of proteins derives from evolutionary-induced cavities or packing defects. In addition, protein aggregates like fibrils are sensitive to pressure and show packing defects as well. Applying high hydrostatic pressures allows to dissolve these aggregates and stabilize a preamyloidogenic conformation, whose structure may be determined through distance restraints derived from NOEs and RDCs. In summary, we can state that the combination of high hydrostatic pressure and high-resolution multidimensional NMR spectroscopy allows to make atomic resolution as a standard practice in high-pressure biochemistry. This promises to contribute enormously to our knowledge of protein folding and misfolding as well as of protein structure and conformational fluctuations in the biologically relevant conformational space.

ACKNOWLEDGMENTS

I thank Professor Dr. Hans Robert Kalbitzer for stimulating discussions and continuing support. I would like to thank my present and former colleagues, especially Prof. Dr. Eike Brunner, Dr. Wolfram Gronwald and Dr. Till Maurer for discussions. I also thank Professor Kazuyuki Akasaka, Dr. Ryo Kitahara and Dr. Yuji Kamatari for discussions and supplying manuscripts prior to publication. Norman Kachel and Peter Geyer are thanked for proofreading the manuscript. Part of this work was financed by the DFG.

REFERENCES

1. J. L. Silva, D. Foguel and C. A. Royer, *Trends Biochem. Sci.*, 2001, **26**, 612–618.
2. K. Akasaka and H. Yamada, *Methods Enzymol.*, 2001, **338**, 134–158.
3. J. Jonas, *Science*, 1982, **216**, 1179–1184.
4. M. Gross and R. Jaenicke, *Eur. J. Biochem.*, 1994, **221**, 617–630.
5. R. Jaenicke, *Annu. Rev. Biophys. Bioeng.*, 1981, **10**, 1–67.
6. E. Morild, *Adv. Protein Chem.*, 1981, **34**, 93–166.
7. K. Heremans, *Annu. Rev. Biophys. Bioeng.*, 1982, **11**, 1–21.
8. G. Weber and H. G. Drickamer, *Q. Rev. Biophys.*, 1983, **16**, 89–112.
9. V. V. Mozhaev, K. Heremans, J. Frank, P. Masson and C. Balny, *Proteins*, 1996, **24**, 81–91.
10. J. L. Silva and G. Weber, *Annu. Rev. Phys. Chem.*, 1993, **44**, 89–113.
11. J. L. Silva, D. Foguel, A. T. Da Poian and P. E. Prevelige, *Curr. Opin. Struct. Biol.*, 1996, **6**, 166–175.
12. T. W. Randolph, M. Seefeldt and J. F. Carpenter, *Biochim. Biophys. Acta*, 2002, **1595**, 224–234.
13. J. Jonas and A. Jonas, *Annu. Rev. Biophys. Biomol. Struct.*, 1994, **23**, 287–318.
14. J. Jonas, L. Ballard and D. Nash, *Biophys. J.*, 1998, **75**, 445–452.
15. J. Jonas, *Biochim. Biophys. Acta*, 2002, **1595**, 145–159.

16. K. E. Prehoda, E. S. Mooberry and J. L. Markley, High pressure effects on protein Structure, in *Protein Dynamics, Function and Design*, O. Jardetzky and J.-F. Lefevre, eds., NATO ASI Series, Plenum press, 1998, 59–86.
17. R. Winter, *Annu. Rep. NMR Spectrosc.*, 2003, **50**, 163–200.
18. K. Akasaka and H. Li, *Biochemistry*, 2001, **40**, 8665–8671.
19. K. Akasaka, *Pure Appl. Chem.*, 2003, **75**, 927–936.
20. K. Akasaka, *Biochemistry*, 2003, **42**, 10875–10885.
21. Y. O. Kamatari, R. Kitahara, H. Yamada, S. Yokoyama and K. Akasaka, *Methods*, 2004, **34**, 133–143.
22. K. Akasaka, Probing conformational fluctuation of proteins by pressure perturbation. *Chem. Rev.* Thematic Issue “Protein Dynamics and Folding” (Guest Editor: Prof. A.J.Wand), 2005.
23. H. Yamada, *Rev. Sci. Instr.*, 1974, **45**, 640.
24. G. Völkl, E. Lang and H. D. Lüdemann, *Berichte Bunsengesellschaft Physikalische Chemie*, 1979, **83**, 722–729.
25. G. Wagner, *FEBS Lett*, 1980, **112**, 280–284.
26. J. Jonas, *Rev. Sci. Instr.*, 1972, **43**, 643.
27. J. Jonas, *Rev. Sci. Instr.*, 1970, **41**, 1240.
28. L. Ballard, C. Reiner and J. Jonas, *J. Magn. Reson. A*, 1996, **123**, 81–86.
29. L. Ballard, A. Yu, C. Reiner and J. Jonas, *J. Magn. Reson.*, 1998, **133**, 190–193.
30. H. Yamada, Glass cell method for high-pressure, high-resolution NMR measurements. Application to the studies of pressure effects on molecular conformation and structure, in J. Jonas, ed., *High Pressure NMR in the Springer Series NMR Basic Principles and Progress*, Vol. 24, P. Diehl, E. Fluck, H. Günther, R. Kosfeld and J. Seelig eds., Springer-Verlag, Berlin, 1990, 233–263.
31. E. W. Lang and H. -D. Lüdemann, *Prog. Nucl. Magn. Reson. Spectrosc.*, 1993, **25**, 507–633.
32. W. E. Price and H.-D. Lüdemann, NMR and diaphragm-cell techniques for the study of molecular dynamics in fluids, in *High Pressure Techniques in Chemistry and Physics: A Practical Approach*, W. B. Holzapfel and N. S. Isaacs, eds., Oxford University Press, Oxford, 1997, 225.
33. C. Roe and D. Sapphire, *J. Magn. Reson.*, 1985, **63**, 388–391.
34. J. L. Urbauer, M. R. Ehrhardt, R. J. Bieber, P. F. Flynn and A. J. Wand, *J. Am. Chem. Soc.*, 1996, **118**, 11329–11330.
35. M. R. Arnold, H. R. Kalbitzer and W. Kremer, *J. Magn. Reson.*, 2003, **161**, 127–131.
36. W. J. Wu, G. Vidugiris, E. S. Mooberry, W. M. Westler and J. L. Markley, *J. Magn. Reson.*, 2003, **164**, 84–91.
37. H. Yamada, K. Nishikawa, M. Honda, T. Shimura, K. Akasaka and K. Tabayashi, *Rev. Sci. Instr.*, 2001, **72**, 1463–1471.
38. C. M. Dobson, *Nature*, 2003, **426**, 884–890.
39. C. M. Dobson, *Semin. Cell Dev. Biol.*, 2004, **15**, 3–16.
40. C. M. Dobson, *Methods*, 2004, **34**, 4–14.
41. D. Foguel and J. L. Silva, *Biochemistry*, 2004, **43**, 11361–11370.
42. T. W. Randolph, M. Seefeldt and J. F. Carpenter, *Biochim. Biophys. Acta*, 2002, **1595**, 224–234.
43. K. Kuwata, H. Li, H. Yamada, G. Legname, S. B. Prusiner, K. Akasaka and T. L. James, *Biochemistry*, 2002, **41**, 12277–12283.
44. T. N. Niraula, K. Haraoka, Y. Ando, H. Li, H. Yamada and K. Akasaka, *J. Mol. Biol.*, 2002, **320**, 333–342.
45. K. Kuwata, Y. O. Kamatari, K. Akasaka and T. L. James, *Biochemistry*, 2004, **43**, 4439–4446.
46. W. Kremer, N. Kachel, R. Zahn and H. R. Kalbitzer, submitted manuscript.
47. T. W. Randolph, M. Seefeldt and J. F. Carpenter, *Biochim. Biophys. Acta*, 2002, **1595**, 224–234.
48. J. Torrent, M. T. Alvarez-Martinez, F. Heitz, J. P. Liautard, C. Balny and R. Lange, *Biochemistry*, 2003, **42**, 1318–1325.
49. J. Torrent, M. T. Alvarez-Martinez, M. C. Harricane, F. Heitz, J. P. Liautard, C. Balny and R. Lange, *Biochemistry*, 2004, **43**, 7162–7170.

50. J. Torrent, M. T. Alvarez-Martinez, J. P. Liautard, C. Balny and R. Lange, *Protein Sci.*, 2005, **14**, 956–967.
51. Y. Cordeiro, J. Kraineva, R. Ravindra, L. M. Lima, M. P. B. Gomes, D. Foguel, R. Winter and J. L. Silva, *J. Biol. Chem.*, 2004, **279**, 32354–32359.
52. A. Bundi and K. Wüthrich, *Biopolymers*, 1979, **18**, 299–311.
53. A. Bundi and K. Wüthrich, *Biopolymers*, 1979, **18**, 285–297.
54. D. S. Wishart, C. G. Bigam, A. Holm, R. S. Hodges and B. D. Sykes, *J. Biomol. NMR*, 1995, **5**, 67–81.
55. D. S. Wishart, C. G. Bigam, J. Yao, F. Abildgaard, H. J. Dyson, E. Oldfield, J. L. Markley and B. D. Sykes, *J. Biomol. NMR*, 1995, **6**, 135–140.
56. R. Hoffmann, I. Reichert, W. O. Wachs, M. Zappezauer and H. R. Kalbitzer, *Int. J. Pept. Protein Res.*, 1994, **44**, 193–198.
57. R. Hoffmann, W. O. Wachs, R. G. Berger, H. R. Kalbitzer, D. Waidelich, E. Bayer, W. Wagner-Redeker and M. Zappezauer, *Int. J. Pept. Protein Res.*, 1995, **45**, 26–34.
58. R. Hoffmann, T. Hoffmann, A. Tholey, A. C. Schulte and H. R. Kalbitzer, *J. Pept. Res.*, 1997, **49**, 163–173.
59. H. Li, H. Yamada and K. Akasaka, *Biochemistry*, 1998, **37**, 1167–1173.
60. H. Li, H. Yamada, K. Akasaka and A. M. Gronenborn, *J. Biomol. NMR*, 2000, **18**, 207–216.
61. M. R. Arnold, W. Kremer, H. D. Lüdemann and H. R. Kalbitzer, *Biophys. Chem.*, 2002, **96**, 129–140.
62. G. Bernhardt, R. Jaenicke and H. D. Lüdemann, *Appl. Environ. Microbiol.*, 1987, **53**, 1876–1879.
63. W. Kremer and H. R. Kalbitzer, *Methods Enzymol.*, 2001, **339**, 3–19.
64. R. C. Neuman, W. Kauzmann and A. Zipp, *J. Phys. Chem.*, 1973, **77**, 2687–2691.
65. H. R. Kalbitzer, A. Görler, H. Li, P. V. Dubovskii, W. Hengstenberg, C. Kowolik, H. Yamada and K. Akasaka, *Protein Sci.*, 2000, **9**, 693–703.
66. G. Némethy and M. P. Printz, *Macromolecules*, 1972, **5**, 755–758.
67. N. Tjandra and A. Bax, *Science*, 1997, **278**, 1111–1114.
68. A. Bax, *Protein Sci.*, 2003, **12**, 1–16.
69. C. Griesinger, W. Peti, J. Meiler and R. Bruschweiler, *Methods Mol. Biol.*, 2004, **278**, 107–121.
70. N. Tjandra, J. Marquardt and G. M. Clore, *J. Magn. Reson.*, 2000, **142**, 393–396.
71. E. Brunner, M. R. Arnold, W. Kremer and H. R. Kalbitzer, *J. Biomol. NMR*, 2001, **21**, 173–176.
72. R. Kitahara, H. Yamada, K. Akasaka and P. E. Wright, *J. Mol. Biol.*, 2002, **320**, 311–319.
73. M. W. Lassalle, H. Li, H. Yamada, K. Akasaka and C. Redfield, *Protein Sci.*, 2003, **12**, 66–72.
74. K. Kuwata, H. Li, H. Yamada, C. A. Batt, Y. Goto and K. Akasaka, *J. Mol. Biol.*, 2001, **305**, 1073–1083.
75. K. Akasaka, H. Li, H. Yamada, R. Li, T. Thoresen and C. K. Woodward, *Protein Sci.*, 1999, **8**, 1946–1953.
76. H. Li, H. Yamada and K. Akasaka, *Biophys. J.*, 1999, **77**, 2801–2812.
77. M. Marchi and K. Akasaka, *J. Phys. Chem. B*, 2001, **105**, 711–714.
78. R. Kitahara, S. Sareth, H. Yamada, E. Ohmae, K. Gekko and K. Akasaka, *Biochemistry*, 2000, **39**, 12789–12795.
79. K. Hata, R. Kono, M. Fujisawa, R. Kitahara, Y. O. Kamatari, K. Akasaka and Y. Xu, *Cell Mol. Biol. (Noisy-le-grand)*, 2004, **50**, 311–316.
80. K. Inoue, H. Yamada, T. Imoto and K. Akasaka, *J. Biomol. NMR*, 1998, **12**, 535–541.
81. M. Hattori, H. Li, H. Yamada, K. Akasaka, W. Hengstenberg, W. Gronwald and H. R. Kalbitzer, *Protein Sci.*, 2004, **13**, 3104–3114.
82. M. Canalia, T. E. Malliavin, W. Kremer and H. R. Kalbitzer, *Biopolymers*, 2004, **74**, 377–388.
83. K. Akasaka, T. Tezuka and H. Yamada, *J. Mol. Biol.*, 1997, **271**, 671–678.
84. Y. O. Kamatari, H. Yamada, K. Akasaka, J. A. Jones, C. M. Dobson and L. J. Smith, *Eur. J. Biochem.*, 2001, **268**, 1782–1793.
85. M. Refaee, T. Tezuka, K. Akasaka and M. P. Williamson, *J. Mol. Biol.*, 2003, **327**, 857–865.
86. M. Iwadate, T. Asakura, P. V. Dubovskii, H. Yamada, K. Akasaka and M. P. Williamson, *J. Biomol. NMR*, 2001, **19**, 115–124.

87. R. Kitahara, C. Royer, H. Yamada, M. Boyer, J. L. Saldana, K. Akasaka and C. Roumestand, *J. Mol. Biol.*, 2002, **320**, 609–628.
88. K. Inoue, H. Yamada, K. Akasaka, C. Herrmann, W. Kremer, T. Maurer, R. Doker and H. R. Kalbitzer, *Nat. Struct. Biol.*, 2000, **7**, 547–550.
89. K. Inoue, T. Maurer, H. Yamada, C. Herrmann, G. Horn, H. R. Kalbitzer and K. Akasaka, *FEBS Lett.*, 2001, **506**, 180–184.
90. R. Kitahara, H. Yamada and K. Akasaka, *Biochemistry*, 2001, **40**, 13556–13563.
91. R. Kitahara and K. Akasaka, *Proc. Natl. Acad. Sci. U.S.A.*, 2003, **100**, 3167–3172.
92. R. Kitahara, S. Yokoyama and K. Akasaka, *J. Mol. Biol.*, 2005, **347**, 277–285.
93. S. Sareth, H. Li, H. Yamada, C. K. Woodward and K. Akasaka, *FEBS Lett.*, 2000, **470**, 11–14.
94. V. Y. Orekhov, P. V. Dubovskii, H. Yamada, K. Akasaka and A. S. Arseniev, *J. Biomol. NMR*, 2000, **17**, 257–263.
95. M. Hattori, H. Li, H. Yamada, K. Akasaka, W. Hengstenberg, W. Gronwald and H. R. Kalbitzer, *Protein Sci.*, 2004, **13**, 3104–3114.
96. L. Ragona, F. Fogolari, L. Zetta, D. M. Perez, P. Puyol, K. De Kruif, F. Lohr, H. Ruterjans and H. Molinari, *Protein Sci.*, 2000, **9**, 1347–1356.
97. L. Ragona, F. Fogolari, M. Catalano, R. Ugolini, L. Zetta and H. Molinari, *J. Biol. Chem.*, 2003, **278**, 38840–38846.
98. R. Riek, K. Pervushin and K. Wüthrich, *Trends Biochem. Sci.*, 2000, **25**, 462–468.
99. K. Pervushin, *Q. Rev. Biophys.*, 2000, **33**, 161–197.
100. C. Fernandez and G. Wider, *Curr. Opin. Struct. Biol.*, 2003, **13**, 570–580.
101. G. Wider, *Methods Enzymol.*, 2005, **394**, 382–398.
102. D. Foguel, M. C. Suarez, A. D. Ferrao-Gonzales, T. C. R. Porto, L. Palmieri, C. M. Einsiedler, L. R. Andrade, H. A. Lashuel, P. T. Lansbury, J. W. Kelly and J. L. Silva, *PNAS*, 2003, **100**, 9831–9836.
103. H. Tachibana, T. Oka and K. Akasaka, *J. Mol. Biol.*, 2001, **314**, 311–320.
104. T. N. Niraula, T. Konno, H. Li, H. Yamada, K. Akasaka and H. Tachibana, *PNAS*, 2004, **101**, 4089–4093.
105. G. Desai, G. Panick, M. Zein, R. Winter and C. A. Royer, *J. Mol. Biol.*, 1999, **288**, 461–475.
106. J. Woenckhaus, R. Kohling, P. Thiagarajan, K. C. Littrell, S. Seifert, C. A. Royer and R. Winter, *Biophys. J.*, 2001, **80**, 1518–1523.
107. R. Winter and W. Dzwolak, *Cell Mol. Biol. (Noisy. -le-grand)*, 2004, **50**, 397–417.
108. R. Winter and W. Dzwolak, *Philos. Trans. A: Math. Phys. Eng. Sci.*, 2005, **363**, 537–562.

This page intentionally left blank

Xenon NMR Spectroscopy

DANIEL RAFTERY

Department of Chemistry, Purdue University, 560 Oval Drive, West Lafayette, IN 47907, USA

1. Introduction	206
2. Conventional Xenon NMR Studies	207
2.1 New studies of bulk xenon	207
2.2 Xenon in solution	209
2.3 Xenon compounds	211
2.4 Xenon as a probe of materials	212
2.5 Xenon ¹³¹ studies	223
2.6 Calculations of xenon parameters	225
3. Hyperpolarized Xenon	227
3.1 Optical pumping methods	227
3.2 HP xenon bulk measurements	231
3.3 HP xenon in materials and on surfaces	234
3.4 Polarization transfer methods	239
3.5 HP xenon in medicine	243
3.6 Bioanalytical HP xenon	247
3.7 HP xenon diffusion studies	250
3.8 HP xenon imaging of materials	252
3.9 New and exotic applications	254
4. Conclusion	260
Acknowledgments	260
References	261

This chapter summarizes the recent developments in both convention and hyperpolarized (HP) xenon NMR experiments. Xenon NMR has been used in a growing number of spectroscopy and imaging approaches to physical, chemical, and biological problems. Because of its sensitivity to chemical environment, its inertness, and now the ability to create high polarization through optical pumping xenon has become an extremely useful NMR nucleus to probe an enormous range of materials. Increasingly, we find that unusual materials are being examined with xenon NMR. In addition, more powerful computational methods are now available, making the calculation of xenon chemical shifts possible under a variety of experimentally simulated situations. Approximately half of the papers published over the past 7 years now involve the use of HP xenon because of the dramatic enhancement in sensitivity it affords, and because the optical pumping technology has become more routine. This advance has given rise to a significant increase in the papers that describe the use of 2D methods for xenon NMR as well as static and

even dynamic imaging. Some of the rather exotic new methods that have been proposed recently promise to enhance the sensitivity and applicability of xenon NMR experiments well into the future.

1. INTRODUCTION

Xenon NMR spectroscopy has evolved in status over the past two decades from exotic to routine such that it is now used to provide detailed information for an enormous variety of applications. Thus, xenon NMR has become a useful and complementary experiment for the investigation of a large range of materials as will be seen below. Also evident is the growing emphasis on the development and use of hyperpolarized (HP) xenon experiments that can provide much enhanced sensitivity. These experiments have therefore greatly enhanced the utility of xenon NMR studies, and exciting new developments promise even more advances to come.

This chapter follows a number of excellent reviews, some comprehensive¹⁻⁴ and others more focused⁵⁻¹⁴ on the subject of xenon NMR spectroscopy. I have chosen to focus this review primarily on the most recent and exciting developments (in my own opinion) during the period 1998 to the present as the previous xenon work has been reviewed comprehensively by Ratcliffe in volume 36 of the *Annual Reports on NMR Spectroscopy*.⁴ Thus, results from approximately 100 papers are described from the over 500 that have been published on Xe NMR during the past 7 years. References are made to many other papers, although not all that have appeared since 1998 due to time and space considerations. I apologize to those authors whose work was not featured in this review.

A number of superb and recent reviews describe xenon NMR studies in an increasingly diverse set of applications. The ability to study biological systems has resulted in a variety of new applications for xenon NMR, and these have been summarized in reviews by Cherubini and Bifone,¹⁵ Goodson,¹⁶ and Oros and Shah.¹⁷ Pietrass^{18,19} has reviewed xenon optical pumping methodologies, the interaction of HP xenon with surfaces and described the various methods used for polarization transfer. Brunner^{20,21} described the literature on polarization transfer from xenon to surfaces and biological systems, as well as the applications of continuous-flow xenon NMR experiments enabled by high-powered laser-diode-based optical pumping systems. Springuel-Huet *et al.*¹⁴ and Bonardet *et al.*²² have reviewed the extensive literature on xenon's interaction with microporous solids, including zeolites. As a result, some topics have received much attention in other reviews, such as the conventional studies of xenon in porous materials (Section 2.5), or the recent work on HP xenon in biomedical applications¹⁷ (Sections 3.5 and 3.6) and thus are not a large focus of the present review. Instead, a significant focus of this review is the development of new methodologies, and thus several experimental apparatuses are described for obtaining new xenon NMR data along with the description of new xenon experiments and the characterization of new materials. Thermal and HP xenon studies are separated in this review in part because the methodology is different.

The important NMR-related properties of xenon have been discussed and are quite well known. First of all, xenon's inertness allows it to act as a superb probe of its chemical environment. However, this also leads to an averaging of its chemical shift in many situations. Perhaps most important to NMR spectroscopy is the relatively high sensitivity of xenon, both in terms of its natural abundance (26.4% for ^{129}Xe and 21.2% for ^{131}Xe), its relatively high detectivity (for ^{129}Xe it is approximately 2% that for ^1H , or 30 times that of ^{13}C), and particularly its enormous chemical shift range of over 7500 ppm. The ^{129}Xe and ^{131}Xe resonance frequencies are 27.66 and 8.199 MHz at 2.3488 T (at which ^1H resonates at 100 MHz). The ^{131}Xe quadrupole interaction is relatively strong, but because of xenon's inertness, it is normally averaged significantly.

As a result of these favorable NMR properties, xenon has been utilized in a wide range of studies, especially as a probe of its host's structure such as in microporous materials and other chemical environments. As should be evident from the discussion below, applications to new materials are appearing every year. In addition, the much higher sensitivity that optical pumping provides has increased the capabilities of xenon NMR significantly. As a result, new studies to investigate biological materials and to carry out diffusion and imaging studies have appeared. These developments, along with a variety of interesting new methods are described at the end of the review.

2. CONVENTIONAL XENON NMR STUDIES

2.1. New studies of bulk xenon

One of the earliest properties of xenon studied by NMR was the gas-phase relaxation, which had been investigated in a detail as early as 1961.²³ Xenon was observed to have a T_1 relaxation time that is inversely dependent on the pressure, indicating the presence of a strong spin-rotation interaction.²⁴ Detailed studies of xenon relaxation in the presence of paramagnetic gases has been studied in detail by the Jamesons.²⁵

The gas-phase relaxation in pure xenon was recently reinvestigated by Modrakovski *et al.*²⁶ Samples were prepared using heavy-walled Pyrex glass tubing and in some cases included either enriched ^{129}Xe or Rb for optical pumping experiments at lower pressures. Three methods were used to measure the T_1 values: standard saturation recovery, field cycling into low magnetic field for long samples at high pressure followed by small-angle pulsing, and optical pumping followed by small-angle pulsing. Results from this detailed study showed linear relaxation behavior as a function of pressure above 20 amagat (1 amagat = density of xenon at 1 atm and 298 K) in accordance with recent high-pressure measurements,²⁷ but below 20 amagat, the behavior was nonlinear, with a minimum relaxation rate of approximately 10^{-4} s^{-1} measured at 3 amagat (see Fig. 1). Interactions with the walls increased the relaxation rate at low pressures. A small factor that was not included was the possibility of further relaxation by Rb atoms present in the

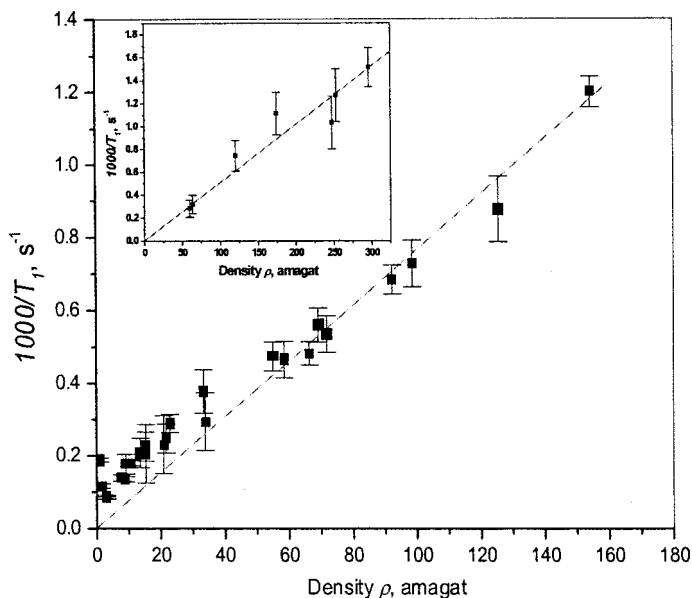


Fig. 1. Density dependence of ^{129}Xe relaxation rate at 295 K in a magnetic field of 9.4 T. The inset shows for comparison the experimental data from ref. 27 (298 K, 1.2 T). (Courtesy of Igor Moudrakovski. Reprinted from ref. 26 with permission. Copyright 2001, American Institute of Physics.)

optically pumped samples. No effect on the relaxation rate was observed due to the presence of xenon-131. A field-dependent relaxation effect was observed, and attributed to the modulation of the chemical shift during xenon–xenon collisions. Also, two opposing temperature dependences were observed, one that was field dependent and the other field independent. The authors found they could account for the temperature-dependent spin-rotation interaction as the major contributor to the relaxation.

The xenon chemical shift has been studied in detail, in all the pure phases of xenon. For example, the pressure-dependent chemical shift of gas-phase xenon was first described in terms of a virial expansion by Jameson *et al.*²⁸ The extreme sensitivity of the xenon chemical shift has often provided the basis for the numerous studies reported in the literature, especially for xenon interacting with materials. However, in terms of pure xenon, to date, few studies have focused on supercritical xenon. Recent studies by Baumer *et al.*²⁹ focused on the measurement of the xenon chemical shift in the supercritical state using thermally polarized xenon. The chemical shift was measured at xenon pressures up to 440 amagat and reported to have a reasonably strong nonlinear dependence on pressure, with deviations from linearity as much as 30 ppm at 300 amagat. Up to 100 amagat, the results follow those obtained by Jameson *et al.*²⁸ Above that density, a five-parameter fit was used to match the data, which gave two inflection points. The first is likely due to three-body interactions, while the second inflection point might be due to wall

interactions. A description of the production and possible uses of HP supercritical xenon^{30,31} are provided in Section 3.2 below.

2.2. Xenon in solution

Over the years, a number of studies have probed the interaction of xenon in numerous liquid environments.⁵ The xenon chemical shift is known to vary widely depending on the particular solvent. For example, the xenon chemical shift in methanol is 148 ppm³² while in methyl iodide it is 333 ppm,³³ with more typical values around 180–220 ppm.⁵ The xenon chemical shift is very sensitive to its liquid environment such that it can detect the difference between protonated and deuterated solvents, with changes of the order of 1–4 ppm seen for various solvents.³⁴ Most liquid-phase studies involving xenon now probe other solute species, as described below, however fundamental studies of xenon in various solvents are still reported.^{35,36}

The xenon relaxation mechanism in aqueous solution was examined in detail recently and determined to result essentially from ^1H – ^{129}Xe dipolar interactions, as might be expected.³⁷ The ^1H – ^{129}Xe nuclear overhauser effect (NOE) interaction was detected using a truncated-driven NOE pulse sequence involving a train of low-power 40 ms saturation pulses on the protons. Xe NMR was used to detect the NOE effect. Cross-relaxation rates from protons to xenon were measured at a range of xenon pressures, with essentially no pressure dependence detected. The cross-relaxation rate was determined to be $3.2 \pm 0.3 \times 10^{-3} \text{ s}^{-1}$. This value is within a factor of 2.5 of the cross-relaxation measurement by Pines and coworkers³⁸ using the spin-polarization-induced nuclear overhauser effect (SPINOE) effect and HP xenon, even though they used benzene as a solvent. As a result of their measurements, Dimitrov *et al.* conclude that dipolar interactions are responsible for the xenon relaxation time in aqueous solution. Because of the low solubility of xenon in H_2O , the Xe–H cross-relaxation rate of the order of 10^{-6} s^{-1} , since the total cross-relaxation rates must be equal: $S(S+1)N_{\text{H}}\sigma_{\text{HXe}} = I(I+1)N_{\text{Xe}}\sigma_{\text{XeH}}$. The low cross-relaxation rate, combined with low-xenon solubility, are the leading factors that make polarization transfer from xenon to other solutes challenging. Mazitov *et al.*³⁹ investigated the effect of paramagnetic ions on xenon relaxation. They found that the relaxation was driven by xenon coupling to the electron spin of the ion, and depended greatly on ion mobility. Xenon did not interact directly with the ion, but rather with the hydrated form.

Locci *et al.*⁴⁰ describe a method to use xenon to monitor chemical transformations, which they describe as the “Spin-Spy” methodology. Xenon was added to a solution of α - and β -D-glucose and the change in concentration of these species was monitored via the Xe chemical shift as equilibrium concentrations of the interconverting sugars were reached over a period of 300 min. The xenon chemical shift difference in a 1 M concentration of these two species is approximately 1.3 ppm. Xenon’s interaction with liquid crystal environments has also been reported over the past several years.^{41–43} This area was reviewed extensively by Jokisaari⁹ in 1994.

In a recent paper Jokisaari and coworkers investigated the effect of long-range attractive van der Waals (vdW) forces on the chemical shift anisotropy due to the anisotropic medium of the liquid crystal.⁴⁴

2.2.1. Xenon interacting with cage molecules

An interest in the interaction between xenon and other solutes has appeared in the past several years. This is largely driven by the increased sensitivity of HP xenon, although several of the studies reported involved thermally polarized xenon. Cage molecules have the potential to trap significant amounts of xenon, and these systems have been reported as possible methods for sensitivity detection of protein-ligand binding⁴⁵ or for xenon delivery to remote locations.⁴⁶ Several studies of xenon interacting with cryptophane-A cages were reported recently.^{47–51} A picture of xenon interacting with the cryptophane-A cage is shown in Fig. 2. Reisse and coworkers⁵⁰ first showed the possibility of using cryptophane-A as a cage molecule to trap xenon in solution. Xenon exchange between solution and the cage is slow, and the linewidth decreases with decreasing temperature as expected. The association constant was estimated to be approximately $3 \times 10^3 \text{ M}^{-1}$ at 278 K. Brotin *et al.*⁴⁹ have synthesized deuterated congeners of cryptophane-A, and carried out variable mixing time xenon-exchange experiments. Xenon's chemical shift is sensitive to the degree of deuteration, a fact that the authors used to probe xenon-exchange dynamics. The experiments showed that xenon had an exchange rate constant of 20–50 between the cages and solution, but direct exchange between cages was much slower, indicating that cage-collision-induced xenon exchange was not important in the dynamics. The authors have also studied cryptophanol hosts.^{52,53}

Xenon was also successfully inserted into the interior of C₆₀.⁵⁴ Incorporating ³He into C₆₀ is relatively easy to accomplish, and has been reported as early as 1994.⁵⁵

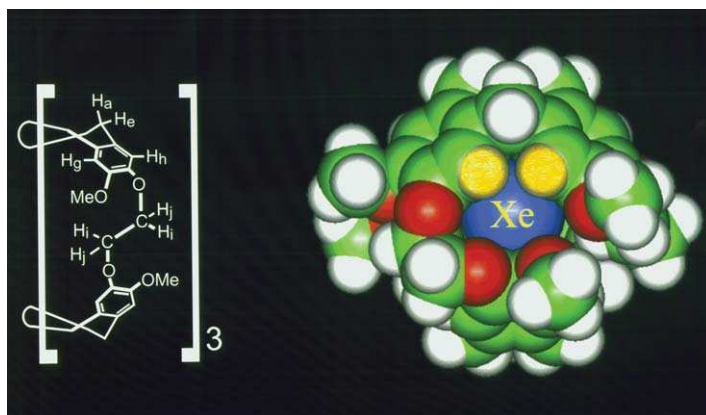


Fig. 2. (Left) Structural formula of cryptophane-A. (Right) Xenon in the hydrophobic pocket of cryptophane-A, shown as one possible conformation based on a CPK model. (Courtesy of Connie Chung and the Pines group. Adapted from ref. 273 with permission. Copyright 1999, American Chemical Society.)

Synthesizing Xe@C₆₀ has been much more difficult. This is primarily because of the larger size of xenon, and the fact that xenon is harder to observe than ³He by NMR. Careful HPLC separation, attention to avoid oxidation of the C₆₀, and use of enriched xenon allowed the collection of both xenon and ¹³C spectra indicating the presence of Xe@C₆₀. The measured ¹²⁹Xe chemical shift, 179.2 ppm, is surprising close to that of xenon dissolved in benzene.

A study of xenon binding to a synthetic receptor, cucurbituril was reported by Haouaj *et al.*^{56,57} Xenon forms a 1:1 complex with the receptor and exchanges on the millisecond timescale as evidenced by the xenon linewidths of 200–800 Hz. However, the linewidth of the bound xenon located at 122 ppm changes linearly with xenon concentration while that of the unbound xenon shows random changes in linewidth, indicating the exchange is more complex than a two-site model would suggest, and may involve a xenon–xenon displacement. Proton resonance shifts were used to determine the equilibrium constant, which was estimated to be approximately 200 M^{−1} at 298 K. This is an order of magnitude smaller than xenon's binding constant in cryptophane-A.

2.2.2. Xenon interactions with proteins

While there have been relatively few reports^{58,59} of xenon interacting with proteins until recently, the possibility of using xenon as a probe of hydrophobic binding has sparked the attention of researchers. Xenon's interactions with metmyoglobin, hen egg white lysozyme, and horse cytochrome *c* were probed in aqueous solution.^{60,61} The authors used a combination of xenon NMR and thermodynamic modeling to obtain quantitative information on the xenon–protein interactions. An important aspect of this work is the use of a three-state model described earlier by the same group.⁶² Careful measurements over a range of pressure conditions and three concentrations of horse metmyoglobin solutions show small, but reproducible increases in the chemical shift with increasing pressure. Xenon is in fast exchange with the binding sites, the protein surface, and the aqueous solvent. Using an equilibrium model, chemical shift values and the equilibrium constant were calculated, resulting in chemical shift values for the bound xenon of approximately 150 ppm and an equilibrium constant of 115–323 M^{−1} depending on the concentration.

Gröger *et al.*⁶³ have explored xenon interacting with a mutant of the phosphocarrier protein from *Staphylococcus carnosus* using ¹H–¹⁵N HSQC experiments. Significant changes in the chemical shift values were observed for the mutant protein, especially those close to the engineered cavity. In contrast, the wild-type protein showed much smaller, nonspecific interactions when xenon was introduced into solution.

2.3. Xenon compounds

A variety of new xenon compounds have been synthesized and characterized by ¹²⁹Xe NMR as well as by NMR of the ligand species. The Seppelt group^{64–68} has reported a number of new compounds, including several xenon–gold compounds.

The first gold–xenon compound to have been discovered was the $[\text{AuXe}_4]^{2+}[\text{Sb}_2\text{F}_{11}]_2^{-64}$ gold(II) complex, but other gold valence states exist, including gold(III) and gold(I). The reaction of $[(\text{F}_3\text{As})\text{Au}]^+[\text{SbF}_6]^-$ with xenon yields the complex $[(\text{F}_3\text{As})\text{AuXe}]^+[\text{Sb}_2\text{F}_{11}]^-$.⁶⁵ ^{129}Xe NMR of this compound shows only a single peak at room temperature because of rapid xenon exchange with the excess atomic xenon in the HF/SbF_5 solution. However, at -30°C , the spectrum from the compound is distinct and is broadened to approximately 0.5 ppm by coupling to both the Au and As quadrupolar nuclei. A somewhat similar HgXe compound $[\text{HgXe}]^{2+}[\text{SbF}_6]^-[\text{Sb}_2\text{F}_{11}]^-$ was also synthesized, although no xenon spectrum was obtained. A XeCl^+ ion species was created by reacting $[\text{XeF}]^+[\text{SbF}_6]^-$ with SbCl_5 to obtain the product $[\text{XeCl}]^+[\text{Sb}_2\text{F}_{11}]^-$.⁶⁷ The ^{129}Xe NMR spectrum of this species was over 100 ppm broad, and contained a splitting resulting from the very large $^{35/37}\text{Cl}$ quadrupole moment. The authors were also successful in forming a XeTe -based compound $[\text{F}_5\text{TeOXe}]^+ \cdot \text{SO}_2\text{ClF}[\text{Sb}(\text{OTeF}_5)_6]^-$.⁶⁸

Gerkin and Schrobilgen⁶⁹ describe experiments to synthesize the highly unstable XeO_4 , which was prepared from $[\text{Na}_4][\text{XeO}_6]$ and 100% sulfuric acid. ^{129}Xe of this compound was obtained for the first time in SO_2ClF , HF , and BrF_5 , and the chemical shift was 5195, 5202.7, and 5193.9 ppm, respectively, with respect to gas-phase xenon. The ^{17}O NMR spectra were also obtained. The authors have also published a review of multinuclear NMR as it pertains to rare-gas compounds.⁷⁰

Frohn and Bardin⁷¹ reported the synthesis of trifluorovinylxenon(II), the first example of an acyclic alkenylxenon(II) compound. A beautiful xenon spectrum, consisting of eight resolved lines displayed in a doublet of doublets pattern with couplings of 248, 146 and 30 Hz, was obtained. Several other examples of alkylxenon(II) compounds have also now been published by the authors.^{72,73} Frohn *et al.*⁷⁴ have also studied the detailed properties of $[\text{C}_6\text{F}_5\text{Xe}]^+$ in $[\text{C}_6\text{F}_5\text{Xe}][\text{AsF}_6]$. This material was very stable as shown by its decomposition temperatures that exceed 150°C . Xenon chemical shifts were measured in several solvents. They also synthesized a number of difluoroalk-1-enyl xenon salts by reacting XeF_2 with appropriate fluoroboranes.⁷⁵ Naumann and coworkers⁷⁶ have also succeeded in preparing a series of alkynylxenon(II) fluorides, $\text{RC}\equiv\text{CXeF}$ ($\text{R} = \text{Me}$, $n\text{-Bu}$, and Ph). A ^{19}F – ^{13}C HMBC experiment was used to prove the $\text{C}\text{--}\text{Xe}\text{--}\text{F}$ structure. ^{19}F – ^{129}Xe and ^{13}C – ^{129}Xe 1J couplings of 4331 and 336 Hz, respectively, were observed. They also succeeded in synthesizing a xenon compound with two carbon bonds, $\text{Xe}(\text{C}_6\text{F}_5)_2$ ⁷⁷ and two amides, $[\text{Xe}(2,6\text{-F}_2\text{C}_6\text{H}_3)][\text{N}(\text{SO}_2\text{R})_2]$ ($\text{R} = \text{F}$, or CF_3).⁷⁸

Table 1 lists the NMR results on xenon compounds reported since 1998. This table follows format established by the comprehensive table compiled by Ratcliffe⁴ covering compounds reported through 1997.

2.4. Xenon as a probe of materials

Xenon continues to be useful to study micro- and mesoporous materials, and this is by far the largest area of application for xenon NMR studies. Variable pressure,

Table 1. Xe NMR parameters for Xe compounds reported after 1998

Compound	Solvent	<i>T</i> (K)	$\delta(\text{Xe})$ (ppm) ^a	$J(^{129}\text{Xe-L})(\text{Hz})^b$		Reference
				L = ¹⁹ F	L = ¹³ C, ¹⁴ N, ¹⁵ N, ¹⁷ O, ¹²⁵ Te	
[(F ₃ As)AuXe] ⁺ [Sb ₂ F ₁₁] [−]	HF/SbF ₅	298	−5180.7			65
[(F ₃ As)AuXe] ⁺ [Sb ₂ F ₁₁] [−]	HF/SbF ₅	243	−5149.9			
[XeCl] ⁺ [Sb ₂ F ₁₁] [−]	HF/SbF ₅	290	−551			67
[Xe(OTeF ₅)] ⁺	SO ₂ ClF	193	−1413.66			68
Xe(OTeF ₅) ₂	SO ₂ ClF	193	−2238			
XeO ₄	SO ₂ ClF	195	−92.9			69
XeO ₄	BrF ₅	223	−94.7			
XeO ₄	HF	198	−85.8			
XeO ₄	SO ₂ ClF	231	−90.0			
XeO ₄	SO ₂ ClF	223	−90.8			
XeO ₄	SO ₂ ClF	213	−91.6			
XeO ₄	SO ₂ ClF	203	−92.5			
XeO ₄	SO ₂ ClF	195	−92.8 ^c			
XeO ₄	BrF ₅	223	−94.5 ^c			
XeO ₄	HF	198	−85.8 ^c			
XeO ₄	SO ₂ ClF	231	8243172Ξ			
XeO ₄	SO ₂ ClF	223	8243163Ξ			
XeO ₄	SO ₂ ClF	213	8243158Ξ			
XeO ₄	SO ₂ ClF	203	8243150Ξ			
XeO ₄	SO ₂ ClF	195	8243148Ξ			
[C ₂ F ¹ F ² _{trans} F ² _{cis} Xe] ⁺ [BF ₄] [−]	HF	243	−3636.1	³ J(F ² _{cis})/30	¹ J(C ¹)/131	71
				³ J(F ² _{trans})/146	² J(C ²)/18	
				² J(F ¹)/248		
C ₆ F ₅ Xe ⁺ /AsF ₆ [−]	HF	263			¹ J(C ¹)/114	
C ₂ F ¹ F ² _{trans} F ² _{cis} Xe ⁺ /BF ₄ [−]	EtCN	233	−3510.6	³ J(F ² _{cis})/27		
				³ J(F ² _{trans})/136		
				² J(F ¹)/197		
C ₂ F ¹ F ² _{trans} F ² _{cis} Xe ⁺ /BF ₄ [−]	EtCN	203		³ J(F ² _{cis})/28		
				³ J(F ² _{trans})/136		
				² J(F ¹)/188		
CF ₂ = C(CF ₃)Xe ⁺ /BF ₄ [−]	HF	213	−3856	³ J(Xe, F ^{2trans})/144		72
				³ J(Xe, F ^{2cis})/4		
CF ₂ = C(CF ₃)Xe ⁺ /BF ₄ [−]	EtCN	213	−3741	³ J(Xe, F ^{2trans})/139		
CF ₂ = CHXe ⁺ /BF ₄ [−]	HF	213	−4059	³ J(Xe, F ^{2trans})/155	² J/H 55	
·CF ₂ = CClXe ⁺ /BF ₄ [−]	HF	213	−3550	³ J(Xe, F ^{2trans})/138		
				³ J(Xe, F ^{2cis})/8		
CF ₃ C≡CXe ⁺ /BF ₄ [−]	HF	213	−3636			73
CF ₃ C≡CXe ⁺ /BF ₄ [−]	HF	243	−3645		−C≡C−Xe−F 343 −C≡C−Xe−F ² J/ 69	
C ₆ F ₅ Xe ⁺ /AsF ₆ [−]	CH ₃ CH ₂ CN/ CD ₃ CN	305		67.29		74
[C ₆ F ₅ Xe ⁺ /AsF ₆ [−]	CH ₃ CH ₂ CN/ CD ₃ CN	272		67.98		
[C ₆ F ₅ Xe ⁺ /AsF ₆ [−]	CH ₃ CH ₂ CN/ CD ₃ CN	253		68.37		
[C ₆ F ₅ Xe ⁺ /AsF ₆ [−]	CH ₃ CH ₂ CN/ CD ₃ CN	233		68.86		
[C ₆ F ₅ Xe ⁺ /AsF ₆ [−]	CH ₃ CH ₂ CN/ CD ₃ CN	213		69.17		
[C ₆ F ₅ Xe ⁺ /AsF ₆ [−]	CH ₃ CH ₂ CN/ CD ₃ CN	193		69.54		
C ₆ F ₅ Xe ⁺ /AsF ₆ [−]	H ₂ O	308		³ J/69.1		

(continued)

Table 1. Continued

Compound	Solvent	<i>T</i> (K)	$\delta(\text{Xe})$ (ppm) ^a	$J(^{129}\text{Xe-L})(\text{Hz})^b$		Reference
				L = ¹⁹ F	L = ¹³ C, ¹⁴ N, ¹⁵ N, ¹⁷ O, ¹²⁵ Te	
C ₆ F ₅ Xe ⁺ /AsF ₆ [−]	MeCN	308		³ J/67.3		
C ₆ F ₅ Xe ⁺ /AsF ₆ [−]	TFE	273		³ J/62.9		
C ₆ F ₅ Xe ⁺ /AsF ₆ [−]	SO ₂	273		³ J/57.0		
C ₆ F ₅ Xe ⁺ /AsF ₆ [−]	H ₂ O	297	−3862.3			
C ₆ F ₅ Xe ⁺ /AsF ₆ [−]	MeCN	297	−3826.2			
C ₆ F ₅ Xe ⁺ /AsF ₆ [−]	SO ₂	233	−3903.0			
C ₆ F ₅ Xe ⁺ /AsF ₆ [−]	AHF	263	−3967.5			
CF ₂ = CFXe ⁺ /AsF ₆ [−]	HF	263	−3641	³ J(Xe,F ^{2trans})/147 ³ J(Xe,F ^{2cis})/31 ² J(Xe,F ¹)/252		75
CF ₂ = CFXe ⁺	HF	243			¹ J/C ¹ 131 ² J/C ² 18	
CF ₂ = CFXe ⁺ / [BF ₄ ,C ₂ F ₅ BF ₃] [−]	EtCN	233	−3511	³ J(Xe,F ^{2trans})/136 ³ J(Xe,F ^{2cis})/27 ² J(Xe,F ¹)/197 ³ J(Xe,F ^{2trans})/136 ³ J(Xe,F ^{2cis})/28 ² J(Xe,F ¹)/188		
[CF ₂ = CFXe ⁺ / [BF ₄ ,C ₂ F ₅ BF ₃] [−]	EtCN	203		³ J(Xe,F ^{2trans})/136 ³ J(Xe,F ^{2cis})/28 ² J(Xe,F ¹)/188		
<i>trans</i> -HCF = CFXe ⁺ / BF ₄ [−]	HF	243	−3693	³ J(Xe,F ²)/60	³ J/H 22	
[<i>cis</i> -CF ₃ CF = CFXe] ⁺ [C ₃ F ₇ BF ₃]/BF ₄ [−]	HF	263	−3431	² J(Xe,F ¹)/20 ⁴ J(Xe,F ³)/38		
[<i>cis</i> -CF ₃ CF = CFXe] ⁺ [C ₃ F ₇ BF ₃]/BF ₄ [−]	EtCN	223		² J(Xe,F ¹)/154 ³ J(Xe,F ²)/183 ⁴ J(Xe,F ³)/36		
<i>cis</i> -ClCF = CFXe ⁺ /BF ₄ [−]	HF	263	−3545	² J(Xe,F ¹)/84 ³ J(Xe,F ²)/163 ² J(Xe,F ¹)/181 ³ J(Xe,F ²)/162 ² J(Xe,F ¹)/204		
<i>trans</i> -ClCF = CFXe ⁺ / BF ₄ [−]	HF	263	−3571	³ J(Xe,F ²)/8 ² J(Xe,F ¹)/153		
<i>cis</i> -C ₂ F ₅ CF = CFXe ⁺ / AsF ₆ [−]	HF	263	−3423	⁴ J(Xe,F ³)/57 ³ J(Xe,F ²)/183 ² J(Xe,F ¹)/85		
<i>cis</i> -C ₂ F ₅ CF = CFXe ⁺ / AsF ₆ [−]	EtCN- CD ₂ CN(3:1)	213		⁴ J(Xe,F ³)/44 ³ J(Xe,F ²)/163		
<i>n</i> -BuC≡ CxeF	CH ₂ Cl	195	−3761* ^d	4231		76
MeC≡ CxeF	CH ₂ Cl ₂	195		4241		
[<i>n</i> -BuC≡ CXe] ⁺ [OSO ₂ - CF ₃] [−]	CH ₂ Cl ₂	195	−4015*			
PhC≡CxeF	CH ₂ Cl ₂	195	−3705*	4301		
PhC≡CxeF	CH ₂ Cl ₂ / 4331		−C≡ C−Xe−F 336		CH ₃ CH ₂ CH ₂ CN	195
−3703*					−C≡ C−Xe−F ² J/ 96	
Xe(C ₆ F ₅) ₂	(CD ₃) ₂ CO	215	−4198**	³ J/45.1 ⁴ J/34.7 ³ J/9.5	¹ J(C)/320 ² J(C ^{2−6})/148	77
C ₆ F ₅ XeF	MeCN	243	−3826.3**	4099.6		

(continued)

Table 1. Continued

Compound	Solvent	<i>T</i> (K)	$\delta(\text{Xe})$ (ppm) ^a	$J(^{129}\text{Xe-L})(\text{Hz})^b$		Reference
				L = ¹⁹ F	L = ¹³ C, ¹⁴ N, ¹⁵ N, ¹⁷ O, ¹²⁵ Te	
[C ₆ F ₅ Xe] ⁺ /B(C ₆ F ₅) ₂ F ₂ [−]	MeCN	243	−3802**	³ J/82		
C ₆ F ₅ XeOCOC ₆ F ₅	CD ₂ Cl ₂	263	−3852**	³ J/69	¹ J(C)/119	
[(C ₆ F ₅ Xe) ₂ Cl] ⁺ AsF ₆ [−]	CD ₃ CN	233	−3938**	³ J/86		
C ₆ F ₅ XeF	CH ₂ Cl ₂	243	−3816**	³ J/81	¹ J(C)/195	
				4035.9		
C ₆ F ₅ XeF	EtCN/MeCN	215		³ J/80		
				4125		
C ₆ F ₅ XeCl	CD ₂ Cl ₂	213	−4117**	³ J/81		
[Xe(2,6-F ₂ C ₆ H ₃)] ⁺ / N(SO ₂ F) ₂ [−]	CH ₃ CN		−3941.9*	³ J/94	¹ J(C)/208	78
[Xe(2,6-F ₂ C ₆ H ₃)] ⁺ / N(SO ₂ F) ₂ [−]	CD ₂ Cl ₂		−3941.9*	³ J/54.8		
[Xe(2,6-F ₂ C ₆ H ₃)] ⁺ / N(SO ₂ F) ₂ [−]	CD ₂ Cl ₂		−3941.9*	³ J/58.5		
[Xe(2,6-F ₂ C ₆ H ₃)] ⁺ / N(SO ₂ CF ₃) ₂ [−]	CH ₃ CN		−3956.2*	³ J/54.3		
[Xe(2,6-F ₂ C ₆ H ₃)] ⁺ / N(SO ₂ CF ₃) ₂ [−]	CH ₂ Cl ₂		−3956.2*	³ J/55.4		
[Xe(2,6-F ₂ C ₆ H ₃)] ⁺ / C(SO ₂ F) ₃ [−]	CH ₃ CN		−3934.9*	³ J/54.4		
[Xe(2,6-F ₂ C ₆ H ₃)] ⁺ / C(SO ₂ F) ₃ [−]	CH ₂ Cl ₂		−3934.9*	³ J/54.9		
[Xe(2,6-F ₂ C ₆ H ₃)] ⁺ / CH(SO ₂ CF ₃) ₂ [−]	CH ₃ CN		−4012.9*	³ J/53.8		
[Xe(2,6-F ₂ C ₆ H ₃)] ⁺ / CH(SO ₂ CF ₃) ₂ [−]	CH ₂ Cl ₂		−4012.9*	³ J/54.8		

^aReferenced with respect to neat XeOF₄ at 24°C unless otherwise noted.

^bOne-bond coupling constants (¹*J*) unless otherwise indicated.

^c $\delta(^{131}\text{Xe})$, $\delta(^{131}\text{XeO}_4)_{\text{XeOF}_4} = \delta(^{131}\text{XeO}_4)_{\text{Xe, Freon 114}} \times \Xi(^{131}\text{Xe, Freon 114}) / \Xi(^{131}\text{Xe O}_4) + \delta(^{129}\text{Xe, Freon 114})_{\text{XeOF}_4}$; Ξ indicates the ¹³¹Xe absolute frequency of XeO₄ in SO₂ClF.

^dAn appended asterisk indicates modified values as follows: for cases referenced to XeF₂ in solution, $\delta^* = [\delta(\text{given}) - 1,818]$; except cases indicated by ** where $\delta^{**} = [\delta(\text{given}) - 1,822]$.

variable temperature, and diffusion measurements provide important information on a variety of key structural properties for understanding and further developing these materials. This work is expanding because of the development of novel nanomaterials and of course because of the increased sensitivity afforded by HP xenon. Zeolites and related materials are still well represented in these studies.

2.4.1. Zeolites

Much of the current xenon NMR work in zeolites dates back to the pioneering work by Fraissard and coworkers,⁷⁹ who showed the utility of xenon as a sensitive probe of its chemical environment. They have mapped out the dependence of the xenon chemical shift δ on a number of different variables, which are summarized by the following expression:

$$\delta = \delta_{\text{ref}} + \delta_{\text{S}} + \delta_{\text{Xe}} + \delta_{\text{SAS}} + \delta_{\text{E}} + \delta_{\text{M}} \quad (1)$$

where δ_{ref} is the reference (gaseous xenon at zero pressure, normally set to 0 ppm), δ_{S} indicates the xenon surface interaction, δ_{Xe} describes contributions from

collisions with other xenon atoms and is prominent at high xenon pressure, δ_{SAS} indicates the presence of strong adsorption sites, which are manifest at lower xenon pressures and δ_{E} and δ_{M} are due to the presence of electric or magnetic fields that can perturb the xenon chemical shift.¹⁴ In addition, the presence of other atoms or molecules can have a significant effect on the xenon chemical shift.⁸⁰ A schematic picture of the variation of the chemical shift as a function of xenon pressure is shown in Fig. 3.

Xenon is very useful to characterize the channel and pore structure and numerous papers have been published on this topic in recent years.^{81–89} Many of the applications of xenon NMR to zeolites have been reviewed previously, including experiments to probe issues related to porosity, crystallinity, the influence of cations, diffusivity of gases as well as coking, and other factors causing the blocking of pores.^{14,22} Therefore, our treatment will be abbreviated.

An example of xenon's ability to probe cation sites is the recent work on the characterization of CuHZSM-5 zeolites and CuSAPO-34 molecular sieves.⁹⁰ Laser-induced fluorescence indicated that there were at least two different sites in both of these zeolites, while ^{129}Xe NMR showed that the copper ions were diamagnetic Cu^+ , and not paramagnetic Cu^{2+} . This was evidenced by the monotonic increase of the xenon chemical shift as a function of xenon pressure (see Curve 2 in Fig. 3). In contrast, paramagnetic ions typically cause a large increase in the xenon chemical shift at low pressure, such as in the case of CoNaY zeolite⁹¹ or Ni^{2+} cations.⁹²

Experiments to study xenon dynamics have become much more prevalent. 2D exchange experiments have been used to probe the movement of xenon among zeolite pores, especially in the interesting NaA zeolite case,⁹³ following studies of the high level of xenon packing in the pores of this zeolite.^{94,95} A recent study of xenon exchange in AgA zeolite has continued this work.⁹⁶ Many of the same phenomena are apparent in the AgA zeolite as were observed in the NaA experiments. Loadings up to 8 Xe per α -cage could be accessed, with faster exchange between

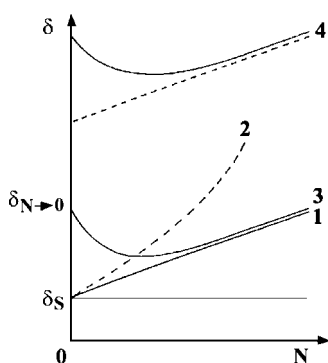


Fig. 3. Variation of the chemical shift δ versus Xe concentration. Different curves indicate the various types of interactions that xenon experiences in microporous materials. (Courtesy of Marie-Anne Springuel-Huet. Reprinted from ref. 14 with permission. Copyright 1999, John Wiley & Sons, Ltd.)

cages occurring above *ca.* $n = 4$. The high degree of loading indicates that the silver ions are most likely located in the β -cages, and thus do not affect xenon exchange appreciably. There is a 40 ppm chemical shift, but it is to low field, not high field as has been observed in AgX and AgY zeolites.⁹⁷ This again points to the location of the silver clusters as being in the β -cages. Xenon-exchange spectra for two different loadings and mixing times can be seen in Fig. 4.

Xenon diffusion in NaX zeolite was examined using pulsed-field gradient methods by BoltWesterhoff *et al.*⁹⁸ using Hahn echo and stimulated echo experiments. Two diffusion rates were observed, a slow rate corresponding to intracrystalline diffusion, and a second rate that indicated faster, long-range diffusion, which was a combination of inter- and intra-crystalline diffusion. The lifetime of xenon inside the 15–25 μm crystallites was estimated to be approximately 20 ms, and essentially all xenon exchange with the gas phase within 70 ms. Fraissard and coworkers^{99,100} studied the adsorption of benzene, *n*-hexane, and paraxylene using a model for xenon diffusion. Careful simulation of the xenon spectra matched the experimental data very well and yielded inter- and intra-particle diffusion constants that were in good agreement with the literature. In addition, ^1H one-dimensional imaging allowed the visualization of the diffusion of the hydrocarbons into the bed.

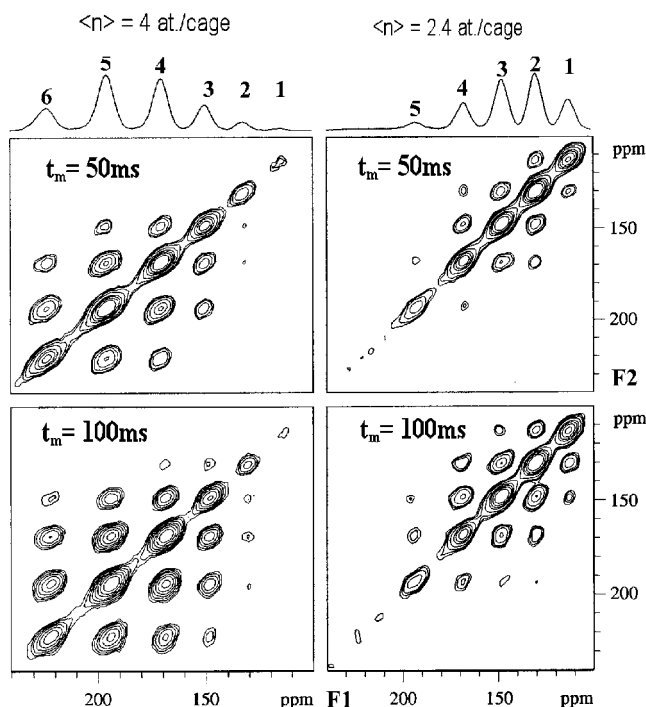


Fig. 4. 2D EXSY spectra of two samples with loadings of 2.4 and 4 atoms per cage, and measured with two different mixing times as indicated. (Courtesy of Igor Moudrakovski. Reprinted from ref. 96 with permission. Copyright 1998, American Chemical Society.)

A variable temperature study of xenon in the α -cages of NaY zeolite was reported by Labouriau *et al.*¹⁰¹ This study extends the temperature range of xenon measurements in NaY zeolite and confirms many of the earlier studies by Fraissard and coworkers. Using a more quantitative statistical mechanical model developed by Cheung,¹⁰² the authors were able to fit their chemical shift data to the following expression:

$$\delta(T) = c\varepsilon/(1 + F \exp(-\varepsilon/kT)) \quad (2)$$

where ε is the depth of a square-well potential, c a constant, and F a geometric term. The vdW interaction energy between xenon and the surface was determined to be 3.3 kJ mol^{-1} .

Zeolites with various guests. Xenon NMR is also very useful in characterizing guests inside the zeolite host structure, and has been used to study a variety of metal/surface interactions, including metal particles deposited on various zeolite substrates.^{103–105} For example, xenon NMR was used to examine platinum nanoparticle clustering in zeolite LTL.¹⁰⁶ Variable temperature measurements showed an increasing chemical shift as the temperature was lowered indicating an increasing interaction of the xenon with the Pt clusters. Xenon chemical shifts for oxidized platinum precursor complexes showed only a small deviation from the shift for the bare zeolite indicating that they occupy a small volume. Larger particles showed reduced xenon chemical shifts indicating that access to the Pt filled zeolite pore was reduced. Horvath *et al.*¹⁰⁷ have prepared gold nanoparticles inside HY zeolite using auto-reduction and ion-exchange methods. These materials have interesting CO oxidation applications. Analysis using Xe NMR and TEM indicated that the gold particles were located inside the zeolite cages, along with the Fe cations. Other applications include the investigation of Pd/Pt clusters in KL zeolite.¹⁰⁸

Other investigations of zeolite host/guest interactions include papers by Kwon *et al.* in which they used Xe to probe C_{60} and anthracene dimer formation inside zeolites,^{109,110} a study of NaCl deposited in NaY,¹¹¹ and work to show the confinement of C_{60} inside VPI-5 zeolites.¹¹²

2.4.2. Mesoporous materials

A growing number of studies have been performed on mesoporous materials ever since their discovery about a decade ago. For example, xenon studies of MCM-22 zeolite^{113,114} were carried out to investigate xenon's adsorption in the two-pore environments, supercages and sinusoidal channels. At low pressures, xenon prefers to adsorb in the supercages, while at high pressure xenon can penetrate the 10-membered rings that form the sinusoidal channels. Exchange between the two pores occurs only through gas-phase interparticle spaces at warmer temperatures. Studies using water adsorption have indicated that water covers the internal roughness in MCM-41 materials.¹¹⁵ Additional studies have probed mesoporous SBA-15 and MCM-41,^{116–119} Si-MCM-48 and Al-MCM-48,¹²⁰ and MAS-7 materials.¹¹⁷

The mechanical stability of these materials has been an important research issue since the walls of many of the mesoporous materials are amorphous, and thus their

high-temperature properties are not as robust as some zeolites. Springuel-Huet *et al.*¹²¹ compared the mechanical properties of MCM-41 and SBA-15 by adsorbing N₂ at various high pressures. Xenon NMR is useful to help determine the amount of pore damage and to assess gas access to the channels from the interparticle region. The authors found that purely siliceous materials were more robust than the Al-containing samples.

An interesting use of high-pressure supercritical xenon was described in which the authors studied the structure of mesoporous FSM-16 with different pore radii at pressures up to 10 MPa.¹²² The linewidth of adsorbed xenon changes significantly over the range of pressures. The data suggest that near 6 MPa, where the linewidths are the largest, the change to supercritical phase causes a large change in density both inside the pores as well as outside, where such behaviour is anticipated. Two-dimensional exchange spectra showed exchange between adsorbed and free xenon occurred with an exchange rate estimated to be approximately 100 Hz.

2.4.3. Silica and other porous materials

An empirical expression that relates the xenon chemical shift to the pore size in porous silica-based materials was developed by Terskikh *et al.*¹²³

$$\delta = \delta_s(1 + D/b) \quad (3)$$

where δ_s is the xenon chemical shift interaction with the silica surface; b a parameter that depends on the pore geometry, adsorption, and temperature; and D the mean pore diameter, which is related to the volume to surface ratio. In their study of 34 materials with pore sizes ranging from 0.5 to 40 nm, the data are well described using $\delta_s = 116 \pm 3$ ppm, and $b = 117 \pm 8$ Å (see Fig. 5). The correlation is

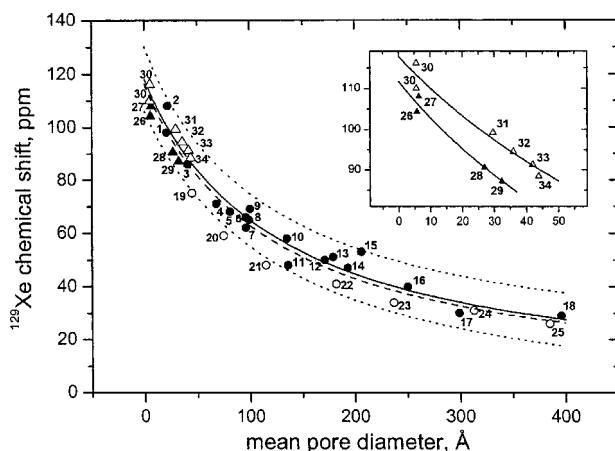


Fig. 5. ¹²⁹Xe NMR chemical shifts versus mean pore diameters for porous silica-based materials. Nonlinear least-squares fit for 18 samples shown as a solid line, and for 34 samples as a dashed line. (Courtesy of Igor Moudrakovski. Reprinted from ref. 123 with permission. Copyright 2002, American Chemical Society.)

extendable to other types of silica-based materials, including porous glasses and organosilicates. Presumably, similar relationships can be developed for other porous materials, although the presence of heteroatoms, and especially metal cations complicates matters as is well-known for the case of zeolites.

A more theoretical study was performed by Cros *et al.*¹²⁴ Fast exchange and vdW interactions with the surface are included in a model based originally on work by Derouane.^{125,126} Inclusion of two-phase exchange between the gas and surface gives a good fit to a series of colloidal silica and silica sol-gel materials with pore radii ranging from 20 to 130 Å. The authors extended their model to account for variable temperature studies. Chen *et al.* have developed a model based on single-file diffusion through the pores or microchannels of a range of microporous materials.¹²⁷ The result of their analysis yielded the following expression for the channel diameter:

$$D = 2\sqrt{2}(\delta_{\text{Xe-Xe}}/\delta_1)^{1/2}d \approx 1.681 \delta_{\text{Xe-Xe}}^{1/2}(\text{nm}) \quad (4)$$

where $\delta_{\text{Xe-Xe}}$ is the pressure-dependent Xe-Xe contribution to the chemical shift from single-file diffusion, δ_1 the pressure-dependent contribution in the bulk (and = 0.548 ppm amagat⁻¹) and d the xenon diameter. The authors calculated the value of $\delta_{\text{Xe-Xe}}$ for 14 different zeolites and showed that their expression gave a very good correlation with the actual channel dimensions of a range of zeolites.

Pietrass *et al.*¹²⁸ also used xenon NMR to examine the porosity of three mesoporous silica materials that were synthesized by sol-gel processing. Xenon did not penetrate the pores of a sample of largely disordered silica. The other two samples showed more typical xenon adsorption and chemical shift behavior. Results from variable temperature and T_1 experiments indicated that xenon had a stronger interaction with the surface of smaller pores and that it was in fast exchange with the gas phase.

Ba and coworkers^{129,130} have used 1D and 2D xenon NMR experiments along with a variety of ¹H and ¹³C conventional NMR experiments to characterize the structure and dynamics of a C₁₈ chromatography stationary phase. While the methods for producing good quality chromatography column materials is highly developed, detailed information on the molecular structure of the bonded phase (C₁₈ in this case) that can describe the performance is sometimes lacking. Differences in density of the bonded phase, as revealed by VT ¹H NMR for example, can give rise to poorer separation results. The authors show that xenon NMR, and especially exchange experiments at low temperatures, can be useful to probe diffusion between four different xenon environments: xenon solvated in the stationary phase, xenon in the pores of silica particles, between silica particles, and xenon outside the stationary phase.

Botto and coworkers^{131,132} combined high-pressure xenon (30 atm) and chemical shift imaging to investigate aero gel samples. The authors characterized the average pore structure and steady-state spatial distributions of xenon atoms in the various parts of the sample. Xenon-exchange rate constants were measured to be of the order of 1 s⁻¹, while PFG diffusion measurements yielded self-diffusivity coefficients of the order of $D = 10^{-3} \text{ cm}^2 \text{ s}^{-1}$.

^{129}Xe NMR has also been used to investigate iron containing silicates and borosilicates,^{133,134} the internal structure of Beta/MCM-41 and ZSM-5/MCM-41 composites,^{135,136} diffusion in silicon imidonitriles,¹³⁷ several carbonaceous materials,^{138,139} transition-metal-complex nanochannels,¹⁴⁰ and sol-gel derived meso- and microporous silica materials.¹⁴¹

2.4.4. Xenon in polymers

Xenon continues to act as a good probe of polymer structure, especially for characterizing free volume, pore size, permittivity, and gas diffusion in a range of different polymer systems, including blends.^{142–149} As an example of recent work, Jones and co-workers¹⁴⁶ studied xenon sorption into high-permeability polymers. Copolymers of tetrafluoroethylene and 2,2-bis(trifluoromethyl)-4,5-difluoro-1,3-dioxole as well as poly(1-trimethylsilyl-1-propyne) showed smaller xenon chemical shifts than other glassy polymers indicating that larger sorption sites are available to xenon. Xenon sorption showed a strong dependence on temperature, which indicated that a large change in adsorption enthalpy was responsible for the exponentially increasing xenon density as the temperature was lowered. The authors also carried out PFG experiments to examine the diffusion of xenon and small hydrocarbons. At short times, the derived diffusion constants were similar, although at longer times the xenon had a much larger mobility indicating the presence of larger pores that connected the smaller adsorption sites. Junker and Veeman¹⁵⁰ have also used PFG methods to determine the xenon self-diffusion constants in elastomeric terpolymer ethylene-propylene-diene (EPDM) and semicrystalline poly(propylene) (PP). Diffusion in EPDM was found to be about 20 times faster.

Morgan *et al.*¹⁵¹ used xenon NMR to investigate the cross-linking and dendritic polymers in order to study the free volume of these systems. Xenon was shown to be a good probe of polymer free volume as the xenon chemical shift increased linearly with the reciprocal of the cross-linking density, which is known to reduce the free volume. The temperature dependence of the free volume was also measured using this method. The xenon chemical shifts as a function of dendrimer generation were also measured and showed an increasing, linear behavior for generations 3–7. Smaller generations were expected to have nonspherical shapes that affected the xenon chemical shifts. Pore sizes in perfluorinated polymers have also been studied using xenon NMR.¹⁴²

Menge *et al.*¹⁴³ used ^{129}Xe NMR to probe cross-linking density in butadiene rubber networks. Structural heterogeneities of the lower cross-linking density were evidenced by the appearance of two peaks around 196 ppm in the spectrum. This effect had been observed in previous deuterium NMR studies. Theoretical models and simulations indicate that extended chain segments are more highly oriented. Polymers with shorter segments give rise to a broader or even a bimodal distribution of orientational order, which is reflected in both the xenon and deuterium NMR. Theoretical and simulation results are in good agreement with these findings.

A high-pressure probe constructed to allow the study of supercritical xenon as it interacts with different polymers (bisphenol-A polycarbonate or polytetrafluoroethylene) was reported by Nagasaka *et al.*¹⁵² The probe, which has a zirconia cell with a Be–Cu flange and indium o-ring can be used in a range of pressure up to 20 MPa, and temperatures from 150 to 400 K (see Fig. 6). Experiments performed up to 10 MPa showed xenon inside the polymer experienced a very different state from that of free xenon, which was attributed to the limitation on xenon cluster size. Essentially no exchange between the supercritical and confined xenon phases occurred on the second timescale.

2.4.5. Xenon in other solid-state materials

Xenon adsorption into three ASTM carbon black materials that are used as filler materials for the curing of rubber was reported by McGrath.¹⁵³ The xenon chemical shifts were different for each of the three samples, ranging from 53 to 94 ppm, and this difference was primarily due to differences in void space area of the three materials. The void space area varied inversely with the surface area of each material as determined by nitrogen BET measurements. A blended sample showed all three distinct resonances, while 2D exchange experiments indicated that the

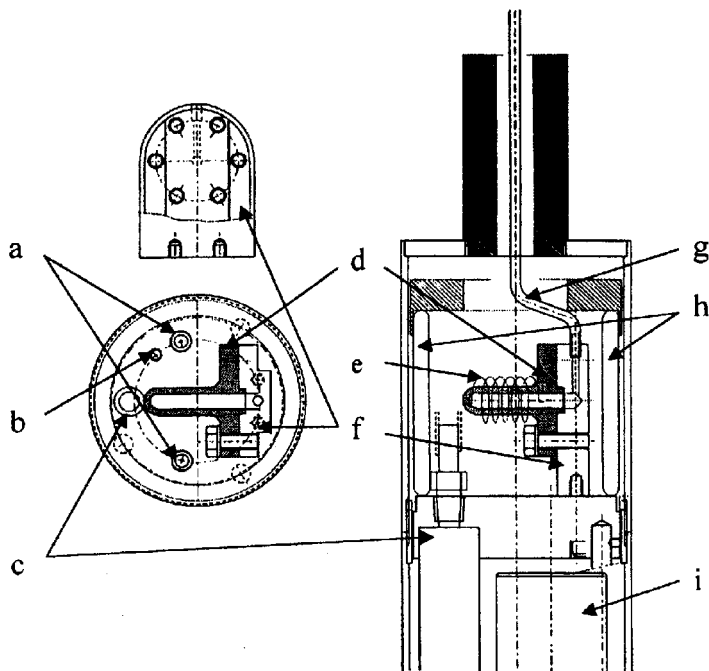


Fig. 6. Schematic drawing of a high-pressure NMR probe used to investigate polymer samples. (Reprinted from ref. 152 with permission. Copyright 2001, Elsevier Science B. V.)

exchange time between samples in the blend was of the order of a few tens of milliseconds.

Xenon has also been applied to the study of humic substances.¹⁵⁴ Previously, there had only been one study on the investigation of surface of soil materials using xenon, namely a study of xenon sorption on to the montmorillonite clay surface.¹⁵⁵ Magusin *et al.* explored the use of xenon NMR to probe the average volume to area ratio in the pore networks of humidified sand as well as carbon black and kaolin model systems. High-pressure xenon NMR experiments were carried out and showed a broad resonance around 45–55 ppm for three different samples of carbon black with different particle sizes. By comparison, the kaolin and humidified sand showed broad resonances near 8 ppm and zero, respectively. The humidified sand spectrum showed xenon spectral intensity at negative ppm values. The authors derived an expression for the pore size given the measured xenon chemical shift and a constant related to xenon adsorption on the surface.

2.5. Xenon 131 studies

Far fewer NMR studies employ ^{131}Xe due to its lower sensitivity (approximately nine times less). Nevertheless, the quadrupolar nucleus allows some unique studies as it provides information on the local electric field gradients. Meersmann and Haake¹⁵⁶ reported the very interesting resolved *field-dependent* quadrupole splitting observed in ^{131}Xe NMR at high magnetic fields between 7.05 and 16.9 T (see Fig. 7). The resolved quadrupole splitting resulting from the coherent motion of ^{131}Xe 's collisions with the small glass NMR tube is to be expected since similar results had been seen earlier at low field.^{157,158} However, the strong dependence of the quadrupole splitting on the magnetic field was unanticipated. This effect was also observed in liquid xenon using a double quantum-filtered experiment that revealed the presence of a quadrupole interaction that was smaller than the observed linewidths. The authors associated this effect with the electrical polarization of the xenon electron shell that was induced by the high magnetic field.

A detailed experimental and theoretical study of xenon-131 interactions with surfaces was carried out by Deschamps *et al.*¹⁵⁹ The observation of coherent and stochastic interactions of the quadrupolar xenon-131 nuclear spin with electric field gradients caused by the distorted electron clouds as xenon transiently adsorbs on surfaces is complicated. In some cases, both splittings and line broadening can be observed using simple pulse-acquire methods. However, if the quadrupolar splittings are small, multiple quantum-filtering experiments can be very useful to determine the presence and magnitude of these interactions in the presence of larger relaxation effects, as reported in other studies.^{160,161} In the work by Deschamps *et al.* single- double- and triple-quantum experiments were used to detect the xenon-131 quadrupolar interactions with the glass container in 6 and 8 mm NMR tubes. The splittings and relaxation effects are on the same order, which prompted the researchers to use multiple quantum-filtered experiments to measure the splittings

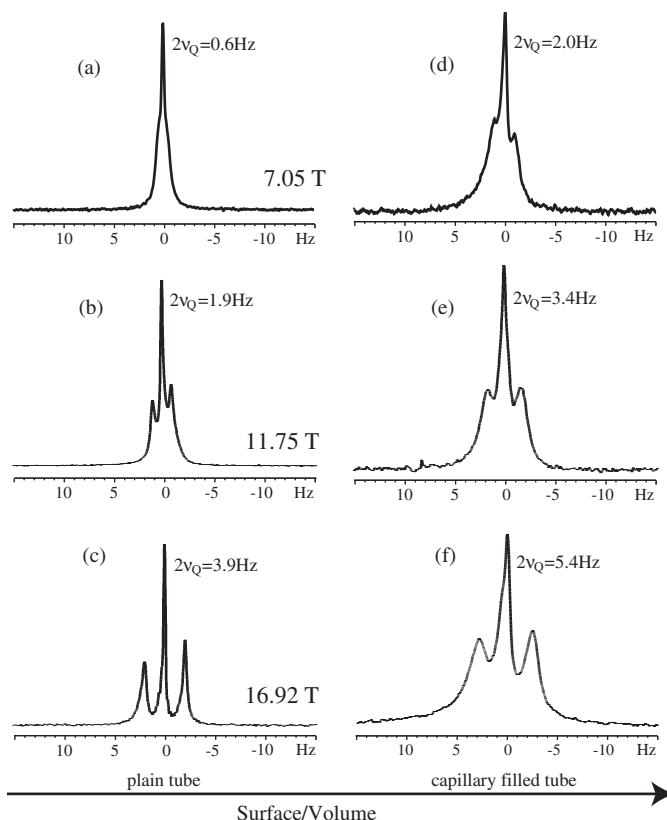


Fig. 7. Gas-phase NMR spectra of natural abundance xenon-131 contained in a cylindrical tube (symmetry axis aligned with the magnetic field) and one filled with small capillary tubes. Experiments were performed at 400 kPa, 305 K and at various field strengths as indicated. (Courtesy of Thomas Meersman. Reprinted from ref. 156 with permission. Copyright 1998, The American Physical Society.)

more accurately. They also developed a calculation procedure using an effective Liouvillian formulation to help analyze the results.

Vaara and Pyykko¹⁶² also studied the quadrupolar interaction of xenon-131 in the liquid and gas phases. The authors carried out *ab initio* calculations that verified the previously proposed diamagnetic mechanism,¹⁶³ and reproduced the experimental results obtained by Meersmann and Haake.¹⁵⁶ The origin of the effect was ascribed primarily to the interaction of the nuclear quadrupole moment with the electric field gradient that was created by the distortion of the electric cloud by the B field, and is quadratic in that field.

Several studies using ^{131}Xe to probe well-known materials in order to gain additional information have also been recently published. Fraissard and coworkers¹⁶⁴ have used xenon-131 NMR to characterize the electric field gradients inside the supercages of Y zeolites. Composite pulses were used in the nutation experiments to

help cancel artifacts from probe ringing. Values of the electric field gradient measured using this approach were 1.25 and $0.81 \times 10^{19} \text{ V m}^{-2}$ for HY and steam-dealuminated zeolites, respectively. Moudrakovski *et al.*¹⁶⁵ explored the utility of xenon-131 as a probe of void spaces in several clathrates. ^{131}Xe in β -quinol showed a very large quadrupole interaction, $\chi = 5.85 \text{ MHz}$, indicating the nonspherical symmetry in this xenon clathrate. Other xenon clathrates examined include Dianin's compound as well as structure I and II hydrates, which also showed large quadrupole interactions in the range of 1.2 – 2.5 MHz . Meersmann and coworkers¹⁶⁶ have examined mesoporous aerogels using xenon-131 and imaging methods. Using a high density of ^{131}Xe , the authors could differentiate aerogels of different densities and changing levels of hydration based on the fact that the different surfaces affect the transverse relaxation in a characteristic manner.

It is anticipated that additional applications of ^{131}Xe will be developed in the coming years since the additional quadrupole parameter allows for further characterization of materials. However, creating optically pumped ^{131}Xe is difficult due to its short T_1 , so sensitivity will still be an issue.

2.6. Calculations of xenon parameters

Ab initio and Monte Carlo methods are becoming much more powerful and therefore more capable of providing information complementary to experiments. These methods have proven invaluable for providing information on the local interactions between xenon and its chemical environment, and for interpreting complex spectral lineshapes.

Cynthia Jameson and coworkers have led the way in developing *ab initio* approaches and investigating interesting applications for xenon-based studies. Over the past several years, she and her colleagues have modeled the xenon chemical shift in a variety of cages,¹⁶⁷ clathrates,^{168,169} and nanochannels,^{170,171} as well as in gas-phase interactions.¹⁷² As an example of this work, Jameson and coworkers reported a grand canonical Monte Carlo (GCMC) simulation on xenon adsorption with methane in NaA zeolite,¹⁷³ after having made similar studies on competitive adsorption with argon and krypton.^{174,175} GCMC calculations were derived from pairwise energy interactions between Xe–Xe, CH_4 – CH_4 and Xe– CH_4 , and the atom–zeolite interactions (which affect the adsorption) as well. Chemical shift calculations were derived from similar pairwise interactions. The xenon chemical shift calculations reproduce the nine experimental mixtures explored by the authors quite well. Especially interesting is the good agreement between the experimental data and an eight-site model described by a hypergeometric distribution, as shown in Fig. 8.

The success of *ab initio* methods have made the calculations of xenon NMR parameters quite popular, with a number of groups now investigating a number of microporous materials, fluids, and even xenon compounds.^{176–182} Many of these studies compare *ab initio* results with experimental data.

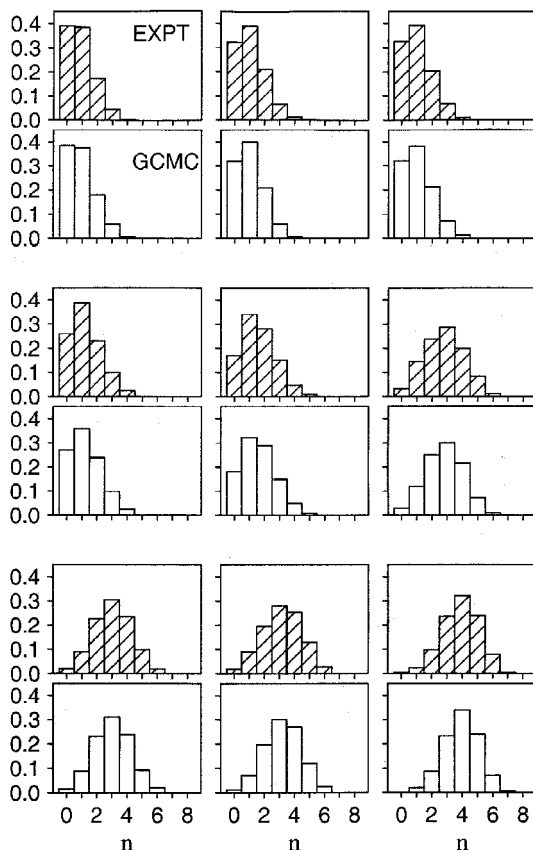


Fig. 8. Experimental and calculated xenon loadings for xenon and methane absorbed on to NaA zeolite. Occupancies for the different loadings in Xe/ α cage are shown. (Courtesy of Cynthia Jameson. Reprinted from ref. 173 with permission. Copyright 2000, American Institute of Physics.)

2.6.1. *Measuring chirality using xenon NMR*

Several interesting papers on the ability of xenon to act as a new probe of chirality have appeared.^{51,183–186} Robert and Barra^{185,186} discuss the possibility of observing two enantiomers in the same NMR sample. A splitting of approximately 10 MHz is predicted for atoms with large Z , such as Pt, Pb and Xe, which arises from the so-called anapolar term¹⁸⁷ that describes the electromagnetic interaction of an electron while it is located inside the nucleus. Elimination of dipolar coupling via deuterium substitution and degassing the sample should increase the relaxation time sufficiently that a 10 MHz splitting could be observed at 600 MHz. These experiments will require temperature regulation to better than 10 mK to eliminate the possibility of temperature-dependent chemical shifts masking the desired observations. The authors suggest Pt and Xe in chiral cages as possible target nuclei.

Bartik *et al.*¹⁸³ described the process in which an achiral species such as xenon interacts with a chiral molecule such as cryptophane-A. The resulting process of “chiralization” is factored into three terms, orientation, atomic, and electronic. Dipolar polarizability of the xenon and higher order polarizabilities are important in this process. Similarly, Harris and coworkers¹⁸⁴ state that for xenon to detect chirality in a molecule, a process of “chiralization” must occur. This process involves the distortion of the xenon electron orbitals, and specifically the paramagnetic currents as felt by the xenon nuclear spin, which depends on the chirality. This can occur through the antisymmetric part of the chemical shift tensor. The authors discuss their goal of interpreting the splittings observed in the NMR spectrum of xenon in the chiral cages of cryptophane-A.

3. HYPERPOLARIZED XENON

3.1. Optical pumping methods

It has now been well established that the use of optical pumping^{3,188–190} to produce HP xenon can provide a dramatic improvement in the S/N signal to noise ratio for a number of applications important to the fields of chemistry, materials science, and medical imaging.^{4,15–18,20,21}

The basic and much used methods of xenon optical pumping have been described in a number of articles. Typically, HP xenon is produced using spin exchange from optically polarized rubidium vapor in a low magnetic field. A variety of detailed experiments have characterized the rubidium–xenon spin-exchange process (see ref. 191 and references therein). The Rb–Xe spin-exchange rate can be described by the following rate expression:¹⁹¹

$$\Gamma_{\alpha} = \frac{1}{T_1^{\text{SE}}} = [\text{Rb}] \left(\langle \sigma v \rangle_{\text{SE}} + \left(\frac{\kappa}{[\text{M}]} \right) \right) = [\text{Rb}] \gamma' \quad (5)$$

where $[\text{Rb}]$ is the Rb density, $\langle \sigma v \rangle_{\text{SE}}$ the velocity-averaged binary spin-exchange rate important at high pressure, κ a constant that describes the rate of Rb–Xe spin exchange within vdW complexes (important at low pressure), and $[\text{M}]$ is the buffer gas pressure that often determines the vdW complex lifetime. Rates for spin exchange are of the order of $10^{-16} \text{ cm}^3 \text{ s}^{-1}$ so high Rb densities and copious laser power are required to produce HP xenon for NMR experiments.

Experimentally, the optical pumping cell contains a small amount of Rb metal and is held in an insulated oven to create Rb vapor at a field of a few tens of G. Optical pumping of the Rb D_1 transition (795 nm) is normally achieved using broadband, high-power (tens of W) semiconductor diode-array lasers that have nominal linewidths of 1–2 nm. A major advance in producing large amounts of HP xenon was achieved by the Happer group¹⁹² some years ago. In that work, a continuous flow of HP ^{129}Xe was produced using an optical pumping setup of the type shown in Fig. 9. The pumping cell is typically pressurized to several atmospheres

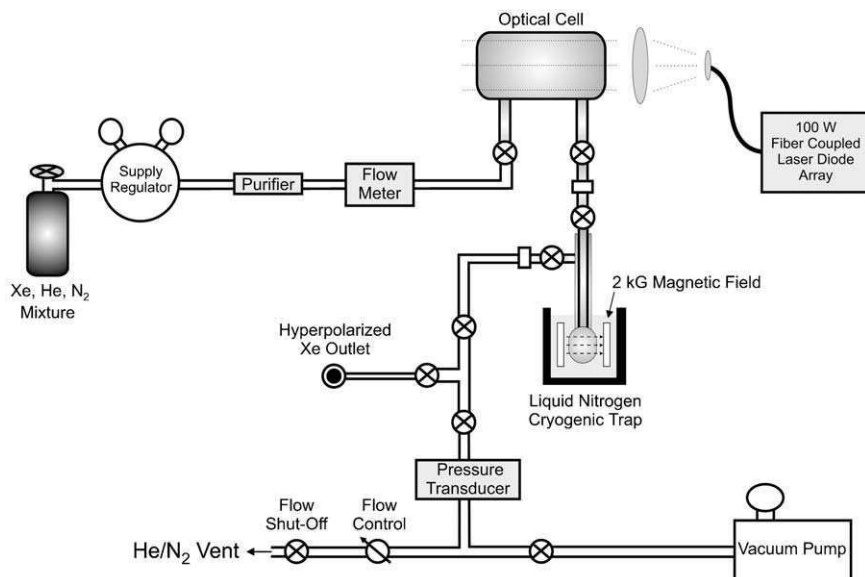


Fig. 9. Apparatus designed to create HP xenon under continuous flow and accumulate polarized xenon ice at cold temperatures. (Courtesy of Bastiaan Driehuys and John Mugler.)

using a mixture of xenon (few %), nitrogen (1–10%), and remainder He gas. N_2 is used to quench Rb fluorescence and improve the polarization, while the He gas pressure broadens the Rb absorption line to ~ 1 nm for better light absorption. Gas flows of several $\text{cm}^3 \text{s}^{-1}$ of HP^{129}Xe can now be produced. Variations to this procedure have been developed and are described below.

3.1.1. Higher polarization methods

New developments in advanced pumping systems that deliver significantly higher xenon polarizations than previous reports have appeared in the past few years. This is largely due to the availability of newer laser systems that have fiber-coupled outputs and thus deliver excellent laser beam quality. For example, early optical pumping systems that utilized continuous flow used high-power (> 100 W) diode-array lasers, although the beam quality was not very good. This often led to light and dark regions in the cell because of nonuniform irradiation, and thereby poor xenon polarization. By 2000, fiber-coupled systems with good beam quality became available that greatly simplified the production of HP xenon without the troublesome laser beam “hotspots” that were sometimes blamed for causing optical pumping cells to explode!

Recent advances in creating HP xenon include the work by the Bowers group,¹⁹³ who were able to create 67% xenon polarization using 210 W of 795 nm light by combining the output of seven laser diode arrays. Their system is also capable of producing 1 L atm h^{-1} at polarizations around 12%. A detailed study of the

polarization as a function of the xenon concentration showed that the xenon polarization was optimized at low xenon concentrations (ca. 1% Xe), as expected from earlier studies. The use of recirculating flow has also contributed to high xenon polarization. Recirculating systems have been used before to carry out xenon studies on static systems in high magnetic field.^{194,195} In the work by Knagge *et al.*¹⁹⁶ a nonmagnetic peristaltic pump was used to recapture much of the residual xenon polarization and fed it back into the optical pumping cell. The result was a gain in polarization of 3–4 times, as can be seen in Fig. 10. The recycled xenon is still highly polarized, which allows the maximum xenon polarization to grow to 61–69%, depending on the gas mixture.

Chupp and coworkers¹⁹⁷ described an automated xenon polarization and delivery system that was optimized for *in vitro* and *in vivo* experiments. The entire system was located in the high-field environment of the nearby 2 T MRI magnet. A mixture of 1700 torr Xe and 150 torr N₂ was used in a batch mode. A laser power of 30 W allowed polarizations of 7.5% to be achieved. HP xenon was frozen and stored as a xenon ice, and then melted and expanded into a glass piston from which small doses of xenon could be delivered for a variety of HP xenon MRI experiments. Meersmann and coworkers¹⁹⁸ recently explored the possibility of creating HP xenon without the use of buffer gases. At the higher pressures used in their studies (approximately 7 atm), the need for N₂ to quench Rb fluorescence is diminished. Using laser powers of 29 and 58 W, polarizations above 10% were realized, although the polarization decreased quickly to below 1% above 2 atm. Nevertheless, the HP xenon NMR signal intensity is nearly constant above 2 atm because the increased xenon number density compensates for the lower polarization. Fukutomi *et al.*¹⁹⁹ studied the polarization dependence on the gas mixture and found that the addition of hydrogen, and especially deuterium was beneficial for xenon optical pumping. However, N₂ and He still provided the best polarization, 35% under their experimental conditions. Happer and coworkers²⁰⁰ investigated the possibility of creating

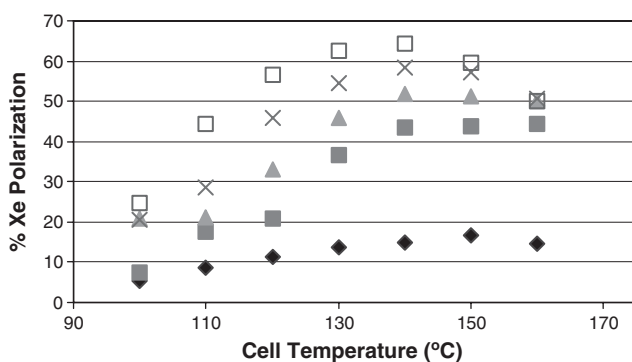


Fig. 10. HP Xe polarization for single pass (diamonds 150 cc min⁻¹) and recirculating flow at different flow rates (filled squares, 250 cc min⁻¹; triangles, 200 cc min⁻¹; crosses, 150 cc min⁻¹; and open squares, 100 cc min⁻¹) and temperatures. (Reprinted from ref. 196 with permission. Copyright 2004, Elsevier B. V.)

HP xenon by spin exchange with optically pumped Cs. A 1 W diode laser tuned at 894.3 nm was used and produced a xenon polarization of 2.5%. Cs is 10% more efficient at polarizing xenon, so the use of higher output diode lasers may make this approach appealing.

Some interesting studies have utilized MRI techniques to visualize the optical pumping process *in situ*. Happer and coworkers²⁰¹ used low-field imaging combined with optical detection to image the Rb polarization using fields of 4 and 35 G. Comparing the signal intensities of the electron spin manifolds, they were able to measure the absolute Rb polarization as a function of position. Shah *et al.*²⁰² used similar MRI techniques to obtain absolute Rb and xenon polarization levels in their pumping cell. Xe polarizations of around 20% were achieved, which were much less than the Rb polarization levels; however this polarization could be transferred to a freezing unit for accumulation. Ishikawa and coworkers²⁰³ first polarized either Rb or Xe by optical pumping and then transferred this magnetization to Cs atoms for detection. Using MRI techniques, they were able to probe the distribution of Cs polarization after polarization transfer. These studies follow in the footsteps of pioneering work by Haroche and Cohen-Tannoudji.²⁰⁴

The use of narrow-band lasers is advantageous because it allows Rb to absorb more of the laser light. Recent laser line-narrowing experiments appear promising,^{205,206} although to date the full potential of line narrowing has not been realized. Therefore, most researchers currently use commercially available diode arrays and He pressure broadening to achieve decent polarizations. In contrast, Jänsch²⁰⁷ has utilized extremely narrow-band TiSapphire laser to polarize small amounts of xenon to very high levels (70%) in a batch-mode operation. Previous studies by many others have used such lasers, although not in a flow system. Different Xe/N₂ ratios (all at 100 mbar pressure) were examined, with the highest polarizations achieved when the xenon pressure was below 10 mbar. Separation of xenon from the gas mixture was achieved by freezing the xenon at 77 K while pumping on the system. The xenon could then be used for low surface area experiments, some of which are described in Section 3.3.3.

3.1.2. *New or alternative methods of optical pumping*

A number of researchers have explored methods to improve the xenon polarization available via optical pumping. Several experiments have explored optical pumping and spin exchange in high magnetic field. Early work by Zeng *et al.*²⁰⁸ and careful studies by Augustine and Zilm,^{209,210} have indicated that although HP xenon can be created at high magnetic field, the spin exchange is quite low and thus polarization levels are not as high as observed in low magnetic field. Rice and Raftery²¹¹ also carried out optical pumping experiments in high magnetic field. Measurement of the xenon polarization buildup over a range of He buffer gas pressures and temperatures allowed measurement of the spin-exchange parameters. One surprising result of this work was the measurement of a significant vdW contribution at high pressure. Very recently, Happer and coworkers^{212,213} studied Xe spin exchange with Rb and Cs at high field, and measured values of $1.60\text{--}1.84 \times 10^{-16} \text{ cm}^3 \text{ s}^{-1}$ for the

binary spin-exchange rate coefficient. They caution the use of either the well-known Killian²¹⁴ or Smithells²¹⁵ formulas for the Rb density, which in their experience can cause errors by factors of 2–3. Instead they suggest using Faraday rotation measurements. Overall, significant differences in the results among these high-field studies, in both the binary collision and vdW contributions to spin exchange, point to the difficulty in making these measurements. Generally, however, it is better to do optical pumping in low field where the spin-exchange rates are somewhat larger, and access to the optical pumping cell is much better.

While the majority of work in creating HP xenon has focused on the development of optical pumping methods, one recent study²¹⁶ shows that at milliKelvin temperatures, xenon can also be polarized to high levels and at a high rate. Normally, the xenon T_1 increases exponentially, with the authors measuring a power law of xenon $T_1 \sim T^{-1.7}$. By adsorbing ^3He along with xenon on a high surface area silica sample, the relaxation of xenon was reduced to approximately 1,000 s. This relaxation was almost independent of temperature, such that xenon could reach its high polarization state much more rapidly.

Saam²¹⁷ has recently designed a novel method to polarize liquid xenon using gas–liquid-phase exchange. Optical pumping takes place in the gas phase, while a convection loop is used to transfer polarized gas to the liquid phase. A steady-state polarization of 8% was measured for 0.1 mL of the xenon liquid.

3.2. HP xenon bulk measurements

HP xenon has been applied to a variety of pure-phase studies. Gas-phase studies are of interest especially for improving the polarization. Liquid xenon is promising because of the high polarization available, and the fact that xenon is a good solvent. Because of the low solubility of xenon in water it is very advantageous to utilize the high polarization afforded by HP xenon. Solid xenon is typically used for polarization storage, while interest in supercritical HP xenon has recently developed.

3.2.1. Gas-phase HP xenon T_1 measurements

Fujiwara *et al.*²¹⁸ have used the high polarization to measure the T_1 values of xenon in high magnetic field in a variety of glass and gelatin containers. Using a pulse sequence with alternating pulses of small angles α and 2α , they were able to determine the T_1 values in a single pumping cycle and verified that the T_1 was inversely dependent on the square of the container diameter ($1/d^2$) as well as the material and its permeability in the case of gelatin. T_1 times of up to 400 s were observed in Pyrex cells with diameters of 20 mm.

A careful reexamination of surface coatings used in optical pumping experiments^{219,220} has shown that the water content used during the coating procedure is important for extending the xenon T_1 . Unexpectedly, replacement of the surface protons with deuterium in the coatings had only a very small effect on the xenon

relaxation time. It appears that xenon adsorption and desorption is more important than magnetic effects.

Chann *et al.*²²¹ examined the gas-phase relaxation of xenon at densities below 14 amagat using a number of different gas mixtures. They concluded that the spin-rotation interaction is responsible for relaxation at low densities and determined a relaxation rate of the form

$$\Gamma = \Gamma_w + \Gamma_{\text{vdW}}^{\text{Xe}} / (1 + r[\text{B}]/[\text{Xe}]) \quad (6)$$

with Γ_w being the wall relaxation rate, which they measured to be 3 h in their cell. $[\text{B}]$ is the buffer gas pressure and r is the ratio of molecular vdW breakup rates for the buffer gas and xenon. The average Xe–Xe relaxation rate for pure xenon was measured to be $6.72 \times 10^{-5} \text{ s}^{-1}$, corresponding to a relaxation time of 4.1 h but was smaller when buffer gases were substituted at the same pressure.

3.2.2. *Highly spin-polarized liquids and solutions*

Several new studies have focused on the strange behavior of highly polarized ^{129}Xe liquids.^{222–224} Nacher and coworkers²²³ investigated the effects of dipole couplings, quantum exchange, and spin diffusion in highly spin-polarized liquids accessed via optical pumping of ^3He and ^{129}Xe . NMR detection after small tip angles showed linear behavior, but at larger tip angles instabilities occurred, causing abrupt relaxation after a delay. It was postulated that the magnetization was preserved, but not measurable because it had dissipated from Zeeman order to an unknown order. They also studied the effect of large pulses on the evolution of xenon magnetization in highly ($\sim 6\%$) polarized liquid xenon.²²² Experiments were carried out at 1.7 mT. Small-pulse angles led to the spatial clustering spin magnetization caused by dipolar coupling over macroscopic lengths, and gave rise to sharp features in the spectrum. At larger pulse angles ($> 35^\circ$) the evolution of the xenon magnetization was unstable, which was ascribed to possible turbulent motion. Similar results have been observed in liquid ^3He ,²²³ and were previously predicted by Jeener,²²⁵ although the magnitude of the instabilities is smaller than that predicted for xenon.

The effect of large dipolar fields on the T_2 spin relaxation time was also investigated by Romalis and Ledbetter.²²⁴ Nonlinear effects caused by the large dipolar fields present in a spherical cell containing HP xenon liquid are readily observed. While the T_1 of HP xenon at 180 K is over 30 min, the transverse magnetization is quickly dissipated in a highly nonexponential manner after just 20 s due to the large dipolar field. A CPMG sequence is used to reduce the effect of dephasing residual field gradients, but it has no effect on the dipolar fields. The authors propose that the highly nonexponential decay of the magnetization is due to the strong dipolar field as being initiated by residual gradients. These gradients cause a helix to form in the xenon liquid, which in turn causes an additional gradient, and thus provides a positive feedback mechanism. In Fig. 11 the rapid decay of the transverse magnetization can be seen. By contrast, the xenon T_1 in liquids is many minutes. However, by miss-setting the π pulses by 3° , the effect of the dephasing dipolar gradients can be eliminated such that T_2 relaxation times as long as 1,360 s were

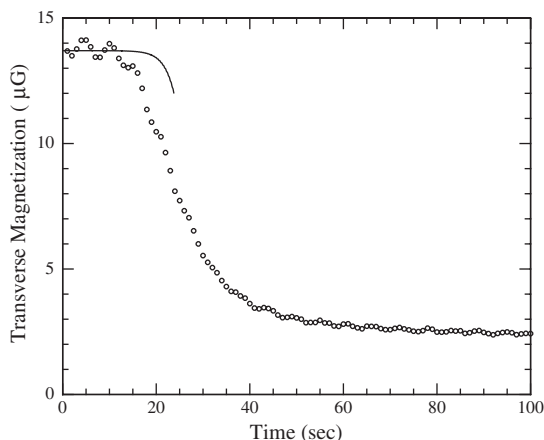


Fig. 11. Onset of nonexponential decay in liquid HP xenon due to dipolar fields. Open circles show envelope of the transverse magnetization signal obtained with CPMG pulse sequence for $\tau = 100$ ms and an applied longitudinal field gradient $dH_{Ez}/dz = 1.4 \text{ mG cm}^{-1}$. Solid line is a model of the initial magnetization gradient growth with no free parameters. (Courtesy of Michael Romalis. Reprinted from Ref. 224 with permission. Copyright 2001, The American Physical Society.)

observed. The authors discuss the use of this system as a sensitive magnetometer in combination with a superconducting quantum interference device (SQUID) detector.

Berthault *et al.*²²⁶ describe a method to invert the high polarization of xenon in an efficient manner that is not affected by radiation damping. A frequency swept CHIRP pulse was applied along with a simultaneous gradient to broaden the resonance during inversion, and evade the potential radiation damping effect. Liquid-phase xenon polarizations as low as 5% would suffer from radiation damping in many cases, but the application of this new approach eliminated radiation damping losses.

Chuang and coworkers²²⁷ have reported a novel method for determining the absolute magnitude of the xenon polarization in liquid xenon. Owing to xenon's high polarization, its dipolar field is large and adds to the normal external field. This effect causes a time-dependent frequency shift of a probe nuclear spin, ^1H in dissolved " CH_3Cl " as the xenon polarization relaxed toward its equilibrium value. The frequency shift was measured to be approximately 6 Hz, corresponding to xenon polarizations of 0.6%.

3.2.3. Highly spin-polarized solid xenon

Experiments on the T_1 of xenon in the solid state showed that it was highly temperature- and field-dependent.²²⁸ A mechanism for the xenon relaxation was described in which a two-photon Raman process was involved that increased the ^{129}Xe relaxation. At colder temperatures, ^{129}Xe is also relaxed by its coupling to

^{131}Xe , which relaxes quickly through a large quadrupole interaction that occurs at grain boundaries. Recently, it was shown that the T_1 of solid xenon could be doubled to 35 h at 4.2 K and 180 G by annealing the solid at 113 K for 10 min after initially freezing it at 77 K.²²⁹ These experiments provided further evidence for the low-temperature cross-relaxation mechanism between ^{129}Xe and ^{131}Xe .

Jänsch and coworkers²³⁰ reported experiments on HP xenon solid thin films at temperatures in the range of 50–100 K. The magnetization field was measured and used to determine the polarization of the solid xenon, which was approximately 80%.

3.2.4. *Highly spin-polarized supercritical xenon*

An interesting report on the production of supercritical xenon using HP gas was described³⁰ using a high-pressure capillary tube. The xenon polarization was approximately 140 times Boltzmann levels. The chemical shift was measured to be 44.5 ppm indicating a pressure of approximately 81.5 amagat.

3.3. HP xenon in materials and on surfaces

The high polarization of xenon allows a variety of new surface experiments to be performed. Many of the studies on porous materials that have previously been carried out using conventional ^{129}Xe are much easier and faster using HP xenon. In addition, lower pressures are available, thus improving the ability of the experiments to investigate the xenon-surface interaction. Methods to deliver HP xenon to surfaces have been developed Pines^{194,195,231} and Raftery²³² groups and more recently by other groups.^{233,234} These efforts have made the study of surfaces much more attractive than previous one-shot experiments,^{235,236} and have allowed an increasingly challenging set of experiments to be performed. Early studies focused on describing the polarization gain by the surface available in static and magic angle spinning (MAS) samples, while later papers have studied an expanding number of interesting materials with important surface properties, as described below.

3.3.1. *Zeolites and mesoporous materials*

Gedeon and coworkers has recently reported HP xenon studies of the nanoporous materials MCM-41, SBA-15, AlPO-41, ITZ-6, AISBA-15 as well as mesoporous SiO_2 and TiO_2 .^{237–242} HP xenon allows one to use low concentration of xenon in the experiments such that the xenon chemical shifts reflect mainly interaction between the adsorbed xenon atoms and the surface. Variable temperature measurements can be used to obtain information on the xenon heats of adsorption on the different materials.²⁴³ The use of a continuous flow system, with an inline, detachable getter makes xenon NMR analysis of microporous materials almost routine.²³⁹ Even with polarizations of a few percent, it is possible to analyze thin film materials, which promises to significantly broaden the applicability of xenon NMR studies. The use of magic-angle spinning combined with HP NMR was also investigated by this

group, and 2D EXSY experiments were performed.²³⁷ A nice example of this work is shown in Fig. 12 in which a 2D EXSY spectrum of HP xenon in ITQ-6 under MAS conditions.

The Canadian group led by Ripmeester^{123,244–247} have explored a number of chemical environments of nanoporous and mesoporous inorganic and organic materials using HP xenon, including the anisotropic voids in a single zeolite crystallite (see below), organic and inorganic nanoporous and mesoporous materials, and organic functionalized inorganic hosts. For example, experiments using HP xenon under continuous flow were used to probe the pore structure of functionalized mesoporous silica with pore sizes between 5 and 30 nm.²⁴⁵ The high polarization allowed measurements at low pressure, such that the researchers could probe the xenon surface interaction directly. Variable temperature measurements were used to probe the adsorption characteristics of xenon. It was observed that xenon NMR was better at characterizing the nonuniformity in the pore size than either N₂ adsorption or TEM. The Liu and Ripmeester groups²⁴⁸ have used xenon NMR to investigate silylated mesoporous MCM-41. The surface properties of these materials were examined using variable temperature HP xenon. MCM-41 samples were

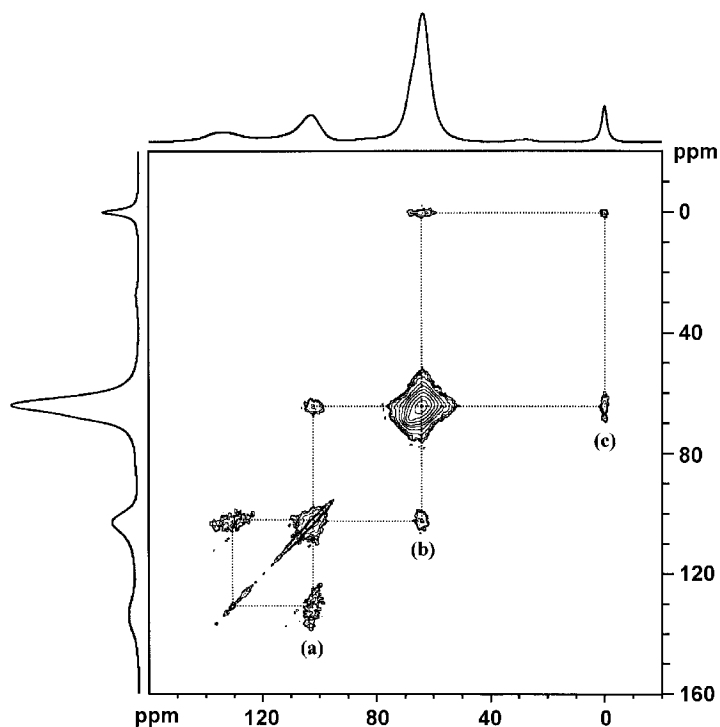


Fig. 12. 2D EXSY spectrum of HP adsorbed in ITQ-6 under MAS conditions showing exchange between channels, cavities, inter-lamellar spaces, and the gas phase. (Reprinted from ref. 237 with permission. Copyright 2003, The Owners Society.)

silylated using butyltrichlorosilane and dodecyltrichlorosilane with surface coverages ranging from 0.26 to 1.33 nm². The chemical shifts increased as a function of coverage and chain length. Individual contributions to the xenon chemical shift from the MCM wall as well as CH₃ and CH₂ surface groups could be extracted from the data.

Terskikh *et al.*²⁴⁷ reported an interesting study in which they used the high polarization of HP xenon to investigate the chemical shift anisotropy of xenon in a single-crystal zeolite sample, (see Fig. 13). A single millimeter-size silicalite (aluminum-free ZSM-5 zeolite) sample was investigated and showed an unanticipated splitting in some of the spectra taken at different orientations. This phenomenon was ascribed to a crystal twinning that was also confirmed with X-ray diffraction. The total surface area of the sample is estimated to be 1 m², which is facilitated by the high xenon polarization.

3.3.2. Other materials

The Canadian group also studied the formation of xenon hydrates on the surface of ice using HP xenon (see Fig. 14).²⁴⁹ Films could be grown up to 1,000 Å until the rate slowed down. It was proposed that a nucleation preceded the hydrate growth because of an observed memory effect in which hydrate formation started immediately after the second cycle of xenon adsorption–desorption. The induction period is reproducible at the same temperature and pressure and follows an exponentially decreasing function of the pressure. The induction period is almost absent upon reintroduction of xenon after desorption, indicating that the surface “remembers”

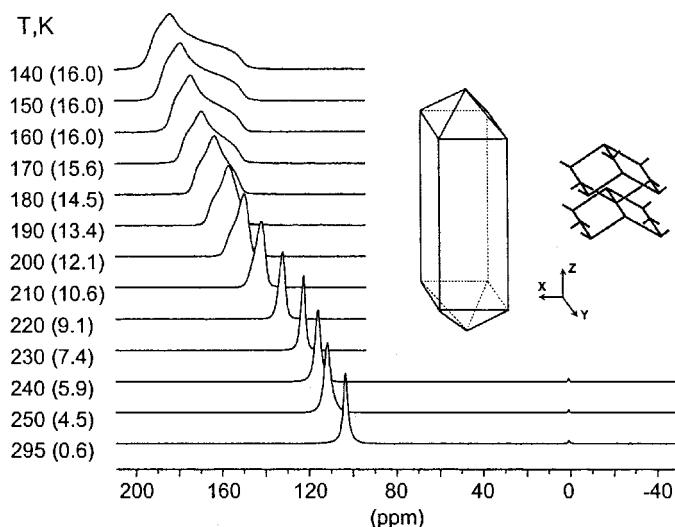


Fig. 13. HP xenon adsorbed in a 1 mm silicalite single crystal at different temperatures. Channel orientation is shown in the inset. (Courtesy of Igor Moudrakovski. Reprinted from ref. 247 with permission. Copyright 2001, American Chemical Society.)

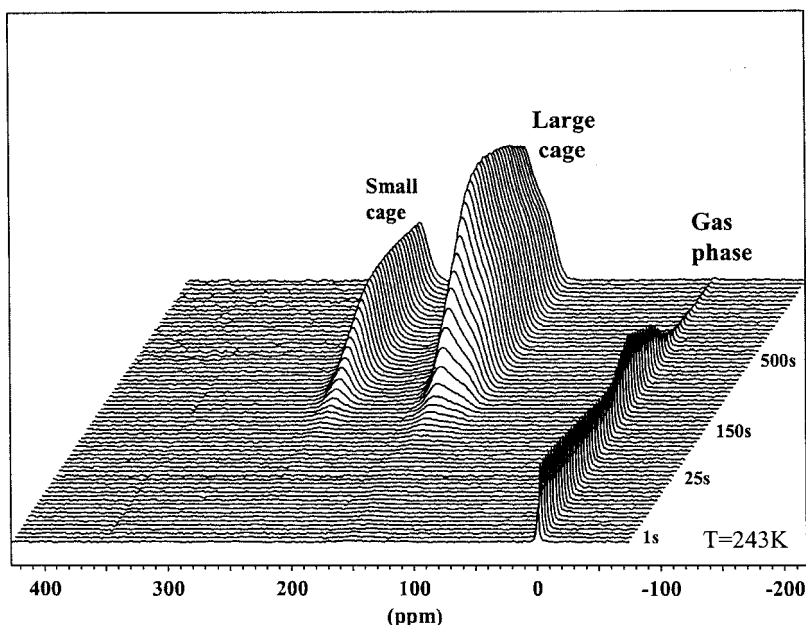


Fig. 14. Formation of xenon hydrates as shown in the time development of the xenon spectrum for the reaction of HP xenon with powdered ice. (Courtesy of Igor Moudrakovski. Reprinted from ref. 249 with permission. Copyright 2001, American Chemical Society.)

the structure needed for hydrate formation, possibly by retention of hydrogen-bonded five-member water rings. Only 2–3% of the xenon is thought to be involved in hydrates left on the surface after evacuation. Nucleation and growth were fitted to an Avrami–Erofeyev model. The authors also reported a transient structure II hydrate of Xe.²⁵⁰ Bowers and co-workers²⁵¹ have also studied xenon clathrates using HP xenon. Xenon clathrates were formed by bringing xenon into contact with preformed acetone/water or SF₆/water type II clathrates. After several minutes, xenon type II clathrates formed, but their formation was in competition with the original SF₆ or acetone guests.

Moudrakovski *et al.*²⁵² investigated the interaction of HP xenon with porous Vycor surfaces and measured the diffusion of xenon through the small 42 Å pore structure of the Vycor. Their measurement of the diffusion constant, $2.2 \times 10^{-8} \text{ m}^2 \text{ s}^{-1}$, compared well with similar experiments using adsorption measurements and conventional xenon experiments.

HP xenon has been used to investigate carbonaceous materials as well, such as the interaction of xenon with C₆₀ and C₇₀ at low temperatures.²⁵³ Laser-polarized xenon has also been used to probe the interaction of xenon in carbon black mesopores of fuel cell materials that contain Pt metal.¹³⁹ The HP xenon technique allows a fast method to determine enthalpy of adsorption in the pores.

Recently, Ripmeester and coworkers²⁵⁴ has investigated the interaction of xenon in dipeptide materials. Two microporous dipeptides, L-Ala-L-Val and L-Val-L-Ala,

were synthesized and studied by adsorption of HP xenon in the chiral channels. High-packing efficiency and remarkably different absorption properties were observed for the two dipeptide materials.

3.3.3. Very low surface areas

Recent progress^{196,255–259} points to the encouraging possibility that SSNMR can access very low surface area systems with surface areas in the 1–1,000 cm² range. In a truly dramatic experiment, Jänsch²⁵⁸ showed that a sub-monolayer coverage of xenon on a 1 cm² Ir(111) surface could be detected with good *S/N* ratio. Experiments were performed under carefully controlled UHV conditions that allowed excellent preparation and control of the metal surface. NMR experiments were performed at 2 T. The isotropic and anisotropic chemical shifts were measured to be 1,032 and 291 ppm, respectively, while the linewidth was a relatively small 20 ppm, indicating a homogeneous surface environment for the xenon. The large chemical shift values provide evidence for a Knight shift which had been seen before in catalytic studies. The adsorption of xenon on the metal surface is unusual in that there is a very strong vdW interaction between the metal electrons and the xenon nucleus that is not accounted for quantitatively by theory, although the general vdW parameters are thought to be reasonably well understood. In Fig. 15, ¹²⁹Xe spectra are shown for xenon adsorbed to Ir(111) substrate that had been chemically altered by adsorption of CO and ethylidene.²⁵⁷

Another approach is to enhance the signal of the adsorbed species itself. Knagge and coworkers¹⁹⁶ recently showed that the adsorbate (methanol) on a low surface area material (titania) could be detected with decent *S/N* ratio using SPINOE

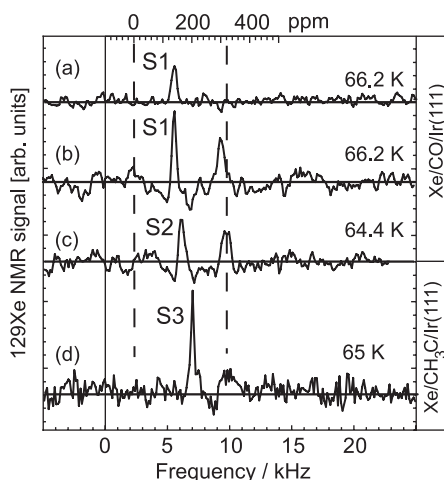


Fig. 15. Monolayer coverage of HP xenon adsorbed on to Ir(111) surface that has been coated with either CO or CH₃C-. Submonolayer surface xenon is seen in the spectrum with peaks marked S1–S3. (Courtesy of Heintz Jänsch. Reprinted from ref. 257 with permission. Copyright 2003, Elsevier Science B. V.)

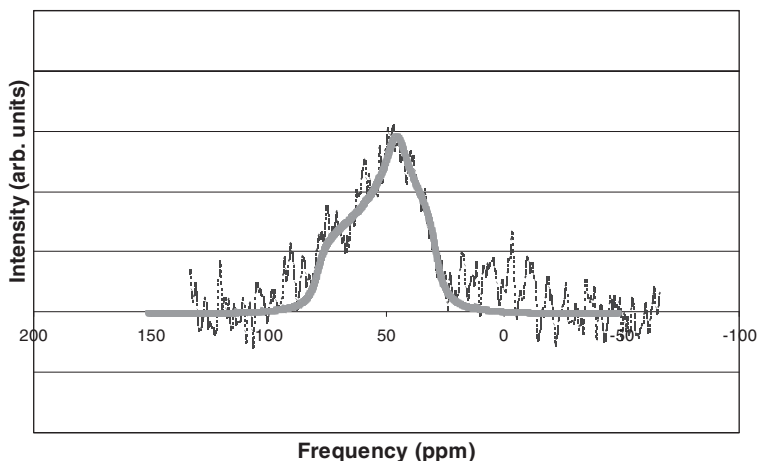


Fig. 16. ^{13}C spectrum of methanol adsorbed on TiO_2 nanoparticles and polarized using HP xenon. The spectrum corresponds to a sample with $2,500\text{ cm}^2$ surface area. (Reprinted from ref. 196 with permission. Copyright 2004, Elsevier B. V.)

polarization transfer. In these experiments, polarization transfer (see below) from xenon to the surface adsorbates ^{13}C nucleus was accomplished for a surface with area of approximately 2500 cm^2 . The CSA pattern from the static sample can be seen in Fig. 16.

3.4. Polarization transfer methods

A long-term goal of HP xenon research is to develop methods to polarize surface nuclei, and thereby enhance surface NMR studies. Applications in a variety of areas of surface science, catalysis, biophysics, semiconductor physics, and many other areas could be envisioned if such methods become routine. Various groups have explored a variety of methods to transfer polarization from HP xenon to other atoms, including rotating-frame cross-polarization (CP),²⁶⁰ thermal mixing in low magnetic field,²⁶¹ and SPINOE,^{38,262} to date, however, successful polarization transfer have been limited to a select subset of materials and experiments.

3.4.1. Polarization transfer to material surfaces

A number of researchers have explored the potential for xenon CP to various high-surface-area materials such as silica.^{195,232,263–265} Pietrass *et al.*²⁶⁶ explored the SPINOE method to transfer HP xenon polarization to the ^1H and ^{29}Si on a silica surface. At 135 K, xenon readily adsorbs to the surface and transfers its polarization to surface hydroxyl protons resulting in a polarization enhancement of 2–5 (see Fig. 17). Conventional ^1H – ^{29}Si CP was then used to move the polarization to the Si atoms at the surface of the material. Happer and coworkers²⁶⁷ observed a coupling

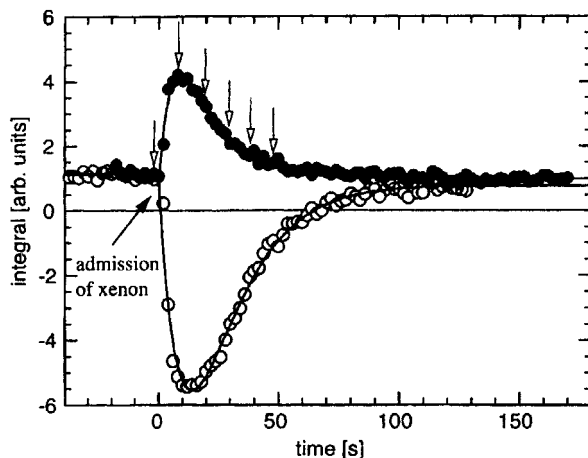


Fig. 17. Time evolution of the ^1H NMR signal from hydroxyl protons of silica Aerosil 300 in contact with optically polarized xenon at a temperature of 135 K. HP xenon with both positive and negative polarizations was used to generate the two different curves. (Reprinted from ref. 266 with permission. Copyright 1998, Academic Press.)

from xenon to protons by matching the surface proton Larmor frequency (ω_0) to xenon rotating frame frequency (ω_1) in a Pyrex cell. The xenon relaxation rate was enhanced when the two frequencies were equal.

Brunner *et al.*²⁵³ examined the polarization transfer to ^{13}C in C_{60} and C_{70} thin films. Experiments were conducted under MAS conditions using SPINOE transfer, and showed differential enhancement for the different atomic sites in C_{70} . Rødøm *et al.*²⁶⁸ studied the polarization transfer from ^{129}Xe and ^3He to protons in polyethylene-oxide-coated aerosol particles as well as to adsorbed $^{13}\text{CO}_2$. Low surface coverage of ^3He limited the polarization transfer to only a factor of 2, but with xenon, polarization enhancements of up to 20 were observed at 130 K. Seydoux *et al.*¹⁹⁵ investigated xenon polarization transfer to silica using a recirculating flow system. The long T_1 time for ^{29}Si nuclei is advantageous for polarization transfer, and as a result, the observed silicon signal built up over 2,000 s. It was estimated that the enhancement was about a factor of 20 times the thermal polarization level. In contrast, the surface ^1H relaxation time is approximately 15 s and thus gives rise to a smaller enhancement signal.

The Raftery group has focused on understanding the details of polarization transfer to surface nuclei, using simple model systems and carrying out detailed studies over a range of temperatures.^{269–271} In an interesting result, they showed that CP was effective even at room temperature and beyond. This was due to relatively fast polarization transfer time constant (ca. 10 ms) and the inherent background subtraction in the CP experiment that allowed the detection of very small signals many times smaller than Boltzmann polarization levels. A careful study of the dynamics of polarization transfer using CP was carried out to develop a model of the polarization transfer under CP²⁷¹ and the results can be seen in Fig. 18.

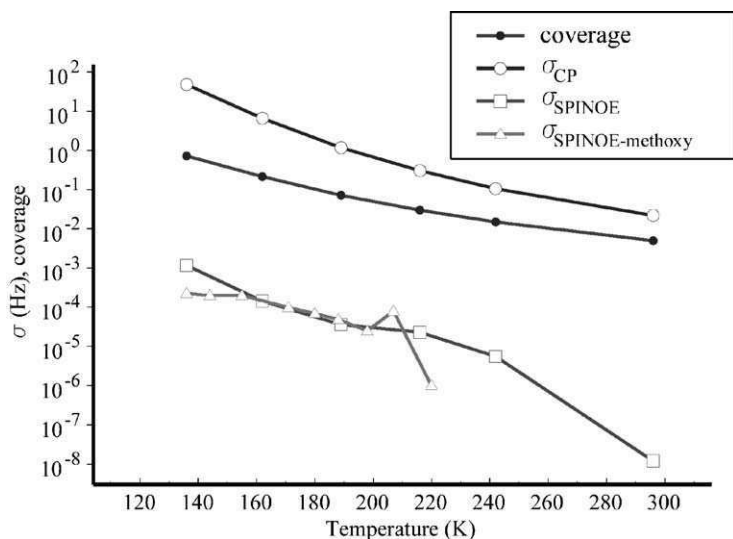


Fig. 18. ^{129}Xe – ^{13}C and ^{129}Xe – ^1H cross-relaxation rates as a function of temperature for different substrates using SPINOE and CP transfer methods. (Reprinted from ref. 271 with permission. Copyright 2002, Academic Press.)

Analysis of the CP dynamics under steady-state conditions of HP xenon flow allowed the determination of an expression for the maximum anticipated polarization enhancement of the surface protons:²¹⁷

$$\xi_{\text{H}}^{\text{SS}} \approx \frac{\gamma_{\text{Xe}}}{\gamma_{\text{H}}} \cdot \theta' \xi_{\text{Xe}}^{\text{Surface}} \left[\frac{\sigma_{\rho\text{XeH}}}{\theta' \rho'_{1\text{Xe}} + \sigma_{\rho\text{XeH}}} \right] \quad (7)$$

where γ_{Xe} and γ_{H} are the xenon and proton gyromagnetic ratios, respectively, θ' the ^{129}Xe surface coverage, $\xi_{\text{Xe}}^{\text{Surface}}$ the xenon surface polarization enhancement (typically ca. 10,000), $\sigma_{\rho\text{XeH}}$ is the xenon–proton cross-relaxation in the rotating frame, and $\rho'_{1\text{Xe}}$ is the ^{129}Xe surface relaxation rate in the rotating frame. This expression is similar to the one derived previously for the steady-state SPINOE enhancement,²⁶⁹ except that the functional form of the cross-relaxation term has an additional $\sigma_{\rho\text{XeH}}$ term in the denominator. In fact, this difference is important in that it explains the unanticipated observation that the surface proton enhancement resulting from CP from HP xenon extends all the way to 323 K.²⁷⁰

3.4.2. Polarization transfer in xenon solutions

A large impetus for solution-phase studies involving xenon was the seminar paper by the Pines group in which they demonstrated xenon polarization transfer to proton-containing solvent molecules.³⁸ The polarization transfer occurs via through-space dipolar coupling, or an NOE process, which the authors termed the SPINOE method. Unfortunately, the cross-relaxation rates from xenon to other nuclear species in solution are often small, of the order of 10^{-6} s^{-1} , due in part to

the low solubility of xenon. As a result, advanced methods to observe the small change in signal intensity, such as difference spectroscopy, have been utilized. The study by Song *et al.*²⁷² which investigated polarization transfer of xenon to surface protons in cyclodextrin is illustrative of this approach.

The Berkeley group used SPINOE transfer methods to study xenon binding in a small-cage molecule, cryptophane-A.²⁷³ Xenon exchanges slowly into and out of the cages leading to two peaks in the xenon solution-phase spectrum. SPINOE transfers to nine distinct protons were observed, with enhancements ranging up to 13% of the Boltzmann signal. Cross-relaxation rates were 5–10 times smaller than that in cyclodextrin,²⁷² most likely due to a larger distance between xenon and the cryptophane-A protons. Selective proton experiments were used to determine preferred conformations of cryptophane-A in the presence of xenon. SPINOE was also used to transfer xenon polarization to ethanol at a very low magnetic field (0.54 T).^{274,275} Large enhancements in the ¹H signal were observed, up to a factor of 15, and showed an inverse temperature dependence. The average xenon to proton spin-exchange cross-relaxation rate σ_{XeH} was measured to be $2.5 \times 10^{-3} \text{ s}^{-1}$.

Polarization transfer has also been observed between HP supercritical xenon and organic solutes.³¹ HP xenon was collected as a solid and then transferred to a 3 mm borosilicate tube containing the organic molecule (toluene or biphenyl) at a field of 1 T to avoid relaxation. Proton enhancements were observed to be three (biphenyl) or seven (toluene) times the Boltzmann equilibrium level as measured at 2 T and with the xenon polarization at 2%. Several proton acquisitions could be made because the xenon T_1 was approximately 7.5 min. The authors suggest that the low cross-relaxation rates observed in both the liquid and now supercritical phases could lead to better polarization transfer in the solid state, albeit with a highly dispersed xenon, such as provided by freezing a supercritical or liquid solution.

Appelt *et al.*²⁷⁶ described experiments to investigate the polarization transfer from liquid xenon to ¹H containing solutes at very low magnetic fields. Because the thermal-equilibrium polarization of nuclei at low magnetic fields is so low, polarization transfer from HP xenon is attractive. The authors showed that even with somewhat unfavorable SPINOE transfer rates, it is still possible to increase the polarization of ¹H in ethanol, butanol, and toluene by a factor of 1,000 when compared to the NMR at 0.001 T. Ethanol/water mixtures showed a somewhat lower enhancement. The authors discuss several applications for low-field NMR, and suggest that by freezing the solutions and carrying out CP methods to increase the polarization transfer would further increase the signal strength and the applicability.

Bifone and coworkers²⁷⁷ have also carried out thermal mixing experiments to transfer xenon polarization to ¹³C, using ¹³CS₂ as the target species. They also compared thermal mixing to SPINOE and found that low-field thermal mixing could provide enhancements as large as 390 times the Boltzmann polarization at 1.5 T, whereas the SPINOE transfer was about five times less efficient. However, even using thermal mixing, the transfer efficiency is only about 5% of the theoretical maximum value.

Xenon polarization was transferred to solid HCl after HP xenon and HCl were mixed in the gas phase and then frozen.²⁷⁸ The NMR signal of ^1HCl was increased by a factor of 6 compared to the Boltzmann level. A ratio between the cross-relaxation rate and the ^1H autorelaxation rate ($\sigma_{\text{IS}}/\rho_{\text{I}}$) was measured to be approximately 1/280. Unfortunately, ρ_{I} was not measured separately.

A table of CP rates measured in various solutions and to materials surfaces is provided in Table 2, and shows a range of rates. The T_1 values of the target nuclei are provided, where available.

3.5. HP xenon in medicine

Following the very promising study of HP xenon gas imaging in a rat lung by Albert *et al.* in 1994,²⁷⁹ a large number of studies have been carried out to explore the utility of HP xenon for medical applications to human and animal biology. A large number of papers discuss experiments to explore the capabilities of HP xenon in biomedical applications in general and MRI specifically. This area has been well summarized²⁸⁰ and an up to date review was very recently published¹⁷ so the discussion below will be brief.

3.5.1. Lung imaging

In the area of lung imaging, significant progress has been achieved in the last 10 years. HP images now show very high resolution, in some cases down to 100 μm , or 0.17 and 0.40 μL voxel sizes for ^3He and ^{129}Xe , respectively.²⁸¹ Although HP ^3He generally provides better S/N ratio than HP xenon, and has thus received more attention, a number of xenon MRI studies in animals and even humans to explore void spaces have been published recently. Xenon interacts more strongly with surfaces than He and thus might be able to provide additional information on the condition of tissue surfaces via changes in the xenon chemical shift. The first *in vivo* human lung study was reported in 1997,²⁷ in part motivated by goal of clinical applications. Results by the Mainz group have shown that polarized gases can distinguish healthy lungs from patients suffering from various diseases, including chronic obstructive pulmonary disease, emphysema, and lung cancer.²⁸² Ruppert *et al.*^{283,284} have studied the diffusion of xenon in the lungs, and derived effective diffusion constant of $3.3 \times 10^{-6} \text{ cm}^2 \text{ s}^{-1}$. Different resonances for the (large) gas-phase peak as well as two dissolved-phase peaks near 200 ppm were observed. Xenon effectively exchanges between the gas and dissolved phases on the timescale of milliseconds. The authors propose that pathological conditions, such as alveolar wall thickening, interstitial and intra-alveolar edema, emphysema, and cysts that affect the alveolar architecture may be diagnosed using HP xenon.

An example of the current state of the art is the HP xenon lung image in a rat shown in Fig. 19, which illustrates an impressive level of detail. The in-plane resolution of the 3D image is $0.39 \times 0.39 \text{ mm}^2$, with a field of view of 5 cm. A 100 mL xenon/oxygen bolus was delivered over the course of 80 breaths, and the image was acquired using a radial projection encoding sequence.

Table 2. Xe cross-relaxation rates and proton relaxation times for different molecules and their target spins interacting with Xe.

Molecule	Target spin	Cross-relaxation rate (Xe → target)	Units	Proton T_1 (s)	Reference
Benzene	H	1.9	10^{-6} s^{-1}	20	38
Fumed SiO ₂	H	2	10^{-3} s^{-1}	4.3	232
Methanol on silica	H	8.6	10^{-4} s^{-1}	3.3	265
Methanol on silica	¹³ C	2.8	10^{-4} s^{-1}	4.5	265
Aerosil coated with polyethylene oxide	H	7	10^{-4} s^{-1}	9.1	268
	¹³ C	4	10^{-4} s^{-1}	1.4	268
Fumed SiO ₂	¹ HO	80	s^{-1}	10	271
<i>p</i> -Nitrotoluene	Methyl H	0.025	$10^{-6} \text{ s}^{-1} \text{ mM}^{-1}$	6.8	272
<i>p</i> -Nitrotoluene	H3, H5	0.032	$10^{-6} \text{ s}^{-1} \text{ mM}^{-1}$	35	272
<i>p</i> -Nitrotoluene	H2, H6	0.028	$10^{-6} \text{ s}^{-1} \text{ mM}^{-1}$	23	272
α -Cyclodextrin	H1	0.44	$10^{-6} \text{ s}^{-1} \text{ mM}^{-1}$	1.1	272
α -Cyclodextrin	H2	1.3	$10^{-6} \text{ s}^{-1} \text{ mM}^{-1}$	1.1	272
α -Cyclodextrin	H3	4.1	$10^{-6} \text{ s}^{-1} \text{ mM}^{-1}$	1.2	272
α -Cyclodextrin	H4	1.6	$10^{-6} \text{ s}^{-1} \text{ mM}^{-1}$	1.1	272
α -Cyclodextrin	H5	4.9	$10^{-6} \text{ s}^{-1} \text{ mM}^{-1}$	0.87	272
α -Cyclodextrin	H6	1.2	$10^{-6} \text{ s}^{-1} \text{ mM}^{-1}$	0.78	272
α -Cyclodextrin	OH(2)	0.7	$10^{-6} \text{ s}^{-1} \text{ mM}^{-1}$	1.2	272
α -Cyclodextrin	OH(3)	0.86	$10^{-6} \text{ s}^{-1} \text{ mM}^{-1}$	1.0	272
α -Cyclodextrin	OH(6)	0.36	$10^{-6} \text{ s}^{-1} \text{ mM}^{-1}$	1.1	272
Cryptophane-A	Aromatic H	1.2	10^{-4} s^{-1} (A-Xe complex) ⁻¹	0.8	273
Cryptophane-A	Axial H	0.47	Relative to aromatic	0.27	273
Cryptophane-A	Linker H	0.67	Relative to aromatic	0.36	273
Cryptophane-A	Linker H	1.55	Relative to aromatic	0.41	273
Cryptophane-A	Methoxy H	0.23	Relative to aromatic	0.83	273
Cryptophane-A	Equatorial H	0.35	Relative to aromatic	0.35	273
Spacer bridge in cryptophane-A	Proximal H	1.55	Relative to aromatic	—	273
	Remote H	0.67	Relative to aromatic	—	273
Ethanol	H	2.5	10^{-3} s^{-1}	0.1–10	274
D ₆ -Ethanol	D	2.1	10^{-5} s^{-1}	—	275

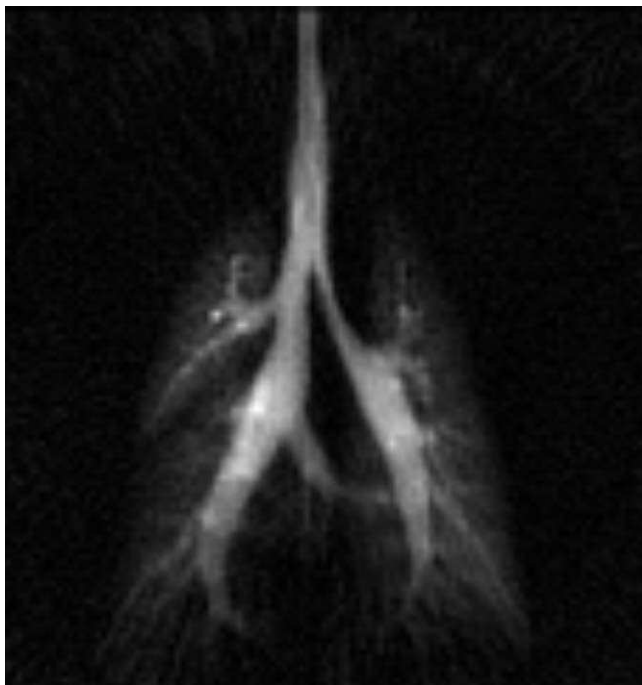


Fig. 19. *In vivo* MRI of rat lung space following respiration of a gas mixture containing 80% enriched laser-polarized Xe with a polarization of 8% and acquired at 2 T. The in-plane resolution was 0.39 mm. (Courtesy of Bastiaan Driehuys and G. Allan Johnson of the Duke Center for *In Vivo* Microscopy, an NCRR National Resource (P41 05959).)

To date, clinical HP gas imaging is still awaiting FDA approval, largely because of concerns for respiratory safety.²⁸⁵ Because xenon is known to be an anesthetic, ^3He is likely to be approved earlier. This coupled with ^3He 's higher sensitivity has made it the focus of most of the recent lung imaging studies.

3.5.2. *Injecting xenon*

Injection of xenon into blood has been proposed as method to direct xenon to important imaging problems, such as cardiac imaging, and a number of studies to explore xenon in blood have appeared.^{286–291} Two peaks are observed in the spectra, xenon in plasma, and a second peak for xenon associated with red blood cells. The T_1 of xenon in blood is an issue because of the desire to deliver HP xenon to remote sites in the body. Bifone and coworkers²⁹² have found that the xenon T_1 is longer (6.4 ± 0.5 s) in oxygenated blood due to the reduced presence of strongly relaxation-inducing paramagnetic deoxyhemoglobin. Xenon's interaction with the protein is apparently stronger than its interaction with free oxygen in the blood, while xenon is in fast exchange between sites in red blood cells and the plasma. The Harvard group also studied the T_1 of xenon in blood using high-pressure thermally

polarized xenon, and found somewhat similar results.^{287,293} Their reported values were 2.86 s for deoxygenated blood and 10.2 s for oxygenated samples measured at 8°C.

Several studies have focused on developing carrier agents for the delivery of HP xenon to remote areas of the body for enhanced MRI.^{46,294–296} The main issues are xenon solubility, biocompatibility, and the effect on xenon T_1 relaxation. Possible liquid-phase carriers include saline, intralipid suspensions, gas-filled liposomes, and perfluorocarbon emulsions. Bifone and coworkers²⁹⁶ showed that perfluorocarbon emulsified with egg yolk phospholipid is promising as a delivery vehicle because of the improved solubility. However, the xenon linewidth is dependent on the emulsion particle size, with larger droplets (10 μm) showing linewidths approaching 5 Hz. The xenon chemical shift inside the droplet is about 110 ppm, far away from its position in water or in association with red blood cells. Exchange with the aqueous phase is likely the origin of the line broadening. Venkatesh *et al.*²⁹⁴ compared four carrier agents by injecting rats with the xenon/carrier mixture and measuring the ^{129}Xe spectra and relaxation times. The study showed that xenon-filled liposomes and perfluorocarbon emulsions are both attractive to increase the solubility of xenon and its relaxation time (54 and 97 s, respectively).

An exciting application of the HP xenon is the study of brain perfusion.^{297–302} Kilian and coworkers³⁰⁰ used a time series of ^{129}Xe spectra after HP Xe inhalation to derive uptake in the brain. Two resonances detected at 196.5 and 193 ppm were assigned to HP Xe dissolved in gray and white matter, respectively. The T_1 values are different, as well. Duhamel *et al.*²⁹⁹ used an intra-carotid injection of HP Xe dissolved in intralipid, a xenon-soluble carrier, to measure cerebral blood flow. Rat brain xenon images were performed to enable regional blood flow measurements.

3.5.3. Xenon's interaction with tissues

An intriguing possibility is to use xenon as an indirect sensor to characterize tissues or plants.³⁰³ Because of the simple nature and sensitivity of the xenon chemical shift it was proposed that xenon could be useful in detecting irregularities (such as cancers) in a variety of tissues. The mobility of xenon in such biomaterials could be a plus because xenon would sample a variety of different environments and thereby give an overall picture of the state of the tissue. A variety of xenon resonances were observed, including both narrow peaks and broad distributions. Cancerous stomach and breast tissues were observed to have significantly different xenon spectra, including additional peaks. Additional research is needed to probe the reliability of the proposed method.

Other xenon experiments to explore the possibility of diagnosing cancerous tissues were carried out by injecting HP xenon dissolved in either saline or perfluorooctyl bromide emulsions and then injected into two types of tumors in rats and mice.³⁰⁴ The perfluorocarbon emulsion is preferred because xenon's resonance in this medium occurs at a much different position (approximately 110 ppm) than that of xenon located in a tissue or tumor (near 200 ppm). A broad peak near 140 ppm was observed for xenon in RIF-1 tumors in mice.

Tremendous progress has been made in the past few years in the area of biomedical studies using xenon NMR and MRI. However, more work is needed before these types of analyses can be made at a diagnostic clinical level.

3.6. Bioanalytical HP xenon

A variety of interesting applications for HP xenon have been reported in the area of bioanalytical NMR, including studies of xenon's interaction with proteins and protein–ligand binding.

3.6.1. HP xenon studies of proteins

Several groups have explored the interaction of xenon with proteins using HP xenon. Early work had shown an affinity for xenon to myoglobin,³⁰⁵ and it is well known that xenon acts as an anesthetic. Bowers *et al.*⁵⁹ investigated xenon's interactions with a number of lyophilized proteins (metmyoglobin, methemoglobin, hen egg white lysozyme, and soybean lipoxygenase) by adsorbing xenon at cold temperatures and measuring the xenon chemical shift and linewidth as a function of temperature. Xenon adsorbs most strongly to lipoxygenase, which had a relatively high affinity for gas molecules. Lipoxygenase also showed a clearly resolved adsorbed ¹²⁹Xe NMR peak. Rubin *et al.*³⁰⁶ explored nonspecific interactions of xenon with myoglobin, which were evidenced by the measurement of two xenon T_1 of, 59 and 291 s, which corresponded to xenon interacting with the hydrophobic binding pocket and xenon's nonspecific interactions with the protein surface, respectively. Rubin *et al.*^{307,308} also showed that the xenon chemical shift can be used to detect a conformational change in maltose-binding protein. A linear chemical shift change was seen as function of the protein concentration corresponding to a slope of 2 ppm Xe chemical shift/mM protein.

Desvaux and coworkers^{309–312} have carried out a series of very interesting and impressive experiments to probe the interactions of xenon with the hydrophobic pockets of proteins. They have developed a rotating-frame version of the popular SPINOE experiment, which they term SPIROE that is useful for transferring xenon to surface protons but at the same time limits the proton–proton spin diffusion.³¹⁰ The authors demonstrated this approach using a cage-molecule cryptophane-233. In proteins, it is advantageous to carry out 2D experiments, and the authors have extended their polarization transfer methodology to a 2D with a SPIROE-TOCSY experiment, which they demonstrated using cryptophane-A camphonate compound.³¹³ The 2D data are shown in Fig. 20. In a third article, the authors show that xenon polarization can be transferred to 26 protons in wheat nonspecific lipid transfer protein.³¹² Four interaction sites were identified that were verified with other xenon experiments and simulations. As opposed to conventional approaches involving the use of X-ray diffraction to study the interaction of high-pressure noble gases with the hydrophobic pockets of proteins, HP xenon appears to offer an attractive alternative. Using 15 known structures, xenon adsorption was simulated

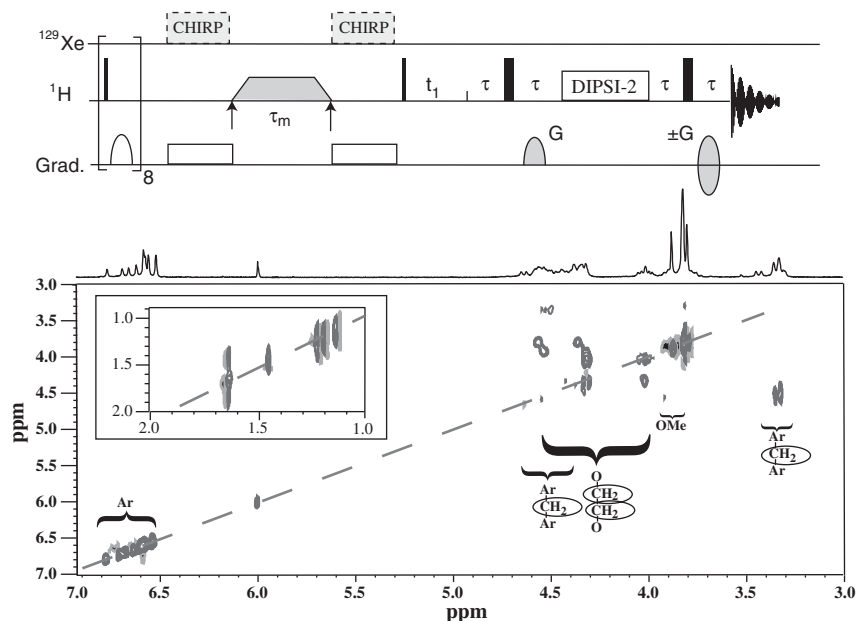


Fig. 20. (Top) SPIROE-TOCSY pulse sequence comprised of proton saturation, adiabatic CHIRP transfer, and proton magnetization buildup during τ_m and TOCSY using the DIPSI-2 mixing sequence. (Bottom) 2D SPIROE-TOCSY performed in deuterated 1,1,2,2-tetrachloroethane. Broken line indicates the diagonal. The inset shows the region of the camp-hanic ester protons. The total experiment time is only 4.5 min. (Courtesy of Hervé Desvaux. Reprinted from ref. 313 with permission. Copyright 2004, Elsevier SAS.)

and showed up to four distinct adsorption sites, often with multiple xenon atoms occupying two sites that are deeply embedded inside the protein. Changes in the proton signal of a few percent were observed using mixing times between 100 and 800 ms, with 200 ms being optimal. Twenty-six proton–xenon interactions were observed, corresponding to 16 hydrophobic amino acids, all of which are located inside the protein cavity. Xenon’s interactions with the protein seem to be more specific than those of small organic molecules.

3.6.2. Protein–ligand binding

Pines and coworkers⁴⁵ have shown a clever approach to using the high polarization and chemical shift sensitivity of HP xenon (see Fig. 21). By containing xenon in a sensitive cage molecule and tethering this system to a ligand they are able to detect binding activity. Cryptophan-A cages had previously been shown to bind xenon^{50,273} with a slow exchange time, and the chemical shift of xenon is extremely sensitive to its chemical environment. A biotin ligand was attached via a short peptide-based linkage and solid-phase synthesis was used to make the biosensor. The biosensor’s binding to avidin was detected as a change in the chemical shift of

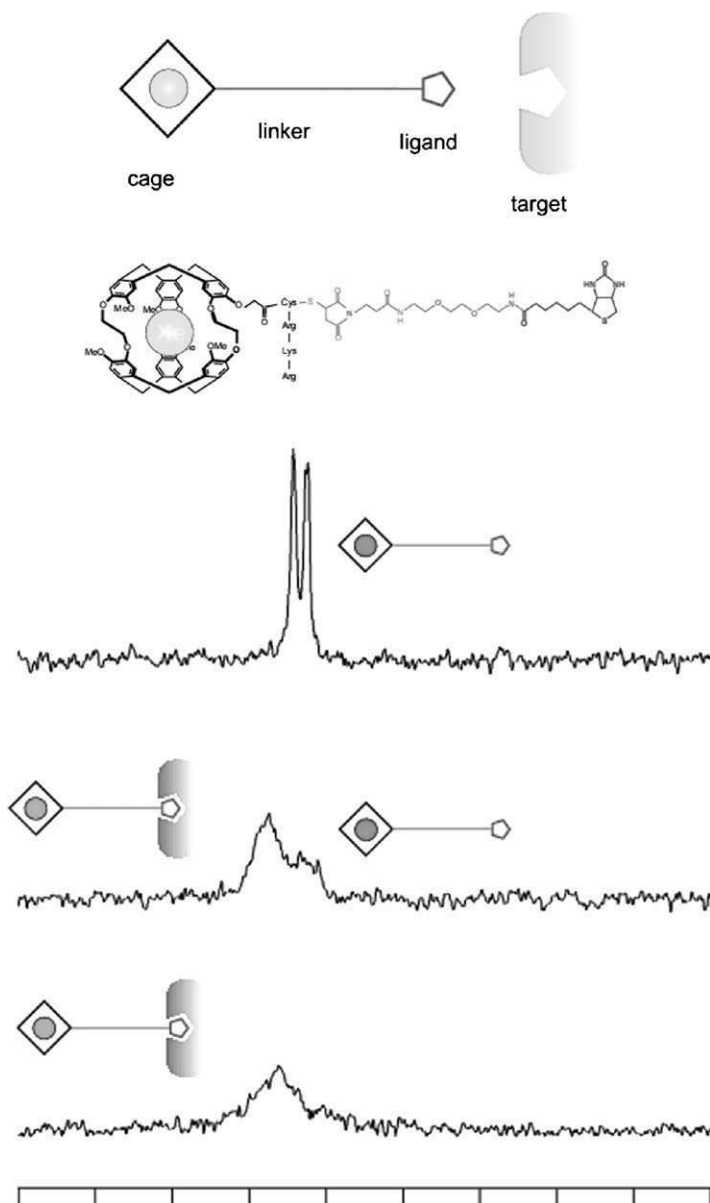


Fig. 21. (Top) Schematic and chemical structure of the biosensor molecule used by Spence *et al.* (Bottom) Detection of biotin–avidin binding with xenon NMR. The HP ^{129}Xe NMR spectra of the functionalized xenon biosensor alone and in the presence of protein. These spectra show a new resonance and marked broadening in response to the increasing amounts of avidin. (Courtesy of Connie Chung and the Pines group, adapted from ref. 314 with permission. Copyright 2004, American Chemical Society.)

xenon from 70 (unbound biotinilated sensor) to 73 ppm (bound). Because of the large chemical shift range of xenon the authors state that it may be possible to multiplex this approach to detect multiple binding events in parallel. Spence *et al.*³¹⁴ explored different modes of employing the xenon biosensor, such as in the detection of competing ligands, and the use of xenon as an indirect binding sensor via the measurement of the free xenon in solution. Methods to increase the sensitivity, such as exchange-signal averaging in which the free xenon in solution acts as a polarization reservoir that slowly exchanges with the encapsulated xenon are also discussed. Finally, it was shown that xenon is sensitive to the chirality of the encapsulating cryptophan-A and its linker (also see Section 2.6.1). It may even be possible to develop a contrast agent based on injecting functionalized HP xenon for protein-specific labeling *in vivo*.³¹⁵

3.7. HP xenon diffusion studies

3.7.1. Diffusion in materials

Mair *et al.* reported the use of thermal³¹⁶ and HP xenon^{316–321} to explore diffusion in various materials. Gas diffusion is advantageous because the diffusion coefficients are much larger, and using HP noble gases such as xenon provide for a good NMR sensitivity with slow relaxation times. Pulsed-gradient stimulated echo with bipolar-gradient pulses were used to collect the data and provided a method to cancel out effects of background gradients while measuring diffusion. The authors point out the advantage of using xenon gas for diffusion studies in porous media as it provides a method to probe on longer length scales due to the higher ($20\text{--}200\text{ mm s}^{-1}$) gas velocities over liquids. The long relaxation time and good signal intensity allows researchers to explore the long time limits of diffusion models where the diffusion goes from a regime described by the surface to volume (S/V) ratio to one where it approaches an asymptotic limit of the reciprocal of the tortuosity of the medium. This behavior can be seen in Fig. 22. Using glass bead samples or Indiana limestone, the authors provided examples where xenon gas-phase NMR diffusion measurements allow access to regimes where liquid diffusion measurements provide limited data.

HP xenon diffusion measurements can also be used to determine S/V ratios in porous materials, including soft materials. Extending the previous work done in liquids by Stejskal and Tanner,³²² Butler *et al.*³²³ determine S/V ratio from the rate of xenon polarization exchange between the gas phase and xenon dissolved in the solid phase. This method was applied to porous polymer samples, but applications to the characterization of lung spaces are envisioned.

3.7.2. Single-file diffusion

Meersmann *et al.*³²⁴ explored one-dimensional diffusion in tris(*o*-phenylenedioxi)cyclophosphazene (TPP) using HP xenon.³²⁵ Materials with nanochannels that are small enough to restrict diffusion to one dimension are of interest to study

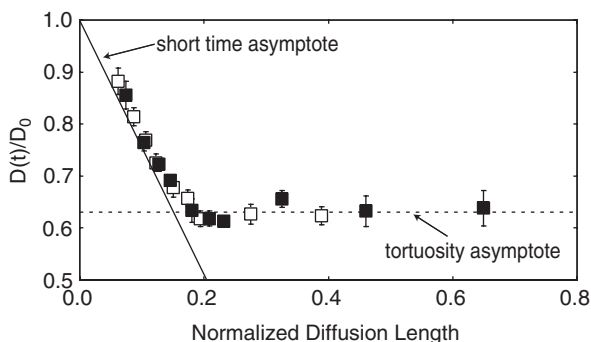


Fig. 22. A comparison of the time-dependent diffusion measurements for laser polarized (filled squares) and thermally polarized (open squares) xenon gas introduced to a sample consisting of randomly packed 3 mm glass beads. (Courtesy of Ross Mair. Reprinted from ref. 321 with permission. Copyright 1999, The American Physical Society.)

fundamental issues in diffusion. The mean displacement for single-file diffusion is given by

$$\langle x^2(t) \rangle = 2F\sqrt{t} \quad (8)$$

where F is the mobility factor (in units of $\text{m}^2 \text{s}^{-1}$), as opposed to its normal time dependence given by the Einstein equation for one-dimensional diffusion:

$$\langle x^2(t) \rangle = 2Dt \quad (9)$$

Experiments to follow the intensity buildup of xenon NMR signal as xenon adsorbed into the channels was monitored to determine whether the diffusion could indeed be described as single file. In fact, the experiments fit the model very well after taking xenon relaxation into account. The authors point out that continuous-flow HP xenon will be useful to investigate other such systems, although determination of the actual diffusion constant will require substantial gradients. Fig. 23 shows xenon spectra for various temperatures and pressures in the channels.

3.7.3. Xenon diffusion in solution

Diffusion measurements of xenon in solution have been described by Wolber *et al.*³²⁶ Using the Burst pulse sequence, diffusion measurements were made in a single-shot measurement. First, a train of small-angle pulses is applied under the influence of a read gradient. After a refocusing of 180° -pulse, and a similar train of pulses, under the same gradient, the magnetization echo train is obtained. The self-diffusion of xenon causes a loss in coherence and a diminution of the echo signal. The measured self-diffusion constant for xenon in water was $2.2 \pm 0.4 \times 10^{-5} \text{ cm}^2 \text{ s}^{-1}$, in agreement with previous experimental and calculated values. The authors discuss a variety of applications for *in vivo* diffusion measurements.

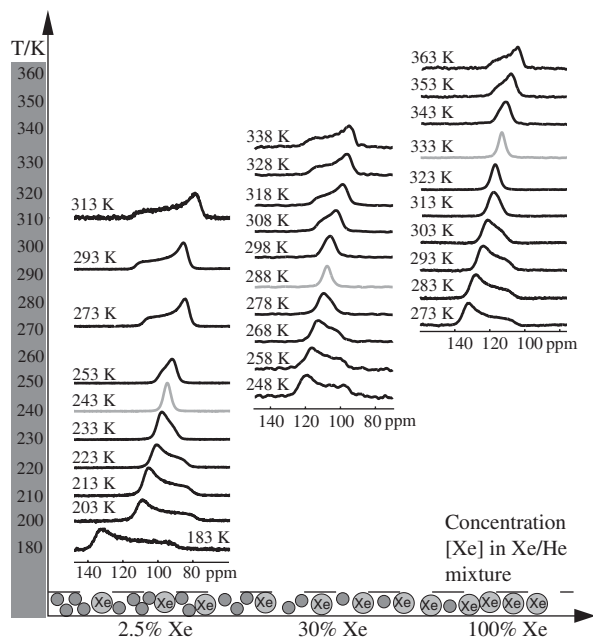


Fig. 23. ^{129}Xe spectra of xenon adsorbed in the subnanometer channels of TPP. The inversion of the ^{129}Xe CSA can be clearly seen as the temperature is raised. (Courtesy of Thomas Meersmann. Reprinted from ref. 324 with permission. Copyright 2004, American Chemical Society.)

3.8. HP xenon imaging of materials

A variety of new experiments have appeared to explore a large range of materials, from void volumes to engineered materials and biosurfaces. HP xenon imaging has also been used to monitor dynamical processes, such as phase transitions and even breathing. A recent review describes the advances in this area.³²⁷

3.8.1. Static imaging

A recent paper by Appelt and coworkers³²⁸ shows that HP xenon can be used to collect time-resolved images of solid xenon ice as it melts and dissolves into several different solvents (see Fig. 24). The authors accumulated xenon ice on the top of a frozen solvent at 77 K, and then used FLASH (fast low angle shot) imaging methods, which allowed the acquisition of images every 30–40 s, to follow xenon as it melted and dissolved into various ethanol/water mixtures. Observations of the different states of xenon were made, including the creation of pores in the xenon ice, and dense liquid xenon layers, which is of interest for the possible injection of xenon into biological systems. Tseng *et al.*³²⁹ investigated the exchange between liquid and vapor phases as well as the evaporation of xenon using MRI techniques. According

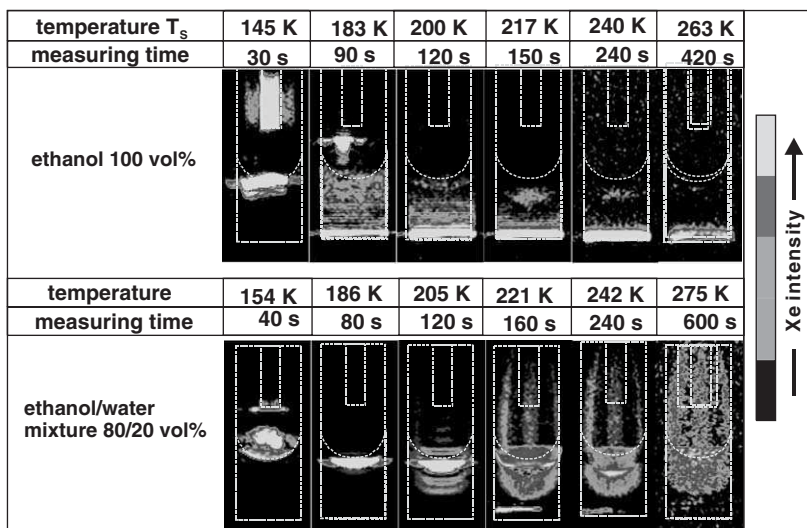


Fig. 24. Series of 2D FLASH images of hyperpolarized Xe ice, which is melting, migrating, and dissolving into the supercooled ethanol (top) or 80 vol% ethanol/water ice (bottom) phase. Within 2 min all Xe polarization is concentrated at the bottom of the outer tube. By 10 min nearly all the Xe polarization is in the gas phase. (Courtesy of Wolfgang Häsing. Reprinted from ref. 328 with permission. Copyright 2004, Elsevier Inc.)

to the authors, the high polarization and density should allow images with resolution down to a few microns to be made with gradient-field strengths of approximately 400 G cm^{-1} , which is well within the range of experimental feasibility.

Song *et al.*³³⁰ used the FLASH pulse sequence to capture the image of xenon solid in an NMR tube and observed that xenon polarization is well preserved on the glass surface, but not on the surface of an included red chili pepper. The spatial resolution was better than 0.05 mm in this 2D experiment.

3.8.2. Flow imaging in materials

Kaiser *et al.*³³¹ reported the use of HP xenon for flow imaging using a chemical shift selective imaging method. Samples of highly porous aerogel and zeolites were examined. Transport of fresh xenon to the sample under flow allowed the experiments to be rapidly recycled. By waiting different delay times between acquisitions, the transport time of polarized xenon to the interior of the aerogel sample could be varied, thus providing information on the diffusion constant through the material. This methodology is useful for mapping out flow dynamics of gases as they interact with particles comprising a particle bed, with applications in areas such as in catalysis, soil science, and petroleum engineering. 2D resolution of the order of $100 \mu\text{m}$ was observed. Moudrakovski *et al.*³³² combined chemical shift imaging and continuous flow of HP xenon to investigate various microporous materials. The use

of chemical shift imaging makes it possible to probe the spatial variation of particular xenon interactions with the materials.

A study of gas-phase Poiseuille flow in a cylindrical tube in a regime where deterministic and stochastic motions were of the same order of magnitude was reported by Kaiser *et al.*³³³ (see Fig. 25). HP xenon imaging of the xenon flowing was made at velocities around 20 mm s^{-1} . Because the displacements due to diffusion are given by $(2Dt)^{1/2}$, where $D = 5.5 \text{ mm}^2 \text{ s}^{-1}$ at 1 atm, it is possible to vary the relative size of diffusion and flow by simply changing the observation time. Indeed, at shorter times, longitudinal diffusion is important, whereas at longer times, transverse diffusion becomes important. These results are in contrast to those obtained with water flow where the diffusion is much smaller. Results match computer simulations quite well.

3.9. New and exotic applications

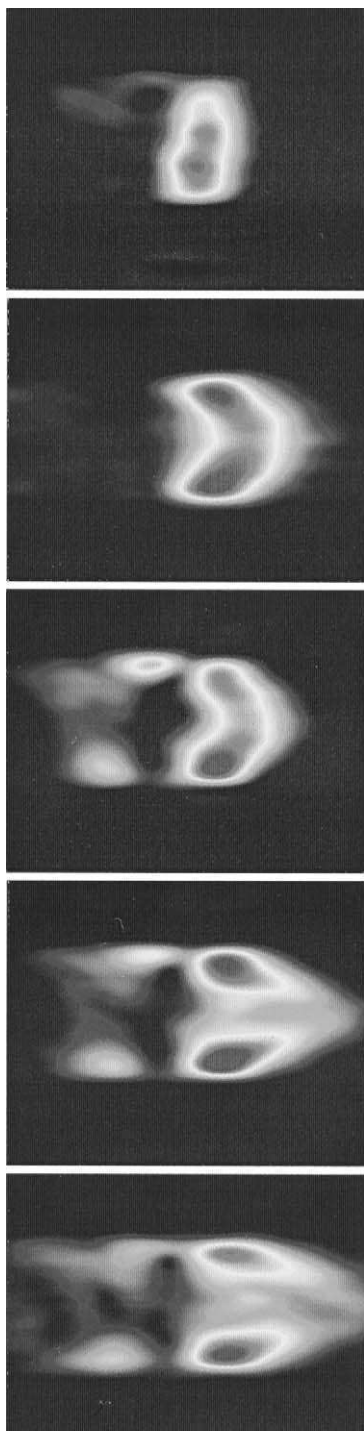
3.9.1. HP xenon studies of combustion

Meersmann³³⁴ has recently reported the use of HP xenon to investigate combustion using a continuous flow of xenon mixed with methane that combusts above a nanoporous zeolite. A small upfield shift was observed when the xenon was in the presence of the combusting gas, with a peak appearing at -3 ppm that was ascribed to xenon located in a small zone just above the zeolite catalyst. 2D EXSY spectra (see Fig. 26) indicated that exchange between xenon located in the bulk of the zeolite and the zone above the catalyst takes place on the 20 ms scale. Exchange with gas-phase xenon also takes place on this timescale. The exchange spectra are asymmetric because xenon is flowing from inside the zeolite to the combustion region above the catalyst bed.

3.9.2. Low field HP xenon studies

One intriguing possibility provided by the enormous polarization of HP xenon is to reduce the magnetic field used in detection. Because the polarization of xenon is fixed by the optical pumping process and laser power, the observed signal does not decrease as quickly with reduced magnetic field as does conventional NMR. This provides a path for the development of NMR and/or MRI experiments that make use of very small magnetic fields. For example, Shao and coworkers³³⁵ have described a low-field MRI system that takes advantage of the high polarization of laser-polarized xenon to produce images at 33.6 mT or 399 kHz. The high polarization of xenon eliminates the need for a polarizing magnet, and the reduction in

Fig. 25. Joint spatial-velocity images of xenon undergoing Poiseuille flow in a pipe. The digital resolution in the spatial direction (y) is $100 \mu\text{m}$. (Figures courtesy of Connie Chung and the Pines group, adapted from ref. 333 with permission. Copyright 1999, Academic Press.)



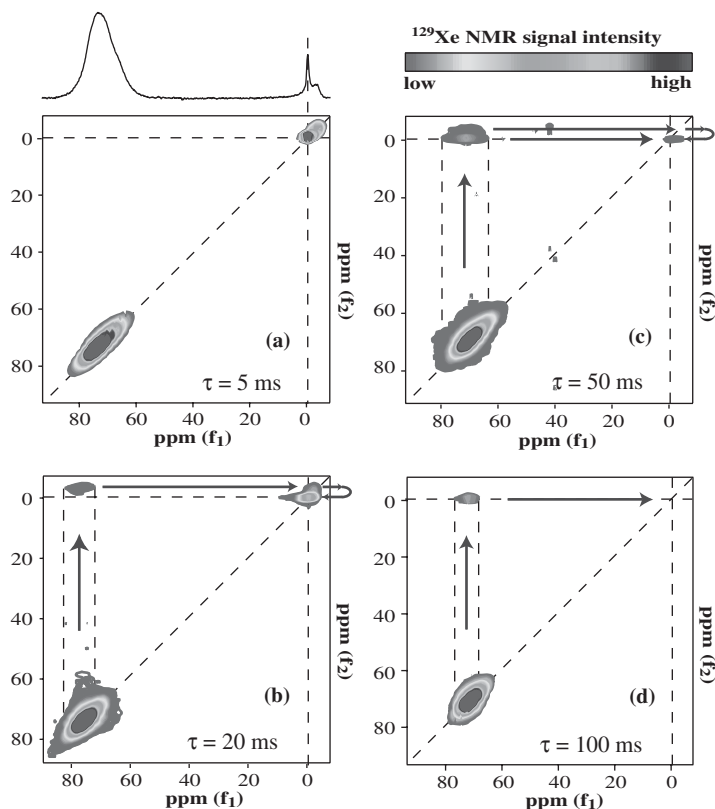


Fig. 26. HP ^{129}Xe 2D EXSY spectra acquired during combustion showing exchange as a function of the mixing time. Experimental time was 40–50 min per spectrum. (Courtesy of Thomas Meersmann. Reprinted from ref. 334 with permission. Copyright 2003, American Chemical Society.)

field has a smaller negative effect on the sensitivity than conventional MRI. A comparison with high-field MRI was made³³⁶ and showed that the S/N ratios measured at 8.5 mT was 32 times less than that at 1.88 T, which was slightly better than the expected ratio of 36. The practical resolution limit was estimated to be 0.5 mm, although it was suggested that fields of 50 mT would be required to create diagnostic images. Others have used ^3He for low-field imaging of materials and for *in vivo* work because the S/N ratio is generally higher.^{337,338}

Pines and coworkers³³⁹ succeeded in improving the spectral resolution of a static sample of frozen HP xenon in low field by rotating the B_0 magnetic field. Experiments were carried out at 3.4 mT where two of the three magnetic fields could be sinusoidally varied on the millisecond timescale in a manner similar to MAS. A factor of 6 in resolution enhancement was achieved. Extensions to higher fields have very interesting potential applications especially for biomedical imaging.

3.9.3. *Alternative detection methods*

A further enhancement is provided by alternative detection methods. Pines and co-workers^{340,341} have coupled the use of HP xenon with a SQUID, which provides very high-sensitivity detection of magnetic fluxes at low resonance frequencies. The authors showed that the use of optically pumped xenon and a high- T_c SQUID device could be coupled to allow the detection of laser-polarized xenon gas at only 27 kHz, corresponding to a magnetic field of 2.3 mT. MRI of xenon adsorbed on a piece of silica aerogel was also shown using this approach (see Fig. 27).³⁴¹ SQUID

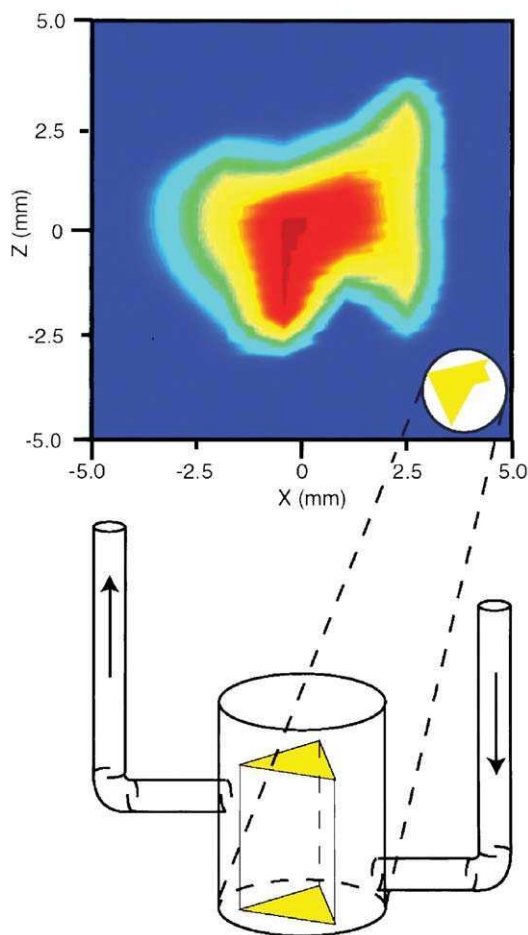


Fig. 27. SQUID-detected MRI of HP xenon gas adsorbed on to an aerogel sample and obtained at a field of 2.26 mT. The MRI is a 2D projection of the xenon interacting with the roughly triangular sample. A schematic drawing of the sample cell is also shown. (Courtesy of Connie Chung and the Pines group. Reprinted from ref. 341 with permission. Copyright 2002, Elsevier Science.)

detectors compete very well with conventional Faraday detection methods at frequencies below 5 MHz, so we anticipate that SQUID detectors could be very useful in the future for HP studies.

Romalis and coworkers³⁴² reported the use of a commercial high- T_c SQUID to observe an enormous enhancement in the NMR signal of simple organic liquids that have been mixed with HP xenon. Experiments were carried out at $0.95\ \mu\text{T}$ where the proton resonance frequency is 40.4 Hz, and the xenon resonance is only 11.2 Hz, as shown in Fig. 28. The authors were able to observe large signals from cyclopentane, acetone, and methanol with S/N ratios of over 1,000. The proton linewidth was 0.04 Hz without shimming! However, due to the low magnetic field, it is not possible to observe chemical shift differences in the proton spectra, although it might be possible to detect proton–xenon dipolar coupling in the solid state, depending on its magnitude.

An interesting approach to increasing the sensitivity of NMR and MRI was reported by Pines and coworkers³⁴³ and involved separating the sample region from

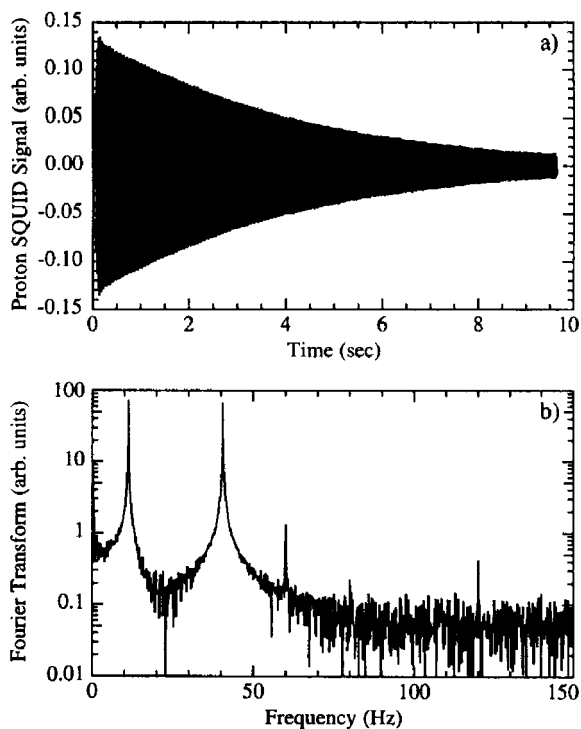


Fig. 28. SQUID-detected proton NMR FID from cyclopentane following a single 90° -pulse enhanced with SPINOE from the liquid HP xenon solvent ($P_{\text{Xe}} = 2\%$). Fourier transformation of the signal shows two peaks at 40.4 and 11.2 Hz, corresponding to ^1H and ^{129}Xe resonances, respectively. The ^1H S/N ratio is approximately 1,000. (Figures courtesy of Michael Romalis. Reprinted from ref. 342 with permission. Copyright 2003, The American Physical Society.)

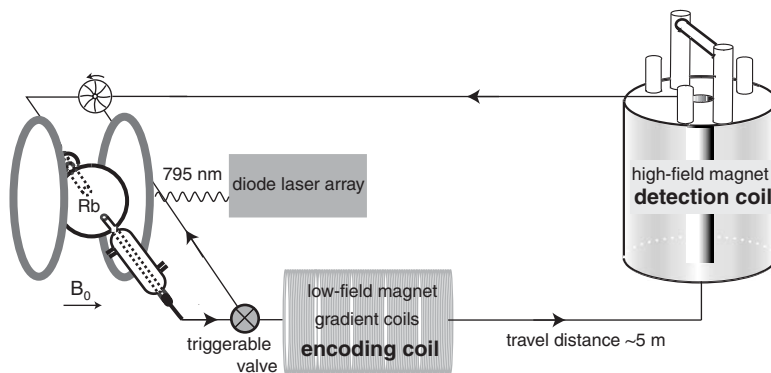


Fig. 29. Basic schematic drawing of remote detection showing the optical pumping hyperpolarization step (left) followed subsequently by the encoding of spectral or image information at one location, the transfer to a different location, and detection in the new location. The encoding time, t_1 , is incremented by the indirect dimension dwell time to map out NMR information in a point-by-point fashion. (Courtesy of Connie Chung and the Pines group. Reprinted from ref. 343 with permission. Copyright 2003, The National Academy of Sciences.)

a remote detection region (see Fig. 29). The authors propose methods to optimize the magnetic resonance sensing, or encoding, and the detection processes separately, which is brought about by physically separating the two in space. In one experiment, the authors used a homebuilt probe with two regions, one a larger region filled with an aerosol sample where xenon magnetization is allowed to evolve before storing along the z direction, and the second region with a smaller volume and therefore higher detection efficiency to measure the point-by-point evolution of the xenon magnetization. In a second experiment, the magnetic resonance of HP xenon gas was encoded in a large, low magnetic field and then the gas was transported by flow to a second, remote region for detection at high magnetic field. The authors were able to collect an image of a phantom sample at 4–7 mT using this approach. An interesting extension of this work is the optical detection of HP xenon using a Rb magnetometer. This approach has the potential for exquisitely sensitive NMR and/or MRI detection.³⁴⁴

3.9.4. Quantum computing

HP xenon has also been used to enhance the polarization of a two-qubit NMR quantum computer using the ^{13}C -enriched chloroform.³⁴⁵ Using the SPINOE transfer mechanism, this approach led to a polarization enhancement of the chloroform that was approximately 10 times the thermal values for ^1H and ^{13}C . Temporal spin-labeling methods along with measurements of the deviation density matrix were used to observe the formation of a pure spin state. The authors then demonstrated their approach by implementing a 2-qubit Grover's search algorithm.

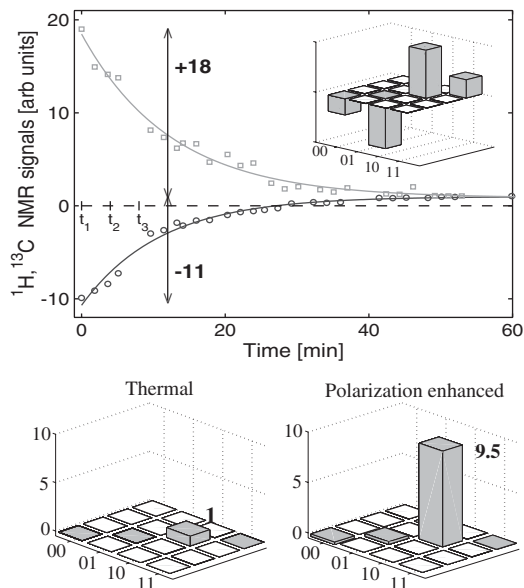


Fig. 30. (Top) Time evolution of the ^{13}C (filled squares) and ^1H (open circles) signals of $^{13}\text{CHCl}_3$ after being dissolved in hyperpolarized ^{129}Xe for 4 min at -40°C showing the initial enhancements of +18 for ^{13}C and -11 for ^1H . Inset shows the deviation density matrix (the diagonal is shifted to obtain a zero average for the nonground states) of the effective pure state. (Courtesy of Isaac Chuang. Reprinted from ref. 345 with permission. Copyright 2001, American Institute of Physics.)

Fig. 30 shows the ^1H and ^{13}C signal enhancements as a function of time, and the deviation density matrix of the pure state under both thermal and HP xenon-enhanced conditions.

4. CONCLUSION

Clearly, the future for advances in xenon NMR spectroscopy is very bright. The growing list of important and interesting applications described in this review give an indication of the increasing impact of xenon NMR experiments and point to at least some of the many exciting future developments that may be anticipated.

ACKNOWLEDGMENTS

I would like to thank former group members, Ernesto MacNamara, Jay Smith, Greg Fisher, Luis J. Smith, Charles Rice, Jonathan Prange, and Kevin Knagge, who have worked on xenon NMR in my group over the past 10 years. I also thank

my current students Carl Murphy and Haiwei Gu for their help with the figures and tables, and Janet Kliever for help with the references. This work was supported by generous grants from the National Science Foundation and the Donors of the Petroleum Research Fund, administered by the American Chemical Society.

REFERENCES

1. G. J. Schrobilgen, in *NMR and the Periodic Table* (ed. R. K. Harris and B. E. Mann), ch. 14, Academic Press, London, 1978.
2. C. J. Jameson, in *Multinuclear NMR* (ed. J. Mason), Ch.18, Plenum Press, London, 1987.
3. D. Raftery and B. F. Chmelka, *NMR Basic Princ. Prog.*, 1994, **30**, 111.
4. C. I. Ratcliffe, *Annu. Rep. NMR Spectrosc.*, 1998, **36**, 123.
5. J. Reisse, *New J. Chem.*, 1986, **10**, 665.
6. J. Fraissard and T. Ito, *Zeolites*, 1988, **8**, 350.
7. C. Dybowski, N. Bansal and T. M. Duncan, *Annu. Rev. Phys. Chem.*, 1991, **42**, 433.
8. P. J. Barrie and J. Klinowski, *Prog. Nucl. Magn. Reson. Spectrosc.*, 1992, **24**, 91.
9. J. Jokisaari, *Prog. Nucl. Magn. Reson. Spectrosc.*, 1994, **26**, 1.
10. J. H. Walton, *Polym. Polym. Compos.*, 1994, **2**, 35.
11. C. Dybowski, *J. Inclusion Phenom. Mol. Recogn. Chem.*, 1995, **21**, 113.
12. M. A. Springuel-Huet, J. L. Bonardet and J. Fraissard, *Appl. Magn. Reson.*, 1995, **8**, 427.
13. M. A. Springuel-Huet, J. L. Bonardet, A. Gedeon and J. Fraissard, *Langmuir*, 1997, **13**, 1229.
14. M. A. Springuel-Huet, J. L. Bonardet, A. Gedeon and J. Fraissard, *Magn. Reson. Chem.*, 1999, **37**, S1.
15. A. Cherubini and A. Bifone, *Prog. Nucl. Magn. Reson. Spectrosc.*, 2003, **42**, 1.
16. B. M. Goodson, *J. Magn. Reson.*, 2002, **155**, 157.
17. A. M. Oros and N. J. Shah, *Phys. Med. Biol.*, 2004, **49**, R105.
18. T. Pietrass, *Colloids Surf. A*, 1999, **158**, 51.
19. T. Pietrass, *Magn. Reson. Rev.*, 2000, **17**, 263.
20. E. Brunner, *Concepts Magn. Reson.*, 1999, **11**, 313.
21. E. Brunner, *Magn. Reson. Chem.*, 1999, **37**, S14.
22. J. L. Bonardet, J. Fraissard, A. Gedeon and M. A. Springuel-Huet, *Catal. Rev. Sci. Eng.*, 1999, **41**, 115.
23. R. L. Streever and H. Y. Carr, *Phys. Rev.*, 1961, **121**, 20.
24. H. C. Torrey, *Phys. Rev.*, 1963, **130**, 2306.
25. C. J. Jameson, A. K. Jameson and J. K. Hwang, *J. Chem. Phys.*, 1988, **89**, 4074.
26. I. L. Moudrakovski, S. R. Breeze, B. Simard, C. I. Ratcliffe, J. A. Ripmeester, T. Seideman, J. S. Tse and G. Santyr, *J. Chem. Phys.*, 2001, **114**, 2173.
27. J. P. Mugler, B. Driehuys, J. R. Brookeman, G. D. Cates, S. S. Berr, R. G. Bryant, T. M. Daniel, E. E. deLange, J. H. Downs, C. J. Erickson, W. Happer, D. P. Hinton, N. F. Kassel, T. Maier, C. D. Phillips, B. T. Saam, K. L. Sauer and M. E. Wagshul, *Magn. Reson. Med.*, 1997, **37**, 809.
28. C. J. Jameson, A. K. Jameson and S. M. Cohen, *J. Chem. Phys.*, 1973, **59**, 4540.
29. D. Baumer, A. Fink and E. Brunner, *Z. Phys. Chem.*, 2003, **217**, 289.
30. M. Haake, B. M. Goodson, D. D. Laws, E. Brunner, M. C. Cyrier, R. H. Havlin and A. Pines, *Chem. Phys. Lett.*, 1998, **292**, 686.
31. J. C. Leawoods, B. T. Saam and M. S. Conradi, *Chem. Phys. Lett.*, 2000, **327**, 359.
32. K. W. Miller, N. V. Reo, A. J. M. S. Uiterkamp, D. P. Stengle, T. R. Stengle and K. L. Williamson, *Proc. Natl. Acad. Sci. USA.*, 1981, **78**, 4946.
33. D. P. Stengle, N. V. Reo and D. Williamson, *J. Phys. Chem.*, 1981, **85**, 3772.
34. Y. K. Grishin, R. K. Mazitov and A. N. Panov, *Appl. Magn. Reson.*, 1998, **14**, 357.
35. A. R. Calhoun and A. D. King, *Appl. Magn. Reson.*, 1998, **15**, 95.
36. B. Patton, N. N. Kuzma and W. Happer, *Phys. Rev. B.*, 2002, **65**, Art. No. 020404.

37. I. E. Dimitrov, R. Reddy and J. S. Leigh, *J. Magn. Reson.*, 2000, **145**, 302.
38. G. Navon, Y. Q. Song, T. Room, S. Appelt, R. E. Taylor and A. Pines, *Science*, 1996, **271**, 1848.
39. R. K. Mazitov, R. Seydoux, P. Diehl, K. M. Enikeev, A. V. Il'yasov and R. Haselmeier, *Z. Phys. Chem.*, 2000, **214**, 1671.
40. E. Locci, J. Reisse and K. Bartik, *ChemPhysChem*, 2003, **4**, 305.
41. J. Bharatam and C. R. Bowers, *J. Phys. Chem. B*, 1999, **103**, 2510.
42. M. Cifelli, J. Saunavaara, J. Jokisaari and C. A. Veracini, *J. Phys. Chem. A*, 2004, **108**, 3973.
43. J. Ruohonen and J. Jokisaari, *Phys. Chem. Chem. Phys.*, 2001, **3**, 3208.
44. M. Ylihautala, J. Lounila and J. Jokisaari, *J. Chem. Phys.*, 1999, **110**, 6381.
45. M. M. Spence, S. M. Rubin, I. E. Dimitrov, E. J. Ruiz, D. E. Wemmer, A. Pines, S. Q. Yao, F. Tian and P. G. Schultz, *Proc. Natl. Acad. Sci. USA.*, 2001, **98**, 10654.
46. J. Wolber, I. J. Rowland, M. O. Leach and A. Bifone, *Appl. Magn. Reson.*, 1998, **15**, 343.
47. T. Brotin, T. Devic, A. Lesage, L. Emsley and A. Collet, *Chem. Eur. J.*, 2001, **7**, 1561.
48. T. Brotin and J. P. Dutasta, *Eur. J. Org. Chem.*, 2003, 973.
49. T. Brotin, A. Lesage, L. Emsley and A. Collet, *J. Am. Chem. Soc.*, 2000, **122**, 1171.
50. K. Bartik, M. Luhmer, J. P. Dutasta, A. Collet and J. Reisse, *J. Am. Chem. Soc.*, 1998, **120**, 784.
51. K. Bartik, M. Luhmer, A. Collet and J. Reisse, *Chirality*, 2001, **13**, 2.
52. M. Darzac, T. Brotin, D. Bouchu and J. P. Dutasta, *Chem. Commun.*, 2002, 48.
53. M. Darzac, T. Brotin, L. Rousset-Arzel, D. Bouchu and J. P. Dutasta, *New J. Chem.*, 2004, **28**, 502.
54. M. S. Syamala, R. J. Cross and M. Saunders, *J. Am. Chem. Soc.*, 2002, **124**, 6216.
55. M. Saunders, H. A. JimenezVazquez, R. J. Cross, S. Mroczkowski, D. I. Freedberg and F. A. L. Anet, *Nature*, 1994, **367**, 256.
- [56] M. El Haouaj, Y. H. Ko, M. Luhmer, K. Kim, K. Bartik, *J. Chem. Soc. Perkins Trans. 2*, 2001 2104.
- [57] M. El Haouaj, M. Luhmer, Y. H. Ko, K. Kim, K. Bartik, *J. Chem. Soc. Perkins Trans. 2* 2001 804.
58. J. Tilton, R. F. and J. Kuntz, I. D., *Biochemistry*, 1982, **21**, 6850.
59. C. R. Bowers, V. Storhaug, C. E. Webster, J. Bharatam, A. Cottone, R. Gianna, K. Betsey and B. J. Gaffney, *J. Am. Chem. Soc.*, 1999, **121**, 9370.
60. E. Locci, Y. Dehouck, M. Casu, G. Saba, A. Lai, M. Luhmer, J. Reisse and K. Bartik, *J. Magn. Reson.*, 2001, **150**, 167.
61. E. Locci, M. Casu, G. Saba, A. Lai, J. Reisse and K. Bartik, *ChemPhysChem*, 2002, **3**, 812.
62. K. Bartik, M. Luhmer, S. J. Heyes, R. Ottinger and J. Reisse, *J. Magn. Reson. Ser. B*, 1995, **109**, 164.
63. C. Groger, A. Moglich, M. Pons, B. Koch, W. Hengstenberg, H. R. Kalbitzer and E. Brunner, *J. Am. Chem. Soc.*, 2003, **125**, 8726.
64. S. Seidel and K. Seppelt, *Science*, 2000, **290**, 117.
65. I. -C. Hwang, S. Seidel and K. Seppelt, *Angew. Chem., Int. Ed.*, 2003, **42**, 4392.
66. T. Drews, S. Seidel and K. Seppelt, *Angew. Chem., Int. Ed.*, 2002, **41**, 454.
67. S. Seidel and K. Seppelt, *Angew. Chem., Int. Ed.*, 2004, **40**, 4225.
68. P. Ulferts and K. Seppelt, *Z. Anorg. Allg. Chem.*, 2004, **630**, 1589.
69. M. Gerken and G. J. Schrobilgen, *Inorg. Chem.*, 2002, **41**, 198.
70. M. Gerken and G. J. Schrobilgen, *Coord. Chem. Rev.*, 2000, **197**, 335.
71. H. J. Frohn and V. V. Bardin, *Chem. Commun.*, 1999, 919.
72. H. J. Frohn and V. V. Bardin, *Z. Anorg. Allg. Chem.*, 2003, **629**, 2465.
73. H. J. Frohn and V. V. Bardin, *Chem. Commun.*, 2003, 2352.
74. H. J. Frohn, A. Klose, T. Schroer, G. Henkel, V. Buss, D. Opitz and R. Vahrenhorst, *Inorg. Chem.*, 1998, **37**, 4884.
75. H. J. Frohn, N. Y. Adonin and V. V. Bardin, *Z. Anorg. Allg. Chem.*, 2003, **629**, 2499.
76. H. Schmidt, H. Scherer, W. Tyrra, J. Hahn and D. Naumann, *Inorg. Chem.*, 2004, **43**, 1837.
77. N. Maggiorosa, D. Naumann and W. Tyrra, *Angew. Chem. Int. Ed.*, 2000, **39**, 4588.
78. Y. L. Yagupolskii, W. Tyrra, R. Gnann, N. Maggiorosa and D. Naumann, *J. Fluorine Chem.*, 2002, **113**, 143.

79. T. Ito and J. Fraissard, *Proceedings of the Fifth International Zeolite Conference*, Naples, L. V. Rees, ed., Heyden, London, 1980, p. 510.
80. L. C. De Menorval, D. Raftery, S. B. Liu, K. Takegoshi, R. Ryoo and A. Pines, *J. Phys. Chem.*, 1990, **94**, 27.
81. A. Seidel and B. Boddenberg, *J. Chem. Soc., Faraday Trans.*, 1998, **94**, 1363.
82. A. Seidel, G. Kampf, A. Schmidt and B. Boddenberg, *Catal. Lett.*, 1998, **51**, 213.
83. A. Seidel, F. Rittner and B. Boddenberg, *J. Chem. Soc., Faraday Trans.*, 1996, **92**, 1815.
84. A. Seidel, F. Rittner and B. Boddenberg, *J. Chem. Soc., Faraday Trans.*, 1996, **92**, 493.
85. J. Nagano, T. Eguchi, T. Asanuma, H. Masui, H. Nakayama, N. Nakamura and E. G. Derouane, *Microporous Mesoporous Mater.*, 1999, **33**, 249.
86. T. Koskela, M. Ylihaata and J. Jokisaari, *Microporous Mesoporous Mater.*, 2001, **46**, 99.
87. W. P. Zhang, X. W. Han, X. C. Liu, H. Lei and X. H. Bao, *Chem. Commun.*, 2001, 293.
88. J. M. Kneller, T. Pietrass, K. C. Ott and A. Labouriau, *Microporous Mesoporous Mater.*, 2003, **62**, 121.
89. T. Koskela, J. Jokisaari and C. Satyanarayana, *Microporous Mesoporous Mater.*, 2004, **67**, 113.
90. A. Lassoued, J. Deson, C. Lalo, A. Gedeon, P. Batamark, J. Fraissard, R. Birjega, R. Ganea and C. Nenu, *Microporous Mesoporous Mater.*, 2001, **43**, 1.
91. J. L. Bonardet, A. Gedeon and J. Fraissard, *Stud. Surf. Sci. Catal.*, 1995, **94**, 139.
92. N. Bansal and C. Dybowski, *J. Phys. Chem.*, 1995, **92**, 2333.
93. R. G. Larsen, J. Shore, K. Schmidtrohr, L. Emsley, H. Long, A. Pines, M. Janicke and B. F. Chmelka, *Chem. Phys. Lett.*, 1993, **214**, 220.
94. B. F. Chmelka, D. Raftery, A. V. McCormick, L. C. Demenorval, R. D. Levine and A. Pines, *Phys. Rev. Lett.*, 1991, **66**, 580.
95. C. J. Jameson, A. K. Jameson, R. Gerald and A. C. Dedios, *J. Chem. Phys.*, 1992, **96**, 1690.
96. I. L. Moudrakovski, C. I. Ratcliffe and J. A. Ripmeester, *J. Am. Chem. Soc.*, 1998, **120**, 3123.
97. R. Grosse, R. Burmeister, B. Boddenberg, A. Gedeon and J. Fraissard, *J. Phys. Chem.*, 1991, **95**, 2443.
98. J. A. BoltWesterhoff, K. P. Datema, A. K. Nowak, F. Stallmach and J. Karger, *Magn. Reson. Imaging*, 1996, **14**, 967.
99. P. Ngokoli-Kekele, M. A. Springuel-Huet, J. L. Bonardet, J. M. Dereppe and J. Fraissard, *Bull. Pol. Acad. Sci. Chem.*, 2002, **50**, 249.
100. P. Ngokoli-Kekele, M. A. Springuel-Huet, J. L. Bonardet and J. Fraissard, *Stud. Surf. Sci. Catal.*, 2000, **130C**, 2939.
101. A. Labouriau, T. Pietrass, W. A. Weber, B. C. Gates and W. L. Earl, *J. Phys. Chem. B*, 1999, **103**, 4323.
102. T. T. P. Cheung, *J. Phys. Chem.*, 1995, **99**, 7089.
103. A. Labouriau, G. Panjabi, B. Enderle, T. Pietrass, B. C. Gates, W. L. Earl and K. C. Ott, *J. Am. Chem. Soc.*, 1999, **121**, 7674.
104. S. Yuvaraj, T. H. Chang and C. T. Yeh, *J. Catal.*, 2004, **221**, 466.
105. A. Seidel, F. Rittner and B. Boddenberg, *J. Phys. Chem. B*, 1998, **102**, 7176.
106. B. A. Enderle, A. Labouriau, K. C. Ott and B. C. Gates, *NanoLett.*, 2002, **2**, 1269.
107. D. Horvath, M. Polisset-Thfoin, J. Fraissard and L. Gucci, *Solid State Ionics*, 2001, **141**, 153.
108. S. J. Cho, S. K. Kang and R. Ryoo, *Sci. Technol. Catal.*, 1999, **121**, 295.
109. O. H. Kwon, H. Yoo, K. Park, B. Tu, R. Ryoo and D. J. Jang, *J. Phys. Chem. B*, 2001, **105**, 4195.
110. O. H. Kwon, H. Yu and D. J. Jang, *J. Phys. Chem. B*, 2004, **108**, 3970.
111. A. Seidel, U. Tracht and B. Boddenberg, *J. Phys. Chem.*, 1996, **100**, 15917.
112. A. Lamrabte, J. M. Janot, A. Elmidaoui, P. Seta, L. C. De Menorval, R. Backov, J. Roziere, J. L. Sauvajol and J. Allegre, *Chem. Phys. Lett.*, 1998, **295**, 257.
113. F. Chen, F. Deng, M. J. Cheng, Y. Yue, C. H. Ye and X. H. Bao, *J. Phys. Chem. B*, 2001, **105**, 9426.
114. F. Chen, F. Deng, M. J. Cheng, Y. Yue and C. H. Ye, *Chin. Sci. Bull.*, 2002, **47**, 542.
115. M. A. Springuel-Huet, K. Sun and J. Fraissard, *Microporous Mesoporous Mater.*, 1999, **33**, 89.
116. A. Davidson, P. Berthault and H. Desvaux, *J. Phys. Chem. B*, 2003, **107**, 14388.

117. F. Chen, M. J. Zhang, Y. Han, F. S. Xiao, Y. Yue, C. H. Ye and F. Deng, *J. Phys. Chem. B*, 2004, **108**, 3728.
118. S. J. Jong, J. F. Wu, A. R. Pradhan, H. P. Lin, C. Y. Mou and S. B. Liu, *Mesoporous Molecular Sieves*, 1998, **117**, 543.
119. W. H. Chen, H. P. Lin, J. F. Wu, S. J. Jong, C. Y. Mou and S. B. Liu, *Stud. Surf. Sci. Catal.*, 2000, **129**, 517.
120. G. Oye, M. A. Springuel-Huet, J. Fraissard, M. Stocker and J. Sjöblom, *Stud. Surf. Sci. Catal.*, 2001, **135**, 1034.
121. M. A. Springuel-Huet, J. L. Bonardet, A. Gedeon, Y. Yue, V. N. Romannikov and J. Fraissard, *Microporous Mesoporous Mater.*, 2001, **44**, 775.
122. H. Omi, B. Nagasaka, K. Miyakubo, T. Ueda and T. Eguchi, *Phys. Chem. Chem. Phys.*, 2004, **6**, 1299.
123. V. V. Tersikh, I. L. Moudrakovski, S. R. Breeze, S. Lang, C. I. Ratcliffe, J. A. Ripmeester and A. Sayari, *Langmuir*, 2002, **18**, 5653.
124. F. Cros, J. P. Korb and L. Malier, *Langmuir*, 2000, **16**, 10193.
125. E. G. Derouane and J. B. Nagy, *Chem. Phys. Lett.*, 1987, **137**, 341.
126. E. G. Derouane, J. M. Andre and A. A. Lucas, *Chem. Phys. Lett.*, 1987, **137**, 336.
127. F. Chen, C. L. Chen, S. W. Ding, Y. Yue, C. H. Ye and F. Deng, *Chem. Phys. Lett.*, 2004, **383**, 309.
128. T. Pietrass, J. M. Kneller, R. A. Assink and M. T. Anderson, *J. Phys. Chem. B*, 1999, **103**, 8837.
129. Y. Ba and D. Chagolla, *J. Phys. Chem. B*, 2002, **106**, 5250.
130. D. Chagolla, G. Ezedine and Y. Ba, *Microporous Mesoporous Mater.*, 2003, **64**, 155.
131. D. M. Gregory, R. E. Gerald and R. E. Botto, *J. Magn. Reson.*, 1998, **131**, 327.
132. D. M. Gregory and R. E. Botto, *Appl. Spectrosc.*, 2003, **57**, 245.
133. S. Faggian, P. Fiscaro, E. Giamello, R. Gobetto, A. Viale, G. Berlier, C. Lamberti and I. Rossetti, *J. Phys. Chem. B*, 2003, **107**, 8922.
134. P. Ngokoli-Kekele, M. A. Springuel-Huet, P. P. Man, J. Thoret, J. Fraissard and D. R. Corbin, *Microporous Mesoporous Mater.*, 1998, **25**, 35.
135. W. P. Guo, L. M. Huang, P. Deng, Z. Y. Xue and Q. Z. Li, *Microporous Mesoporous Mater.*, 2001, **44**, 427.
136. W. P. Guo, L. M. Huang, C. S. Ha and Q. Z. Li, *Stud. Surf. Sci. Catal.*, 2003, **146**, 367.
137. F. Junker and W. S. Veeman, *Chem. Phys. Lett.*, 1999, **305**, 39.
138. P. A. Simonov, S. V. Filimonova, G. N. Kryukova, E. M. Moroz, V. A. Likholobov, T. Kuretzky and H. P. Boehm, *Carbon*, 1999, **37**, 591.
139. K. Saito, A. Kimura and H. Fujiwara, *Magn. Reson. Imaging*, 2003, **21**, 401.
140. T. Ueda, T. Eguchi, N. Nakamura and R. E. Wasylshen, *J. Phys. Chem. B*, 2003, **107**, 180.
141. A. Julbe, L. C. De Menorval, C. Balzer, P. David, J. Palmeri and C. Guizard, *J. Porous Mater.*, 1999, **6**, 41.
142. G. Golemme, J. B. Nagy, A. Fonseca, C. Algieri and Y. Yampolskii, *Polymer*, 2003, **44**, 5039.
143. H. Menge, H. Kuhn, B. Blumich, P. Blumler and H. Schneider, *Macromol. Mater. Eng.*, 2000, **282**, 1.
144. G. Meresi, Y. Wang, A. Bandis, P. T. Inglefield, A. A. Jones and W. Y. Wen, *Polymer*, 2001, **42**, 6153.
145. T. Suzuki, M. Miyauchi, M. Takekawa, M. Yoshimizu, Y. Tsujita and T. Kinoshita, *Macromolecules*, 2001, **34**, 3805.
146. Y. Z. Wang, P. T. Inglefield and A. A. Jones, *Polymer*, 2002, **43**, 1867.
147. T. Suzuki, H. Yoshimizu and Y. Tsujita, *Polymer*, 2003, **44**, 2975.
148. T. C. Merkel, L. G. Toy, A. L. Andrady, H. Gracz and E. O. Stejskal, *Macromolecules*, 2003, **36**, 353.
149. Y. Z. Wang, P. T. Inglefield and A. A. Jones, *J. Polym. Sci., Part B: Polym. Phys.*, 2002, **40**, 1965.
150. F. Junker and W. S. Veeman, *Macromolecules*, 1998, **31**, 7010.
151. D. R. Morgan, E. O. Stejskal and A. L. Andrady, *Macromolecules*, 1999, **32**, 1897.
152. B. Nagasaka, H. Omi, T. Eguchi, H. Nakayama and N. Nakamura, *Chem. Phys. Lett.*, 2001, **340**, 473.

153. K. J. McGrath, *Carbon*, 1999, **37**, 1443.
154. P. C. M. M. Magusin, A. Bolz, K. Sperling and W. S. Veeman, *Geoderma*, 1997, **80**, 449.
155. P. J. Barrie, G. F. Mccann, I. Gameson, T. Rayment and J. Klinowski, *J. Phys. Chem.*, 1991, **95**, 9416.
156. T. Meersmann and M. Haake, *Phys. Rev. Lett.*, 1998, **81**, 1211.
157. Z. Wu, W. Happer and J. M. Daniels, *Phys. Rev. Lett.*, 1987, **59**, 1480.
158. D. Raftery, H. W. Long, D. Shykind, P. J. Grandinetti and A. Pines, *Phys. Rev. A*, 1994, **50**, 567.
159. M. Deschamps, I. Burghardt, C. Derouet, G. Bodenhausen and D. Belkic, *J. Chem. Phys.*, 2000, **113**, 1630.
160. T. Meersmann, M. Deschamps and G. Bodenhausen, *J. Am. Chem. Soc.*, 2001, **123**, 941.
161. T. Meersmann, S. A. Smith and G. Bodenhausen, *Phys. Rev. Lett.*, 1998, **80**, 1398.
162. J. Vaara and P. Pyykko, *Phys. Rev. Lett.*, 2001, **86**, 3268.
163. F. R. Salsbury and R. A. Harris, *J. Chem. Phys.*, 1998, **109**, 8338.
164. Y. Millot, P. P. Man, M. A. Springuel-Huet and J. Fraissard, *C. R. Acad. Sci. Ser. IIc: Chim.*, 2001, **4**, 815.
165. I. L. Moudrakovski, C. I. Ratcliffe and J. A. Ripmeester, *J. Am. Chem. Soc.*, 2001, **123**, 2066.
166. G. Pavlovskaya, A. K. Blue, S. J. Gibbs, M. Haake, F. Cros, L. Malier and T. Meersmann, *J. Magn. Reson.*, 1999, **137**, 258.
167. D. N. Sears and C. J. Jameson, *J. Chem. Phys.*, 2003, **119**, 12231.
168. D. Stueber and C. J. Jameson, *J. Chem. Phys.*, 2004, **120**, 1560.
169. C. J. Jameson and D. Stueber, *J. Chem. Phys.*, 2004, **120**, 10200.
170. C. J. Jameson and A. C. de Dios, *J. Chem. Phys.*, 2002, **116**, 3805.
171. C. J. Jameson, *J. Chem. Phys.*, 2002, **116**, 8912.
172. C. J. Jameson, D. N. Sears and A. C. de Dios, *J. Chem. Phys.*, 2003, **118**, 2575.
173. C. J. Jameson, A. K. Jameson, P. Kostikin and B. I. Baello, *J. Chem. Phys.*, 2000, **112**, 323.
174. C. J. Jameson, A. K. Jameson and H. M. Lim, *J. Chem. Phys.*, 1996, **104**, 1709.
175. C. J. Jameson, A. K. Jameson and H. M. Lim, *J. Chem. Phys.*, 1997, **107**, 4364.
176. A. Bagno and G. Saielli, *Chem. Eur. J.*, 2003, **9**, 1486.
177. M. A. M. Forgeron, R. E. Wasylshen and G. H. Penner, *J. Phys. Chem. A*, 2004, **108**, 4751.
178. J. H. Yang, L. A. Clark, G. J. Ray, Y. J. Kim, H. Du and R. Q. Snurr, *J. Phys. Chem. B*, 2001, **105**, 4698.
179. J. Vaara and P. Pyykko, *J. Chem. Phys.*, 2003, **118**, 2973.
180. C. J. Jameson and S. Murad, *Chem. Phys. Lett.*, 2003, **380**, 556.
181. B. A. Fir, H. P. A. Mercier, J. C. P. Sanders, D. A. Dixon and G. J. Schrobilgen, *J. Fluorine Chem.*, 2001, **110**, 89.
182. A. Hori and T. Hondoh, *Can. J. Phys.*, 2003, **81**, 33.
183. K. Bartik, M. El Haouaj, M. Luhmer, A. Collet and J. Reisse, *ChemPhysChem*, 2000, **1**, 221.
184. D. N. Sears, C. J. Jameson and R. A. Harris, *J. Chem. Phys.*, 2003, **119**, 2685.
185. A. L. Barra and J. B. Robert, *Mol. Phys.*, 1996, **88**, 875.
186. J. B. Robbert and A. L. Barra, *Chirality*, 2001, **13**, 699.
187. C. S. Wood, S. C. Bennett, D. Cho, B. P. Masterson, J. L. Robert, C. E. Tanner and C. E. Wieman, *Science*, 1997, **275**, 1759.
188. T. G. Walker and W. Happer, *Rev. Mod. Phys.*, 1997, **69**, 629.
189. R. J. Knize, Z. Wu and W. Happer, *Adv. Atom. Mol. Phys.*, 1989, **24**, 223.
190. R. Tycko and J. A. Reimer, *J. Phys. Chem.*, 1996, **100**, 13240.
191. G. D. Cates, R. J. Fitzgerald, A. S. Barton, P. Bogorad, M. Gatzke, N. R. Newbury and B. Saam, *Phys. Rev. A*, 1992, **45**, 4631.
192. B. Driehuys, G. D. Cates, E. Miron, K. Sauer, D. K. Walter and W. Happer, *Appl. Phys. Lett.*, 1996, **69**, 1668.
193. A. L. Zook, B. B. Adhyaru and C. R. Bowers, *J. Magn. Reson.*, 2002, **159**, 175.
194. M. Haake, A. Pines, J. A. Reimer and R. Seydoux, *J. Am. Chem. Soc.*, 1997, **119**, 11711.
195. R. Seydoux, A. Pines, M. Haake and J. A. Reimer, *J. Phys. Chem. B*, 1999, **103**, 4629.
196. K. Knagge, J. Prange and D. Raftery, *Chem. Phys. Lett.*, 2004, **397**, 11.

197. M. S. Rosen, T. E. Chupp, K. P. Coulter, R. C. Welsh and S. D. Swanson, *Rev. Sci. Instrum.*, 1999, **70**, 1546.
198. M. G. Mortuza, S. Anala, G. E. Pavlovskaya, T. J. Dieken and T. Meersmann, *J. Chem. Phys.*, 2003, **118**, 1581.
199. J. Fukutomi, E. Suzuki, T. Shimizu, A. Kimura and H. Fujiwara, *J. Magn. Reson.*, 2003, **160**, 26.
200. D. Levron, D. K. Walter, S. Appelt, R. J. Fitzgerald, D. Kahn, S. E. Korbly, K. L. Sauer, W. Happer, T. L. Earles, L. J. Mawst, D. Botez, M. Harvey, L. DiMarco, J. C. Connolly, H. E. Moller, X. J. Chen, G. P. Cofer and G. A. Johnson, *Appl. Phys. Lett.*, 1998, **73**, 2666.
201. A. B. Baranga, S. Appelt, C. J. Erickson, A. R. Young and W. Happer, *Phys. Rev. A*, 1998, **58**, 2282.
202. N. J. Shah, T. Unlu, H. P. Wegener, H. Halling, K. Zilles and S. Appelt, *NMR Biomed.*, 2000, **13**, 214.
203. K. Ishikawa, S. Morii, K. Enomoto and T. Yabuzaki, *J. Opt. Soc. Am. B*, 2000, **17**, 182.
204. S. Haroche and C. Cohen-Tannoudji, *Phys. Rev. Lett.*, 1970, **24**, 974.
205. J. N. Zerger, M. J. Lim, K. P. Coulter and T. E. Chupp, *Appl. Phys. Lett.*, 2000, **76**, 1798.
206. I. A. Nelson, B. Chann and T. G. Walker, *Appl. Phys. Lett.*, 2000, **76**, 1356.
207. U. Ruth, T. Hof, J. Schmidt, D. Fick and H. J. Jansch, *Appl. Phys. B Lasers Opt.*, 1999, **68**, 93.
208. X. Zeng, C. J. Wu, M. X. Zhao, S. L. Li, L. Y. Li, X. Zhang, Z. D. Liu and W. Liu, *Chem. Phys. Lett.*, 1991, **182**, 538.
209. M. P. Augustine and K. W. Zilm, *Mol. Phys.*, 1996, **89**, 737.
210. M. P. Augustine and K. W. Zilm, *Chem. Phys. Lett.*, 1997, **280**, 24.
211. C. V. Rice and D. Raftery, *J. Chem. Phys.*, 2002, **117**, 5632.
212. Y. Y. Jau, N. N. Kuzma and W. Happer, *Phys. Rev. A*, 2002, **66**, No. 052710.
213. Y. Y. Jau, N. N. Kuzma and W. Happer, *Phys. Rev. A*, 2004, **69**, No. 061401.
214. T. Killian, *Phys. Rev.*, 1926, **27**, 578.
215. C. J. Smithells, *Metals Reference Book*, Vol. 2, Butterworths, London, 1962, p. 655.
216. N. Biskup, N. Kalechofsky and D. Candela, *Phys. B*, 2003, **329**, 437.
217. T. Su, G. L. Samuelson, S. W. Morgan, G. Laicher and B. Saam, *Appl. Phys. Lett.*, 2004, **85**, 2429.
218. H. Fujiwara, A. Kimura, Y. Yanagawa, T. Kamiya, M. Hattori and T. Hiraga, *J. Magn. Reson.*, 2001, **150**, 156.
219. S. R. Breeze, S. Lang, I. Moudrakovski, C. I. Ratcliffe, J. A. Ripmeester, G. Santyr, B. Simard and I. Zuger, *J. Appl. Phys.*, 2000, **87**, 8013.
220. S. R. Breeze, S. Lang, I. Moudrakovski, C. I. Ratcliffe, J. A. Ripmeester, B. Simard and G. Santyr, *J. Appl. Phys.*, 1999, **86**, 4040.
221. B. Chann, I. A. Nelson, L. W. Anderson, B. Driehuys and T. G. Walker, *Phys. Rev. Lett.*, 2002, **88**, Art. No. 113201.
222. K. L. Sauer, F. Marion, P. J. Nacher and G. Tastevin, *Phys. Rev. B*, 2001, **63**, Art. No. 184427.
223. P. J. Nacher, G. Tastevin, B. Villard, N. Piegay, F. Marion and K. Sauer, *J. Low Temp. Phys.*, 2000, **121**, 743.
224. M. V. Romalis and M. P. Ledbetter, *Phys. Rev. Lett.*, 2001, **87**, Art. No. 067601.
225. J. Jeener, *Phys. Rev. Lett.*, 1999, **82**, 1772.
226. P. Berthault, H. Desvaux, G. Le Goff and M. Petro, *Chem. Phys. Lett.*, 1999, **314**, 52.
227. A. S. Verhulst, O. Liivak, M. H. Sherwood and I. L. Chuang, *J. Magn. Reson.*, 2002, **155**, 145.
228. M. Gatzke, G. D. Cates, B. Driehuys, D. Fox, W. Happer and B. Saam, *Phys. Rev. Lett.*, 1993, **70**, 690.
229. S. Lang, I. L. Moudrakovski, C. I. Ratcliffe, J. A. Ripmeester and G. Santyr, *Appl. Phys. Lett.*, 2002, **80**, 886.
230. P. Gerhard, M. Koch and H. J. Jansch, *C. R. Phys.*, 2004, **5**, 297.
231. E. Brunner, R. Seydoux, M. Haake, A. Pines and J. A. Reimer, *J. Magn. Reson.*, 1998, **130**, 145.
232. D. Raftery, E. MacNamara, G. Fisher, C. V. Rice and J. Smith, *J. Am. Chem. Soc.*, 1997, **119**, 8746.
233. J. M. Kneller, R. J. Soto, S. E. Surber, J. F. Colomer, A. Fonseca, J. B. Nagy and T. Pietrass, *J. Magn. Reson.*, 2000, **147**, 261.

234. I. L. Moudrakovski, A. Nosssov, S. Lang, S. R. Breeze, C. I. Ratcliffe, B. Simard, G. Santyr and J. A. Ripmeester, *Chem. Mater.*, 2000, **12**, 1181.
235. D. Raftery, H. Long, T. Meersmann, P. J. Grandinetti, L. Reven and A. Pines, *Phys. Rev. Lett.*, 1991, **66**, 584.
236. D. Raftery, L. Reven, H. Long, A. Pines, P. Tang and J. A. Reimer, *J. Phys. Chem.*, 1993, **97**, 1649.
237. A. Nosssov, F. Guenneau, M. A. Springuel-Huet, E. Haddad, V. Montouillout, B. Knott, F. Engelke, C. Fernandez and A. Gedeon, *Phys. Chem. Chem. Phys.*, 2003, **5**, 4479.
238. A. Nosssov, E. Haddad, F. Guenneau, A. Galarneau, F. Di Renzo, F. Fajula and A. Gedeon, *J. Phys. Chem. B*, 2003, **107**, 12456.
239. A. Nosssov, E. Haddad, F. Guenneau and A. Gedeon, *Phys. Chem. Chem. Phys.*, 2003, **5**, 4473.
240. E. Haddad, A. Nosssov, F. Guenneau, M. Nader, D. Grosso, C. Sanchez and A. Gedeon, *Stud. Surf. Sci. Catal.*, 2004, **154**, 1464.
241. E. Haddad, J. -B. d'Espinose, A. Nosov, F. Guenneau and A. Gedeon, *Stud. Surf. Sci. Catal.*, 2002, **142B**, 1173.
242. A. Nosssov, E. Haddad, F. Guenneau, C. Mignon, A. Gedeon, D. Grosso, F. Babonneau, C. Bonhomme and C. Sanchez, *Chem. Commun.*, 2002, 2476.
243. E. Haddad, A. Nosssov, F. Guenneau and A. Gedeon, *C. R. Chim.*, 2004, **7**, 305.
244. A. V. Nosssov, D. V. Soldatov and J. A. Ripmeester, *J. Am. Chem. Soc.*, 2001, **123**, 3563.
245. I. L. Moudrakovski, V. V. Terskikh, C. I. Ratcliffe, J. A. Ripmeester, L. Q. Wang, Y. Shin and G. J. Exarhos, *J. Phys. Chem. B*, 2002, **106**, 5938.
246. I. L. Moudrakovski, L. Q. Wang, T. Baumann, J. H. Satcher, G. J. Exarhos, C. I. Ratcliffe and J. A. Ripmeester, *J. Am. Chem. Soc.*, 2004, **126**, 5052.
247. V. V. Terskikh, I. L. Moudrakovski, H. B. Du, C. I. Ratcliffe and J. A. Ripmeester, *J. Am. Chem. Soc.*, 2001, **123**, 10399.
248. S. J. Huang, C. H. Huang, W. H. Chen, X. P. Sun, X. Z. Zeng, H. K. Lee, J. A. Ripmeester, C. Y. Mou and S. B. Liu, *J. Phys. Chem.*, 2005, **109**, 681.
249. I. L. Moudrakovski, A. A. Sanchez, C. I. Ratcliffe and J. A. Ripmeester, *J. Phys. Chem. B*, 2001, **105**, 12338.
250. I. L. Moudrakovski, C. I. Ratcliffe and J. A. Ripmeester, *Angew. Chem. Int. Ed.*, 2001, **40**, 3890.
251. V. J. Storhaug, F. Liebigh and C. R. Bowers, *J. Phys. Chem. B*, 2002, **106**, 2884.
252. I. L. Moudrakovski, A. Sanchez, C. I. Ratcliffe and J. A. Ripmeester, *J. Phys. Chem. B*, 2000, **104**, 7306.
253. E. Brunner, M. Haake, A. Pines, J. A. Reimer and R. Seydoux, *Chem. Phys. Lett.*, 1998, **290**, 112.
254. D. V. Soldatov, I. L. Moudrakovski and J. A. Ripmeester, *Angew. Chem. Int. Ed.*, 2004, **43**, 6308.
255. H. J. Jansch, *Appl. Phys. A: Mater. Sci. Process.*, 1997, **65**, 567.
256. H. J. Jansch, T. Hof, U. Ruth, J. Schmidt, D. Stahl and D. Fick, *Chem. Phys. Lett.*, 1998, **296**, 146.
257. H. J. Jansch, P. Gerhard, M. Koch and D. Stahl, *Chem. Phys. Lett.*, 2003, **372**, 325.
258. H. J. Jansch, P. Gerhard and M. Koch, *Proc. Natl. Acad. Sci. USA*, 2004, **101**, 13715.
259. D. Stahl and H. J. Jansch, *Hyperfine Interact.*, 2000, **127**, 469.
260. H. W. Long, H. C. Gaede, J. Shore, L. Reven, C. R. Bowers, J. Kritzenberger, T. Pietrass, A. Pines, P. Tang and J. A. Reimer, *J. Am. Chem. Soc.*, 1993, **115**, 8491.
261. C. R. Bowers, H. W. Long, T. Pietrass, H. C. Gaede and A. Pines, *Chem. Phys. Lett.*, 1993, **205**, 168.
262. Y. Q. Song, *Concepts Magn. Reson.*, 2000, **12**, 6.
263. H. C. Gaede, Y. Q. Song, R. E. Taylor, E. J. Munson, J. A. Reimer and A. Pines, *Appl. Magn. Reson.*, 1995, **8**, 373.
264. E. MacNamara, G. Fisher, J. Smith, C. V. Rice, S. J. Hwang and D. Raftery, *J. Phys. Chem. B*, 1999, **103**, 1158.
265. E. MacNamara, C. V. Rice, J. Smith, L. J. Smith and D. Raftery, *Chem. Phys. Lett.*, 2000, **317**, 165.
266. T. Pietrass, R. Seydoux and A. Pines, *J. Magn. Reson.*, 1998, **133**, 299.
267. K. Sauer, R. J. Fitzgerald and W. Happer, *Phys. Rev. A*, 1999, **59**, R1746.
268. T. Room, S. Appelt, R. Seydoux, E. L. Hahn and A. Pines, *Phys. Rev. B*, 1997, **55**, 11604.

269. L. J. Smith, J. Smith, E. MacNamara, K. Knagge and D. Raftery, *J. Phys. Chem. B*, 2001, **105**, 1412.
270. J. Smith, L. J. Smith, K. Knagge, E. MacNamara and D. Raftery, *J. Am. Chem. Soc.*, 2001, **123**, 2927.
271. J. Smith, K. Knagge, L. J. Smith, E. MacNamara and D. Raftery, *J. Magn. Reson.*, 2002, **159**, 111.
272. Y. Q. Song, B. M. Goodson, R. E. Taylor, D. D. Laws, G. Navon and A. Pines, *Angew. Chem. Int. Ed.*, 1997, **36**, 2368.
273. M. Luhmer, B. M. Goodson, Y. Q. Song, D. D. Laws, L. Kaiser, M. C. Cyrier and A. Pines, *J. Am. Chem. Soc.*, 1999, **121**, 3502.
274. K. Ishikawa, H. Imai and Y. Takagi, *J. Chem. Phys.*, 2004, **120**, 7602.
275. K. Ishikawa, H. Imai and Y. Takagi, *Phys. Rev. B*, 2004, **70**, 42712.
276. S. Appelt, F. W. Haesing, S. Baer-Lang, N. J. Shah and B. Blumich, *Chem. Phys. Lett.*, 2001, **348**, 263.
277. A. Cherubini, G. S. Payne, M. O. Leach and A. Bifone, *Chem. Phys. Lett.*, 2003, **371**, 640.
278. X. Zhou, J. Luo, X. P. Sun, X. Z. Zeng, S. W. Ding, M. L. Liu and M. S. Zhan, *Phys. Rev. B*, 2004, **70**, Art. No. 052405.
279. M. S. Albert, G. D. Cates, B. Driehuys, W. Happer, B. Saam, C. S. Springer and A. Wishnia, *Nature*, 1994, **370**, 199.
280. M. S. Albert and D. Balamore, *Nucl. Instrum. Methods Phys. Res. Sect. A*, 1998, **402**, 441.
281. H. E. Moller, X. J. Chen, M. S. Chawla, G. P. Cofer, B. Driehuys, L. W. Hedlund, S. A. Suddarth and G. A. Johnson, *Magn. Reson. Med.*, 1999, **41**, 800.
282. H. U. Kauczor, D. Hofmann, K. F. Kreitner, H. Nilgens, R. Surkau, W. Heil, A. Potthast, M. V. Knopp and E. W. Otten, *Radiology*, 1996, **201**, 564.
283. K. Ruppert, J. F. Mata, J. R. Brookeman, K. D. Hagspiel and J. P. Mugler, *Magn. Reson. Med.*, 2004, **51**, 676.
284. K. Ruppert, J. R. Brookeman, K. D. Hagspiel and J. P. Mugler, *Magn. Reson. Med.*, 2000, **44**, 349.
285. M. P. Ramirez, K. C. E. Sigaloff, L. V. Kubatina, M. A. Donahue, A. K. Venkatesh and M. S. Albert, *NMR Biomed.*, 2000, **13**, 253.
286. M. S. Albert, V. D. Schepkin and T. F. Budinger, *J. Comput. Assist. Tomogr.*, 1995, **19**, 975.
287. M. S. Albert, D. F. Kacher, D. Balamore, A. K. Venkatesh and F. A. Jolesz, *J. Magn. Reson.*, 1999, **140**, 264.
288. A. Bifone, Y. Q. Song, R. Seydoux, R. E. Taylor, B. M. Goodson, T. Pietrass, T. F. Budinger, G. Navon and A. Pines, *Proc. Natl. Acad. Sci. USA*, 1996, **93**, 12932.
289. J. Wolber, A. Cherubini, M. O. Leach and A. Bifone, *Magn. Reson. Med.*, 2000, **43**, 491.
290. B. M. Goodson, Y. Q. Song, R. E. Taylor, V. D. Schepkin, K. M. Brennan, G. C. Chingas, T. F. Budinger, G. Navon and A. Pines, *Proc. Natl. Acad. Sci. USA*, 1997, **94**, 14725.
291. C. Lavini, G. S. Payne, M. O. Leach and A. Bifone, *NMR Biomed.*, 2000, **13**, 238.
292. J. Wolber, A. Cherubini, A. S. K. Dzik-Jurasz, M. O. Leach and A. Bifone, *Proc. Natl. Acad. Sci. USA*, 1999, **96**, 3664.
293. M. S. Albert, D. Balamore, D. F. Kacher, A. K. Venkatesh and F. A. Jolesz, *NMR Biomed.*, 2000, **13**, 407.
294. A. K. Venkatesh, L. Zhao, D. Balamore, F. A. Jolesz and M. S. Albert, *NMR Biomed.*, 2000, **13**, 245.
295. A. K. Venkatesh, L. Zhao, D. Balamore, F. A. Jolesz and M. S. Albert, *Acad. Radiol.*, 2002, **9**, S270.
296. J. Wolber, I. J. Rowland, M. O. Leach and A. Bifone, *Magn. Reson. Med.*, 1999, **41**, 442.
297. G. Duhamel, P. Choquet, E. Grillon, L. Lamalle, J. L. Leviel, A. Ziegler and A. Constantinesco, *Magn. Reson. Med.*, 2001, **46**, 208.
298. G. Duhamel, P. Choquet, E. Grillon, J. L. Leviel, M. Decorps, A. Ziegler and A. Constantinesco, *Acad. Radiol.*, 2002, **9**, S498.
299. G. Duhamel, P. Choquet, E. Grillon, J. L. Leviel, A. Ziegler and A. Constantinesco, *C. R. Acad. Sci. Ser. IIc Chim.*, 2001, **4**, 789.
300. W. Kilian, F. Seifert and H. Rinneberg, *Magn. Reson. Med.*, 2004, **51**, 843.

301. G. Duhamel, P. Choquet, J. L. Leviel, J. Steibel, L. Lamalle, C. Julien, F. Kober, E. Grillon, J. Derouard, M. Decorps, A. Ziegler and A. Constantinesco, *C. R. Acad. Sci. Ser. III.*, 2000, **323**, 529.
302. P. Choquet, J. N. Hyacinthe, G. Duhamel, E. Grillon, J. L. Leviel, A. Constantinesco and A. Ziegler, *Magn. Reson. Med.*, 2003, **49**, 1014.
303. A. V. Il'yasov, R. K. Mazitov, K. M. Enikeev, A. N. Panov, N. A. Il'yasov and R. Z. Khasanov, *Appl. Magn. Reson.*, 1999, **17**, 77.
304. J. Wolber, D. J. O. McIntyre, L. M. Rodrigues, P. Carnochan, J. R. Griffiths, M. O. Leach and A. Bifone, *Magn. Reson. Med.*, 2001, **46**, 586.
305. B. P. W. Schoenborn, H. C. and J. C. Kendrew, *Nature*, 1965, **207**, 760.
306. S. M. Rubin, M. M. Spence, B. M. Goodson, D. E. Wemmer and A. Pines, *Proc. Natl. Acad. Sci. USA*, 2000, **97**, 9472.
307. S. M. Rubin, M. M. Spence, I. E. Dimitrov, E. J. Ruiz, A. Pines and D. E. Wemmer, *J. Am. Chem. Soc.*, 2001, **123**, 8616.
308. S. M. Rubin, S. Y. Lee, E. J. Ruiz, A. Pines and D. E. Wemmer, *J. Mol. Biol.*, 2002, **322**, 425.
309. H. Desvaux, T. Gautier, G. Le Goff, M. Petro and P. Berthault, *Eur. Phys. J. D.*, 2000, **12**, 289.
310. H. Desvaux, J. G. Huber, T. Brotin, J. P. Dutasta and P. Berthault, *ChemPhysChem*, 2003, **4**, 384.
311. L. Dubois, S. Parres, J. G. Huber, P. Berthault and H. Desvaux, *J. Phys. Chem. B*, 2004, **108**, 15952.
312. C. Landon, P. Berthault, F. Vovelle and H. Desvaux, *Protein Sci.*, 2001, **10**, 762.
313. L. Dubois, P. Berthault, J. G. Huber and H. Desvaux, *C. R. Phys.*, 2004, **5**, 305.
314. M. M. Spence, E. J. Ruiz, S. M. Rubin, T. J. Lowery, N. Winssinger, P. G. Schultz, D. E. Wemmer and A. Pines, *J. Am. Chem. Soc.*, 2004, **126**, 15287.
315. T. J. Lowery, S. M. Rubin, E. J. Ruiz, M. M. Spence, N. Winssinger, P. G. Schultz, A. Pines and D. E. Wemmer, *Magn. Reson. Imaging*, 2003, **21**, 1235.
316. R. W. Mair, M. S. Rosen, R. Wang, D. G. Cory and R. L. Walsworth, *Magn. Reson. Chem.*, 2002, **40**, S29.
317. R. W. Mair, D. G. Cory, S. Peled, C. H. Tseng, S. Patz and R. L. Walsworth, *J. Magn. Reson.*, 1998, **135**, 478.
318. R. W. Mair, R. Wang, M. S. Rosen, D. Candela, D. G. Cory and R. L. Walsworth, *Magn. Reson. Imaging*, 2003, **21**, 287.
319. R. W. Mair, M. N. Sen, M. D. Hurlimann, S. Patz, D. G. Cory and R. L. Walsworth, *J. Magn. Reson.*, 2002, **156**, 202.
320. R. W. Mair, M. D. Hurlimann, P. N. Sen, L. M. Schwartz, S. Patz and R. L. Walsworth, *Magn. Reson. Imaging*, 2001, **19**, 345.
321. R. W. Mair, G. P. Wong, D. Hoffmann, M. D. Hurlimann, S. Patz, L. M. Schwartz and R. L. Walsworth, *Phys. Rev. Lett.*, 1999, **83**, 3324.
322. E. O. Stejskal and C. E. Tanner, *J. Chem. Phys.*, 1968, **42**, 288.
323. J. P. Butler, R. W. Mair, D. Hoffmann, M. I. Hrovat, R. A. Rogers, G. P. Topulos, R. L. Walsworth and S. Patz, *J. Phys.: Condens. Matter*, 2002, **14**, L297.
324. T. Meersmann, J. W. Logan, R. Simonutti, S. Caldarelli, A. Comotti, P. Sozzani, L. G. Kaiser and A. Pines, *J. Phys. Chem. A*, 2000, **104**, 11665.
325. P. Sozzani, A. Comotti, R. Simonutti, T. Meersmann, J. W. Logan and A. Pines, *Angew. Chem., Int. Ed.*, 2000, **39**, 2695.
326. J. Wolber, S. J. Doran, M. O. Leach and A. Bifone, *Chem. Phys. Lett.*, 1998, **296**, 391.
327. R. W. Mair and R. L. Walsworth, *Appl. Magn. Reson.*, 2002, **22**, 159.
328. S. Han, H. Kuhn, F. W. Hasing, K. Munnemann, B. Blumich and S. Appelt, *J. Magn. Reson.*, 2004, **167**, 298.
329. C. H. Tseng, R. W. Mair, G. P. Wong, D. Williamson, D. G. Cory and R. L. Walsworth, *Phys. Rev. E*, 1999, **59**, 1785.
330. Y. Q. Song, R. E. Taylor and A. Pines, *Solid State Nucl. Magn. Reson.*, 1998, **10**, 247.
331. L. G. Kaiser, T. Meersmann, J. W. Logan and A. Pines, *Proc. Natl. Acad. Sci. USA*, 2000, **97**, 2414.
332. I. L. Moudrakovski, S. Lang, C. I. Ratcliffe, B. Simard, G. Santyr and J. A. Ripmeester, *J. Magn. Reson.*, 2000, **144**, 372.
333. L. G. Kaiser, J. W. Logan, T. Meersmann and A. Pines, *J. Magn. Reson.*, 2001, **149**, 144.

- 334. S. Anala, G. E. Pavlovskaya, P. Pichumani, T. J. Dieken, M. D. Olsen and T. Meersmann, *J. Am. Chem. Soc.*, 2003, **125**, 13298.
- 335. W. J. Shao, G. D. Wang, R. Fuzesy, E. W. Hughes, B. A. Chronik, G. C. Scott, S. M. Conolly and A. Macovski, *Appl. Phys. Lett.*, 2002, **80**, 2032.
- 336. A. R. Cross, M. McDonald, J. P. Robles and G. E. Santyr, *J. Magn. Reson.*, 2003, **162**, 241.
- 337. C. H. Tseng, G. P. Wong, V. R. Pomeroy, R. W. Mair, D. P. Hinton, D. Hoffmann, R. E. Stoner, F. W. Hersman, D. G. Cory and R. L. Walsworth, *Phys. Rev. Lett.*, 1998, **81**, 3785.
- 338. A. K. Venkatesh, A. X. Zhang, J. Mansour, L. Kubatina, C. H. Oh, G. Blasche, M. S. Unlu, D. Balamore, F. A. Jolesz, B. B. Goldberg and M. S. Albert, *Magn. Reson. Imaging*, 2003, **21**, 773.
- 339. C. A. Meriles, D. Sakellariou, A. Moule, M. Goldman, T. F. Budinger and A. Pines, *J. Magn. Reson.*, 2004, **169**, 13.
- 340. S. Saxena, A. Wong-Foy, A. J. Moule, J. A. Seeley, R. McDermott, J. Clarke and A. Pines, *J. Am. Chem. Soc.*, 2001, **123**, 8133.
- 341. A. Wong-Foy, S. Saxena, A. J. Moule, H. M. L. Bitter, J. A. Seeley, R. McDermott, J. Clarke and A. Pines, *J. Magn. Reson.*, 2002, **157**, 235.
- 342. J. J. Heckman, M. P. Ledbetter and M. V. Romalis, *Phys. Rev. Lett.*, 2003, **91**, Art. No. 067601.
- 343. A. J. Moule, M. M. Spence, S. I. Han, J. A. Seeley, K. L. Pierce, S. Saxena and A. Pines, *Proc. Natl. Acad. Sci. USA*, 2003, **100**, 9122.
- 344. V. V. Yashchuk, J. Granwehr, D. F. Kimball, S. M. Rochester, A. H. Trabesinger, J. T. Urban and D. Budker, *A. Pines, Phys. Rev. Lett.*, 2004, **93**, Art. No. 160801.
- 345. A. S. Verhulst, O. Liivak, M. H. Sherwood, H. M. Vieth and I. L. Chuang, *Appl. Phys. Lett.*, 2001, **79**, 2480.

Index

Note: Italicized page numbers denote entries taken from figures or tables.

- ab initio* methods 224, 225
- accidental overlaps, ^{13}C NMR signals 111, 112–13
- acid–alkaline transition
 - ferric myoglobin 79–83
- acid blue membrane 132, 133, 135
- active spins 24, 25
- acyclic alkenylxenon(II) 212
- alternative detection methods, HP xenon 257–9
- amino-acid specific ^{13}C enrichment, NMR signal 105–8
 - TS and M9 media 106
- amyloidogenic protein 197
- anapolar term 226
- apomyoglobin
 - conformational order 195
- archaeal rhodopsins 158–9
- Arg 140, 149, 151
- aromatic side-chains, two-site jump motions 119–21
- Asn, side chain amide protons 189
- b*-type haemoproteins, NMR studies
 - ^{19}F labeling, reconstitution 53–6
 - haem orientation 74–7
 - ring-fluorinated haem 51
- bacteriorhodopsin (bR), interfacial domains
 - blue membrane 132–4
 - mutants, 2D lattice formation 153–5
 - surface dynamics 125–32
 - surface structure 134–42
- basic pancreatic trypsin inhibitor (BPTI) 178, 192, 193, 194
- bioanalytical HP xenon
 - protein-ligand binding 248–50
 - protein studies 247–8
- blue membrane 132–4
 - acid 132, 133
 - deionized 132, 133, 134, 135
- borosilicate glass 181, 183, 184
- Burst pulse sequence
 - diffusion measurement 251
- [1,2,3- ^{13}C]Ala-labeled bR 112, 116, 124, 137, 138, 143, 144, 150, 153, 154, 155
- [3- ^{13}C]Ala-labeled bO 141, 153
- [3- ^{13}C]Ala-labeled D85N 115, 141
- [3- ^{13}C]Ala-labeled proteins, ^{13}C NMR spectra 102, 108, 111, 113, 153, 155
 - DD-MAS and CP-MAS techniques, comparison 104, 108–9, 132–3, 135, 141–2, 154, 156, 161, 163, 166, 167, 168
- [1- ^{13}C]glucose/[2- ^{13}C]glycerol
 - of NMR signal enrichment 104–5
- [1- ^{13}C]Gly-labeled bR 117 118, 130
- [1- ^{13}C]Phe-labeled bR 128
- [1- ^{13}C]Pro-bR 114, 122
- [1- ^{13}C]Pro-labeled wild type bR 122, 123
- [1- ^{13}C]Trp labeled bR 119, 121, 128
- [1- ^{13}C]Val-labeled bR 104, 112, 113–14, 153, 155, 157
- [1- ^{13}C]Val-labeled protein, ^{13}C NMR spectra 119, 121, 140–1, 142, 146, 153, 155, 157, 160, 167
 - DD-MAS and CP-MAS techniques, comparison 104, 115, 130, 133–4, 150
- ^{13}C NMR peaks of membrane proteins, site-directed assignment
 - conformation-dependent ^{13}C chemical shifts, membrane proteins 123–5
 - conformation-dependent ^{13}C chemical shifts, solids 109–11
 - regio-specific assignment 108–9
 - site-directed mutagenesis 111–16
 - spectral editing, Mn^{2+} -induced spectral broadening 116–23
- cage molecules, xenon interaction 210–11
- chemical shift and pressure 187, 188
 - models 185–6

- chemical shift anisotropy (CSA) 5–6
 - xenon 236
- chemical shifts, $\delta^{29}\text{Si}$
 - calculated and experimental values 11–12
 - general 9–10
 - isotope-induced 19–23
 - patterns 10–19
- chirality measurement
 - xenon NMR 226–7
- chiralization 227
- cis*- and *trans*-conformation 190
- cognate transducer, phoborhodopsin 158–65
 - pHtrII* 162–4
- combustion, HP xenon studies 254, 256
- conformation-dependent ^{13}C chemical shifts
 - in membrane proteins 123–5
 - in solid 109–11
- conventional xenon NMR studies 207
 - bulk xenon 207–9
 - compounds 211–12
 - parameters calculations 225–7
 - probe of materials 212–23
 - in solution 209–11
 - xenon 131 studies 223–5
- coupling constants $^nJ(^{29}\text{Si}, \text{X})$ 24
 - general 24–5
 - indirect nuclear spin–spin coupling 24
 - $^1J(^{29}\text{Si}, \text{X})$ 25
 - $^2J(^{29}\text{Si}, \text{X})$ and $^3J(^{29}\text{Si}, \text{X})$ 36–9
 - long-range $^nJ(^{29}\text{Si}, \text{X})$ 39
 - nuclei, types 24
- cross-linking density 221
- cross polarization (CP) 5, 112, 129, 163, 239, 240–1, 242
 - dynamics 241
- cryptophan-A cages 210, 226, 248, 250
- cyclic structures, ^{29}Si 18–19
- 2D EXSY spectrum 217
 - of HP xenon 234–5, 235, 254, 256
- D85N mutant 147, 148–9
 - [3- ^{13}C]Ala-labeled 115, 126, 141
 - D85N/D96N mutant 144–5
 - D85N/V49A mutant 147
- DD-MAS NMR technique 104
- deionized blue membrane 132, 133, 134, 135
- deoxy Mbs 74
 - ^{19}F NMR spectra 64, 72
 - ^1H NMR spectra 61, 64, 77
- DEPT pulse sequences 3–4
 - indirect nuclear 24
- 3,7-DF 54, 60, 67–8, 84, 86–7, 88
- 3,7-DFP 58
- diacylglycerol kinase (DGK) 165–7, 176, 170
 - from *E. coli* 165
 - topology 165, 166
- dihexanoylphosphatidylcholine (DHPC)
 - bilayer 191
- dihydrofolate reductase (DHFR) 195
- dimyristoylphosphatidylcholine (DMPC)
 - bilayer 153, 155, 156, 191
- dipalmytoylphosphatidylcholine (DPPC)
 - bilayer 156, 167
- dipolar and chemical shift (DIP-SHIFT)
 - correlation technique 130–1
- dipolar interactions
 - xenon relaxation time 209
- dipole–dipole interactions 5, 7, 88, 116
- disulphide-deficient lysozyme variant (0SS) 197
- egg phosphatidylcholine (egg PC) 155, 156, 160, 162, 163
- elastomeric terpolymer ethylene-propylene-diene (EPDM) 221
- electron-deficient hydrogen bridges 18, 20, 23, 29
- Escherichia coli*, membrane proteins 157–67
 - cognate transducer 162–4
 - diacylglycerol kinase (DGK) 165–7
 - phoborhodopsin 158–61
 - signal transduction 164–5
- experimental techniques, ^{29}Si NMR
 - spectra measurement
 - referencing 3
 - ^{29}Si resonance observation 3–5
- ^{19}F labeling 52, 61, 63
 - of *b*-type haemoproteins 53–6
 - effect on porphyrin electronic structure 56–8
 - reconstitution technique 53–5
- ^{19}F NMR spectra 56, 72, 83
 - of deoxy Mbs 66, 72, 74, 77, 87
 - of Mb(2-MF) 63, 78–9
 - of Mb(7-PF) 63, 77–9
 - of MbCO 64, 67–8, 68, 84–5, 86
 - MbO2 64, 84–5, 86

- of met-aquo Mbs 66, 74
- of met-cyano Mbs 66, 69–70, 74, 87
- ^{19}F relaxation mechanism 87–92
 - nuclear relaxation 87
- Fermi contact (FC) term 24, 31–2, 34
- ferric myoglobin
 - acid–alkaline transition 79–83
- fixed frequency 3
- FLASH imaging methods 252–3
- flexible interfacial domains of bR, distinction
 - ^{13}C – ^1H dipolar coupling 130
 - cross-polarization 129
 - order parameters 131–2
 - relaxation parameters 129–32
- flow imaging 253–4
- fluorinated haems, myoglobins
 - ^{19}F NMR spectral properties 63–6
 - ^{19}F NMR studies 66
- frequency-switched Lee Goldburg (FSLG)
 - decoupling scheme 131
- G-protein-coupled receptors (GPCRs) 108
- gas diffusion 250
- gas-phase HP xenon T_1 measurements 231–2
- gas-phase relaxation, xenon 207–8, 232
- geminal coupling constants 37
 - $^2J(^{29}\text{Si}, \text{X})$ 36
 - see also* two- and three-bond coupling constants
- Gln 189
- global conformational changes,
 - protein backbone 143–4, 145–6
- Glu, side chain 185
 - amide protons 189
- Glu residue 141, 185
- Gly residue 117, 129
- ^1H NMR spectra 56, 58–9, 74
 - of deoxy Mbs 61, 77
 - of met-aquo Mbs 62
 - of met-cyano Mbs 61
 - of reconstituted protein 56
- haem 53, 54
- haem bis-cyano complexes
 - NMR spectral comparison 58–61
- haem electronic structure 66–74
 - deoxy myoglobin 77–9
 - haem–protein interaction effects, difficulties 67–8, 75
 - protein-induced rhombic perturbation 66–7, 72
- haem methyl proton shift patterns
 - axial His imidazole plane orientation 67, 68, 71–2
- haem orientation 74–7
 - normal form 74–5, 82
 - reconstituted Mbs 75, 86
 - reversed form 75, 82
- haemoprotein 53
- Halobacteria* 155, 160
 - acyl chain of phospholipids 156
- Halobacterium salinarum* 158–9
- HEED-DEPT technique 20
- HEED-INEPT technique 8, 20, 23, 32
- hen egg white lysozyme (HEWL) 194, 211, 247
- hexafluoroisopropanol (HFIP) solution 111, 124, 162
- high-hydrostatic pressure 178, 179–80, 195, 196, 200
- high-pressure NMR spectroscopy
 - in proteins 177
- highly spin-polarized xenons
 - liquid state 232–3
 - solid state 233–4
 - supercritical 234
- His, side chains 185
- His F8 53, 55
- His-Fe bonding 61, 72
- His imidazole 67, 68, 78, 80, 87
- His residue 53, 54, 55, 185
- hyperpolarized (HP) xenon
 - bioanalytical 247–50
 - bulk measurements 231–4
 - diffusion studies 250–2
 - imaging, of materials 252–4
 - in materials and on surfaces 234–9
 - in medicine 243–7
 - new and exotic applications 254–60
 - optical pumping methods 227–31
 - transfer methods 239–43
- Ile FG5 δ -CH₃ proton 61, 75
- Ile-labeled bR 128
- INEPT pulse sequence 4, 20, 21, 23, 24, 33

- information transfer
 - among residues 148–52
- isotope enrichment
 - [1-¹³C]glucose/[2-¹³C]glycerol 104–5
 - site-directed ¹³C enrichment 105–8
 - uniform/extensive 103–4
 - see also* amino-acid specific ¹³C enrichment
- isotope-induced ²⁹Si chemical shifts 19–23, 38
- kinked structure 142–3
 - Pro residues, PM 143
 - spectral change 143
- Leu residue
 - N- or C-terminal moieties 118
- linear tetrapeptides 185–90
- lipid bilayer, bR structure 155–7
- lipoxygenase 247
- liquid xenon
 - highly spin-polarized 233–4
 - long-range ⁿJ(²⁹Si,X) 39–40
 - low field HP xenon studies 254–6
 - lung imaging 243–5
- M-like state 143–8
 - Schiff base 144, 144–5
- magic angle spinning 103, 105, 125, 128
- materials, HP xenon studies 236–8
 - HP xenon diffusion 250–2
 - HP xenon imaging 252–4
 - mesoporous materials 234–6
 - very low surface area 238–9
 - zeolites 234–6
- Mb(2-MF), ¹⁹F NMR spectra 63, 68
- Mb(3,7-DF), ¹⁹F NMR spectra 63, 67
- Mb(7-PF), ¹⁹F NMR spectra 63, 66
- MbCO 53, 69–70, 87
 - ¹⁹F NMR spectra 67, 68, 77, 84–5, 86, 87–8
 - ¹H NMR spectra 61
 - haem methyl proton signals 77
- MbO₂, ¹⁹F NMR spectra 53, 64, 84–5, 86–7
- medicine, HP xenon application
 - lung imaging 243–5
 - xenon injection 245–6
 - xenon's interaction with tissues 246–7
- membrane-binding protein 167–70
- membrane proteins, site-directed solid-state NMR 99
 - bR interfacial domains, backbone dynamics and structures 125
 - ¹³C NMR peaks, assignment 108
 - E. coli* 157–67
 - isotope enrichment 103–8
 - membrane-binding protein 167–70
 - monomers, backbone structures and dynamics 153–6
 - transmembrane α -helices, backbone dynamics 142
- mesohaem 54, 59
 - relative to His F8 76
- mesoporous materials
 - xenon NMR 218–19
 - xenon studies 234–6
- mesoporous silica materials
 - porosity 220
- mesoporphyrin 54, 56, 57–8
- met-aquo Mbs ¹⁹F NMR spectra 66, 74, 87–8, 92
- met-cyano Mbs 61, 64, 66, 69–70, 71, 72, 73, 74, 90
- metMb
 - acid-alkaline transition 79–83
 - ferrihaem 80–1, 82
- 2-MF 54, 59, 60–1, 76
- 2-MFP 57–8
- Mn²⁺ ion
 - spectral broadening 116–23
- monomers, backbone structures and dynamics
 - bR mutants, 2D lattice formation 153–5
 - lipid bilayer, bR structure 155–7
- Monte Carlo methods
 - grand canonical Monte Carlo (GCMC) simulation 225
- MRI techniques 230, 252
- myoglobin (Mb) 53
- myoglobins, reconstituted with fluorinated haems
 - ¹⁹F NMR spectral properties 63–6
 - ¹⁹F NMR studies 66
 - fluorinated haems 66
 - properties 61–3

- Natronobacterium pharonis*
 ppR 159
 neutral lipid bilayers
 egg PC 155
 DMPC 155
 DPPC 155
 NMR characterization, difficulties 84
 NMR properties
 of quadrupole nuclei 2
 of spin-1/2 nuclei 2
 NOESY 191, 198
 non-contact terms 24–5
 non-magnetic metal autoclaves 180, 181–2
 nuclear overhauser effect (NOE) 211
 nuclear spin relaxation, ^{29}Si
 mechanisms 5–9
 scalar relaxation 6–8
 one-bond couplings, $^1J(^{29}\text{Si}, \text{X})$
 calculated and experimental values 26–8
 $^1J(\text{M}, ^{29}\text{Si})$ 35–6
 $^1J(^{31}\text{P}, ^{29}\text{Si})$ 33, 34
 $^1J(^{207}\text{Pb}, ^{29}\text{Si})$ 30–1, 32
 $^1J(^{29}\text{Si}, ^{11}\text{B})$ 29
 $^1J(^{29}\text{Si}, ^9\text{Be})$ 29, 30
 $^1J(^{29}\text{Si}, ^{13}\text{C})$ 29–30
 $^1J(^{29}\text{Si}, ^{19}\text{F})$ 34–5
 $^1J(^{29}\text{Si}, ^1\text{H})$ 25, 29
 $^1J(^{29}\text{Si}, ^{15}\text{N})$ 31–4
 $^1J(^{29}\text{Si}, ^{29}\text{Si})$ 30–1, 31
 $^1J(^{77}\text{Se}, ^{29}\text{Si})$ 34
 $^1J(^{119}\text{Sn}, ^{29}\text{Si})$ 30–1, 31
 $^1J(^{125}\text{Te}, ^{29}\text{Si})$ 34
 optical pumping methods 227–31
 polarization methods 228–30
 new/alternative methods 230–1
 oxy and carbonmonoxy myoglobins 83–7
 π spin delocalization
 ^{19}F signals, Mb(7-PF) 77–9, 85–6
 haem methyl proton signals, Mb(7-PF) 77
 passive spin 24
 perfluorocarbon emulsion 246
 7-PF 54, 60, 66, 78
 7-PFP 58
 pH dependence
 of met Mb(7-PF), ^{19}F NMR spectrum 80
pharaonis phoborhodopsin (ppR) 157–8
 Phe-labeled bR 119
 phoborhodopsin 158–61, 162–4
 cognate transducer 160, 162–4
 phospholipase C- $\delta 1$ (PLC- $\delta 1$)
 pleckstrin homology (PH) domain
 167–70
 phospholipids bicelles
 decay pressure 191
 DMPC, DHPC 190–1
 pleckstrin homology (PH) domain 167–70
 polarization transfer methods, HP xenon
 to material surfaces 239–41
 in xenon solutions 241–3
 polymers, xenon 221–2
 porous materials, silica 219–21
 porous Vycor surfaces
 with HP xenon 237
 porphyrin electronic structure
 ^{19}F labeling effect 56–8
 porphyrins, iron-free 54
 pressure effects
 on protein structures 198–9
 pressure-jump studies 197
 pressure stability
 functional important conformers 191–8
 phospholipid bicelles 190–1
 prion protein 180, 196, 197, 198
 proline effect 115
 proline (Pro) residue 121–2, 147, 190
 protein-ligand binding 248–50
 proteins, high-pressure NMR spectroscopy
 177–8, 180–2
 application on 182
 linear tetrapeptides 185–90
 methods 180
 phospholipids bicelles, pressure-stability
 190–1
 protein function, pressure-stability
 191–8
 protein structures 198–200
 responses 178
 volume change, depending interaction
 178–9
 proteins, HP xenon studies 247–8
 proteins, xenon interactions 211
 protohaem 53, 54, 59
 proton decoupling 103, 126, 127, 130, 164
 protoporphyrin 54, 57, 58
 purple membrane, bacteriorhodopsin 114,
 125–42

- quantum computing, HP xenon 259–60
quartz 181
- R82Q mutant 150–1
Rb–Xe spin-exchange rate 227
regio-specific assignment
 ^{13}C NMR peaks 108–9
residual dipolar couplings (RDCs)
 measurement 190–1
ring-fluorinated haem 51
- S. carnosus* *see Staphylococcus carnosus*
sapphire-cell system 181–2
 O-ring gasket 183
scalar coupling
 ^{29}Si – ^1H 4
 ^{29}Si –X 36
scalar relaxation 5, 6, 8
Schiff base (SB) 141, 144, 146, 149
shaPrP(90–231) 180, 197
SHIFTY 123
 ^{29}Si chemical shifts ($\delta^{29}\text{Si}$), patterns 10–19
 base-free silylenes-metal complexes 10, 13
 coordination number change 16, 17
 cyclic structures, effects 18–19
 extreme values, divalent silicon 10
 monomeric silylenes 12
 non-cyclic derivatives 15, 18
 organosilicon compounds 3, 16
 relative to $\delta^{29}\text{Si}$ (SiMe_4) 9, 10, 12
 Si–H bonds, activation 17–18
 silacyclopentadiene derivative 18–19
 7-silanorbornadiene derivative 18, 21
 silicon and electronic structure, coordina-
 tion number 10–17
 silicon-element multiple bonds 14, 15
 silyl cations 10, 13
 silylene adducts 10, 13
 ^{29}Si NMR parameters
 applications 1
 chemical shifts, $\delta^{29}\text{Si}$ 9
experimental techniques 3–5
 indirect nuclear spin–spin coupling con-
 stants $^nJ(^{29}\text{Si}, \text{X})$ 24
 nuclear spin relaxation 5–9
signal transduction
 TM2 motion, decoupling 164
signaling cascade 159
7-silanorbornadienes 18, 21
silicon and electronic structure
 coordination number 10–17
 N-silylaminophosphanes 38, 39
 single-file diffusion 220, 250–1
 site-directed ^{13}C enrichment *see* amino-acid
 specific ^{13}C enrichment
 site-directed suppression, ^{13}C NMR signals
 125–9
 ^{13}C NMR signals, relative contribution
 127, 128
 conformational fluctuation motions 126,
 128
 residues, predicted proportion
 127–8
 transverse relaxation rate 125, 126
solid-state materials, xenon 222–3
solid-state ^{29}Si NMR spectra 3, 4–5, 8–9, 10,
 35
solid xenon, highly spin-polarized 233–4
Solomon–Bloembergen equation 91, 117
solution, xenon diffusion 251
spectral editing
 Mn^{2+} -ion-induced spectral broadenings
 116–23
 Solomon–Bloembergen equation 117
spin–lattice relaxation time 5, 108–9, 119,
 122, 126, 130
spin–rotation (SR) mechanism 5, 7, 207, 208
spin–spin coupling 5, 19
 ^{31}P – ^{29}Si 9
 ^{29}Si – ^1H 4
 ^{29}Si –X 38
“Spin-Spy” methodology 209
SPINOE 209, 238–9, 240, 241, 242, 247, 249
SPIROE 247, 248
Staphylococcus carnosus 189, 211
static imaging 252–3
sulfoglycolipid 153
superconducting quantum interference de-
 vice (SQUID) 232, 257–9
supercritical xenon, highly spin-polarized
 234
surface dynamics, bacteriorhodopsin
 flexible interfacial domains, distinction
 129–32
 site-directed suppression, ^{13}C NMR sig-
 nals 125–9
surface structure, membrane proteins 134–42
 probe technique 134–5

- TALOS 123
 tetrapeptides Gly–Gly–X–Ala 185, 186, 187, 188, 190
 thermal mixing, low field 242
Thermotoga maritima 182, 184
 Thr 150
 torsion angles 123, 124, 193
 transmembrane α -helices, backbone dynamics
 kinked structure 142–3
 long-distance interaction, among residues 148–52
 M-like state 143–8
 transthyretin (TTR) 179, 197
 trifluorovinylxenon(II)synthesis 212
 trimeric structure, bR mutant 153
 Trp-labeled bR 128
 Trp residues 121, 145, 153
 two- and three-bond coupling constants, $^2J(^{29}\text{Si}, \text{X})$ and $^3J(^{29}\text{Si}, \text{X})$
 $^2J(^{31}\text{P}, ^{29}\text{Si})$ 38–9
 $^2J(^{207}\text{Pb}, ^{29}\text{Si})$ 37
 $^2J(^{29}\text{Si}, ^{15}\text{N})$ 38–9
 $^{2,3}J(^{29}\text{Si}, ^{13}\text{C})$ 37
 $^{2,3}J(^{29}\text{Si}, ^{19}\text{F})$ 36
 $^{2,3}J(^{29}\text{Si}, ^1\text{H})$ 36
 $^{2,3}J(^{29}\text{Si}, ^{29}\text{Si})$ 37
 $^{2,3}J(^{119}\text{Sn}, ^{29}\text{Si})$ 37
 uniform/extensive isotope enrichment, NMR signal
 ^{13}C -labeled proteins, spectral resolution 103–4
 Val E11 γ -CH3 proton 61
 vicinal coupling constants
 $^3J(^{29}\text{Si}, \text{X})$ 36
 see also two- and three-bond coupling constants
 ^{129}Xe spectra, of xenon 238, 246, 252
 xenon diffusion 217, 250, 251
 xenon magnetization, evolution 232, 259
 xenon NMR spectroscopy 205
 conventional studies 207
 hyperpolarized xenon 227
 xenon relaxation, mechanism 209, 233
 xenon sorption 221, 223
 Yamada glass cell method 178, 180–2
 zeolites, xenon NMR 215–18
 guests 218

This page intentionally left blank